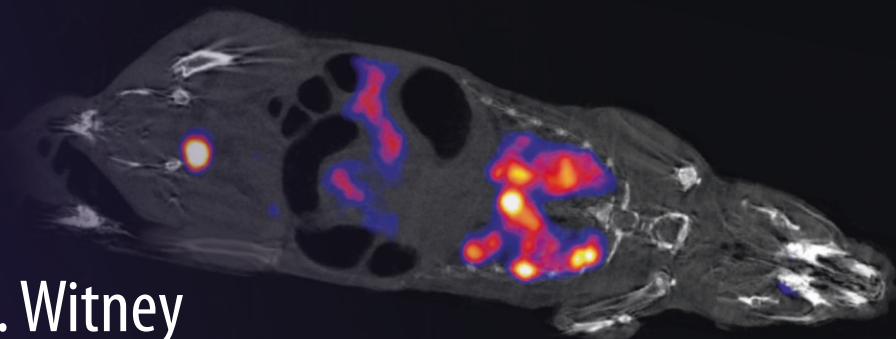Springer Protocols

Timothy H. Witney
Adam J. Shuhendler *Editors*

Positron Emission Tomography

Methods and Protocols

Humana Press

METHODS IN MOLECULAR BIOLOGY

For further volumes:
http://www.springer.com/series/7651

For over 35 years, biological scientists have come to rely on the research protocols and methodologies in the critically acclaimed *Methods in Molecular Biology* series. The series was the first to introduce the step-by-step protocols approach that has become the standard in all biomedical protocol publishing. Each protocol is provided in readily-reproducible step-by-step fashion, opening with an introductory overview, a list of the materials and reagents needed to complete the experiment, and followed by a detailed procedure that is supported with a helpful notes section offering tips and tricks of the trade as well as troubleshooting advice. These hallmark features were introduced by series editor Dr. John Walker and constitute the key ingredient in each and every volume of the *Methods in Molecular Biology* series. Tested and trusted, comprehensive and reliable, all protocols from the series are indexed in PubMed.

Positron Emission Tomography

Methods and Protocols

Edited by

Timothy H. Witney

School of Biomedical Engineering and Imaging Sciences, King's College London, London, UK

Adam J. Shuhendler

Department of Chemistry and Biomolecular Sciences, University of Ottawa, Ottawa, ON, Canada

Editors
Timothy H. Witney
School of Biomedical Engineering
and Imaging Sciences
King's College London
London, UK

Adam J. Shuhendler
Department of Chemistry and Biomolecular Sciences
University of Ottawa
Ottawa, ON, Canada

Paper in this product is recyclable.

Dedication

In memory of Sanjiv Sam Gambhir and Bin Shen

What remains after people are gone are the lessons learned from their words and actions, which ruminate and distill in our minds, populating the standard operating procedures for our lives. Sam and Bin taught us many different things in very different ways, and after reflection, these are the SOPs they inspired:

Never say no; say how

Never quench a dream; dream big

Never miss a chance to smile; share this with everyone around you

Never overvalue your own time; share of yourself

Never weigh others down; raise them up and take pride in their heights

Never go it alone; build community to foster strength

Never forget why we are here; be the conduit for change

Never forget where you began; wayfind for others along the same path

Never underestimate your impact; a key moment, a few true and kind words, and a pat on the shoulder can inspire for a lifetime

The lives you have touched are innumerable, your legacy immeasurable, and your kindness infinite. In our work and in our hearts, you are far from gone.

Preface

Medical imaging has revolutionized the way we diagnose and treat disease. In many cases, invasive surgical procedures prevalent at the beginning of the last century have been replaced by anatomical scans, such as magnetic resonance imaging and computed tomography, that reveal whole-body anatomy in fine detail. Positron emission tomography (PET) enables an even deeper look into health and disease by illuminating functional and molecular changes in the body. The ability to probe living subjects with molecular precision is not only continuing to change the way we can study and diagnose disease, but it is also opening up new frontiers in precision medicine, predicting therapy response, and the creation of theranostic agents with diagnostic and therapeutic duality. This volume of the Methods in Molecular Biology series will explore the key concepts and experimental design related to PET imaging that have revolutionized our understanding of human biology. The first part focuses on recent advances in radiotracer probe development to enable the detection of large macromolecules to complicated drug-like structures. The next section describes how key physiological and pathophysiological processes can be interrogated and quantifiably measured with this imaging technique. Finally, we will describe important technological developments in the field which are revolutionizing the way these innovative PET probes are utilized in the clinic.

London, UK   *Timothy H. Witney*
Ottawa, ON, Canada   *Adam J. Shuhendler*

Contents

Part III   PET Technology

Contributors

ARTURO ALIAGA • *Translational Neuroimaging Laboratory, Research Centre for Studies in Aging, Douglas Research Institute, McGill University, Montreal, QC, Canada; McConnell Brain Imaging Centre, Montreal Neurological Institute-Hospital (The Neuro), McGill University, Montreal, QC, Canada*

ALEJANDRO ARROYO • *Department of Radiology, Memorial Sloan Kettering Cancer Center, New York, NY, USA*

FRIEDRICH BAARK • *School of Biomedical Engineering and Imaging Sciences, King's College London, St Thomas' Hospital, London, UK*

RAMSEY D. BADAWI • *Department of Radiology, University of California-Davis, Sacramento, CA, USA; Department of Biomedical Engineering, University of California-Davis, Davis, CA, USA*

JUSTIN J. BAILEY • *Department of Oncology, Division of Oncological Imaging, University of Alberta, Edmonton, AB, Canada*

VIKTORIA BALOGH • *Queen's Medical Research Institute, Edinburgh, UK*

PETER BARTENSTEIN • *Department of Nuclear Medicine, University Hospital, LMU Munich, Munich, Germany*

HUSSEIN BDAIR • *Department of Neurology and Neurosurgery, McGill University, Montreal, QC, Canada; Department of Psychiatry, McGill University, Montreal, QC, Canada; McConnell Brain Imaging Centre, Montreal Neurological Institute-Hospital (The Neuro), McGill University, Montreal, QC, Canada*

LEONIE BEYER • *Department of Nuclear Medicine, University Hospital, LMU Munich, Munich, Germany*

STEPHAN BLINDER • *McConnell Brain Imaging Centre, Montreal Neurological Institute-Hospital (The Neuro), McGill University, Montreal, QC, Canada; PERFORM Centre, Concordia University, Montreal, QC, Canada*

MILOU BOSWINKEL • *Department of Medical Imaging, Nuclear Medicine, Radboud University Medical Center, Nijmegen, The Netherlands*

KIMBERLY D. BREWER • *School of Biomedical Engineering, Dalhousie University, Halifax, NS, Canada; Department of Physics and Atmospheric Science, Dalhousie University, Halifax, Canada; Diagnostic Radiology, Dalhousie University, Halifax, Canada*

KEVIN M. BRINDLE • *Cancer Research UK Cambridge Institute, University of Cambridge, Cambridge, UK*

ALLEN F. BROOKS • *Department of Radiology, University of Michigan, Ann Arbor, MI, USA*

FLAVIU BULAT • *Cancer Research UK Cambridge Institute, University of Cambridge, Cambridge, UK*

CHRISTOPHER J. CAWTHORNE • *Nuclear Medicine and Molecular Imaging, Department of Imaging and Pathology, Katholieke Universiteit Leuven, Leuven, Belgium*

ZHEN CHENG • *State Key Laboratory of Drug Research, Molecular Imaging Center, Shanghai Institute of Materia Medica, Chinese Academy of Sciences, Shanghai, China; Shandong Laboratory of Yantai Drug Discovery, Bohai Rim Advanced Research Institute for Drug Discovery, Yantai, Shandong, China*

SIMON R. CHERRY • *Department of Radiology, University of California-Davis, Sacramento, CA, USA; Department of Biomedical Engineering, University of California-Davis, Davis, CA, USA*

TAEMOON CHUNG • *Cold Spring Harbor Laboratory, Cold Spring Harbor, NY, USA*

CHIARA DA PIEVE • *Preclinical Molecular Imaging, Division of Radiotherapy and Imaging, The Institute of Cancer Research, London, UK*

DREW R. DEBAY • *Biomedical Translational Imaging Centre (BIOTIC), Halifax, Canada; Department of Physics and Atmospheric Science, Dalhousie University, Halifax, Canada*

RICHARD K. G. DO • *Department of Radiology, Memorial Sloan Kettering Cancer Center, New York, NY, USA*

THOMAS R. EYKYN • *School of Biomedical Engineering and Imaging Sciences, King's College London, St Thomas' Hospital, London, UK*

GERBEN M. FRANSSEN • *Department of Medical Imaging, Nuclear Medicine, Radboud University Medical Center, Nijmegen, The Netherlands*

JENS FRIGELL • *GE Healthcare, GEMS PET Systems, Uppsala, Sweden*

GILBERT O. FRUHWIRTH • *Imaging Therapies and Cancer Group, Comprehensive Cancer Centre, School of Cancer and Pharmaceutical Sciences, King's College London, London, UK*

KATHERINE GAGNON • *GE Healthcare, GEMS PET Systems, Uppsala, Sweden*

ARMANDO GARCIA • *Azrieli Centre for Neuro-Radiochemistry, Brain Health Imaging Centre, Centre for Addiction and Mental Health, Toronto, ON, Canada*

MITHAT GONEN • *Department of Epidemiology & Biostatistics, Memorial Sloan Kettering Cancer Center, New York, NY, USA*

ANDREA GONZALEZ-MONTORO • *Department of Radiology, Stanford University, Stanford, CA, USA*

LEXI GOWER-FRY • *Department of Oncology, Division of Oncological Imaging, University of Alberta, Edmonton, AB, Canada*

BEN GRIMSDELL • *Imaging Therapies and Cancer Group, Comprehensive Cancer Centre, School of Cancer and Pharmaceutical Sciences, King's College London, London, UK*

SANDRA HESKAMP • *Department of Medical Imaging, Nuclear Medicine, Radboud University Medical Center, Nijmegen, The Netherlands*

HEATHER HUNT • *Department of Radiology, University of California-Davis, Sacramento, CA, USA*

TERRY JONES • *Department of Radiology, University of California-Davis, Sacramento, CA, USA*

KYUNG OH. JUNG • *Department of Radiation Oncology, Stanford University, Stanford, CA, USA; Department of Anatomy, Chung-Ang University, Seoul, South Korea*

KLAUS JURKSCHAT • *Fakultät für Chemie und Chemische Biologie, Technische Universität Dortmund, Dortmund, Germany*

MIN SU KANG • *Translational Neuroimaging Laboratory, Research Centre for Studies in Aging, Douglas Research Institute, McGill University, Montreal, QC, Canada; LC Campbell Cognitive Neurology Unit, Hurvitz Brain Sciences Program, Sunnybrook Research Institute, University of Toronto, Toronto, ON, Canada*

ALEXIA KIRBY • *Department of Biology, University of Ottawa, Ottawa, ON, Canada; University of Ottawa Heart Institute, Ottawa, ON, Canada*

AGNE KNYZELIENE • *Queen's Medical Research Institute, Edinburgh, UK*

ALEXEY KOSTIKOV • *Department of Neurology and Neurosurgery, McGill University, Montreal, QC, Canada; Translational Neuroimaging Laboratory, Research Centre for Studies in Aging, Douglas Research Institute, McGill University, Montreal, QC, Canada; McConnell Brain Imaging Centre, Montreal Neurological Institute-Hospital (The Neuro), McGill University, Montreal, QC, Canada; Department of Chemistry, McGill University, Montreal, QC, Canada*

GABRIELA KRAMER-MAREK • *Preclinical Molecular Imaging, Division of Radiotherapy and Imaging, The Institute of Cancer Research, London, UK*

PETER KUNACH • *Department of Neurology and Neurosurgery, McGill University, Montreal, QC, Canada; Translational Neuroimaging Laboratory, Research Centre for Studies in Aging, Douglas Research Institute, McGill University, Montreal, QC, Canada*

CRAIG S. LEVIN • *Department of Radiology, Stanford University, Stanford, CA, USA; Departments of Radiology, Bioengineering, Physics, and Electrical Engineering, Stanford University, Stanford, CA, USA*

DAVID Y. LEWIS • *Cancer Research UK Scotland Institute, Glasgow, UK; School of Cancer Sciences, University of Glasgow, Glasgow, UK*

JASON S. LEWIS • *Department of Radiology, Memorial Sloan Kettering Cancer Center, New York, NY, USA; Radiochemistry and Imaging Probes Core, Memorial Sloan Kettering Cancer Center, New York, NY, USA; Molecular Pharmacology Program, Memorial Sloan Kettering Cancer Center, New York, NY, USA*

MARCO LEYTON • *Department of Neurology and Neurosurgery, McGill University, Montreal, QC, Canada; Department of Psychiatry, McGill University, Montreal, QC, Canada; McConnell Brain Imaging Centre, Montreal Neurological Institute-Hospital (The Neuro), McGill University, Montreal, QC, Canada; Department of Psychology, McGill University, Montreal, QC, Canada; Center for Studies in Behavioral Neurobiology, Concordia University, Montreal, QC, Canada*

ANTON LINDBERG • *Azrieli Centre for Neuro-Radiochemistry, Brain Health Imaging Centre, Centre for Addiction and Mental Health, Toronto, ON, Canada*

SIMON LINDNER • *Department of Nuclear Medicine, University Hospital, LMU Munich, Munich, Germany*

SERGE K. LYASHCHENKO • *Department of Radiology, Memorial Sloan Kettering Cancer Center, New York, NY, USA; Radiochemistry and Imaging Probes Core, Memorial Sloan Kettering Cancer Center, New York, NY, USA*

SCOTT K. LYONS • *Cold Spring Harbor Laboratory, Cold Spring Harbor, NY, USA*

XIAOWEI MA • *Department of Nuclear Medicine, The Second Xiangya Hospital, Central South University, Changsha, China*

KRISTIN MCBRIDE • *Department of Radiology, University of California-Davis, Sacramento, CA, USA*

JOSEPH R. MERRILL • *Cold Spring Harbor Laboratory, Cold Spring Harbor, NY, USA*

MARIA MORALES • *Department of Chemistry, University of Michigan, Ann Arbor, MI, USA*

EMILY MURRELL • *Azrieli Centre for Neuro-Radiochemistry, Brain Health Imaging Centre, Centre for Addiction and Mental Health, Toronto, ON, Canada*

ANDRÉ A. A. NEVES • *Cancer Research UK Cambridge Institute, University of Cambridge, Cambridge, UK*

JULIE OTTOY • *LC Campbell Cognitive Neurology Unit, Hurvitz Brain Sciences Program, Sunnybrook Research Institute, University of Toronto, Toronto, ON, Canada*

D. CHRISTIAN PARR • *GE Healthcare, GEMS PET Systems, Uppsala, Sweden*

ALEKSANDRA PEKOŠAK • *Department of Radiology and Nuclear Medicine, Radionuclide Center, Amsterdam UMC, Amsterdam, the Netherlands*

ALEX J. POOT • *Department of Radiology and Nuclear Medicine, Radionuclide Center, Amsterdam UMC, Amsterdam, the Netherlands*

GUILLEM PRATX • *Department of Radiation Oncology, Stanford University, Stanford, CA, USA*

SEAN PRESHLOCK • *Department of Radiology, University of Michigan, Ann Arbor, MI, USA*

ERIC PRICE • *Department of Chemistry, College of Arts and Science, University of Saskatchewan, Saskatoon, SK, Canada*

CATERINA RAMOGIDA • *Department of Chemistry, Simon Fraser University, Burnaby, BC, Canada; Life Sciences Division, TRIUMF, Vancouver, BC, Canada*

MELISSA E. RODNICK • *Department of Radiology, University of Michigan, Ann Arbor, MI, USA*

PEDRO ROSA-NETO • *Department of Neurology and Neurosurgery, McGill University, Montreal, QC, Canada; Translational Neuroimaging Laboratory, Research Centre for Studies in Aging, Douglas Research Institute, McGill University, Montreal, QC, Canada; McConnell Brain Imaging Centre, Montreal Neurological Institute-Hospital (The Neuro), McGill University, Montreal, QC, Canada*

ADEEL SALEEM • *Imaging Therapies and Cancer Group, Comprehensive Cancer Centre, School of Cancer and Pharmaceutical Sciences, King's College London, London, UK*

MELANIE S. SANFORD • *Department of Chemistry, University of Michigan, Ann Arbor, MI, USA*

RALF SCHIRRMACHER • *Department of Oncology, Division of Oncological Imaging, University of Alberta, Edmonton, AB, Canada*

PETER J. H. SCOTT • *Department of Radiology, University of Michigan, Ann Arbor, MI, USA*

LIAM S. SHARNINGHAUSEN • *Department of Chemistry, University of Michigan, Ann Arbor, MI, USA*

ROBERT SHAW • *Queen's Medical Research Institute, Edinburgh, UK*

ADAM J. SHUHENDLER • *University of Ottawa Heart Institute, Ottawa, ON, Canada; Department of Chemistry and Biomolecular Sciences, University of Ottawa, Ottawa, ON, Canada*

AMBER L. SIMPSON • *School of Computing and Department of Biomedical and Molecular Sciences, Queen's University, Kingston, ON, Canada*

THOMAS A. SINGLETON • *Department of Neurology and Neurosurgery, McGill University, Montreal, QC, Canada; McConnell Brain Imaging Centre, Montreal Neurological Institute-Hospital (The Neuro), McGill University, Montreal, QC, Canada*

CARINA SOLLERT • *GE Healthcare, GEMS PET Systems, Uppsala, Sweden*

JEAN-PAUL SOUCY • *Department of Neurology and Neurosurgery, McGill University, Montreal, QC, Canada; McConnell Brain Imaging Centre, Montreal Neurological Institute-Hospital (The Neuro), McGill University, Montreal, QC, Canada; PERFORM Centre, Concordia University, Montreal, QC, Canada*

RICHARD SOUTHWORTH • *School of Biomedical Engineering and Imaging Sciences, King's College London, St Thomas' Hospital, London, UK*

BENJAMIN A. SPENCER • *Department of Radiology, University of California-Davis, Sacramento, CA, USA; Department of Biomedical Engineering, University of California-Davis, Davis, CA, USA*

ADRIANA A. S. TAVARES • *Queen's Medical Research Institute, Edinburgh, UK*

OSKAR VILHELMSSON TIMMERMAND • *School of Biomedical Engineering & Imaging Sciences, King's College London, London, UK*

NEIL VASDEV • *Azrieli Centre for Neuro-Radiochemistry, Brain Health Imaging Centre, Centre for Addiction and Mental Health, Toronto, ON, Canada; Institute of Medical Science and Department of Psychiatry, University of Toronto, Toronto, ON, Canada*

ALESSIA VOLPE • *Molecular Imaging Group, Department of Radiology, Memorial Sloan Kettering Cancer Center, New York, NY, USA*

BJÖRN WÄNGLER • *Molecular Imaging and Radiochemistry, Department of Clinical Radiology and Nuclear Medicine, Medical Faculty Mannheim of Heidelberg University, Mannheim, Germany*

CARMEN WÄNGLER • *Biomedical Chemistry, Department of Clinical Radiology and Nuclear Medicine, Medical Faculty Mannheim of Heidelberg University, Mannheim, Germany*

EDWARD C. T. WATERS • *School of Biomedical Engineering and Imaging Sciences, King's College London, St Thomas' Hospital, London, UK*

TRAVIS L. WILLIAMS • *Department of Epidemiology & Biostatistics, Memorial Sloan Kettering Cancer Center, New York, NY, USA*

ALBERT D. WINDHORST • *Department of Radiology and Nuclear Medicine, Radionuclide Center, Amsterdam UMC, Amsterdam, the Netherlands*

TIMOTHY H. WITNEY • *School of Biomedical Engineering & Imaging Sciences, King's College London, London, UK*

RICK WRAY • *Department of Radiology, Memorial Sloan Kettering Cancer Center, New York, NY, USA*

JAY S. WRIGHT • *Department of Radiology, University of Michigan, Ann Arbor, MI, USA*

Part I

Radiochemistry

Chapter 1

^{11}C-Fixation Techniques

Emily Murrell, Anton Lindberg, Armando Garcia, and Neil Vasdev

Abstract

This protocol describes the application of cyclotron-generated $[^{11}C]CO_2$ fixation reactions for direct ^{11}C-carboxylation reactions and $[^{11}C]CO$ for ^{11}C-carbonylations. Herein we describe one-pot methods wherein the radioactive gas is first trapped in a reaction mixture at room temperature and atmospheric pressure prior to the radiolabeling reactions. Such procedures are widely applicable to numerous small molecules to form ^{11}C-labeled carboxylic acids, amides, esters, ketones, oxazolidinones, carbamates, and ureas. The steps for ^{11}C-fixation techniques described herein are tailored for a commercial automated synthesis unit and are readily adapted for routine radiopharmaceutical production.

Key words Carbon-11, Carbon dioxide, Carbon monoxide, Carbonylation, Carboxylation

1 Introduction

Carbon-11 (^{11}C, $t_{1/2} = 20.4$ min) is a widely used radionuclide for the development of positron emission tomography (PET) imaging radiotracers because of its ubiquitous composition in organic compounds and small molecule drugs. ^{11}C-labeling is typically performed through the robust chemistry of *N*-, *O*-, or *S*-^{11}C-methylations, *via* methyl iodide ($[^{11}C]CH_3I$), or methyl triflate ($[^{11}C]CH_3OTf$). While several PET radiopharmaceuticals are produced by ^{11}C-methylation reactions, the synthetic versatility of this chemistry for producing new tracers is limited to drug structures containing accessible methyl functionalities. Conversely, carbonyl groups are more common in small molecule drugs, and it is not surprising that major efforts have been ongoing for developing a wide scope of ^{11}C-fixation reactions to increase the number of labeled drugs accessible from combinatorial libraries by generating ^{11}C $= $O bonds [1].

Syntheses of positron-emitting radiopharmaceuticals are generally conducted remotely to limit exposure to ionizing radiation. Hence, there are several commercially available synthesis units for ^{11}C-chemistry, as well as various units built in-house at

radiochemistry facilities around the world. While the protocol herein describes the use of a specific commercial radiosynthesis unit, the steps and notes are applicable to other available commercial units, as well as those built in-house for carbon-11 radiotracers.

Cyclotron-generated $[^{11}C]CO_2$ is produced *via* the nuclear reaction $^{14}N(p,\alpha)^{11}C$ by proton bombardment of a gas target containing a nitrogen:oxygen mixture (>99% nitrogen). Fixation based on $[^{11}C]CO_2$ has been traditionally restricted to labeling *via* ^{11}C-synthons such as Grignard and organolithium reagents, which have limited functional group tolerance. Recent developments in CO_2-fixation have allowed the use of less sensitive reactions to produce ^{11}C-carboxylated compounds (see [2–4] for extensive reviews). Particularly, the use of organic fixating bases (e.g., DBU or BEMP) have greatly improved the solubility of CO_2 in organic solvents, and it has facilitated direct $[^{11}C]CO_2$ fixation to form ^{11}C-labeled oxazolidinones, carbamates, and ureas [5]. Using this advancement, copper-catalyzed $[^{11}C]CO_2$ fixation into organoboron [6] or organotin [7] precursors have also been shown to produce ^{11}C-carboxylic acids, which can be subsequently transformed into ^{11}C-labeled esters or amides. A representative intramolecular ^{11}C-carboxyaltion is demonstrated below for the radiosynthesis of $[^{11}C]SL25.1188$, a PET radiopharmaceutical used for imaging monoamine oxidase B (MAO-B) [8] (Fig. 1) (*see* **Note 1**).

Historically, labeling with $[^{11}C]CO$ was limited due to its low solubility in organic solvents. Approaches to mitigate this challenge include devices that recirculate the $[^{11}C]CO$, high pressure reactors (mini-autoclave methodology), or utility of heavy carrier gases (e.g., xenon) [9–12]. Trapping of $[^{11}C]CO$ has been demonstrated at low and atmospheric pressures (see [13, 14] for comprehensive reviews of various techniques). Boron-based trapping of $[^{11}C]CO$ was performed using a borane-THF complex that subsequently releases $[^{11}C]CO$ upon heating [15]. Another approach is Cu-based $[^{11}C]CO$ trapping using the Cu(I) scorpionate Cu (Tp*), which can release $[^{11}C]CO$ in the presence of the competing ligand PPh_3 [16]. These trapping approaches are followed by various Pd or Rh-mediated ^{11}C-carbonylation reactions to form ^{11}C-amides, ureas, ketones, carboxylic acids, esters, carbamate esters, acid chlorides, and aldehydes, among other carbonyl-containing functional groups [14]. More recently, the use of Pd (II)-ligand complexes to both trap the $[^{11}C]CO$ and insert it has been demonstrated as a method to produce ^{11}C-amides, esters, carboxylic acids, aldehydes, and ketones [17, 18]. For example, a one-pot ^{11}C-aminocarbonylation is demonstrated herein to produce the N-^{11}C-acrylamide, $[^{11}C]$tolebrutinib [19] (Fig. 2) (*see* **Note 2**).
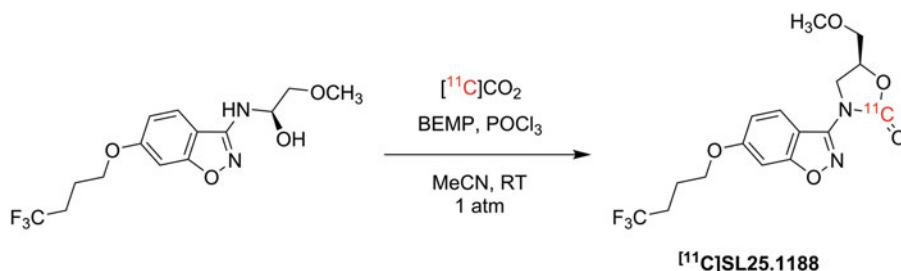
Fig. 1 Example of an intramolecular ^{11}C-carboxylation for the synthesis of [^{11}C]SL25.1188, a neuro-PET radiopharmaceutical used for imaging monoamine oxidase B
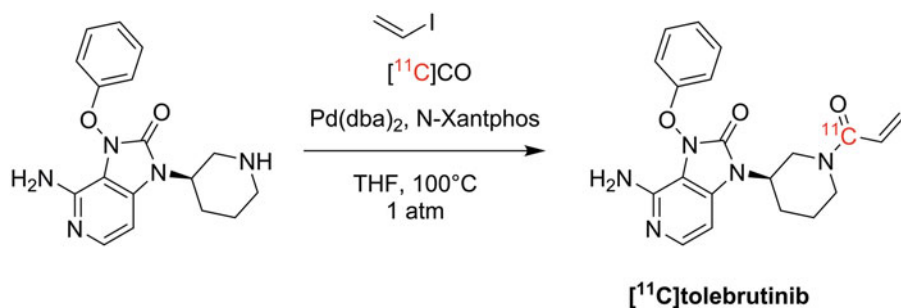
Fig. 2 Example of an ^{11}C-aminocarbonylation for the synthesis of [^{11}C]tolebrutinib

2   Materials

2.1   [^{11}C]CO$_2$ Carboxylation

1. Cyclotron-generated [^{11}C]CO$_2$.

2. HayeSep D column: (700 mg HayeSep D) (*see* **Notes 3** and **4**).

3. Amino alcohol precursor, e.g., (*S*)-1-methoxy-3-[6-(4,4,4-tri-fluorobutoxy)benzo[d]isoxazol-3-ylamino]propan-2-ol   (*see* **Note 1**).

4. Trapping base, e.g., 2-*tert*-butylimino-2-diethylamino-1,3-dimethyl-perhydro-1,3,2-diazaphorine (BEMP).

5. POCl$_3$.

6. Anhydrous acetonitrile.

7. Water.

8. Ammonium formate.

9. Nitrogen gas.

10. 4 mL glass reaction vial with septum

11. Helium gas.

12. Liquid nitrogen.

13. Commercial radiosynthesis unit (TracerMaker™; Scansys Laboratorierteknik, Denmark) (*see* **Notes 5–7**).

14. HPLC mobile phase and system as needed.

2.2 [^{11}C]CO Production

See Fig. 3 for set up scheme of columns and traps (*see* **Note 3**)

1. Cyclotron-generated [^{11}C]CO$_2$.

2. HayeSep D column: (700 mg HayeSep D) (*see* **Note 4**).

3. Molybdenum column: 26 cm quartz tube (4 mm ID, 6.35 mm OD) packed with 6 cm molybdenum powder (~2 g, 350 micron) and packed with 5 cm of quartz wool on both sides (*see* **Note 8**).

4. Ascarite/Sicapent column: Containing half sodium hydroxide-coated silica (Ascarite II, 20–30 mesh) and half Sicapent (*see* **Note 9**).

5. Silica trap: 1/16″ stainless steel tube (1/25" ID) in hairpin shape. Packed at turn with silica (60 Å, 60–100 mesh) and packed with a frit on each side (*see* **Note 10**). The silica trap is attached to an electric circuit for heating (*see* **Note 11**).

6. Helium gas.

7. Liquid nitrogen.

8. Commercial radiosynthesis unit (TracerMaker™; Scansys Laboratorierteknik, Denmark)) (*see* **Notes 5** and **6**).

2.3 [^{11}C]CO (Amino) Carbonylation

1. Amine precursor, e.g., des-acrylamide tolebrutinib precursor ((*R*)-4-amino-3-phenoxy-1-(piperidin-3-yl)-1,3-dihydro-2*H*-imidazo[4,5-*c*]pyridin-2-one) [19]) (*see* **Notes 12–13**).

2. Vinyl or aryl halide, e.g., vinyl iodide (*see* **Note 14**).

3. Ligand, e.g., *N*-Xantphos (*see* **Note 15**).

4. Palladium source, e.g., Pd(dba)$_2$ (*see* **Note 16**).

5. Anhydrous tetrahydrofuran (THF) (*see* **Note 17**).

6. Oven-dried 4 mL glass reaction vessel with Teflon-lined silicone septum (*see* **Note 18**).

7. Argon gas.

8. Nitrogen gas.

9. Helium gas.

10. Liquid nitrogen.

11. Commercial radiosynthesis unit (TracerMaker™; Scansys Laboratorierteknik, Denmark) (*see* **Notes 5–7**).

12. HPLC mobile phase and system as needed.
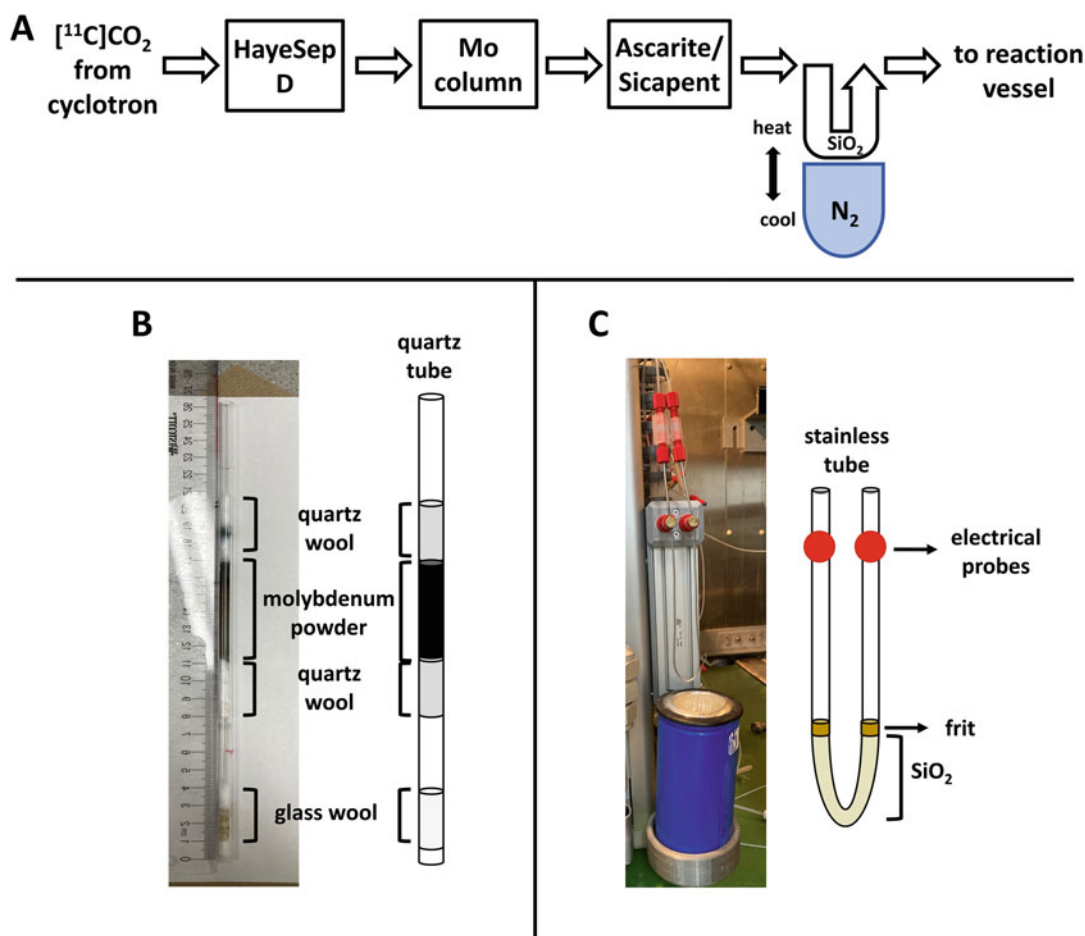
Fig. 3 (a) Flow scheme for [11C]CO production. (b) Molybdenum column set up. (c) Silica trap set up

3 Methods

Due to strong ionization radiation, all procedures (other than reaction preparations) should be performed in an adequately shielded radiochemical hot cell.

3.1 [11C]CO2 Carboxylation

Steps 1–5: Preparation

1. Prepare a 1 mg/mL precursor stock solution of amino alcohol (e.g., (S)-1-methoxy-3-[6-(4,4,4-trifluorobutoxy)benzo[d]iso-xazol-3-ylamino]propan-2-ol) in anhydrous acetonitrile (*see* **Note 1**).

2. Dispense 100 μL of the precursor stock solution into a conical reaction vessel (4 mL) and add 1 μL BEMP (1% overall). Seal the reaction vessel tight with a septum and flush the reaction vessel with inert gas.

3. Prepare a solution of $POCl_3$ (2 μL) in anhydrous acetonitrile (1 mL) (0.2% overall) in a dry vial with a septum.

4. Prepare a vial containing a quench solution of acetonitrile:H_2O (1 mL; 10:90 v/v) with ammonium formate (0.1 M).

5. At 5 min before end of bombardment, place the prepared reaction vial (**Step 2**) in the reactor and transfer the prepared $POCl_3$ solution (**Step 3**) to the addition vial on the radiosynthesis unit. Make sure the hot cell is closed.

Steps 6–11: $[^{11}C]CO_2$ production and trapping

This process has been automated and controlled and monitored through an external computer outside the hot cell (see **Notes 3– 7**).

6. Fill the dewar for the HayeSep D column on the radiosynthesis unit with liquid nitrogen.
   *Handle with appropriate PPE for cryogens according to institutional guidelines.

7. Make sure all gas lines are open and confirm sufficient pressure to the synthesis unit.

8. Produce $[^{11}C]CO_2$ in a cyclotron using the $^{14}N(p,\alpha)^{11}C$ nuclear reaction.

9. Trap cyclotron-produced $[^{11}C]CO_2$ on HayeSep D column cooled to −180 °C with liquid nitrogen.

10. Heat HayeSep D column slowly to −40 °C under helium flow (100 mL/min) over 2 min to remove any by-product impurities from the $[^{11}C]CO_2$.

11. Heat HayeSep D column to room temperature under helium flow (10 mL/min) to release $[^{11}C]CO_2$ into the prepared and sealed reaction vessel at room temperature (*see* **Note 19**).

Steps 12–14: Reaction and purification and/or analysis

This process has been automated and controlled and monitored through an external computer outside the hot cell (see **Notes 5– 7**).

12. After 1 min, add $POCl_3$ solution to the precursor and BEMP solution in the reaction vial at room temperature.

13. After 30 s, add quench solution to reaction vial.

14. Analyze reaction mixture and/or purify reaction mixture using RP-HPLC and an appropriate system for the substrate.

3.2 $[^{11}C]CO$ (Amino) Carbonylation

Steps 1–5: Reaction preparation

1. Prepare a solution of vinyl halide (vinyl iodide, 10 μL) in anhydrous THF (4 mL) solution (33.8 mM). Vinyl iodide has a very

low boiling point. Cap tight when not in use and handle only in a fumehood (*see* **Note 20**).

2. Prepare an oven-dried vial containing coupling reagents (Pd source, Xantphos ligand) with a septum (2.0 (± 0.2) mg Pd(dba)$_2$ and 2.0 (± 0.2) mg *N*-Xantphos). Minimize exposure to air while performing this and flush vial with nitrogen gas (*see* **Note 21**).

3. Prepare an oven-dried reaction vessel (4 mL) with a septum containing the precursor (des-acrylamide tolebrutinib precursor, 3 mg). Flush the reaction vessel with nitrogen gas.

4. 20 min before end of bombardment, add alkyl halide in THF (600 μL) to the vial with the Pd and ligand, through the septum. Vortex for 2 min and let stand at room temperature for 20 min for the complex intermediates to form.

5. Five minutes before the end of bombardment, add the reagents mixture to the precursor in the reaction vessel through the septum. Vortex for 2 min (*see* **Note 13**), then quickly replace with a new unpunctured septum and install the reaction vessel on the radiosynthesis unit. Make sure the hot cell is closed.

***Steps 6–15**: [^{11}C]CO production and trapping*

*This process has been automated and controlled and monitored through an external computer outside the hot cell (*see* **Notes 3– 7**). See Fig. 3 for a scheme.*

6. Fill appropriate dewars on the radiosynthesis unit with liquid nitrogen (for the silica trap and for the HayeSep column).
      *Handle with appropriate PPE for cryogens.

7. Make sure all gas lines are open and confirm sufficient pressure to the synthesis unit.

8. Produce [^{11}C]CO$_2$ in a cyclotron using the ^{14}N(p,α)^{11}C nuclear reaction.

9. Trap cyclotron-produced [^{11}C]CO$_2$ on HayeSep D column that has been cooled to −180 °C with liquid nitrogen.

10. Heat HayeSep D column slowly to −40 °C under helium flow (100 mL/min) over 2 min to remove any by-product impurities from the [^{11}C]CO$_2$.

11. Heat HayeSep D column to room temperature under helium flow (10 mL/min) to release [^{11}C]CO$_2$. Helium flow rate is maintained at 10 mL/min until trapping on silica trap.

12. Pass [^{11}C]CO$_2$ through the molybdenum column heated to 850 °C to produce [^{11}C]CO.

13. Pass [^{11}C]CO over Ascarite II column to remove any remaining [^{11}C]CO$_2$.

14. Trap $[^{11}C]CO$ on silica trap cooled by immersion in liquid nitrogen.

15. Remove silica trap from liquid nitrogen and heat trap to release $[^{11}C]CO$ into the prepared and sealed reaction vessel at room temperature. (Under helium flow at 10 mL/min) (*see* **Note 19**).

Steps 16–19: Reaction and purification and/or analysis

This process has been automated and controlled and monitored through an external computer outside the hot cell (see **Notes 5–7**).

16. Shut off helium flow and close valves to the reaction vessel. Heat the reaction mixture at 100 °C for 5 min.

17. Heat reaction vessel to 110 °C under nitrogen flow (100 mL/min) for 90 s to remove the THF.

18. Dilute reaction mixture with HPLC mobile phase.

19. Analyze reaction mixture and/or purify reaction mixture using RP-HPLC and an appropriate system for the substrate.

4   Notes

1. This ^{11}C-carboxylation reaction can also be achieved intermolecularly using a suitable amine precursor, followed by addition of an alcohol-based building block after the formation of the isocyanate with $POCl_3$ (*see* [20] *for an example).*

2. This reaction has potential to be modified to access a variety of other functional groups. Esters can be prepared by replacing the precursor amine with an alcohol, an aldehyde was prepared by replacing the amine with triethylsilane, a ketone by replacing the amine with a tributylstannane precursor, and a carboxylic acid by replacing the amine with tetraethylammonium hydroxide solution. Necessary reaction conditions for these scaffolds may need optimization [18].

3. All columns and traps need to be pre-conditioned prior to use to ensure complete removal of atmospheric gases. This is usually performed with a He flush.

4. Molecular sieves can be used to trap cyclotron-produced $[^{11}C]CO_2$ in place of the liquid nitrogen cooled Hayesep D column. In this case, $[^{11}C]CO_2$ is trapped on molecular sieves at room temperature, the column is flushed with helium to remove target gas and nitrogenous impurities, and the $[^{11}C]CO_2$ is released by heating the column to 350 °C under helium flow.

5. The TracerMaker™ is an automated radiosynthesis module equipped to handle all carbon-11 transformations and

manipulations. Other modules may be appropriate or modified for the needs herein.

6. All tubing on the TracerMaker™ are polytetrafluoroethylene (PTFE).

7. Stainless steel needles are used for the TracerMaker™ reactor (delivery needle and vent needle).

8. The molybdenum column needs to be conditioned after packing. With the outlet disconnected, condition under He flow at 5-10 mL/min: 100 °C for 5 min, ramp to 350 °C and hold for 10 min, ramp to 850 °C over 10 min and hold for 5 min, ramp down to room temperature slowly.

9. An Ascarite (or NaOH) column must always follow the molybdenum column. We have found that placing an Ascarite/Sicapent column directly before the silica trap helps to remove any residual moisture and maintain the longevity of the silica trap. The Ascarite column can also be placed inside the quartz tube of the molybdenum column at the outlet end; however, this placement results in more connections and/or valves between the desiccant and the silica trap, which increased the possibility of introduction of moisture to the trap.

10. When filling the stainless tube with silica, use a dipstick to measure and even the silica height on each side. Tap the tube repeatedly to pack the silica. Use small pieces of frit material and push down on each side to hold the silica in place.

11. On the Tracermaker™, the stainless tube is attached to electrical probes to heat the trap with an electrical current in order to speed the release of [^{11}C]CO from the silica.

12. This method has been reported for the synthesis of [^{11}C] ibrutinib as well using 3-(4-phenoxyphenyl)-1-(piperidin-3-yl)-2,3-dihydro-1H-pyrazolo[3,4-d]pyrimidin-4-amine as precursor [21].

13. We have found that using free base of precursor gives higher radiochemical yields and less radioactive by-products than salt forms. It is common for amino bases to be commercially sold as salts, which will make them difficult to dissolve in aprotic solvents such as THF. Addition of 2 equivalents amine base (e.g., diisopropylethylamine) is known to aid solubility in those cases.

14. It is also often possible to use a vinyl/aryl bromide or vinyl/aryl triflate in place of the vinyl/aryl iodide.

15. Other Xantphos and diphosphine ligands have been tested with some efficacy [18].

16. Other Pd(0) or Pd(II) catalysts have also have been used with varying success in trapping efficiencies and yields [18].

17. Freshly distilled, or SureSeal™ (with or without butylated hydroxytoluene (BHT)) THF is important for the yield of the reaction. When using THF with trace water or impurities (peroxides), a common by-product is the ^{11}C-labeled carboxylic acid. Yields were also lower when using alternate dry aprotic solvents such as 1,4-dioxane, acetonitrile, or DMF (which also have higher boiling points making them more difficult to remove).

18. These methods have also been adapted to "in-loop" carbonylation reactions using an HPLC loop as the reaction vessel [22, 23].

19. Ensure that when trapping $[^{11}C]CO_2$ or $[^{11}C]CO$ in the reaction mixture solution, the dispensing needle is submerged in the solvent and confirm that the gas is bubbling into it.

20. Vinyl iodide in THF solution can be prepared ahead of time. A solution of vinyl iodide (10 μL) in 4 mL anhydrous THF is prepared as follows: Handle vinyl iodide in a fumehood. Store vinyl iodide in the fridge and dispense into THF while the vial is still cold. The vinyl iodide/THF mixture has a shelf life of 1 week in a jar with desiccant (Drierite) at room temperature. Sealed vials should be wrapped with parafilm and covered with aluminum foil to protect from light.

21. Palladium source and ligand vial can be prepared ahead of time. To make in advance add both compounds to vial with septum. Store under inert atmosphere, seal vial with parafilm, and store the sealed vial in a jar with desiccant (Drierite) at −5 to 20 °C.

References

1. Rotstein BH, Liang SH, Placzek MS et al (2016) [11]C=O bonds made easily for positron emission tomography radiopharmaceuticals. Chem Soc Rev 45:4708–4726

2. Rotstein BH, Liang SH, Holland JP et al (2013) [11]CO_2 fixation: a renaissance in PET radiochemistry. Chem Commun (Camb) 49:5621–5629

3. Taddei C, Gee AD (2018) Recent progress in [11]Ccarbon dioxide ($[^{11}C]CO_2$) and ^{11}C carbon monoxide ($[^{11}C]CO$) chemistry. J Labelled Comp Radiopharm 61:237–251

4. Dahl K, Halldin C, Schou M (2017) New methodologies for the preparation of carbon-11 labeled radiopharmaceuticals. Clin Transl Imaging 5:275–289

5. Wilson AA, Garcia A, Houle S et al (2011) Synthesis and application of isocyanates radiolabeled with carbon-11. Chem A Eur J 17:259–264

6. Riss PJ, Lu S, Telu S et al (2012) CuI-catalyzed ^{11}C carboxylation of boronic acid esters: a rapid and convenient entry to ^{11}C-labeled carboxylic acids, esters, and amides. Angew Chemie Int Ed 51:2698–2702

7. Duffy IR, Vasdev N, Dahl K (2020) Copper(I)-mediated ^{11}C-carboxylation of (hetero)-arylstannanes. ACS Omega 5:8242–8250

8. Vasdev N, Sadovski O, Garcia A et al (2011) Radiosynthesis of $[^{11}C]SL25.1188$ via ^{11}C CO_2 fixation for imaging monoamine oxidase B. J Label Compd Radiopharm 54:678–680

9. Lidström P, Kihlberg T, Långström B (1997) [11]Carbon monoxide in the palladium-mediated synthesis of ^{11}C-labelled ketones. J Chem Soc Perkin Trans 1:2701–2706

10. Dahl K, Itsenko O, Rahman O et al (2015) An evaluation of a high-pressure [11]CO carbonylation apparatus. J Label Compd Radiopharm 58:220–225

11. Kihlberg T, Långström B (1999) Biologically active ^{11}C-labeled amides using palladium-mediated reactions with aryl halides and [^{11}C] carbon monoxide. J Org Chem 64:9201–9205

12. Eriksson J, Hoek J van den, Windhorst AD (2012) Transition metal mediated synthesis using [^{11}C]CO at low pressure – a simplified method for ^{11}C-carbonylation. J Label Compd Radiopharm 55:223–228

13. Taddei C, Pike VW (2019) [^{11}C]Carbon monoxide: advances in production and application to PET radiotracer development over the past 15 years. EJNMMI Radiopharm Chem 4:25

14. Eriksson J, Antoni G, Långström B et al (2020) The development of ^{11}C-carbonylation chemistry: a systematic view. Nucl Med Biol. https://doi.org/10.1016/j.nucmedbio.2020.02.005

15. Audrain H, Martarello L, Gee A et al (2004) Utilisation of [^{11}C]-labelled boron carbonyl complexes in palladium carbonylation reaction. Chem Commun:558–559

16. Kealey S, Miller PW, Long NJ et al (2009) Copper(i) scorpionate complexes and their application in palladium-mediated [^{11}C]carbonylation reactions. Chem Commun:3696–3698

17. Miller PW, Audrain H, Bender D et al (2011) Rapid carbon-11 radiolabelling for PET using microfluidics. Chem A Eur J 17:460–463

18. Dahl K, Schou M, Amini N et al (2013) Palladium-mediated [^{11}C]carbonylation at atmospheric pressure: a general method using Xantphos as supporting ligand. Eur J Org Chem 2013:1228–1231

19. Dahl K, Turner T, Vasdev N (2020) Radiosynthesis of a Bruton's tyrosine kinase inhibitor, [^{11}C]Tolebrutinib, via palladium-NiXantphos-mediated carbonylation. J Label Compd Radiopharm 63:482–487

20. Wilson AA, Garcia A, Parkes J et al (2011) [^{11}C]CURB: Evaluation of a novel radiotracer for imaging fatty acid amide hydrolase by positron emission tomography. Nucl Med Biol 38:247–253

21. Lindberg A, Boyle AJ, Tong J et al (2021) Radiosynthesis of [^{11}C]Ibrutinib via Pd-Mediated [^{11}C]CO Carbonylation: preliminary PET Imaging in Experimental Autoimmune Encephalomyelitis Mice. Front Nucl Med 1:772289

22. Ferrat M, Dahl K, Halldin C, Schou M (2020) "In-loop" carbonylation-A simplified method for carbon-11 labelling of drugs and radioligands. J Labelled Comp Radiopharm 63:100–107

23. Donnelly DJ, Preshlock S, Kaur T et al (2022) Synthesis of Radiopharmaceuticals via "In-Loop" ^{11}C-Carbonylation as Exemplified by the Radiolabeling of Inhibitors of Bruton's Tyrosine Kinase. Front Nucl Med 1:820235

Chapter 2

Enantioselective Synthesis of Carbon-11-Labeled Amino Acids and Peptides

Aleksandra Pekošak, Albert D. Windhorst, and Alex J. Poot

Abstract

Radiolabeled amino acids (AAs), their derivatives, and peptides are essential radiotracers in nuclear imaging. Despite its potential, the preparation of enantiopure radiopharmaceuticals poses several challenges, demanding a great need for rapid and stereocontrolled reactions. This chapter describes a highly stereoselective carbon-11 alkylation of Schiff bases, to obtain radiolabeled AAs and small peptides. The method uses chiral quaternary ammonium salt phase-transfer catalyst with two alkylating agents, namely, $[^{11}C]$ methyl iodide and $[^{11}C]$benzyl iodide. This methodology allows the radiolabeling of AAs and peptides with excellent regioselectivity and enantiomeric or diastereomeric excess.

Key words Carbon-11, Amino acid, Peptide, Stereoselective synthesis, Radiolabeling, PET imaging

1 Introduction

Positron emission tomography (PET) is a noninvasive technique that is routinely used for diagnosis in, e.g., oncology and neurology. PET relies on the visualization and quantification of molecules equipped with positron-emitting nuclides, PET radiopharmaceuticals, or tracers [1]. Therefore, the distribution and kinetics as well as the biochemical and physiological behavior of the PET tracer can be assessed, and as such cellular processes in vivo can be studied [2].

Important classes of compounds for PET tracer development are amino acids (AAs) and peptides. AAs play a crucial role in virtually all biological processes, e.g., protein synthesis, cell signaling, precursors for biomolecular transmission, redox homeostasis, and as neurotransmitters [3]. AAs can passively diffuse into cells; however, the main transmembrane transport of AAs into cells occurs through specific membrane-associated proteins, so-called AA-transporters. Due to the imperative role of generally existing or tissue-specific AA-transport systems and their consumption in many cellular processes, radiolabeled AAs have become important

PET tracers to diagnose, stage, and study cancer biology, considering that malignant tissue often relies on increased AA uptake [4]. The value of AA-based PET tracers is best demonstrated by [^{11}C]methionine and O-(2-[^{18}F]fluoroethyl)-L-tyrosine, which are used routinely in clinical settings for tumor diagnosis. Furthermore, multiple AAs and analogs thereof, e.g., [^{11}C]glutamine or derivatives (2S,4S)-4-(3-[^{18}F]fluoropropyl)glutamine and 3-(1-[^{18}F]fluoromethyl)-L-alanine, are under (pre)clinical development [5–9].

In addition, peptides have gained increasing importance as imaging agents and PET tracers. Peptides generally have a high affinity and specificity for receptor targets expressed on the cellular membrane, which often occur in nanomolar concentrations in diseased tissue. Due to many favorable properties for molecular imaging, such as advantageous pharmacokinetics and specific tumor targeting characteristics, combined with the overexpression of peptide receptors on the tumor cells, radiolabeled peptides are important for the PET imaging of cancer, especially when they are used as companion diagnostic with targeted radionuclide therapy [10]. Peptide-based radiopharmaceuticals have been successfully employed for imaging of somatostatin receptor (SSTR) expression using radiolabeled analogs of somatostatin as natural ligand, bombesin analogs for cholecystokinin/gastrin receptor-overexpressing tumors, and specific radiolabeled peptides targeting CXC receptor 4-expressing cancer cells [11–14]. As PET tracers, both AAs and peptides are used for disease diagnosis and treatment strategies and to establish new biological targets for therapy. Though their role in vivo and in biology and thus their potential and possible application as PET tracers are different, structurally AAs as building blocks of peptides are chemically related.

Many methodologies have been developed since the 1980s for radiolabeling AAs or peptides using organic approaches employing ^{11}C, ^{18}F, or iodine isotopes, as well as radiometals. Excellent reviews have been published that describe these different strategies for labeling AAs or peptides [15–17]. Only very few generally applicable methodologies are developed that can be used both for labeling AAs and peptides that result in high yields and a high enantiomeric purity and without adjustments to the chemical structure of the lead compound (Fig. 1) [18–20]. Here we describe the enantioselective radiolabeling of AAs and peptides with ^{11}C by employing the chiral alkylation of a Schiff base precursor with a ^{11}C-labeled alkyl iodide. By conducting a comprehensive reaction condition optimization and a strategic analysis of several phase-transfer catalysts that facilitate enantioselective alkylation, we describe the radiolabeling of L/D-[^{11}C]alanine, L/D-[^{11}C]phenyl alanine, dipeptides, and tetrapeptides (Fig. 2) [21–24]. This methodology here described is broadly applicable and can potentially also be used for the ^{11}C-labeling of other AAs and peptides. The
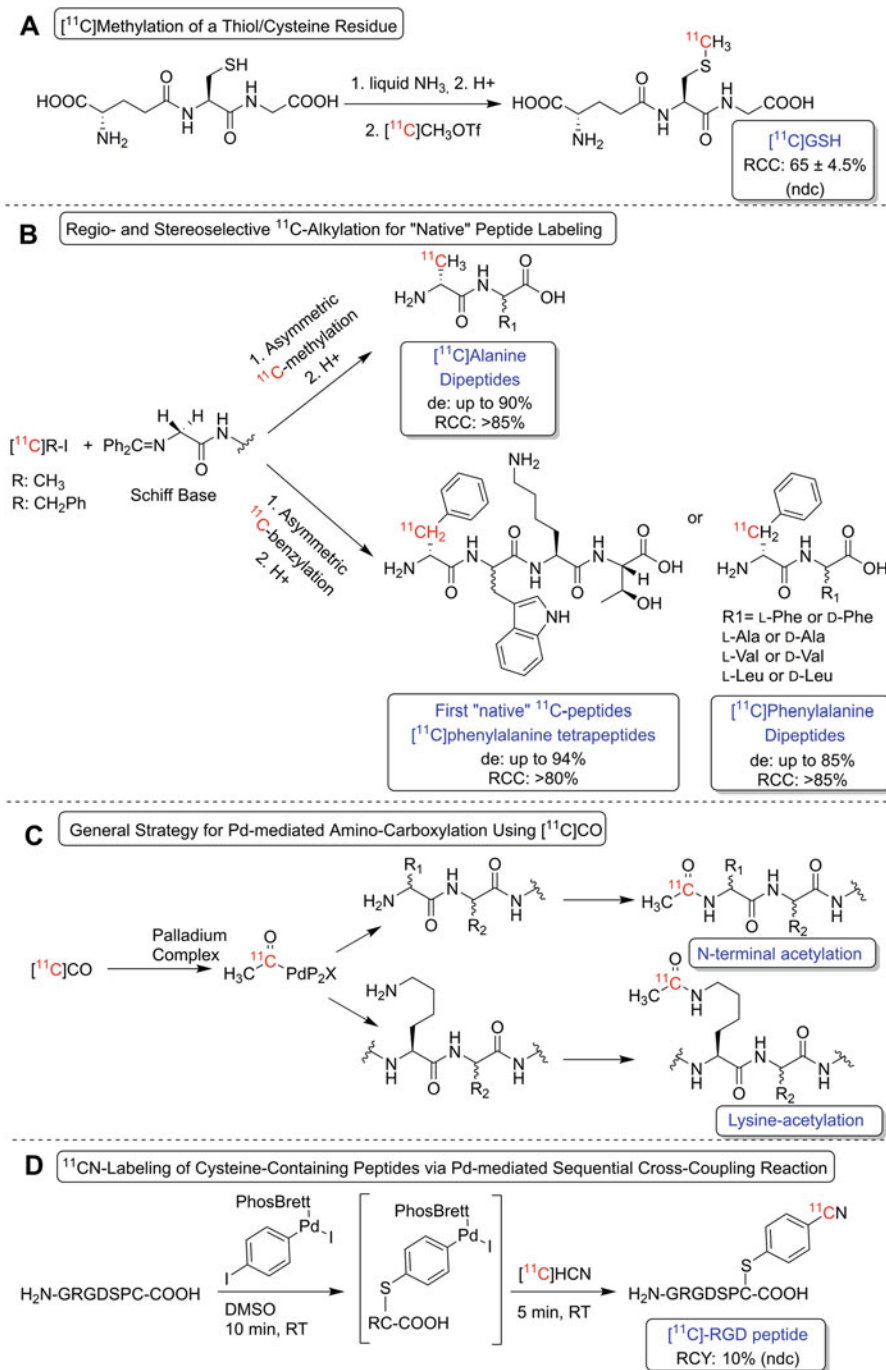
Fig. 1 Reported radiosynthetic methods for the carbon-11 labeling of peptides. (**a**) The alkylation of a cysteine with [^{11}C]MeI to form an [^{11}C]methionine residue. (**b**) The chiral alkylation of an N-terminal glycine Schiff base to form an [^{11}C]alanine or an [^{11}C]phenylalanine residue. (**c**) The acetylation of free primary amines in the peptide by [^{11}C]CO. (**d**) The cyanation of a modified cysteine residue in the peptide by [^{11}C]HCN
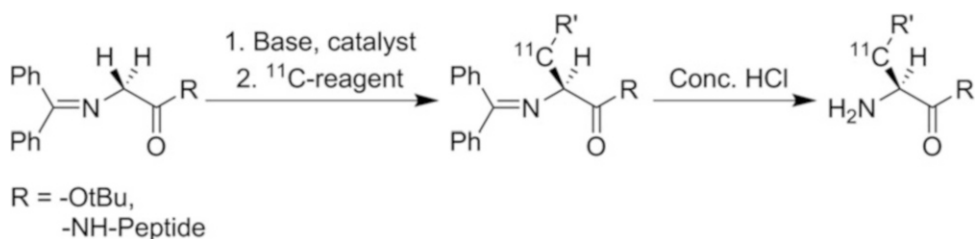
Fig. 2 Iodinated building block production for chiral alkylation. Synthesis of [^{11}C]MeI and [^{11}C]BnI as synthons for Schiff base alkylation. Schematic representation of the enantioselective ^{11}C-labeling of AAs and di- and tetrapeptides using the chiral alkylation of Schiff base precursors

radiosynthesis of L/D-[^{11}C]alanine has been adopted by other research groups, and the PET tracer is used for the imaging of tumors and bacterial infections [25].

In the addition to the synthesis of unfunctionalized AAs and peptides, we investigated the application of this methodology to radiolabel functionalized AAs, such as glutamine or glutamic acid. Therefore, a Michael addition reaction of the Schiff base precursor was exploited. Though comparable reactions have been described in organic chemistry, it is to date not possible to translate this methodology to radiochemistry and the enantioselective synthesis of [^{11}C]glutamine and [^{11}C]glutamic acid [23].

2 Materials

Prepare all solutions using ultrapure water and analytical grade reagents. Prepare and store all reagents at room temperature; and radiosynthesis reagents, precursors, and phase-transfer catalysts at 2–8 °C. Diligently follow all waste disposal regulations when disposing waste materials.

2.1 Analytical HPLC

Use the following columns and mobile phases for analytical HPLC of reference compounds:

1. Alltima 5 μm C18 250 × 4.6 mm column. Mobile phase: 4 mM sodium formate and 4% dimethylformamide (DMF) (v/v) ACN/buffer, isocratic, 80/20, wavelength 254 nm, column T—ambient, flow 1 mL/min.

2. ReproSil 100 Chiral-AA 8 μm 250 × 4.0 mm. Mobile phase: MeOH/H$_2$O (v/v), isocratic, 90/10, wavelength 254 nm, column T—ambient, flow 1 mL/min.

3. Phenomenex Luna 5 μm C18(2) 250 × 4.6 mm. Mobile phase: ACN/buffer 1 (4 mM sodium formate and 4% DMF (v/v)), linear gradient, 0–2 min: 65% ACN; 2–20 min: 65–97% ACN; 20–23 min: 97–65% CAN, 23–25 min: 65% D; wavelength 220 nm, column T—ambient, flow 1 mL/min.

4. Phenomenex Luna 5 μm C18(2) 250 × 4.6 mm. Mobile phase: ACN/buffer 1 (4 mM sodium formate and 4% DMF (v/v)), linear gradient, 0–2 min: 90% ACN; 2–10 min: 90–96% ACN; 10–13 min: 96% ACN; 13–15 min: 96–90% ACN; wavelength 254 nm, column T—ambient, flow 1 mL/min.

2.2 Preparative HPLC Use the following column and mobile phases for semi-preparative HPLC of the radiolabeled intermediate:

1. Phenomenex Luna 10 μm C18(2) 250 × 10 mm. Mobile phase: ACN/4 mM sodium formate, isocratic, 96/4, wavelength 254 nm, column T—ambient, flow 6 mL/min.

2.3 Production Units Adjustable universal home-build synthetic units allow the implementation of simple to complex radiochemistry [26]. All the steps of the process can be customized and controlled: reaction temperature, helium flow, activity, reagent placement, stirring, HPLC fraction collection switch, formulation solvents, etc. The methodology could be applied on commercially available carbon-11 radiosynthesis modules as well.

The following production modules, two for synthesis (Fig. 3a, b), one for purification (Fig. 3c), and one for formulation (Fig. 3d), are used (see the letters in red) [26]:

1. Synthesis unit with four valves for reagent addition, a temperature range from −50 to 150 °C, controlled He flow and vacuum, connection to liquid nitrogen for rapid cooling.

2. Synthesis unit with four valves for reagent addition, a temperature range from −50 to 150 °C, controlled He flow and vacuum, connection to liquid nitrogen for rapid cooling.

3. Prep HPLC unit with automated syringe for injection and a loop of 5 mL.

4. Formulation unit with fraction collector and homogenizer, placement for the SPE cartridge, valves for formulation solvents, etc.

The universal home-build synthesis modules were controlled using operating software with a graphical interface as depicted in Fig. 4.

2.4 Radiosynthesis 1. [^{11}C]CO2: produced by the ^{14}N(p,α)^{11}C nuclear reaction performed in a 0.5% O_2/N_2 gas mixture using an 18 MeV cyclotron.

2. Two synthesis modules (Fig. 3a, b).

3. Two glass reaction vessels (conical vial with a diameter 7–10 mm) with septum (blue septa), lid, and stirrer (PTFE Micro Stirrer Bar 7 × 2 mm).
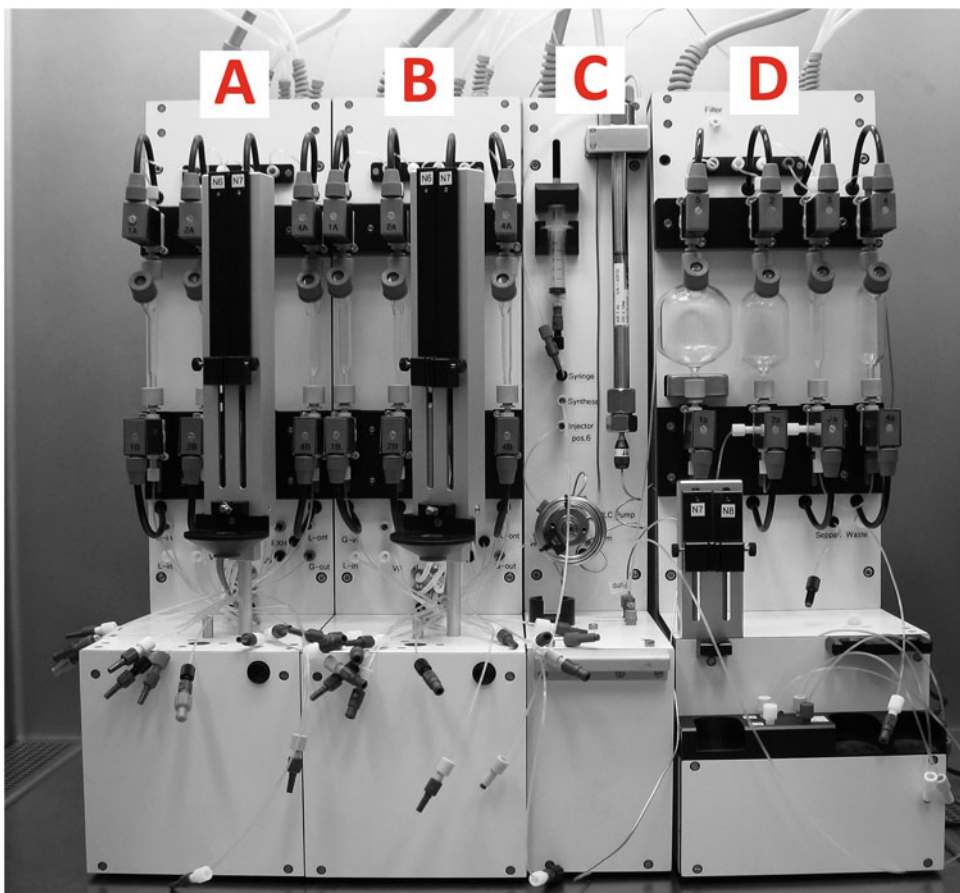
Fig. 3 Production modules required with: (**a**) synthesis module for the production of the iodinated building block; (**b**) synthesis module for the chiral alkylation reaction; (**c**) purification module for semi-preparative HPLC; and (**d**) product reformulation module to obtain injectable solutions

4. Needles with the following specifications: 0.80 × 120 mm BL/B; 0.90 × 70 mm BL/B; 0.80 × 40 mm BL/B; 1.20 × 40 mm BL/B; 0.45 × 12 mm BL/B; 0.70 × 50 mm BL/B.

5. 5 × 0.5 cm columns (ISOLUTE® Reservoir 3 mL; ISOLUTE® Column Adapter 1, 3, 6 mL columns; ISOLUTE® Frits 3 mL (9 mm) 20 μm PE), including filling material (phosphorus pentoxide, KOH).

6. Sep-Pak® Plus Short tC18 cartridges.

7. Various tubings: 1.0 × 2.0 mm, L.50 cm, vol. 0.66 mL; 1.0 × 2.0 mm, L.10 cm, vol. 0.30 mL; 1.0 × 2.0 mm, L.50 cm, vol. 0.66 mL.

8. Connectors with the following specifications: Male Luer Slip coupler; Female Luer Slip coupler; Male Luer to Female Luer Lock.
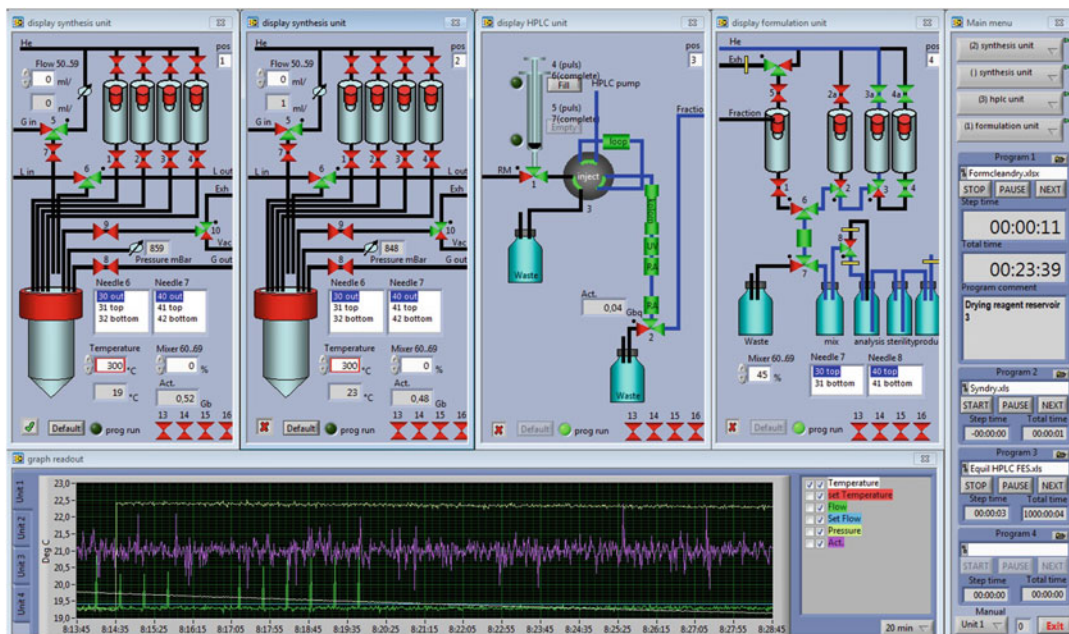
Fig. 4 Graphical interface of the operating software. Where each valve can be switched manually using this software. For optimized production protocols, automated synthesis programs can be loaded using an Excel sheet containing the required commands

9. Nitrogen and helium gas (grade 6.0).

10. 1 M and 0.1 M lithium aluminum hydride ($LiAlH_4$) solution in tetrahydrofuran (THF) (*see* **Note 1**).

11. 1 M phenylmagnesium bromide (PhMgBr) in THF (*see* **Note 1**).

12. 57% hydriodic acid (HI).

13. Purification column: 5×0.5 cm column (ISOLUTE® Reservoir 3 mL; ISOLUTE® Column Adapter 1, 3, 6 mL columns; ISOLUTE® Frits 3 mL (9 mm) 20 μm PE) filled with sodium hydroxide, potassium carbonate, and magnesium sulfate (approx. 5/3/2 by volume) (*see* **Note 2**).

14. Reaction solvent of choice (e.g., toluene (optimal solvent), DCM).

15. Schiff base precursor: for alanine: 1 eq, 1.9 mg, 7 μmol; for phenylalanine: 1 eq, 5.0 mg, 17 μmol; for dipeptides: 1 eq, 1.2–1.7 mg, 4–7 μmol; for tetrapeptide: 1 eq, 3.0 mg, 3.1 μmol, 350 eq of $CsOH \cdot H_2O$.

16. Chiral phase-transfer catalysts (Fig. 5): Cat 1, O-allyl-N-(9-anthracenylmethyl)cinchonidinium bromide, CAS: 200132-54-3; Cat 2, O-allyl-N-(9-anthracenylmethyl)cinchonidinium bromide, synthesized in-house [24]; Cat 3, (11bS)-(+)-4,4-dibutyl-4,5-dihydro-2,6-bis(3,4,5-trifluorophenyl)-3H-
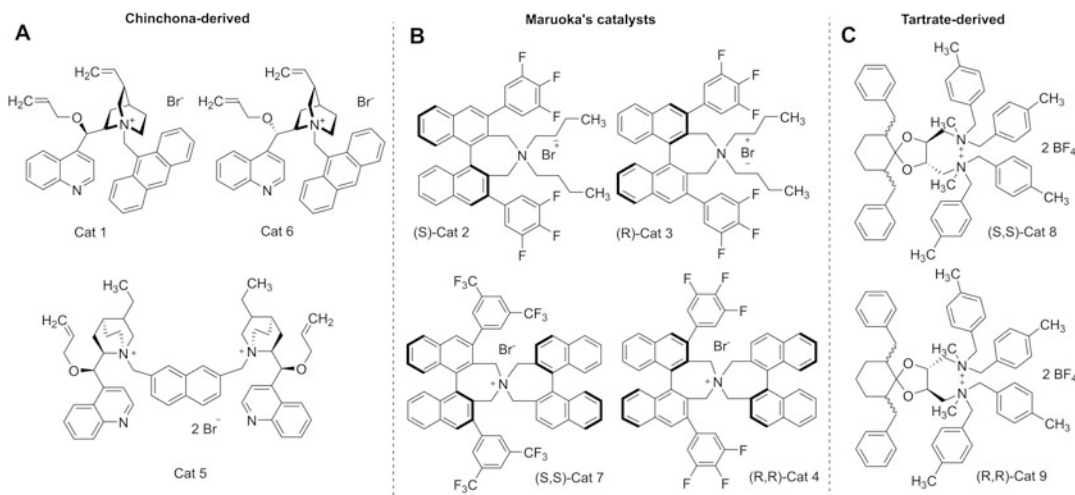
Fig. 5 Chiral phase-transfer catalysts explored for the radiosynthesis of carbon-11-labeled amino acids, dipeptides, and tetrapeptides. (**a**) Cinchona-based catalysts. (**b**) Maruoka's quaternary ammonium-based and tartrate-derived catalysts (**c**)

dinaphth[2,1-c:1′,2′-e]azepiniumbromide, CAS: 851942-89-7; Cat 4, (11bR)-(−)-4,4-dibutyl-4,5-dihydro-2,6-bis(3,4,5-trifluorophenyl)-3H-dinaphth[2,1-c:1′,2′-e]azepinium bromide, CAS: 887938-70-7; Cat 5, O,O′-diallyl-N,N′-(2,7-naphthalenediyldimethyl)bis(hydrocinchonidinium)dibromide, CAS: 480427-57-4; Cat 6, 6,10-dibenzyl-N,N′-dimethyl-N,N,N′,N′-tetrakis(4-methylbenzyl)-1,4-dioxaspiro[4.5]decane-(2S,3S)-diylbis(methylammonium)tetrafluoroborate, CAS: not available; Cat 7, 6,10-dibenzyl-N,N′-dimethyl-N,N,N′,N′-tetrakis(4-methylbenzyl)-1,4-dioxaspiro[4.5]decane-(2R,3R)-diylbis(methylammonium)tetrafluoroborate, CAS: not available; Cat 8, (S,S)-3,5-bistrifluoromethylphenyl-NAS bromide, CAS: 438002-03-0; Cat 9 (R,R)-3,4,5-trifluorophenyl-NAS bromide, CAS: 287384-12-7.

17. *N*-(diphenylmethylene)glycine *tert*-butyl ester or N-terminal *N*-(diphenylmethylene)glycine peptide.

18. Cesium hydroxide monohydrate (CsOH·H$_2$O).

19. Hydrochloric acid (HCl).

20. Acetonitrile (acn).

21. Analytical and preparative HPLC system, including the UV and radioactivity detector.

22. Saline solution.

23. 96% ethanol (EtOH).

3 Methods

3.1 Carbon-11 Alkylating Agents

Important: All materials have to be prepared and connected in the hot cell before transferring the $[^{11}C]CO_2$ into the hot cell.

3.1.1 Procedure to Activate Schiff Base Precursors

1. Add a solution of the N-terminally free amino acid or peptide H-XXX-O^{t}Bu (1 eq) in dichloromethane (DCM) to benzophenone imine (1.1 eq), dissolved in DCM.
2. Stir reaction overnight at ambient temperature.
3. Follow the progress of the reaction with TLC.
4. After completion, concentrate reaction mixture and purify it by flash chromatography (mixture of EtOAc/n-hexane) to yield white solid with >95% purity.

3.1.2 [^{11}C]Methyl Iodide ([^{11}C]MeI) [27–29]

1. Pre-dry the reaction vessel at elevated temperature (120 °C) under a stream of helium of 50 mL/min for 5 min. Cool down the vessel under inert atmosphere to room temperature before adding the 0.1 mL of 0.1 M LiAlH$_4$ in THF.
2. Transfer $[^{11}C]CO_2$ through a P$_2$O$_5$ column with a stream of helium to a hot cell (10 mL/min). Trap $[^{11}C]CO_2$ in a reaction vessel containing 0.1 M LiAlH$_4$ at room temperature under a helium flow of 10 mL/min.
3. After obtaining the maximum radioactivity in the vessel, increase gas flow to 20 mL/min and temperature to 130 °C to evaporate the vial to dryness (approximately 60 s).
4. Add 0.2 mL of 57% HI.
5. Distil $[^{11}C]MeI$ under a stream of helium with flow of 20 mL/min to the second reaction vessel for alkylation.

3.1.3 [^{11}C]Benzyl Iodide ([^{11}C]BnI)

1. Pre-dry the reaction vessel at elevated temperature (120 °C) under a stream of helium (50 mL/min) for 5 min. Cool down the vessel under inert atmosphere to room temperature before adding the 0.1 mL of a 1 M PhMgBr in THF.
2. Transfer $[^{11}C]CO_2$ through a P$_2$O$_5$ column with a stream of helium to a hot cell (50 mL/min). Trap $[^{11}C]CO_2$ in a reaction vessel containing PhMgBr at 35 °C under a helium flow of 10 mL/min.
3. After obtaining the maximum radioactivity in the vessel, stir reaction mixture using helium flow of 10 mL/min for 1 min and additional 1 min at a He flow of 50 mL/min to remove possible untrapped $[^{11}C]CO_2$.
4. Add 100 μL 1 M LiAlH$_4$. Heat the reaction vial to 130 °C under helium flow of 50 mL/min for 90 s.

5. Decrease temperature of synthesis unit to 0 °C (*see* **Note 3**). Add 100 µL of 57% HI and leave to react for 2 min at 120 °C.

6. Add desired amount of toluene (*see* **Note 4**) and pass it through a purification column (*see* **Note 2**) into a second reaction vial for alkylation under a helium flow of 50 mL/min.

3.2 Carbon-11 Stereoselective Alkylation with [^{11}C] MeI

1. Prepare the following chemicals in the second alkylation reaction vessel (*see* **Note 5**): Schiff base precursor (1 eq; *see* **Note 6**), CsOH·H$_2$O (40 eq), the catalyst of choice (*see* **Note 7**), and a small magnetic stirrer. Required amount of phase-transfer catalyst: 0.1 eq to precursor for amino acid; 0.5 eq for dipeptide; 2 eq for tetrapeptides.

2. [^{11}C]MeI is added in the second alkylation reaction vessel with a helium flow of 10 mL/min.

3. Stir the reaction vigorously for 10 min at desired temperature with the aid of helium flow (25 mL/min) bubbling through the solution and a magnetic stirrer. All needles in the vial need to be in elevated position that the stirrer can stir excess of CsOH·H$_2$O. Alkylation time can be decreased to 5 min for alanine.

4. Temperature: For alanine use 5 °C, for dipeptides −10 °C, and for tetrapeptide −10 °C.

3.3 Carbon-11 Stereoselective Alkylation with [^{11}C] BnI

1. Prepare the following chemicals in the second alkylation reaction vessel: Schiff base precursor (1 eq; *see* **Note 6**), CsOH·H$_2$O (40 eq), the catalyst of choice (*see* **Note 7**), and a small magnetic stirrer. Required amount of phase-transfer catalyst: 0.1 eq to precursor for amino acid; 0.5 eq for dipeptide; 2 eq for tetrapeptides.

2. [^{11}C]BnI is added in the second alkylation reaction vessel by elution from a purification column with toluene.

3. Stir the reaction vigorously for 10 min at desired temperature with the aid of helium flow (25 mL/min) bubbling through the mixture and a magnetic stirrer. All needles in the vial need to be in elevated position that the stirrer can stir excess of CsOH·H$_2$O. Alkylation time can be decreased to 7 min for phenylalanine.

4. Optimal temperature to achieve chiral alkylation: for phenylalanine 0 °C, for dipeptides −10 °C, and for tetrapeptide −10 °C.

3.4 Purification and Deprotection of Carbon-11-Labeled Amino Acids

1. Add 200 µL of 37% HCl to the reaction vessel and heat it to 120 °C for 2 min.

2. Cool the vessel to ambient temperature with the aid of liquid nitrogen.

3. Quench the reaction mixture with 1.5 mL of CH_3CN and load it onto a 5 mL injection loop.

4. Perform purification using a semi-preparative reversed-phase HPLC (*see* Subheading 2.3).

5. Collect the desired peak into a collection vessel. Collection is based on the radioactivity readout of the detector present at the end of the installed semi-preparative reversed-phase HPLC column.

3.5 Purification and Deprotection of Carbon-11-Labeled Peptides

1. After completion of the alkylation, quench the reaction mixture with 1.5 mL of CH_3CN and load it onto a 5 mL injection loop.

2. Perform purification using a semi-preparative reversed-phase HPLC (*see* Subheading 2.3).

3. Collect the desired peak into a collection vessel containing 40 mL of water.

4. Stir the solution to homogenize it.

5. Load aqueous solution on Sep-Pak C18.

6. Elute the product with 1.5 mL of ACN into a reaction vessel.

7. Gently evaporate ACN at 70 °C using vacuum.

8. After evaporation, add 100 μL of 12 M HCl and heat it to 100 °C for 2 min.

9. Cool the vessel to ambient temperature.

4   Notes

1. Container of $LiAlH_4$ and PhMgBr can be stored for maximum 1 month after opening. The container should be sealed with parafilm and stored under 4–8 °C. Before the start of the synthesis, the container should warm up to ambient temperature.

2. All purification columns needed for the production should be freshly prepared for radiosynthesis (up to 2 h before start of synthesis).

3. The temperature can be less than 0 °C, but below 25 °C is essential. It is important that the waste is closed during the addition of HI to avoid loss of the iodinated intermediate building blocks required for the alkylation reaction.

4. The amount of toluene depends on the tubing and should be reduced to a minimum (e.g., using our setting we use 1 mL of toluene for peptide labeling and 3 mL for amino acid labeling). For labeling a single amino acid, the desired volume in the second reaction vessel is 400 μL of toluene, while for the peptides the volume should be 100 μL. It should be

acknowledged that even a 100 μL of toluene produces broad peaks during the preparative HPLC purification.

5. Second reaction vial needs to be precooled to desired temperature.

6. For each chiral alkylation reaction to synthesize a radiolabeled AA or peptide, the combination of precursor, 11C-labeled alkylating reagent and chiral catalyst required optimization.

7. The appropriate semi-preparative reversed-phase HPLC method is determined prior to the synthesis. The retention time of the desired peak is determined by co-injection of the reference standard.

Acknowledgments

References

1. Phelps ME (2000) Inaugural article: positron emission tomography provides molecular imaging of biological processes. Proc Natl Acad Sci U S A 97:9226–9233

2. Van Dongen GAMS, Poot AJ, Vugts DJ (2012) PET imaging with radiolabeled antibodies and tyrosine kinase inhibitors: immuno-PET and TKI-PET. Tumour Biol 33:607–615

3. Christensen HN (1990) Role of amino acid transport and countertransport in nutrition and metabolism. Physiol Rev 70:43–77

4. Huang C, McConathy J (2013) Radiolabeled amino acids for oncologic imaging. J Nucl Med 54:1007–1010

5. Langstrom B, Antoni G, Gullberg P et al (1987) Synthesis of L- and D-[methyl-^{11}C]methionine. J Nucl Med 28:1037–1041

6. Dunet V, Rossier C, Buck A et al (2012) Performance of ^{18}F-fluoro-ethyl-tyrosine (^{18}F-FET) PET for the differential diagnosis of primary brain tumor: a systematic review and metaanalysis. J Nucl Med 53:207–214

7. Oya S, Qu W, Ponde D et al (2009) Preparation of [^{11}C]glutamine as a metabolic tracer for imaging glutaminolysis in tumor cells. J Nucl Med 50(suppl 2):264

8. Wu Z, Zha Z, Li G et al (2014) [^{18}F](2S,4S)-4-(3-fluoropropyl)glutamine as a tumor imaging agent. Mol Pharm 11:3852–3866

9. Wang L, Zha Z, Qu W et al (2012) Synthesis and evaluation of ^{18}F labeled alanine derivatives as potential tumor imaging agents. Nucl Med Biol 39:933–943

10. Cremonesi M, Gerrari M, Bodei L et al (2006) Dosimetry in peptide radionuclide receptor therapy: a review. J Nucl Med 47:1467–1475

11. Sanli Y, Garg I, Kandathil A et al (2018) Neuroendocrine tumor diagnosis and management: ^{68}Ga-DOTATATE PET/CT. Am J Roentgenol 2:267–277

12. Nicolas GP, Beykan S, Bouterfa H et al (2018) Safety, biodistribution, and radiation dosimetry of ^{68}Ga-OPS202 in patients with gastroenteropancreatic neuroendocrine tumors: a prospective phase I imaging study. J Nucl Med 59:909–914

13. Zhang H, Abiraj K, Thorek DLJ et al (2012) Evolution of bombesin conjugates for targeted PET imaging of tumors. PLoS One 7:e44046

14. Kircher M, Herhaus P, Schottelius M et al (2018) CXCR4-directed theranostics in oncology and inflammation. Ann Nucl Med 32:503–511

15. Huang C, Mcconathy J (2013) Fluorine-18 labeled amino acids for oncologic imaging with positron emission tomography. Curr Top Med Chem 13:871–891

16. Cutler CS, Hennkens HM, Sisay N et al (2013) Radiometals for combined imaging and therapy. Chem Rev 113:858–883

17. Pekošak A, Filp U, Poot AJ et al (2018) From carbon-11-labeled amino acids to peptides in positron emission tomography: the synthesis and clinical application. Mol Imaging Biol 20: 510–532

18. Fasth K, Antoni G, Langstrom B (1988) Asymmetric synthesis of L-[3-^{11}C]alanine and L-[^{11}C]phenylalanine by a phase-transfer alkylation reaction. J Chem Soc Perkin Trans I (12): 3081–3084

19. Popkov A, Nádvorník M, Kružberská P et al (2007) Towards stereoselective radiosynthesis of α-[^{11}C]methyl-substituted aromatic α-amino acids—a challenge of creation of quaternary asymmetric centre in a very short time. J Label Compd Radiopharm 50:370–374

20. Andersen TL, Nordeman P, Christoffersen HF et al (2017) Application of methyl bisphosphine-ligated palladium complexes for low pressure N-^{11}C-acetylation of peptides. Angew Chem Int Ed 56:4549–4553

21. Filp U, Pekošak A, Poot AJ et al (2016) Enantioselective synthesis of carbon-11 labeled L-alanine using phase transfer catalysis of Schiff bases. Tetrahedron 72:6551–6557

22. Pekošak A, Filp U, Škrinjar J et al (2017) A rapid and highly enantioselective C-^{11}C bond formation of L-[^{11}C]phenylalanine via chiral phase-transfer catalysis. Org Biomol Chem 15:570–575

23. Filp U, Pekošak A, Poot AJ, Windhorst AD (2017) Stereocontrolled ^{11}C-alkylation of N-terminal glycine Schiff bases to obtain dipeptides. Eur J Org Chem 2017:5592–5596

24. Pekošak A, Rotstein BH, Collier TL et al (2017) Stereoselective ^{11}C-labeling of a "native" tetrapeptide using asymmetric phase-transfer catalyzed alkylation reactions. Eur J Org Chem 2017:1019–1024

25. Parker MFL, Luu JM, Schulte B et al (2020) Sensing living bacteria in vivo using d-alanine-derived ^{11}C radiotracers. ACS Cent Sci 6:155–165

26. Windhorst AD, ter Linden T, de Nooij A et al (2001) A complete, multipurpose, low cost, fully automated and GMP compliant radiosynthesis system. J Label Compd Radiopharm 44:S1052–S1054

27. Comar D, Cartron JC, Maziere M, Marazano C (1976) Labelling and metabolism of methionine-methyl-^{11}C. Eur J Nucl Med 1:11–14

28. Crouzel C, Langstrom B, Pike VW, Coenen HH (1987) Recommendations for a practical production of [^{11}C]methyl iodide. Appl Radiat Isot 38:601–603

29. Langstrom B, Lundqvist H (1976) The preparation of ^{11}C-methyl iodide and its use in the synthesis of ^{11}C-methyl-L-methionine. Int J Appl Radiat Isot 27:357–363

Chapter 3

Silicon–Fluoride Acceptors (SiFA) for ^{18}F-Radiolabeling: From Bench to Bedside

Lexi Gower-Fry, Carmen Wängler, Peter Bartenstein, Leonie Beyer, Simon Lindner, Klaus Jurkschat, Björn Wängler, Justin J. Bailey, and Ralf Schirrmacher

Abstract

Fluorine-18 (^{18}F) is undoubtedly one of the most frequently applied radionuclides for the development of new radiotracers for positron emission tomography (PET) in the context of clinical cancer, neurological, and metabolic imaging. Until recently, the available radiochemical methodologies to introduce ^{18}F into organic molecules ranging from small- to medium- and large-sized compounds were limited to a few applicable protocols. With the advent of late-stage fluorination of small aromatic, nonactivated compounds and various noncanonical labeling strategies geared toward the labeling of peptides and proteins, the molecular toolbox for PET radiotracer development was substantially extended. Especially, the noncanonical labeling methodologies characterized by the formation of Si–[18]F, B–[18]F, and Al–[18]F bonds give access to kit-like ^{18}F-labeling of complex and side-group unprotected compounds, some of them already in clinical use. This chapter will particularly focus on silicon–fluoride acceptor (SiFA) chemistry and cover the history of its conceptual design and its translation into the clinical practice.

Key words Isotope exchange, Radiofluorination, SiFA, Peptides, Proteins

1 Introduction

1.1 Noncanonical Labeling Methods

As fluorine-18 has been found to be extremely useful in PET imaging due to its low mean β^+ energy of 250 keV and ideal half-life of $t_{1/2} = 109.5$ min, its incorporation into targeting vectors has been the subject of many studies into ^{18}F-labeling strategies [1]. The method of ^{18}F incorporation into organic molecules originally was done through nucleophilic or electrophilic substitutions generating a carbon–[18]F bond. However, these reactions typically are slow and occur under harsh conditions that are not suitable for peptide and protein targeting vectors. Additionally, the reactions are not very specific, and the generation of by-products requires timely and expensive separation techniques [1]. More recently,
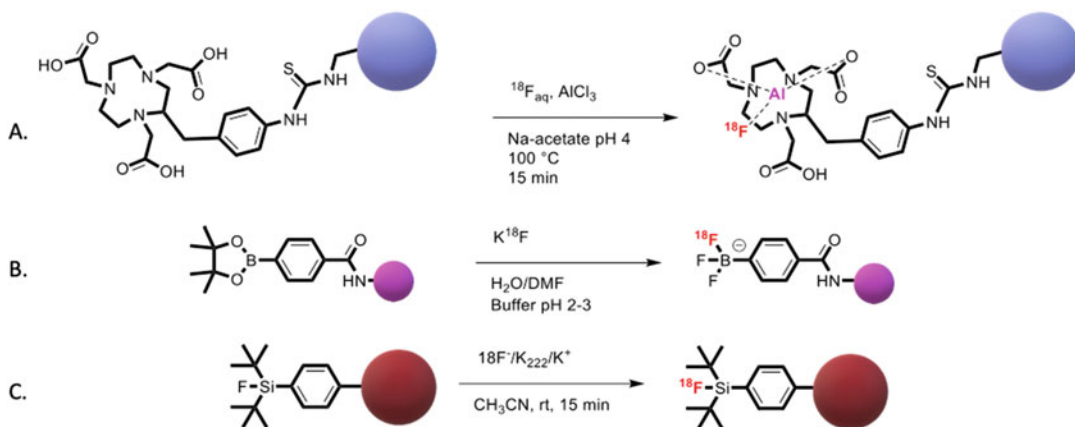
Fig. 1 General schemes of common fluorine-18 labeling reactions. (**a**) Aluminum–[18]F-labeling approach. (**b**) Boron–[18]F-labeling approach. (**c**) Silicon–[18]F-labeling approach [3, 4]

methods have been implemented that take advantage of boronic ester and hypervalent iodonium ylide leaving group chemistry [2]. These procedures all require metal catalysts and more time-intensive purification techniques such as high-performance liquid chromatography (HPLC), limiting their efficacy as PET radiotracer synthesis methods. Ideally, radiolabeling of compounds with fluorine-18 should take place by relatively simple and fast procedures that are reliable and highly standardized and result in a high molar activity of the radiotracer, yielding PET images with better contrast and specificity [2]. As well, purification should be timely and efficient, without the need to use HPLC.

The development of methods to introduce ^{18}F using silicon–[18]F, boron–[18]F, and aluminum–[18]F radiochemistry has been a great advancement to the field of PET imaging (Fig. 1). Perrin et al. introduced labeling methods based on boron–[18]F bond formation that have been shown to significantly improve the labeling of peptides for PET imaging [2]. Ametamey et al. established silicon-based ^{18}F chemistry concurrently with the Schirrmacher, Wängler, and Jurkschat groups' development of silicon–fluoride acceptor (SiFA) chemistry, which will be discussed in more detail below [2]. Conversely, Goldenberg et al. instigated a method of ^{18}F-labeling that incorporates chelator chemistry usually implemented in radiometal-labeling [5, 6]. In this approach, ^{18}F interacts with Al^{3+} and is consecutively stabilized via chelator complexation.

Even though a Si–[18]F bond energy is known to be 90 kJ higher than a C–F bond, some initial studies exploiting the use of organo-fluorosilanes were hampered due to the kinetic lability of the Si–F bond toward hydrolysis [2]. Rosenthal et al. observed this when they labeled chlorotrimethylsilane with [18]F⁻, resulting in [^{18}F] fluorotrimethylsilane with very low in vivo stability to result in silanole formation and ^{18}F bone uptake [1, 7]. Due to this

disadvantage, researchers sought to determine the effects of adding bulky groups on the silicon core to prevent hydrolysis of the Si–F bond. Blower et al. as well as Schirrmacher and Jurkschat were able to show that, indeed, the incorporation of sterically hindered groups improved the stability of the Si–F bond. The first few compounds investigated had a combination of aryl and *tert*-butyl substituents on the silicon atom, and their in vivo stability was probed. These initial studies found that [^{18}F]triorganofluorosilane (with 2 *tert*-butyl and one aryl group) had exceptional stability in vivo and thus was used as a building block to further develop ^{18}F-radiolabeling methods using Si–F chemistry. The Perrin group was able to generate radioactive organotetrafluorosilicate salts at approximately the same time as Schirrmacher and Jurkschat were developing methods for isotopic exchange of "cold" fluorine to radioactive [18]F [1, 8, 9].

1.2 The Development of ^{18}F-SiFA Labeling

Usually, isotopic exchange reactions as a way of radiolabeling are considered to be less than ideal as they tend to result in lower molar activities of the tracers, meaning the amount of ^{18}F relative to ^{19}F-bearing pharmaceutical is low (measured in units of activity *per* mol) [10]. In the case of C–[18]F chemistry, isotopic exchange reactions yield molar activities in the low kBq/μmol range [1]. This is a significant issue as high molar activity is required for successful in vivo applications, especially when the target is present in low quantities such as enzymes or cell surface receptors. If the molar activity is too low, a considerable fraction of target structures is saturated by nonradioactive "carrier," resulting in low target specificity or even failure to visualize the target. Additionally, the lower the molar activity, the more tracer is required to be injected to produce adequate PET images, thus leading to potential adverse pharmacological effects in patients. Moreover, in receptor target systems, only less than 1% of receptors should be occupied by a radiotracer to limit any erroneous receptor function [1, 11]. Importantly, since ^{18}F and ^{19}F have the same chemical and physical properties, the nonradioactive compound cannot be separated from that with the ^{18}F-label, which could also significantly decrease the molar activity. However, due to this characteristic, labeled agents obtained by isotopic exchange do not require a purification procedure which could greatly improve the efficiency of the preparation of the radiotracers. Due to this advantage, radiolabeling of organosilicon compounds with ^{18}F using isotopic exchange chemistry was investigated to determine if the molar activity and radiochemical yield would be sufficient for in vivo applications. The first experiment was done with Ph_3SiF in 2006, which proved that isotopic exchange could be a viable option. This was due to the easy exchange of ^{19}F to ^{18}F at room temperature in only a few minutes in acetonitrile that gave radiochemical yields of over 90% [2, 12]. Unfortunately, this compound was found to be unstable at

physiological pH as it underwent hydrolysis. Further results of reactions done with the organofluorosilane tBu$_2$PhSiF proved that the isotopic exchange method could produce high radiochemical yields and molar activities (~230 GBq/μmol) [1]. Moreover, this compound proved to be more stable against hydrolysis as animal studies only showed minimal ^{18}F uptake in the bones over a 2 h period. Additionally, the purification process was facile and time efficient as no side products were formed and only the unreacted [^{18}F]fluoride had to be removed after the labeling reaction. Due to this, the purification could occur by flushing them through a C18 solid phase cartridge. The radiolabeled compound would stay stuck in the cartridge as impurities are flushed out, and then using an elution solution the pure radiotracer could be obtained. Furthermore, reactions could be done under mild conditions with short reaction times. This substantial contribution to the field of PET radiotracer synthesis is known as SiFA chemistry. It was first introduced as a way to label peptides and has since been used in a wide variety of compounds as a potential way of introducing ^{18}F onto targeting vectors for PET imaging [12].

1.3 Synthesis

The synthesis and isolation of SiFA compounds (Fig. 2) have been well reported and follow a straightforward procedure. The first step is a metal–halogen exchange reaction that takes place when the silyl-protected 4-bromobenzene is treated with *tert*-butyllithium. Next, the resulting aryllithium derivative undergoes a salt metathesis reaction with di-*tert*-butyldifluorosilane where the carbanion acts as a strong nucleophile, undergoing substitution with one of the silicon-bound fluoride atoms and forming the Si–C bond. This works to attach the t-Bu$_2$SiF moiety to the functionalized benzene ring allowing for its attachment to a targeting vector after a final deprotection step.

1.4 Peptides and Limitations of the SiFA-Based ^{18}F-Labeling Approach

One of the first SiFA-derivatized peptides synthesized was SiFA-TATE, where the SiFA moiety is attached to the peptide Tyr^3-octreotate. This peptide is important for the diagnosis of neuroendocrine tumors (NET), which are characterized by their increase in somatostatin receptors (SSTR) [13]. To image these tumors, octreotide-derivative peptides have been found to be the most useful due to their high affinity toward SSTR2 as well as having an ideal biological half-life of ~72–98 min [14]. Significantly, the radiochemical half-life of ^{18}F is a great match, allowing enough time for the distribution of the ^{18}F-labeled peptide to its intended target receptors without too much loss of radioactivity. Successful radiolabeling of this peptide–SiFA conjugate through isotopic exchange was instrumental in demonstrating the ability of SiFA to have preference for ^{18}F/^{19}F isotopic exchange over any ^{18}F$^-$/peptidic acidic group interactions [2]. Acidic group interactions are a significant issue when it comes to isotopic exchange chemistry due
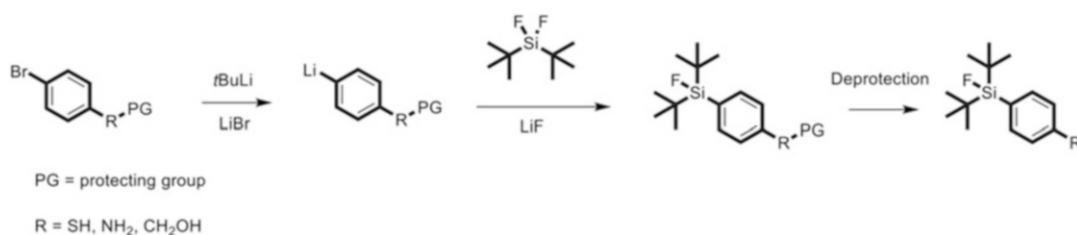
Fig. 2 General scheme for SiFA synthesis [1]

to their potential interaction with nucleophilic [^{18}F]fluoride and thus suppression of the labeling reaction. The alternative, using a protecting group to decrease the reactivity of the acidic functional groups, is also not optimal as the introduction and removal of protecting groups can be difficult and have negative consequences on the peptide, as well as the purification process being demanding. Therefore, the reaction of SiFA-TATE with ^{18}F at room temperature producing a radiochemical yield of 95% within 10 min was a massive achievement and improvement in the field [2]. This result demonstrated the ability of SiFA to label clinically significant compounds with ^{18}F in a one-step isotopic exchange process under mild conditions, fast time frames and with high selectivity.

Although SiFA chemistry provides many advantages in the world of ^{18}F-labeling and PET imaging, it does come with some limitations. A major drawback is its intrinsic lipophilicity that can conversely affect the ability of the radiotracer to have the appropriate biodistribution needed. If the lipophilicity is too high, the compound will not have the time to adequately distribute in the organism to enable target interaction and thus visualization. Instead, the radiotracer will be trapped and metabolized in the liver in what is known as the first pass effect, removing it out of the blood to be excreted. This issue simply means that the compound would never make it to its intended targets and that tumor imaging would be impossible. This was seen when bis-*tert*-butyl SiFA was applied to rats and its accumulation was primarily in the liver before excretion [1]. Furthermore, SiFA derivatives of small molecule brain-imaging agents fallypride and desmethoxyfallypride showed no uptake in the brain of healthy rats due to the lipophilicity concerns [2]. This issue was confirmed when in vivo studies of SiFA-TATE showed most of its uptake primarily in the liver. Further, this signifies that attachment of lipophilic SiFA to a peptide was enough to affect the overall lipophilicity of the compound and cause adverse biodistribution [15]. This limitation could possibly be overcome through the addition of a charge or hydrophilic groups to the SiFA group, or to the peptide itself. It has been shown that TATE derivatives with hydrophilic groups attached at the N-terminus such as carbohydrates or charged amino acids are
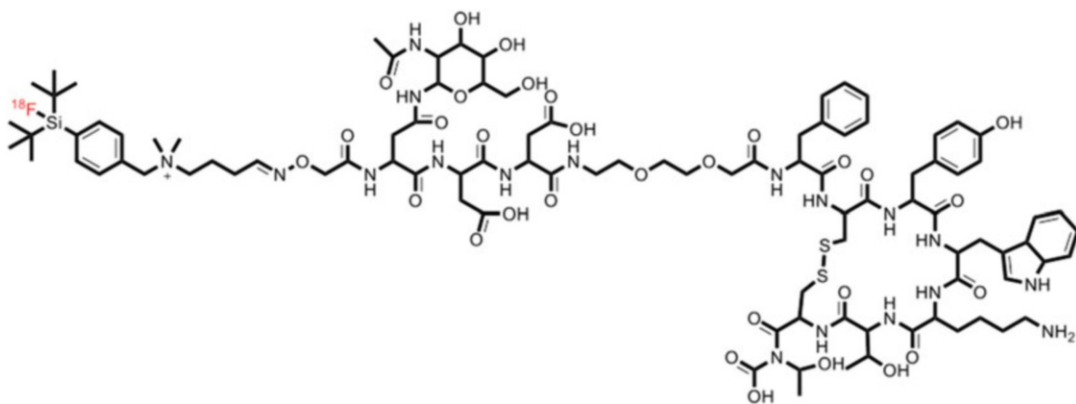
Fig. 3 Schematic drawing of [^{18}F]-SiTATE

more flexible to SiFA modification without losing their ability to bind to their target receptor [2]. Wängler et al. used a derivative where a polyethylene glycol (PEG) group and glycosylated aspartic acid were added in between the SiFA and TATE to produce [^{18}F] SiFA-Asn(AcNH-β-Glc)-PEG-Tyr^{3}-octreotate [16]. Lipophilicity and in vivo studies in comparison to SiFA-TATE showed a remarkable decrease in lipophilicity (2.20 to 0.96) and elevation in tumor uptake (0 to −7.7%) [15]. Additional modifications were tested until [^{18}F]SiTATE (previously known as [^{18}F]SiFA*lin*-TATE) (Fig. 3) was developed, which consists of a permanently positively charged SiFA, two aspartic acids, and an Asn(AcNH-β-Glc)-PEG$_{1}$ spacer [17].

[^{18}F]SiTATE was able to yield extremely high tumor uptake, similar to that of the gold standard [^{68}Ga]Ga-DOTA-TATE when applied to NET-bearing mice (Fig. 4) [18, 19]. Significantly, ^{18}F also offers further advantages over using a ^{68}Ga radiotracer, such as its widespread availability, its ideal positron energy (offering higher spatial resolution images), longer half-life, and less expensive production [20].

The first human clinical studies reported by Ilhan et al. in 2019 evaluated [^{18}F]-SiTATE in 13 patients diagnosed with NET and compared the scans to [^{68}Ga]Ga-DOTA-TOC [20]. Results showed that [^{18}F]-SiTATE had higher tumor-to-normal tissue uptake, also seen in the preclinical studies, as well as comparable image quality and biodistribution (Fig. 5), thus making [^{18}F]-SiTATE an excellent candidate as a PET imaging radiotracer.

More recently, Unterrainer et al. compared an [^{18}F]-SiTATE PET/CT to [^{68}Ga]Ga-DOTA-TOC PET/CT in a patient with falx meningioma and transosseous extension, which are known to have high SSTR expression on cell surfaces [21]. They found that the tumor uptake was extremely similar, and since the use of ^{18}F resolves some limitations inherent with ^{68}Ga use, it may become the future gold standard in NET and meningioma PET imaging
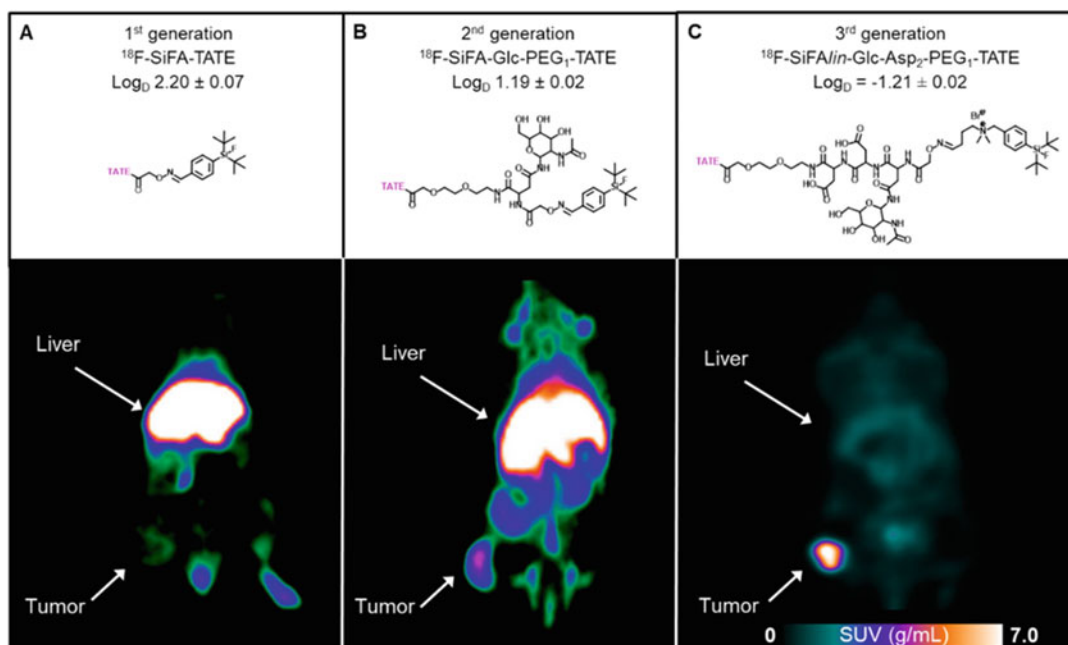
Fig. 4 Comparison of the biodistribution of different ^{18}F-SiFA-TATE analogs in tumor-bearing mice. The successive decrease in Log$_D$ from first (**a**)- to second (**b**)- to third (**c**)-generation radiotracers simultaneously enhances hepatobiliary clearance while increasing tumor SUV. (Reprinted with permission from ref. [17])

(Fig. 6). Further clinical studies done by Beyer et al. in 2021 looked into tracer kinetics by evaluating PET images over several time points in eight patients with different NET tumor types [22]. They found that lower administered radiotracer activities (~100–120 MBq) are adequate in producing a sufficient image quality as well as an increasing tumor-to-background ratio over time. Based on their results, and with patient logistics taken into consideration, it was determined that the ideal imaging strategy would be to start the image acquisition 90 min after injection [22]. Additionally, efforts have recently been made by Linder et al. to fully automate the production of [^{18}F]-SiTATE so that it will be widely accessible by diagnostic centers and medical clinics [23]. The process uses a cassette-method Scintomics GRP™ platform where all steps take place in a timed sequence on two manifolds with ten valves [23]. Clinical studies using this automated system resulted in no reported acute side effects of the tracer and typical tumor uptake and biodistribution. This further exemplifies the accessibility and potential ease of incorporation of [^{18}F]-SiTATE into full clinical application.

1.5 Proteins

In contrast to peptide labeling, protein labeling requires a small molecule prosthetic group to be radiolabeled before being attached to the protein of interest. This is essential as proteins have a great
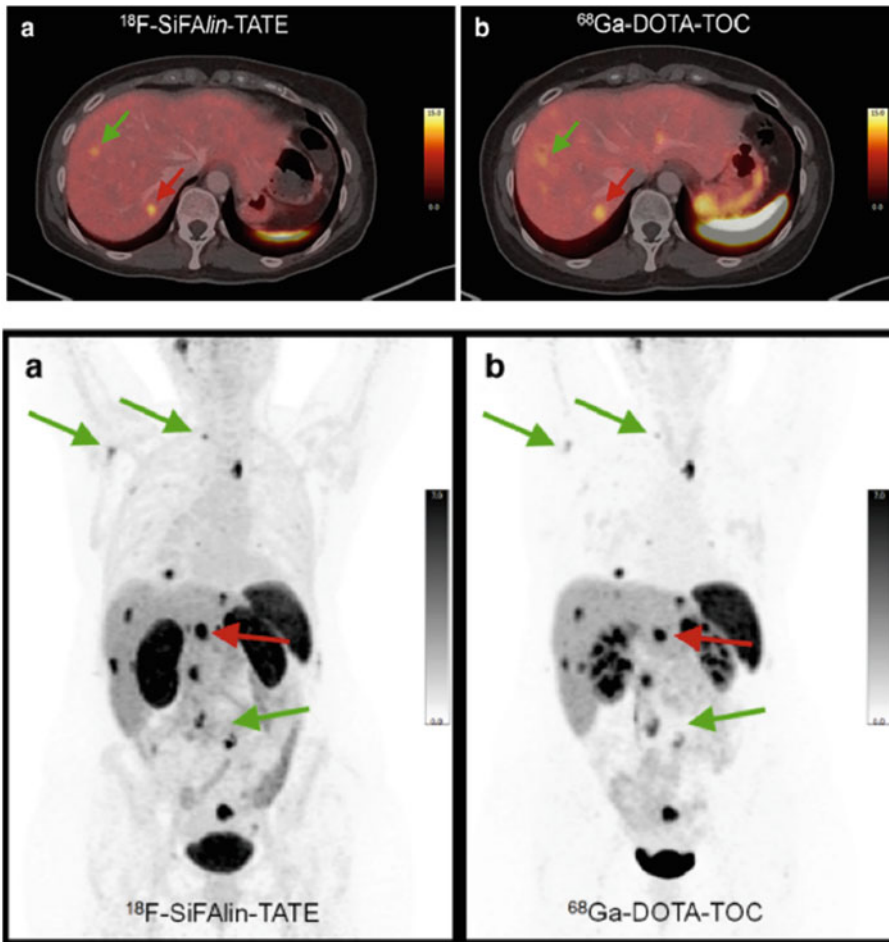
Fig. 5 Patient examples of (**a**) [^{18}F]-SiTATE and (**b**) [^{68}Ga]Ga-DOTA-TOC targeting ileum NET. (Reprinted by permission from Springer Nature: Springer Eur. J. Nucl. Med. Mol. Imaging. Reference [20])

quantity of side chains and functionalities that would potentially interact with the [18]F. Therefore, the prosthetic groups require a functional moiety that would allow it to be easy coupled to the protein such as an active ester or click chemistry amenable group [4]. A specific way of protein labeling with a prosthetic SiFA group was explored by attaching an isothiocyanate group to the SiFA building block. That way the protein in question does not need any modification prior to the SiFA attachment, since isothiocyanates are reactive with the amine groups on preexisting lysine side chains. Flourine-18 labeling of SiFA isothiocyanate compounds resulted in high radiochemical yields (~95%), and further incorporation into three varying proteins gave radiochemical yields of ~30–80% [1, 24]. Conversely, when labeling SiFA building blocks comprising active ester moieties, a challenge arose. It was found that the basic labeling conditions resulted in degradation of the
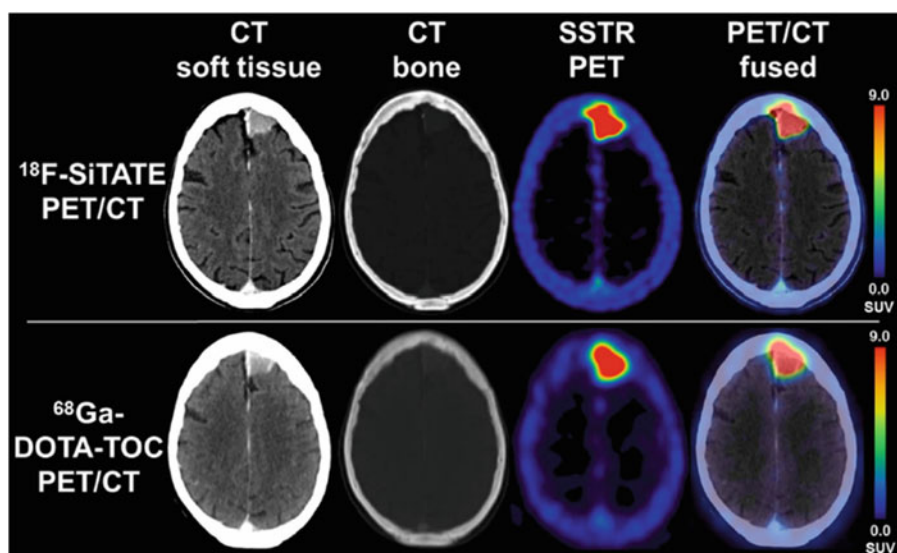
Fig. 6 Visualization of somatostatin receptors (SSTRs) on meningiomas by PET/CT using either [^{18}F]-SiTATE or [^{68}Ga]Ga-DOTA-TOC. (Reprinted by permission from Wolters Kluwer Health, Inc.: Clin. Nucl. Med. Reference [21])

compounds due to active ester hydrolysis. Thus, the acidity of the labeling mixture was altered by addition of oxalic acid [1]. In addition, the active ester moiety being situated at the *meta* position as opposed to the *para* position greatly increased the stability of the compound. Moreover, Glaser et al. have been able to show the applicability of SiFA labeling toward affibodies. They demonstrated the ability to ^{18}F-label those large biomolecules with high selectivity and efficiency [25].

1.6   Small Molecules   Due to the increased similarity in size between small molecules and the SiFA moiety, the lipophilicity issue is greatly enhanced. Yet, recent studies into negating this unfortunate consequence have shown that increasing the number of ligands relative to the number of SiFA groups in a multivalent ligand strategy may be successful. Hazari et al. used a SiFA-derivatized bivalent 5-hydroxytryptamine 1A (5-HT$_{1A}$)-selective compound with an affinity for serotonin receptors and found high uptake in areas with upregulated receptors [15, 26]. Previous studies done on silicon–[18]F analogs of FMISO used for hypoxia imaging, which seemed promising, showed low stability and low target uptake [27, 28]. Further, nucleosides and nucleotides were derivatized with SiFA for their labeling via isotopic exchange. The radiolabeling experiments resulted in average radiochemical yields ~40%, yet elevated temperatures were required [26].
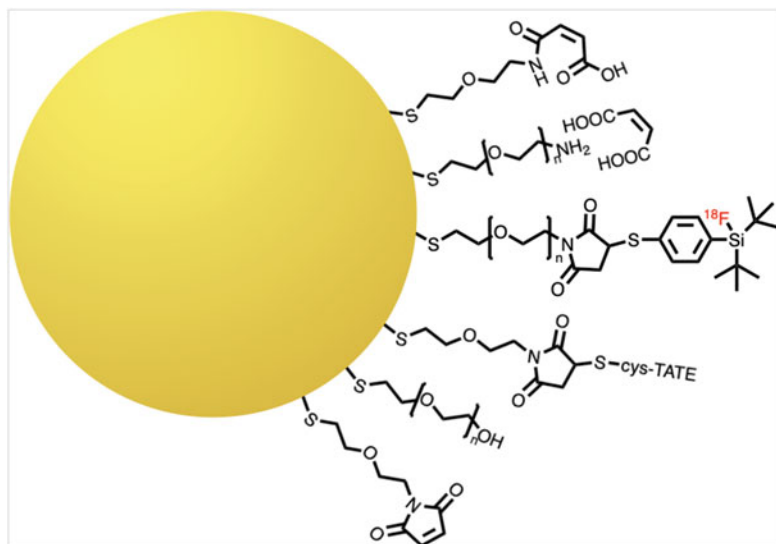
Fig. 7 Schematic drawing of [^{18}F]SiFA-labeled AuNP

1.7 Other Applications

The ease and efficiency that SiFA chemistry offers for ^{18}F-labeling makes it a good candidate for areas outside of radiotracer development as well. For instance, Schirrmacher et al. used the SiFA methodology to label maleimide-terminated PEGylated gold nanoparticles (AuNP) (Fig. 7) [29]. High radiochemical yields were obtained (60–80%), and in vivo studies using healthy rats showed substantial brain uptake. This technique with SiFA-tetrazine (SiFA-O-Tz) has been used as a sensor to demonstrate the ability to modify sp^2-hybridized graphite surfaces through an inverse electron Diels–Alder reaction.

More recently, SiFA has been introduced into a prostate-specific membrane antigen (PSMA) radiohybrid ligand by Wester et al. in 2020 [30]. Essentially, these radiohybrid PSMA inhibitors (rhPSMAs) contain a SiFA moiety as well as a chelator. Initially, the chelator was introduced as a way to increase hydrophilicity; however, it became apparent there was a greater advantage to having a molecule with both isotopic exchange and chelation-labeling strategies available. Either the SiFA moiety could be labeled with ^{18}F and a nonradioactive metal for PET imaging or the chelator could be labeled with other radioisotopes available for imaging (e.g., ^{68}Ga or ^{111}In) or therapy (e.g., ^{177}Lu) [30]. This is also useful as medical centers with no access to a cyclotron could still use ^{68}Ga to generate a nearly identical PET image [31]. Moreover, the use of ^{18}F-^{nat}Lu-rhPSMA and ^{19}F-^{177}Lu-rhPSMA as molecules with the same chemical properties can generate, for the first time, an ^{18}F-^{177}Lu "theranostic" pair, effectively combining the ability of PET diagnostics and radiotherapy into one radiopharmaceutical. This also allows for more personalized treatment plans as the radiotracer used for
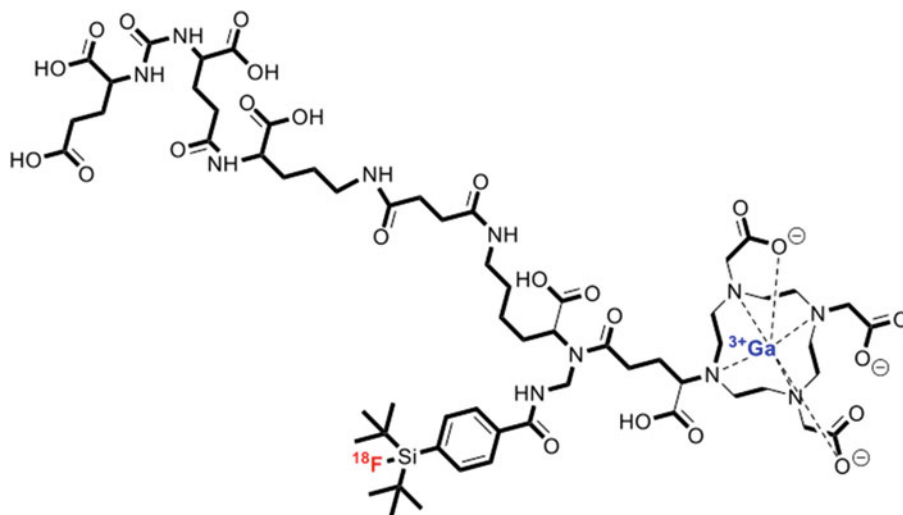
Fig. 8 Schematic drawing of [^{18}F]Ga-rhPSMA-7 [31]

imaging could be exploited as a tool for pretherapeutic dosimetry and patient stratification [30]. Interestingly, in vitro experiments with the synthesized rhPSMAs showed that they had lower lipophilicity (log P of −2.0 to −3.5) than any other SiFA compound currently reported in literature [30]. Additionally, when compared to established ^{18}F-PSMA reference compounds DCFPyL and PSMA-1007, they showed comparable uptake in most nonspecific tissues yet lower uptake in the liver in addition to higher blood levels. These results suggest that rhPSMA inhibitors have the potential to greatly enhance diagnosis and treatment options for patients suffering from prostate cancer. Further clinical studies with [18]F-[nat]Ga-rhPSMA-7 (Fig. 8) showed remarkable results in imaging high-risk primary prostate cancer, even when patients had low antigen levels [31]. One of the rhPSMA isomers ([^{18}F]Ga-rhPSMA-7.3) was identified as the best candidate for theranostic applications and is presently in phase III clinical trials. Due to its success, an automated synthesis was developed using the Munich method where the azeotropic drying step is eliminated and the entirety of the labeling process is done at room temperature [31]. Instead of azeotropic drying, they were able to use an on-cartridge drying procedure where ^{18}F was subjected to a QMA cartridge and allowed to dry rapidly on the column through purging with air and elution of anhydrous acetonitrile [31]. Further elution of the ^{18}F with K_{222} in acetonitrile resulted in almost no loss of activity (96% retained). The whole automation process uses a double-cassette setup and a nine-step procedure and has superb reliability (98.8%) and radiochemical yields (~50%) [31]. The development of an adequate automated process effectively enhances the ability to introduce SiFA-derivatized compounds into the clinic.

Overall, the SiFA methodology has come a long way since its first arrival in literature in 2006. As discussed, it presents a great improvement in the PET imaging field. The labeling procedure can be carried out under mild conditions, with fast reaction times and high selectivity. The whole synthesis and procedure is able to be highly automated as seen with $[^{18}F]$-SiTATE and $[^{18}F]$Ga-rhPSMA-7.3. The reliable and easy automation process along with the present clinical study results highlights its exceptional ability to be translated into future clinical applications.

2   Materials

1. Cyclotron produced $[^{18}F]F^-/[^{18}O]H_2O$.
2. QMA cartridge.
3. Potassium carbonate.
4. Deionized water.
5. Anhydrous acetonitrile.
6. Anhydrous ethanol.
7. [2.2.2]Cryptand (Kryptofix 2.2.2).
8. C18 cartridge.
9. HPLC.
10. HPLC C18 column.
11. RadioTLC plate scanner.

3   Methods

3.1   Azeotropic Drying

1. Pass 10 mL of 0.5 M K_2CO_3 and then 10 mL of deionized H_2O through a quaternary methyl ammonium (QMA) cartridge.
2. Turn the QMA cartridge upside down and pass the aqueous solution of $[^{18}F]F^-/[^{18}O]H_2O$ through using a male-to-male adapter.
3. Discard the eluted $[^{18}O]H_2O$.
4. Turn the cartridge back around and pass through an elution solution consisting of [2.2.2]cryptand, 0.2 M K_2CO_3, and acetonitrile.
5. Collect the first four drops into a thick-walled v-vial.
6. Heat the sealed vial to 90 °C and have a steady flow of argon passing through the vial.
7. Wait for approximately 5 min for the solvents to evaporate.

8. Add 1 mL of acetonitrile to help remove any remaining water via azeotropic co-evaporation.

9. Repeat evaporation step.

10. Once all the solvent is visibly removed, resuspend the [^{18}F] fluoride in the preferred reaction solvent.

3.2 SiFA Labeling

1. Pass 10 mL of ethanol and then 10 mL of distilled H$_2$O through a C18 cartridge.

2. Add the [^{18}F]fluoride solution to the SiFA precursor compound (100 μL, ~20–100 nmol) and allow the labeling reaction to sit at room temperature for 5 min.

3. Draw reaction solution up into a syringe that contains 9 mL 0.1 M phosphate buffer.

4. Pass the resulting solution through the C18 cartridge.

5. Pass 5 mL of distilled H$_2$O through the cartridge to wash and then 300 μL of ethanol to elute the [^{18}F]SiFA compound.

6. Dilute with 3 mL phosphate buffer for HPLC injection onto a C18 column to assess the radiochemical purity (RCP).

7. Monitor reaction by radioTLC to determine radiochemical yields (RCY).

4   Notes

All necessary precautions should be taken when working with radioactive isotopes including using lead shielding, wearing a dosimeter, checking for contamination with Geiger counters, and wearing appropriate PPE. Only the first four drops of the eluted [^{18}F]fluoride need to be taken as most of the radioactivity is eluted in those initial drops. This is important to minimize any base-related degradation to the SiFA moiety as it limits the amount of base in the reaction solution [32].

References

1. Wängler C, Kostikov A, Zhu J, Chin J, Wängler B, Schirrmacher R (2012) Silicon-[18F]fluorine radiochemistry: basics, applications and challenges. Appl Sci 2(2):277–302

2. Schirrmacher R, Bernard-Gauthier V, Schirrmacher E, Bailey JJ, Jurkschat K, Wängler C, Wängler B (2019) Silicon-based 18F-radiopharmaceuticals: from basic SiFA chemistry toward its clinical application. In: *Fluorine in life sciences: pharmaceuticals, medicinal diagnostics, and agrochemicals progress in fluorine science series.* Elsevier, pp 551–574

3. Bernard-Gauthier V, Lepage ML, Waengler B, Bailey JJ, Liang SH, Perrin DM, Vasdev N, Schirrmacher R (2018) Recent advances in 18F radiochemistry: a focus on B-18F, Si-18F, Al-18F, and C-18F radiofluorination via spirocyclic iodonium ylides. J Nucl Med 59(4):568–572

4. Jacobson O, Kiesewetter DO, Chen X (2015) Fluorine-18 radiochemistry, labeling strategies and synthetic routes. Bioconjug Chem 26(1):1–18

5. Mcbride WJ, D'Souza CA, Sharkey RM, Goldenberg DM (2012) The radiolabeling of proteins by the [18F]AlF method. Appl Radiat Isot 70(1):200–204

6. Laverman P, D'Souza CA, Eek A, Mcbride WJ, Sharkey RM, Oyen WJG, Goldenberg DM, Boerman OC (2012) Optimized labeling of NOTA-conjugated octreotide with F-18. Tumour Biol 33(2):427–434

7. Rosenthal MS, Bosch AL, Nickles RJ, Gatley SJ (1985) Synthesis and some characteristics of no-carrier added [18F]fluorotrimethylsilane. Int J Appl Radiat Isot 36(4):318–319

8. Ting R, Harwig CW, Lo J, Li Y, Adam MJ, Ruth TJ, Petrin DM (2008) Substituent effects on aryltrifluoroborate solvolysis in water: implications for Suzuki-Miyaura coupling and the design of stable 18F-labeled aryltrifluoroborates for use in PET imaging. J Org Chem 73(12):4662–4670

9. Ting R, Adam MJ, Ruth TJ, Perrin DM (2005) Arylfluoroborates and alkylfluorosilicates as potential PET imaging agents: high-yielding aqueous biomolecular 18F-labeling. J Am Chem Soc 127(38):13094–13095

10. Svoboda K (1985) Short review of specific activity phenomena. Phenomena dependent on specific activity but not changing it. J Radioanal Nucl Chem 88(1):13–29

11. Hevesy G (1923) The absorption and translocation of lead by plants: a contribution to the application of the method of radioactive indicators in the investigation of the change of substance in plants. Biochem J 17(4–5):439–445

12. Schirrmacher R, Bradtmöller G, Schirrmacher E, Thews O, Tillmanns J, Siessmeier T, Buchholz HG, Bartenstein P, Wängler B, Niemeyer CM (2006) 18F-labeling of peptides by means of an organosilicon-based fluoride acceptor. Angew Chem Int Ed 45(36):6047–6050. https://doi.org/10.1002/anie.200600795

13. Pauwels E, Cleeren F, Bormans G, Deroose CM, Leuven UZ (2018) Somatostatin receptor PET ligands – the next generation for clinical practice. Am J Nucl Med Mol Imaging 8(5):311–331

14. Waldmann CM, Stuparu AD, van Dam RM, Slavik R (2019) The search for an alternative to [68Ga]Ga-DOTA-TATE in neuroendocrine tumor theranostics: current state of 18F-labeled somatostatin analog development. Theranostics 9(5):1336–1347

15. Bernard-Gauthier V, Bailey JJ, Liu Z, Wängler B, Wängler C, Jurkschat K, Perrin DM, Schirrmacher R (2015) From

unorthodox to established: the current status of 18F-trifluoroborate- and 18F-SiFA-based radiopharmaceuticals in PET nuclear imaging. Bioconjug Chem 27(2):267–279

16. Wängler C, Waser B, Alke A, Iovkova L, Buchholz H-G, Niedermoser S, Jurkschat K, Fottner C, Bartenstein P, Schirrmacher R, Reubi J-C, Wester H-J, Wängler B (2010) One-step 18F-labeling of carbohydrate-conjugated octreotate-derivatives containing a silicon-fluoride-acceptor (SiFA): in vitro and in vivo evaluation as tumor imaging agents for positron emission tomography (PET). Bioconjug Chem 21(12):2289–2296

17. Lindner S, Wängler C, Bailey JJ, Jurkschat K, Bartenstein P, Wängler B, Schirrmacher R (2020) Radiosynthesis of [18F]SiFA*lin*-TATE for clinical neuroendocrine tumor positron emission tomography. Nat Protoc 15:3827–3843

18. Bernard-Gauthier V, Wängler C, Schirrmacher E, Kostikov A, Jurkschat K, Wängler B, Schirrmacher R (2014) 18F-labeled silicon-based fluoride acceptors: potential opportunities for novel positron emitting radiopharmaceuticals. Biomed Res Int 2014:454503

19. Niedermoser S, Chin J, Wängler C, Kostikov A, Bernard-Gauthier V, Vogler N, Soucy J-P, McEwan AJ, Schirrmacher R (2015) In vivo evaluation of 18F-SiFA*lin*-modified TATE: a potential challenge for 68Ga-DOTATATE, the clinical gold standard for somatostatin receptor imaging with PET. J Nucl Med 56(7):1100–1105

20. Ilhan H, Lindner S, Todica A, Cyran CC, Tiling R, Auernhammer CJ, Spitzweg C, Boeck S, Unterrainer M, Gildehaus FJ, Böning G, Jurkschat K, Wängler C, Wängler B, Schirrmacher R, Bartenstein P (2020) Biodistribution and first clinical results of 18F-SiFA*lin*-TATE PET: a novel 18F-labeled somatostatin analog for imaging of neuroendocrine tumors. Eur J Nucl Med Mol Imaging 47(4):870–880

21. Unterrainer M, Lindner S, Beyer L, Gildehaus FJ, Todica A, Mittlmeier LM, Jurkschat K, Wängler C, Wängler B, Schirrmacher R, Tonn JC, Albert NL, Bartenstein P, Ilhan H (2021) PET imaging of meningioma using the novel SSTR-targeting peptide 18F-SiTATE. Clin Nucl Med 46(8):667–668

22. Beyer L, Gosewisch A, Lindner S, Völter F, Mittelmeier LM, Tiling R, Brendel M, Cyran CC, Unterrainer M, Rübenthaler J, Auerhammer CJ, Spitzweg C, Böning G, Gildehaus FJ, Jurkschat K, Wängler C, Wängler B, Schirrmacher R, Wenter V, Todica A,

Bartenstein P, Ilhan H (2021) Dosimetry and optimal scan time of [18F]SiTATE-PET/CT in patients with neuroendocrine tumours. Eur J Nucl Med Mol Imaging 48(11):3571–3581

23. Lindner S, Simmet M, Gildehaus FJ, Jurkschat K, Wängler C, Wängler B, Bartenstein P, Schirrmacher R, Ilhan H (2020) Automated production of [18F] SiTATE on a Scintomics GRP™ platform for PET/CT imaging of neuroendocrine tumors. Nucl Med Biol 88–89:86–95

24. Rosa-Neto P, Wängler B, Iovkova L, Boening G, Reader A, Jurkschat K, Schirrmacher E (2009) [18F]SiFA-isothiocyanate: a new highly effective radioactive labeling agent for lysine-containing proteins. Chembiochem 10:1321–1324

25. Glaser M, Iveson P, Hoppmann S, Indrevoll B, Wilson A, Arukwe J, Danikas A, Bhalla R, Hiscock D (2013) Three methods for 18F labeling of the HER2-binding affibody molecule Z (HER2:2891) including preclinical assessment. J Nucl Med 54(11):1981–1988

26. Hazari PP, Schulz J, Vimont D, Chadha N, Allard M, Szlosek-Pinaud M, Fouquet E, Mishra AK (2014) A new SiF-Dipropargyl glycerol scaffold as a versatile prosthetic group to design dimeric radioligands: synthesis of the [18F] BMPPSiF tracer to image serotonin receptors. ChemMedChem 9:337–349

27. Bohn P, Deyine A, Azzouz R, Bailly L, Fiol-Petit C, Bischoff L, Fruit C, Marsais F, Vera P (2009) Design of silicon-based misonidazole

analogues and 18F-radiolabelling. Nucl Med Biol 36(8):895–905

28. Joyard Y, Azzouz R, Bischoff L, Papamicaël C, Labar D, Bol A, Bol V, Vera P, Grégoire V, Levacher V, Bohn P (2013) Synthesis of new 18F-radiolabeled silicon-based nitroimidazole compounds. Bioorg Med Chem 21(13):3680–3688

29. Zhu J, Chin J, Wängler C, Wängler B, Lennox RB, Schirrmacher R (2014) Rapid 18F-labeling and loading of PEGylated gold nanoparticles for in vivo applications. Bioconjug Chem 25:1143–1150

30. Wurzer A, Carlo D, Schmidt A, Beck R, Eiber M, Schwaiger M, Wester H-J (2020) Radiohybrid ligands: a novel tracer concept exemplified by 18F- or 68Ga-labeled RhPSMA inhibitors. J Nucl Med 61(5):735–742

31. Wurzer A, Carlo D, Herz M, Richter A, Robu S, Schirrmacher R, Mascarin A, Weber W, Eiber M, Schwaiger M, Wester H-J (2021) Automated synthesis of [18F]Ga-RhPSMA-7/-7.3: results, quality control and experience from more than 200 routine productions. EJNMMI Radiopharm Chem 6(41):4. https://doi.org/10.1186/s41181-021-00120-5

32. Connolly D, Bailey JJ, Ilhan H, Bartenstein P, Wangler C, Wangler B, Wuest F, Schirrmacher R (2020) 18F-labeling of radiotracers functionalized with a silicon fluoride acceptor (SiFA) for positron emission tomography. J Vis Exp 155:e60623. https://doi.org/10.3791/60623

Chapter 4

Tandem Iridium-Catalyzed C–H Borylation/Copper-Mediated Radiofluorination of Aromatic C–H Bonds with [18F]TBAF

Maria Morales, Sean Preshlock, Liam S. Sharninghausen, Jay S. Wright, Allen F. Brooks, Melanie S. Sanford, and Peter J. H. Scott

Abstract

Direct C–H functionalization of (hetero)aromatic C–H bonds with iridium-catalyzed borylation followed by copper-mediated radiofluorination of the *in situ* generated organoboronates affords fluorine-18 labeled aromatics in high radiochemical conversions and *meta*-selectivities. This protocol describes the benchtop reaction assembly of the C–H borylation and radiofluorination steps, which can be utilized for the fluorine-18 labeling of densely functionalized bioactive scaffolds.

Key words Late-stage fluorination, Fluorine-18, PET radiochemistry, Copper-mediated radiofluorination

1 Introduction

Transition-metal-catalyzed radiofluorination has emerged as a powerful method for the formation of aromatic C–18F bonds, enabling complementary electronic selectivity to traditional methods such as S_NAr radiofluorination [1, 2]. In particular, copper-mediated radiofluorination (CMRF) has become an attractive approach for the practical synthesis of 18F-labeled radiopharmaceuticals due to its advantageous operational simplicity (i.e., labeling can be conducted without rigorous exclusion of air and/or moisture) and the low-cost and toxicity of copper [3–7]. CMRF of aromatic precursors such as boronic acids and esters [8–10], organostannanes [11], iodonium salts [12], and aryl halides [13] have been studied for the late-stage radiofluorination of (hetero)aromatic substrates. Notably, organoboron precursors are most commonly used in CMRF reactions owing to a high functional group compatibility with radiofluorination conditions and the good availability of borylation methodologies [14, 15].

Fig. 1 Ir/Cu-mediated C–H radiofluorination of electronically diverse (hetero)aromatics

The radiofluorination of organoborons has been used to radio-label many different molecules for preclinical and clinical PET imaging [3], and detailed protocols have been reported for executing the technique [16, 17]. However, challenges can arise when preparing, handling, and storing these precursors long term, or when dealing with unstable organoborons, which can hamper translation to clinical applications. A convenient alternative to address these drawbacks is the nucleophilic radiofluorination of C(sp^2)–H bonds, as such precursors are more readily available and stable. However, few reports have studied the CMRF of (hetero)-aromatic C–H bonds and high selectivity is difficult in the presence of multiple C–H bonds [18, 19]. Herein, we present an operationally simple, benchtop setup for a cascade Ir/Cu-mediated C–H radiofluorination of electronically diverse (hetero)aromatics (Fig. 1) [20]. This protocol describes a *meta*-selective Ir-catalyzed C(sp^2)–H borylation that is compatible with Cu-mediated radiofluorination to achieve the synthesis of ^{18}F-labeled substrates. Overall, this one-pot transformation circumvents the isolation, handling, and storage of unstable organoboron precursors, exhibits complimentary and high selectivity for a wide substrate scope compared to other methods, and does not require stringent exclusion of air and/or moisture, demonstrating enhanced clinical applicability.

2 Materials

Conduct reactions under inert atmosphere in 1 dram/4 mL vials using PTFE and silicone-lined septa caps at the allotted temperature with a magnetic stirrer hotplate fitted with a reaction block carousel attachment. Ensure local procedures are observed with regard to radiation safety and when disposing of chemical waste.

2.1 *C–H Borylation*

1. [Ir(cod)OMe]$_2$: Store at 4 °C [Ir(cod)(OMe)]$_2$ exhibits optimal catalytic performance when obtained as a rich, lemon-yellow color. Darker colors indicate decomposition and exhibit reduced activity. Therefore, replacing the catalyst every 6 months is advised [21].

2. 3,4,7,8-tetramethyl-1,10-phenanthroline.

3. 1,3,5-trimethoxybenzene.

4. Anhydrous 2-methyltetrahydrofuran.

5. Pinacolborane (HBPin). Store HBPin at 4 °C under inert atmosphere.

6. Varian NMR spectrometer (or equivalent).

2.2 *Synthesis Module Setup*

1. General Electric TRACERLab FX$_{FN}$ automated fluorine-18 synthesis module (or equivalent).

2. Waters Sep-Pak cartridge Sep-Pak Accell Plus Quaternary Methyl Ammonium (QMA) Plus Light.

3. Deionized water, ethanol, 0.5 M KOTf aqueous solution for QMA conditioning.

4. Tetraethylammonium bicarbonate.

5. Tetrabutylammonium triflate.

6. Ethanol.

7. Deionized water.

8. Acetonitrile.

9. Anhydrous N,N-dimethylacetamide (DMA).

2.3 *Production of [^{18}F]Fluoride*

1. General Electric PETtrace cyclotron (or equivalent) equipped with a fluorine-18 target.

2. ^{18}O-Water.

2.4 *Small-Scale Radiofluorination*

1. 1-Butanol(n-butanol, nBuOH).

2. Cu(py)$_4$OTf$_2$.

3. DMA.

4. Deionized water.

5. Bioscan AR 2000 Radio-TLC scanner (or equivalent).

6. EMD Millipore TLC silica gel 60 plates (3.0 cm wide × 6.5 cm long).

7. Shimadzu LC-20 AD/T LPGEKIT HPLC system equipped with a CBM-20A controller, SIL 20AHT injector, SPD 20A UV detector, DGU 20A SR degasser, and CTO-20A column oven with an in-series B-FC-3300 radiation detector for observing gamma emissions (or equivalent).

3   Methods

3.1   C–H Borylation (see Note 1)

1. Add 3.2 mg [Ir(cod)OMe]$_2$ (4.8μmol) (*see* **Note 2**), 2.3 mg 3,4,7,8-tetramethyl-1,10-phenanthroline (tmphen, 4.8μmol), and 25 mg 1,3,5-trimethoxybenzene (0.15 mmol, NMR standard) to a 4 mL vial equipped with a stir bar. Cap the vial using a PTFE-lined screw cap.

2. For liquid arene substrates: Add 1.1 mL 2-methyltetrahydrofuran (*see* **Note 3**) to the vial and sparge with argon for ca. 2 min (*see* **Note 4**). The arene is added in **Step 4**.

3. For solid arene substrates: Add 0.55 mL 2-methyltetrahydrofuran (*see* **Note 3**) to the vial and sparge with argon for ca. 2 min (*see* **Note 4**). To a second 4 mL vial, add arene (0.54 mmol) and 0.55 mL 2-methyltetrahydrofuran and sparge with argon for ca. 2 min.

4. After sparging (*see* **Note 5**), add 70μL pinacolborane (*see* **Note 6**) (0.48 mmol) to the vial (*see* **Note 7**). For heteroaryl substrates or aryl iodide substrates, after the addition of pinacolborane, heat the vial at 60 °C, stir for 2 min, and remove from the heat source before proceeding to **Step 4**.

5. For liquid arene substrates, add arene substrate (0.54 mmol) to the reaction vial prepared in **Step 3**. For solid arene substrates, transfer the solution of arene in 2-methyltetrahydrofuran to the vial prepared in **Step 3** (*see* **Note 8**).

6. Heat the reaction vial to 80 °C (electron-rich or -neutral arenes) or keep at room temperature (electron-poor arenes) and stir overnight.

7. Allow the reaction to cool to room temperature. Analyze crude aromatic organoboronates with NMR and use in radiolabeling (Subheading 3.4) within 12 h of preparation. For NMR analysis, take a ~50μL aliquot of the reaction mixture, remove the solvent, and perform ^{1}H and ^{13}C NMR analysis using CDCl$_3$.

3.2   Synthesis Module Setup

1. Condition a Sep-Pak Accell Plus QMA Plus Light cartridge by sequentially rinsing with >6 mL ethanol, >6 mL deionized water, 10 mL 0.5 M KOTf aqueous solution, and finally 10 mL deionized water.

2. Prepare the [^{18}F]fluoride eluent solution by dissolving 2 mg tetraethylammonium bicarbonate and 15 mg of tetrabutylammonium triflate in 200μL of EtOH then dilute with 400μL of deionized water. This solution should be prepared fresh prior to use and, if using a TRACERLab FX$_{FN}$ automated fluorine-18 synthesis module, added to Vial 1.

3. Add acetonitrile (1 mL) to Vial 2.

4. Add DMA (3 mL) to Vial 3.

5. Seal the hot-cell door and proceed to production of [^{18}F] fluoride (Subheading 3.3).

3.3 Production of [^{18}F]Fluoride

1. Produce nucleophilic [^{18}F]fluoride via the ^{18}O(p,n)^{18}F nuclear reaction in a cyclotron.

2. Load ^{18}O-water (approx. 2 mL) into the cyclotron target and irradiate for 1–2 min proton beam at 55 μA.

3. After completion of irradiation, transfer the solution of [^{18}F] fluoride to a General Electric TRACERLab FX$_{FN}$ automated fluorine-18 synthesis module (or equivalent) and proceed to radiofluorination (Subheading 3.4).

3.4 Small-Scale Radiofluorination (see Notes 9 and 10)

1. Using a radiosynthesis module (e.g., GE TRACERlab FX$_{FN}$), transfer the aqueous [^{18}F]fluoride solution from the cyclotron onto the QMA cartridge and use the module's software to elute into the reactor with the [^{18}F]fluoride eluent solution.

2. Add 1 mL of acetonitrile from Vial 2 and evaporate the mixture by heating to 100 °C and drawing vacuum for 5 min and then further drying under a stream of argon while maintaining the vacuum pull for an additional 8 min (*see* **Note 11**).

3. Dissolve the [^{18}F]TBAF residue in 3 mL DMA from Vial 3, and transfer to an external vial for use outside the hot cell. Typically, 1.5 to 3.5 GBq is sufficient activity to run ca. 30 small-scale experiments utilizing 100 μL of this solution (*see* **Notes 12** and **13**).

4. Under ambient air, dispense 50 μL nBuOH into a 4 mL vial equipped with a stir bar and containing 20 μmol [Cu (OTf)$_2$(py)$_4$] dissolved in 300 μL DMA (see **Note 14**). Add 50 μL of crude borylation mixture in 2-MeTHF (see Subheading 3.1) and finally 100 μL of [^{18}F]TBAF solution in DMA. Cap the vial using a PTFE-lined screw cap (*see* **Note 15**).

5. Heat the reaction vial to 120 °C for 20 min with stirring. The reactions should be heated directly after combining the reactants. Allowing the reactants to remain in solution for prolonged periods of time in the presence of [Cu(OTf)$_2$(py)$_4$] before heating can lead to diminished yields (*see* **Note 16**). The rate of this degradation is highly substrate dependent. Allow the sample to return to room temperature and quench with 150 μL deionized water.

6. Analyze the reaction mixture by radio-TLC and radio-HPLC. Note that due to radioactive decay, the samples should be of an appropriate radioactive concentration and examined in a timely manner to obtain satisfactory signal-to-noise ratios. Typically, a 10 μL injection of a sample with a radioactivity concentration of

40–100 MBq/mL is adequate for radio-HPLC analysis and an aliquot from a sample at an activity concentration of 4–100 MBq/mL is sufficient for radio-TLC analysis. This can vary depending on the sensitivity and setup of the radioactivity detectors.

7. Work areas should be cleaned, and radioactive samples stored and allowed to decay in accordance with local regulations.

4   Notes

1. Protocol for benchtop borylation is given here. The process can alternatively be performed in an inert atmosphere drybox.

2. For long-term storage, keep solid hygroscopic reagents like [Ir(cod)OMe]$_2$ in a vacuum desiccator over drierite at room temperature.

3. Store 2-methyltetrahydrofuran over activated molecular sieves. For long-term storage (>1 month), keep reaction solvents in an mBraun N$_2$ drybox (or equivalent).

4. Use narrow gauge sparging and exit needles to avoid compromising the integrity of the cap. For example, Air-Tite 22-gauge x 4″ as sparging needle and BD 22-gauge x 1.5″ as exit needle. Sparging can be conducted with an argon-filled balloon or directly from a compressed gas cylinder. Adjust gas pressure to give a steady stream of bubbles but avoid high flow rates to prevent drastic reduction of solvent volume.

5. Remove the exit needle prior to adding pinacolborane and arene substrate. Raise the sparging needle out of the solvent but keep it in the vial during reagent addition.

6. For long-term storage of pinacolborane, blow a gentle stream of argon or nitrogen into the container for a few seconds and store at 4 °C.

7. The color of the solution should change from pale orange to dark brown upon addition of pinacolborane.

8. Perform all reagent additions and transfers using a syringe equipped with a narrow-gauge needle to avoid compromising the septum. Prior to reagent additions and transfers, first purge out the needle by drawing in and expelling argon to avoid transferring air into the reaction vial.

9. Protocol for small-scale radiolabeling using aliquots of a [^{18}F] TBAF stock solution prepared on a GE TRACERlab FX$_{FN}$ synthesis module is given here. Equivalent synthesis modules can alternatively be used.

10. Procedures should only be carried out in areas designated for the use of radioactivity and in accordance with local rules regarding the safe handling and use of radioactivity.

11. Prior to the preparation of the [^{18}F]TBAF stock solution, the GE TRACERlab FX$_{FN}$ synthesis module should be adequately cleaned in accordance with standard operating procedures and the vacuum pump and push gases should be operating at levels acceptable for routine production. Argon can be substituted with an alternative inert push gas such as nitrogen or helium. Dry, high purity gases are recommended.

12. The total amount of activity used for the preparation of this solution should be in agreement with local rules and activity limits, while also taking into account the appropriate amount of activity required for proper analysis. Typically, a concentration of 40–100 MBq/mL will be adequate for radio-HPLC analysis and 4–10 MBq/mL will be sufficient for radio-TLC analysis.

13. The volume of the stock solution can be adjusted for the required number of reactions. For single experiments requiring the entire batch of [^{18}F]TBAF, it may be beneficial to dissolve the [^{18}F]TBAF residue in the reactant solutions to keep the concentration of reactants at levels consistent to those described in **Step 6**. The higher concentration of tetraethylammonium bicarbonate may also yield lower results. Substituting the 2 mg tetraethylammonium bicarbonate in the preparation of the [^{18}F]fluoride eluent solution described in **Step 2** with 50μL of a 0.075 M aqueous tetrabutylammonium bicarbonate solution (ABX Prod. No. 808.0000.6) can improve results but is much less cost-effective. In cases where the full batch of [^{18}F]TBAF is used for a single reaction, an additional dissolution/evaporation cycle, described in **Step 4**, can lead to a more anhydrous [^{18}F]TBAF residue.

14. Electron-deficient substrates afford better yields using Cu(impy)$_4$(OTf)$_2$ (impy = imidazo[1,2-b]pyridazine) in place of Cu(py)$_4$(OTf)$_2$. Prepare Cu(impy)$_4$OTf$_2$ from Cu(OTf)$_2$ and imidazo[1,2-*b*]pyridazine as previously described [22].

15. Multiple reaction variables such as the type of Cu complex, solvent, concentrations, and molar equivalents can be varied during this step.

16. Multiple reactions can be set up and run simultaneously.

References

1. Brooks AF, Topczewski JJ, Ichiishi N, Sanford MS, Scott PJH (2014) Late-stage [F-18]fluorination: new solutions to old problems. Chem Sci 5:4545–4553

2. Sanford MS, Scott PJH (2016) Moving metal-mediated F-18-fluorination from concept to clinic. ACS Cent Sci 2:128–130

3. Wright JS, Kaur T, Preshlock S, Tanzey SS, Winton WP, Sharninghausen LS, Wiesner N, Brooks AF, Sanford MS, Scott PJH (2020) Copper-mediated late-stage radiofluorination: five years of impact on preclinical and clinical PET imaging. Clin Transl Imaging 8:167–206

4. Mossine AV, Tanzey SS, Brooks AF, Makaravage KJ, Ichiishi N, Miller JM, Henderson BD, Erhard T, Bruetting C, Skaddan MB, Sanford MS, Scott PJH (2020) Synthesis of high-molar-activity [^{18}F]6-fluoro-L-DOPA suitable for human use via Cu-mediated fluorination of a BPin precursor. Nat Protoc 15:1742–1759

5. Mossine AV, Brooks AF, Ichiishi N, Makaravage KJ, Sanford MS, Scott PJH (2017) Development of customized [^{18}F]fluoride elution techniques for the enhancement of copper-mediated late-stage radiofluorination. Sci Rep 7:233

6. Guibbal F, Isenegger PG, Wilson TC, Pacelli A, Mahaut D, Sap JBI, Taylor NJ, Verhoog S, Preshlock S, Hueting R, Cornelissen B, Gouverneur V (2020) Manual and automated Cu-mediated radiosynthesis of the PARP inhibitor [^{18}F]olaparib. Nat Protoc 15:1525–1541

7. Zischler J, Kolks N, Modemann D, Neumaier B, Zlatopolskiy BD (2017) Alcohol-enhanced Cu-mediated radiofluorination. Chem Eur J 23:3251–3256

8. Tredwell M, Preshlock SM, Taylor NJ, Gruber S, Huiban M, Passchier J, Mercier J, Genicot C, Gouverneur V (2014) A general copper-mediated nucleophilic F-18 fluorination of arenes. Angew Chem Int Ed 53:7751–7755

9. Mossine AV, Brooks AF, Makaravage KJ, Miller JM, Ichiishi N, Sanford MS, Scott PJH (2015) Synthesis of [^{18}F]arenes via the copper-mediated [^{18}F]fluorination of boronic acids. Org Lett 17:5780–5783

10. Preshlock S, Calderwood S, Verhoog S, Tredwell M, Huiban M, Hienzsch A, Gruber S, Wilson TC, Taylor NJ, Cailly T, Schedler M, Collier TL, Passchier J, Smits R, Mollitor J, Hoepping A, Mueller M, Genicot C, Mercier J, Gouverneur V (2016) Enhanced copper-mediated ^{18}F-fluorination of aryl boronic esters provides eight radiotracers for PET applications. Chem Commun 52:8361–8364

11. Makaravage KJ, Brooks AF, Mossine AV, Sanford MS, Scott PJH (2016) Copper-mediated radiofluorination of arylstannanes with [^{18}F]KF. Org Lett 18:5440–5443

12. Ichiishi N, Brooks AF, Topczewski JJ, Rodnick ME, Sanford MS, Scott PJH (2014) Copper-catalyzed [^{18}F]fluorination of (mesityl)(aryl)-iodonium salts. Org Lett 16:3224–3227

13. Sharninghausen LS, Brooks AF, Winton WP, Makaravage KJ, Scott PJH, Sanford MS (2020) NHC-copper mediated ligand-directed radiofluorination of aryl halides. J Am Chem Soc 142:7362–7367

14. Ishiyama T, Takagi J, Ishida K, Miyaura N, Anastasi NR, Hartwig JF (2002) Mild iridium-catalyzed borylation of arenes. High turnover numbers, room temperature reactions, and isolation of a potential intermediate. J Am Chem Soc 124:390–391

15. Cho JY, Tse MK, Holmes D, Maleczka RE Jr, Smith MR III (2002) Remarkably selective iridium catalysts for the elaboration of aromatic C-H bonds. Science 295:305–308

16. Mossine AV, Tanzey SS, Brooks AF, Makaravage KJ, Ichiishi N, Miller JM, Henderson BD, Skaddan MB, Sanford MS, Scott PJH (2020) Synthesis of high molar activity 6-[^{18}F]fluoro-L-DOPA suitable for human use by Cu-mediated fluorination of a BPin precursor. Nat Prot 15:1742–1759

17. Guibbal F, Isenegger PG, Wilson TC, Pacelli A, Mahaut D, Sap JBI, Taylor NJ, Verhoog S, Preshlock S, Hueting R, Cornelissen B, Gouverneur V (2020) Manual and automated Cu-mediated radiosynthesis of the PARP inhibitor [^{18}F]Olaparib. Nat Protoc 15:1525–1541

18. Lee SJ, Makaravage KJ, Brooks AF, Scott PJH, Sanford MS (2019) Copper-mediated amino-quinoline-directed radiofluorination of aromatic C-H bonds with K^{18}F. Angew Chem Int Ed 58:3119–3122

19. McCammant MS, Thompson S, Brooks AF, Krska SW, Scott PJH, Sanford MS (2017) Cu-mediated C-H ^{18}F-fluorination of electron-rich (hetero)arenes. Org Lett 19:3939–3942

20. Wright JS, Sharninghausen LS, Preshlock S, Brooks AF, Sanford MS, Scott PJH (2021) Sequential Ir/Cu-mediated method for the meta-selective C-H radioluorination of

(hetero)arenes. J Am Chem Soc 143:6915–6921

21. Preshlock SM, Ghaffari B, Maligres PE, Krska SW, Maleczka RE, Smith MS III (2013) High-throughput optimization of Ir-catalyzed C−H borylation: a tutorial for practical applications. J Am Chem Soc 135:7572–7582

22. Taylor N, Emer E, Preshlock S, Schedler M, Tredwell M, Verhoog S, Mercier J, Genicot C, Gouverneur V (2017) Derisking the Cu-mediated ^{18}F-fluorination of heterocyclic positron emission tomography radioligands. J Am Chem Soc 139:8267–8276

Chapter 5

Preparation of [^{68}Ga]GaCl$_3$ Using a Cyclotron

Melissa E. Rodnick, Carina Sollert, D. Christian Parr, Jens Frigell, Katherine Gagnon, and Peter J. H. Scott

Abstract

Recent developments in ^{68}Ga-radiopharmaceuticals, including a number of regulatory approvals for clinical use, has created a hitherto unprecedented demand for ^{68}Ga. Reliable access to enough ^{68}Ga to meet growing clinical demand using only ^{68}Ge/^{68}Ga generators has been problematic in recent years. To address this challenge, we have optimized the direct production of ^{68}Ga on a cyclotron *via* the ^{68}Zn(p,n)^{68}Ga reaction using a liquid target. This protocol describes the cyclotron-based production of [^{68}Ga]GaCl$_3$ implemented at the University of Michigan using a liquid target on GE PETtrace instrumentation. The protocol provides 56 ± 4 mCi ($n = 3$) of [^{68}Ga]GaCl$_3$ that meets the necessary quality control criteria to use for the preparation of ^{68}Ga-radiopharmaceuticals for human use.

Key words Radiotheranostics, Gallium-68, Cyclotron-produced gallium-68, PSMA-11

1 Introduction

Nuclear medicine is entering into a new age of radiotheranostics in which precision diagnostic imaging with positron emission tomography (PET) is combined with targeted radiotherapeutics to enable precision therapy in diseases such as cancer [1]. Given the relatively straightforward chemistry development offered with radioactive metal ions (radiometals), there has been significant focus on the development of theranostics consisting of a targeting ligand decorated with a chelating group that complexes radioactive metal ions selected for diagnostic (e.g., ^{64}Cu, ^{68}Ga) or therapeutic (e.g., ^{225}Ac, ^{213}Bi (alpha), ^{177}Lu, ^{90}Y (beta)) applications [2]. Initial efforts concentrated on the development of radiometal theranostic pairs targeting somatostatin receptors (SSTRs) for PET imaging and radiotherapeutic management of neuroendocrine tumors (NETs) [3]. In the past 5 years in the United States, [^{68}Ga]Ga-DOTA-TATE (NETSPOT) [4], [^{68}Ga]Ga-DOTA-TOC [5], [^{64}Cu]Cu-DOTA-TATE (Detectnet) [6], and [^{177}Lu]Lutathera

[7] were approved by the US FDA, while the European Union approved [^{68}Ga]Ga-DOTA-TOC (SomaKIT TOC) and Lutathera (Fig. 1). Subsequently, [^{68}Ga]Ga-PSMA-11 has also been approved by the FDA for imaging of prostate cancer [8], along with [^{177}Lu]Lu-PSMA-617 for treatment. [^{225}Ac]Ac-PSMA-617 is in advanced clinical trials for alpha therapy of prostate cancer [9]. Translation of numerous other radiotheranostics is also underway, with theranostic agents targeting C-X-C chemokine receptor type 4 (CXCR4) ligands [10] and, most recently, fibroblast activation protein inhibitors (FAPI) [11] also entering clinical trials (Fig. 1).

To date, diagnostic radiopharmaceuticals based on PET radiometals have typically been radiolabeled with ^{68}Ga (89% β+, $t_{1/2}$ = 68 min) (Fig. 1) and, reflecting this, there has been a surge in demand for access to the radionuclide in recent years. Historically, for agents targeting SSTRs, ^{68}Ga has usually been eluted from a ^{68}Ge/^{68}Ga generator, a process that can easily be implemented in PET facilities that do not own a cyclotron [12]. However, the unprecedented demand for [^{68}Ga]Ga-PSMA-11 expected after approval of a prostate cancer radiotherapeutic, as well as the newer agents in clinical trials, is further driving demand for ^{68}Ga and highlights the need for access to a reliable (and economical) supply of the radionuclide. While generators offer operational simplicity for ^{68}Ga-tracer production, there are certain limitations:

- Current generators cost ~ $100,000.00 USD and typically have a maximum activity (1.85 GBq, 50 mCi) that restricts elution to 4 h increments (i.e., 2 production runs *per* day with 2–4 doses *per* day).

- Commercial supply has not kept pace with the clinical demand and lead times for generator delivery can be significant (up to 18 months [13]).

Meeting the growing demand for ^{68}Ga is challenging using generators alone. Thus, additional sources of ^{68}Ga are required to meet the current and future patient demand [13]. To this end, we have investigated the direct production of ^{68}Ga on a cyclotron *via* the ^{68}Zn(p,n)^{68}Ga reaction [14]. This approach is being increasingly used around the world, evidenced by recent research publications [15–25] and publication of a European Pharmacopeia monograph for the direct accelerator-based production of [^{68}Ga]GaCl3 [26]. Moreover, the International Atomic Energy Agency (IAEA) has published a technical document in support of direct production of ^{68}Ga *via* liquid (hundreds of millicuries) and solid targets (multiple Curies) [27], and also begun a coordinated research project on cyclotron production of ^{68}Ga [28]. Notably, two of the FDA-approved ^{68}Ga radiotracers ([^{68}Ga]Ga-DOTA-TOC and [^{68}Ga]Ga-PSMA-11) have explicit approval for production using cyclotron-based ^{68}Ga.
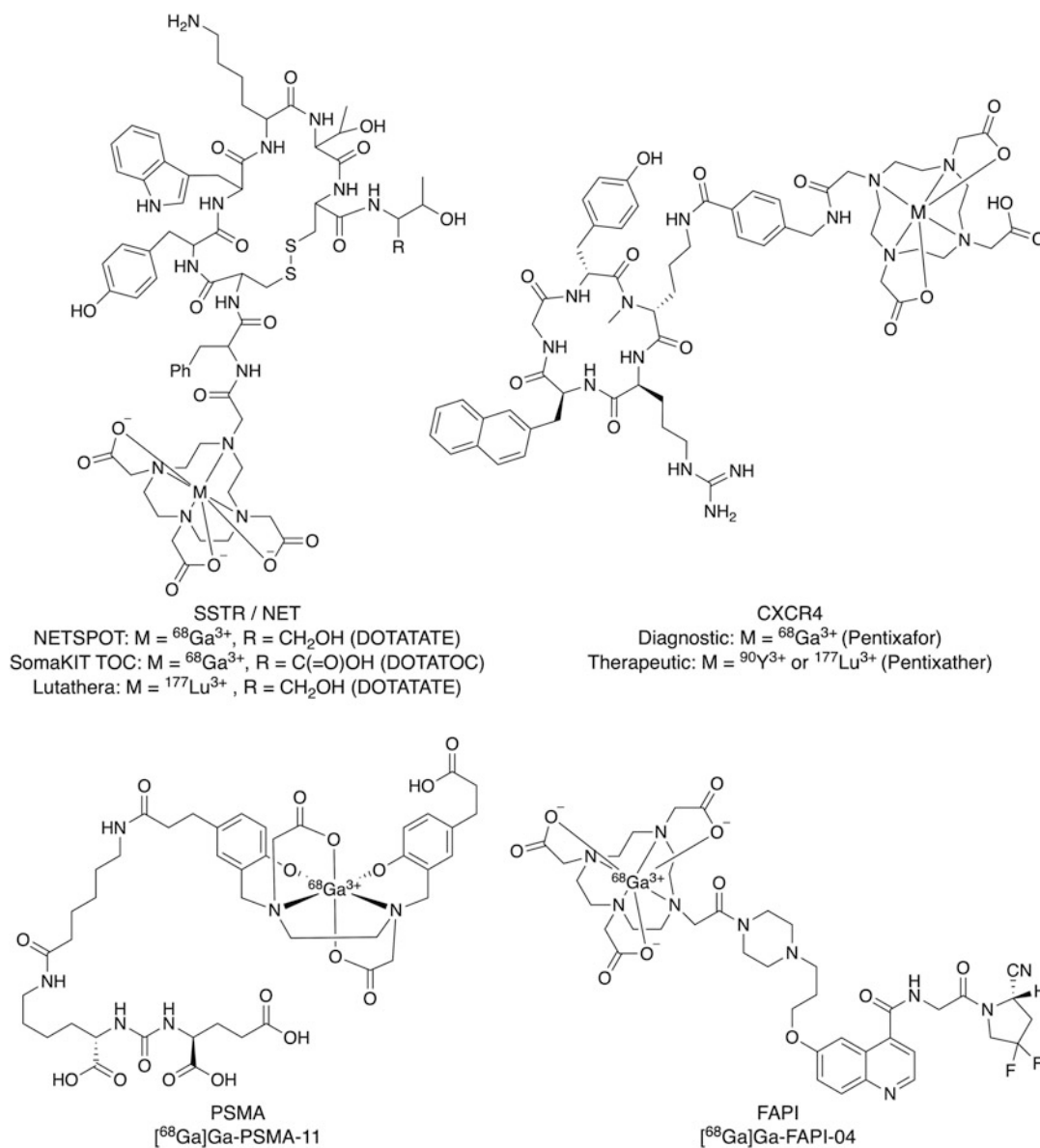
Fig. 1 New theranostic agents. (Reproduced from Ref. [14] under a Creative Commons License)

This protocol describes the cyclotron production of ^{68}Ga from a liquid target. The workflow is analogous to production of [^{18}F] fluoride and is compatible with laboratory setups in existing PET radiopharmaceutical production centers. The protocol provides 56 ± 4 mCi ($n = 3$) of [^{68}Ga]GaCl$_3$ at end-of-synthesis that meets the necessary quality control criteria (Table 1) to use for the preparation of ^{68}Ga-radiopharmaceuticals for human use.

Table 1
Quality control data for [^{68}Ga]GaCl$_3$ validation runs (*see* Note 9)

Quality control test (*see* Note 9)	Release criteria (U of Michigan)	Batch 1	Batch 2	Batch 3
Radiochemical yield at end-of-synthesis	Record for information	52	60	57
Radiochemical purity [^{68}Ga]GaCl$_3$ (rTLC)	≥95	99	98	98
Rf [^{68}Ga]GaCl$_3$ (TLC)	≤0.2	<0.2	<0.2	<0.2
Rf Ref B^a (TLC)	≥0.7	>0.7	>0.7	>0.7
pH	<2	<2	<2	<2
Visual inspection	Clear, colorless, free of particulates	Passed	Passed	Passed
Radionuclidic identity (half-life)	64.6–71.4 min	67.2	68.8	69.1
Endotoxin analysis	≤58.3 EU/mL^b	<2	<2	<2
Residual Fe$^{2+/3+}$ (*see* Note 10)	<10 μg/GBq	< 5 μg/GBq	< 5 μg/GBq	<5 μg/GBq
Residual Zn^{3+} (*see* Note 11)	<10 μg/GBq	<1.25 μg/GBq	<1.25 μg/GBq	<1.25 μg/GBq
Radionuclidic purity (MCA) @ EOB	98% ^{c}	99.8	99.8	99.8

^{a}Reference solution B (Pentetic acid solution) from the European Pharmacopoeia (Gallium (^{68}Ga) chloride (accelerator-produced) solution for radiolabeling [26]); ^{b} for a 3 mL batch; ^{c}<2% combined ^{66}Ga and ^{67}Ga at end of bombardment

2   Materials

2.1   Prepare Liquid Target Solution

1. [^{68}Zn]Zn(NO$_3$)$_2$.
2. 0.3 M HNO$_3$.
3. 4 mL borosilicate glass vial with PTFE septum.
4. Ultrapure water.

2.2   Produce and Purify ^{68}Ga

1. General Electric PETtrace cyclotron (or equivalent) equipped with a gallium-68 liquid target.
2. ZR hydroxamate-based and TK200 resins (Triskem).
3. Nitric acid.
4. Hydrochloric acid.
5. Sodium chloride (optional).
6. Optionally, if labeling with chelators such as DOTA or NOTA which are more sensitive to trace metal impurities than the

HBED-CC chelator, an additional anion exchange resin may be warranted in between the ZR and TK200 resins [29].

2.3 Quality Control of ^{68}Ga

1. Capintec dose calibrator or equivalent.
2. Bioscan AR 2000 Radio-TLC scanner or equivalent.
3. ColorpHast pH Strips or equivalnet pH paper.
4. MQuant test strips for Fe and Zn (Merck).
5. Charles River Endosafe PTS endotoxin system (or equivalent).
6. Canberra multichannel analyzer (or equivalent).

3 Methods

All hazardous laboratory chemicals should be used by trained personnel under the supervision of an environmental health and safety officer. Radioactivity can only be used with institutional, state, and/or federal authorization and according to ALARA principles. Users should be properly shielded against radiation. All reactions involving radioactivity should be performed in a lead-shielded fume hood or hot cell, according to appropriate institutional, state, and/or federal radiation safety guidelines. Workers handling radioactive material must ensure that all appropriate personal protective equipment is worn and that shielding, dosimeters, and survey meters are always used. Ensure local procedures are observed when disposing of radioactive and chemical waste.

3.1 Prepare Liquid Target Solution

1. Add isotopically enriched [^{68}Zn]ZnO (2 g, elemental weight) to ultrapure water (~10 mL) in a falcon tube and vortex to form a slurry.
2. Slowly add 70% nitric acid (1 mL) and vortex for 20 s. Repeat with additional nitric acid (3×1 mL and 1×0.3 mL aliquots for the total cumulative volume of 70% nitric acid added $= 4.3$ mL).
3. Add ultrapure water so the final solution volume is 30 mL to yield a 1.0 M solution of [^{68}Zn]Zn(NO$_3$)$_2$ in 0.3 M HNO$_3$.
4. Vortex the final solution for 4 min, let the solution stand for at least 4 h and then filter through a 0.22 μm Millex-GS (or equivalent) filter prior to irradiation. Store for up to 6 months at room temperature in the dark.

3.2 Produce and Purify ^{68}Ga

1. Produce gallium-68 in the cyclotron via the ^{68}Zn(p,n)^{68}Ga nuclear reaction. Load ~2.2 mL of 1.0 M solution of [^{68}Zn]Zn(NO$_3$)$_2$ in 0.3 M HNO$_3$ solution prepared in Subheading 3.1 into the ^{68}Ga target and irradiate (30–40 μA for ~60 min) (*see* **Note 1**). Upon completion of irradiation, transfer the
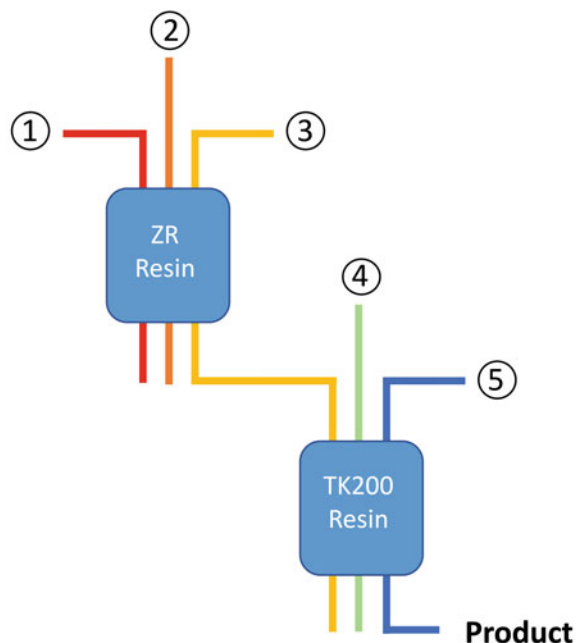
Process steps:

0. Condition ZR cartridge with 0.1 M HNO_3 (7 mL) and TK200 resin with sterile water for injection (7 mL) followed by 1.75 M HCl (4 mL) prior to use.
1. Trapping of ^{68}Ga on a hydroxamate-based resin (2 mL [~700 mg] ZR resin, Triskem) —
2. Rinsing of the resin with 0.1 M HNO_3 (15 mL) to remove residual zinc —
3. Elution onto a TOPO-based resin (2 mL [~700 mg]) TK200 resin, Triskem) with 1.75 M HCl (5-6 mL) —
4. Optional: Rinse with 3.5 mL 2 M NaCl in 0.13 M HCl to decrease residual acid —
5. Final elution with water, volumes of which can be varied, to yield [^{68}Ga]$GaCl_3$ in the desired formulation (e.g. 5 mL of 0.1 M HCl) —

Fig. 2 Two-column approach for ^{68}Ga chemical separation. (Reproduced from Ref. [14] under a Creative Commons License)

solution of ^{68}Ga/Zn in HNO_3 to the FASTlab synthesis module, or equivalent, with suitable automated synthesis sequence (*see* **Note 2**).

2. Dilute the ^{68}Ga target solution with water from the synthesis unit (5.5 mL) to achieve a nitric acid concentration of <0.1 M, which is necessary for subsequent processing.

3. Pass the solution of ^{68}Ga through 2 mL [~ 700 mg] of theZR hydroxamate-based resin (Triskem) to trap ^{68}Ga (Fig. 2).

4. Rinse the ZR resin with 0.1 M HNO_3 (15 mL) to remove residual ^{68}Zn (Fig. 2).

5. Elute ^{68}Ga off the ZR resin with 1.75 M HCl (5–6 mL) (Fig. 2), prepared from hydrochloric acid 4 M (From Trace Metals HCl) solution (Aqua Solutions, cat. no. AM426).

6. Transfer the eluent through 2 mL [~ 700 mg] of the TK200 resin (Triskem) to trap ^{68}Ga onto the TK200 (Fig. 2).

7. Optional step: Rinse TK200 resin with 3.5 mL 2 M NaCl in 0.13 M HCl to decrease residual acid (Fig. 2).

8. Elute [^{68}Ga]GaCl$_3$ from the TK200 resin with water (3 mL) (Fig. 2) (*see* **Note 3**).

9. Transfer [^{68}Ga]GaCl$_3$ through a Cathivex 0.22 μm sterile filter (or equivalent) into a sterile dose vial (or other reaction vessel for downstream chemistry).

10. Aseptically remove 0.5 mL of the batch and place it into the 2 mL sterile QC vial for QC testing.

11. Complete quality control testing according to local regulatory requirements and using published procedures (see Table 1 for results of QC testing) (*see* **Note 4**).

12. Use [^{68}Ga]GaCl$_3$ to prepare desired ^{68}Ga-radiopharmaceuticals (*see* **Notes 5–8**).

3.3   Quality Control Testing of ^{68}Ga

1. Establish radiochemical yield by measuring the dose activity using a dose calibrator.

2. Determine radiochemical purity using radio-TLC.

3. Complete a visual inspection to determine dose is clear, colorless, and free of particulates.

4. Determine the pH of the solution by applying a sample to pH paper and comparing to the provided scale.

5. Confirm radionuclidic identity by measuring the activity in a sample over a defined time period using a dose calibrator, and verifying that the half-life of the solution matches that of ^{68}Ga (68 min).

6. Verify the solution is free of bacterial endotoxins via the limulus amoebocyte lysate (LAL) test using a Charles River Endosafe (or equivalent) system.

7. Determine radionuclidic purity using a multichannel analyzer (MCA) or equivalent test.

8. Determine residual metal content in the solution using dedicated test strips or ICP-MS.

3.4   Site Cleaning

1. Work areas and synthesis module should be cleaned, and radioactive samples stored and allowed to decay in accordance with local regulations.

2. For optimal liquid target performance, a conditioning run should be completed daily. Load ~2.2 mL 0.6 M HNO$_3$ into the gallium-68 target and irradiate with a 30–40 μA proton beam for >15 min. Upon completion of irradiation, transfer the solution to waste and allow to decay in place (*see* **Note 2**).

4 Notes

1. Enriched ^{68}Zn is utilized to produce ^{68}Ga in a cyclotron (GE PETtrace or equivalent) via the ^{68}Zn(p,n)^{68}Ga reaction with energy degraded or selected to reduce the ^{68}Zn (p,2n)^{67}Ga competing reaction (e.g., ~13–14 MeV). The protocol for 1 h irradiation of a single liquid target is given here. Irradiation time can be reduced if less activity is needed, or additional targets can be irradiated simultaneously if more activity is needed.

2. Significant ^{13}N is generated during the production of ^{68}Ga and target conditioning via the ^{16}O(p,α)^{13}N reaction. Proper infrastructure configuration and containment must be considered.

3. Volume of water can be varied to yield [^{68}Ga]GaCl$_3$ in the desired formulation (e.g., 5 mL of 0.1 M HCl).

4. Complete QC testing using methods outlined in Subheading 3.3 as well as previously published procedures [14].

5. For example, [^{68}Ga]Ga-DOTA-TATE and [^{68}Ga]Ga-PSMA-11 can be prepared as previously described [14, 27].

6. Radiopharmaceuticals can be prepared by transferring [^{68}Ga]GaCl$_3$ to a synthesis module or a kit. Alternatively, depending on the synthesis module and process, it may be possible to execute both the [^{68}Ga]GaCl$_3$ purification and subsequent labeling in a single module/process [14].

7. Procedures should only be carried out in areas designated for the use of radioactivity and in accordance with local rules regarding the safe handling and use of radioactivity.

8. Radiolabeling with radiometals and chelators is a process which is generally sensitive to trace metal impurities. Suitable quality reagents and consumables (e.g., needles) and material handling/processing should be considered to minimize introduction of such impurities throughout ^{68}Ga production and radiolabeling.

9. Local quality assurance and quality control requirements should be met when preparing radioactive materials for human use.

10. Determined on validation runs and/or annual process verification runs using MQuant test strips or ICP-MS.

11. Determined on validation runs and/or annual process verification runs using ICP-MS.

References

1. Herrmann K, Schwaiger M, Lewis JS, Solomon SB, McNeil BJ, Baumann M, Gambhir SS, Hricak H, Weissleder R (2020) Radiotheranostics: a roadmap for future development. Lancet Oncol 21:e146–e156

2. Qaim SM, Scholten B, Neumaier B (2018) New developments in the production of theranostic pairs of radionuclides. J Radioanal Nucl Chem 318:1493–1509

3. Pencharz D, Gnanasegaran G, Navalkissoor S (2018) Theranostics in neuroendocrine tumours: somatostatin receptor imaging and therapy. Br J Radiol 91:20180108

4. FDA approves new diagnostic imaging agent to detect rare neuroendocrine tumors. [new release]. https://www.fda.gov/news-events/press-announcements/fda-approves-new-diagnostic-imaging-agent-detect-rare-neuroendocrine-tumors. Published 1 Jun 2016; Accessed 2 Jun 2021

5. Sunderland JJ (2020) The Academic NDA: justification, process, and lessons learned. J Nucl Med 61:480–487

6. RadioMedix and Curium Announce FDA Approval of Detectnet (copper Cu 64 dotatate injection) in the U.S. [news release]. https://www.curiumpharma.com/2020/09/08/radiomedix-and-curium-announce-fda-approval-of-detectnet-copper-cu-64-dotatate-injection-in-the-u-s/. Published 7-Sept-2020; Accessed 2 Jun 2021

7. Hennrich U, Kopka K (2019) Lutathera®: The first FDA- and EMA-approved radiopharmaceutical for peptide receptor radionuclide therapy. Pharmaceuticals (Basel) 12:114

8. Carlucci G, Ippisch R, Slavik R, Mishoe A, Blecha J, Zhu S (2021) ^{68}Ga-PSMA-11 NDA approval: a novel and successful academic partnership. J Nucl Med 62:149–155

9. Wester HJ, Schottelius M (2019) PSMA-targeted radiopharmaceuticals for imaging and therapy. Semin Nucl Med 49:302–312

10. Kircher M, Herhaus P, Schottelius M, Buck AK, Werner RA, Wester HJ, Keller U, Lapa C (2018) CXCR4-directed theranostics in oncology and inflammation. Ann Nucl Med 32:503–511

11. Calais J (2020) FAP: the next billion dollar nuclear theranostics target? J Nucl Med 61:163–165

12. Fani M, André JP, Maecke HR (2008) ^{68}Ga-PET: a powerful generator-based alternative to cyclotron-based PET radiopharmaceuticals. Contrast Media Mol Imaging 3:67–77

13. Cutler CS, Minoshima S. (2018) Shortage of Germanium68/gallium68 generators in the United States. https://s3.amazonaws.com/rdcms-snmmi/files/production/public/Ga68%20shortage%20letter.pdf. Accessed 1 Jun 2021

14. Rodnick ME, Sollert C, Stark D, Clark M, Katsifis A, Hockley BG, Parr DC, Frigell J, Henderson BD, Abghari-Gerst M, Piert MR, Fulham MJ, Eberl S, Gagnon K, Scott PJH (2020) Cyclotron-based production of ^{68}Ga, [^{68}Ga]GaCl$_3$, and [^{68}Ga]Ga-PSMA-11 from a liquid target. EJNMMI Radiopharm Chem 5:25

15. Alves F, Alves VHP, Do Carmo SJC, Neves ACB, Silva M, Abrunhosa AJ (2017) Production of copper-64 and gallium-68 with a 481 medical cyclotron using liquid targets. Mod Phys Lett A 32:1740013

16. Engle JW, Lopez-Rodriguez V, Gaspar-Carcamo RE, Valdovinos HF, Valle-Gonzalez M, Trejo-Ballado F et al (2012) Very high specific activity ^{66}/^{68}Ga from zinc targets for PET. Appl Radiat Isot 70:1792–1796

17. Graves SA, Engle JW, Eriksson TE, Gagnon K (2018) Dosimetry of cyclotron-produced [^{68}Ga]Ga-PSMA-11, [^{68}Ga]Ga-DOTA-TATE, and [^{68}Ga]Ga-DOTA-TOC. J Nucl Med 59(Suppl. 1):1003

18. Jensen M, Clark JC. (2011) Direct production of Ga-68 from proton bombardment of concentrated aqueous solutions of [Zn-68] Zinc Chloride. In The 13th International Workshop on Targetry and Target Chemistry Proceedings by Horoun S, Givskov and Jensen M (Eds). Risø DTU, National Laboratory for Sustainable Energy, Technical University of Denmark. Roskilde. 288–292. Available online: https://inis.iaea.org/collection/NCLCollectionStore/_Public/43/006/43006750.pdf. Accessed 12 Aug 2020

19. Lin M, Waligorski GJ, Lepera CG (2018) Production of curie quantities of ^{68}Ga with a medical cyclotron via the ^{68}Zn(p,n)^{68}Ga reaction. Appl Radiat Isot 133:1–3

20. Nair M, Happel S, Eriksson T, Pandey M, DeGrado T, Gagnon K (2017) Cyclotron production and automated new 2-column processing of [^{68}Ga]GaCl$_3$. Eur J Nucl Med Mol Imaging 44(Suppl 2):S119–S956

21. Pandey MK, Byrne JF, Jiang H, Packard AB, DeGrado TR (2014) Cyclotron production of ^{68}Ga via the ^{68}Zn(p,n) ^{68}Ga reaction in aqueous solution. Am J Nucl Med Mol Imaging 4:303–310

22. Pandey MK, Byrne JF, Schlasner KN, Schmit NR, DeGrado TR (2019) Cyclotron production of ^{68}Ga in a liquid target: Effects of solution composition and irradiation parameters. Nucl Med Biol 74/75:49–55

23. Riga S, Cicoria G, Pancaldi D, Zagni F, Vichi S, Dassenno M et al (2018) Production of Ga-68 with a General Electric PETtrace cyclotron by liquid target. Phys Med 55:116–126

24. Zeisler S, Limoges A, Kumlin J, Siikanen J, Hoehr C (2019) Fused zinc target for the production of gallium radioisotopes. Instruments 3:10

25. Sadeghi M, Kakavand T, Rajabifar S, Mokhtari L, Rahimi-Nezhad A (2009) Cyclotron production of ^{68}Ga via proton-induced reaction on ^{68}Zn target. Nukleonika 54:25–28

26. Gallium (^{68}Ga) Chloride (accelerator produced) solution for radiolabelling. European Pharmacopoeia 2020;10(Suppl. 10.3): 4864–4865

27. International Atomic Energy Agency (2019) Gallium-68 Cyclotron Production, IAEA-TECDOC-1863. IAEA, Vienna

28. New CRP: Production of Cyclotron-Based Gallium-68 Radioisotope and Related Radio-pharmaceuticals (F22073). https://www.iaea.org/newscenter/news/new-crp-production-of-cyclotron-based-gallium-68-radioisotope-and-related-radiopharmaceuticals-f22073. Accessed 2 Jun 2021

29. Rinne SS, Abouzayed A, Gagnon K, Tolmachev V, Orlova A (2021) ^{66}Ga-PET-imaging of GRPR-expression in prostate cancer: production and characterization of [^{66}Ga]Ga-NOTA-PEG$_2$-RM26. Sci Rep 11:3631

Chapter 6

Transition and Post-Transition Radiometals for PET Imaging and Radiotherapy

Caterina Ramogida and Eric Price

Abstract

Radiometals are an exciting class of radionuclides because of the large number of metallic elements available that have medically useful isotopes. To properly harness radiometals, they must be securely bound by chelators, which must be carefully matched to the radiometal ion to maximize radiolabeling performance and the stability of the resulting complex. This chapter focuses on practical aspects of radiometallation chemistry including chelator selection, radiolabeling procedures and conditions, radiolysis prevention, purification, quality control, requisite equipment and reagents, and useful tips.

Key words Radiometals, Bifunctional chelators, PET, TRT, Radiolabeling

1 Introduction

There are a large number of metal and metalloid elements with useful radioactive isotopes (radionuclides) for potential use in PET imaging via positron emission, and targeted radiotherapy via emission of *alpha particles*, *beta particles*, or Auger electrons. In order to utilize radiometals for radiopharmaceutical purposes, they must be incorporated into a drug delivery compound that has affinity for a specific tissue or disease type. The term "radiolabeling" refers to a radiometal being incorporated into such drug compounds. The most common way to incorporate an inorganic nuclide into a radiopharmaceutical is via the bifunctional chelate (BFC) strategy, in which a disease delivery molecule (a.k.a. targeting vector) is covalently attached to a BFC. The BFC has the dual capability of (1) being chemically reactive for bioconjugation (attachment to a targeting vector) and (2) possessing a chelate for the stable attachment of a radiometal ion (Fig. 1). The terms "chelator" and "ligand" are used interchangeably.

This methods chapter describes the general theory and techniques used for radiometal labeling, radiolabeling yield analysis,
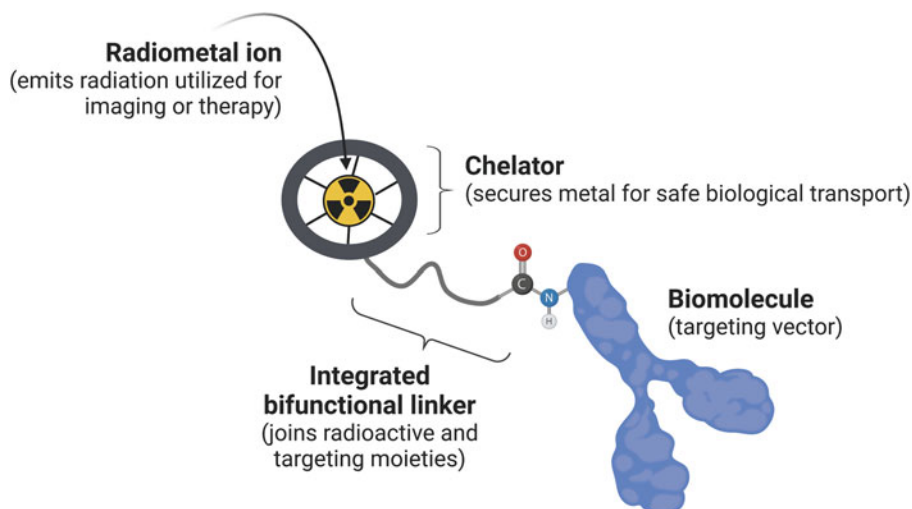
Fig. 1 Depiction of the bifunctional chelate strategy. (Figure created using BioRender.com)

tracer purification, and quality control analysis. A selection of the most common and attractive radiometal ions have been selected; however, many of the methods described herein can be transferred to other radiometal ions. The general premise, which is described in detail in the Methods section, is to prepare a solution of chelator or bioconjugate in buffer, to which radiometal (typically in dilute acid) is added. Following incubation/reaction for a certain amount of time and at an appropriate temperature, the incorporation yield of the radiometal (% radiochemical yield, %RCY) can be determined by chromatography (e.g., thin layer chromatography, TLC, or high-pressure liquid chromatography, HPLC). If needed, the radiotracer can be subsequently purified (e.g., by HPLC, or size-exclusion chromatography, or C18 plug), and quality control performed afterwards. Radiolytic protectant may be added before the radiometal is added or after the radiotracer is purified.

Before we delve into the experimental protocols and technical details, pertinent background information has been provided for the reader so that one understands the importance of each step in radiometal labeling.

1.1 Radiometals and Considerations for Radiolabeling

An important concept in radiometal chemistry is that different isotopes (radioactive and stable) of the same element possess effectively identical chemistry. This means that the solubility, pK_a, and ligand affinity are the same. As such, if a non-radioactive isotope of a metal is available, we can prepare and study ligand complexes and expect that the behavior will be the same with a radioactive isotope of that metal. One factor that will be drastically different is the concentration, as the mole/mass quantity of radionuclides is tiny (e.g., nmol-pmol) and the ligand is always in excess. The oxidation

state of most medically relevant radiometals is not easily changed, as they possess high enough standard reduction potentials to be reduction/oxidation inactive in living systems; notable exceptions include technetium and copper.

As radiometals are typically radiolabeled in aqueous buffers in varying pH and molarity, both the pH of the buffer and the pK_a of the metal ion is very important. The speciation curve of a metal ion shows the pH ranges at which different hydrates/hydroxides are formed and can guide the selection of appropriate pH buffers for optimum solubility and radiolabeling yields. Many metal ions such as Ga^{3+}, In^{3+}, and Zr^{4+} have a propensity to form hydroxide complexes at neutral pH ranges, which are insoluble and inhibit ligand binding. For example, the metal ions Y^{3+} ($pK_a = \sim 7.7$) and Lu^{3+} ($pK_a = \sim 7.6$) are not as acidic (less solvent activation) or prone to hydrolysis as metal ions such as Ga^{3+} ($pK_a = \sim 2.6$) or Zr^{4+} ($pK_a = \sim 0.22$) [1, 2]. A lower pK_a value means strong solvent activation effects, which means increasing polarization of coordinated water molecules and a decrease in the pK_a of those coordinated waters (more acidic). The full speciation curve of a metal ion provides more information; for example, above pH 2–3 the metal ions Y^{3+}, Lu^{3+}, Ga^{3+}, and In^{3+} still have a tendency to form insoluble $[M(OH)_3]$ species. Zr^{4+} has much more complicated aqueous chemistry, where it tends to form a mixture of insoluble hydroxides (including hydroxo-bridged species) [2, 3]. The extremely small quantity of radiometal ions (~nmol-pmol) present in radiolabeling reactions render the system into extremely dilute conditions. This dilution allows even insoluble metal hydroxide species to retain at least partial solubility during radiolabeling reactions, which is one reason why gallium-68 can be radiolabeled effectively at pH 4–5 even though its speciation curve would suggested only the presence of insoluble $Ga(OH)_3$ at those pH ranges. As such, a majority of radiometals are typically formulated in solutions of 0.01 or 0.1 M HCl or HNO_3 to ensure uniform speciation and prevent the formation of insoluble hydroxides (zirconium-89 typically in oxalic acid, 1.0 M).

Despite the possibility of forming insoluble hydroxide species above pH ~2–4, the buffers used for radiolabeling with a majority of radiometals are typically between pH 4 and 7. This is partially because at low pH (e.g., 1–3), the acidic coordinating groups of ligands (e.g., carboxylic acids: $pK_a \sim 4–5$, hydroxamates: $pK_a \sim 9$) may become protonated, a process which can disrupt the coordination of the radiometal. Further, secondary and tertiary amines can become protonated, forming positive charges which could repel radiometal ions as they are all cationic. The reason that zirconium-89 is typically radiolabeled at pH 7.0–7.5 is because hydroxamic acid groups are typically used for coordination (e.g., desferrioxamine, DFO), which have high pK_a values of ~9–10 (some aryl hydroxamic acids being in the 8–9 range).

All of these factors considered together, the take-home lesson is that the pH of both the pure radiometal solution and of the radiolabeling buffer are very important and often need optimization to ideally match both the specific radiometal and the specific ligand being used. An ideal radiolabeling pH will satisfy the following conditions as much as possible:

1. Be somewhere in the middle of the pK_a values of your specific ligand's ionizable functional groups so that amine protonation is minimized and oxygen deprotonation is maximized (although oxygen deprotonation is not strictly required for metal ion chelation).

2. Minimize the formation of insoluble metal hydroxides species.

3. Be gentle enough to ensure the stability of your conjugated targeting vector (e.g., antibody, peptide, nanoparticle).

When considering these three general guidelines, the requisite reaction time for your specific ligand and radiometal are very important. Some targeting vectors might survive higher temperatures or lower pH values for short periods of time, and an acyclic ligand with fast binding kinetics at ambient temperature, or a macrocyclic ligand at high temperatures can often afford quantitative radiolabeling yields in ~5–15 min. Once a radiometal is stably coordinated by an appropriate ligand, it becomes mostly protected from water coordination and hydroxide formation and can be formulated for injection at neutral/physiological pH regardless of the metal ions pK_a value.

1.2 Bifunctional Chelators

The role of the BFC in a fully functioning metal-based radiopharmaceutical is essential. Ideally, the chelator should possess the following properties:

- Ability to efficiently complex the radiometal under radiochemical conditions: the ligand should display high radiolabeling (incorporation) yields of the radiometal (quantitative is best) at low ligand concentration (sub-micromolar or lower) at mild temperature (ambient temperature is preferred) and quickly (preferably <20 min). Macrocyclic ligands typically require temperatures of 60–90 °C to achieve quantitative RCYs and are therefore only matched with thermally stable targeting vectors.

- Ability to form highly stable and inert radiometal-chelate complexes: the resulting radiometal complex must be experimentally determined to be highly stable and inert. Can the complex withstand transchelation to endogenous metal-binding proteins, and remain intact at the extremely dilute conditions encountered in vivo (μg-ng of radiotracer diluted into blood stream) [4, 5]? Macrocyclic ligands are typically more stable and inert than acyclic ligands.

- Possess a chemically reactive handle for conjugation and covalent attachment to targeting vectors: the conjugation should ideally be regio- and chemo-selective such that it does not affect the metal-binding properties of the chelator, or the biological target binding of the vector. Often, a carboxylate arm that is essential in metal binding is used in conjugation reactions via peptide bond formation with a primary amine of the targeting vector to form a carboxamide; however, this bioconjugation could alter radiolabeling ability and/or complex stability and so a careful assessment of these changes must be conducted to ensure sufficient stability/inertness is retained.

When choosing a BFC for a particular radiometal, one must consider the coordination number, coordination geometry, and donor atom preferences for the radiometal, which is tied to the metal ion properties such as atomic number, charge, and radius [6]. It is important to note that each individual ligand, whether macrocyclic (closed chained) or acyclic (open chained), will possess their own radiolabeling kinetics and properties with specific radiometal ions. The ideal conditions for specific ligands should be determined from literature, or if a ligand is new, from extensive radiochemical study. Several seminal reviews and summaries of BFCs in radiopharmaceutical elaboration have been published which outline the most appropriate chelate-radiometal pairings, as such the reader is referred to these works for further details [4–10].

Radiolabeling time and temperature is highly dependent on the chelate (e.g., acyclic vs. macrocyclic), and the vector (e.g., heat sensitive protein vs. heat impervious peptides). Typically, macrocycles such as DOTA (1,4,7,10-tetraaza-cyclododecane-1,4,7,10-tetraacetic acid) require radiolabeling temperatures of 60–90 °C for 5–30 min, which is compatible with free ligands and most peptides; however, these conditions are not tolerated by antibodies, which should not be heated much above physiological temperatures (~40 °C), otherwise they may denature. When radiolabeled at temperature of 40 °C, macrocycles often suffer from lower radiochemical yields, and longer reaction times (e.g., 30–120 min). Acyclic chelators tend to complex radiometals with high radiochemical yields at ambient temperatures in short reaction times (5–30 min); however, the resulting complex may be kinetically labile.

The commercially available macrocyclic chelator DOTA is by far the most promiscuous ligand in radiopharmaceutical design. This ligand often forms thermodynamically stable metal complexes, due to the macrocyclic effect, but at the cost of sluggish radiolabeling kinetics, requiring elevated temperatures and long reaction times. These properties obviate its utility for complexing radiometals with short half-lives and/or when working with heat sensitive molecules (e.g., antibodies). Nonetheless, DOTA is available
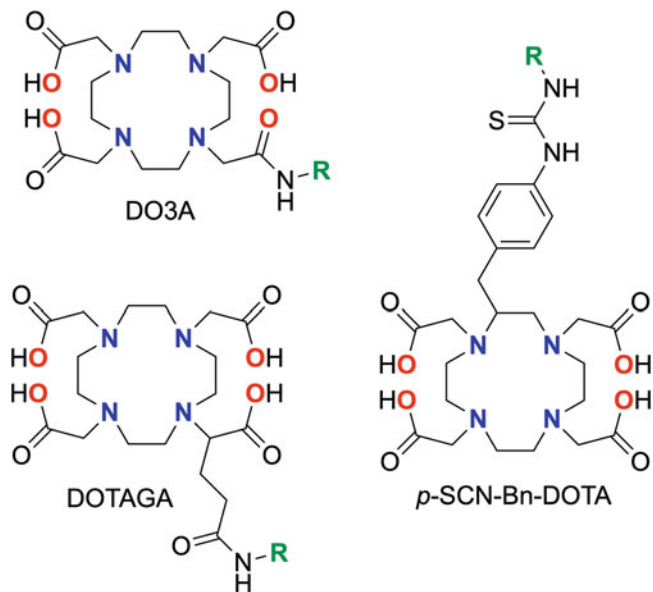
Fig. 2 Chemical structures of selected bifunctional DOTA (1,4,7,10-tetraaza-cyclododecane-1,4,7,10-tetraacetic acid) derivatives. Donor atoms used in metal coordination have been highlighted in blue (N donor) and red (O donor), "R" denotes the targeting vector. DO3A: the native DOTA ligand has been conjugated via one carboxymethyl arm. DOTAGA: (GA = glutaric acid) an additional ethyl carboxylate arm is incorporated for bioconjugation leaving four available carboxylic acids for metal binding. *p*-SCN-Bn-DOTA: C-functionalized DOTA analog that incorporates an isothiocyanate as a reactive moiety, which forms thiourea bonds via primary amine conjugation of a targeting vector

commercially in several bifunctional forms (Fig. 2), and its utility in radiopharmaceutical design is driven by its ease of accessibility and established radiolabeling protocols, rather than an ideal metal-chelate pairing.

1.3 Radiolytic Protectants

Radiation chemistry in aqueous media is complicated, but perhaps the most relevant process to radiochemistry and radiopharmaceutical production is water radiolysis. This is a topic that we believe is not typically discussed in enough detail, and it can have a profound effect on radiopharmaceuticals. Water radiolysis occurs through the interaction of high-energy ionization radiation with water to produce free radicals such as hydroxyl, superoxide, and solvated electrons [11]. Generally speaking, the higher the quantity and/or concentration of radionuclide in an aqueous radiolabeling solution, the greater the extent of water radiolysis. The same is true of administering beams of high-energy X-ray or gamma-ray radiation, which is the principle by which external beam radiation therapy of cancer works. Similarly, targeted radionuclide therapy, which is the site-specific delivery of radionuclides inside of tumors, operates

largely via the production of free radicals through water radiolysis. The presence of oxygen increases the damage done to tissue by these free radicals, which could be a reason why radiation therapy of hypoxic tumors is less effective than for normoxic tumors (*see* Eq. 7 below) [12]. As with other types of ionizing radiation, *alpha* particles can generate large quantities of free radicals as the ejected *alpha* particles ($_2^4\text{He}^{2+}$) have an extremely high linear energy transfer (LET, ~50–230 keV/µm) and deposit a huge amount of energy over a very small distance (~50–100 µm) [13]. *Alpha* particles are capable of directly inducing single strand and double strand DNA breaks; therefore, they are effective with or without free radical production.

Radiation sources relevant to radiochemistry include photons (X-ray, gamma ray) and charged particles such as *beta* (β^+, β^-) and *alpha* (α^{2+} [$_2^4\text{He}^{2+}$]). Regardless of the type of ionizing radiation, the radiation chemistry of water for all of these is remarkably similar [14]. In brief, ionizing radiation creates a *sparse track* of ionization and excitation events, initiating a complex chain of reactions, beginning with a water radical cation $[\text{H}_2\text{O}]^{\bullet+}$ and a solvated electron e_{aq}^- (Eq. 1):

$$\text{H}_2\text{O} + (\text{ionizing radiation}) \rightarrow [\text{H}_2\text{O}]^{\bullet+} + e_{\text{aq}}^- \tag{1}$$
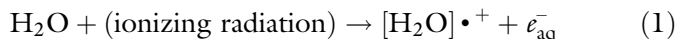
For a single H_2O molecule, the excited electron can originate from any of the five occupied H_2O molecular orbitals, giving rise to a series of different $[\text{H}_2\text{O}]^{\bullet+}$ excited states. These in turn can decay in a variety of ways by emitting photons or secondary electrons, giving rise to so-called *ionization spurs* in proximity to the primary ionization event and serving to amplify any chemical changes. The radical cation $[\text{H}_2\text{O}]^{\bullet+}$ can react to give hydronium ions and hydroxyl radicals (Eq. 2) [14]:

$$[\text{H}_2\text{O}]^{\bullet+} + \text{H}_2\text{O} \rightarrow [\text{H}_3\text{O}]^+ + \text{HO}\bullet \tag{2}$$

The resultant hydroxyl radical, HO•, a strong oxidizing agent, is a primary suspect for radiopharmaceutical degradation. Both e_{aq}^- and HO• are highly mobile entities [15] and can give rise to a range of other reactive species, for example, two HO• can react to make H_2O_2, and if O_2 is present then this can be reduced by e_{aq}^- to the superoxide radical anion $\text{O}_2\bullet^-$ (Eq. 3):

$$\text{O}_2 + e_{\text{aq}}^- \rightarrow \text{O}_2\bullet^- \tag{3}$$

Despite these complexities, most products of water irradiation are consumed through reactions that are effectively the reverse of those producing them, regenerating water and heat [14]. Thus, both $[\text{H}_2\text{O}]^{\bullet+}$ and HO• react with e_{aq}^- to regenerate H_2O (Eqs. 4, 5) [14].

$$[\text{H}_2\text{O}]^{\bullet+} + e_{\text{aq}}^- \rightarrow \text{H}_2\text{O} + \Delta \tag{4}$$

$$HO \cdot + e_{aq}^- + [H_3O]^+ \rightarrow 2H_2O + \Delta \qquad (5)$$
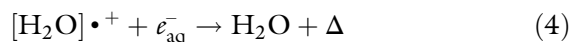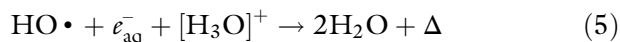
Although saline (0.9% NaCl) is an ideal solution for injectable radiopharmaceutical formulations since it is isotonic with blood, it is not ideal for storing these solutions, and high concentrations of NaCl present during radiolabeling reactions can exacerbate water radiolysis [16]. Chloride can react with hydroxyl radicals to produce hypochlorous acid (HOCl), which is a potent oxidizing agent (Eqs. 6 and 7) [17]. It is also possible to produce chlorine radicals through interaction of chloride with photons [18]. Recent methods for radiolabeling chelator-peptide conjugates with gallium-68 have utilized high concentrations of NaCl for gallium-generator elution (~0.5–1.0 M NaCl in radiolabeling mixture) [19], which can lead to high levels of hypochlorous acid. This can cause radiolytic damage even to small peptides if a radioprotectant such as ascorbic acid is not used, even with relatively small quantities of activity (e.g., ~10–40 MBq). As such, high concentrations of NaCl present during radiolabeling or radiopharmaceutical storage/shipment should be avoided, or it should necessitate the use of a chemical radioprotectant as a buffer additive. Stability of the molecule/injectate can be assessed in-house via common radioanalytical methods described below (e.g., radio-HPLC, radio-TLC).

$$Cl^- + HO \cdot \rightarrow Cl \cdot + HO^- \qquad (6)$$

$$HO \cdot + Cl^- + O_2 \rightarrow HOCl + O_2 \cdot^- \qquad (7)$$
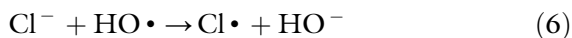
Radiolysis has been studied most commonly in biology as it can intentionally or unintentionally cause biological damage, and also in nuclear reactors for its deleterious effects on water cooling systems [20]. Although free radical production and radiolysis is desirable inside of tumors where biological destruction and therefore treatment of diseased tissues is desired, radiolysis is a major obstacle for radiochemists who need to prepare sensitive radiopharmaceutical drugs in aqueous media. This is particularly critical for peptides and proteins containing amino acids such as methionine, which are highly sensitive to free radical damage [21]. Radioprotectants are molecules that can be added to radiolabeling reactions to quench free radicals and inhibit the deleterious effects of water radiolysis. Radioprotectants such as ascorbic acid, gentisic acid, ethanol, and methionine are perhaps the best-known examples, and they can quench these free radicals and prevent damage, to varying extents and depending on factors such as concentration and pH [21–23].

The radioprotectants, L-ascorbic acid and gentisic acid, are perhaps the most well known. Vitamin C (L-ascorbic acid) is typically added to radiolabeling buffers in concentrations of ~25–200 mM [21–23]. A recent study investigated the radioprotective effects of ethanol (10% v/v) and methionine (3.5 mM) and

found they were more effective over a 25 h period at preventing radiolytic damage to [^{177}Lu]Lu-DOTA-PSMA-617 (~62.5 MBq, ~1.7 mCi, ~100 μL reaction) than both ascorbic acid and gentisic acid at 3.5 mM (~0.6 mg/mL and ~0.54 mg/mL, respectively), providing ~90% stability vs. 75%, respectively [21]. In this study, a combination of ~7% ethanol with 3.5 mM methionine was optimum, providing stability of ~96%. Without any radioprotectant, these radiolabeling reactions showed stability of only ~25%, demonstrating the crucial role of radioprotectants. It is important to note that although 3.5 mM of ascorbic acid or gentisic acid did not provide adequate radioprotection in this study, a previous study with ascorbic acid demonstrated that concentrations of 100–500 mM (20–100 mg/mL) were effective at preventing radiolytic damage to [^{90}Y]Y-DOTA-vitronectin peptide conjugates (37 GBq, 100 mCi) [23]. Another study by Liu et al. demonstrated that with 20 mCi (~740 mBq) of [^{90}Y]Y-DOTA-RP697 peptide conjugate (0.5 mL total volume), concentrations of ~20–25 mM gentisic acid or ascorbic acid were not sufficient to prevent degradation over a period of 6 days, but ~110–130 mM was sufficient [22]. Several recent studies demonstrated that for radiolabeling of DOTA-TATE/TOC with gallium-68 (~300–1800 MBq, ~10–50 mCi), adding a portion of a 1.4% (w/v) ascorbic acid solution to the reaction mixture (~5–10 mg/mL, ~25–50 mM) was effective as a radioprotectant when radiolabeling [19]. A common example of ethanol being used as a radioprotectant is for 2-[^{18}F]fluoro-2-deoxy-D-glucose [^{18}F]FDG, where ethanol is often present in the final formulated product, although the effectiveness is limited and recent studies suggest that more radioprotection would be beneficial [24].

Interestingly, another study compared the post-radiolabeling radioprotectant ability of histidine, glycine, tryptophan, methionine, cysteine, gentisic acid, ascorbic acid, human serum albumin, and ethanol for stabilizing a lutetium-177 peptide conjugate ([^{177}Lu]Lu-AMBA) [25]. These additives were all prepared at a final concentration of 6.6 mg/mL (or 6.6%v/v for ethanol) with ~83 MBq (~2.2 mCi) of [^{177}Lu]Lu-AMBA in a total volume of 150 μL. Methionine as a buffer additive was one of the most effective at preventing radiolytic damage to methionine residues present in the AMBA peptide, but it was not sufficient to offer full protection to the entire peptide. Although ascorbic acid and gentisic acid were effective, 6.6 mg/mL was not high enough to inhibit all radiolysis. Interestingly, seleno-methionine was found to be the most effective overall for radioprotection of this particular peptide conjugate; however, quantities of 1–10 mg total seleno-methionine was tested and at higher quantities the radiolabeling yields were significantly lowered. The final recommendations from this comprehensive study were to utilize seleno-methionine during radiolabeling (1 mg/mL) and to add ascorbic acid post-radiolabeling to

help stabilize. The authors state that seleno-methionine is safe for injection into humans, and ascorbic acid is known to be safe (vitamin C).

A recent study used fluorescent dyes as optical markers to measure radioprotectant effectiveness against hydroxyl radical-induced radiobleaching [26]. In this work, the authors used variable quantities of indium-111, gallium-68, and bismuth-213 mixed with IRDye 800CW and radioprotectants, such as ethanol, ascorbic acid, or gentisic acid. Ascorbic acid was the most effective radioprotectant in this study, with concentrations of 0.001–0.1% (w/v) being effective in inhibit radiobleaching from gallium-68 and indium-111 (20 MBq, ~0.5 mCi). The authors attribute the greater radioprotecant ability of ascorbic acid to its ability to quench two radicals per molecule and its very high rate constant for reaction with hydroxyl radicals ($k = 1.1 \times 10^{10}$ L mol^{-1} s^{-1}), which is nearly an order of magnitude higher than ethanol or gentisic acid [27–29]. None of these radioprotectants could effectively prevent radiobleaching from the *alpha* particles emitted by bismuth-213. This study did not investigate methionine or a methionine/ethanol combination [26].

These examples suggest that each specific radionuclide and radiolabeling situation might require adjustment of radioprotectant levels; therefore, the concentration ranges reported here should be taken as guidelines with the expectation that some optimization is likely needed when applying to a new radionuclide/molecule. A special consideration for using radioprotectants is to always prepare the solutions fresh for each radiolabeling reaction. Although a radioprotectant solution might remain "fresh" for several days or even weeks, to ensure reliable protection they should be prepared fresh each day they are used. For example, ascorbic acid solutions will turn yellow/brown over time as it reversibly degrades into dehydroascorbic acid.

Another important consideration for these radioprotectants include caution around their functional groups, with ascorbic acid and gentisic acid possibly causing interference when added to radiolabeling reactions with oxophilic metal ions such as zirconium-89, and so methionine or a methionine/ethanol mixture might be preferred. If any reactive functional groups (e.g., electrophiles for bioconjugation) are present on the molecule that is being radiolabeled, methionine could be problematic due to the presence of a primary amine (good nucleophile). Organic solvents such as ethanol are used to elute radiopharmaceuticals from reverse-phase C18 stationary phases such as C18 Sep-paks and C18 HPLC columns. As such, when ethanol is used as a radioprotectant, the final reaction mixture should be diluted with water/aqueous buffer before loading onto a reverse-phase media (e.g., <5% ethanol). Although ascorbic acid appears to be a superior radioprotectant to gentisic acid or ethanol alone, the ability of ascorbic acid to act as a mild

reducing agent (e.g., $Cu(II) \rightarrow Cu(I)$) means it should not be used with radionuclides of copper.

Although a single study suggested that a combination of methionine and ethanol are excellent radioprotectants, and adding methionine is effective at protecting methionine residues in proteins at far lower concentrations than ascorbic acid or gentisic acid, radioprotection can vary greatly between molecules and radionuclides. Limited examples are available of methionine being used as a radioprotectant, and so its effectiveness with different radionuclides is not clear. However, it does appear excellent for preventing radiolytic damage to other methionine residues present in protein vectors. Work with seleno-methionine suggests that it is far superior to regular methionine, and perhaps an ethanol/seleno-methionine mixture would be ideal for many reactions. As a post-radiolabeling additive for imparting radioprotection, ascorbic acid appears to be ideal. Ascorbic acid has also been shown to be effective for preventing radiolysis damage to antibodies during radiolabeling [30], but presumably seleno-methionine could be used instead (e.g., for zirconium-89 radioimmunoconjugate formation) with ascorbic acid being added post-radiolabeling during purification and/or formulation.

1.4 Radiolabeling Yield Analysis, Radiotracer Purification, and Quality Control (HPLC and TLC)

Following a radiolabeling reaction, the radiochemical yield (%RCY) must be assessed; radioactive TLC (a.k.a. radio-TLC) and radioactive HPLC (radio-HPLC) are the most common methods for this purpose. If the radiotracer may also need to be purified, HPLC, or C_{18} plugs (Sep-pak), or size exclusion (PD-10 desalting columns) can be used for this process depending on the type and molecular weight of bioconjugate labeled (e.g., small molecules, peptides, or antibodies). The premise of radio-TLC and HPLC is the same for non-radioactive chemistry, the difference being that a radiation detector is used to measure the distribution of radioactivity (number of counts) along the length of the plate (for TLC) or measure the radioactivity of the compounds in the eluate (in HPLC).

2 Materials

Prepare all solutions using ultrapure water (prepared by purifying deionized/reverse osmosis water, to attain a sensitivity of 18 MΩ·cm at 25 °C), ultrapure nitric (HNO_3), hydrochloric (HCl) acids (trace metal grade) (*see* **Note 1**), and other reagents of the highest purity possible. Diligently follow all safety and waste disposal regulations when handling radioactive isotopes which cause ionizing radiation. Ultrapure water and buffers can be further demetallated using Chelex resin treatment (~1.2 g/L, 24 h stirring at room temp, followed by 0.22 micron filtration, e.g., media filters).

2.1 Radiolabeling Buffers

A selection of the most common radiolabeling buffers can be found in Table 1. Radiolabeling reaction mixtures have typical volumes of 10–2000 μL total. Thus, preparing 100 mL solution of buffer should suffice for several radiochemical studies. Buffer solutions can be stored at ambient temperature for several months in preferably acid washed plastic or glass containers (e.g., 1–3% nitric acid bath, 24 h soak).

2.2 Radiolytic Protectants

A selection of common radiolytic protectants, which can be added to radiolabeling reaction mixtures, can be found in Table 2. Radiolytic protectant can be added before the reaction begins (i.e., before the addition of radiometal), or after radiolabeling yield has been determined and/or after radiotracer purification and formulation. Many of the radiolytic protectants can degrade over time in solution; thus, it is preferred that each radiolytic protectant solution be prepared fresh daily.

2.3 Chelates (Ligands)
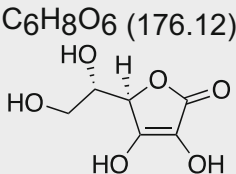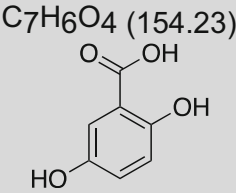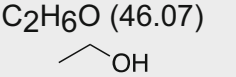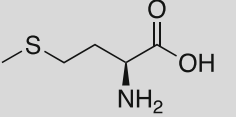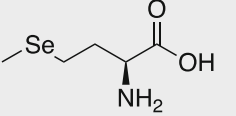
A selection of both commercially available and popular literature chelators employed in radiometal chelation can be found in Figs. 3, 4, and 5. For simplicity, only the non-bifunctional (native) chelator structure is shown; however, in some cases several bifunctional derivatives have been tested and/or are available commercially. BFCs can be used on their own (native chelates for radiolabeling studies and complex stability assays), or conjugated to small molecules, peptides, antibodies (MW ~ 150 kDa), antibody fragments, or attached to the surface of nanoparticles. Bioconjugation strategies are not covered in this chapter, and here we assume the chelator has been prepared in appropriate form desired for radiolabeling [5, 6, 8–10, 35–41].

1. Native chelates, small molecule or peptide bioconjugates:
   - Prepare a stock solution of chelator or bioconjugate: accurately weigh ~1–5 mg of chelator or bioconjugate, dissolve in ultrapure water (*see* **Note 4**) or biology grade DMSO such that the final concentration of ligand/bioconjugate is in the range of 10^{-2}–10^{-3} M (~20–200 μL).
   - For concentration-dependent labeling studies, using the stock solution from above prepare 1-to-10 serial dilutions of the ligand/bioconjugate with final concentrations of approximately 10^{-3}–10^{-7} M.
2. Antibody, antibody fragments, and nanoparticle conjugates:
   - Received in solution (e.g., PBS) at appropriate concentrations (e.g., 1–20 mg/mL).
   - ~1–2 chelators per antibody/antibody fragment is typically desired. Nanoparticles are dependent on too many factors to generalize.

Table 1
A selection of the most common radiolabeling buffers (*see* Note 2) employed in radiometal labeling chemistry, and some of their relevant properties

Name (*see* Note 3)	Short name	Chemical formula/structure and (MW g mol^{-1}) or composition	Usable pH range	Properties and uses	Typical molarities used (M)	Typical pH used
Sodium acetate	NaOAc	$C_2H_3O_2Na$ (82.03)	3.6–5.6	pK_a (25 °C) = 4.75	0.01–2.0	4.0–5.5
Ammonium acetate	NH$_4$OAc	$C_2H_7NO_2$ (77.08)	3.5–6.0, 8.5–10.5	p$K_{a,\text{acetic acid}}$ (25 °C) = 4.75 p$K_{a,\ NH4+}$ (25 °C) = 9.25	0.01–2.0	4.0–7.2
Phosphate buffered saline	PBS (1x)	NaCl (137 mmol/L) KCl (2.7 mmol/L) Na$_2$HPO$_4$ (10 mmol/L) KH$_2$PO$_4$ (1.8 mmol/L)	5.7–8.0	Typical pH is 7.4 (biological pH)	n/a	7.0–7.4
2-[4-(2-hydroxyethyl)piperazin-1-yl]ethanesulfonic acid	HEPES	$C_8H_{18}N_2O_4S$ (238.30)	2.5–3.5 or 6.8–8.2	pK_{a1} (25 °C) = 3 pK_{a2} (25 °C) = 7.5	0.1–2.0	2.0, 7.0
2-(N-morpholino)ethanesulfonic acid	MES	$C_6H_{13}NO_4S$ (195.2)	5.5–6.7	pK_{a1} (25 °C) = 6.10	0.1–2.0	5.0–6.5
2-amino-2-(hydroxymethyl)-1,3-propanediol	Tris-HCl	$C_4H_{11}NO_3$ (121.14)	7.0–9.0	pK_{a1} (25 °C) = 8.06	0.1–2.0	7.4–9.0.

Table 2
Common chemical radioprotectants and their relevant attributes

Name	Chemical Formula/ Structure and (MW g mol^{-1})	Concentration used in radiolabeling buffer	Special considerations
L-ascorbic acid	$C_6H_8O_6$ (176.12)	25–500 mM (5–100 mg/mL) [19, 21–23, 25, 33]	Can decrease radiolabeling yields with oxophilic metal ions, e.g., [^{89}Zr]Zr^{4+}, can reduce Cu(II) → Cu(I)
Gentisic acid	$C_7H_6O_4$ (154.23)	100–500 mM (15–80 mg/mL) [21, 25, 34]	Can decrease radiolabeling yields with oxophilic metal ions, e.g., [^{89}Zr]Zr^{4+}
Ethanol	C_2H_6O (46.07)	10% v/v [21, 25]	Too much ethanol could impact retention on C18 HPLC/sep-pak columns when loading
L-methionine	$C_5H_{11}NO_2S$ (149.21)	3.5–45 mM (~0.5–6.6 mg/ mL) [21, 25]	Amino acid, contains unprotected primary amine which can act as a potent nucleophile
Seleno-methionine (se-met)	$C_5H_{11}NO_2Se$ (196.11)	5 mM (1 mg/mL) [25]	Amino acid, contains unprotected primary amine which can act as a potent nucleophile
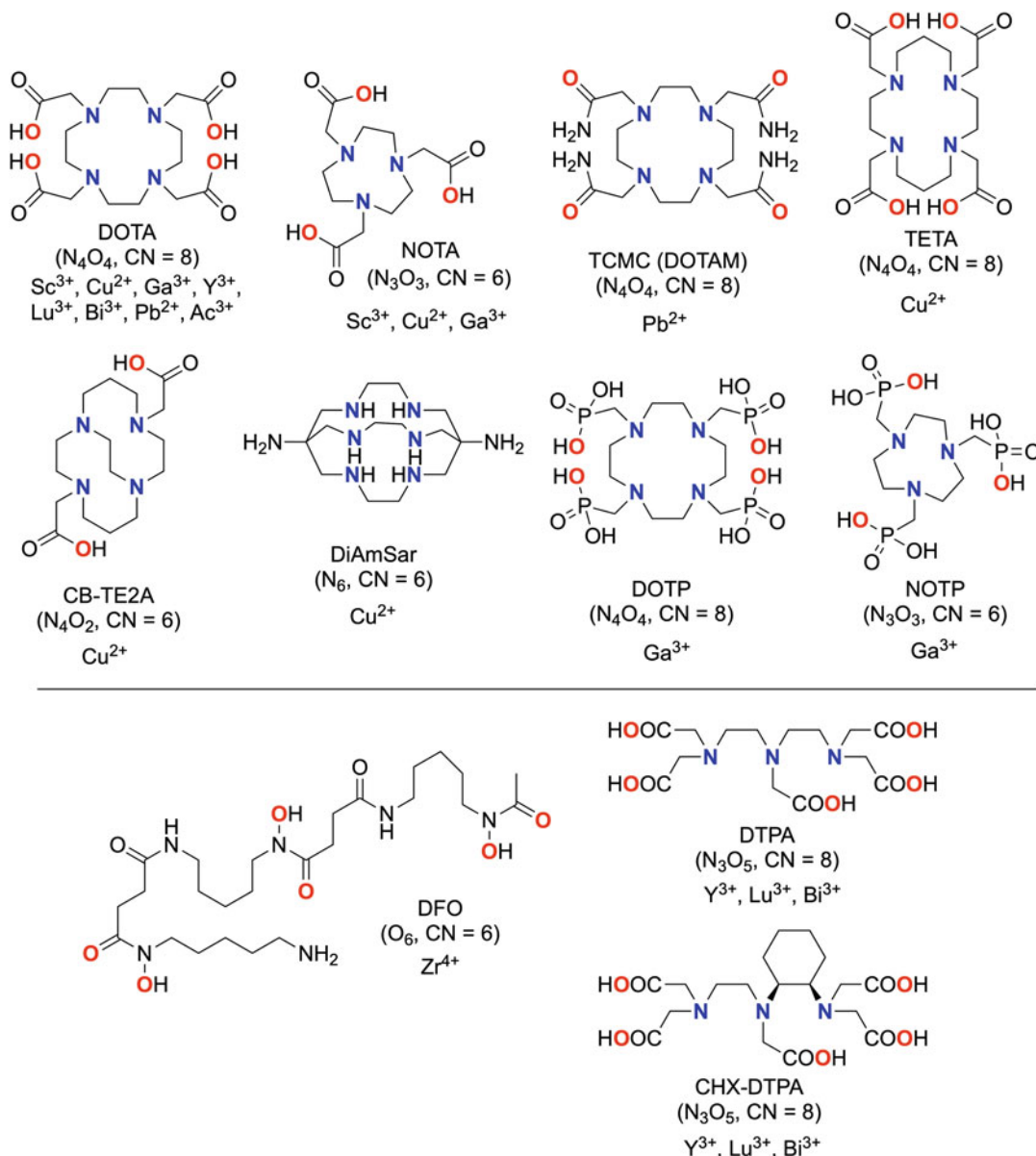
Fig. 3 Chemical structures of a selection of commercially available macrocyclic (closed-chain) chelators (top), and acyclic (open-chain) chelators (bottom). Metal-binding donor atoms highlighted in blue (N-donor) and red (O-donor). *CN* coordination number

2.4 Radiometals

Radiometals can be sourced from several suppliers (e.g., ITG, DOE, academic cyclotron labs), received as radionuclide generators (e.g., $[^{68}Ge]Ge^{4+}/[^{68}Ga]Ga^{3+}$ generator), or made in-house with medical cyclotrons. A table of the PET and therapeutic radiometals, which are of focus in this chapter, are listed in Table 3. The radiometals will be formulated in dilute acid (most commonly
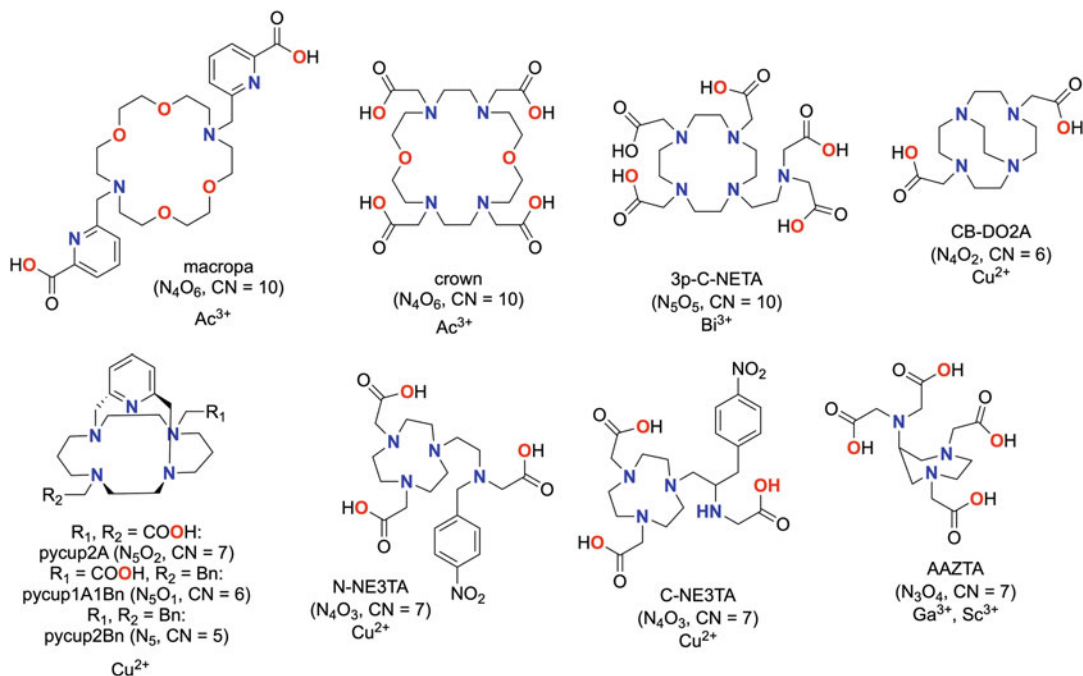
Fig. 4 Chemical structures of selected non-commercial macrocyclic chelators. Metal-binding donor atoms highlighted in blue (N-donor) and red (O-donor). *CN* coordination number

0.04–0.1 M HCl or HNO_3). With the exception of $[^{89}Zr]Zr^{4+}$, the radiometal solutions can be added directly into radiolabeling reactions without further preparation. However, if the specific activity is too high or volume of solution is too low to pipet accurate volumes into a reaction mixture, the radiometal solutions can be diluted with excess dilute acid (or whichever solution the radionuclide was formulated in) (*see* **Note 5**).

2.5 Equipment

2.5.1 Dose Calibrator

Radioactivity of bulk samples can be measured using a dose calibrator. Read the instruction manual and ensure the instrument is set at the appropriate calibration for the correct radionuclide.

2.5.2 Radio-HPLC

A high-performance liquid chromatography (HPLC) system equipped with a binary or quaternary pump, UV-Vis absorbance detector (or equivalent), coupled to a radiation detector (e.g., inorganic scintillation detector) is required for HPLC analysis of radiolabeling reactions, or HPLC purification of radiotracers.

2.5.3 Radioactive TLC Plate Reader

A gas-filled continuous flow proportional counter or an inorganic scintillation detector can be used for measuring radioactive TLC (radio-TLC) plates. The inorganic scintillation detector will be efficient at measuring β-emitting sources, while the proportional counters will provide better sensitivity for low activity sources of all
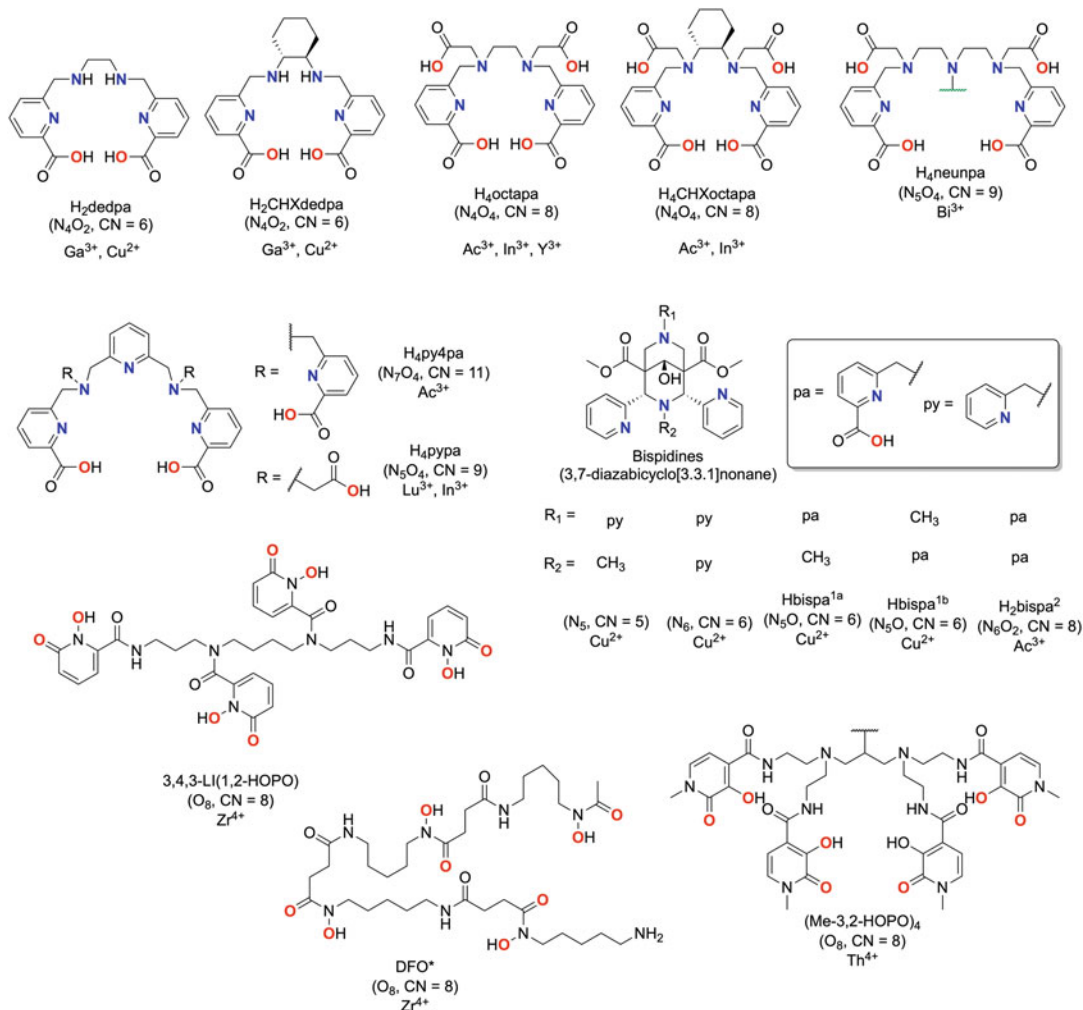
Fig. 5 Chemical structures of selected non-commercial chelators. Metal-binding donor atoms highlighted in blue (N-donor) and red (O-donor). *CN* coordination number

types. TLC strips can also be chopped into sections (halfs, thirds, or quarters), placed into individual containers, and counted on an automated gamma counter to obtain an approximate distribution of radioactivity across the TLC strip if no radio-TLC reader is available.

2.5.4 Thermomixer — This device both heats and shakes reactions, can be purchased from several vendors.

2.5.5 Centrifuge — Small for microcentrifuge tubes, large for 15–50 mL falcon tubes. Can be used for size-exclusion filter purification. An actively cooled centrifuge is ideal for cell-based assays and for heat-sensitive vectors.

Table 3

A selection of "common" radiometals and some of their relevant nuclear properties including average particle emission energy and most prominent gamma emissions

Radionuclide	$t_{1/2}$ (h)	Formulation	Application	Decay mode	E (keV)[a]	Production method
$[^{44}Sc]Sc^{3+}$	4.04	0.04–0.1 M HCl	PET	β^+ (94%) EC (6%)	γ, 1157; β^+, 632	$[^{44}Ti/^{44}Sc$ generator] $^{44}Ca(p,n)^{44}Sc$
$[^{47}Sc]Sc^{3+}$	80.4	0.04–0.1 M HCl	SPECT Therapy: β^-	β^- (100%)	γ, 159; β^-, 162	$^{47}Ti(n,p)^{47}Sc$ $^{46}Ca(n,\gamma)^{47}Ca\diamond^{47}Sc$
$[^{64}Cu]Cu^{2+}$	12.7	0.04–0.1 M HCl	PET	β^+ (19%) EC (41%) β^- (40%)	γ, 1346; β^+, 278; β^-, 579	Cyclotron $^{64}Ni(p,n)^{64}Cu$
$[^{67}Cu]Cu^{2+}$	61.8	0.04–0.1 M HCl	SPECT Therapy: β^-	β^- (100%)	γ, 91, 93, 184; β^-, 141	$^{67}Zn(n,p)^{67}Cu$ $^{68}Zn(\gamma,p)^{67}Cu$
$[^{68}Ga]Ga^{3+}$	1.1	0.05–1 M HCl	PET	β^+ (89%) EC (11%)	γ, 1077; β^+, 836	$[^{68}Ge/^{68}Ga$ generator] $^{68}Zn(p,n)^{68}Ga$
$[^{86}Y]Y^{3+}$	14.7	0.04–0.1 M HCl	PET	β^+ (33%) EC (66%)	γ, 443–1920 (9); β^+, 535, 681, 883 (664 avg)	Cyclotron $^{86}Sr(p,n)^{86}Y$
$[^{90}Y]Y^{3+}$	64.1	0.04–0.1 M HCl	Therapy: β^-	β^- (100%)	β^-, 934	$^{90}Zr(n,p)^{90}Y$ $[^{90}Sr/^{90}Y$ generator]
$[^{89}Zr]Zr^{4+}$	78.5	1.0 M Oxalic acid	PET	β^+ (23%) EC (77%)	γ, 909; β^+, 396	Cyclotron $^{89}Y(p,n)^{89}Zr$
$[^{177}Lu]Lu^{3+}$	159.4	0.04–0.1 M HCl	SPECT Therapy: β^-	β^- (100%)	γ, 112, 208; β^-, 134	$^{176}Lu(n,\gamma)^{177}Lu$
$[^{212}Bi]Bi^{3+}$	1.0	0.04–0.1 M HCl	Therapy: α and β^-	α (36%) β^- (64%)	α, 6210; β^-, 771	$[^{228}Th/^{212}Pb/^{212}Bi$ generator]

$[^{213}Bi]Bi^{3+}$	0.76	0.1 M HCl/0.1 M NaI	Therapy: α and β^-	α (2%) β^- (98%)	γ, 440 α, 8350 β^-, 435	$[^{228}Th/^{212}Pb$ generator]
$[^{212}Pb]Pb^{2+}$ (daughter is $[^{212}Bi]Bi^{3+}$)	10.6	0.04–0.1 M HCl 1 M NH_4OAc	Therapy: β^- (daughters emit α/β^-)	β^- (100%)	β^-, 570	$[^{224}Ra/^{212}Pb$ generator]
$[^{225}Ac]Ac^{3+}$	238 (9.9 d)	0.04–0.1 M HCl 0.01–0.1 M HNO_3	Therapy: α(daughters emit α/β^-)	α (100%)	α, 5800–8400 MeV[47],b	$^{226}Ra(p,2n)^{225}Ac$ $^{232}Th(p,2p6n)^{225}Ac$ $[^{229}Th \rightarrow {}^{225}Ac$ generator]
$[^{227}Th]Th^{4+}$	449 (18.7 d)	0.01–0.1 M HCl 0.01–0.1 M HNO_3 Oxalic acid (1 M)	Therapy: α(daughters emit α/β^-)	α (100%)	α, 5900b	$^{226}Ra(n,\gamma)^{227}Ra$ ($t_{1/2} = 42$ m) $\rightarrow {}^{227}Ac$ $[^{227}Ac$ ($t_{1/2} = 21.8$ y) $\rightarrow {}^{227}Th$ generator]

EC electron capture [6, 8, 42–46]. [a]Particle energies are mean values (weighted averages). [b]Actinium-225 and thorium-227 have complicated decay chains with a series of radioactive daughters, which also emit α and β^- particles

2.6 Supplies

2.6.1 Plastic snap-top vials (0.5–2 mL; preferably acid washed). Low-protein bind tubes can be used for "sticky" antibodies/vectors.

2.6.2 Micropipettes (0–10, 10–100, 100–1000 μL) with tips (preferably acid washed).

2.6.3 pH paper (0–14 or narrow ranges depending on radiolabeling pH).

2.6.4 TLC plates.

2.6.4.1 Paper-backed instant TLC (iTLC) silica gel (iTLC-SG).

2.6.4.2 Paper-backed iTLC silicic acid (iTLC-SA).

2.6.4.3 Aluminum-backed silica TLC.

2.6.4.4 C_{18} TLC.

2.6.5 HPLC vials or HPLC compatible syringe and needle.

2.6.6 Falcon tubes (15 or 50 mL).

2.6.7 Purification consumables.

Small molecule and peptide conjugates:

- 0.2 μm filters.

- Sep-pak C_{18} cartridges. Equilibrated with ethanol (5 mL) followed by aqueous radiolabeling buffer or water (5–10 mL). Elution in methanol/ethanol/acetonitrile, with ethanol being idea (can inject up to ~10% ethanol). A mixture of ethanol-saline can help elute stubborn peptides/chelators that are "stuck" on the filter (e.g., 50–70% ethanol, 30–50% saline).

Antibody, antibody-fragment, and nanoparticle conjugates:

- PD-10 desalting columns. Equilibrated with the loading solvent as per manufacturer instructions.

- Corning Amicon Ultra centrifugation filters spin filters (ranges from 3–100 kDa MW cut-offs available).

3 Methods

A summary of the common radiolabeling buffers and conditions used for various radiometals can be found in Table 4. A general written procedure for a typical radiolabeling reaction is also found below, along with standard procedures for radiochemical yield analysis, and radiotracer purification.

Table 4
Summary of radiolabeling buffers and conditions used for various radiometal ions discussion in this chapter

Radiometal	Buffer (molarity, pH)	Selection of used chelators (BFCs)	Radioprotectant
[$^{64/67}$Cu] Cu^{2+}	NH$_4$OAc (0.1–0.5 M, pH 5.4–8) Ammonium or sodium citrate (0.1 M, pH 6.5–8) NaOAc (0.5 M, pH 5.5)	Sar [47–51] TETA, DOTA [52] Bispidine-N$_4$O [53, 54] N-NE3TA C-NE3TA [55] CB-TE2A [56], CB-DO2A [52] H$_2$dedpa, H$_2$CHXdedpa [57, 58] Pycup2A, pycup1A1Bn, pycup2Bn [59]	None reported
[^{225}Ac] Ac^{3+}	NH$_4$OAc (0.1–1 M, pH 5–7) Tris–HCl (0.1 M, pH 9)	Macropa [60] H$_4$py4pa [61] Crown [62] H$_2$bispa [63] H$_4$octapa, H$_6$phospa, H$_4$neunpa, DOTA [64] DOTA [65]	Ascorbic acid and DTPA added after reaction
[^{213}Bi]Bi^{3+}	NH$_4$OAc (0.1–1 M, pH 5.5–6) Tris–HCl (2 M) MES (0.5 M, pH 5.5–6)	DOTA [66, 67] CHX-A"-DTPA [68, 69]	L-ascorbic acid added after reaction
[^{212}Pb] Pb^{2+}	NH$_4$OAc (0.15–5 M, pH 5.3–7) NaOAc (0.4 M, pH 4–5)	DOTA, TCMC [67, 70–74]	L-ascorbic acid added prior radiometal addition [73] or prior to purification (for ^{212}Pb labeling)
[^{44}Sc]Sc^{3+} and [^{47}Sc] Sc^{3+}	NH$_4$OAc (0.25–0.5 M, pH 4) NaOAc (0.25–0.5 M, pH 4–4.5)	DOTA [75–82], AAZTA [83–86], CHX-A"-DTPA [84–86]	
[^{68}Ga]Ga^{3+}	NH$_4$OAc (0.25–0.6 M, pH 6.5–7.2) NaOAc (0.01–0.1 M, pH 4.5–5.5) Tris–HCl (pH 7.4) HEPES (0.3–1 M, pH 2)	NOTA [85, 86], DOTA [87, 88], H$_2$dedpa [89–92], H$_2$CHXdedpa [93], TRAP [94–97], AAZTA [98]	EtOH [99], ascorbic acid
[^{86}Y]Y^{3+} and [^{90}Y]Y^{3+}	NH$_4$OAc (0.1–0.4 M, pH 4.5–6) NaOAc (0.05–0.4 M, pH 4–5.5)	DOTA [100–104], CHX-A"-DTPA [105–107], H$_4$octapa [91, 108], NETA [109]	

(continued)

Table 4
(continued)

Radiometal	Buffer (molarity, pH)	Selection of used chelators (BFCs)	Radioprotectant
$[^{177}Lu]$ Lu^{3+}	NaAscorbate (0.5 M, pH 4.5) NH$_4$OAc (0.2–0.3 M, pH 5.5–7)	DOTA [110–112], NETA [109, 113], H$_4$octapa [114–116]	
$[^{89}Zr]Zr^{4+}$ (*see* **Note** **6**)	Saline PBS, HEPEs, pH 7.0–7.4	DFO [117–121], HOPO [122–124], DFO* [125–128], DFO2 [129]	Gentisic acid
$[^{227}Th]$ Th^{4+}	Citrate buffer (0.03 M with 0.07 M NaCl, 0.02 M EDTA, 0.5 mg/mL PABA, 5% DMSO, pH 5.5)	(Me-3,2-HOPO)$_4$ [130–132]	

3.1 General Radiolabeling Procedures

A variety of vector-types are depicted in Fig. 6, such as proteins and nanoparticles, but any molecule or structure can be radiometallated if the appropriate bifunctional ligand can be stably conjugated. A number of the instruments and concepts that are summarized in this figure have been explained in more detail above in Subheadings 2 and 3. Detailed methodologies for each step are outlined as follows.

- **In step 1**, the exact buffer volume, pH, and molarity are customized to the type of vector used and the buffering strength needed to balance the acidic radiometal solution (e.g., gallium-68 delivered in 0.05 M or 0.5 M HCl). If working with zirconium-89, you would first neutralize its 1 M oxalic acid mixture to pH ~7–7.4, typically using a sodium carbonate (1 M) solution. Therefore, for zirconium-89 even phosphate buffered saline is sufficient *buffering power*. For those gallium-generators that elute in 0.5–1.0 M HCl, ammonium acetate at a high concentration of 1.0–1.5 M is often used as buffer (including radioprotectant) to neutralize the higher quantity of acid.

- **For step 2**, the temperature is dependent on your vector/molecule, but *speaking very broadly*, small peptides (e.g., <20–30 amino acids) can often handle temperatures of 80–90 °C for periods of 5–30 min at pH ~4–7. Larger proteins—and certainly antibodies—do not fare well above 40 °C and those temperatures should be avoided, unless you have specific knowledge that your protein/antibody will remain stable and functional at higher temperatures. Basically, the temperature of radiolabeling
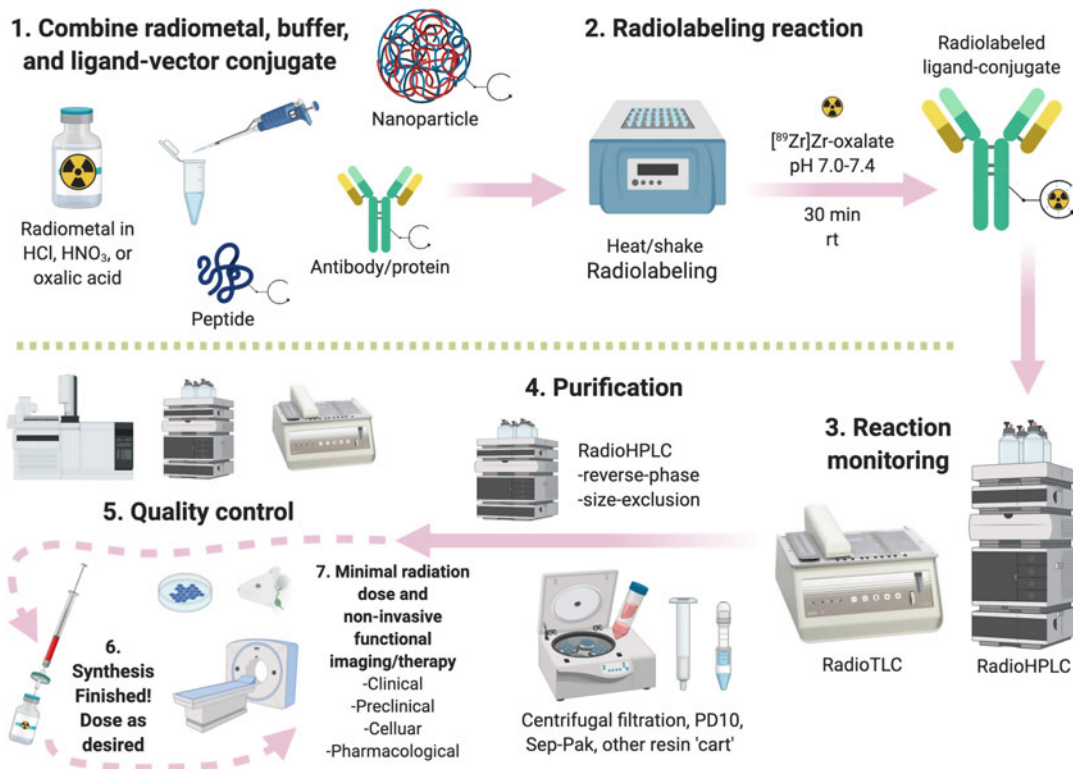
Fig. 6 Stepwise graphical depiction of the full radiometallation process (radiolabeling with chelator-radiometal complexes), with major differences in analysis and purification attributed to the type and size of the targeting vector (e.g., peptide, antibody, nanoparticle, cell). **Step 1**: The radiometal solution (typically 0.01–0.1 M HCl or HNO$_3$, or neutralized 1.0 M oxalic acid) is transferred via pipet into the reaction vessel, which contains the ligand-conjugate (vector, e.g., protein). **Step 2**: The pH of the final radiolabeling reaction mixture is checked and then heated with shaking. **Step 3**: Radiolabeling progress is evaluated by techniques such as radio-TLC and/or radio-HPLC (reverse-phase or size-exclusion) to obtain a crude radiochemical yield. **Step 4**: When the reaction is deemed complete, purification is performed (if needed) using radio-HPLC (reverse-phase or size-exclusion), stand-alone manual size exclusion columns (e.g., PD10), or centrifugal spin filters (e.g., vivaspin, amicon). **Step 5**: Final quality control analysis is performed to ensure purification was successful and a high radiochemical purity has been achieved. **Steps 6–7**: The final purified radiopharmaceutical is formulated for injection (e.g., sterile saline, buffered water) for administration/injection for any desired application such as imaging or cell studies. (Figure created using BioRender.com)

is selected to provide sufficient radiolabeling kinetics with your chosen radiometal and chelator, while ensuring your targeting vector remains stable.

- **In step 3**, the radiolabeling reaction is monitored to determine when it is completed, or if a standard protocol is being followed (e.g., [^{68}Ga]Ga-DOTA-TATE) it is checked at the end of the prescribed reaction time. The two main techniques used for monitoring reaction yields (radiochemical yield, RCY) are

radio-TLC and radio-HPLC (reverse phase for peptides and small molecules, size exclusion for proteins and antibodies). Radio-TLC is fastest and often best for a quick yield analysis to know when to end the radiolabeling (i.e., completion). Radio-HPLC adds UV/Vis detection as another dimension on top of just the retention time/factor obtained via radio-TLC, but radioHPLC takes far longer to run a single analysis (~15–30 min, ~5–10 min UPLC).

- **In step 4** it is time for purification and this step is mostly explained in Fig. 6. A useful tip is that pre-packed PD10 columns (GE, Sephadex G25) are the fastest way to purify large proteins (>5–10 kDa) from free radiometal and can aid in buffer exchange. Centrifugal spin filters (e.g., Vivaspin, Amicon) also work well to remove radiometals and small molecules/buffer, and can be purchased with molecular weight cut-offs ranging from 3 to 100 kDa. These should be spun down via centrifuge *generally* at 4 K rpm for the bigger 50 mL and 15 mL versions and 10-14 K rpm for the small microcentrifuge size, but read the manual as each brand/type has specific speed requirements! These spin filters should be re-filled with your desired final buffer (e.g., injectate solution/buffer) and spun down an additional 2–3 times (which takes much longer than PD10). The free radiometal and other small molecules pass through the size-exclusion membrane and are collected in the bottom of the tube. Both methods produce high-purity radiometallated-protein, but neither methods give you information about protein aggregates or if there is appreciable protein degradation into smaller fragments. To obtain this information, a final size-exclusion HPLC column/system (buffer is typically saline) must be used to observe—and if desired—remove lower and higher molecular weight impurities/aggregates. Final filtration through a 0.22 micron syringe filter also renders the injectate sterile (if prepared under sterile aseptic conditions, e.g., GMP), but some vectors may be sensitive to 0.22 micron filtration.

- **Step 5** is usually a re-injection onto an analytical radio-HPLC column, or another radio-TLC for quality control. Clinical tracers might have other quality control requirements to test for things such as residual solvent or reagent and long-term pyrogen/sterility testing.

- **Steps 6 and 7** are up to the user to decide how to use this new radioactive imaging probe or targeted radionuclide therapy agent. Common applications are covered elsewhere, but include studying/treating cells, infectious bacteria, animals, tumor models, humans, and even the environment. Various types of drugs are commonly radiolabeled to study their pharmacology in animal and human patients (e.g., pharmacokinetics).
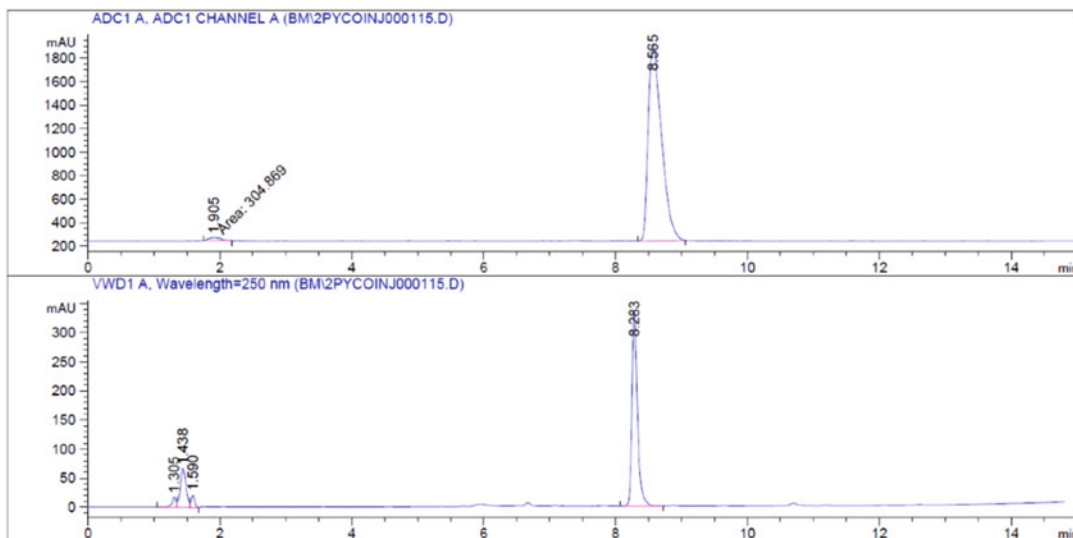
Fig. 7 Representative radioactive (top) and UV (absorbance at 250 nm; bottom) RP-HPLC chromatogram of co-injected radioactive and non-radioactive metal complex on a C_{18} analytical column using mobile phase: A—0.1% TFA in water, B—0.1% TFA in acetonitrile, 1 mL/min, 0–100% B over 20 min. Unchelated radiometal elutes at early retention times ($t_R = 3.9$ min), while radiometal complex is retained and elutes later ($t_R = 8.2$–8.6 min). Note that the radioactive chromatogram is slightly later in retention compared to the UV due to the radiation detector being placed after the UV detector in series. Highly polar species might also elute at the void volume of your column along with free radiometal, so a cold-standard is required to determine the retention time

3.2 Radiolabeling Yield Analysis

3.2.1 Radio-HPLC

A small aliquot of (approx. 1–10 µL, for radiolabeling yield analysis) or the entire radiolabeling reaction (for radiotracer purification) will be injected onto the radio-HPLC system, and species are passed through and separated on a column (stationary phase) with a solvent or mixture of solvents (mobile phase). The concentration of species that elute off the column will be measured by the UV detector, which is proportional to the concentration of solute present, and the radiation detector measures the radioactivity of the compounds in the eluate (Fig. 7).

The column packing used will depend on the nature of the radiotracer. Most commonly, for small molecule or peptide-based conjugates, reverse phase (RP) columns consisting of fully porous, silica microparticles chemically bonded with alkyl chains such as octyl-(C_8) and octadecyl-(C_{18}) are used which retain molecules based on their polarity. Mobile phases for RP-HPLC are polar solvents such as water, to which miscible organic solvents such as methanol and acetonitrile are added. Since protonation of metal complexes and biomolecules can affect retention time and resolution, the pH of the mobile phase is often controlled by addition of acid or base (e.g., 0.1% trifluoroacetic acid). The solvent strength can be varied by changing the solvent ratio of the aqueous (water) and organic (acetonitrile or methanol) solvents overtime, to create a gradient, or kept at a constant ratio for an isocratic method.

For large molecular weight conjugates such as monoclonal antibodies (MW = 150 kDa), size exclusion chromatography (SEC) HPLC columns are employed. SEC separates molecules based on their size by running the molecules through a column consisting of spherical beads containing pores of specific size distribution. Separation is achieved when the molecules of different sizes are included or excluded from the pores within the matrix; smaller sized particles will diffuse into the pores more readily and thus will travel slower than larger molecules that do not enter the pores. As such, large molecules elute first (shorter retention times). Since the elution of compounds is determined solely by their size, the solvent systems used in SEC are typically isocratic.

For reaction monitoring, analytical (4.6 mm diameter) HPLC columns can be employed, while semi-preparative (10 mm diameter) HPLC columns can be used in radiotracer purification (either column is typically between 15 and 30 cm in length). For example, a C18 stationary phase (e.g., Luna 5 μm C18 100 Å, Hydro RP C18) can be used for radiolabeling yield monitoring and tracer purification, respectively.

3.2.2 Radio-TLC   Thin layer chromatography (TLC) can be used to assess radiolabeling and radiochemical yields. Small strips (approx. 0.5–2 cm W × 5–15 cm H) of paper or aluminum-backed plates are employed. Typically, a small aliquot (1–10 μL) of a radiolabeling reaction mixture is spotted at the baseline (retention factor, $R_f = 0$; approx. 1–1.5 cm above the bottom of the strip of paper), the spot dried, and the plate is placed vertically in a chamber containing mobile phase solution such that the spot is not immediately immersed in the solution. The TLC plate is left in the chamber until the mobile phase has sufficient time to migrate up to the top of the plate ($R_f = 1$).

After developing, the TLC plate can be read in a TLC plate reader (*see* **Note** 7). TLC plate readers will produce a chromatogram of the number of counts (y-axis) versus the position on the plate (x-axis) (Fig. 8), which can be used to calculate percent radiochemical yield (%RCY), or equivalent, by integrating the area under each peak. The quantity of radioactivity spotted onto the TLC strips is dependent on the detector used, where for Eckert and Ziegler AR2000 (previously BioScan) a *maximum* of ~1 μCi per TLC strip is ideal.

If a radio-TLC plate reader is not available, developed TLC plates may be cut in half and the activity (counts) of each counted in a gamma counter (such as a Perkin-Elmer Automated Wizard Gamma Counter) and number of counts in each half compared. The cut-and-count method assumes good peak separation between the radiolabeled and unchelated radiometal. Typically the radiometal complex sticks to the baseline ($R_f = 0$), while unchelated radiometal migrates with the solvent from ($R_f = 1$); this is not
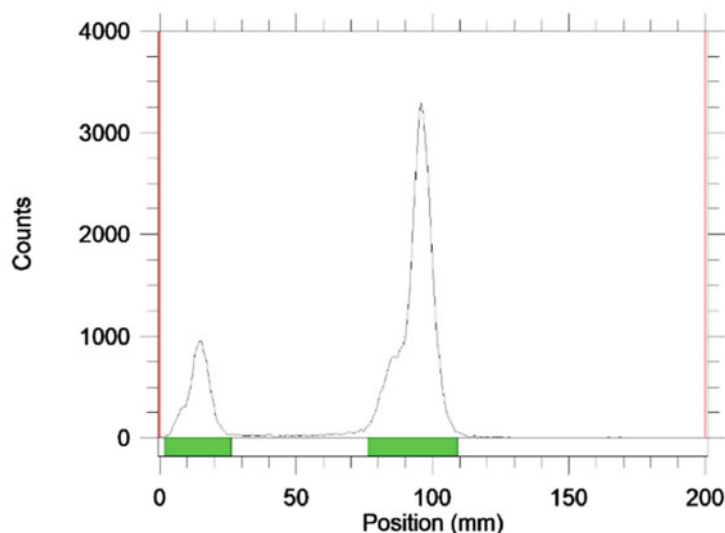
Fig. 8 Representative radio-TLC chromatogram showing separation of radio-metal complex (15 mm, $R_f = 0$) from unchelated radiometal (100 mm, $R_f = 1$). Integration of area under the peaks gives radiochemical yield. In this example, RCY is 20%

Table 5
Typical TLC stationary and mobile phase pairings

Stationary phase	MobilepPhase	R_f (complex (see Note 8)	R_f (unchelated metal)
Silica gel	Conc. aq. NH_3/MeOH/H_2O 1/2/1 (v/v/v)	>0.5	<0.1
C-18	MeOH/10% NH_4OAc (3:7)	>0	<0.1
Silica gel or C-18	MeOH/10% NH_4OAc (50:50)	~0.5–0.6	<0.1
iTLC-SA or iTLC-SG or Al-backed silica TLC	EDTA (50–100 mM, pH 4–7)	0	1
iTLC-SG or Al-based silica	Citric acid (0.4 M, pH 4) with or without 10% methanol	0	1
iTLC-SG	10 mM NaOH/9% NaCl	>0.1	0

always the case and depends on the nature of the labeled compounds and the mobile phase used, thus each system must be validated with proper controls prior to use. For a list of commonly used elution solvents (TLC mobile phases) see Table 5.

3.3   Conclusions   In summary, radiometallation chemistry is required to create radiometal-based radiopharmaceuticals and involves an intricate balance of many parameters. Key concepts have been covered including bifunctional chelators, coordination chemistry, water radiolysis and radioprotectants, aqueous chemistry of radiometals, buffers and pH considerations, and basic equipment and procedural considerations. This chapter should provide the reader with both the requisite scientific foundation for understanding radiometallation chemistry, and practical tips and workflows for performing it yourself.

4   Notes

1. Careful attention should be made to eliminate the introduction of non-radioactive metal impurities in radiolabeling reactions that may interfere with BFC labeling.

2. Evidence suggests that radiolabeling in the presence of organic solvents such as ethanol, isopropyl alcohol, and acetonitrile may improve radiolabeling yield. Recently, Rösch and co-workers have shown that [^{68}Ga]Ga-, [^{44}Sc]Sc-, and [^{177}Lu]Lu-DOTA labeling yields can be increased at significantly lower temperature than 95 °C when binary water/organic solvent mixtures are used [31, 32]; however, these conditions will not be discussed in this chapter.

3. In general, buffers that can interact or bind with metal ions should be avoided, as these can interfere with radiolabeling and cause aberrant results. Tris–HCl should not be used for bioconjugations (-NH$_2$).

4. A small amount (~10–20% v/v) of ethanol or DMSO may be added in the case that the chelator/bioconjugate is not entirely soluble. Ensure that the percent of organic solvent in the final radiolabeling reaction mixture does not exceed ~10% v/v, or <2–3% DMSO for antibodies.

5. IMPORTANT: Maintain your stock radiometal solution in acidic medium, unless otherwise noted. Do not use buffered solutions to dilute radiometal stock solutions and only adjust the pH of aliquots that you plan to immediately use for radiolabeling. Neutralizing radiometal stock solutions can cause the formation of insoluble metal hydroxide species rendering your isotope unusable for radiolabeling.

6. See Subheading 3.1 for important pre-conditioning and neutralization requirements of [^{89}Zr]Zr^{4+} prior to radiolabeling.

7. For radiometals with several radioactive progeny (e.g., ^{225}Ac, ^{212}Pb, ^{227}Th), plates cannot be counted immediately, instead TLC plates can be stored and counted after secular/transient equilibrium has been reached. Similarly, ^{213}Bi plates should be read immediately to eliminate interference from grow-in of grand-daughter ^{209}Pb ($t_{1/2} = 3.2$ h).

8. The specified retention factors are for small molecule or native chelate structures only and should be verified for each radiometal-chelate pairing used.

References

1. Baes CF, Mesmer RE (1981) The thermodynamics of cation hydrolysis. Am J Sci 281(7): 935–962. https://doi.org/10.2475/ajs.281.7.935

2. Baes CF Jr, Mesmer RE (1976) The hydrolysis of cations. The Hydrolysis of Cations; Wiley-Interscience, New York

3. Martell AE, Smith RM (1977) Critical stability constants, *vol. 3: other organic ligands*. Plenum Press, New York

4. Ramogida CF, Orvig C (2013) Tumour targeting with radiometals for diagnosis and therapy. Chem Commun Camb Engl 49(42):4720–4739. https://doi.org/10.1039/c3cc41554f

5. Price EW, Orvig C (2014) Matching Chelators to Radiometals for radiopharmaceuticals. Chem Soc Rev 43(1):260–290. https://doi.org/10.1039/c3cs60304k

6. Kostelnik TI, Orvig C (2019) Radioactive main group and rare earth metals for imaging and therapy. Chem Rev 119(2):902–956. https://doi.org/10.1021/acs.chemrev.8b00294

7. Boros E, Packard AB (2019) Radioactive transition metals for imaging and therapy. Chem Rev 119(2):870–901. https://doi.org/10.1021/acs.chemrev.8b00281

8. Wadas TJ, Wong EH, Weisman GR, Anderson CJ (2010) Coordinating radiometals of copper, gallium, indium, yttrium, and zirconium for PET and SPECT imaging of disease. Chem Rev 110(5):2858–2902. https://doi.org/10.1021/cr900325h

9. Price EW, Orvig C (2014) The chemistry of inorganic nuclides (86Y, 68Ga, 64Cu, 89Zr, 124I). In: The chemistry of molecular imaging. Wiley, pp 105–135. https://doi.org/10.1002/9781118854754.ch5

10. Khozeimeh Sarbisheh, E.; Price, E. W. The radiopharmaceutical chemistry of the radioisotopes of lutetium and yttrium. In Radiopharmaceutical chemistry; Lewis, J. S., Windhorst, A. D., Zeglis, B. M., Eds.; Springer Cham, 2019; pp. 359–370. https://doi.org/10.1007/978-3-319-98947-1_20

11. Wren JC (2010) Steady-state radiolysis: effects of dissolved additives. In: Nuclear energy and the environment; ACS symposium series, vol 1046. Am Chem Soc, pp 271–295. https://doi.org/10.1021/bk-2010-1046.ch022

12. Sørensen BS, Horsman MR (2020) Tumor hypoxia: impact on radiation therapy and molecular pathways. Front Oncol 10:562–562. https://doi.org/10.3389/fonc.2020.00562

13. Targeted Alpha Therapy Working Group (2018) Targeted alpha therapy, an emerging class of cancer agents: a review. JAMA Oncol 4(12):1765–1772. https://doi.org/10.1001/jamaoncol.2018.4044

14. Garrett BC, Dixon DA, Camaioni DM, Chipman DM, Johnson MA, Jonah CD, Kimmel GA, Miller JH, Rescigno TN, Rossky PJ, Xantheas SS, Colson SD, Laufer AH, Ray D, Barbara PF, Bartels DM, Becker KH, Bowen KH, Bradforth SE, Carmichael I, Coe JV, Corrales LR, Cowin JP, Dupuis M, Eisenthal KB, Franz JA, Gutowski MS, Jordan KD, Kay BD, LaVerne JA, Lymar SV, Madey TE, McCurdy CW, Meisel D, Mukamel S, Nilsson AR, Orlando TM, Petrik NG, Pimblott SM, Rustad JR, Schenter GK, Singer SJ, Tokmakoff A, Wang L-S, Zwier TS (2005) Role of water in electron-initiated processes and radical chemistry: issues and scientific advances. Chem Rev 105(1):355–390. https://doi.org/10.1021/cr030453x

15. Codorniu-Hernández E, Kusalik PG (2012) Mobility mechanism of hydroxyl radicals in aqueous solution via hydrogen transfer. J Am Chem Soc 134(1):532–538. https://doi.org/10.1021/ja208874t

16. Bhatt NB, Pandya DN, Rideout-Danner S, Gage HD, Marini FC, Wadas TJ (2018) A comprehensively revised strategy that improves the specific activity and long-term stability of clinically relevant (89)Zr-immuno-PET agents. Dalton Trans 47(37):13214–13221. https://doi.org/10.1039/c8dt01841c

17. Anbar M, Thomas JK (1964) Pulse radiolysis studies of aqueous sodium chloride solutions1. J Phys Chem 68(12):3829–3835. https://doi.org/10.1021/j100794a050

18. Mishra OP, Popov AV, Pietrofesa RA, Christofidou-Solomidou M (2016) Gamma-irradiation produces active chlorine species (ACS) in physiological solutions: secoisolariciresinol diglucoside (SDG) scavenges ACS – a novel mechanism of DNA radioprotection. Biochim Biophys Acta 1860(9):1884–1897. https://doi.org/10.1016/j.bbagen.2016.05.037

19. Mueller D, Breeman WAP, Klette I, Gottschaldt M, Odparlik A, Baehre M, Tworowska I, Schultz MK (2016) Radiolabeling of DOTA-like conjugated peptides with generator-produced (68)Ga and using NaCl-based cationic elution method. Nat Protoc 11(6):1057–1066. https://doi.org/10.1038/nprot.2016.060

20. Zacchia NA, Martinez DM, Hoehr C (2020) Radiolysis reduction in liquid solution targets for the production of 89Zr. Appl Radiat Isot 155:108791. https://doi.org/10.1016/j.apradiso.2019.06.037

21. de Zanger RMS, Chan HS, Breeman WAP, de Blois E (2019) Maintaining radiochemical purity of [177Lu]Lu-DOTA-PSMA-617 for PRRT by reducing radiolysis. J Radioanal Nucl Chem 321(1):285–291. https://doi.org/10.1007/s10967-019-06573-y

22. Liu S, Edwards DS (2001) Stabilization of 90Y-labeled DOTA-biomolecule conjugates using gentisic acid and ascorbic acid. Bioconjug Chem 12(4):554–558. https://doi.org/10.1021/bc000145v

23. Liu S, Ellars CE, Edwards DS (2003) Ascorbic acid: useful as a buffer agent and radiolytic stabilizer for metalloradiopharmaceuticals. Bioconjug Chem 14(5):1052–1056. https://doi.org/10.1021/bc034109i

24. Jacobson MS, Dankwart HR, Mahoney DW (2009) Radiolysis of 2-[18F]fluoro-2-deoxy-d-glucose ([18F]FDG) and the role of ethanol and radioactive concentration. Appl Radiat Isot 67(6):990–995. https://doi.org/10.1016/j.apradiso.2009.01.005

25. Chen J, Linder KE, Cagnolini A, Metcalfe E, Raju N, Tweedle MF, Swenson RE (2008) Synthesis, stabilization and formulation of [177Lu]Lu-AMBA, a systemic radiotherapeutic agent for gastrin releasing peptide receptor positive tumors. Appl Radiat Isot 66(4):497–505. https://doi.org/10.1016/j.apradiso.2007.11.007

26. Hernandez R, Heskamp S, Rijpkema M, Bos DL, Goldenberg DM, McBride WJ, Morgenstern A, Bruchertseifer F, Cai W, Boerman OC (2017) Preventing radiobleaching of cyanine fluorophores enhances stability of nuclear/NIRF multimodality imaging agents. Theranostics 7(1):1–8. https://doi.org/10.7150/thno.15124

27. Buxton GV, Greenstock CL, Helman WP, Ross AB (1988) Critical review of rate constants for reactions of hydrated electrons, hydrogen atoms and hydroxyl radicals (·OH/·O− in aqueous solution. J Phys Chem Ref Data 17(2):513–886. https://doi.org/10.1063/1.555805

28. Oturan M, Pinson J, Deprez D, Terlain B (1992) Polyhydroxylation of salicylic acid by electrocheically generated OH radicals. New J Chem 16:705–710

29. Redpath J, Willson R (1973) Reducing compounds in radioprotection and radiosensitization: model experiments using ascorbic acid. Int J Radiat Biol Relat Stud Phys Chem Med 23(1):51–65

30. Chakrabarti MC, Le N, Paik CH, De Graff WG, Carrasquillo JA (1996) Prevention of radiolysis of monoclonal antibody during labeling. J Nucl Med 37(8):1384–1388

31. Pérez-Malo M, Szabó G, Eppard E, Vagner A, Brücher E, Tóth I, Maiocchi A, Suh EH, Kovács Z, Baranyai Z, Rösch F (2018) Improved efficacy of synthesizing∗MIII-labeled DOTA complexes in binary mixtures of water and organic solvents. A combined radio- and physicochemical study. Inorg Chem 57(10):6107–6117. https://doi.org/10.1021/acs.inorgchem.8b00669

32. Eppard E, Pèrez-Malo M, Rösch F (2017) Improved radiolabeling of DOTATOC with trivalent radiometals for clinical application by addition of ethanol. EJNMMI Radiopharm Chem 1(1):6. https://doi.org/10.1186/s41181-016-0010-8

33. Tworowska I, Ranganathan D, Thamake S, Delpassand E, Mojtahedi A, Schultz MK, Zhernosekov K, Marx S (2016) Radiosynthesis of clinical doses of 68Ga-DOTATATE (GalioMedix™) and validation of organic-matrix-based 68Ge/68Ga generators. Nucl

Med Biol 43(1):19–26. https://doi.org/10.1016/j.nucmedbio.2015.08.004

34. Joshi R, Gangabhagirathi R, Venu S, Adhikari S, Mukherjee T (2012) Antioxidant activity and free radical scavenging reactions of gentisic acid: in-vitro and pulse radiolysis studies. Free Radic Res 46(1):11–20. https://doi.org/10.3109/10715762.2011.633518

35. Ramogida CF, Orvig C (2013) Tumour targeting with radiometals for diagnosis and therapy. Chem Commun 49(42):4720–4739. https://doi.org/10.1039/c3cc41554f

36. Bartholomä MD (2012) Recent developments in the design of bifunctional chelators for metal-based radiopharmaceuticals used in positron emission tomography. Inorganica Chim Acta 389(0):36–51. https://doi.org/10.1016/j.ica.2012.01.061

37. Anderson CJ, Welch MJ (1999) Radiometal-labeled agents (non-technetium) for diagnostic imaging. Chem Rev 99(9):2219–2234. https://doi.org/10.1021/cr980451q

38. Cutler CS, Hennkens HM, Sisay N, Huclier-Markai S, Jurisson SS (2013) Radiometals for combined imaging and therapy. Chem Rev 113(2):858–883. https://doi.org/10.1021/cr3003104

39. Zeglis BM, Houghton JL, Evans MJ, Viola-Villegas N, Lewis JS (2013) Underscoring the influence of inorganic chemistry on nuclear imaging with radiometals. Inorg Chem. https://doi.org/10.1021/ic401607z

40. Zeglis BM, Mohindra P, Weissmann GI, Divilov V, Hilderbrand SA, Weissleder R, Lewis JS (2011) Modular strategy for the construction of radiometalated antibodies for positron emission tomography based on inverse electron demand Diels-Alder click chemistry. Bioconjug Chem 22(10):2048–2059. https://doi.org/10.1021/bc200288d

41. Zeglis BM, Lewis JS (2011) A practical guide to the construction of radiometallated bioconjugates for positron emission tomography. Dalton Trans 40(23):6168–6195. https://doi.org/10.1039/C0DT01595D

42. Lederer CM, Shirley VS (1978) Table of isotopes, 7th edn. Wiley, New York

43. Holland JP, Williamson MJ, Lewis JS (2010) Unconventional nuclides for radiopharmaceuticals. Mol Imaging 9(1):1–20

44. Qaim SM (2008) Decay data and production yields of some non-standard positron emitters used in PET. Q J Nucl Med Mol Imaging 52:111–120

45. Chu SYF, Ekström LP (1999) Firestone, R. B. WWW Table Radioact. Isot. Database Version 2281999 Httpnucleardatanuclearlusenucleardatatoi

46. Conti M, Eriksson L (2016) Physics of pure and non-pure positron emitters for PET: a review and a discussion. EJNMMI Phys 3(1):8. https://doi.org/10.1186/s40658-016-0144-5

47. Keinänen O, Fung K, Brennan JM, Zia N, Harris M, van Dam E, Biggin C, Hedt A, Stoner J, Donnelly PS, Lewis JS, Zeglis BM (2020) Harnessing 64Cu/67Cu for a theranostic approach to pretargeted radioimmunotherapy. Proc Natl Acad Sci U S A 117(45):28316–28327. https://doi.org/10.1073/pnas.2009960117

48. Di Bartolo N, Sargeson AM, Smith SV (2006) New 64Cu PET imaging agents for personalised medicine and drug development using the Hexa-Aza cage. SarAr Org Biomol Chem 4(17):3350–3357

49. Di Bartolo NM, Sargeson AM, Donlevy TM, Smith SV (2001) Synthesis of a new cage ligand, SarAr, and its complexation with selected transition metal ions for potential use in radioimaging. Dalton Trans 0(15):2303–2309. https://doi.org/10.1039/b103242a

50. Lears KA, Ferdani R, Liang K, Zheleznyak A, Andrews R, Sherman CD, Achilefu S, Anderson CJ, Rogers BE (2011) In vitro and in vivo evaluation of 64Cu-labeled SarAr-bombesin analogs in gastrin-releasing peptide receptor–expressing prostate cancer. J Nucl Med 52(3):470–477. https://doi.org/10.2967/jnumed.110.082826

51. Mume E, Asad A, Di Bartolo NM, Kong L, Smith C, Sargeson AM, Price R, Smith SV (2013) Synthesis of hexa aza cages, SarAr-NCS and AmBaSar and a study of their metal complexation, conjugation to nanomaterials and proteins for application in radioimaging and therapy. Dalton Trans 42:14402–14410. https://doi.org/10.1039/c3dt51199e

52. Boswell CA, Sun X, Niu W, Weisman GR, Wong EH, Rheingold AL, Anderson CJ (2004) Comparative in vivo stability of copper-64-labeled cross-bridged and conventional tetraazamacrocyclic complexes. J Med Chem 47(6):1465–1474. https://doi.org/10.1021/jm030383m

53. Roux A, Gillet R, Huclier-Markai S, Ehret-Sabatier L, Charbonnière LJ, Nonat AM (2017) Bifunctional bispidine derivatives for copper-64 labelling and positron emission

tomography. Org Biomol Chem 15(6): 1475–1483. https://doi.org/10.1039/C6OB02712A

54. Roux A, Nonat AM, Brandel J, Hubscher-Bruder V, Charbonnière LJ (2015) Kinetically inert bispidol-based cu(II) chelate for potential application to $^{64/67}$ cu nuclear medicine and diagnosis. Inorg Chem 54(9): 4431–4444. https://doi.org/10.1021/acs.inorgchem.5b00207

55. De Silva RA, Jain S, Lears KA, Chong H-S, Kang CS, Sun X, Rogers BE (2012) Copper-64 radiolabeling and biological evaluation of bifunctional chelators for radiopharmaceutical development. Nucl Med Biol 39(8): 1099–1104. https://doi.org/10.1016/j.nucmedbio.2012.05.009

56. Boswell CA, Regino CAS, Baidoo KE, Wong KJ, Bumb A, Xu H, Milenic DE, Kelley JA, Lai CC, Brechbiel MW (2008) Synthesis of a cross-bridged cyclam derivative for peptide conjugation and 64Cu radiolabeling. Bioconjug Chem 19(7):1476–1484. https://doi.org/10.1021/bc800039e

57. Boros E, Cawthray JF, Ferreira CL, Patrick BO, Adam MJ, Orvig C (2012) Evaluation of the H2dedpa scaffold and Its CRGDyK conjugates for labeling with 64Cu. Inorg Chem 51(11):6279–6284. https://doi.org/10.1021/ic300482x

58. Ramogida CF, Boros E, Patrick BO, Zeisler SK, Kumlin J, Adam MJ, Schaffer P, Orvig C (2016) Evaluation of H 2 CHXdedpa, H 2 dedpa- and H 2 CHXdedpa-N,N′-Propyl-2-NI ligands for 64 Cu(Ii) radiopharmaceuticals. Dalton Trans 45(33):13082–13090. https://doi.org/10.1039/C6DT00932H

59. Boros E, Rybak-akimova E, Holland JP, Rietz T, Rotile N, Blasi F, Day H, Lati R, Caravan P (2014) Pycup - a bifunctional, cage-like ligand for 64Cu radiolabeling. Mol Pharm 11:617–629

60. Thiele NA, Brown V, Kelly JM, Amor-Coarasa A, Jermilova U, MacMillan SN, Nikolopoulou A, Ponnala S, Ramogida CF, Robertson AKH, Rodríguez-Rodríguez C, Schaffer P, Williams C, Babich JW, Radchenko V, Wilson JJ (2017) An eighteen-membered macrocyclic ligand for actinium-225 targeted alpha therapy. Angew Chem Int Ed 56(46):14712–14717. https://doi.org/10.1002/anie.201709532

61. Li L, Rousseau J, Jaraquemada-Peláez M de G, Wang X, Robertson A, Radchenko V, Schaffer P, Lin KS, Bénard F, Orvig C (2020) 225 Ac-H 4 Py4pa for targeted alpha therapy. Bioconjug Chem acs.bioconjchem.0c00171. https://doi.org/10.1021/acs.bioconjchem.0c00171

62. Yang H, Zhang C, Yuan Z, Rodriguez-Rodriguez C, Robertson A, Radchenko V, Perron R, Gendron D, Causey P, Gao F, Bénard F, Schaffer P (2020) Synthesis and evaluation of a macrocyclic actinium-225 chelator, quality control and in vivo evaluation of 225 ac-crown-αMSH peptide. Chem Eur J 26(50):11435–11440. https://doi.org/10.1002/chem.202002999

63. Comba P, Jermilova U, Orvig C, Patrick BO, Ramogida CF, Rück K, Schneider C, Starke M (2017) Octadentate picolinic acid-based bispidine ligand for radiometal ions. Chem Eur J 23(63):15945–15956. https://doi.org/10.1002/chem.201702284

64. Ramogida CF, Robertson AKH, Jermilova U, Zhang C, Yang H, Kunz P, Lassen J, Bratanovic I, Brown V, Southcott L, Rodrí-guez-Rodríguez C, Radchenko V, Bénard F, Orvig C, Schaffer P (2019) Evaluation of polydentate picolinic acid chelating ligands and an α-melanocyte-stimulating hormone derivative for targeted alpha therapy using ISOL-produced 225Ac. EJNMMI Radio-pharm Chem 4(1):21. https://doi.org/10.1186/s41181-019-0072-5

65. Kratochwil C, Bruchertseifer F, Giesel FL, Weis M, Verburg FA, Mottaghy F, Kopka K, Apostolidis C, Haberkorn U, Morgenstern A (2016) 225Ac-PSMA-617 for PSMA-targeted -radiation therapy of metastatic castration-resistant prostate cancer. J Nucl Med 57(12):1941–1944. https://doi.org/10.2967/jnumed.116.178673

66. Norenberg JP, Krenning BJ, Konings IRHM, Kusewitt DF, Nayak TK, Anderson TL, de Jong M, Garmestani K, Brechbiel MW, Kvols LK (2006) 213Bi-[DOTA0, Tyr3]octreotide peptide receptor radionuclide therapy of pancreatic tumors in a preclinical animal model. Clin Cancer Res Off J Am Assoc Cancer Res 12(3 Pt 1):897–903. https://doi.org/10.1158/1078-0432.CCR-05-1264

67. Li M, Zhang X, Quinn TP, Lee D, Liu D, Kunkel F, Zimmerman BE, McAlister D, Olewein K, Menda Y, Mirzadeh S, Copping R, Johnson FL, Schultz MK (2017) Automated cassette-based production of high specific activity [(203/212)Pb]peptide-based Theranostic radiopharmaceuticals for image-guided radionuclide therapy for cancer. Appl Radiat Isot Data Instrum Methods Use Agric Ind Med 127:52–60. https://doi.org/10.1016/j.apradiso.2017.05.006

68. Nikula TK, Curcio MJ, Brechbiel MW, Gansow OA, Finn RD, Scheinberg DA (1995) A rapid, single vessel method for preparation of clinical grade ligand conjugated monoclonal antibodies. Nucl Med Biol 22(3):387–390.

https://doi.org/10.1016/0969-8051(94)00126-5

69. Rosenblat TL, McDevitt MR, Mulford DA, Pandit-Taskar N, Divgi CR, Panageas KS, Heaney ML, Chanel S, Morgenstern A, Sgouros G, Larson SM, Scheinberg DA, Jurcic JG (2010) Sequential cytarabine and alpha-particle immunotherapy with bismuth-213-lintuzumab (HuM195) for acute myeloid leukemia. Clin Cancer Res Off J Am Assoc Cancer Res 16(21):5303–5311. https://doi.org/10.1158/1078-0432.CCR-10-0382

70. Westrøm S, Generalov R, Bønsdorff TB, Larsen RH (2017) Preparation of 212Pb-Labeled monoclonal antibody using a novel 224Ra-based generator solution. Nucl Med Biol 51:1–9. https://doi.org/10.1016/j.nucmedbio.2017.04.005

71. McNeil BL, Robertson AKH, Fu W, Yang H, Hoehr C, Ramogida CF, Schaffer P (2021) Production, purification, and radiolabeling of the 203Pb/212Pb theranostic pair. EJNMMI Radiopharm Chem 6(1):6. https://doi.org/10.1186/s41181-021-00121-4

72. Shah MA, Zhang X, Rossin R, Robillard MS, Fisher DR, Bueltmann T, Hoeben FJM, Quinn TP (2017) Metal-free cycloaddition chemistry driven pretargeted radioimmunotherapy using α-particle radiation. Bioconjug Chem 28(12):3007–3015. https://doi.org/10.1021/acs.bioconjchem.7b00612

73. Baidoo KE, Milenic DE, Brechbiel MW (2013) Methodology for labeling proteins and peptides with Lead-212 (212Pb). Nucl Med Biol 40(5):592–599. https://doi.org/10.1016/j.nucmedbio.2013.01.010

74. Stallons TAR, Saidi A, Tworowska I, Delpassand ES, Torgue JJ (2019) Preclinical investigation of ^{212}Pb-DOTAMTATE for peptide receptor radionuclide therapy in a neuroendocrine tumor model. Mol Cancer Ther 18(5):1012. https://doi.org/10.1158/1535-7163.MCT-18-1103

75. Koumarianou E, Loktionova NS, Fellner M, Roesch F, Thews O, Pawlak D, Archimandritis SC, Mikolajczak R 44Sc-DOTA-BN[2–14]NH2 in comparison to 68Ga-DOTA-BN[2–14]NH2 in pre-clinical investigation. Is 44Sc a potential radionuclide for PET? Appl Radiat Isot 12, 70(12):2669–2676. https://doi.org/10.1016/j.apradiso.2012.08.004

76. Huclier-Markai S, Kerdjoudj R, Alliot C, Bonraisin AC, Michel N, Haddad F, Barbet J. Optimization of reaction conditions for the radiolabeling of DOTA and DOTA-peptide with 44m/44Sc and experimental evidence of the feasibility of an in Vivo PET generator. Nucl Med Biol 5, 41, Supplement (0):e36–e43. https://doi.org/10.1016/j.nucmedbio.2013.11.004

77. Nagy G, Dénes N, Kis A, Szabó JP, Berényi E, Garai I, Bai P, Hajdu I, Szikra D, Trencsényi G (2017) Preclinical evaluation of melanocortin-1 receptor (MC1-R) specific ^{68}Ga- and ^{44}Sc-labeled DOTA-NAPamide in melanoma imaging. Eur J Pharm Sci Off J Eur Fed Pharm Sci 106:336–344. https://doi.org/10.1016/j.ejps.2017.06.026

78. Honarvar H, Müller C, Cohrs S, Haller S, Westerlund K, Karlström AE, van der Meulen NP, Schibli R, Tolmachev V (2017) Evaluation of the first 44Sc-labeled affibody molecule for imaging of HER2-expressing tumors. Nucl Med Biol 45:15–21. https://doi.org/10.1016/j.nucmedbio.2016.10.004

79. Eppard E, de la Fuente A, Benešová M, Khawar A, Bundschuh RA, Gärtner FC, Kreppel B, Kopka K, Essler M, Rösch F (2017) Clinical translation and first in-human use of [44Sc]Sc-PSMA-617 for PET imaging of metastasized castrate-resistant prostate cancer. Theranostics 7(18):4359–4369. https://doi.org/10.7150/thno.20586

80. Hernandez R, Valdovinos HF, Yang Y, Chakravarty R, Hong H, Barnhart TE, Cai W (2014) 44Sc: an attractive isotope for peptide-based PET imaging. Mol Pharm 11(8):2954–2961. https://doi.org/10.1021/mp500343j

81. Müller C, Bunka M, Haller S, Köster U, Groehn V, Bernhardt P, van der Meulen N, Türler A, Schibli R (2014) Promising prospects for 44Sc-/47Sc-based theragnostics: application of 47Sc for radionuclide tumor therapy in mice. J Nucl Med 55(10):1658–1664. https://doi.org/10.2967/jnumed.114.141614

82. Domnanich KA, Müller C, Benešová M, Dressler R, Haller S, Köster U, Ponsard B, Schibli R, Türler A, van der Meulen NP (2017) 47Sc as useful β--emitter for the radiotheragnostic paradigm: a comparative study of feasible production routes. EJNMMI Radiopharm Chem 2(1):5. https://doi.org/10.1186/s41181-017-0024-x

83. Nagy G, Szikra D, Trencsényi G, Fekete A, Garai I, Giani AM, Negri R, Masciocchi N, Maiocchi A, Uggeri F, Tóth I, Aime S, Giovenzana GB, Baranyai Z (2017) AAZTA: an ideal chelating agent for the development of 44Sc PET imaging agents. Angew Chem Int Ed 56(8):2118–2122. https://doi.org/10.1002/anie.201611207

84. Chakravarty R, Goel S, Valdovinos HF, Hernandez R, Hong H, Nickles RJ, Cai W

(2014) Matching the decay half-life with the biological half-life: immunoPET imaging with 44Sc-labeled cetuximab fab fragment. Bioconjug Chem. https://doi.org/10.1021/bc500415x

85. Engle JW, Hong H, Zhang Y, Valdovinos HF, Myklejord DV, Barnhart TE, Theuer CP, Nickles RJ, Cai W (2012) Positron emission tomography imaging of tumor angiogenesis with a 66Ga-labeled monoclonal antibody. Mol Pharm 9(5):1441–1448. https://doi.org/10.1021/mp300019c

86. Prata MIM, André JP, Kovács Z, Takács AI, Tircsó G, Tóth I, Geraldes CFGC (2017) Gallium(III) chelates of mixed phosphonate-carboxylate triazamacrocyclic ligands relevant to nuclear medicine: structural, stability and in vivo studies. J Inorg Biochem 177:8–16. https://doi.org/10.1016/j.jinorgbio.2017.08.015

87. Walker RC, Smith GT, Liu E, Moore B, Clanton J, Stabin M (2013) Measured human dosimetry of ^{68}Ga-DOTATATE. J Nucl Med 54(6):855. https://doi.org/10.2967/jnumed.112.114165

88. Heppeler A, André JP, Buschmann I, Wang X, Reubi J-C, Hennig M, Kaden TA, Maecke HR (2008) Metal-ion-dependent biological properties of a Chelator-derived somatostatin analogue for tumour targeting. Chem Eur J 14(10):3026–3034. https://doi.org/10.1002/chem.200701264

89. Boros E, Ferreira CL, Patrick BO, Adam MJ, Orvig C (2011) New Ga derivatives of the H2dedpa scaffold with improved clearance and persistent heart uptake. Nucl Med Biol 38(8):1165–1174. https://doi.org/10.1016/j.nucmedbio.2011.05.004

90. Boros E, Cawthray JF, Ferreira CL, Patrick BO, Adam MJ, Orvig C (2012) Evaluation of the H2dedpa scaffold and its CRGDyK conjugates for labeling with 64Cu. Inorg Chem 51(11):6279–6284

91. Price EW, Cawthray JF, Adam MJ, Orvig C (2014) Modular syntheses of H4octapa and H2dedpa, and yttrium coordination chemistry relevant to 86Y/90Y radiopharmaceuticals. Dalton Trans 43(19):7176–7190. https://doi.org/10.1039/C4DT00239C

92. Boros E, Ferreira CL, Cawthray JF, Price EW, Patrick BO, Wester DW, Adam MJ, Orvig C (2010) Acyclic chelate with ideal properties for 68Ga PET imaging agent elaboration. J Am Chem Soc 132(44):15726–15733. https://doi.org/10.1021/ja106399h

93. Ramogida CF, Cawthray JF, Boros E, Ferreira CL, Patrick BO, Adam MJ, Orvig C (2015) H2CHXdedpa and H4CHXoctapa—chiral acyclic chelating ligands for 67/68Ga and 111In radiopharmaceuticals. Inorg Chem 54(4):2017–2031. https://doi.org/10.1021/ic502942a

94. Notni J, Pohle K, Wester H-J (2012) Comparative gallium-68 labeling of TRAP-, NOTA-, and DOTA-peptides: practical consequences for the future of gallium-68-PET. EJNMMI Res 2(1):1–5. https://doi.org/10.1186/2191-219x-2-28

95. Notni J, Šimeček J, Hermann P, Wester H-J (2011) TRAP, a powerful and versatile framework for gallium-68 radiopharmaceuticals. Chem Eur J 17(52):14718–14722. https://doi.org/10.1002/chem.201103503

96. Notni J, Pohle K, Wester H-J (2013) Be spoilt for choice with radiolabelled RGD peptides: preclinical evaluation of 68 Ga-TRAP(RGD)3. Nucl Med Biol 40(1):33–41. https://doi.org/10.1016/j.nucmedbio.2012.08.006

97. Notni J, Plutnar J, Wester H-J (2012) Bone-seeking TRAP conjugates: surprising observations and their implications on the development of gallium-68-labeled bisphosphonates. EJNMMI Res 2(1):1–4. https://doi.org/10.1186/2191-219x-2-13

98. Waldron BP, Parker D, Burchardt C, Yufit DS, Zimny M, Roesch F (2013) Structure and stability of hexadentate complexes of ligands based on AAZTA for efficient PET labelling with gallium-68. Chem Commun 49(6):579–581. https://doi.org/10.1039/c2cc37544c

99. Eppard E, Wuttke M, Nicodemus PL, Rösch F (2014) Ethanol-based post-processing of generator-derived ^{68}Ga toward kit-type preparation of ^{68}Ga-radiopharmaceuticals. J Nucl Med 55(6):1023. https://doi.org/10.2967/jnumed.113.133041

100. Nayak TK, Garmestani K, Milenic DE, Baidoo KE, Brechbiel MW (2011) HER1-targeted 86Y-panitumumab possesses superior targeting characteristics than 86Y-cetuximab for PET imaging of human malignant mesothelioma tumors xenografts. PLoS One 6(3):e18198

101. Rösch F, Herzog H, Stolz B, Brockmann J, Köhle M, Mühlensiepen H, Marbach P, Müller-Gärtner H-W (1999) Uptake kinetics of the somatostatin receptor ligand [86Y]DOTA-d Phe1-Tyr3-octreotide ([86Y]SMT487) using positron emission tomography in non-human primates and calculation of radiation doses of the 90Y-labelled analogue. Eur J Nucl Med Mol Imaging 26(4):358–366. https://doi.org/10.1007/s002590050398

102. Banerjee SR, Foss CA, Pullambhatla M, Wang Y, Srinivasan S, Hobbs R, Baidoo KE, Brechbiel MW, Nimmagadda S, Mease RC, Sgouros G, Pomper MG (2015) Preclinical evaluation of 86Y-labeled inhibitors of prostate-specific membrane antigen for dosimetry estimates. J Nucl Med. https://doi.org/10.2967/jnumed.114.149062

103. Perk L, Visser O, Stigter-van Walsum M, Vosjan M, Visser G, Zijlstra J, Huijgens P, van Dongen G (2006) Preparation and evaluation of 89Zr-zevalin for monitoring of 90Y-zevalin biodistribution with positron emission tomography. Eur J Nucl Med Mol Imaging 33(11):1337–1345. https://doi.org/10.1007/s00259-006-0160-0

104. Helisch A, Förster GJ, Reber H, Buchholz H-G, Arnold R, Göke B, Weber MM, Wiedenmann B, Pauwels S, Haus U, Bouterfa H, Bartenstein P (2004) Pre-therapeutic dosimetry and biodistribution of 86Y-DOTA-Phe1-Tyr3-octreotide versus 111In-pentetreotide in patients with advanced neuroendocrine tumours. Eur J Nucl Med Mol Imaging 31(10):1386–1392. https://doi.org/10.1007/s00259-004-1561-6

105. Lee FT, Mountain AJ, Kelly MP, Hall C, Rigopoulos A, Johns TG, Smyth FE, Brechbiel MW, Nice EC, Burgess AW, Scott AM (2005) Enhanced efficacy of radioimmunotherapy with 90Y-CHX-A″-DTPA-Hu3S193 by inhibition of epidermal growth factor receptor (EGFR) signaling with EGFR tyrosine kinase inhibitor AG1478. Clin Cancer Res 11(19):7080s–7086s. https://doi.org/10.1158/1078-0432.ccr-1004-0019

106. Schneider DW, Heitner T, Alicke B, Light DR, McLean K, Satozawa N, Parry G, Yoo J, Lewis JS, Parry R (2009) In vivo biodistribution, PET imaging, and tumor accumulation of 86Y- and 111In-antimindin/RG-1, engineered antibody fragments in LNCaP tumor-bearing nude mice. J Nucl Med 50(3):435–443. https://doi.org/10.2967/jnumed.108.055608

107. Brechbiel MW, Gansow OA (1991) Backbone-substituted DTPA ligands for Yttrium-90 radioimmunotherapy. Bioconjug Chem 2(3):187–194. https://doi.org/10.1021/bc00009a008

108. Price EW, Edwards KJ, Carnazza KE, Carlin SD, Zeglis BM, Adam MJ, Orvig C, Lewis JS A comparative evaluation of the chelators H4octapa and CHX-A″-DTPA with the therapeutic radiometal 90Y. Nucl Med Biol 43(9):566–576. https://doi.org/10.1016/j.nucmedbio.2016.06.004

109. Kang CS, Sun X, Jia F, Song HA, Chen Y, Lewis M, Chong H-S (2012) Synthesis and preclinical evaluation of bifunctional ligands for improved chelation chemistry of 90Y and 177Lu for targeted radioimmunotherapy. Bioconjug Chem 23(9):1775–1782. https://doi.org/10.1021/bc200696b

110. Vallabhajosula S, Kuji I, Hamacher KA, Konishi S, Kostakoglu L, Kothari PA, Milowski MI, Nanus DM, Bander NH, Goldsmith SJ (2005) Pharmacokinetics and biodistribution of 111In- and 177Lu-labeled J591 antibody specific for prostate-specific membrane antigen: prediction of 90Y-J591 radiation dosimetry based on 111In or 177Lu? J Nucl Med 46(4):634

111. Kwekkeboom DJ, Bakker WH, Kooij PP, Konijnenberg MW, Srinivasan A, Erion JL, Schmidt MA, Bugaj JL, de Jong M, Krenning EP (2001) [177Lu-DOTA0,Tyr3]Octreotate: comparison with [111In-DTPA0]Octreotide in patients. Eur J Nucl Med 28(9):1319–1325. https://doi.org/10.1007/s002590100574

112. Ahmadzadehfar H, Rahbar K, Kürpig S, Bögemann M, Claesener M, Eppard E, Gärtner F, Rogenhofer S, Schäfers M, Essler M (2015) Early side effects and first results of radioligand therapy with (177)Lu-DKFZ-617 PSMA of castrate-resistant metastatic prostate cancer: a two-centre study. EJNMMI Res 5(1):114. https://doi.org/10.1186/s13550-015-0114-2

113. Kang CS, Chen Y, Lee H, Liu D, Sun X, Kweon J, Lewis MR, Chong H-S (2015) Synthesis and evaluation of a new bifunctional NETA chelate for molecular targeted radiotherapy using90y Or177Lu. Nucl Med Biol 42(3):242–249. https://doi.org/10.1016/j.nucmedbio.2014.10.004

114. Price EW, Cawthray JF, Bailey GA, Ferreira CL, Boros E, Adam MJ, Orvig C (2012) H4octapa: an acyclic chelator for 111In radiopharmaceuticals. J Am Chem Soc 134(20):8670–8683. https://doi.org/10.1021/ja3024725

115. Price EW, Zeglis BM, Cawthray JF, Lewis JS, Adam MJ, Orvig C (2014) What a difference a carbon makes: H4octapa vs. H4C3octapa, ligands for in-111 and Lu-177 radiochemistry. Inorg Chem 53(19):10412–10431. https://doi.org/10.1021/ic501466z

116. Price EW, Zeglis BM, Cawthray JF, Ramogida CF, Ramos N, Lewis JS, Adam MJ, Orvig C (2013) H4octapa-trastuzumab: versatile acyclic chelate system for 111In and 177Lu imaging and therapy. J Am Chem Soc

135(34):12707–12721. https://doi.org/10.1021/ja4049493

117. Price EW, Carnazza KE, Carlin SD, Cho A, Edwards KJ, Sevak KK, Glaser JM, de Stanchina E, Janjigian YY, Lewis JS (2017) 89Zr-DFO-AMG102 Immuno-PET to determine local HGF protein levels in tumors for enhanced patient selection. J Nucl Med 58(9):1386–1394. https://doi.org/10.2967/jnumed.116.187310

118. Sharma SK, Glaser JM, Edwards KJ, Khozeimeh Sarbisheh E, Salih AK, Lewis JS, Price EW (2020) A systematic evaluation of antibody modification and 89Zr-radiolabeling for optimized Immuno-PET. Bioconjug Chem. https://doi.org/10.1021/acs.bioconjchem.0c00087

119. Summers KL, Sarbisheh EK, Zimmerling A, Cotelesage JJH, Pickering IJ, George GN, Price EW (2020) Structural characterization of the solution chemistry of zirconium (IV) desferrioxamine: a coordination sphere completed by hydroxides. Inorg Chem. https://doi.org/10.1021/acs.inorgchem.0c02725

120. Holland JP, Divilov V, Bander NH, Smith-Jones PM, Larson SM, Lewis JS (2010) 89Zr-DFO-J591 for ImmunoPET of prostate-specific membrane antigen expression in vivo. J Nucl Med 51(8):1293–1300. https://doi.org/10.2967/jnumed.110.076174

121. Vosjan MJWD, Perk LR, Visser GWM, Budde M, Jurek P, Kiefer GE, van Dongen GAMS (2010) Conjugation and radiolabeling of monoclonal antibodies with zirconium-89 for PET imaging using the bifunctional chelate p-isothiocyanatobenzyl-desferrioxamine. Nat Protoc 5(4):739–743

122. Allott L, Da Pieve C, Meyers J, Spinks T, Ciobota DM, Kramer-Marek G, Smith G (2017) Evaluation of DFO-HOPO as an octadentate chelator for zirconium-89. Chem Commun 53(61):8529–8532. https://doi.org/10.1039/C7CC03572A

123. Deri MA, Ponnala S, Kozlowski P, Burton-Pye BP, Cicek HT, Hu C, Lewis JS, Francesconi LC (2015) P-SCN-Bn-HOPO: a superior bifunctional chelator for 89Zr ImmunoPET. Bioconjug Chem 26(12):2579–2591. https://doi.org/10.1021/acs.bioconjchem.5b00572

124. Deri MA, Ponnala S, Zeglis BM, Pohl G, Dannenberg JJ, Lewis JS, Francesconi LC (2014) Alternative chelator for 89Zr radiopharmaceuticals: radiolabeling and evaluation of 3,4,3-(LI-1,2-HOPO). J Med Chem

57(11):4849–4860. https://doi.org/10.1021/jm500389b

125. Raavé R, Sandker G, Adumeau P, Jacobsen CB, Mangin F, Meyer M, Moreau M, Bernhard C, Da Costa L, Dubois A, Goncalves V, Gustafsson M, Rijpkema M, Boerman O, Chambron J-C, Heskamp S, Denat F (2019) Direct comparison of the in vitro and in vivo stability of DFO, DFO* and DFOcyclo* for 89Zr-ImmunoPET. Eur J Nucl Med Mol Imaging 46(9):1966–1977. https://doi.org/10.1007/s00259-019-04343-2

126. Vugts DJ, Klaver C, Sewing C, Poot AJ, Adamzek K, Huegli S, Mari C, Visser GWM, Valverde IE, Gasser G, Mindt TL, van Dongen GAMS (2017) Comparison of the octadentate bifunctional chelator DFO*-PPhe-NCS and the clinically used hexadentate bifunctional chelator DFO-PPhe-NCS for (89)Zr-immuno-PET. Eur J Nucl Med Mol Imaging 44(2):286–295. https://doi.org/10.1007/s00259-016-3499-x

127. Patra M, Bauman A, Mari C, Fischer CA, Blacque O, Haussinger D, Gasser G, Mindt TL (2014) An octadentate bifunctional chelating agent for the development of stable zirconium-89 based molecular imaging probes. Chem Commun 50(78):11523–11525. https://doi.org/10.1039/C4CC05558F

128. Briand M, Aulsebrook ML, Mindt TL, Gasser G (2017) A solid phase-assisted approach for the facile synthesis of a highly water-soluble zirconium-89 chelator for radiopharmaceutical development. Dalton Trans 46(47):16387–16389. https://doi.org/10.1039/C7DT03639F

129. Sarbisheh EK, Salih AK, Raheem SJ, Lewis JS, Price EW (2020) A high-denticity chelator based on desferrioxamine for enhanced coordination of zirconium-89. Inorg Chem. https://doi.org/10.1021/acs.inorgchem.0c01629

130. Hagemann UB, Wickstroem K, Hammer S, Bjerke RM, Zitzmann-Kolbe S, Ryan OB, Karlsson J, Scholz A, Hennekes H, Mumberg D, Cuthbertson AS (2020) Advances in precision oncology: targeted thorium-227 conjugates as a new modality in targeted alpha therapy. Cancer Biother Radiopharm 35(7):497–510. https://doi.org/10.1089/cbr.2020.3568

131. Ramdahl T, Bonge-Hansen HT, Ryan OB, Larsen Å, Herstad G, Sandberg M, Bjerke RM, Grant D, Brevik EM, Cuthbertson AS (2016) An efficient chelator for complexation of thorium-227. Bioorg Med Chem Lett

26(17):4318–4321. https://doi.org/10.1016/j.bmcl.2016.07.034

132. Hammer S, Hagemann UB, Zitzmann-Kolbe S, Larsen A, Ellingsen C, Geraudie S, Grant D, Indrevoll B, Smeets R, von Ahsen O, Kristian A, Lejeune P, Hennekes H, Karlsson J, Bjerke RM, Ryan OB, Cuthbertson AS, Mumberg D (2020) Preclinical efficacy of a PSMA-targeted thorium-227 conjugate (PSMA-TTC), a targeted alpha therapy for prostate cancer. Clin Cancer Res 26(8):1985. https://doi.org/10.1158/1078-0432.CCR-19-2268

Chapter 7

Rapid Radiolabeling for Peptide Radiotracers

Xiaowei Ma and Zhen Cheng

Abstract

Peptide-based radiopharmaceuticals (PRPs) have been developed and introduced into research and clinic diagnostic imaging and targeted radionuclide therapy for more than two decades. In order to efficiently prepare PRPs, some rapid radiolabeling methods have been demonstrated. This chapter presents six common approaches for PRPs radiolabeling with metallic radioisotopes and Fluorine-18.

Key words Radiolabeling, Peptide, Peptide-based radiopharmaceuticals, Metallic radioisotopes, Fluorine-18, Radiochemistry

1 Introduction

Peptide-based radiopharmaceuticals (PRPs) are a series of radionuclide-labeled peptides that specifically bind to target receptors related to biological processes of diseases, such as tumors, neurological disorders, and cardiological diseases. PRPs have been applied in clinical diagnostic and therapeutic purposes for over 20 years. The advantage of high binding affinity and specificity, good pharmacokinetics, ease of synthesis, and rapid radiolabeling has encouraged the investigation of a wide variety of PRPs targeting different receptors or enzymes, including fibroblast activation protein inhibitor (FAPI) [1], somatostatin receptors (SSTRs) [2, 3], and prostate-specific membrane antigen (PSMA) [4, 5]. Peptide precursors can be synthesized using an automatic peptide synthesizer and modified to achieve the desired pharmacokinetic characteristics by changing peptide sequence and/or by adding a bifunctional prosthetic group, such as a small polyethylene glycol (PEG) [4], small peptide linker [6], or a small molecule [7]. Meanwhile, rapid radiolabeling methods have been developed to synthesize PRPs within a few minutes, depending on the properties of the conjugated chelator and radioisotope to be used. Fluorine-18 and radioactive metallic radionuclides (e.g., Galium-68, Copper-64,

Table 1
Summary of chelators for the different radioisotopes and general labeling conditions

Radioisotopes	Chelators [#]	Labeling conditions[*] (buffer, temperature, and time)
^{68}Ga ($T_{1/2} = 1.1$ h)	DOTA or DOTAGA [10, 11] NOTA or NODAGA [12] HBED-CC [13, 14]	0.1 M NaAc (pH 5.5), 95 °C, 5–15 min 0.1 M NaAc (pH 4.5), RT, 10 min 0.1 M NaAc (pH 3.9–4.2), 90 °C, 5–10 min
^{64}Cu ($T_{1/2} = 12.7$ h)	DOTA or DOTAGA [15, 16] NOTA or NODAGA [15] CB-TE2A [17, 18] TETA [18, 19]	0.1 M NaAc (pH 5.5), 95 °C, 15 min 0.1 M NaAc (pH 4.5), RT, 15 min 0.1 M NaAc (pH 8.0), 95 °C, 2 h 0.1 M NaAc (pH 5.5), RT, 30 min
^{177}Lu ($T_{1/2} = 159.4$ h)	DOTA [20, 21]	0.1 M NaAc (pH 5.5), 95 °C, 20 min
^{90}Y ($T_{1/2} = 64.1$ h)	DOTA [21, 22]	0.1 M NaAc (pH 6.0–7.8), 50 °C, 10 min or 100 °C, 5 min
^{111}In ($T_{1/2} = 67.2$ h)	DTPA [23] DOTA [24]	0.1 M HEPES (pH 5.5), RT, 20 min 0.1 M NaAc (pH 5.5), 95 °C, 20 min
^{89}Zr ($T_{1/2} = 78.42$ h)	DFO [25]	0.5 M HEPES (pH 7.0–7.3) with 0.2 M oxalic acid, RT, 2 h
^{225}Ac ($T_{1/2} = 240$ h)	DOTA [1]	0.2 M NH$_4$Ac (pH 5.0) and 7% sodium ascorbate, 80 °C, 2 h
^{99m}Tc ($T_{1/2} = 6.02$ h)	HYNIC [26–28]	Tricine/EDDA in 0.1 M PBS (pH 6), 95 °C, 15 min
^{18}F ($T_{1/2} = 1.83$ h)	NOTA [2, 29] (*see* **Note 1**) SiFA [30, 31]	0.1 M NaAc (pH 4.5), 100 °C, 10 min 1 M oxalic acid, RT, 5 min

[#]   2,2′,2″-(10-(2,6-Dioxotetrahydro-2H-pyran-3-yl)-1,4,7,10-tetraazacyclododecane-1,4,7triyl)triacetic acid (DOTAGA); 1,4,7-triazacyclononane,1-glutaric acid-4,7-acetic acid (NODAGA); N,N′-bis [2-hydroxy-5-(carboxyethyl)benzyl]ethylenediamine-N,N′-diacetic acid (HBED-CC); 1,4,8,11-tetraazacyclododecane1,4,8,11-tetra-acetic acid (TETA); 4,11-bis(carboxymethyl)-1,4,8,11-tetraazabicyclo[6.6.2]hexadecane (CB-TE2A); Deferoxamine (DFO). [*]The labeling conditions list here were generally used, but the buffer, pH, and temperature could be adjusted to achieve higher labeling efficiency and meanwhile protect the precursor.

Lutetium-177, and Technetium-99 m) are preferred for peptide labeling because they have a suitable half-life matched to PRP pharmacokinetics, mild labeling condition requirements, and good chemical properties that suit radiochemistry. However, there are many different chelators for metallic radionuclide labeling (Table 1). The radiolabeling approach mainly depends on the properties of the chelator pre-conjugated to the peptide, such as 1,4,7-triazacyclononane-1,4,7-triacetic acid (NOTA) conjugated peptides are mainly suitable for ^{68}Ga, ^{64}Cu, ^{90}Y, ^{177}Lu, or Al^{18}F labeling at room temperature or mild heating,
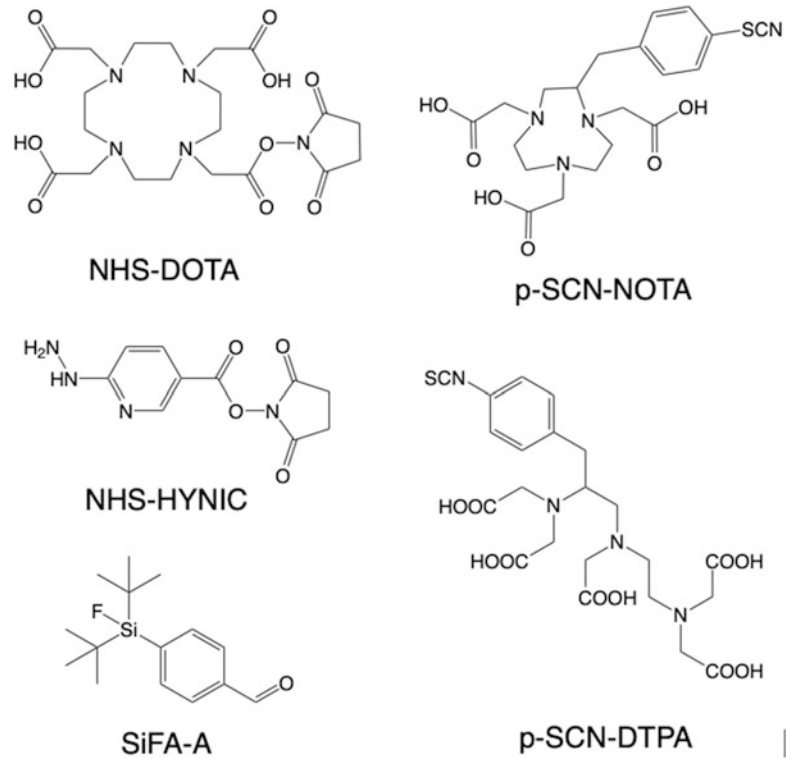
Fig. 1 Schematic illustrates of the structures of four different chelators, NOTA, DOTA, HYNIC, DTPA, and SiFA-A

6-hydrazinonicotinic acid (HYNIC) conjugated peptides are mainly used for ^{99m}Tc labeling, and diethylenetriamine pentaacetate (DTPA) conjugated peptides could be labeled with ^{111}In at room temperature. It is important to remember that the attachment of a chelator to the probe will impact the stability, pharmacokinetics, and binding affinity of the probe and, ultimately, the imaging outcomes [8, 9]. Thus, a proper bifunctional chelator should be considered when designing metallic radionuclide labeled probes. This chapter describes the general protocols of four popular chelators, DOTA-, NOTA-, HYNIC-, and DTPA-conjugated peptides for rapid metallic radionuclides labeling and NOTA- and silicon-fluoride acceptor (SiFA)-conjugated peptides for ^{18}F labeling. The structure of the chelators is shown in Fig. 1.

2   Materials

Prepare all solutions using deionized water and analytical grade reagents at room temperature (unless indicated otherwise). Diligently follow all waste disposal regulations when disposing of waste materials, especially radioactive and biohazard wastes. Operators

must wear the necessary personal protective equipment (PPE) according to the requirement of the working environment and government regulations. Prepare all materials and solutions at room temperature unless otherwise specified.

2.1 Chemicals and Buffers

1. Sodium acetate (≥99.9%, BioUltra).
2. Sodium chloride (≥99.9%, BioUltra).
3. Aluminum chloride (anhydrous, powder, 99.999%, trace metals basis).
4. Disodium hydrogen phosphate (Na_2HPO_4; ACS reagent).
5. Sodium dihydrogen phosphate monohydrate (NaH_2PO_4; ACS reagent).
6. Sodium hydroxide solution (NaOH; ACS reagent).
7. Hydrogen chloride (HCl, 37%, conc. Aqueous, ACS reagent).
8. Potassium hydroxide (KOH, 99.995%, Suprapur).
9. Oxalic acid (anhydrous, ≥99.0%, BioUltra).
10. Ascorbic acid (Sigma-Aldrich, United States Pharmacopeia).
11. Ethylenediaminetetraacetic acid (EDTA, ≥99%).
12. Tricine (PharmaGrade).
13. Ethylenediamine-N,N′-diacetic acid (EDDA, ≥98%).
14. Tin chloride ($SnCl_2$, ≥99%).
15. Kryptofix 222 (K2.2.2; United States Pharmacopeia).
16. Ultrapure water.
17. Sterilized 0.9% NaCl (saline).
18. 0.9% (wt/vol) NaCl (trace metals basis).
19. Sterilized deionized water (di-water).
20. Acetic acid (glacial, ≥99.85%).
21. N-2-Hydroxyethylpiperazine-N′-2-ethanesulfonic acid (HEPES; ≥99.5%, BioUltra grade).
22. 0.1 M Sodium acetate (NaAc) buffer (pH 5.5): Mix 410 mg of sodium acetate in 50 ml of ultrapure water and adjust with acetic acid (glacial) to a pH of 5.5.
23. 0.1 M Sodium acetate (NaAc) buffer (pH 4.5): Mix 410 mg of sodium acetate in 50 ml of ultrapure water and adjust with acetic acid (glacial) to a pH of 4.5.
24. 0.05 M Phosphate buffer (pH 7.4): Dissolve 7.098 g of Na_2HPO_4 in 1 L of sterilized di-water. Adjust the pH to 7.4 using 1 M NaOH.
25. 0.1 M phosphate buffered saline (PBS) (pH 6.5): Dissolve 10.9 g of Na_2HPO_4 and 3.2 g NaH_2PO_4 in 1000 mL of

sterilized di-water. Adjust the pH to 6.5 using 1 M HCl and 1 M NaOH.

26. 0.1 M HEPES buffer (pH 5.5): Dissolve 2.38 g HEPES in 100 mL sterilized di-water and the pH was adjusted to 5.5 with 1 M NaOH.

27. 0.1 M HEPES buffer (pH 2): Dissolve 2.38 g HEPES in 100 mL sterilized di-water and the pH was adjusted to 2 with 1 M HCl.

28. 1 M HCl: Dilute 8.3 ml of 37% HCl with ultrapure water to 100 ml.

29. 1 M NaOH: Dissolve 40 g NaOH in 1 L di-water.

30. Anhydrous dimethylsulfoxide (DMSO, ≥99.7%).

31. Anhydrous acetonitrile (≥99.5%, ACS reagent).

32. Acetonitrile (≥99.5%, ACS reagent).

33. Ethanol (≥99.5%, ACS reagent).

34. DOTA-, NOTA-, HYNIC-, and DTPA-conjugated peptides: Dissolve peptide in ultrapure water at desired concentration (usually 1 mg/mL) and divide into aliquots in metal-free vials, then lyophilize overnight. Seal and store all vials in a freezer at −20 °C for later use (*see* **Note 2**).

35. SiFA-conjugated peptide: Dissolve peptide in anhydrous DMSO at desired concentration (usually 1 mM). Then divide and seal into aliquots of 25 μL *per* vial for later use.

36. 50 mM EDTA solution: Dissolve 185 mg EDTA in 10 ml of 0.1 M NH4Ac.

37. 2 mg/mL SnCl2: Dissolve 10 mg Tin chloride in 5 mL of 0.1 M HCl. This solution must be freshly prepared prior to use.

38. Tricine/EDDA solution: 20 mg Tricine and 10 mg EDDA in 1 mL 0.1 M PBS buffer (pH 6.5).

39. 2 mM $AlCl_3$ solution: Dissolve 26.6 mg of aluminum chloride (anhydrous, trace metals basis) in 100 ml of 0.1 M sodium acetate buffer (pH 4.5).

40. 1 M oxalic acid in anhydrous acetonitrile: Dissolve 6.03 g oxalic acid in 50 mL anhydrous acetonitrile.

41. 1.0 M KOH solution: Dissolve 5.61 g of KOH in 100 mL of ultrapure water.

42. K.2.2.2/KOH elution: Dissolve 205 mg of Kryptofix 222 in 500 μL of 1 M KOH solution and 500 μL of ultrapure water. Then divide the solution into five aliquots and lyophilize overnight. Seal and store the lyophilized K222/KOH in −20 °C freezer. When ready to use, dissolve lyophilisate with 0.5 mL

anhydrous acetonitrile for ^{18}F elution. Critical: K.2.2.2 solution must be freshly prepared before use.

43. 1.4% ascorbic acid solution: Dissolve 1.4 g ascorbic acid in 100 mL sterilized di-water. This solution must be freshly prepared before use.

2.2   Radioisotopes

1. Gallium-68 chloride (^{68}GaCl$_3$): Can be obtained by eluting a ^{68}Ge/^{68}Ga generator with hydrogen chloride (*see* **Note 3**). Alternatively, ^{68}Ga could be produced by a cyclotron.

2. Copper-64 chloride (^{64}CuCl$_2$): ^{64}CuCl$_2$ is usually produced by a cyclotron.

3. Technetium-99 m (^{99m}Tc): ^{99m}Tc in the form of the pertechnetate (^{99m}TcO$_4{}^-$) in saline is easily obtained from eluting a generator with saline.

4. Lutetium-177 chloride (^{177}LuCl$_3$).

5. Yittrium-90 chloride (^{90}YCl$_3$).

6. Indium-111 chloride (^{111}InCl$_3$).

7. Actinium-225 chloride (^{225}AcCl3): ^{225}Ac can be produced by radiochemical extraction from 229Th.

8. [^{18}F]-Fluoride: [^{18}F]-Fluoride produced in cyclotron *via* the ^{18}O(p,n)^{18}F nuclear reaction.

2.3   Other Materials

1. 0.22 μm membrane (sterile syringe filter). Some membranes may require preconditioning, and please follow the manufacture's instruction.

2. Sep-Pak QMA light cartridge: Precondition the cartridge properly according to the reaction requirement (*see* **Note 4**).

3. C18 light Sep-Pak cartridge: Precondition the C18 cartridge with 10 ml of ethanol and then 10 ml of di-water (no air). Do not dry the cartridge with air.

4. Syringes.

5. Sterile glass vials (10 mL and 20 mL).

2.4   Equipment

1. Instant thin layer chromatography (iTLC) with a radiation detector, accessories (Silicon-coated strips or filter paper, chamber), and mobile phase (NaAc buffer/acetonitrile).

2. High-performance liquid chromatography (HPLC) with radiation detector and mobile phase.

3. Biosafety fume hood.

4. Radiation protective fume hood.

5. Radiosynthesis module.

6. Hot plate or a heat gun.

7. pH meter to validate the pH value of buffers, and pH paper to validate the pH of reaction mixtures.

8. Dose calibrator.

3 Methods

Operators should wear PPE and carry out all procedures in a fume hood purposed for radiation work unless otherwise specified. Direct exposure to the radiation should be kept to a minimum, and radiation exposure must be monitored with appropriate devices. Radiation protection should meet the requirements of the department. Qualified operators and GMP environment may be required by government regulations in some countries if these probes are using for humans. For each labeling procedure, please refer to Table 1 to choose an optimized condition.

3.1 DOTA-Conjugated Peptide Labeling

1. Thaw out an aliquot of the DOTA-conjugated peptide.

2. Transfer radionuclides to reaction vial.

3. Add 500 μL 1 M NaAc buffer (pH 5.5) to metallic radionuclide solution (*see* **Note 5**).

4. Check the pH value of the solution; adjust pH to 5.5 with 1 M HCl and 1 M NaOH (*see* **Note 6**).

5. Add peptide solution to the reaction vial and check the pH at 5.5.

6. Mix well and incubate the labeling reaction at 95 °C for 10–15 min.

7. Add 1 mL 50 mM EDTA solution.

8. Purify and formulate following the procedure described in Subheading 3.3.

9. Measure the radiolabeling efficiency and perform quality control (QC) tests described in Subheading 3.4.

10. 1.4% ascorbic acid solution could be used to reduce radiolysis of the peptide.

3.2 NOTA-Conjugated Peptide Labeling

1. Thaw out an aliquot of the NOTA-conjugated peptide.

2. Transfer metallic radionuclide to reaction vial.

3. Add 500 μL 1 M NaAc buffer (pH 4.5) to metallic radionuclide solution (*see* **Note 5**).

4. Check the pH value of the solution; adjust pH to 4.5 with 1 M HCl and 1 M NaOH (*see* **Note 6**).

5. Add peptide solution to the reaction vial and check the pH at 4.5.

6. Mix well and incubate the labeling reaction at room temperature or 37 °C for 10–15 min.

7. Add 1 mL 50 mM EDTA solution.

8. Purify and formulate following the procedure described in Subheading 3.3.

9. Measure the radiolabeling efficiency and perform QC tests following described in Subheading 3.4.

10. 1.4% ascorbic acid solution could be used to reduce radiolysis of the peptide.

3.3   HYNIC-Conjugated Peptide with ^{99m}Tc Labeling

1. Thaw out an aliquot of the HYNIC-conjugated peptide.

2. Add 500 μL tricine/EDDA solution to peptide solution.

3. Add 20 μL $SnCl_2$ solution (40 μg) (*see* **Note** 7).

4. Add $^{99m}TcO_4^-$ in saline (*see* **Note 8**).

5. Incubate the reaction at 95 °C for 15 min (*see* **Note 9**).

6. Measure the radiolabeling efficiency and perform QC tests following described in Subheading 3.4.

3.4   DTPA-Conjugated Peptide with ^{111}In Labeling

1. Thaw out an aliquot of the DTPA-conjugated peptide.

2. Add 500 μL 0.1 M HEPES buffer (pH 5.5).

3. Add $^{111}InCl_3$ (<300 MBq/nmol peptide) and check pH is about 5.5.

   Optional Step: Add 1.4% ascorbic acid solution to reduce radiolysis of the peptide.

4. Incubate the reaction at room temperature for 20 min.

5. Purify and formulate following the procedure described in Subheading 3.3.

6. Measure the radiolabeling efficiency and perform QC tests following described in Subheading 3.4.

3.5   NOTA-Conjugated Peptide with Al^{18}F Labeling

Al^{18}F labeling strategy allows rapid one-step ^{18}F labeling of NOTA- or RESCA-conjugated peptides in aqueous, which is suitable for some peptides that are thermosensitive. The following procedure describes Al^{18}F for NOTA-conjugated peptide labeling.

1. Produce [^{18}F]fluoride in a cyclotron.

2. Precondition QMA cartridge with 5 mL of di-water at a flow rate of 5 mL/min, then dry the cartridge with 5 mL air (*see* **Note 10**).

3. Thaw out an aliquot of the NOTA-conjugated peptide. If needed, it can be diluted with 50–200 μL of 0.1 M NaAc buffer (pH 4.5).

4. Transfer and trap [^{18}F]fluoride on the Sep-Pak QMA cartridge.

5. Rinse QMA with 5 mL of ultrapure water, followed by 2 min of air flow (10 mL/min).

6. Slowly elute [^{18}F]fluoride from QMA with 0.5 ml of 0.9% (wt/vol) NaCl (trace metals basis) into the reaction vial.

7. Add 10 μL of 2 mM aluminum chloride solution into the [^{18}F] fluoride solution (*see* **Note 11**).

8. Incubate the solution at room temperature for 5 min.

9. Add NOTA-conjugated peptide solution (30–50 nmol) and then incubated the reaction at 100 °C for 10 min.

10. Cool down the reaction to room temperature.

11. Dilute with 15 mL saline.

12. Purify and formulate the product following the procedure described in Subheading 3.3.

13. Perform quality control procedures described in Subheading 3.4.

14. 1.4% ascorbic acid solution could be used to reduce radiolysis of the peptide.

3.6 SiFA-Conjugated Peptide for ^{18}F Labeling

1. Produce [^{18}F]fluoride in a cyclotron.

2. Precondition QMA cartridge with 10 mL of di-water at a flow rate of 10 mL/min. Do not dry the cartridge with air.

3. Transfer and trap [^{18}F]fluoride on a Sep-Pak QMA cartridge.

4. Dry the cartridge by air flow for 2 min (10 mL/min).

5. Rinse QMA with 5 mL of anhydrous acetonitrile, followed by 2 min air flow (10 mL/min).

6. Slowly Elute [^{18}F]fluoride from the QMA into a reaction vial using 0.5 mL freshly prepared K222/KOH solution.

7. Add 30 μL of 1 M oxalic acid solution to the reaction vial.

8. Add 25 μL SiFA-conjugated peptide solution to the reaction mixture.

9. Incubate at room temperature for 5 min without stirring.

10. Dilute the mixture with 15 mL of 0.1 M HEPES buffer (pH 2).

11. Inject the solution to pass through a Sep-Pak C18 light cartridge.

12. Rinse the C18 cartridge with 10 mL of 0.05 M phosphate buffer (pH 7.4).

13. Elute the C18 cartridge with 0.5 mL of EtOH to a 10 mL sterile vial.

14. Dilute the product solution with 9.5 mL saline.

15. Inject the elution through a 0.22 μm sterile filter and collect the filtration into a sterilized vial.

16. Measure the radiolabeling efficiency and perform quality control (QC) tests following the procedure described in Subheading 3.4.

3.7 General Procedure for Purification and Formulation

1. Dilute the reaction, containing product, with 10- to 20 times the volume of sterile di-water.

2. Load the solution onto a C18 light Sep-Pak cartridge.

3. Wash the C18 cartridge with 10 mL sterile di-water.

4. Elute the product from the C18 cartridge into a 15 mL sterilized vial with 1 mL ethanol followed by 10 mL saline (*see* **Note 12**).

   OPTION STEP: Add 1 mL ascorbic acid or sodium ascorbate for some peptides that sensitive to radiation to prevent radioautolysis.

5. Inject the elution through a 0.22 μm sterile filter and collect the filtration into a sterilized vial (*see* **Note 13**).

3.8 Measure Radiolabeling Efficiency by iTLC

1. Drop 1–2 μl sample (crude product for calculating radiolabeling efficiency or final produce for purity test) onto the start point (about 1 cm from the end) of the iTLC strip.

2. Pour the iTLC mobile phase solution into a chamber until it is about 0.5 cm deep and covers the chamber's bottom.

3. Gently place the iTLC strip upright in the chamber. Cover the chamber and allow the solvent to extend up about 8 cm (or about 1 cm from the top of the strip).

4. Carefully dry the strip and place it onto a thin plastic sheet set on the iTLC scanner.

5. Start scan to get the radioactive count curve and calculate the radiolabeling efficiency and radiochemical purity. Radiolabeling yield (or purity) = (CPM of radiolabeled peptide)/(CPM total) × 100%.

3.9 Measure Radiolabeling Efficiency by HPLC

The radiolabeling efficiency and radiochemical purity can be measured by iTLC or by HPLC. The HPLC is more accurate than iTLC to detect radiolysis, and to detect unlabeled radionuclides and peptides for calculation of radiolabeling efficiency.

1. Take a sample (10–100 μCi) of the sample solution and inject it onto the HPLC.

2. Calculate the radiolabeling efficiency and radiochemical purity using chromatography.

3.10 QC Test

QC test should be performed according to the government regulations. It usually includes radionuclide identity, radionuclide purity, radiochemical purity, chemical purity, visual examination, content of solvents, and sterility.

4   Notes

1. The labeling conditions described here may not be the best condition for producing highest yield and stabled labeling. Depending on the properties of the peptide, the labeling method should be optimized by changing buffer, pH, temperature, and incubation time. Some reactions may need auxiliary reagents, such as sodium ascorbate, oxalic acid, and glycerol.

2. For rapid radioactive metallic isotope labeling, the optimized dose of DOTA- and NOTA- conjugated peptides are different. Usually, 5–50 nmol could achieve high radiochemistry yield and good specific activity. It is highly recommended to eliminate air bubbles when aliquoting peptides with nitrogen and then seal under nitrogen protection.

3. $^{68}Ge/^{68}Ga$ generators are different based on the carrier material (stationary generator phase). Thus, the concentration of eluent HCl may vary from 0.05 M to 1.0 M. The pH of the reaction solution should be checked before incubation.

4. The QMA cartridge is usually preconditioned with 10 mL of di-water at a flow rate of 10 mL/min and then the cartridge is dried with 5 mL air for $Al^{18}F$ labeling. Do not dry the cartridge when it is used for SiFA-conjugated peptide labeling.

5. The volume of the NaAc buffer could be changed according to the volume of radioisotope solution, usually equal to 10% of radioisotope solution. The same concentration of ammonium acetate (NH4Ac) buffer could be a replacement for NaAc buffer.

6. The pH has a significant effect on radionuclide labeled NOTA (optimal pH = 3.5–5.0, 4.5 is usually used as a start) and DOTA-conjugated peptides (optimal pH = 4.0–6.0, 5.5 is generally used at beginning). Thus, the pH should be optimized to get a higher labeling yield.

7. The ^{99m}Tc-HYNIC-peptide labeling depends on maintaining the stannous ion in a reduced state. Therefore, the tin chloride solution must be freshly prepared. Nitrogen purge is recommended to prepare all solutions for at least 10 min. To get the highest yield, the amount of $SnCl_2$ should be optimized. Meanwhile, for ^{99m}Tc labeling with HYNIC as chelator, additional co-ligands are usually required to complete the coordination sphere, such as tricine alone, or in combination with EDDA, ternary phosphines (e.g., triphenylphosphine-3,3′,3″--trisulfonate, TPPTS), or aromatic amines (e.g., nicotinic). The ^{99m}Tc-HYNIC/co-ligand complexes exhibit different pharmacokinetic properties and biological stability. The ^{99m}Tc-HYNIC/tricine complexes are formed in high yield,

but isomers are observed, and the biological stability is relatively low. The ^{99m}Tc-HYNIC/EDDA complexes are more stable and exhibit better homogeneity but require high reaction temperature. Thus, the use of EDDA along with tricine is common to improve stability, homogeneity, and labeling yield.

8. ^{99m}TcO$_4$$^-$ volume also affects the radiolabeling yield. Usually, 0.5 mL to 5 mL is sufficient.

9. For ^{99m}Tc labeling of HYNIC-conjugated peptide, it usually achieves higher than 95% yield and purity. Thus, no further purification step is needed for routine application.

10. An optimal pH (4.4–4.6) is important to produce high-yield Al^{18}F chelation. A QMA cartridge in the chloride form instead of the carbonate form is highly recommended to reduce the pH change during elution since the QMA cartridge in the carbonate form usually generates a basic solution (pH = 11) after elution.

11. The ^{18}F-to-Al ratio and the chelator-to-Al$_3$$^+$ ratio in the reaction mixture positively affect the radiolabeling yield. An optimal ratio is 50 mCi ^{18}F to 20 nmol AlCl$_3$ and 20–50 nmol peptides. The amount of AlCl$_3$ could be increased depending on the activity of the [^{18}F]fluoride. However, higher amounts of radioactivity may cause increased radiolysis of the peptide.

12. The concentration of ethanol of eluting solution could be optimized according to the peptide's properties to reduce ethanol residue in the final product.

13. Some peptides may stick to the membrane. Different types of membranes could be tried to reduce product loss.

References

1. Watabe T et al (2020) Theranostics targeting fibroblast activation protein in the tumor stroma: (64)Cu- and (225)Ac-labeled FAPI-04 in pancreatic cancer xenograft mouse models. J Nucl Med 61:563–569

2. Tshibangu T et al (2020) Automated GMP compliant production of [(18)F]AlF-NOTA-octreotide. EJNMMI Radiopharm Chem 5:4

3. Chan K, Luong TV, Navalkissoor S (2018) 111In-DTPA-octreotide SPECT (OctreoScan) uptake in metastatic renal cell carcinoma to the pancreas. Clin Nucl Med 43:e29–e30

4. Gai Y et al (2019) Comparison of Al18F- and 68Ga-labeled NOTA-PEG4-LLP2A for PET imaging of very late antigen-4 in melanoma. JBIC J Biol Inorg Chem 25:99–108

5. Kratochwil C et al (2016) 225Ac-PSMA-617 for PSMA-Targeted alpha-Radiation Therapy of Metastatic Castration-Resistant Prostate Cancer. J Nucl Med 57:1941–1944

6. Cardinale J et al (2020) Development of PSMA-1007-related series of (18)F-labeled glu-ureido-type PSMA inhibitors. J Med Chem 63:10897–10907

7. Sun Y et al (2016) Preclinical study on GRPR-targeted (68)Ga-probes for PET imaging of prostate cancer. Bioconjug Chem 27:1857–1864

8. Xia Y et al (2020) Comparative evaluation of (68)Ga-labelled TATEs: the impact of chelators on imaging. EJNMMI Res 10:36

9. Guleria M, Das T, Amirdhanayagam J, Sarma HD, Dash A (2018) Comparative evaluation of using NOTA and DOTA derivatives as bifunctional chelating agents in the preparation of (68)Ga-labeled porphyrin: impact on

pharmacokinetics and tumor uptake in a mouse model. Cancer Biother Radiopharm 33:8–16

10. Tsionou MI et al (2017) Comparison of macrocyclic and acyclic chelators for gallium-68 radiolabelling. RSC Adv 7:49586–49599

11. Sosabowski JK, Mather SJ (2006) Conjugation of DOTA-like chelating agents to peptides and radiolabeling with trivalent metallic isotopes. Nat Protoc 1:972–976

12. Notni J, Pohle K, Wester HJ (2012) Comparative gallium-68 labeling of TRAP-, NOTA-, and DOTA-peptides: practical consequences for the future of gallium-68-PET. EJNMMI Res 2:28

13. Eppard E, Homann T, de la Fuente A, Essler M, Rosch F (2017) Optimization of labeling PSMA(HBED) with ethanol-postprocessed (68)Ga and its quality control systems. J Nucl Med 58:432–437

14. Eder M et al (2012) 68Ga-complex lipophilicity and the targeting property of a urea-based PSMA inhibitor for PET imaging. Bioconjug Chem 23:688–697

15. Ghosh SC et al (2015) Comparison of DOTA and NODAGA as chelators for 64Cu-labeled immunoconjugates. Nucl Med Biol 42:177–183

16. De Silva RA et al (2012) Copper-64 radiolabeling and biological evaluation of bifunctional chelators for radiopharmaceutical development. Nucl Med Biol 39:1099–1104

17. Pandya DN et al (2012) New macrobicyclic chelator for the development of ultrastable 64Cu-radiolabeled bioconjugate. Bioconjug Chem 23:330–335

18. Wadas TJ, Anderson CJ (2006) Radiolabeling of TETA- and CB-TE2A-conjugated peptides with copper-64. Nat Protoc 1:3062–3068

19. Bass LA, Wang M, Welch MJ, Anderson CJ (2000) In vivo transchelation of copper-64 from TETA-octreotide to superoxide dismutase in rat liver. Bioconjug Chem 11:527–532

20. Guleria M, Das T, Amirdhanayagam J, Sarma HD, Dash A (2019) Preparation of [(177)Lu]Lu-DOTA-Ahx-Lys40-Exendin-4 for radiotherapy of insulinoma: a detailed insight into the radiochemical intricacies. Nucl Med Biol 78-79:31–40

21. Liu S, Cheung E, Ziegler MC, Rajopadhye M, Edwards DS (2001) (90)Y and (177)Lu labeling of a DOTA-conjugated vitronectin receptor antagonist useful for tumor therapy. Bioconjug Chem 12:559–568

22. Onthank DC et al (2004) 90Y and 111In complexes of a DOTA-conjugated integrin alpha v beta 3 receptor antagonist: different but biologically equivalent. Bioconjug Chem 15:235–241

23. Brom M, Joosten L, Oyen WJ, Gotthardt M, Boerman OC (2012) Improved labelling of DTPA- and DOTA-conjugated peptides and antibodies with 111In in HEPES and MES buffer. EJNMMI Res 2:4

24. Boubaker A et al (2012) Biokinetics and dosimetry of 111In-DOTA-NOC-ATE compared with 111In-DTPA-octreotide. Eur J Nucl Med Mol Imaging 39:1868–1875

25. Bauman A, Valverde IE, Fischer CA, Vomstein S, Mindt TL (2015) Development of 68Ga- and 89Zr-labeled exendin-4 as potential radiotracers for the imaging of insulinomas by PET. J Nucl Med 56:1569–1574

26. Guggenberg EV, Mikolajczak R, Janota B, Riccabona G, Decristoforo C (2004) Radiopharmaceutical development of a freeze-dried kit formulation for the preparation of [99mTc-EDDA-HYNIC-D-Phe1, Tyr3]-octreotide, a somatostatin analog for tumor diagnosis. J Pharm Sci 93:2497–2506

27. Erfani M, Shafiei M, Mazidi M, Goudarzi M (2013) Preparation and biological evaluation of [(99m)Tc/EDDA/Tricine/HYNIC(0), BzThi(3)]-octreotide for somatostatin receptor-positive tumor imaging. Cancer Biother Radiopharm 28:240–247

28. Mogadam HY, Erfani M, Nikpassand M, Mokhtary M (2020) Preparation and assessment of a new radiotracer technetium-99m-6-hydrazinonicotinic acid-tyrosine as a targeting agent in tumor detecting through single photon emission tomography. Bioorg Chem 104:104181

29. Giesel FL et al (2021) FAPI-74 PET/CT Using Either (18)F-AlF or Cold-Kit (68)Ga labeling: biodistribution, radiation dosimetry, and tumor delineation in lung cancer patients. J Nucl Med 62:201–207

30. Wangler C et al (2010) One-step (1)(8)F-labeling of carbohydrate-conjugated octreotate-derivatives containing a silicon-fluoride-acceptor (SiFA): in vitro and in vivo evaluation as tumor imaging agents for positron emission tomography (PET). Bioconjug Chem 21:2289–2296

31. Lindner S et al (2020) Radiosynthesis of [(18)F]SiFAlin-TATE for clinical neuroendocrine tumor positron emission tomography. Nat Protoc 15:3827–3843

Chapter 8

Methods for the Production of Radiolabeled Bioagents for ImmunoPET

Alejandro Arroyo, Serge K. Lyashchenko, and Jason S. Lewis

Abstract

Immunoglobulin-based positron emission tomography (ImmunoPET) is making increasingly significant contributions to the nuclear imaging toolbox. The exquisite specificity of antibodies combined with the high-resolution imaging of PET enables clinicians and researchers to localize diseases, especially cancer, with a high degree of spatial certainty. This review focuses on the radiopharmaceutical preparation necessary to obtain those images—the work behind the scenes, which occurs even before the patient or animal is injected with the radioimmunoconjugate. The focus of this methods review will be the chelation of four radioisotopes to their most common and clinically relevant chelators.

Key words ImmunoPET, antibody radiolabeling, radioimmunoconjugate, chelator, ^{89}Zr, ^{64}Cu, ^{86}Y, ^{124}I

1 Introduction

ImmunoPET is a novel imaging technique that blends two areas of science, immunology and nuclear imaging, taking advantage of each of their strengths. Rather than using small molecules, such as 18F-Fluorodeoxyglucose, an radiofluorineted glucose (FDG), immunoPET uses the exquisite specificity of antibodies to deliver the radionuclide to a given target tissue. Antibodies are part of a class of proteins called immunoglobulins [1]. The specificity of these antibodies and other related targeted biologicals is crucial for the identification of their target, enabling the precise detection of the disease site in the affected tissue [2]. Antibodies are Y-shaped, in which a highly specific and variable region is present in the inside part of the bifurcation. The potential for high variation gives researchers the capacity to customize the antibody to a specific antigen. Antigens contain defined chemical signatures, which are usually found in the surface layers of xenobiotic agents, such as bacteria. However, antigens are also present in disease sites such as

cancer cells, where they can be detected by immunoPET. For targeted imaging purposes—be it optical, nuclear, or any other modality—antigens should be exclusively either expressed or over-expressed, ideally in the cell surface, of the cancer cells, thus decreasing background signal in the resulting image and increasing the contrast between healthy tissue and disease.

Antibodies are not the only strategy for the development of immunoPET imaging. Other targeting strategies that have recently emerged include the use of antibody fragments such as minibodies [3–6]. These have the potential to decrease the blood half-life of the compound, thus reducing overall bodily exposure to the radioisotope.

Several isotopes have been used for the development of immu-noPET as an imaging technique in the clinical setting [7]. The focus of this chapter will be the complexation of four positron-emitting radioisotopes (^{89}Zr, ^{64}Cu, ^{86}Y, and ^{124}I) to their most common chelators and the provision of adaptions from the litera-ture with some chelate–antibody examples. The methodology described in examples below for each ligand, chelator, and radio-nuclide combination could be seamlessly adapted to a variety of macromolecules where the described chelator–radionuclide combi-nation is used.

2   Materials

2.1   Radionuclides

1. ^{89}Zr can be obtained from commercial sources or produced by in-house cyclotrons [8].
2. ^{64}Cu can be produced in an in-house cyclotron [9] or obtained from commercial/academic sources.
3. ^{86}Y can be produced in an in-house cyclotron [10] or obtained from commercial/academic sources.
4. ^{124}I can be produced in an in-house cyclotron or obtained from commercial sources.

2.2   Bifunctional Chelators

1. *p*-SCN-Bn-deferoxamine (B-705).
2. DOTA-NHS ester (B-280).
3. *p*-SCN-NOTA (B-605).
4. *p*-SCN-Bn-DTPA (B-305).
5. *p*-SCN-PCTA (B-405).
6. Sarcophagine provided to the researchers by a collaborator.
7. TE2A-Ph-NCS was synthesized in house by the researchers [11].
8. TE1A1P was synthesized in house by the researchers [12].

2.3   Antibodies (Ligands)

1. Trastuzumab (HERCEPTIN®; Roche).
2. Pembrolizumab (Merck).
3. Cetuximab (Merck).
4. Onartuzumab (Genentech).
5. L19-SIP (Bayer Schering Pharma).
6. B43.13 antibody from B43.13 hybridoma.
7. J591.
8. 9E7.4 was produced by the researchers using a hybridoma model.
9. Hu3S193.

2.4   Buffer Preparation

General instructions on how to make 1 L of any buffer:

1. Weigh the required amount of buffering compound (*see* below for amounts).
2. Dissolve it in around 800 mL of Ultrapure water (18 MΩ-cm at 25 °C; *see* **Note 1**) in a 1 L beaker or Erlenmeyer flask (*see* **Note 2**).
3. Using a pH meter, measure the pH of the solution and adjust it to the desired pH by adding aliquots of 1 M HCl (to lower the pH) or 1 M NaOH (to increase the pH).
4. Transfer the solution to a volumetric flask and add water up to the line to make 1 L and mix gently (*see* **Note 3**).
5. Transfer 250 mL of the buffer to a 500 mL beaker or Erlenmeyer flask and place a magnetic stirring bar.
6. Add 12.5 g of the Chelex resin to the buffer and place the flask on a magnetic stir plate for a minimum 1 h (*see* **Note 4**).
7. Decant or filter the buffer to a clean flask to remove the resin (*see* **Note 5**).

2.5   Buffers

1. 0.1 M sodium bicarbonate, pH 8.7: weigh 8.401 g for 1 L, or 0.8401 g for 100 mL.
2. 50 mM Ethylenediaminetetraacetic acid (EDTA), pH 5 and pH 6: weigh 14.612 g EDTA for 1 L, or 1.4612 g EDTA for 100 mL.
3. 50 mM sodium acetate, 200 mM sucrose, pH 5.4–5.6: weigh 4.1015 g sodium acetate and 68.460 g sucrose for 1 L, or 0.4102 g sodium acetate and 6.8460 g sucrose for 100 mL.
4. 0.5 M 4-(2-Hydroxyethyl)piperazine-1-ethanesulfonic acid, N-(2-hydroxyethyl)piperazine-N′-(2-ethanesulfonic acid) (HEPES) buffer, pH 7, pH 7.4, and pH 7.5: weigh 119.15 g HEPES for 1 L, or 11.915 g HEPES for 100 mL.
5. 50 mM Diethylenetriaminepentaacetic acid (DTPA): weigh 19.6675 g DTPA for 1 L, or 1.9668 g DTPA for 100 mL.

6. 0.9% saline, 5 mg/mL hydroquinonecarboxylic acid (gentisic acid).

7. 0.25 M sodium acetate, 5 mg/mL gentisic acid: weigh 20.5075 g sodium acetate for 1 L, or 2.0508 g sodium acetate for 100 mL.

8. 1 M HEPES buffer, 0.1 M sodium carbonate, pH 8.5: weigh 238.3 g HEPES and 10.599 g sodium carbonate for 1 L, or 23.83 g HEPES and 1.0599 g sodium carbonate for 100 mL.

9. 1 M HEPES buffer, pH 7.5–8.0: weigh 238.3 g HEPES for 1 L, or 23.83 g HEPES for 100 mL.

10. 0.1 M ammonium acetate buffer, pH 5.5, pH 6, pH 8.0, and pH 8.2: weigh 7.708 g ammonium acetate for 1 L, or 0.7708 g ammonium acetate for 100 mL.

11. 0.1 M EDTA, pH 8: weigh 29.224 g EDTA for 1 L, or 2.9224 g EDTA for 100 mL.

12. 0.1 M HEPES buffer, pH 8.5: weigh 23.83 g HEPES for 1 L, or 2.383 g HEPES for 100 mL.

13. 0.3 M sodium carbonate: weigh 31.797 g sodium carbonate for 1 L, or 3.1797 sodium carbonate for 100 mL.

14. 0.3 M sodium acetate, pH 7: weigh 24.609 g sodium acetate for 1 L, or 2.4609 g sodium acetate for 100 mL.

15. 2.5 M ammonium acetate, pH 7: weigh 192.7 g ammonium acetate for 1 L, or 19.27 g ammonium acetate for 100 mL.

16. 10 mM EDTA, pH 7: weigh 2.9224 g EDTA for 1 L, or 0.2922 g EDTA for 100 mL.

17. 0.1 M citrate, pH 4.5: weigh 29.410 g sodium citrate dihydrate for 1 L, or 2.9410 g sodium citrate dihydrate for 100 mL.

18. 0.1 M sodium acetate, pH 5: weigh 8.203 g sodium acetate for 1 L, or 0.8203 g sodium acetate for 100 mL.

19. 3 M ammonium acetate, pH 5: weigh 231.24 g ammonium acetate for 1 L, or 23.124 g ammonium acetate for 100 mL.

20. 0.5 M disodium phosphate, pH 7.4: weigh 70.98 g disodium phosphate for 1 L, or 7.098 g disodium phosphate for 100 mL.

21. 0.1 M disodium phosphate, pH 6.8: weigh 14.196 g disodium phosphate for 1 L, or 1.4196 g disodium phosphate for 100 mL.

22. 0.9% NaCl, 5 mg/mL ascorbic acid, pH 5.

23. 0.02 M citrate, pH 5: weigh 5.882 g sodium citrate dihydrate for 1 L, or 0.5882 g sodium citrate dihydrate for 100 mL.

24. 0.05 M disodium phosphate, 0.15 M NaCl, pH 6.8: weigh 7.098 g disodium phosphate and 8.766 g NaCl for 1 L, or 0.7098 g disodium phosphate and 0.8766 g NaCl for 100 mL.

2.6 Other Aqueous Solutions	1. 10 mM EDTA: weigh 2.9224 g EDTA for 1 L, or 0.29224 g EDTA for 100 mL.
	2. 1 M sodium carbonate: weigh 105.99 g sodium carbonate for 1 L, or 10.599 g sodium carbonate for 100 mL.
	3. 0.1 M sodium carbonate: Weigh10.599 g sodium carbonate for 1 L, or 1.0599 g sodium carbonate for 100 mL.
	4. 2 M sodium carbonate: weigh 211.98 g sodium carbonate for 1 L, or 21.198 g sodium carbonate for 100 mL.
	5. 0.9% NaCl.
	6. Phosphate buffered saline (PBS) pH 7.4 (137 mM NaCl, 2.7 mM KCl, 10 mM Na_2HPO_4, and 1.8 mM KH_2PO_4).
	7. 25 mg/mL ascorbic acid.
2.7 General Reagents	1. Water.
	2. Sodium bicarbonate.
	3. Dimethyl sulfoxide (DMSO).
	4. Sodium carbonate.
	5. Ethylenediaminetetraacetic acid (EDTA).
	6. Sodium acetate.
	7. Sucrose.
	8. 4-(2-Hydroxyethyl)piperazine-1-ethanesulfonic acid, N-(2- hydroxyethyl)piperazine-N′-(2-ethanesulfonic acid) HEPES.
	9. Diethylenetriaminepentaacetic acid (DTPA).
	10. Hydroquinonecarboxylic acid (gentisic acid).
	11. Ammonium acetate.
	12. Sodium citrate dihydrate.
	13. Ascorbic acid.
	14. Disodium hydrophosphate.
	15. Sodium chloride.
	16. Chelex-100.
2.8 Consumables	1. Centrifugal filters Vivaspin 30 kDa.
	2. Centricon 100.
	3. Amicon Ultra-4.
	4. IODO-GEN.
	5. Acrodisc filters.
	6. Silica-gel impregnated glass fibers.
	7. 10-DG columns.
	8. Sephadex G-25 M PD10 desalting columns.

9. Superdex™ 200 10/300 GL size exclusion column.

10. Instant thin layer chromatography (iTLC) silica glass fiber paper.

11. Lo-bind protein tubes.

2.9 Instruments

1. Thermomixer.

2. Nanodrop or similar spectrophotometric device.

3 Methods

3.1 How to Perform a Radio-TLC and Determine the Radiochemical Yield (Adapted from Zeglis et al. [13])

1. Spot 37 kBq (1 μCi) of the radiolabeling reaction mixture on a 1 cm–wide silica-impregnated TLC strip (*see* **Note 6**).

2. Allow the sample dot to dry.

3. Gently, place the strip in a chamber containing the mobile phase (usually EDTA or DTPA at pH 5.5).

4. Allow the solvent to run until the leading edge reaches around 1 cm from the top edge of the paper (*see* **Note 7**).

5. Analyze the TLC strip using a radio-TLC scanner (*see* **Note 8**).

6. Radiolabeled immunoconjugates will remain at or close to the spotted location. Free unbound radioactive isotopes will travel with the solvent front.

7. Calculate the radiolabeling yield of the reaction by integrating the radio-chromatogram using the following equation:

Radiochemical yield of the reaction

$$= \frac{\text{Radioactivity isolated from the purified radioimmunoconjugate}}{\text{Radioactivity initially added to the antibody solution}} \times 100$$

3.2 Getting Your Reaction Mixture Ready for Syringes

If your reaction mixture shows a labeling of 100%, you may not need further workup in the reaction mixture to prepare the syringes (*see* **Note 9**).

1. If your radiolabeling yield is not 100%, two methods could be used to get rid of the free radioactive ions in the reaction mixture: filtering the reaction using a centrifugal filter system with an appropriate molecular weight cutoff (MWCO) or a prepackaged PD-10 desalting column to exchange the buffer system (*see* **Note 10**).

2. Pipette the reaction mixture into the filter part of the centrifugal filter system, add buffer to reach 500 μL, snap close, and place in the centrifuge with the appropriate counterweight (if needed). Run the centrifuge up to a maximum of 14,000 × *g* for 10 min. Around 100 μL of radiolabeled antibody solution will remain in the filter part.

3. To check the purity and the efficiency of the filtering part, run an iTLC of the antibody fraction to assure that there is no longer free radionuclide ions.

4. Usually one to two washes through the filter gets rid of all free ions.

3.3 Preparation of Syringes

1. The syringes can become a source of lost activity by attracting antibodies to stick to the plastic. A way to overcome this is to "block" or pretreat the syringes with PBS with 1% FBS.

2. Running the radioimmunoconjugate solution through a 0.2 μm filter is a good practice to assure that injection can be as sterile as possible.

3. As a delivery control for immunoPET studies, an isotype control IgG similarly modified with the chelator and labeled with the radioisotope choice should be used for in vitro and in vivo studies.

3.4 Storing Antibody and Antibody Conjugates

1. Upon receipt of the antibody, thaw and spin the vial to assure that any antibody present in the cap or in the walls is pulled down to the bottom of the vial.

2. A good lab practice is to measure the concentration and compare it to the one recorded in the documentation provided by the supplier or the collaborators providing the antibody.

3. Freeze-thaw cycles affect the integrity of the antibody or the antibody conjugate. It is important to aliquot the bulk stock solution. A good rule of thumb amount should be to aliquot the amount that you would use per experiment. In other words, aliquot the amount of antibody that could be used in one in vivo experiment and freeze. Usually a cage of mice has 5 mice, thus aliquots could be made to be used per cage of mice.

4. The Abcam Antibody Storage guide notes that storing the antibodies in a −20 °C freezer vs a −80 °C one has no particular advantage. However, they recommend that antibody storage should be in a freezer area with minimal fluctuations in temperature (think the back of the freezer rather than the door).

5. Once aliquots are thawed, they should not be refrozen. According to the Abcam Antibody Storage guide, these aliquots should remain stable and usable for 1–2 weeks when stored at +4 °C.

6. If the concentration of the antibody or antibody-chelator is too diluted for either the chelator addition to the antibody or the radiolabeling step, a centrifugation step with an ultrafiltration tube with an appropriate MWCO can help concentrate the sample.

3.5 Further Considerations for ImmunoPET Experiments

1. As a delivery control for immunoPET studies, an isotype-control IgG similarly modified with the chelator and labeled with the radioisotope choice should be used for in vitro and in vivo studies.

2. To determine the number of chelators per antibody, a MALDI-TOF-MS analysis can be performed to compare the immunoconjugate vs. the unreacted antibody.

3. For in vivo experiments, unlabeled antibody can be added to achieve a total mAb dose of 100 µg per mouse.

3.6 Making a Calibration Curve

Calibration curves are a great way to determine the concentration of a sample by comparing with a standard measurement of stock solutions at a set range of concentrations. The way a calibration curves works is by determining the linear correlation between concentration of an analyte and a certain physical measurement such as absorbance. For this specific method, the Nanodrop will be the instrument referenced.

1. Make 7 solutions of the desired antibody in different concentrations. Usually a good spread of concentrations should be between 5 and 0.1 mg/mL. For example: 5, 2.5, 1.25, 0.625, 0.3125, 0.156, 0.08 mg/mL.

2. Place 2 µL in the measurement pedestal and gently lower the arm of the instrument. The drop should bead up. If it flattens out, the pedestal should be delicately cleaned with deionized water and a KimWipe.

3. Measure the absorbance of the sample at 280 nm.

4. Raise the arm, and clean the pedestal with water and a KimWipe.

5. Repeat the **steps 2–4** for the other concentrations.

6. Once all samples are measured, plot the data in a graph with *x*-axis "concentration" and *y*-axis "absorbance" and add a linear regression to determine the equation of the linear regression.

7. The equation will be used to determine the concentration of an unknown sample.

The figures referenced in the title of each complexation methods show a representative PET image of the probe.

3.7 [^{89}Zr]Zr-DFO-MAb-B43.13 [14] (Fig. 1)

1. Mix a known amount of the B43.13 antibody with a 10-time molar excess of *p*-SCN-DFO in a 0.1 M sodium bicarbonate buffer at pH 8.7 (*see* **Note 11**).

2. Allow the antibody-DFO mixture to react for 1 h at 37 °C.

3. Purify the reaction mixture using a Sephadex G-25 M PD-10 desalting column previously equilibrated with phosphate buffered saline (PBS) at pH 7.4 (*see* **Note 12**).
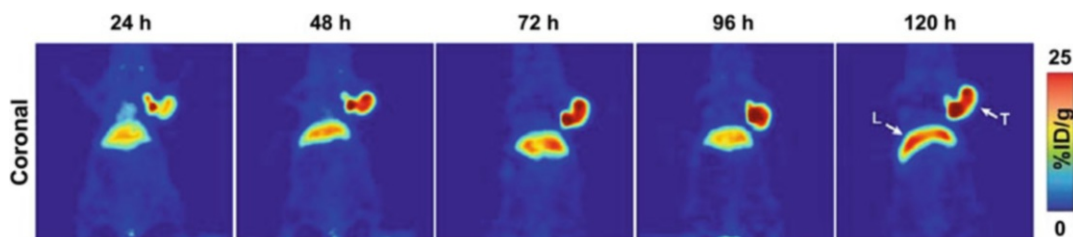
Fig. 1 CA125-targeted PET imaging with ^{89}Zr-DFO-mAb-B43.13. Serial PET images of an athymic nude mouse bearing a CA125-positive OVCAR3 xenograft after the administration of ^{89}Zr-DFO-mAb-B43.13 via tail vein injection (10.2–12.0 MBq). Coronal planar images intersect the middle of the tumor. L liver, T tumor. (This adapted figure was originally published in the *Journal of Nuclear Medicine*, issue 57(5) [14])

4. Measure between 74 and 95 MBq (2–2.5 mCi) of zirconium-89 oxalate ([^{89}Zr]Zr(C$_2$O$_4$)$_2$) in oxalic acid.

5. Adjust the [^{89}Zr]Zr(C$_2$O$_4$)$_2$ solution to pH 7.0–7.5 using small aliquots of 1.0 M sodium carbonate solution. To adjust the pH of the ^{89}Zr solution, start by adding 250 μL of 1.0 M Na$_2$CO$_3$ followed by smaller (< 10 μL) aliquots of the Na$_2$CO$_3$ solution.

6. Dissolve 300–400 μg of DFO-MAb-B43.13 in 200 μL of PBS buffer at pH 7.4.

7. Pipette the pH-adjusted zirconium solution into the DFO-labeled B43.13 solution and incubate this reaction mixture for 1 h at room temperature.

8. Monitor the reaction via radio-thin layer chromatography (radio-TLC) using silica-impregnated paper and 50 mM EDTA at pH 5.

9. After 1 h, quench the reaction with 50 μL of 50 mM EDTA at pH 5 (*see* **Note 13**).

10. Purify the [^{89}Zr]Zr-DFO-B43.13 using a PD-10 desalting column for size-exclusion chromatography.

11. Assess the radiochemical purity of the eluate by radio-TLC using 50 mM EDTA at pH 5 as the mobile phase (*see* Subheading 3.1).

3.8 [^{89}Zr]Zr-DFO-Trastuzumab [15] (Fig. 2)

1. Dissolve 5 mg of trastuzumab (33 nmol) in 1 mL of 0.9% NaCl to a concentration of 5 mg/mL and adjust the pH of the solution to 8.9–9.1 with 0.1 M sodium carbonate.

2. Add 20 μL of a 5 mM p-SCN-DFO in DMSO to the trastuzumab solution (*see* **Note 11**).

3. Allow the mixture to react for 45 min at 37 °C. Keep the DMSO concentration below 2% in all the reaction mixtures.
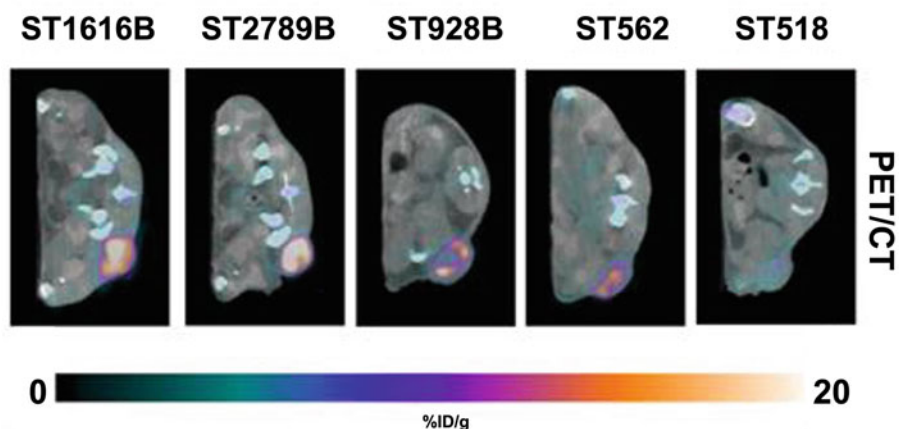
Fig. 2 Site-specific [89]Zr-DFO-trastuzumab PET/CT imaging in PDX models with varying HER2 expression. Representative axial PET/CT images of 89Zr-DFO-trastuzumab (endoS2) tumor uptake in ST518 (breast), ST562 (gastric), ST928B (breast), ST2789B (breast), and ST1616B (breast) PDX models 70 h post-injection. (This adapted figure was originally published in the journal *Theranostics*, issue 9(15) [15])

4. Purify the reaction mixture using a PD-10 column and 50 mM sodium acetate and 200 mM sucrose (pH 5.4–5.6) buffer as the solvent. Collect fractions of the eluent.

5. Measure the concentration of DFO-trastuzumab using a Nanodrop and a previously established calibration curve (*see* Subheading 3.6).

6. Mix 200 μL of [89Zr]-Zr oxalate in 1 M oxalic acid solution with 90 μL of a 2 M sodium carbonate solution and allow to equilibrate for 3 min.

7. Dissolve around 1.5 mg of DFO-NCS-trastuzumab in 0.5 M HEPES buffer (pH 7.0) to reach a volume of 1.71 mL.

8. Mix the [89Zr]-Zr oxalate solution and the DFO-NCS-trastuzumab solution and allow the reaction to progress for 60 min at room temperature under constant agitation.

9. Purify the [89Zr]Zr-DFO-NCS-trastuzumab immunoconjugate reaction mixture using a PD-10 column and collect in 2 mL of 50 mM sodium acetate and 200 mM sucrose buffer at pH 5.4–5.6. Using HPLC, the radiolabeling yield is usually 80–85% with a concentration of 0.6 mg/mL.

3.9 [89Zr]Zr-DFO-SCN-Cetuximab [16] (Fig. 3)

1. Add 30 mg of cetuximab to a PD-10 column and run through a 0.9% NaCl solution to exchange with the storage buffer (*see* **Note 14**).

2. Concentrate the eluate using a 30 kDa ultrafiltration centrifuge tube at $14{,}000 \times g$ for 16 min.

3. Determine the final concentration using a Nanodrop or a similar spectrophotometric device and a previously established
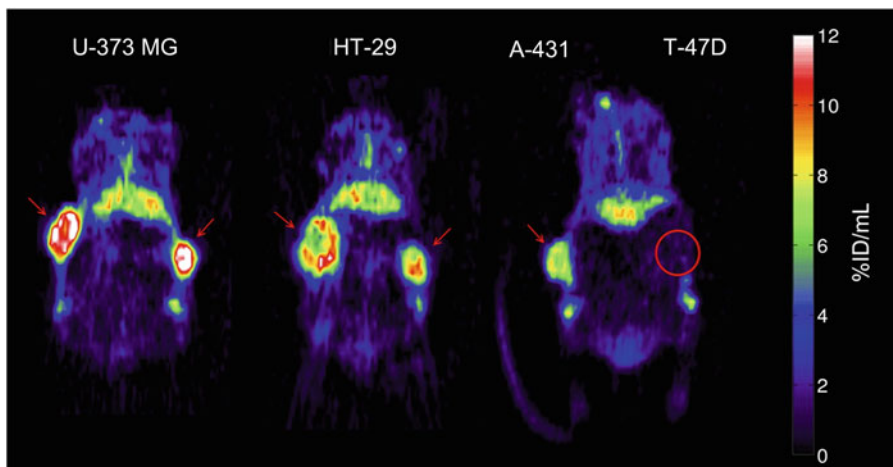
Fig. 3 Representative small-animal PET images 72 h after injection of [89]Zr-cetuximab. Mouse bearing U-373 MG (left) or HT-29 (center) tumors in both flanks. Mouse (right) bearing A-431 and T-47D (circled) tumor in right and left flanks, respectively. Red arrows indicate tumors. Images at mid-plane cross-section through tumor are shown. Images are corrected for injected dose and decay, represented as %ID/mL. High uptake is found in EGFR-expressing tumors (HT-29, U-373 MG, A-431), whereas uptake of low-expression tumor (T-47D) is comparable with overall uptake in surrounding normal tissue. [89]Zr-cetuximab uptake was also found in catabolic organs: in liver and kidneys (below tumors). (This adapted figure was originally published in the *Journal of Nuclear Medicine*, issue 50(1) [28])

    calibration curve with a cetuximab reference standard (*see* Subheading 3.6).

4. Dilute 10 mg of cetuximab (66 nmol) in 1 mL with 0.9% NaCl and adjust the pH to 8.9–9.0 with 0.1 M sodium carbonate.

5. Add 40 μL of a 5 mM solution of *p*-SCN-DFO in DMSO (3 equivalents) to the cetuximab solution and allow this mixture to react for 45 min at 37 °C (*see* **Note 11**).

6. Purify the DFO-SCN-cetuximab reaction mixture using a PD-10 column and a 50 mM sodium acetate, 200 mM sucrose buffer at pH 5.4–5.6.

7. Determine the concentration of the DFO-SCN-cetuximab following Subheading 3.9, **step 3**.

8. Mix 200 μL of [[89]Zr]-Zr oxalate in 1 M oxalic acid solution with 90 μL of 2 M sodium carbonate and allow to equilibrate for 3 min.

9. Dissolve around 1.5 mg of DFO-SCN-cetuximab in up to 1.71 mL of 0.5 M HEPES buffer at pH 7.0.

10. Mix both solutions and allow to react for 60 min at room temperature under constant agitation.

11. Purify the reaction mixture in a PD-10 column using a 50 mM sodium acetate and 200 mM sucrose buffer (pH 5.4–5.6).
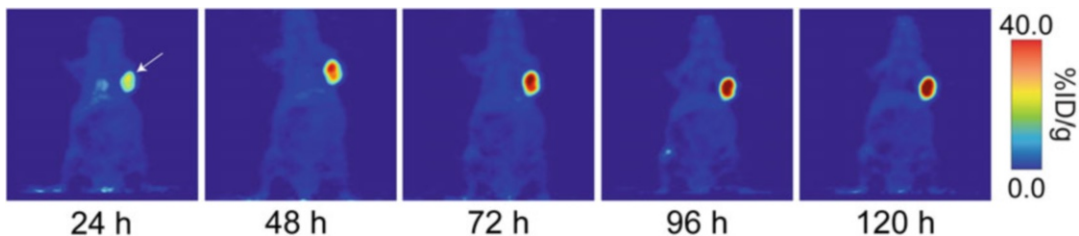
Fig. 4 Coronal PET images of ^{89}Zr-DFO-J591 (11.1–12.9 MBq [300–345 μCi] injected via tail vein in 200 μL 0.9% sterile saline) in athymic nude mice bearing subcutaneous, PSMA-expressing LNCaP prostate cancer xenografts (white arrows) between 24 and 120 h post-injection. (This adapted figure was originally published in the *Journal of Visualized Experiments*, issue 96 [13])

3.10 [^{89}Zr]Zr-DFO-J591 [13] (Fig. 4)

1. Prepare a 2–5 mg/mL solution of J591 in 1 mL of PBS pH 7.4 or in 1 mL of 0.5 M HEPES buffer pH 7.4 (*see* **Note 15**).

2. Prepare a 5–10 mM solution of DFO-NCS in dry DMSO (*see* **Note 11**).

3. Increase the pH of the antibody solution to 8.8–9.0 using small aliquots of 0.1 M Na$_2$CO$_3$.

4. Add a 3–4 molar excess of the DFO-NCS solution to the antibody solution and incubate for 30 min at 37 °C on a thermomixer at 350 rpm.

5. Purify the immunoconjugate using a pre-packed disposable size exclusion desalting column with a 50,000 kDa molecular weight cutoff (MWCO) and 0.5 M HEPES buffer at pH 7.4 as the mobile phase. Measure the concentration using a spectrophotometer or NanoDrop. The J591-DFO immunoconjugate solution can be stored at −20 °C in the dark.

6. Prepare a solution of 0.5–2.0 mg of the immunoconjugate in 200 μL of 0.5 M HEPES buffer at pH 7.5.

7. Add between 37 and 222 MBq (1.0–6.0 mCi) of the ^{89}Zr stock solution into a screw-cap centrifuge tube and add 1.0 M oxalic acid to reach a total volume of 300 μL.

8. Adjust the pH of the radioactive solution between 6.8 and 7.5 using 1.0 M Na$_2$CO$_3$.

9. Add the desired amount of ^{89}Zr^{4+} solution to the immunoconjugate solution and incubate for 60 min at RT on a thermomixer at 350 rpm.

10. Measure the radiochemical yield of the reaction using radio-TLC. If the radiolabeling yield is around 74 MBq/mg (2 mCi/mg), quench the reaction with 5 μL of 50 mM DTPA at pH 5.5 (*see* Subheading 3.1).

11. Run the radioimmunoconjugate reaction mixture through a pre-packed disposable size exclusion desalting column with a 50,000 MWCO with one of the following as mobile phase: 0.9% sterile saline with 5 mg/mL gentisic acid and 0.25 M sodium acetate (pH 5.5) with 5 mg/mL gentisic acid (*see* **Note 16**).

12. Rerun the radio-TLC to check the radiochemical purity of the ^{89}Zr-DFO-J591 (*see* Subheading 3.1).

3.11 Copper-64 [^{64}Cu]Cu-DOTA-Pembrolizumab [17, 18] (Fig. 5)

The most common chelators of copper-64 for antibody applications are DOTA, NOTA, TE2A, TE1A1P, and sarcophagine [19].

1. Purify the antibody using a size exclusion column HPLC with PBS at pH 8.0 (*see* **Note 12**).

2. Exchange the buffer of the antibody solution using 1 M HEPES and 0.1 M sodium carbonate buffer (pH 8.5 ± 0.5) (*see* **Note 14**).

3. Concentrate the pembrolizumab to ~5 mg/mL with a 30 kDa centrifugal filter (*see* **Note 17**).

4. Mix 5 mg of pembrolizumab in 1 mL of 1 M HEPES buffer at pH 7.5–8.0 with 34 μL of 10 mM DOTA-NHS in DMSO using molar excess of the chelator (*see* **Note 11**).
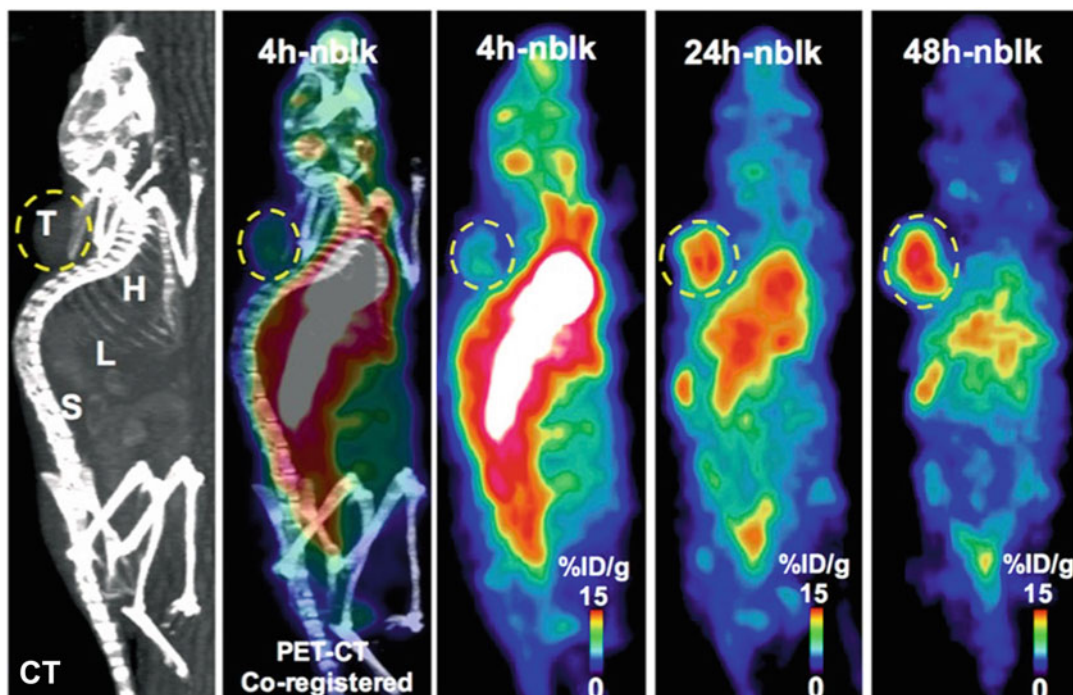
Fig. 5 PET-CT image showing ^{64}Cu-pembrolizumab immunoPET in NSG/293 T/hPD-1 mouse model. Representative PET images scanned at 4, 24, and 48 h post-injection of 64Cu-pembrolizumab tracer (7.4 MBq/200 μL) in NSG/293 T/hPD-1-nblk (non-blocking) mice. L liver, H heart, X xenograft, S spleen. (This adapted figure was originally published in the journal *Scientific Reports*, issue 8(1) [17])

5. Allow the reaction to progress for 60 min at 37 °C.

6. Purify the antibody–chelator reaction mixture with a SEC 2000 HPLC using a mobile phase of 0.1 M ammonium acetate buffer (pH 5.5) eluted at 1 mL/min. Store the immunoconjugate in 200 μL aliquots after the centrifugal concentration in 0.1 M ammonium acetate buffer (pH 5.5) at −20 °C.

7. Concentrate the eluate with a 30 kDa MWCO centrifugal filter to 3–5 mg/mL (*see* **Note 17**).

8. Add 0.5 mg of DOTA-pembrolizumab to a reaction vial (~100 μL) and 750 μL [^{64}Cu]CuCl$_2$ (260–270 MBq) at pH 5.5 ± 0.5.

9. Incubate the reaction mixture at 37 °C for 1 h.

10. Add around 90 μL of a 0.1 M EDTA at pH 8.0 to the reaction vial for a final concentration of 10 mM and allow to react for 15 min (*see* **Note 13**).

11. Purify the radioimmunoconjugate, ^{64}Cu-DOTA-pembrolizumab, using a SEC-2000 HPLC with PBS buffer as the mobile phase at a flow rate of 1 mL/min. Collect the radioimmunoconjugate at 8 ± 2 min.

12. Concentrate the product to ~5 mg/mL using a 30 kDa MWCO centrifugal filter (*see* **Note 17**).

3.12 [^{64}Cu]Cu-NOTA-Trastuzumab [20] (Fig. 6)

1. Exchange the buffer of the trastuzumab antibody solution with 0.1 M HEPES buffer at pH 8.5 and concentrate the resulting solution to 10 mg/mL using a centrifugal concentrator (*see* **Notes 14** and **17**).

2. Mix the trastuzumab solution in HEPES buffer with a 20-fold molar excess of p-SCN-Bn-NOTA in 100% ethanol. Addition of ethanol solution should be done dropwise.

3. Incubate the reaction overnight at 4 °C.

4. Exchange the buffer of the reaction mixture with 0.1 M ammonium acetate buffer at pH 6 and concentrate it to 5 mg/mL using a Vivaspin-20 filter (*see* **Notes 14** and **17**).

5. Mix 1 mg of the newly synthesized NOTA-trastuzumab with 74 MBq (2 mCi) of [^{64}Cu]CuCl$_2$ and incubate the reaction mixture for 1 h at room temperature with constant agitation.

6. Determine the radiolabeling yield and purity with radio-TLC using silica gel and a mobile phase of 0.1 M ammonium acetate buffer and 0.05 M EDTA at pH 6 (*see* Subheading 3.1).

3.13 [^{64}Cu]Cu-TE2A-9E7.4 [21] (Fig. 7)

1. Incubate the antibody for 2 h in a solution of 0.1 M EDTA to chelate contaminant metals.

2. Exchange the buffer with 0.3 M carbonate buffer at pH 8.6 and concentrate the antibody solution to 4 mg/mL using a disposable Amicon Ultra-4 filter (*see* **Note 17**).
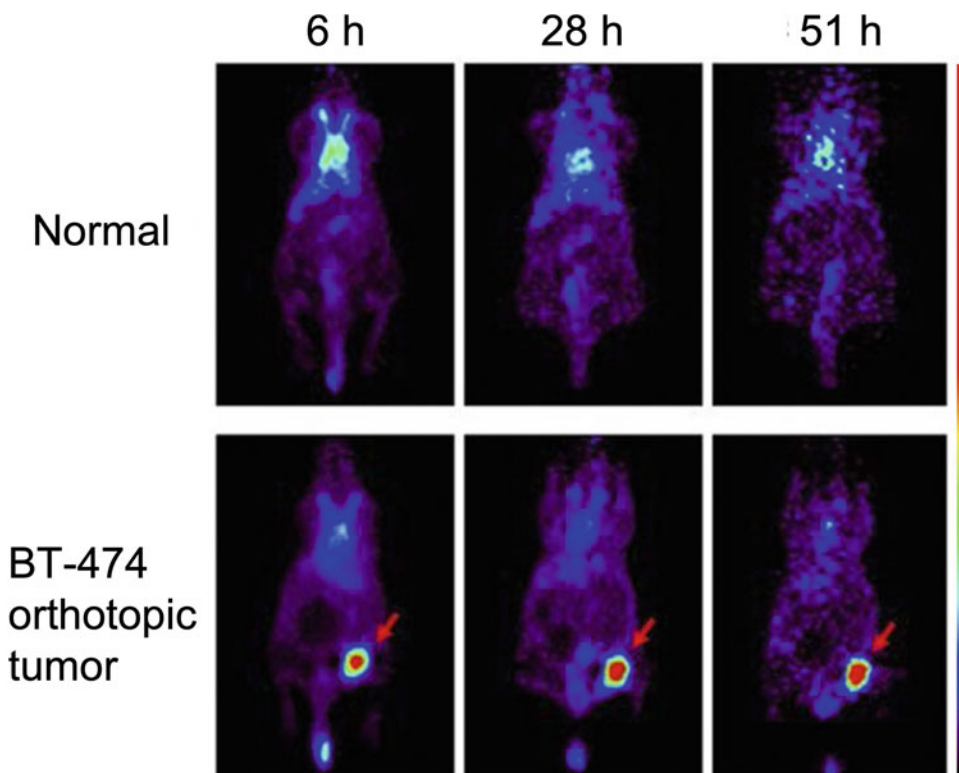
Fig. 6 ^{64}Cu-NOTA-trastuzumab PET in orthotopic HER2-positive BT-474 breast tumor model. Tumor uptake of ^{64}Cu-NOTA-trastuzumab was clearly visible at 6 h and peaked at 51 h. (This adapted figure was originally published in the *Journal of Nuclear Medicine*, issue 60(1) [20])

3. Add 20 molar excess of TE2A-benzyl isothiocyanate (usually in a 12 mg/mL solution) to the antibody and incubate overnight at 4 °C (*see* **Note 11**).

4. Purify the immunoconjugate using a PD-10 disposable gel filtration column with 0.3 M ammonium acetate buffer at pH 7 and concentrate the solution using a disposable Amicon Ultra-4 filter (*see* **Notes 12** and **17**).

5. Add 408 MBq of [^{64}Cu]CuCl$_2$ in 0.1 M HCl (around 244 μL) and 60 μL of 2.5 M ammonium acetate buffer at pH 7.0 to the immunoconjugate solution and incubate for 20 min at 40 °C.

6. Add 10 μL of 10 mM EDTA at pH 7 to the reaction mixture and stir for 5 min at 40 °C (*see* **Note 13**).

7. Determine the radiochemical purity by thin layer chromatography radio-TLC-SG using a 0.1 M citrate buffer at pH 4.5 as the mobile phase (*see* Subheading 3.1).

8. Further purify the radio immunoconjugate using a Sephadex PD-10 column (*see* **Note 12**).
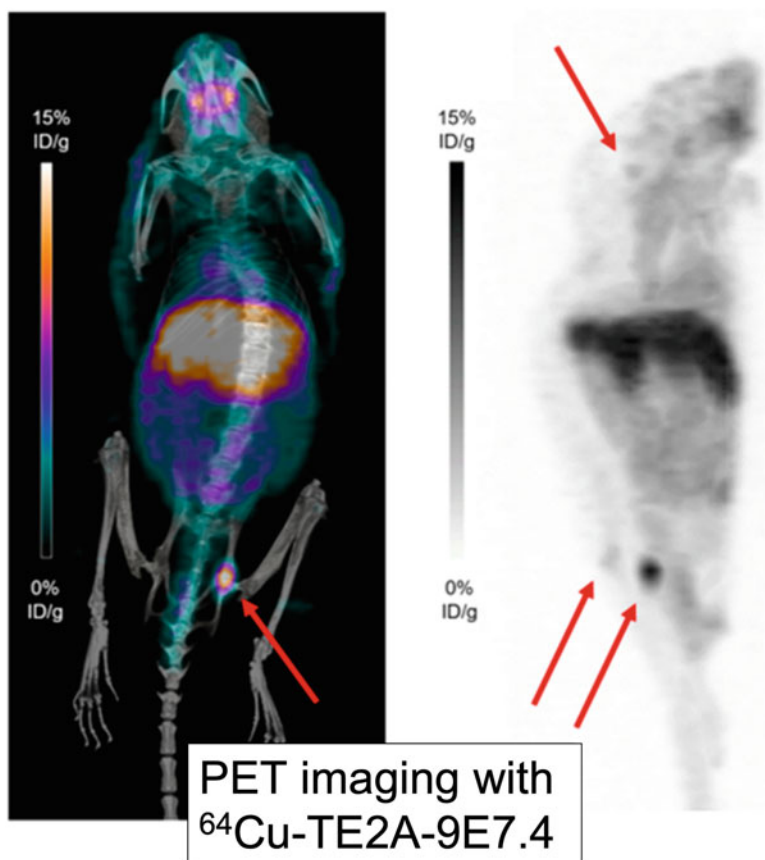
Fig. 7 PET imaging with ^{64}Cu-TE2A-9E7.4 showing maximum intensity projections of PET and CT imaging with ^{64}Cu-TE2A-9E7.4 at 24 h post-injection. (This research was originally published in the *International Journal of Molecular Sciences*, issue 20(10) [29])

3.14 [^{64}Cu]Cu-CB-TE1A1P-Cetuximab [22] (Fig. 8)

1. Mix 5.8 mg of CB-TE1A1P, 1.7 mg of sulfo-N-hydroxysucci-nimide, and 2.0 mg of hydroxybenzotriazole (HOBT) in 1 mL of DMF and place the reaction on ice (*see* **Note 11**).

2. Add 2.9 mg of 1-ethyl-3-(3-(dimethylamino)propyl) carbodii-mide hydrochloride (EDC) to the reaction mixture. Stir for 30 min to evaporate the DMF. The proportion of this activation reaction in **steps 1** and **2** is 1:1:1:1. The EDC solution degrades quickly. Therefore, the solution must be used immediately post-preparation.

3. Mix 2.9 mL concentrated solution of cetuximab (20 mg/mL) with the activated CB-TE1A1P to achieve a molar ration of 100:1 (CB-TE1A1P:cetuximab) and incubate the reaction for 2 days at 4 °C using an end-over-end rotation mixing method.

4. Transfer the reaction mixture to a Centricon 100 filter unit, wash twice with 0.1 M ammonium acetate at pH 8.0 and concentrate the immunoconjugate solution (*see* **Note 17**).
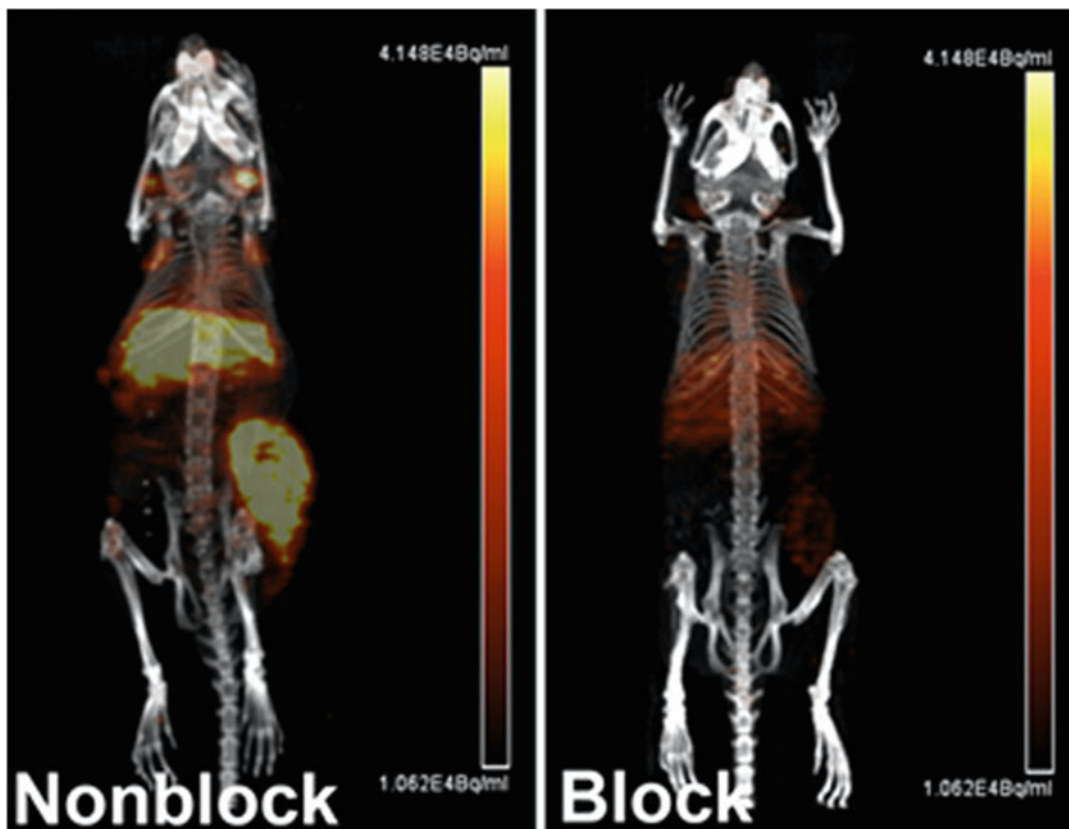
Fig. 8 Small animal PET/CT maximum intensity projection images of HCT116 tumor bearing female nude mice at 48 h post-injection 64Cu-CB-TE1A1P–cetuximab. One group of mice was pretreated with ~166–33 equiv. of unlabeled cetuximab 24 h prior to probe injection (right panel) while the other group was not pretreated (left panel). (This adapted figure was originally published in *Molecular Pharmaceutics*, issue 11(11) [22])

5. Extract unreacted small molecules by flowing the mixture through a desalting column 2–3 times (*see* **Note 12**).

6. Mix ~70 μL CB-TE1A1P—cetuximab (2.0 mg/mL) and 250 μL of 0.1 M ammonium acetate at pH 8.2 in a 1.5 mL tube.

7. Add 18.5 MBq (500 μCi) [^{64}Cu]CuCl$_2$ in 0.1 M ammonium acetate buffer, vortex for 10 s, and incubate the reaction for 2 h at 40 °C.

8. Determine the radiolabeling yield by FPLC.

3.15 [^{64}Cu]Cu-Sar-ch14.18-Δ C$_H$2 [23] (Fig. 9)

1. Exchange the buffer of the ch14.18-ΔC$_H$2 antibody to sodium acetate and concentrate using Centricon centrifugal filter units with 30 kDa MWCO (*see* **Note 17**).

2. Mix 50 μL of a 400 mg/mL solution of (NH$_2$)(CO$_2$H)sar in DMSO with 150 μL of 0.1 M sodium acetate buffer at pH 5.0 for a final sarcophagine concentration of 100 mg/mL (*see* **Note 11**).
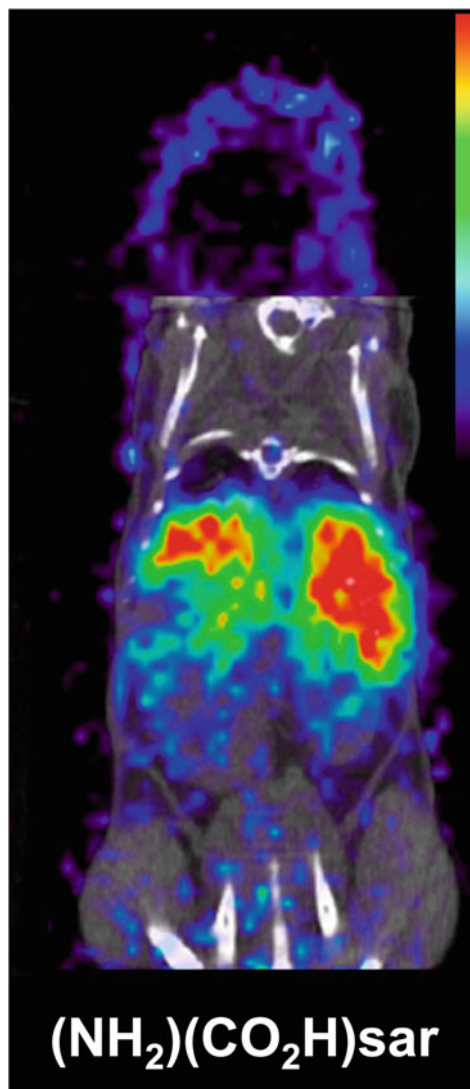
Fig. 9 Coronal small animal PET/CT images of mice injected with ch14.18-ΔCH2 labeled with 64Cu via (NH$_2$)(CO$_2$H)sar at 48 h post-injection. PET data is in color scale; CT data is in gray scale. (This adapted figure was originally published in *Bioconjugate Chemistry*, issue 26(4) [23])

3. Adjust the pH to 5.0 by addition of small aliquots of 1 N NaOH.

4. Add 200 μL of chelator to the ch14.18-ΔC$_H$2 solution at a molar ratio of 250:1 and add sodium acetate buffer to achieve a final antibody concentration of 5 mg/mL (*see* **Note 11**).

5. Add 500 molar equivalents of EDC to the reaction mixture and allow the reaction to progress for 30 min. The EDC solution must be prepared right before it is going to be used in a concentration of 50 mg/mL using ultrapure water (*see* **Note 1**).

6. Purify the immunoconjugate by size-exclusion HPLC using a BioSep SEC-S3000 column with 0.1 M sodium acetate at pH 5.0 as the solvent at a flow rate of 1 mL/min. The retention time of the Sar-ch14.18-$\Delta C_H 2$ is around 8.1 min. Fractions containing the immunoconjugate can be mixed together, concentrated using Centricon filters, and stored at -80 °C.

7. Mix 74 MBq (2 mCi) $[^{64}Cu]CuCl_2$ in 5–10 μL HCl (0.04 N) with 15–30 mL of sodium acetate buffer 0.1 M at pH 5.0.

8. Add 75 μL of the immunoconjugate at a concentration of 3.33 mg/mL to the $[^{64}Cu]CuCl_2$ solution and incubate the reaction for 30 min at 25 °C.

9. Confirm radiolabeling efficiency using radio-iTLC (*see* Subheading 3.1).

10. Purify the $[^{64}Cu]Cu$-Sar-ch14.18-$\Delta C_H 2$ radioimmunoconjugate using a centrifugal filter and dilute the purified solution to achieve a final concentration of 0.5 mg/mL (*see* **Note 17**).

11. Before injection, filter the radioimmunoconjugate through a 0.2 μm sterile filter.

3.16 Yttrium-86 [^{86}Y] Y-DTPA-hu3S193 [24] (Fig. 10)

Conjugation of the 3S193 to DTPA is adapted from [25].

1. Incubate the humanized 3S193 (hu3S193) overnight in EDTA at a final concentration of 1 mM in an Amicon filter with a cutoff of 30 kDA MWCO (*see* **Note 17**).

2. Add 40 mL of carbonate buffer to the humanized 3S193 solution and connect the reservoir and the filter unit.

3. Exchange buffer of the antibody solution with a carbonate buffer by dropwise dilution with 800 mL of carbonate buffer over ~2 h (*see* **Note 14**).

4. Concentrate the antibody solution to around 20 mL using a flow of N_2.

5. Dissolve between 3 and 11 mg of the chelator (2-*p*-SCN-Bz)-cyclohexyl-DTPA into an antibody solution containing around 60–100 mg.
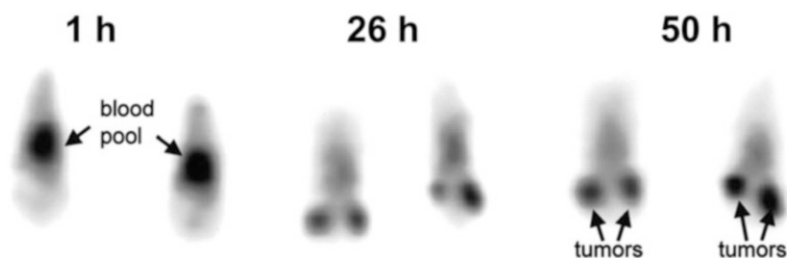
Fig. 10 Serial coronal PET images of 2 mice injected with ^{86}Y-hu3S193. (This adapted figure was originally published in *Journal of Nuclear Medicine*, issue 42(8) [24])

6. Allow the reaction mixture to react for 19 h at room temperature.

7. Exchange the buffer of immunoconjugate reaction mixture to an acetate buffer by continuous dilution with 750 mL of buffer over ~2 h.

8. Concentrate the DTPA-hu3S193 immunoconjugate to 12–21 mL using a ultracentrifuge filter. Transfer into 15 mL vials and store at 4 °C.

9. Mix between 51.8 and 148 MBq ^{86}Y with 3 M ammonium acetate to a final pH of around 5.

10. Add around 100–250 μg of the DTPA-hu3S193 and incubate the reaction mixture for 30 min at room temperature.

11. Quench the reaction by adding 50 nmol EDTA.

12. Purify the radioimmunoconjugate with 0.050 M PBS using a 10-DG desalting column pre-equilibrated with 0.050 M PBS (*see* **Note 12**).

13. To assess the radiolabeling, perform a radio-TLC on silica gel using a solution of EDTA 10 mmol/L at pH 4.5 as a mobile phase (*see* Subheading 3.1).

3.17 ^{124}**I-L19-SIP**
[26] (Fig. 11)

Currently, the method of choice for iodination of antibodies is the direct radioiodination of tyrosine residues of the antibodies with I^+ species created by oxidation of ^{124}I with oxidizing agents such as IODOGEN or chloramine-T [27].

1. Pipette 25 μg of IODO-GEN in dichloromethane in a scintillation vial and dry the solution under a gentle flow of N_2 gas to achieve a thin coat in the bottom of the vial (*see* **Note 18**).

2. Using the prepared IODO-GEN glass vial, add 50 μL of 0.5 M Na_2HPO_4 at pH 7.4, 218 μL of 0.1 M Na_2HPO_4 at pH 6.8, 142 μL (175 μg, 2.33 nmol) of L19-SIP, and 90 μL ^{124}I solution (38.5 MBq, 232 pmol NaI) and gently shake the mixture for 4 min at room temperature.

3. Add 0.1 mL of ascorbic acid (25 mg/mL) at pH 5 and gently shake for 5 min (*see* **Note 19**).

4. Transfer the reaction mixture to a syringe connected to an Acrodisc 0.22 μm filter and wash the reaction vessel with 400 μL of 0.1 M Na_2HPO_4 at pH 6.8. Combine this washout with the reaction mixture in the syringe.

5. Filter the solution through a PD-10 column using 0.9% NaCl/ascorbic acid buffer solution (5 mg/mL, pH 5) as the mobile phase.

6. Discard the first 2.5 mL of eluate and collect the radiolabeled antibody in the following 1.5 mL.
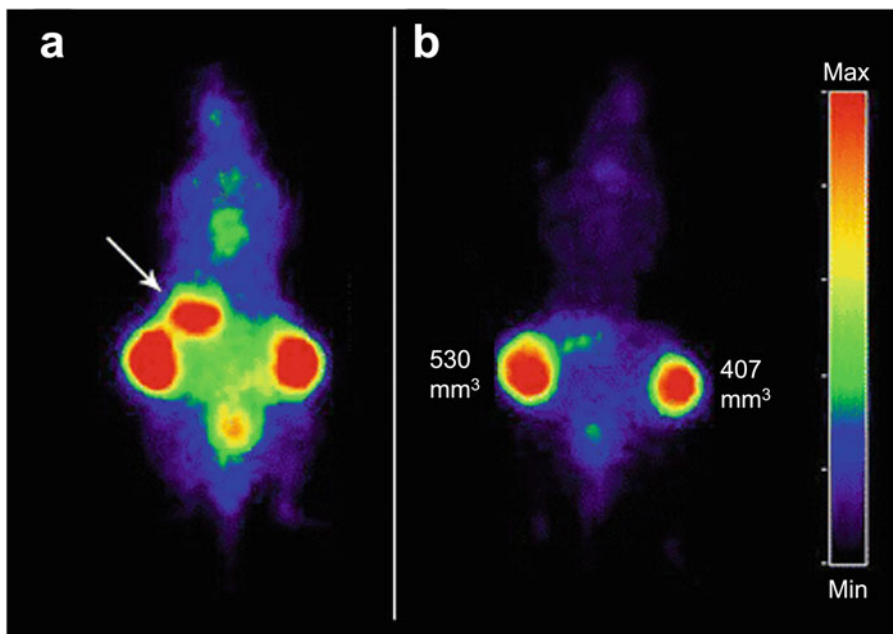
Fig. 11 PET images of FaDu xenograft-bearing nude mouse injected with ^{124}I-L19-SIP (3.7 MBq, 25 μg). Coronal images were acquired at 24 (**a**) and 48 h (**b**) after injection. Image planes have been chosen where both tumors were visible. Uptake of 124I in the stomach (arrow) and to some extent in bladder (urine) is visible at 24 h post-injection, but has disappeared at 48 h post-injection. (This adapted research was originally published in the *European Journal of Nuclear Medicine and Molecular Imaging*, issue 36(8) [26])

7. Perform radio-TLC analysis using silica gel glass fiber sheets using 20 mM citrate buffer (pH 5) as a mobile phase.

8. Run an HPLC of the final product using a size exclusion column and 0.05 M sodium phosphate/0.15 M sodium chloride (pH 6.8) mixture at a flow rate of 0.5 mL/min.

4   Notes

1. Water should be distilled and deionized using a MilliQ water filtration system or similar system to achieve the 18 MΩ-cm.

2. If the compound is not dissolving, place the solution on a heating plate and increase the temperature. Heating up the solution will help to dissolve the compound if there are issues getting it into solution. However, it is important to wait until the solution cools down to room temperature (25 °C) before measuring and adjusting the pH.

3. The buffer is now ready. However, due to the possible presence of heavy metals traces in the solution, adding Chelex to the solution will remove these contaminants that can affect the chelation steps.

4. When labeling biomolecules with radiometals, it is important to use metal-free or trace-metals-grade solvents and buffers to prevent the presence of any unwanted metal ions in the working solutions. These metal contaminant ions can compete for the same chelator as the radiometal, resulting in lower radiolabeling yield.

5. Turn the stirring off and allow the Chelex resin to accumulate in the bottom of the flask. There are two ways to remove the Chelex polymer from the solution, depending on the supplies available in the lab. One is to decant the chelexed buffer through a filter paper in a funnel in a clean flask and allow for gravity filtration. The other more faster way is to use a Millipore filtering unit (or similar device) to remove the traces of Chelex resin in solution. Though the Chelex should have no effect on the pH of the buffer, it is good practice to verify the pH of the final solution.

6. Silica-impregnated paper is very fragile—it can crack and crease very easily. Cut it carefully. Once cut to the desired width (between 0.5 and 1 cm should be enough), a dot of ink from a pen (we use red ink) around 1–2 cm from the edge of the iTLC paper—the sample should be placed around the same paper height. The color dot is used to monitor the progress of the iTLC.

7. The iTLC chamber should contain mobile phase solvent around 1–2 cm from the bottom of the chamber. If a glass TLC chamber is unavailable, a 50 mL conical tube can be used as a replacement.

8. To prevent the instrument from radioactive contamination from the samples, the iTLC paper should be covered with either cling wrap or parafilm.

9. Some chelations are reacted in a buffer that is approved for injection into mice. Each antibody usually has a specific buffer system that works optimally for mouse injection. Some mouse-safe buffers are PBS and 0.9% buffered saline, among others. However, the buffers to be used in mouse studies need to be confirmed with those approved in the animal protocol in each lab and institution.

10. Rather than a quick selection between two methods, either one or both methods should be selected based on the situation. To inject into mice, radiolabeled antibodies should be the only source of radiation in the sample; thus, no free radioactive ions can linger in the solution. Free ions affect the final images obtained as they usually have a different distribution to that of the radiolabeled antibody. For example, free iodine-124 ends up in the thyroid, free zirconium-89 in the bones, and copper-64 in the liver, among other examples. Once the radiolabeled antibody solution is 100% radioactively pure, another question that must be asked is whether the buffer system the

compound is in compatible with in vivo tail vein injection. If yes, then the sample just needs to be diluted into the full volume needed, and then the syringes are prepared. If no, then a buffer exchange column (size exclusion column) should be run. Sometimes, if the biological probe (antibody, minibody, monobody, targeting peptide) is considered "sticky" (it easily gets adsorbed or stuck in the stationary phase), several filtration steps might be a better option to prevent loss of product.

11. Compounds like *p*-SCN-DFO can be tricky to dissolve in DMSO and, therefore, sonication or vortexing can be used. Ideally, a concentrated working solution of the chelator in DMSO will prevent the reaction solution to have a percentage of DMSO higher than 1–2%. When adding the DMSO solution to the antibody sample, a dropwise addition followed by gentle agitation reassures that the reaction solution remains homogeneous and the compounds are well mixed. This prevents the chelator to crash out of solution, thus affecting the yield of the reaction.

12. Pretreating your PD-10 column with the elution buffer is a key step in the purification of both the modified antibody and the radioimmunoconjugate. Pretreatment involves replacing the solution in the column with the buffer appropriate for the antibody. Run around 20 mL of the antibody buffer through the column to get it ready for use.

13. Adding EDTA to the reaction scavenges any unchelated radionuclides in the reaction mixture and stops the reaction.

14. The storage buffer of an antibody may not be optimal for the reaction to occur. Exchanging the buffer of an antibody using a PD10 column removes the buffer used for storage and replaces it with the ideal buffer for the conjugation step.

15. Either buffer can be used and have been used in the past. The main goal of using these buffers is to get the reaction to pH ~7.0.

16. Gentisic acid is used to stabilize and protect the radiolabeled molecule.

17. Centrifugal filters are a very useful tool to concentrate antibodies and other large molecular weight materials. These filters contain molecular weigh based size exclusion membranes that retain molecules larger that the molecular weigh specification while allowing smaller molecular weight molecules to pass through the membrane. Since the molecular weight of antibodies and proteins is much larger than the molecular weight of small molecules and salts, they can easily stay in solution above the membrane while salts and water will pass through the memembrane, effectively concentrating the antibody concentration in solution upstream of the filter. And centrifugation provides the necessary force for solution upstream of the

membrane to pushed across the membrane. The filter membrane size exclusion specification should be carefully selected based on the molecular weight of the antibody or protein of interest in order to minimize the loss of product during filtration. A good practice is to select a filter membrane cutoff specification that is around half the size of your biological of interest.

18. The vials containing thin layers of IODO-GEN can be stored under a nitrogen atmosphere for future use.

19. Ascorbic acid reduces the IODO-GEN and protects the L19-SIP against radiation damage.

Acknowledgments

References

1. Schroeder HW Jr, Cavacini L (2010) Structure and function of immunoglobulins. J Allergy Clin Immunol 125(2 Suppl 2):S41–S52. https://doi.org/10.1016/j.jaci.2009.09.046

2. Ljungars A, Martensson L, Mattsson J, Kovacek M, Sundberg A, Tornberg UC, Jansson B, Persson N, Emruli VK, Ek S, Jerkeman M, Hansson M, Juliusson G, Ohlin M, Frendeus B, Teige I, Mattsson M (2018) A platform for phenotypic discovery of therapeutic antibodies and targets applied on Chronic Lymphocytic Leukemia. NPJ Precis Oncol 2:18. https://doi.org/10.1038/s41698-018-0061-2

3. Sundaresan G, Yazaki PJ, Shively JE, Finn RD, Larson SM, Raubitschek AA, Williams LE, Chatziioannou AF, Gambhir SS, Wu AM (2003) 124I-labeled engineered anti-CEA minibodies and diabodies allow high-contrast, antigen-specific small-animal PET imaging of xenografts in athymic mice. J Nucl Med 44(12):1962–1969

4. Lepin EJ, Leyton JV, Zhou Y, Olafsen T, Salazar FB, McCabe KE, Hahm S, Marks JD, Reiter RE, Wu AM (2010) An affinity matured minibody for PET imaging of prostate stem cell antigen (PSCA)-expressing tumors. Eur J Nucl Med Mol Imaging 37(8):1529–1538. https://doi.org/10.1007/s00259-010-1433-1

5. Pandit-Taskar N, Postow MA, Hellmann MD, Harding JJ, Barker CA, O'Donoghue JA, Ziolkowska M, Ruan S, Lyashchenko SK, Tsai F, Farwell M, Mitchell TC, Korn R, Le W, Lewis JS, Weber WA, Behera D, Wilson I, Gordon M, Wu AM, Wolchok JD (2020) First-in-humans imaging with (89)Zr-Df-IAB22M2C anti-CD8 minibody in patients with solid malignancies: preliminary pharmacokinetics, biodistribution, and lesion targeting. J Nucl Med 61(4):512–519. https://doi.org/10.2967/jnumed.119.229781

6. Farwell M, Gamache R, Pandit-Taskar N, Postow M, Gordon M, Wilson I, Mascioni A, Wu A, Le W, Weiss A, Korn R (2020) 294 CD8 PET imaging of tumor infiltrating T cells in advanced solid tumors: a phase I first-in-human study of 89Zr-IAB22M2C, a radiolabeled anti-CD8 minibody. J Immunother Cancer 8(Suppl 3):A179–A180. https://doi.org/10.1136/jitc-2020-SITC2020.0294

7. Wei W, Rosenkrans ZT, Liu J, Huang G, Luo QY, Cai W (2020) ImmunoPET: concept, design, and applications. Chem Rev 120(8):3787–3851. https://doi.org/10.1021/acs.chemrev.9b00738

8. Holland JP, Sheh Y, Lewis JS (2009) Standardized methods for the production of high specific-activity zirconium-89. Nucl Med Biol

36(7):729–739. https://doi.org/10.1016/j.nucmedbio.2009.05.007

9. Anderson CJ, Ferdani R (2009) Copper-64 radiopharmaceuticals for PET imaging of cancer: advances in preclinical and clinical research. Cancer Biother Radiopharm 24(4):379–393. https://doi.org/10.1089/cbr.2009.0674

10. Sadeghi M, Aboudzadeh M, Zali A, Zeinali B (2009) (86)Y production via (86)Sr(p,n) for PET imaging at a cyclotron. Appl Radiat Isot 67(7–8):1392–1396. https://doi.org/10.1016/j.apradiso.2009.02.038

11. Halime Z, Frindel M, Camus N, Orain PY, Lacombe M, Bernardeau K, Cherel M, Gestin JF, Faivre-Chauvet A, Tripier R (2015) New synthesis of phenyl-isothiocyanate C-functionalised cyclams. Bioconjugation and (64)Cu phenotypic PET imaging studies of multiple myeloma with the te2a derivative. Org Biomol Chem 13(46):11302–11314. https://doi.org/10.1039/c5ob01618e

12. Ferdani R, Stigers DJ, Fiamengo AL, Wei L, Li BT, Golen JA, Rheingold AL, Weisman GR, Wong EH, Anderson CJ (2012) Synthesis, Cu (II) complexation, 64Cu-labeling and biological evaluation of cross-bridged cyclam chelators with phosphonate pendant arms. Dalton Trans 41(7):1938–1950. https://doi.org/10.1039/c1dt11743b

13. Zeglis BM, Lewis JS (2015) The bioconjugation and radiosynthesis of 89Zr-DFO-labeled antibodies. J Vis Exp 96. https://doi.org/10.3791/52521

14. Sharma SK, Sevak KK, Monette S, Carlin SD, Knight JC, Wuest FR, Sala E, Zeglis BM, Lewis JS (2016) Preclinical 89Zr Immuno-PET of high-grade serous ovarian cancer and lymph node metastasis. J Nucl Med 57(5):771–776. https://doi.org/10.2967/jnumed.115.167072

15. Kristensen LK, Christensen C, Jensen MM, Agnew BJ, Schjoth-Frydendahl C, Kjaer A, Nielsen CH (2019) Site-specifically labeled (89)Zr-DFO-trastuzumab improves immunoreactivity and tumor uptake for immuno-PET in a subcutaneous HER2-positive xenograft mouse model. Theranostics 9(15):4409–4420. https://doi.org/10.7150/thno.32883

16. Vugts DJ, Klaver C, Sewing C, Poot AJ, Adamzek K, Huegli S, Mari C, Visser GWM, Valverde IE, Gasser G, Mindt TL, van Dongen G (2017) Comparison of the octadentate bifunctional chelator DFO*-pPhe-NCS and the clinically used hexadentate bifunctional chelator DFO-pPhe-NCS for (89)Zr-immuno-PET. Eur J Nucl Med Mol Imaging 44(2):286–295. https://doi.org/10.1007/s00259-016-3499-x

17. Natarajan A, Patel CB, Habte F, Gambhir SS (2018) Dosimetry prediction for clinical translation of (64)Cu-pembrolizumab Immuno-PET targeting human PD-1 expression. Sci Rep 8(1):633. https://doi.org/10.1038/s41598-017-19123-x

18. Natarajan A, Mayer AT, Reeves RE, Nagamine CM, Gambhir SS (2017) Development of novel ImmunoPET tracers to image human PD-1 checkpoint expression on tumor-infiltrating lymphocytes in a humanized mouse model. Mol Imaging Biol 19(6):903–914. https://doi.org/10.1007/s11307-017-1060-3

19. Cai Z, Anderson CJ (2014) Chelators for copper radionuclides in positron emission tomography radiopharmaceuticals. J. Label. Compd. Radiopharm 57(4):224–230. https://doi.org/10.1002/jlcr.3165

20. Woo SK, Jang SJ, Seo MJ, Park JH, Kim BS, Kim EJ, Lee YJ, Lee TS, An GI, Song IH, Seo Y, Kim KI, Kang JH (2019) Development of (64)Cu-NOTA-Trastuzumab for HER2 targeting: a radiopharmaceutical with improved pharmacokinetics for human studies. J Nucl Med 60(1):26–33. https://doi.org/10.2967/jnumed.118.210294

21. Bailly C, Gouard S, Lacombe M, Remaud-Le Saec P, Chalopin B, Bourgeois M, Chouin N, Tripier R, Halime Z, Haddad F, Faivre-Chauvet A, Kraeber-Bodere F, Cherel M, Bodet-Milin C (2018) Comparison of Immuno-PET of CD138 and PET imaging with (64)CuCl2 and (18)F-FDG in a preclinical syngeneic model of multiple myeloma. Oncotarget 9(10):9061–9072. https://doi.org/10.18632/oncotarget.23886

22. Zeng D, Guo Y, White AG, Cai Z, Modi J, Ferdani R, Anderson CJ (2014) Comparison of conjugation strategies of cross-bridged macrocyclic chelators with cetuximab for copper-64 radiolabeling and PET imaging of EGFR in colorectal tumor-bearing mice. Mol Pharm 11(11):3980–3987. https://doi.org/10.1021/mp500004m

23. Dearling JL, Paterson BM, Akurathi V, Betanzos-Lara S, Treves ST, Voss SD, White JM, Huston JS, Smith SV, Donnelly PS, Packard AB (2015) The ionic charge of copper-64 complexes conjugated to an engineered antibody affects biodistribution. Bioconjug Chem

26(4):707–717. https://doi.org/10.1021/acs.bioconjchem.5b00049

24. Lovqvist A, Humm JL, Sheikh A, Finn RD, Koziorowski J, Ruan S, Pentlow KS, Jungbluth A, Welt S, Lee FT, Brechbiel MW, Larson SM (2001) PET imaging of (86)Y-labeled anti-Lewis Y monoclonal antibodies in a nude mouse model: comparison between (86)Y and (111)In radiolabels. J Nucl Med 42(8):1281–1287

25. Nikula TK, Curcio MJ, Brechbiel MW, Gansow OA, Finn RD, Scheinberg DA (1995) A rapid, single vessel method for preparation of clinical grade ligand conjugated monoclonal antibodies. Nucl Med Biol 22(3):387–390. https://doi.org/10.1016/0969-8051(94)00126-5

26. Tijink BM, Perk LR, Budde M, Stigter-van Walsum M, Visser GW, Kloet RW, Dinkelborg LM, Leemans CR, Neri D, van Dongen GA (2009) (124)I-L19-SIP for immuno-PET imaging of tumour vasculature and guidance of (131)I-L19-SIP radioimmunotherapy. Eur J Nucl Med Mol Imaging 36(8):1235–1244. https://doi.org/10.1007/s00259-009-1096-y

27. Kumar K, Ghosh A (2021) Radiochemistry, production processes, labeling methods, and ImmunoPET imaging pharmaceuticals of Iodine-124. Molecules 26(2). https://doi.org/10.3390/molecules26020414

28. Aerts HJWL, Dubois L, Perk L, Vermaelen P, van Dongen GAMS, Wouters BG, Lambin P (2009) Disparity between in vivo EGFR expression and (89)Zr-labeled cetuximab uptake assessed with PET. J Nucl Med 50(1): 123–131. https://doi.org/10.2967/jnumed.108.054312

29. Bailly C, Gouard S, Guerard F, Chalopin B, Carlier T, Faivre-Chauvet A, Remaud-Le Saec P, Bourgeois M, Chouin N, Rbah-Vidal L, Tripier R, Haddad F, Kraeber-Bodere F, Bodet-Milin C, Cherel M (2019) What is the best radionuclide for Immuno-PET of multiple myeloma? A comparison study between (89) Zr- and (64)Cu-labeled anti-CD138 in a preclinical syngeneic model. Int J Mol Sci 20(10). https://doi.org/10.3390/ijms20102564

Radiolabeled Antibodies for Immune Checkpoint PET in Preclinical Research

Milou Boswinkel, Gerben M. Franssen, and Sandra Heskamp

Abstract

Antibodies that block immune checkpoints, also called immune checkpoint inhibitors (ICI), have demonstrated impressive anti-tumor efficacy. The success of ICIs results from a complex interplay between cancer cells and their immune microenvironment. One of the predictors for ICI efficacy is the expression of the targeted immune checkpoint, such as programmed death ligand 1 (PD-L1). Immune checkpoints can be expressed on tumor cells and/or subsets of immune cells. PET imaging offers unique possibilities to study the dynamics of immune checkpoint expression in tumor and normal tissues in a longitudinal manner. In this chapter, we describe the methodology to use zirconium-89-labeled antibodies to assess the expression of immune checkpoint molecules in syngeneic murine tumor models by PET imaging.

Key words Immune checkpoints, Cancer, PET, Antibody, Zirconium-89

1 Introduction

Recent developments in cancer immunotherapy have demonstrated impressive anti-tumor efficacy, especially for antibodies targeting immune checkpoint molecules (immune checkpoint inhibitors; ICI). Immune checkpoints are expressed by various cell types, including tumor cells and subsets of immune cells. These checkpoints tightly regulate the immune response and play a key role in maintaining immune homeostasis and prevention of autoimmunity. Tumor cells that (over)express inhibitory immune checkpoint molecules are capable of escaping immune surveillance and attack. ICI block the interaction of these checkpoints and thereby reinvigorate the anti-tumor immune response, resulting in enhanced tumor cell recognition and killing. As a consequence of its own success, numerous clinical trials are currently investigating new ICI treatment regimens. Although subgroups of patients show durable response, many patients do not respond, which leads to the search

for more effective treatment combination strategies. Furthermore, the treatment costs are high, and there is a considerable risk of immune-related side effects [1, 2].

There is a growing demand for tools that allow the use of immune therapy in a more effective way by maximizing the likelihood of response for the individual patient. Accurate pretreatment patient selection to identify responders from nonresponders is essential. Currently, the gold standard for therapy stratification is immunohistochemichal analysis of immune checkpoint expression of tumor biopsies. However, various studies have demonstrated the limitations of biopsies, namely, sampling errors and the invasiveness of the procedure. Being noninvasive, sensitive, and quantitative, positron emission tomography (PET) imaging allows for longitudinal and repetitive assessment of immune checkpoint expression on a whole body scale [3–5]. The aim of this chapter is to describe how to use radiolabeled antibodies to study the expression of immune checkpoint molecules in syngeneic murine tumor models by PET imaging. We will discuss the selection of the right combination of antibody and animal model, antibody conjugation and radiolabeling, inoculation of the tumor cells, injection of the radiolabeled antibody, and, finally, the PET image acquisition, reconstruction, and analysis.

2 Materials

2.1 Animal Model

1. Syngeneic murine tumor cells: PD-L1+ Renca cells
2. Immunocompetent mice: Balb/c mice, age 10–12 weeks
3. Phosphate-Buffered Saline (PBS): 137 mM NaCl, 2.7 mM KCl, 10 mM Na2HPO4, 1.8 mM KH2PO4, pH 7.4
4. 1 mL syringe
5. 0.6 × 30 mm injection needle
6. Caliper to measure tumor size

2.2 Desferrioxamine (DFO) Conjugation

1. 5 mg antibody of choice: anti-mouse PD-L1, clone 10F.9G2, 5 mg/mL in PBS
2. p-NCS-Bn-DFO: 15 mg/mL in dimethyl sulfoxide (DMSO), freshly prepared in a metal-free tube
3. 1 M NaHCO$_3$, pH 9.5
4. 0.25 M NH$_4$Ac, 2 g/L chelex 100 cation exchange resin mesh 200–400, pH 5.5
5. 0.5–3 mL slide-A-Lyzer 20 K
6. Metal-free 1.5 mL Eppendorf tubes
7. 1 mL syringe

8. 0.5 × 16 mm injection needle

9. pH strips: range pH 7.0–14.0

10. Balance

11. Vortex

12. Shaker

13. HPLC/FPLC system

14. Size Exclusion Chromotography (SEC) column: particle size 3 μm, pore size 200 Å

15. HPLC buffer: 250 mM NaCl in PBS

16. Nanodrop or spectrophotometer

2.3 ^{89}Zr Radiolabeling

1. 2 M Na_2CO_3

2. DFO-conjugated antibody

3. ^{89}Zr in 1 M oxalic acid

4. 0.5 M 4-(2-hydroxyethyl)-1-piperazineethanesulfonic acid (HEPES), pH 7.5

5. 0.1 M Citrate, pH 6.0

6. PBS

7. Screw cap vial

8. pH strips

9. Disposable G25M sephadex column

10. Silica gel chromatography strips

11. Storage phosphor screen

12. Phosphor imager

13. HPLC/FPLC system

14. SEC column: particle size 3 μm, pore size 200 Å

15. HPLC buffer: 250 mM NaCl in PBS

16. Tweezers

2.4 Radiotracer Preparation

1. PBS

2. Optionally: unlabeled antibody

3. Optionally: vials to store 1% injection standards suitable for measurements in a gamma counter

4. 1 mL syringe

5. 0.5 × 16 mm injection needle

2.5 Radiotracer Injection

1. Tumor-bearing mice

2. Heat lamp or warming chamber

3. Dose calibrator

4. Restrainer

5. Fixation tape

6. Animal balance

7. 5 mL round-base test tubes

2.6 PET Scanning

1. Small animal PET/CT scanner with integrated heating bed and optionally animal respiratory and temperature monitoring

2. Isoflurane

3. Isoflurane anesthetic machine with air supply

4. Animal balance

5. Dose calibrator

2.7 PET Image Analysis

1. Image analysis software (e.g., VivoQuant, PMOD, and Inveon research workplace)

3 Methods

3.1 Animal Model

This protocol describes the use of PD-L1-expressing Renca cells, which are derived from a tumor that arose spontaneously as a renal cortical adenocarcinoma in Balb/cCr mice (*see* **Note 1** for more information about the selection of the right tumor cells and mouse strain).

1. Prepare a solution of Renca cells to a final concentration of 2.5×10^6 cells/mL in PBS.

2. Transfer the cells into a 1 mL syringe, and place a 0.6×30 mm injection needle on the syringe. Remove the air from the syringe.

3. Restrain the mouse and inject 5×10^5 Renca cells (0.2 mL) subcutaneously on one of the flanks of a 10–12 weeks old BALB/c mouse.

4. Wait until the tumor reaches a size of approximately 100–200 mm^3 before injecting the radiolabeled antibody (*see* **Note 2**).

3.2 DFO Conjugation

1. Transfer 5 mg antibody (1 mL) into a metal-free 1.5 mL Eppendorf tube (*see* **Notes 3**, **4**, and **5**).

2. Add 100 μL (1/10 volume) of 1 M NaHCO$_3$ to the antibody solution.

3. Add a 3- to 10-fold molar excess of p-NCS-Bn-DFO. 5 mg of antibody is 33.3 nmol, with a 3-fold excess of p-NCS-Bn-DFO corresponding to 100 nmol. To achieve this, add 50.2 μL of p-NCS-Bn-DFO to the antibody solution (*see* **Notes 4** and **6**).
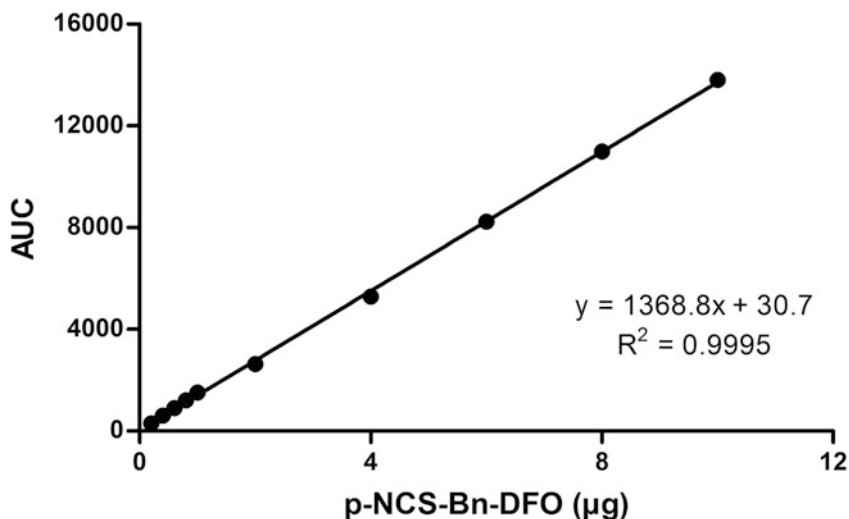
Fig. 1 Example of a p-NCS-Bn-DFO calibration curve using HPLC SEC

4. Vortex and incubate for 2 h at room temperature (RT) on a shaker.

5. Transfer a 20–100 μL sample of the reaction mixture to a new tube for conjugation ratio analysis by SEC.

6. Produce a calibration curve of p-NCS-Bn-DFO from original 15 mg/mL stock solution. First, dilute the 15 mg/mL p-NCS-Bn-DFO to 1 mg/mL in PBS. Next, analyze a minimum of five different amounts of p-NCS-Bn-DFO using HPLC SEC as determined by measurement of the UV signal at 280 nm (e.g., 0.2 μg, 0.6 μg, 1 μg, 4 μg, and 8 μg p-NCS-Bn-DFO). For HPLC conditions, use 250 mM NaCl in PBS as an isocratic buffer with a flow rate of 1.0 mL/min and a runtime of 30 min. Determine the area under the curve (AUC) and create a calibration curve using the AUC as a function of the amount (μg) of p-NCS-Bn-DFO. *See* Fig. 1 for an example calibration curve.

7. Analyse 20–100 μL of the conjugation reaction mixture by HPLC SEC.

8. Calculate the conjugation ratio. First, determine the AUC of the peak that represents the amount of nonconjugated p-SCN-Bn-DFO in the reaction mixture. *See* Fig. 2 for examples of different conjugation reactions, where Reg#2 represents the amount of nonconjugated p-SCN-Bn-DFO. Use the calibration curve $y = ax + b$, where y is the AUC of the unconjugated p-SCN-Bn-DFO, to calculate the amount of nonconjugated p-NCS-Bn-DFO (x). To calculate the conjugation ratio, substract the amount of nonconjugated p-NCS-Bn-DFO (x) from the total amount of p-NCS-Bn-DFO (m) that
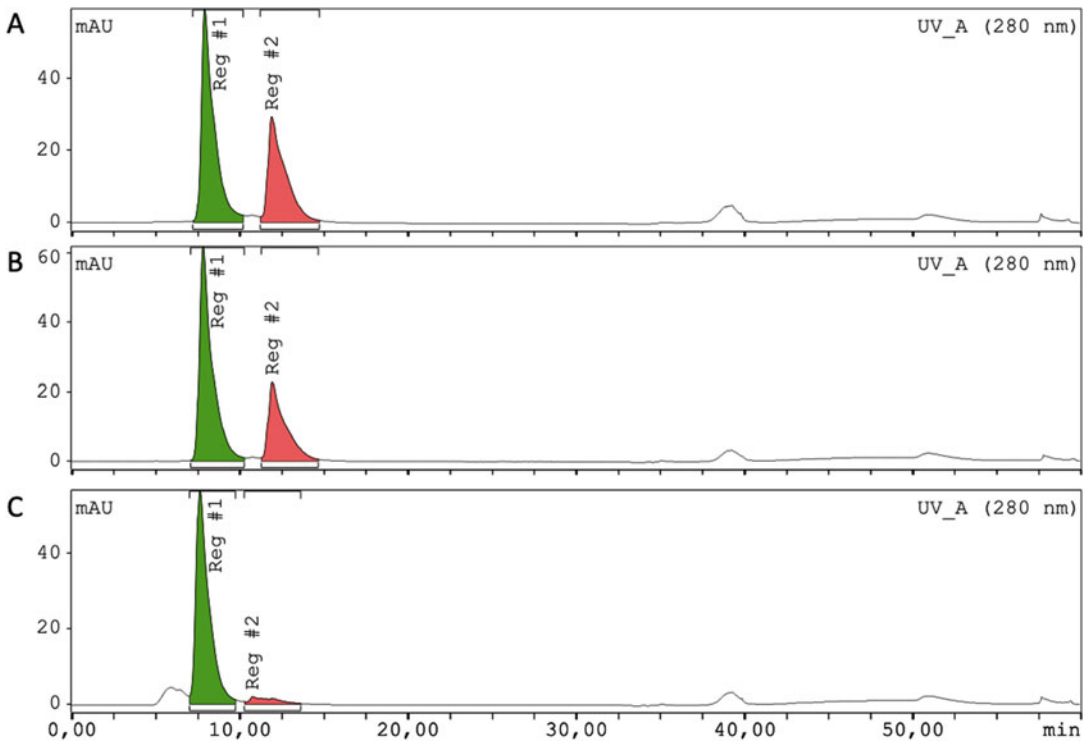
Fig. 2 HPLC SEC analysis examples of a conjugation reaction of 5 mg monoclonal antibody ($3.33.10^{-8}$ mol) with 10 times molar excess of p-SCN-Bn-DFO chelator (251 µg; $3.33.10^{-7}$ mol) by UV detection (280 nm). Reg#1 (retention time 7.9 min) is the UV signal of the monoclonal antibody, and Reg#2 (retention time 11.9) is the UV signal of the nonconjugated p-SCN-Bn-DFO. (**a**) Sample of the conjugation reaction before incubation; where none of the p-SCN-Bn-DFO is conjugated to the monoclonal antibody, conjugation ratio 1:0. (**b**) Example of the conjugation reaction during incubation, where part of the p-SCN-Bn-DFO is conjugated to the monoclonal antibody and a part is nonconjugated available; conjugation ratio 1:4. (**c**) Example of the conjugation reaction after extreme incubation, where almost all p-SCN-Bn-DFO is conjugated to the mono-clonal antibody and only one molar part is nonconjugated available; conjugation ratio 1:9

was added at the start of the conjugation reaction. Divide this by the total amount of p-NCS-Bn-DFO (m) and multiply by the molar excess (n). The result of this equation is the conjugation ratio.

$$\text{conjugation ratio } (\%) = \left(\frac{m\ (\mu g) - x(\mu g)}{m\ (\mu g)} \right) * n$$

9. Transfer the reaction mixture into a 1 mL syringe and place a 0.5 × 16 mm injection needle on the syringe.

10. Transfer the reaction mixture from the syringe into a Slide-A-Lyzer 20 K.

11. Dialyze the sample in the Slide-A-Lyzer 20 K against 0.25 M NH_4OAc buffer, 2 g/L chelex-100 buffer at 4 °C. Refresh the dialysis buffer every 12–24 h for at least 5 times. After exchanging the last dialysis buffer, the total amount of buffer used should be a minimum of 5 L.

12. After dialysis, transfer the sample into a new metal free vial and measure the protein concentration using a Nanodrop or spectrophotometer.

13. Dilute the conjugated antibody to final concentration of 1 mg/mL in 0.25 M NH_4Ac buffer.

14. Store the conjugated antibody in aliquots of 100–200 μL at 4 °C, −20 °C, or −70 °C, depending on the recommendation storing conditions of the antibody.

3.3 ^{89}Zr Radiolabeling

The following radiolabeling procedure is based on 20 μL of ^{89}Zr in 1 M oxalic acid (*see* **Notes 7**, **8**, and **9**).

1. Add to a metal-free screw cap vial 100 MBq of ^{89}Zr, and make up to a total of 20 μL in oxalic acid.

2. Add to the same vial 9 μL of Na_2CO_3.

3. Incubate for 3 min without closing the cap due to the production of CO_2.

4. Mix well by pipetting up and down at least three times.

5. Add 100 μL of HEPES.

6. Add 100 μg of DFO-conjugated antibody.

7. Close the vial and vortex.

8. Check pH of the reaction mixture (should be around pH 7.2–7.5, *see* **Note 10**).

9. Incubate the sample for at least 1 h at RT.

10. Perform quality control using HPLC using a Phenomonex Yarra Bio-SPE-SEC s3000, or similar, and 250 mM NaCl in PBS as isocratic buffer (Flow rate 1.0 mL/min; runtime 30 min). The elution time of the radiolabeled antibody is approximately 8 min. Use the radiodector signal as read out (Fig. 3).

11. Alternatively, for Instant thin layer chromatography (ITLC), pipette 1–3 μL of radiolabeling mixture on a silica gel chromatography strip. Place the bottom of the strip in citrate buffer, and wait until the buffer runs to the top of the strip. When the buffer has run through the whole strip, place the strip on tissues using tweezers. Be careful not to grasp the upper part of the strip, because this may contain radioactivity. Expose the strip (including the tissues) to a phopholuminescence plate (depending on the activity concentration, the exposure time

ranges from a few seconds to minutes), and scan the plate using a phosphor imager. Calculate the fraction of radioactivity that is labeled to the antibody using an image analysis software, such as Aida Image Analyzer. The radiolabeled antibody remains at the bottom of the ITLC strip (Rf: 0.0–0.2), while the non-labeled ^{89}Zr will run toward the top of the ITLC strip (Rf: 0.6–1.0; Fig. 3).
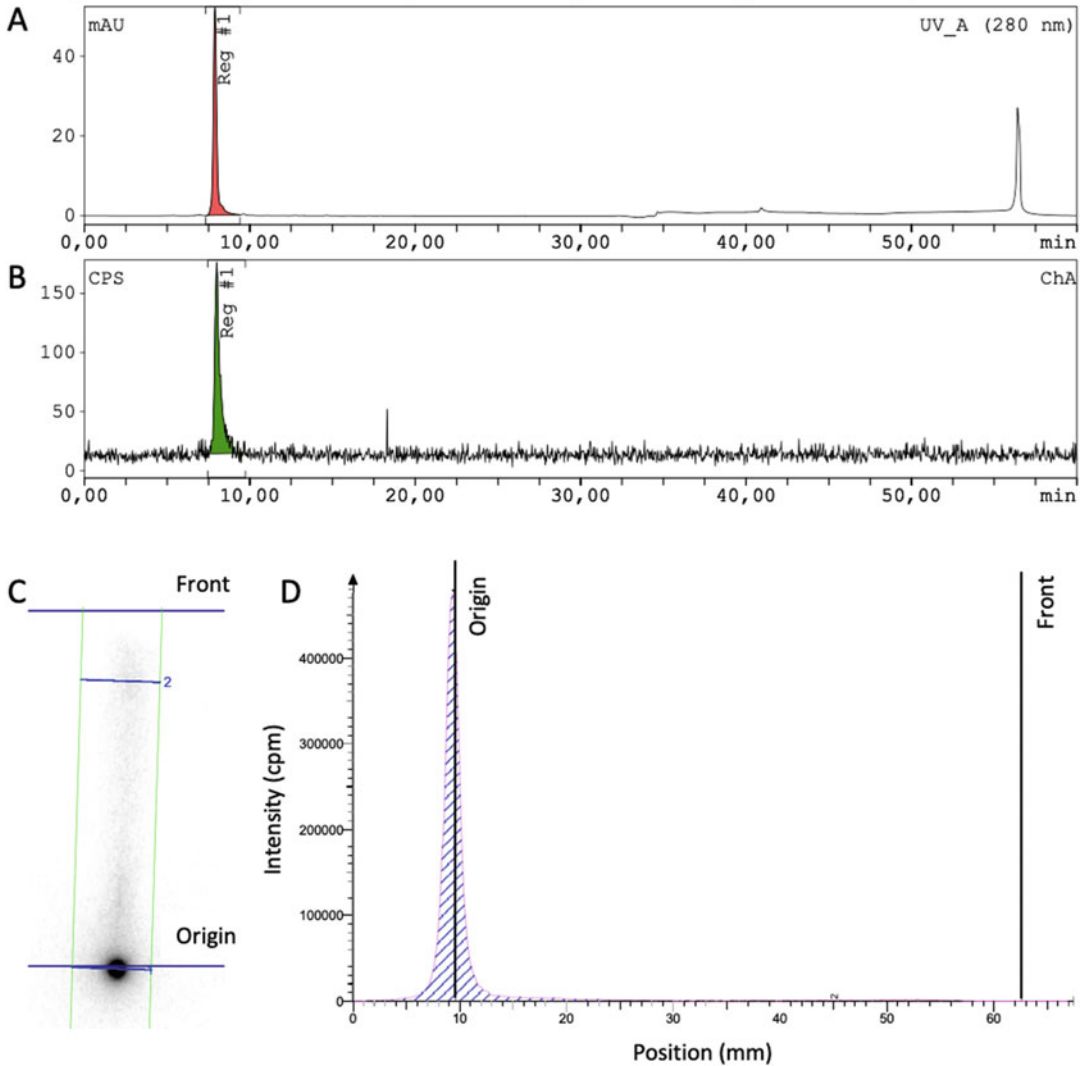
Fig. 3 HPLC SEC and ITLC analysis example of a labeling reaction of DFO conjugated monoclonal antibody with ^{89}Zr (**a**) HPLC SEC analysis by UV detection (280 nm). (**b**) HPLC SEC analysis by radiodetection (cps). In A and B, Reg#1 (retention time 7.9 min) is the UV signal and the radio signal of the ^{89}Zr-labeled monoclonal antibody. (**c**) Scan of the phospholuminscence plate exposed to an ITLC strip. (**d**) quantitative analysis of ITLC. The radiolabeled antibody remains at the bottom of the ITLC strip (Rf: 0.0–0.2), while the nonlabeled ^{89}Zr will run toward the top of the ITLC strip (Rf: 0.6–1.0)

3.4 ^{89}Zr Radiolabeling Quality Control

If quality control shows that the labeling efficiency is below 95%, purify the sample using a disposable G25M sephadex column.

1. Wash the column with 5 mL PBS.

2. Add the reaction mixture.

3. Wash the reaction vial with 0.5 mL PBS, and add to the column. The reaction mixture and wash should be completely absorbed by the column.

4. Add a further 5 mL of PBS.

5. Collect 10 fractions of 0.5 mL.

6. Measure the activity of each fraction in a dose calibrator.

7. Determine the radiochemical purity of the fractions by ITLC, as described above.

8. Pool the fractions containing ^{89}Zr-labeled antibody with a radiochemical purity >95%.

9. Determine the radiochemical purity of the pooled ^{89}Zr-labeled antibodies by ITLC or HPLC, as described previously.

3.5 Radiotracer Preparation

1. Prepare the stock solution for in vivo imaging by diluting the purified radiotracer to a concentration of 10–50 MBq/mL in PBS (*see* **Notes 11** and **12**).

2. The final concentration of the antibody should be 150 μg/mL. If necessary, add nonlabeled antibody to reach this concentration (*see* **Note 13**).

3. Optionally, pipet 10 μL of stock solution in 990 μL PBS. Store 3 × 200 μL (injection volume) of this dilution. This is a 1% standard of the injected activity per mouse and can be used to quantify the radioactivity concentration in tissues dissected from the scanned mice. Make sure to use the same tubes for the 1% standards as for the samples that you intend to measure at the end of the experiment, for example, 5 mL round-base test tubes.

4. Transfer the stock solution into a 1 mL syringe, and place a 0.5 × 16 mm injection needle on the syringe.

5. Remove all air from the syringe.

6. Fill the syringe to a volume of 0.2 mL. Make sure that when filling the syringe, the needle does not touch the wall of the vial because this will cause the needle to become blunt and will make it harder to intravenously administer the tracer (as described below).

3.6 Radiotracer Injection

1. Transport the mouse from the housing lab to the imaging lab.

2. Measure the body weight of the mouse.

3. Measure the activity of the radiotracer in the syringe in a dose calibrator. Note the amount of radioactivity and time of the measurement.

4. Put the mouse under a heat lamp or heat chamber to ensure it is warm and tail veins are fully dilated. Care must be taken not to place the heat lamp too close to the mice to prevent it from overheating.

5. Put the mouse in a restrainer and stroke the tail by moving from a proximal to distal direction to further dilate the vein.

6. To inject the radiotracer, grasp the mouse tail using the non-dominant hand. Hold the needle of the syringe in the dominant hand, insert the needle into the lateral tail vein of the mouse, and advance the needle a few millimeters.

7. Inject 0.2 mL of the radiotracer and note the time of injection.

8. Close the injection site using fixation tape.

9. Measure the activity of the empty syringe. Note amount of radioactivity and time of the measurement.

10. Calculate the injected dose by subtracting the activity in syringe post injection from the activity in the syringe prior to injection.

11. Transport the mouse back to the housing lab until PET/CT acquisition.

3.7 PET/CT Acquisition

1. Transport the mouse from the housing lab to the imaging lab.

2. Record the body weight of the mouse.

3. Prepare the anesthesia machine by filling the isoflurane vaporizer and switching on the medical air delivery (2–3% isoflurane).

4. Warm the PET/CT scanner bed to 37 °C.

5. Once the induction chamber is filled with isoflurane, place the mouse into the chamber.

6. When the mouse is fully anesthetized, place it on the PET/CT scanner bed, ensuring the nose is placed in the anesthetic nose cone. Next, change the concentration of isoflurane to 1.5–2.5%. If the mouse is breathing steadily, the isoflurane can be reduced further to ~1% for maintenance. The exact isoflurane concentration will be model- and strain-dependent. The respiration rate should be in the range of 60–100 breaths/min.

7. Acquire a scout view to select the scan area for the PET and CT scan. Make sure the tumor and other tissues of interest are in the field of view (FOV).

8. For the PET acquisition parameters, set the radionuclide to ^{89}Zr and select an acquisition time of 15 min (*see* **Note 12**).

9. The CT acquisition parameters can differ between scanners. For example, for the Siemens Inveon PET/CT scanner, the following settings can be used: 80 kV, 500 μA, 300 ms exposure time.

10. To improve the accuracy of the image quantification, attenuation correction can be applied using the PET transmission method or CT-method. Although the effect of attenuation is limited in mice because of their small size (*see* **Note 14**).

11. After the scan, turn off the anesthesia and place the mouse back into its cage. If necessary, put the cage on a heating mattress to keep the mouse warm while recovering from the anesthesia. When the mouse is fully recovered, bring it back to the housing lab.

12. The imaging procedure can be repeated at different time points post injection. Typical time points where sufficient contrast is visible between tumor and normal tissues are 24 h, 72 h, and 168 h post injection (*see* **Note 12** and **15**).

13. Euthanize the mouse after the last scan. Tissues of interest can be collected for ex vivo analysis, such as immunohistochemistry, or to quantify the concentration of radioactivity in different tissues. For the latter, weigh the dissected tissues and measure the samples in a gamma counter, simultaneously with the 1% standards as previously described. The results can be expressed as percentage of injected activity per gram tissue (%IA/g).

14. Image reconstruction parameters are specific to each PET/CT scanner and require optimization depending on your application. In general, we recommend a dynamic 3D iterative reconstruction technique such as OSEM3D/SPMAP for PET and the modified Feldkamp algorithm for CT. The recommended output format is DICOM as this is compatible with most image analysis software.

3.8 PET/CT Image Analysis

1. Transfer the reconstructed PET and CT scans to the image analysis software.

2. Co-register the PET and CT scans if the alignment is not performed automatically.

3. Tumor and normal tissue uptake can be quantified from the PET scan by manual drawing a volume of interest (VOI) using the PET or CT scan. Depending on the image acquisition settings and the image analysis software, the results are commonly expressed as Bq/mL, %IA/mL, or standardized uptake values (SUVs). If the output is only in Bq/mL, you can use the information regarding the injected activity dose, time between injection and scanning, and weight of the animal to calculate %IA/mL or SUV manually.
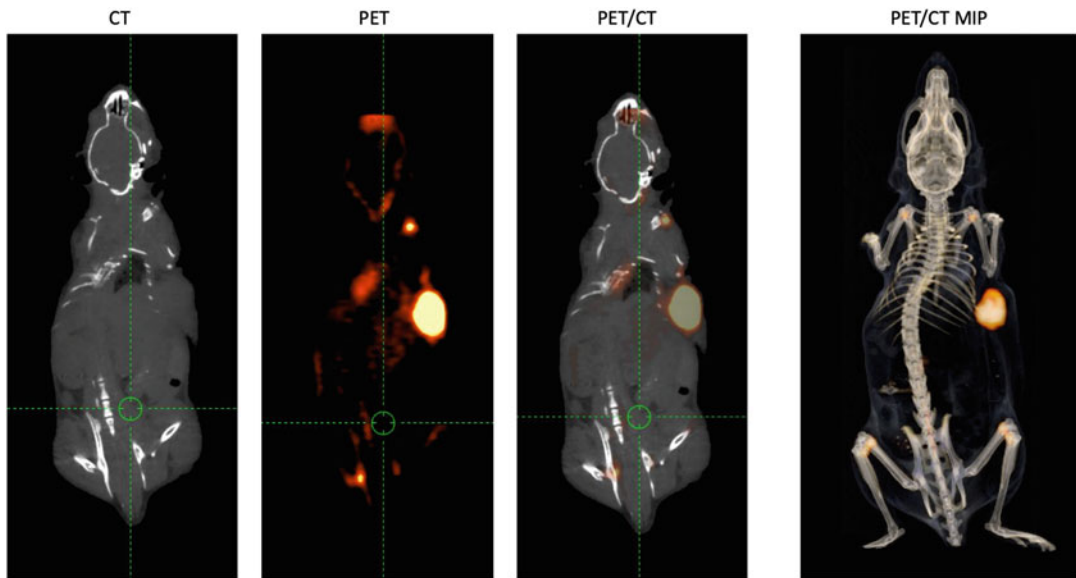
Fig. 4 Example of a PET and CT scan of a mouse with a subcutaneous tumor on the right flank, injected with a ^{89}Zr-labeled antibody. The scan was acquired 7 days post injection. Representative cross sections of the PET, CT, and merged PET/CT scans are presented, as well as a maximum intensity projection (MIP) of the merged PET/CT

4. Finally, cross sections or a maximum intensity projection (MIP) of the PET/CT can be displayed, with a scale bar, using appropriate thresholds to visualize the tumor or other tissues of interest (Fig. 4).

4   Notes

1. Traditionally, preclinical PET imaging studies are carried out in immunodeficient mice bearing human xenografts, using antibodies that specifically bind the human target of interest. Often, these antibodies are not cross-reactive with murine immune checkpoints, which can be (abundantly) expressed on subsets of immune cells and other tissues. Therefore, humanized mice or syngeneic murine tumor models are more realistic models for the human situation [6]. In this chapter, we describe the methodology for syngeneic murine tumor models. Here, murine tumor cells will be engrafted in immunocompetent mice. To image immune checkpoints, the used antibodies should be cross-reactive with the murine immune checkpoint. Selection of the cancer cell line used for the experiments depends not only on the type of cancer which is subject of the research (e.g., prostate cancer and melanoma) but also on the immunological status of the tumor (e.g., immunogenic or nonimmunogenic) and the presence of the immune checkpoint

of interest on the cancer cell (e.g., PD-L1 positive of negative tumor cells). After selecting the tumor cell line, the matching mouse strain should be selected. For example, the immunogenic melanoma cell line B16F10 originates from C57/Bl6 mice.

2. The uptake of the radiolabeled antibody can be influenced by tumour growth rate and size. Murine tumor cells tend to develop very rapidly and large tumors might have a poorer vascularization and a higher interstitial fluid pressure. This can hamper the penetration of the antibody into a large tumor, even though the immune checkpoint is expressed. Therefore, it is important to start experiments with relatively small tumors ($100–200$ mm^3) and to make sure that tumor sizes are comparable between groups and experiments. Furthermore, it is important to ensure that the injected tumor cells are viable. The presence of many dead tumor cells during tumor cell inoculation can initiate an anti-tumor immune response, which will delay or even prevent the formation of a tumor.

3. The most commonly used chelator to label antibodies with ^{89}Zr is DFO. This combination has been applied widely in preclinical and clinical research. However, a drawback is that a fraction of the ^{89}Zr is released from DFO, resulting in accumulation of ^{89}Zr in mineral bone. This may hamper the detection of bone metastases and could result in undesired radiation dose to bone marrow. Release of ^{89}Zr is the result of suboptimal complexation, as ^{89}Zr^{4+} demands octacoordination to form stable complexes, while the three hydroximate groups of DFO only offer hexacoordination. To overcome this, several new chelators and new labeling strategies have been developed, such as ^{89}ZrCl$_4$ for ^{89}Zr complexation using DOTA. However, a drawback of this approach is the temperature required for efficient complexation (95 °C), which is a limiting factor for antibodies. Recently, newly developed chelators such as DFO*-NCS, DFO-cyclo*-pPhe-NCS, or p-SCN-Bn-HOPO showed improved retention of ^{89}Zr. Nowadays, DFO*-NCS is commercially available. Clinical studies will have to demonstrate the relevance of these preclinical findings in the clinical setting [7–11].

4. The concentration of the antibody is preferable between 2.5 and 10 mg/mL to increase the chance of an effective conjugation reaction. The ratio of antibody to p-NCS-Bz-DFO can be varied in case the reaction is very inefficient. The preferred conjugation ratio is around 2 chelators per antibody. More chelators per antibody could potentially influence the antigen binding properties or clearance rate of the antibody, while less chelators might result in inefficient ^{89}Zr-labeling.

5. Avoid metal contaminations of filter tips and vials to prevent incorporation of metals in p-NCS-Bn-DFO, as this will disturb the radiolabeling with ^{89}Zr: Use metal-free plastics and filter tips for pipetting, or remove unwanted metals by washing plastics overnight in 2 M HCl, followed by 2 washing steps with metalfree water and subsequent drying of the plastics. Use metal-free buffers, with metals removed through the addition of 2 g/L chelex. After overnight incubation, chelex should be removed with, for example, a 0.2 μm filter.

6. p-NCS-Bn-DFO is a bifunctional chelator that can be coupled rapidly and efficiently to the lysine-NH$_2$ groups of antibodies. The protocol has been extensively described by Vosjan et al. [12] An alternative approach is to use *N*-succinyldesferrioxamine B (*N*-sucDf). However, this chelator requires a more complex multi-step procedure [13].

7. The radiolabeling as described under Subheading 3.3. can be adjusted, for example, if a different amount of antibody or radioactivity is need. However, it is important to keep the volume ratios the same. A volume of 20 μL of ^{89}Zr in 1 M oxalic acid is the minimal starting volume.

8. Next to positrons, ^{89}Zr emits high energy gammas of 909 keV. Shield them with lead and work in a flow hood for radiation protection purposes.

9. At the moment, ^{89}Zr is the most commonly used radionuclide for PET imaging with radiolabeled antibodies. It has favorable characteristics: Its half-life of 78.4 h matches the tissue kinetics of antibodies, it is a residualizing radionuclide that provides high-contrast images, and its positrons have a relatively low energy, which results in high-resolution PET images. Therefore, ^{89}Zr is preferred over other long-lived positron emitters, such as ^{124}I [14].

10. To achieve efficient labeling with ^{89}Zr, the pH of the reaction mixture should be between pH 7.2–7.5. The pH of reaction mixture may differ depending on, for example, the time between irradiation and performing the radiolabeling. Always check the pH and adjust if necessary.

11. To prevent adverse reactions when injecting the radiolabeled antibody in mice, it is important that the solution is pH neutral and physiological (e.g., physiological saline) and/or isotonic with blood (e.g., PBS). Furthermore, the solution should not contain proteins such as bovine serum albumin. If necessary, add 1/10 volume of 10× concentrated PBS to achieve a pH neutral and isotonic solution. Also, prevent the use bovine serum albumin during the purification process.

12. The minimum amount of ^{89}Zr injected per mouse depends on time between injection and scanning, total scan time, and

sensitivity of the PET scanner. On average, 5 MBq/mouse is sufficient for PET imaging 1–7 days post injection, using an acquisition time of 15–30 min. This will result in sufficient counts to reconstruct a representative image. However, in case the sensitivity of the scanner is for example very high, lower amounts of activity can be administered.

13. The circulation time and in vivo distribution of radiolabeled antibodies directed against immune checkpoints is often dose-dependent. For example, PD-L1 is not only expressed on tumor cells but also on subsets of immune cells in lymphoid tissues, such as the spleen and lymph nodes. At low antibody concentrations, PD-L1 antibodies are rapidly cleared from the circulation by binding to PD-L1 positive immune cells in the spleen. Therefore, the spleen acts as a so-called sink organ and prevents the antibody from reaching PD-L1 in the tumor. By increasing the amount of injected antibody the PD-L1-mediated uptake in the spleen can be saturated, resulting in increased levels of circulating antibody and, as a consequence, increased tumor uptake. The optimal antibody dose is target and model dependent. For PD-L1, the optimal amount is in the range of 20–50 μg [15, 16].

14. In humans, attenuation correction is required to obtain quantitative PET data. However, this is less of a problem in preclinical research because of the small size of mice. In case it is desirable to perform attenuation correction, the two most common methods are PET-based, by acquiring a transmission scan using a ^{57}Co-point source, or CT-based [17, 18].

15. Repeated anesthesia within short time intervals can cause significant discomfort for the mouse. Ensure that body temperature remains constant during the scan by using a proper heating mattress during the scan and keep the animals warm when recovering from the anesthesia. A drop in body temperature affects the anesthesia making it more effective. If the animal cools down too much, it may take longer for it to recover and it may increase the discomfort.

References

1. Sharma P, Allison JP (2015) The future of immune checkpoint therapy. Science 348(6230):56–61. https://doi.org/10.1126/science.aaa8172

2. de Miguel M, Calvo E (2020) Clinical challenges of immune checkpoint inhibitors. Cancer Cell 38(3):326–333. https://doi.org/10.1016/j.ccell.2020.07.004

3. Verhoeff SR, van den Heuvel MM, van Herpen CML, Piet B, Aarntzen E, Heskamp S (2020) Programmed cell Death-1/Ligand-1 PET imaging: a novel tool to optimize

immunotherapy? PET Clin 15(1):35–43. https://doi.org/10.1016/j.cpet.2019.08.008

4. Bensch F, van der Veen EL, Lub-de Hooge MN, Jorritsma-Smit A, Boellaard R, Kok IC, Oosting SF, Schroder CP, Hiltermann TJN, van der Wekken AJ, Groen HJM, Kwee TC, Elias SG, Gietema JA, Bohorquez SS, de Crespigny A, Williams SP, Mancao C, Brouwers AH, Fine BM, de Vries EGE (2018) (89)Zr-atezolizumab imaging as a non-invasive approach to assess clinical response to PD-L1 blockade in cancer. Nat

Med 24(12):1852–1858. https://doi.org/10.1038/s41591-018-0255-8

5. Niemeijer AN, Leung D, Huisman MC, Bahce I, Hoekstra OS, van Dongen G, Boellaard R, Du S, Hayes W, Smith R, Windhorst AD, Hendrikse NH, Poot A, Vugts DJ, Thunnissen E, Morin P, Lipovsek D, Donnelly DJ, Bonacorsi SJ, Velasquez LM, de Gruijl TD, Smit EF, de Langen AJ (2018) Whole body PD-1 and PD-L1 positron emission tomography in patients with non-small-cell lung cancer. Nat Commun 9(1):4664. https://doi.org/10.1038/s41467-018-07131-y

6. Olson B, Li Y, Lin Y, Liu ET, Patnaik A (2018) Mouse Models for cancer immunotherapy research. Cancer Discov 8(11):1358–1365. https://doi.org/10.1158/2159-8290.CD-18-0044

7. Heskamp S, Raave R, Boerman O, Rijpkema M, Goncalves V, Denat F (2017) (89)Zr-Immuno-Positron emission tomography in oncology: State-of-the-Art (89)Zr radiochemistry. Bioconjug Chem 28(9):2211–2223. https://doi.org/10.1021/acs.bioconjchem.7b00325

8. Vugts DJ, Klaver C, Sewing C, Poot AJ, Adamzek K, Huegli S, Mari C, Visser GWM, Valverde IE, Gasser G, Mindt TL, van Dongen G (2017) Comparison of the octadentate bifunctional chelator DFO*-pPhe-NCS and the clinically used hexadentate bifunctional chelator DFO-pPhe-NCS for (89)Zr-immuno-PET. Eur J Nucl Med Mol Imaging 44(2):286–295. https://doi.org/10.1007/s00259-016-3499-x

9. Chomet M, Schreurs M, Bolijn MJ, Verlaan M, Beaino W, Brown K, Poot AJ, Windhorst AD, Gill H, Marik J, Williams S, Cowell J, Gasser G, Mindt TL, van Dongen G, Vugts DJ (2020) Head-to-head comparison of DFO* and DFO chelators: selection of the best candidate for clinical (89)Zr-immuno-PET. Eur J Nucl Med Mol Imaging. https://doi.org/10.1007/s00259-020-05002-7

10. Raave R, Sandker G, Adumeau P, Jacobsen CB, Mangin F, Meyer M, Moreau M, Bernhard C, Da Costa L, Dubois A, Goncalves V, Gustafsson M, Rijpkema M, Boerman O, Chambron JC, Heskamp S, Denat F (2019) Direct comparison of the in vitro and in vivo stability of DFO, DFO* and DFOcyclo* for (89)Zr-immunoPET. Eur J Nucl Med Mol Imaging 46(9):1966–1977. https://doi.org/10.1007/s00259-019-04343-2

11. Pandya DN, Bhatt N, Yuan H, Day CS, Ehrmann BM, Wright M, Bierbach U, Wadas TJ (2017) Zirconium tetraazamacrocycle complexes display extraordinary stability and provide a new strategy for zirconium-89-based radiopharmaceutical development. Chem Sci 8(3):2309–2314. https://doi.org/10.1039/c6sc04128k

12. Vosjan MJ, Perk LR, Visser GW, Budde M, Jurek P, Kiefer GE, van Dongen GA (2010) Conjugation and radiolabeling of monoclonal antibodies with zirconium-89 for PET imaging using the bifunctional chelate p-isothiocyanatobenzyl-desferrioxamine. Nat Protoc 5(4):739–743. https://doi.org/10.1038/nprot.2010.13

13. Verel I, Visser GW, Boellaard R, Stigter-van Walsum M, Snow GB, van Dongen GA (2003) 89Zr immuno-PET: comprehensive procedures for the production of 89Zr-labeled monoclonal antibodies. J Nucl Med 44(8):1271–1281

14. Verel I, Visser GW, Boerman OC, van Eerd JE, Finn R, Boellaard R, Vosjan MJ, Stigter-van Walsum M, Snow GB, van Dongen GA (2003) Long-lived positron emitters zirconium-89 and iodine-124 for scouting of therapeutic radioimmunoconjugates with PET. Cancer Biother Radiopharm 18(4):655–661. https://doi.org/10.1089/108497803322287745

15. Heskamp S, Wierstra PJ, Molkenboer-Kuenen JDM, Sandker GW, Thordardottir S, Cany J, Olive D, Bussink J, Boerman OC, Dolstra H, Aarntzen E, Hobo WA (2019) PD-L1 microSPECT/CT imaging for longitudinal monitoring of PD-L1 expression in syngeneic and humanized Mouse Models for cancer. Cancer Immunol Res 7(1):150–161. https://doi.org/10.1158/2326-6066.CIR-18-0280

16. Josefsson A, Nedrow JR, Park S, Banerjee SR, Rittenbach A, Jammes F, Tsui B, Sgouros G (2016) Imaging, biodistribution, and dosimetry of radionuclide-labeled PD-L1 antibody in an immunocompetent Mouse Model of breast cancer. Cancer Res 76(2):472–479. https://doi.org/10.1158/0008-5472.CAN-15-2141

17. Habte F, Ren G, Doyle TC, Liu H, Cheng Z, Paik DS (2013) Impact of a multiple mice holder on quantitation of high-throughput MicroPET imaging with and without Ct attenuation correction. Mol Imaging Biol 15(5):569–575. https://doi.org/10.1007/s11307-012-0602-y

18. El Ali HH, Bodholdt RP, Jorgensen JT, Myschetzky R, Kjaer A (2012) Importance of Attenuation Correction (AC) for small animal PET imaging. Diagnostics (Basel) 2(4):42–51. https://doi.org/10.3390/diagnostics2040042

Chapter 10

Radiolabeled Affibody Molecules for PET Imaging

Chiara Da Pieve and Gabriela Kramer-Marek

Abstract

Owing to their ease of engineering and production, chemical stability, size, and high target affinity and specificity, radiolabeled affibody molecules have been recognized as very promising molecular imaging probes in both preclinical and clinical settings. Herein we describe the methods for the preparation of affibody-chelator conjugates and their subsequent radiolabeling with ^{18}F-AlF, ^{68}Ga, ^{89}Zr.

Key words Conjugation, chelators, ^{18}F-AlF, ^{68}Ga, ^{89}Zr

1 Introduction

Affibody molecules are a class of small (approximately 58 amino acids, 6.5–7 kDa) nonimmunoglobulin affinity proteins generated by combinatorial protein engineering [1]. By randomizing 13 amino acids on two of the three-helix bundle, large libraries can be generated, from which potent binders can be isolated by a variety of display methods [2]. The selected binders have a high target specificity and binding affinity (K_D in the low-nanomolar to picomolar range) [3]. A large variety of affibody molecules toward major cancer-associated molecular targets (e.g., EGFR, HER2, HER3, VEGFR, PD-L1) have been selected and radiolabeled with positron emitters such as ^{18}F [4–11], ^{68}Ga [12–16], ^{64}Cu [17, 18], and ^{89}Zr [19–21]. When radiometals (e.g., ^{68}Ga, ^{89}Zr) or radioactive metal-halogen complexes (i.e., ^{18}F-AlF) are used, the attachment of a suitable chelator to the protein must be carried out prior to radiolabeling. The site-specific conjugation of chelators (as well as dyes) to the affibody molecule can be achieved by introducing a unique cysteine residue at its C-terminus [1]. The quick and straightforward maleimide–thiol conjugation reaction is usually performed to prepare affibody-based conjugates [22]. High product yields can be achieved through a one-pot reaction containing the affibody molecule (that is most likely present as a dimer in
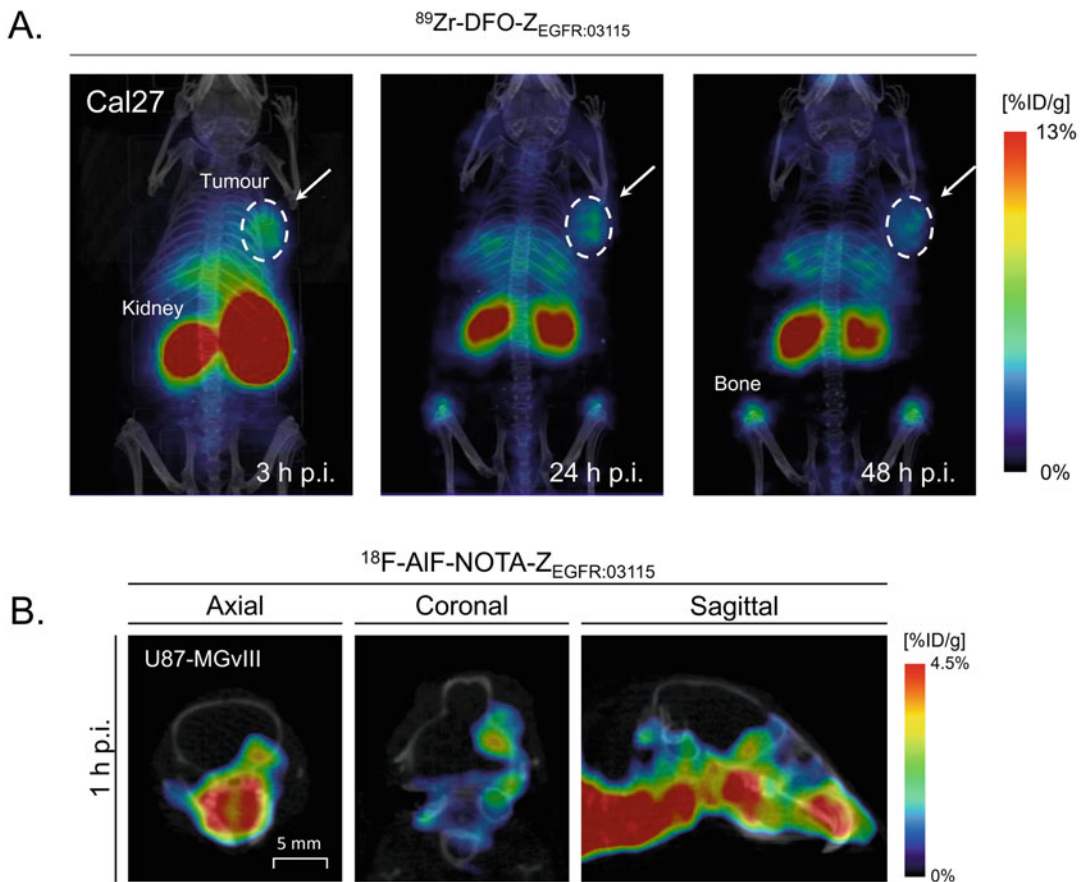
Fig. 1 Representative whole-body coronal PET/CT images of a subcutaneous tumor-bearing mouse 3, 24, and 48 h after administration of the ^{89}Zr-labeled EGFR targeting affibody molecule $Z_{EGFR:03115}$. Clearly visible are the kidneys, as a result of the glomerular filtration, reabsorption, and retention of affibody molecules. Additionally, the high uptake in bone is caused by free ^{89}Zr from some degree of demetallation of the ^{89}Zr-DFO complex in vivo (**a**). In vivo uptake of ^{18}F-AlF labeled $Z_{EGFR:03115}$ in a brain orthotopic tumor model 1 h post-radioactive agent injection (**b**)

solution), maleimide-bearing chelator, and tris(2-carboxyethyl) phosphine hydrochloride (TCEP-HCl) as the reducing agent required to restore the reactive monomeric-free sulfhydryl form of the protein [8]. Importantly, affibody molecules are characterized by high chemical and thermic stability, allowing the protein conjugates to be radiolabeled at high temperatures (up to 95 °C) without compromising the structural integrity and the target recognition ability of the radioconjugate [23]. Additionally, affibody molecules are compatible with a broad range of pH and organic solvents used during the radiolabeling reaction and purification step (e.g., ethanol, DMSO) [24]. All these properties make the molecules attractive vectors for imaging purposes (Fig. 1).

2   Materials

Prepare all aqueous solutions using either ultrapure water or water for injection and analytical grade reagents. Use Reagent or ACS grade organic solvents. Prepare and store buffers and solutions at room temperature, if not stated otherwise. Follow the local waste disposal indications when discarding waste material. A metal-free environment is preferable when working with radiometals. For this reason, the use of plastic spatulas (instead of metal ones) and plastic vials (instead of glass ones) is recommended.

The described procedure are suitable for the preparation of affibody conjugates and their radiolabeled products for preclinical use only.

2.1   Conjugation Reaction

1. The affibody molecule is delivered either as a lyophilized powder or in solution in a buffer established by the manufacturer based on the solubility of the protein. In the latter case, the concentration of the affibody molecule stock solution can vary depending on the production batch and will be indicated, as well as the buffer constituency, in the delivery sheet sent by the supplier. Store at −20 °C. Prepare a 1.2–1.5 mg/mL affibody molecule solution (*see* **Note 1**) by either dissolving the lyophilized affibody molecule in a suitable volume of buffer (e.g., PBS; *see* **Note 2**) or by diluting the supplied stock solution with an appropriate volume of buffer (e.g., PBS). For example: mix 300 μL of a 2.3 mg/mL solution of affibody molecule with 250 μL of PBS (*see* **Note 3**).

2. 50 mg/mL TCEP-HCl, pH 5.0–5.5 (*see* **Note 4**): Weigh 5 mg of TCEP-HCl and transfer to a 1.5 mL microcentrifuge tube. Add 100 μL of PBS and mix. Since TCEP is not particularly stable in phosphate buffers, this solution should be freshly prepared immediately before use. Do not store it.

3. 0.1 M Ethylenediaminetetraacetic acid (EDTA): Dissolve 1.46 mg of EDTA in 50 mL of water.

4. Maleimide functionalised chelators (i.e., NOTA-maleimide, DOTA-maleimide, deferoxamine-maleimide): Purchase from either CheMatech or Macrocyclics. Store at −20 °C. Freshly prepare a chelator-maleimide stock solution (e.g., 10 mM in buffer or DMSO depending on solubility; *see* **Note 5**).

5. Low-protein binding 1.5 mL microcentrifuge tubes.

6. pH meter.

7. Thermoshaker.

8. HPLC system with UV detector.

9. Analytical (e.g., 4.6 × 250 mm) and semi-preparative (7.8 × 250 mm) wide pore (300 Å) C18 HPLC columns.

10. HPLC eluents, 0.1% trifluoroacetic acid (TFA) in water or acetonitrile: Add 1 mL of TFA to either 1 L of water or 1 L acetonitrile.

11. HPLC gradient depends on the affibody molecule analyzed. No universal gradient can be applied.

12. Lyophilizer or a centrifugal concentrator.

13. UV-VIS spectrophotometer.

14. Mass spectrometer.

2.2 ^{18}F-AlF Radiolabelling

1. NOTA-affibody conjugate (Scheme 1) either lyophilized or in water. In the latter case, determine the concentration of the affibody conjugate stock solution by UV-VIS spectrophotometry (*see* **Note 6**). Store at −20 °C.

2. 0.5 M sodium acetate buffer, pH 4 (metal-free): Prepare the buffer from sodium acetate (base) and acetic acid (acid) using the Henderson-Hasselbach equation to determine each component's concentration in the final solution based on the desired pH:

$$pH = pK_a + \log\ [base]/[acid]$$
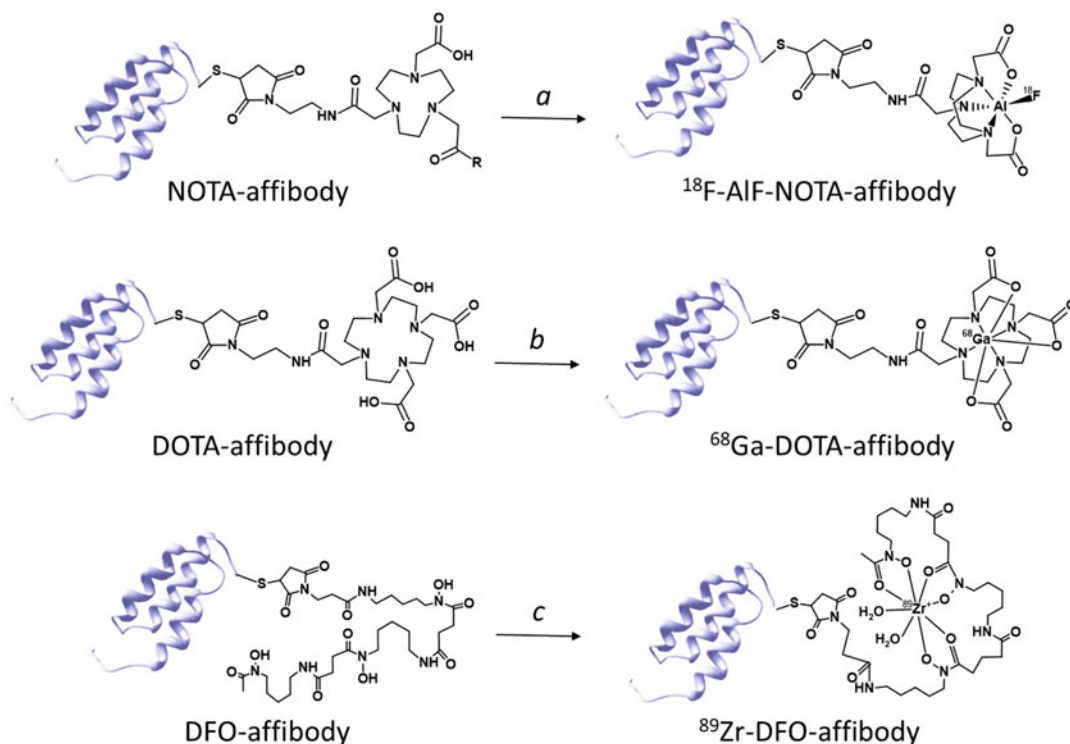
Scheme 1 Structures of NOTA-, DOTA-, and deferoxamine- (DFO-) affibody conjugates and their respective ^{18}F-AlF, ^{68}Ga, and ^{89}Zr radioconjugates. Reaction conditions: (*a*) AlCl$_3$, ^{18}F$^-$, sodium acetate/ethanol 1:1 (v/v), pH 4, 15 min, 95 °C; (*b*) ^{68}GaCl$_3$, sodium acetate, pH 4, 15 min, 80 °C; (*c*) ^{89}Zr-oxalate, Na$_2$CO$_3$, and HEPES, pH 7, rt, 1 h

Considering a final pH of 4 and a pK_a of 4.75 for acetate. Concentration of sodium acetate in final solution = 0.075 M. Concentration of acetic acid in final solution = 0.425 M. To prepare 50 mL of the buffer, weigh 306.6 mg of sodium acetate and transfer to a 100 mL beaker. Add 1.22 mL of glacial acetic acid and 40 mL of water. Calculate the required amount of each component based on the volume of the buffer. Check the pH with a pH meter, and correct it with few drops of either acetic acid or sodium hydroxide solution. Quantitatively transfer the solution to a 50 mL volumetric flask, and bring to 50 mL with water. Add 0.5–2.5 g of Chelex 100 chelating ion exchange resin (see **Note 7**), and gently shake the solution at room temperature for 1 h. Filter the solution through a 0.2 μm filter (hydrophilic membrane, 30 mm diameter) twice. Confirm the pH of the final double-filtered solution with a pH meter. Store at 4 °C.

3. 2 mM aluminium chloride ($AlCl_3$) in 0.5 M sodium acetate pH 4: To prepare 5 mL of the solution, weigh 2.4 mg of aluminium chloride hexahydrate and transfer to a 15 mL plastic centrifuge tube. Add 5 mL of metal-free 0.5 M sodium acetate buffer, pH 4. Store at 4 °C.

4. 4–20 GBq ^{18}F-fluoride in approximately 2.5 mL water produced from irradiation of an enriched $[^{18}O]H_2O$ target.

5. Organic solvent of choice: e.g., ethanol, acetonitrile, dimethyl sulfoxide (DMSO), dimethylformamide (DMF).

6. 0.1% trifluoroacetic acid (TFA) in water: Add 100 μL of TFA to 100 mL of HPLC grade water.

7. Water for injection.

8. 0–14 pH test strips.

9. Low-protein binding 1.5 mL microcentrifuge tubes.

10. 5 mL and 1 mL disposable syringes.

11. Oasis HLB solid phase extraction (SPE) cartridges, 1 mL tube, 30 mg sorbent: Prepare the HLB-SPE cartridge by washing it with 3 mL of ethanol, followed by 3 mL of aqueous 0.1% TFA. Store the cartridge at room temperature until needed.

12. 20 mL glass/plastic vials.

13. Heating block with thermometer.

14. HPLC system with UV detector and radiodetector.

15. Analytical (e.g., 4.6 × 250 mm) wide pore (300 Å) C18 HPLC columns.

16. HPLC eluents, 0.1% trifluoroacetic acid (TFA) in water or acetonitrile: Add 1 mL of TFA to either 1 L of water or 1 L acetonitrile.

17. HPLC gradient depends on the kind of affibody molecule analyzed. No universal gradient can be applied.

18. UV-VIS spectrophotometer.

19. Dose calibrator.

2.3 ^{68}Ga Radiolabelling

1. DOTA-affibody conjugate (Scheme 1) either lyophilized or in water. In the latter case, determine the concentration of the affibody conjugate stock solution by UV-VIS spectrophotometry (*see* **Note 6**). Store at −20 °C.

2. ^{68}Ga generator eluate: depending on the kind of ^{68}Ge/^{68}Ga generator used, the solution volume will range from 1.1 to 5 mL of 0.1 M hydrochloric acid (HCl). Depending on the age of the generator used, the activity will range from 500 MBq to 1.2 GBq.

3. 5 M NaCl and 5.5 M HCl solution: Initially, prepare 50 mL of 5 M sodium chloride solution by weighing 14.61 g of NaCl and transfer in a 50 mL volumetric flask. Add water up to 50 mL volume, and shake vigorously until all solid is dissolved. Then prepare the 5.5 M HCl solution by adding 22.9 mL of 37% (12 M) hydrochloride acid into a 50 mL volumetric flask and bring to volume with water. Finally, to prepare a 5 M NaCl and 5.5 M HCl solution, add 250 μL of 5.5 M HCl to 10 mL of 5 M NaCl.

1. 0.2 M sodium acetate buffer, pH 6, metal-free: To prepare 50 mL of the buffer, weigh 775 mg of sodium acetate and transfer to a 100 mL beaker. Add 31.6 μL of glacial acetic acid and 40 mL of water. Check the pH with a pH meter and correct it with few drops of either acetic acid or sodium hydroxide solution. Quantitatively transfer the solution to a 50 mL volumetric flask and bring to 50 mL volume with water. Add 0.5–2.5 g of Chelex 100 chelating ion exchange resin (*see* **Note** 7), and gently shake the solution at room temperature for 1 h. Filter the solution through a 0.2 μm filter (hydrophilic membrane, 30 mm diameter) twice. Confirm the pH of the final double-filtered solution with a pH meter. Store at 4 °C.

4. 0.1 M EDTA: Dissolve 1.46 mg of EDTA in 50 mL of water.

5. Commercially available phosphate-buffered saline (PBS).

6. ITLC eluents (either 0.1 M ammonium acetate with 25 mM EDTA, or 20 mM sodium citrate or 1 M ammonium acetate): Prepare 50 mL of 0.1 M ammonium acetate with 25 mM EDTA, pH 5.5 by dissolving 385.4 mg of ammonium acetate and 365.3 mg of EDTA in 50 mL of water. To prepare 50 mL of 20 mM sodium citrate, pH 5, dissolve 294.1 mg of sodium citrate dehydrate in 50 mL of water. Store at room

temperature. Prepare 50 mL of 1 M ammonium acetate pH 4.5 by dissolving 3.854 g of ammonium acetate in 50 mL of water. Store at room temperature.

7. Low-protein binding 1.5 mL microcentrifuge tubes.

8. 0–14 pH test strips.

9. 5 mL and 1 mL disposable syringes.

10. Strong cation exchange (SCX) SPE cartridge (e.g. Chromabond, 100 mg sorbent): condition the sorbent with 2–3 column volumes of ethanol followed by 2–3 column volumes of 0.1 M HCl. The conditioning step should be performed just before the use of the cartridge since the adsorbent bed should not run dry to avoid compromising its functionality.

11. 20 mL glass/plastic vials.

12. Disposable size exclusion spin-desalting column (*see* **Note 8**) or SPE column: conditioned the spin column with PBS or other suitable buffer following the manufacturer instructions. Alternatively, prepare Oasis HLB-SPE cartridges (1 mL tube, 30 mg sorbent) by washing it with 3 mL of ethanol, followed by 3 mL of aqueous 0.1% TFA. Store the cartridge/column at room temperature until needed.

13. pH meter.

14. Heating block with thermometer.

15. HPLC system with UV detector and radiodetector.

16. Analytical (e.g., 4.6 × 250 mm) wide pore (300 Å) C18 HPLC columns.

17. HPLC eluents, 0.1% trifluoroacetic acid (TFA) in water or acetonitrile: Add 1 mL of TFA to either 1 L of water or 1 L acetonitrile.

18. The HPLC gradient depends on the kind of affibody molecule analysed. No universal gradient can be applied.

19. Silica gel impregnated instant thin liquid chromatography (ITLC-SG) strips.

20. UV-VIS spectrophotometer.

21. Dose calibrator.

2.4 ^{89}Zr Radiolabeling

1. DFO-affibody conjugate (Scheme 1) either lyophilized or in 0.5 M HEPES buffer, pH 7. In the latter case, determine the concentration of the affibody conjugate stock solution by UV-VIS spectrophotometry (*see* **Note 6**). Store at −20 °C.

2. ^{89}Zr-oxalate solution in 1 M oxalic acid. The needed activity is decided based on the number and type of experiment (e.g., 3–10 MBq if used for in vitro studies, 20–50 MBq for in vivo studies). If purchased from a commercial source, the solution volume (generally <200 μL) is indicated on the product data sheet together with the ordered activity.

3. 2 M sodium carbonate (Na_2CO_3): Dissolve 10 mg of anhydrous Na_2CO_3 in 48 μL of water. Freshly prepare the solution, do not store it.

4. 0.5 M HEPES buffer, pH 7–7.3, metal-free: To prepare 50 mL of the buffer, weigh 5.95 g of HEPES and transfer to a 100 mL beaker. Add 40 mL of water. Check the pH with a pH meter, and adjust it with 10 M sodium hydroxide. Quantitatively transfer the solution to a 50 mL volumetric flask and bring to volume with water. Add 0.5–2.5 g of Chelex 100 chelating ion exchange resin (*see* **Note 7**), and gently shake the sospension at room temperature for 1 h. Filter through a 0.2 μm filter (hydrophilic membrane, 30 mm diameter) twice. Confirm the pH of the final double-filtered solution with a pH meter. Alternatively, dilute commercially available sterile-filtered 1 M HEPES solution pH 7.0-7.6 with water (1:1 v/v). Store at 4 °C.

5. 0.1 M EDTA: Dissolve 1.46 mg of EDTA in 50 mL of water.

6. PBS or 25 mM sodium acetate pH 7: PBS is commercially available. Prepare 50 mL of 25 mM sodium acetate pH 7 by dissolving 340.2 mg of sodium acetate trihydrate in 100 mL of water. Confirm the pH using a pH meter or a pH strip.

7. ITLC eluent: Prepare 20 mM sodium citrate buffer, pH 5 by dissolving 294.1 mg of sodium citrate dehydrate in 50 mL of water. Confirm the pH using a either a pH meter or pH strips.

8. Low-protein binding 1.5 mL microcentrifuge tubes.

9. 0–14 pH test strips.

10. Disposable size exclusion-desalting column (*see* **Note 8**): conditioned with PBS or 25 mM sodium acetate pH 7, following the manufacturer instructions.

11. pH meter.

12. ITLC-SG strips.

13. UV-VIS spectrophotometer.

14. Dose calibrator.

3   Methods

3.1   One-Pot Conjugation Reaction (See *Note 9*)

The following procedure is suitable for the conjugation of any maleimide functionalysed chelators (e.g., DOTA-maleimide, NOTA-maleimide, DFO-maleimide) to any cysteine-bearing affibody molecule.

1. Transfer an appropriate volume of the affibody molecule solution (1 equiv.) into a 1.5 mL low-protein binding microcentrifuge tube and add a volume of 0.1 M EDTA (*see* **Note 10**)
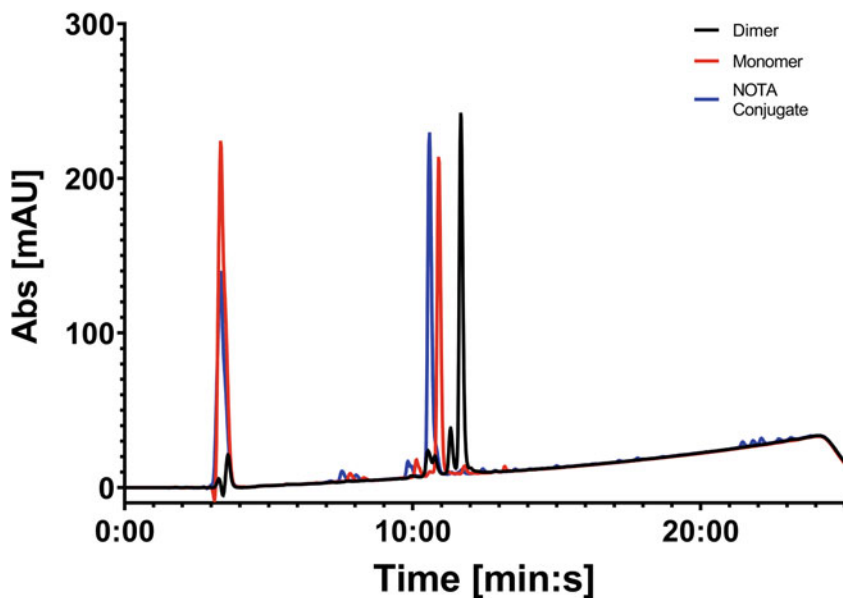
Fig. 2 Overlay of representative RP-HPLC traces for the affibody dimer (black line; elution at approximately 12 min:s), monomer (red line; elution at approximately 10:80 min:s; reduction reaction mixture containing TCEP eluting at 3 min:s), and NOTA-affibody conjugate in the conjugation reaction mixture (blue line; elution at approximately 10:50 min:s; presence of TCEP eluting at 3 min:s). The absorbance was measured at the wavelength of 230 nm

       solution corresponding to 60–90 equiv. Incubate for 30 min at room temperature.

2. To the affibody molecule solution, add a volume of the fresh 50 mg/mL TCEP-HCl stock solution corresponding to a 25 molar excess (*see* **Note 11**).

3. Incubate the mixture at 85 °C for 5 min, followed by 25 min at 24 °C with gentle shaking in a thermoshaker (*see* **Note 12**).

4. Add an amount of maleimide functionalised chelator corresponding to a 40 molar excess to the protein solution (*see* **Note 5**).

5. Incubate the reaction mixture at 40 °C for 2 h with gentle shaking (*see* **Note 13**).

6. Take a sample of the reaction mixture and analyze it by analytical RP-HPLC. Inject 7–10 μg of protein. The presence of the product peak and the disappearance of the unconjugated affibody molecule peak (both monomer and dimer) indicate that the conjugation reaction has reached completion (Fig. 2).

7. Purify the conjugate by semipreparative RP-HPLC to remove any residual free chelator and TCEP. Collect the product peak from the column output.

8. Evaporate the solvent of the collected fractions containing the product (e.g., using a lyophilizer or a centrifugal concentrator) and re-dissolve the conjugate in a known volume of water to have a concentration of 0.4–1.0 mg/mL.

9. Measure the concentration of the conjugate by UV-VIS spectroscopy (*see* **Note 6**).

10. Characterize the products by RP-HPLC and mass spectrometry (e.g., MALDI or ESI).

11. Store the conjugate stock solution at −20 °C until needed. Alternatively, divide the bioconjugate solution into aliquots, containing an amount of protein according to the radiolabeling reaction requirements (e.g., 10–15 nmol). Lyophilize the aliquots. The solid affibody conjugate can be stored at −20 °C until needed.

3.2 ^{18}F-AlF Radiolabeling

The following procedure is suitable for the manual ^{18}F-AlF radiolabeling (*see* **Note 14**) of any affibody-conjugates containing pentadentate macrocyclic chelators, such as NOTA (*see* **Note 15**).

1. To the NOTA-affibody conjugate (solid or in solution, 10–15 nmol), add a 2 mM solution of AlCl$_3$ (1:0.8 protein to AlCl$_3$ molar ratio) and 2–5 μL of 0.5 M sodium acetate (*see* **Notes 7** and **16**).

2. Add nonpurified aqueous ^{18}F-fluoride (300–500 MBq). Alternatively, the aqueous ^{18}F-fluoride can be purified from target generated impurities (e.g., various radionuclides and metals) through a quaternary methyl ammonium (QMA) SPE cartridge before it is added to the reaction. For that purpose, equilibrate a commercially available Sep-Pak QMA-SPE cartridge (130 mg sorbent) with 5 mL of 0.9% NaCl, followed by a 5 mL water rinse. Meanwhile, prepare a 0.36% NaCl solution by diluting the commercially available 0.9% NaCl solution with water (1:2.5 v/v). Preferably using a syringe drive or an automated synthesiser, transfer the ^{18}F target wash (0.5–2 GBq in water) onto the QMA cartridge. To ensure the removal of possible longer-lived contaminants, wash the QMA with 2 ml water. Finally, recover the ^{18}F-fluoride by eluting the QMA cartridge with 0.5 mL of 0.36% NaCl into a 1.5 mL microcentrifuge tube. Add purified aqueous ^{18}F-fluoride (300–500 MBq) to the conjugate buffered solution.

3. Take a small aliquot (approximately 0.5 μL) of the solution, and test the pH on a pH strip. It should be 4 (*see* **Note 17**).

4. Add a volume of organic solvent (e.g., ethanol, acetonitrile, DMSO, DMF) equal to the volume of the aqueous solution (*see* **Notes 18** and **19**). Measure the radioactivity of the mixture using a dose calibrator.

5. Incubate the solution at 95 °C for 15 min.

6. Purify the product by RP-HPLC: Inject the whole reaction solution into an analytical wide pore C18 HPLC column, and
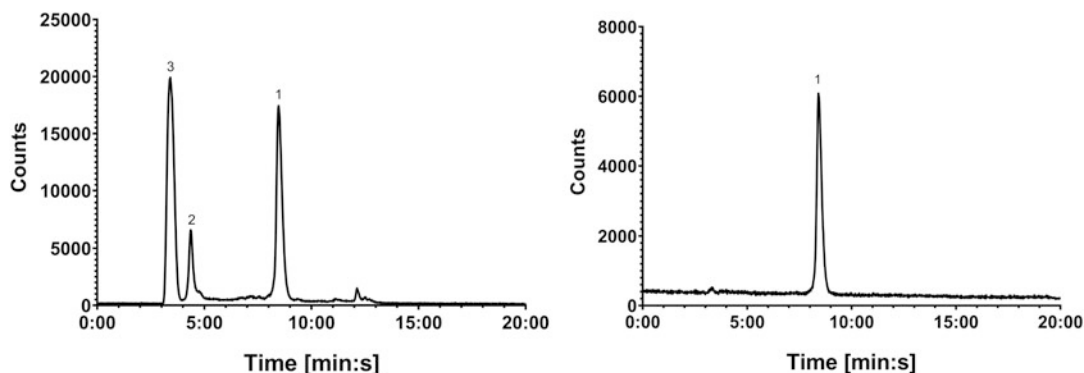
Fig. 3 Representative radiochromatograms of ^{18}F-AlF-NOTA-affibody reaction mixture (left), showing the radioconjugate (*1*), a side-product from thermolysis (*2*) and free ^{18}F-fluoride (*3*), and of the isolated product (*1*) (right)

collect the eluate corresponding to the product peak in a 20 mL glass/plastic vial containing 3 mL of aqueous 0.1% TFA. Leave the rest go to waste (*see* **Notes 20** and **21**).

7. Collect the product solution with a 5 mL disposable syringe, and load it onto the previously prepared HLB-SPE cartridge. Discard the eluate (*see* **Note 22**).

8. Wash the cartridge with 3 mL aqueous 0.1% TFA, followed by 3 mL water. Discard the washings (they should contain just free ^{18}F-fluoride) after measuring the activity in a dose calibrator.

9. Elute the product with 130–150 μL of a mixture of ethanol and water (*see* **Note 23**), and collect it in a 1.5 mL low-protein binding vial.

10. Determine the protein concentration, in the product solution, by UV-VIS spectroscopy (*see* **Note 6**), and measure the radioactivity of the product using a dose calibrator (*see* **Notes 24** and **25**).

11. Analyze the product by RP-HPLC to determine the radio-chemical purity (RCP) (Fig. 3).

12. The total preparation time is 40–50 min.

3.3 ^{68}Ga Radiolabeling

The following procedure is suitable for the manual ^{68}Ga radiolabeling of any affibody-conjugates containing DOTA- or NOTA-based chelators.

1. Slowly load the ^{68}Ga solution from the elution of a ^{68}Ge/^{68}Ga generator (generally in a hydrochloric acid solution of various dilutions) onto the freshly conditioned strong cation exchange cartridge (*see* **Note 26**). Flush the column with air. Measure the activity of the eluate in a dose calibrator. Discard the eluate after confirming that the activity has been retained in the column (*see* **Notes 27** and **28**).

2. Elute the ^{68}Ga with the 5 M NaCl and 5.5 M HCl solution (*see* **Note 29**) with a flow rate of 1 drop/second. Measure the activity of the eluate in a dose calibrator.

3. Add 0.42 mL 0.2 M sodium acetate buffer, pH 6 to the solution containing ^{68}Ga; mix and check the pH to be 4 on a pH strip (*see* **Note 30**). If the pH is lower than 4, adjust it adding a suitable extra volume of 0.2 M sodium acetate buffer, pH 6. Measure the activity of the final solution in a dose calibrator.

4. To 5–10 nmol of the affibody conjugate (solid or in solution), add approximately 400 MBq of the buffered ^{68}Ga solution and heat the reaction mixture at 80 °C for 15 min (*see* **Notes 31** and **19**).

5. After storing the solution at room temperature for few minutes to cool down, add 0.1 M EDTA solution to the radiolabeling mixture to a final concentration of 5 mM (*see* **Note 32**). Incubate at room temperature for 10–15 min.

6. Take a small sample to be analyzed by RP-HPLC and ITLC to determine the ^{68}Ga incorporation. Perform ITLC by loading 1–3 μL sample on an ITLC-SG strip. Run the strip and, once dry, analyze it using either a phosphorimager or a radio-TLC scanner. Alternately, the strip can be cut in half and the two parts measured in a gamma counter. Use either 50 mM EDTA pH 4.5 or 0.1 M ammonium acetate with 25 mM EDTA pH 5.5 or 20 mM sodium citrate pH 5 as mobile phase: the radioconjugate remains at the loading site (retention factor $R_f = 0$) and nonaffibody-associated ^{68}Ga (present in solution as either ^{68}Ga-EDTA or ^{68}Ga-citrate/acetate) runs with the solvent front ($R_f = 0.8$–1.0).

7. To purify the radioconjugate, apply the reaction mixture to a freshly conditioned spin desalting column and elute the radiolabeled product with PBS following the manufacturer instructions (*see* **Note 33**). Alternatively, load the mixture onto the previously prepared HLB-SPE cartridge. Discard the eluate. Wash the cartridge with 3 mL aqueous 0.1% TFA, followed by 3 mL water. Discard the washings (they should contain just free ^{68}Ga) after measuring the activity in a dose calibrator. Elute the product with 130–150 μL of a mixture of ethanol and water (*see* **Note 23**), and collect it in a 1.5 mL low-protein binding vial.

8. To verify the RCP of the product, take a sample and analyze it by RP-HPLC and ITLC as previously described.

9. Determine the protein concentration by UV-VIS spectroscopy (*see* **Note 6**), and measure the radioactivity using a dose calibrator (*see* **Notes 24** and **34**).

10. The total preparation time is approximately 40 min.

3.4 ^{89}Zr Radiolabeling

The following procedure is an adaptation of the general procedure developed for the ^{89}Zr radiolabeling of monoclonal antibodies [25, 26] and is suitable for the radiolabeling of any DFO-containing affibody-conjugates (*see* **Note 35**).

1. Pipette a volume/activity of ^{89}Zr-oxalate solution in a 1.5 mL microcentrifuge tube, based on the experiment design (e.g., 3–10 MBq if used for in vitro studies, 20–50 MBq for in vivo studies). Confirm the activity of the solution using a dose calibrator.

2. Add freshly prepared 2 M Na_2CO_3 to increase the pH of the ^{89}Zr solution to 5–6 (*see* **Note 36**). Expect some bubbling due to the production of CO_2. Shake vigorously for few seconds and then centrifuge the solution. Incubate the solution for 3 min at room temperature.

3. Add a suitable volume of 0.5 M HEPES pH 7–7.4 (*see* **Note 37**). Shake vigorously for few seconds and then centrifuge the solution.

4. Take a 0.5–1 µL aliquot of the solution and check the pH on a pH strip. The pH of the solution should be in the 6.8–7.2 range for an efficient radiolabeling. If the pH is too low, add a small volume of 2 M Na_2CO_3 (1–3 µL) to adjust it to the desired value. Measure the activity of the solution in a dose calibrator.

5. Add an amount of DFO-affibody conjugate in 0.5 M HEPES pH 7 according to the experiment design (e.g., 2.5–3.0 µg/MBq). Mix vigorously for a few seconds and then centrifuge the solution.

6. Incubate the reaction mixture for 1 h at room temperature with gentle shaking.

7. Determine the ^{89}Zr incorporation by ITLC analysis. Load a 0.5–1 µL sample on an ITLC-SG strip and use 0.1 M sodium citrate pH 5 as mobile phase (*see* **Note 38**).

8. Add 0.1 M EDTA solution to the radiolabelling mixture to a final concentration of 5 mM (*see* **Note 32**). Incubate at room temperature for 10–15 min.

9. Purify the radioconjugate by applying the reaction mixture to a freshly conditioned spin-desalting column (*see* **Note 33**), and elute the radiolabeled product either in PBS or 25 mM sodium acetate pH 7 following the manufacturer instructions.

10. Verify the RCP of the product by ITLC using ITLC-SG strips and 0.1 M sodium citrate pH 5 as mobile phase. Load 0.5–1 µL sample on an ITLC-SG strip. Run the strip, and once dry, analyze it using either a phosphorimager or a radio-TLC scanner. Alternately, the strip can be cut in half and the two parts measured in a gamma counter. Using 0.1 M sodium citrate

pH 5 as mobile phase, the radioconjugate remain at the loading site ($R_f = 0$) and non-affibody-associated [89]Zr (present as [89]Zr-citrate or [89]Zr-EDTA) runs with the solvent front ($R_f = 0.8$–1.0).

11. Determine the protein concentration by UV-VIS spectroscopy (*see* **Note 6**), and measure the radioactivity using a dose calibrator (*see* **Notes 24** and **39**).

12. The total preparation time is approximately 2 h.

4   Notes

1. Prepare an affibody molecule solution that is neither too diluted (<1 mg/mL) nor too concentrated (>1.5 mg/mL) to optimize the conjugation yield and avoid the reformation of disulfide bonds. The tendency of thiol groups to reform disulfides after reduction is dependent on the concentration of the generated free SH groups and the elapsed time after the reduction. Therefore, perform the conjugation reaction using the reduced sample immediately and keep TCEP in the reaction mixture. A relatively diluted affibody solution (1.2–1.5 mg/mL) and a molar excess of the reactive bifunctional chelator will favor the conjugation reaction over the formation of disulfide bonds.

2. The TCEP-mediated reduction can be performed in most buffers (not exclusively PBS), as well as in ultrapure water. Select the solvent based on the affibody molecule's solubility in these solutions.

3. Some reduction procedures in the literature suggest purging the solution from oxygen using a stream of nitrogen gas to minimize the oxidation of thiol group and the formation of disulfide bonds. From our experience, this step is not crucial for the success of the reaction.

4. A reducing agent is necessary when using a cysteine-bearing affibody molecule supplied as a stock solution. In that case, following the formation of a disulfide bond, the solution most likely contains the affibody molecule as a stable and inert dimer. If the cysteine-bearing affibody molecule is supplied as a powder, the addition of a reducing agent in the conjugation mixture might be unnecessary. A confirmation, for instance by PAGE or HPLC analysis, of the molecular form of the affibody molecule (i.e., monomer or dimer) would be recommended before planning a conjugation reaction.

5. Prepare the bifunctional chelators stock solutions immediately before use and discard them after use. The maleimide ring is susceptible to hydrolysis, especially in mildly alkaline aqueous

solutions, therefore old solutions will yield either low or no conjugation.

6. The determination of the concentration of the affibody conjugate by UV spectroscopy can be performed in two ways: (1) When the molar extinction (ε_{280}) is known, measure the absorbance of the protein solution at 280 nm and calculate the concentration (in M) using the Beer-Lambert law; (2) When a correction coefficient is available (indicating the absorbance at 280 nm of a mg/mL solution of the affibody molecule and usually given by the affibody molecule supplier), measure the mg/mL concentration at 280 nm and multiply it by the coefficient. Of note, usually the conjugated chelator has no absorbance at 280 nm, therefore the product concentration is calculated from the affibody molecule absorbance only. In case the chelator is UV active at 280 nm, its contribution to the absorbance should be considered when calculating the product concentration.

7. The use of metal-free solutions is advisable (in both conjugation and radiolabelling reactions) since metal ions can potentially compete with the radiometals for the same chelator. Generally, radiometals are present in a very low concentration; therefore, the presence of competing metal ions can seriously compromise the radiolabeling yield. Prepare metal-free buffers by treating them with metal-chelating resins, such as Chelex 100. These kinds of resins contain chelating groups that are able to bind polyvalent metal ions (especially heavy metal ions). Among the available resins, Chelex is the most widely used. It is a weakly acidic cation exchange resin, but different from ordinary exchangers; it is characterized by a high selectivity for metal ions and forms high strength bonds at basic, neutral, and weakly acidic pH (pH ≥ 4).

8. Size exclusion chromatography (or gel filtration) is very often used in protein purification processes. This technique involves the separation of molecules based on their different dimensions, molecular weight, shape or size (i.e., hydrodynamic radius) using columns filled with resins with varied pore sizes. Gel-filtration pre-packed columns are routinely used to separate and remove unwanted small molecules from a macromolecule of interest (i.e., desalting), or exchange the buffer. A wide range of such columns are commercially available and they differ based on the sample processing (i.e., gravity-flow or centrifuge-columns), resin's pore size (i.e., molecular weight cut off), and sample volumes. Spin columns (e.g., Vivaspin protein concentrators, Zeba spin desalting columns) offer a quicker purification process and a smaller sample elution volume compared to gravity driven columns (e.g., PD-10,

NAP-10, and CentriPure P10). Importantly, before use, select the most suitable format for the application.

9. The reducing agent can be removed from the affibody molecule solution using desalting columns before proceeding with the conjugation reaction, which is then followed by another purification step to achieve the final product. This multi-steps conjugation procedure might result in a poor protein recovery mostly due to the closeness of the molecular weight cut off (MWCO) of the membrane of the commercially available size exclusion columns (usually 5–7 kDa MWCO) to the molecular weight of the affibody conjugate (approximately 7 kDa). Additionally, such two-step conjugation process can be time-consuming and requires the use of multiple purification steps. A one-pot conjugation reaction using TCEP-HCl as the reducing agent, which is not removed from the mixture, can improve the product yield and simplify its purification [8].

10. Manufacturer protocols suggest to add a metal chelating agent such as EDTA (final concentration of 5–20 mM) to the sample solution to remove free metals that could promote the oxidation of the generated free sulfhydryl groups. This is a precautionary measure that should be added to the use of plastic tools, such as vials and spatulas, to keep the quantity of free metals ions in solution as low as possible.

11. For most applications, concentrations of TCEP in the 5–50 mM range, in the reaction mixture, provide sufficient molar excess to effectively reduce disulphide bonds in peptides or proteins. Differently from other reducing agents (e.g., DTT), TCEP does not contain thiols, and there should be no need to remove it from solution before adding the maleimide-functionalised chelator. The manufacturer reports that TCEP concentrations <10–20 mM are compatible with maleimide reaction chemistry. However, TCEP interacts with maleimide to some degree and can affect the conjugation reaction yield. To compensate for that, add a molar excess of maleimide functionalized chelator to achieve a high yielding conjugation. The extra amount of TCEP and chelator can be easily removed during the RP-HPLC purification of the conjugate.

12. Efficient disulfide reduction occurs over a wide range of pH (pH 4.0–9.0) and temperature (0–95 °C) with highest temperatures promoting the reaction. Due to the presence of the highly acidic TCEP-HCl and the low buffering capacity of PBS, the pH of the conjugation solution is usually around 5 and does not need to be adjusted to help the conjugation. However, if necessary, higher pH values can be achieved using 1 M phosphate buffer pH 6.5–7.0 instead of PBS.
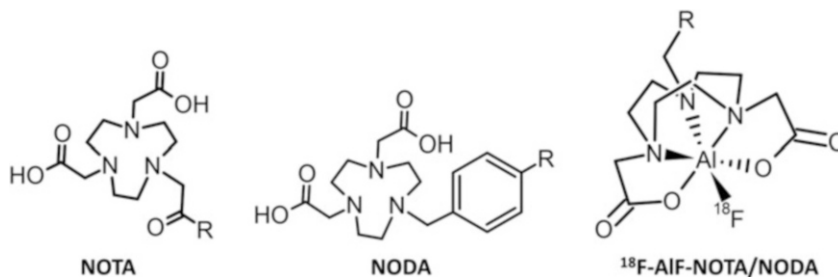
Fig. 4 Structures of derivatives of NOTA and NODA chelating agents and of the ^{18}F-AlF complex

13. The protein type and its concentration determine the incubation time. Generally, >1 mg/mL protein solutions with require minimum 1 h reaction time. If needed, monitor the reaction kinetics by HPLC.

14. The procedure described herein is suitable for the manual preparation of ^{18}F-AlF-labeled affibody conjugates. Although not applied to the preparation of affibody-based radioconjugates yet, some methodologies for the automated production of ^{18}F-AlF-labeled peptides has been reported by Allott et al. [27] and Tshibangu et al. [28].

15. A stable chelation of the ^{18}F-AlF^{2+} core can be achieved using derivatives of macrocyclic chelator 1,4,7-triazacyclononane (TACN). Owing to its commercially availability, also in its bifunctional form, 1,4,7-triazacyclononane-triacetic acid (NOTA) is the most frequently used chelator for the development of ^{18}F-AlF agents, especially in its pentadentate form. However, chelators containing the 1,4,7-triazacyclononane-1,4-diacetate (NODA) motif showed high radiolabeling yields due to the presence of just two carboxylic groups adjacent to the nitrogen atoms in the ring instead of three (Fig. 4). The third carbonyl group in the NOTA molecule, although not being directly involved in the coordination of the aluminum center, could affect the formation of a stable complex due to its electron-withdrawing ability [8, 29, 30]. The mentioned pentadentate chelators form octahedral complexes with the aluminum ion, leaving a single coordination site for strongly binding fluoride (Fig. 4).

16. Add an amount of acetate buffer to a final concentration of 25–35 mM (considering the aqueous solution volume only), which is the lowest concentration capable to maintain the optimal pH of 4. Based on our experience, higher acetate quantities lead to low ^{18}F incorporation. The reason has not been investigated yet. However, it is known that acetate buffers can form coordination complexes with metals ions. Such effect

can be beneficial for an efficient chelation of radiometals. In particular, for radiometal ions such as $^{111}In^{3+}$ and $^{68}Ga^{3+}$, it has been suggested that a weak prechelation effect by the acetate ions is necessary for the efficient labeling of conjugates since it would prevent the formation of insoluble $^{111}In/^{68}Ga$-hydroxides. On the other hand, coordinating buffers can have the same effect on metal contaminants that are present in the radiolabeling mixture and that will then compete with the radiometal, hindering the formation of the radiolabeled product [31]. The same might happen with the ^{18}F-AlF complex, but no studies on the subject have been performed yet.

17. Perform the reaction at pH 4–4.5 to achieve the highest yielding ^{18}F radiolabeling [29]. The pH is very critical for the formation of the ^{18}F-AlF complex: at too low pH, the 18-fluoride ion would be available in very low quantities since it would be mostly protonated (i.e. $H^{18}F$). At too high pH $(4 > pH > 6)$, the aluminum ion would be forming the insoluble, and, therefore, unreactive, hydroxide form $Al(OH)_3$ [32]. The optimal pH for the radiolabeling reaction is, therefore, around 4, in which both the Al^{3+} cation and the $^{18}F^-$ anion are the dominant species in solution.

18. The addition of an organic cosolvent is recommended to increase the radiolabel incorporation [33]. Choose the type of organic solvent to use depending on the protein solubility in that solvent and the use of the product (e.g., higher % of ethanol can be tolerated in radiopharmaceuticals formulations for the clinical use than other organic solvents. Additionally, differently from other organic solvents, ethanol is a known radioprotector).

19. The presence of multiple radioactive products in the HPLC trace could indicate that the radioconjugate is affected by radiolysis. In that case, the addition of a radioprotector, such as ascorbic acid, is highly recommended.

20. The HPLC purification step is not always required. It has been observed that low molecular weight byproducts can be formed during the radiolabeling reaction due to the high reaction temperature. This is observed mostly when the chelator is conjugated to the affibody molecule via a maleimide-thiol bond. In those cases, an HPLC purification can efficiently eliminate the side products from the final radioconjugate. However, not all affibody conjugates show such thermal instability, and therefore, in those cases, the HPLC purification step can be skipped and the final radioconjugates can be isolated by performing just a straightforward SPE (e.g., with HLB cartridges) or gel filtration purification.

21. Differently from ^{18}F-labeled small molecules, radiolabeled affibody conjugates show the same retention time of their

precursors on the HPLC trace independently from the gradient, mobile phase system, and type of column used. For that reason, the two molecules co-elute when purified by liquid chromatography (e.g., HPLC, SPE) and a no-carrier-added affibody-based radioactive product has so far not been achieved.

22. If loaded slowly (e.g., 1 drop/s), this solution from the HLB-SPE cartridge contains only free ^{18}F-fluoride. If some radiolabeled affibody conjugate goes through, decrease the loading speed.

23. The ethanol-to-water ratio in the eluent depends on the hydrophilicity/lipophilicity of the affibody conjugate. Generally an aqueous solution containing 50–70% of ethanol (v/v) is able to elute the majority of affibody radioconjugates from an HLB-SPE cartridge.

24. Use these data to determine the RCY (after decay correction), the protein recovery, and the apparent specific/molar activity of the product.

25. When using a nonpurified ^{18}F-fluoride solution, apparent molar activities up to 11 MBq/nmol (at the end of synthesis) and RCYs of 30–40% can be achieved.

26. In the clinic, ^{68}Ga radiopharmaceuticals are prepared by adding the generator eluate directly into the kit containing the molecule to radiolabel. However, for research purposes, it is advisable to process the generator eluate before use for the following important reasons: First, the eluate from the commercial generator contains long-lived ^{68}Ge (i.e., germanium breakthrough) in variable amounts depending on the age and the make of the generator; In addition, metallic impurities such as Zn(II), Fe(III), and residuals from the generator column material are present in the eluate. Because these trace metal impurities can compete with ^{68}Ga for the chelator, labeling yields and specific activities can be affected. Furthermore, the large volume and the hydrochloric acid content of the generator eluate can limit its direct use in radiolabeling reactions. Large reaction volumes enhance the risk of insufficient ^{68}Ga-labeling yields and specific activities, especially in preclinical settings, when low amounts of precursors are used. Several approaches for processing generator-derived ^{68}Ga can be found in the literature, including fractionation (i.e., the use of just the 1–2 mL of the eluate, which contains the highest ^{68}Ga activity) [34], anion-exchange chromatography, and cation-exchange chromatography [35]. All methods aim to obtain more concentrated and metal-free ^{68}Ga solutions and consequent efficient and reproducible ^{68}Ga-labelling results. After testing and confirming the efficacy of the different

methods, the choice of describing herein the cation-exchange approach is based on personal experience and preference.

27. Sample application with a flow rate of 1 drop/second showed efficient trapping of the radioactivity onto the column. Faster loading speeds might result in insufficient retention of the activity by the sorbent of the SPE column.

28. The handling of PET nuclides may result in significant radiation doses to the hands of workers, particularly the fingers. The contribution of positrons to the skin dose is dominant, especially in the case of high-energy positron emitters, such as ^{68}Ga. Therefore, avoid the direct contact of the fingers with unshielded vials, syringes, tubing, or valves containing such radionuclides. If possible, connect the ^{68}Ge/^{68}Ga generator to the SPE cartridge and load the generator eluate directly onto the column. Alternatively, transfer the generator eluate onto the cartridge using a syringe drive. Additionally, always use long forceps or tweezers during the whole preparation of the radioconjugate.

29. Use a cartridge with a quantity of sorbent suitable for the retention of all ^{68}Ga activity. A cartridge with a low amount of sorbent (i.e., smaller bed weight) (30–100 mg) allows for a small elution volume (ca 150–350 μL), which results in a higher protein concentration in the radiolabeling reaction mixture and consequently in favorable radiometal incorporation (and final RCY). Additionally, by using high concentration buffers (i.e., great buffer capacity; 0.5–1.5 M, pH 6) the desired pH value can be secured by the addition of small volumes, thus keeping the protein concentration in the reaction mixture as high as possible.

30. During ^{68}Ga radiolabeling, the control of the pH is very important. Gallium (III) ions are present as the main form of gallium in solution when the pH is lower than 4. At higher pH (4–8), the main product is the insoluble $Ga(OH)_3$, also called Ga-colloid, since it precipitates from solution. Once precipitated, this form of gallium is not reactive and the radiolabeling reaction is compromised. The buffering capacity of acetate is very good in the pH 4–5 range, and therefore, the acetate buffer can maintain the desired pH during the reaction preventing the formation of Ga-colloid and allowing an efficient radiolabeling.

31. The temperature can be increased up to 95 °C to improve the radiolabel incorporation. Differently from DOTA, the radiolabeling of NOTA-affibody conjugates with ^{68}Ga could be

performed either at 80–95 °C or at lower temperature (e.g., 40 °C or even room temperature) [36].

32. Use EDTA to chelate the nonincorporated radiometal ions. Being the radiometal-EDTA complex stable at a large range of pH values, this step avoid the possibility of formation and precipitation of insoluble ^{68}Ga-colloid during the purification step and QC analysis.

33. Salt and small molecules removal using size exclusion/desalting columns is typically 95–100%. However, the recovery of the final product generally depends on the protein concentration and the sample volume loaded onto the column. Some protein loss occurs at the lowest sample volumes and protein concentrations (<0.2 mg/mL). Of note, the removal of impurities and protein recovery depend also on the individual characteristics of the biomolecules (e.g., molecular weight, shape, hydrophobicity, solubility, binding sites). Based on our experience, expect protein recovery of approximately 40% when using resins with an exclusion limit (MWCO) very similar to the size of the biomolecule of interest.

34. Apparent molar activity of the radiolabeled conjugate in the range of 2.8–5.2 MBq/nmol at the end of synthesis are expected.

35. Due to their small size, affibody molecules are characterized by a rapid pharmacokinetics and fast tumor uptake (i.e., within 30 min post injection), which are perfectly compatible with short-lived radionuclides (i.e., ^{18}F, ^{68}Ga). However, at times, PET imaging using biomolecules with fast pharmacokinetics shows an improved contrast at time points beyond 3–4 h p.i. In that event, long-lived radiometals (such as ^{89}Zr, half-life of 3.27 days) should be employed.

36. Freshly produced ^{89}Zr-oxalate solutions might require smaller volumes of 2 M Na_2CO_3 compared to older solutions. Possibly because oxalate concentration in older ^{89}Zr solution is higher as the result of the slow evaporation of the water during either its storage at room temperature or its transfer from the supplier to the customer. Sometimes, the presence of a precipitate (i.e., oxalic acid) has been observed. This precipitate can be removed, but as it can include some ^{89}Zr, the activity of the leftover solution will decrease. Alternatively, the precipitate can be dissolved by adding water or buffer to the ^{89}Zr-oxalate stock solution. In this case, the smallest possible volume of water or buffer should be added to keep the oxalic acid concentration above 13 μM and avoid the formation of insoluble and unreactive Zr(IV) hydroxide species [37].

37. To achieve and sustain an adequate pH, alternative buffers to HEPES can be used (e.g., phosphate, ammonium acetate).

Alternatively, the pH of ^{89}Zr-oxalate solution can be adjusted to 7 using just Na$_2$CO$_3$ solution (pH >9). The amount of the carbonate solution should be rigorously determined and the pH of the solution carefully monitored. Importantly, the radiolabeling protocol (e.g., quantity of buffer and reaction time) should be prepared based on the reaction conditions (e.g., type of buffer and freshness of ^{89}Zr-oxalate solution). Based on our experience, a reproducible neutralization of a 3-day-old ^{89}Zr-oxalate solution is achieved using a combination of Na$_2$CO$_3$ and HEPES. A 2 M Na$_2$CO$_3$ to ^{89}Zr-oxalate ratio of 1:2.2 (v/v) is required to increase the pH of the ^{89}Zr-oxalate solution to 4.5–5. A 0.5 M HEPES, pH 7 to ^{89}Zr-oxalate ratio of 2.5:1 (v/v) is then required to adequately adjust the pH to 7.

38. Although ^{89}Zr incorporations of >95% can be achieved following the radiolabelling procedure and a product with such high RCP could be used without further processing, the reaction mixture contains oxalic acid that is highly toxic and should be removed before performing in vivo studies. A purification step is therefore highly recommended.

39. When using a 3-day-old ^{89}Zr-oxalate solution, apparent molar activity in the 11–21 MBq/nmol range (at the end of synthesis) and ^{89}Zr incorporation of 80–98% can be achieved.

Acknowledgments

References

1. Ståhl S, Gräslund T, Eriksson Karlström A et al (2017) Affibody molecules in biotechnological and medical applications. Trends Biotechnol 35:691–712

2. Frejd FY, Kim K-T (2017) Affibody molecules as engineered protein drugs. Exp Mol Med 49: e306

3. Löfblom J, Feldwisch J, Tolmachev V et al (2010) Affibody molecules: engineered proteins for therapeutic, diagnostic and biotechnological applications. FEBS Lett 584:2670–2680

4. Kramer-Marek G, Kiesewetter DO, Martiniova L et al (2008) [^{18}F]FBEM-Z(HER2:342)-Affibody molecule-a new molecular tracer for in vivo monitoring of HER2 expression by positron emission tomography. Eur J Nucl Med Mol Imaging 35:1008–1018

5. Namavari M, Padilla De Jesus O, Cheng Z et al (2008) Direct site-specific radiolabeling of an Affibody protein with 4-[^{18}F]fluorobenzaldehyde via oxime chemistry. Mol Imaging Biol 10:177–181

6. Glaser M, Iveson P, Hoppmann S et al (2013) Three methods for ^{18}F labeling of the HER2-binding affibody molecule Z$_{HER2:2891}$ including preclinical assessment. J Nucl Med 54: 1981–1988

7. Heskamp S, Laverman P, Rosik D et al (2012) Imaging of human epidermal growth factor receptor Type 2 expression with ^{18}F-labeled affibody molecule Z$_{HER2:2395}$ in a mouse model for ovarian cancer. J Nucl Med 53: 146–153

8. Da Pieve C, Allott L, Martins CD et al (2016) Efficient [^{18}F]AlF radiolabeling of Z$_{HER3:8698}$

affibody molecule for imaging of HER3 positive tumors. Bioconjug Chem 27:1839–1849

9. Cleeren F, Lecina J, Ahamed M et al (2017) Al[18]F-labeling of heat-sensitive biomolecules for positron emission tomography imaging. Theranostics 7:2924–2939

10. Chiotellis A, Sladojevich F, Mu L et al (2016) Novel chemoselective ^{18}F-radiolabeling of thiol-containing biomolecules under mild aqueous conditions. Chem Commun 52: 6083–6086

11. Miao Z, Ren G, Liu H et al (2012) PET of EGFR expression with an ^{18}F-labeled affibody molecule. J Nucl Med 53:1110–1118

12. Kramer-Marek G, Shenoy N, Seidel J et al (2011) ^{68}Ga-DOTA-affibody molecule for in vivo assessment of HER2/neu expression with PET. Eur J Nucl Med Mol Imaging 38: 1967–1976

13. Sörensen J, Velikyan I, Sandberg D et al (2016) Measuring HER2-receptor expression In metastatic breast cancer using [^{68}Ga]ABY-025 affibody PET/CT. Theranostics 6:262–271

14. Velikyan I, Schweighöfer P, Feldwisch J et al (2019) Diagnostic HER2-binding radiopharmaceutical, [^{68}Ga]Ga-ABY-025, for routine clinical use in breast cancer patients. Am J Nucl Med Mol Imaging 9:12–23

15. Strand J, Varasteh Z, Eriksson O et al (2014) Gallium-68-labeled affibody molecule for PET imaging of PDGFRβ expression in vivo. Mol Pharm 11:3957–3964

16. Oroujeni M, Garousi J, Andersson KG et al (2018) Preclinical evaluation of [^{68}Ga]Ga-DFO-ZEGFR:2377: a promising affibody-based probe for noninvasive PET imaging of EGFR expression in tumors. Cell 7:141. https://doi.org/10.3390/cells7090141

17. Cheng Z, De Jesus OP, Kramer DJ et al (2010) ^{64}Cu-labeled affibody molecules for imaging of HER2 expressing tumors. Mol Imaging Biol 12:316–324

18. Tolmachev V, Gronroos TJ, Yim CB et al (2018) Molecular design of radiocopper-labelled Affibody molecules. Sci Rep 8:6542. https://doi.org/10.1038/s41598-018-24785-2

19. Garousi J, Andersson KG, Mitran B et al (2016) PET imaging of epidermal growth factor receptor expression in tumours using [89]Zr-labelled ZEGFR:2377 affibody molecules. Int J Oncol 48:1325–1332

20. Martins CD, Da Pieve C, Burley TA et al (2018) HER3-mediated resistance to Hsp90 inhibition detected in breast cancer xenografts by affibody-based PET imaging. Clin Cancer Res 24:1853–1865

21. Burley TA, Da Pieve C, Martins CD et al (2019) Affibody-based PET imaging to guide EGFR-targeted cancer therapy in head and neck squamous cell cancer models. J Nucl Med 60:353–361

22. Ahlgren S, Orlova A, Rosik D et al (2008) Evaluation of maleimide derivative of DOTA for site-specific labeling of recombinant affibody molecules. Bioconjug Chem 19:235–243

23. Garousi J, Orlova A, Frejd FY et al (2020) Imaging using radiolabelled targeted proteins: radioimmunodetection and beyond. EJNMMI Radiopharm Chem 5(1):16–42

24. Tolmachev V, Orlova A (2020) Affibody molecules as targeting vectors for PET imaging. Cancers 12:651–672

25. Vosjan MJ, Perk LR, Visser GW et al (2010) Conjugation and radiolabeling of monoclonal antibodies with zirconium-89 for PET imaging using the bifunctional chelate p-isothiocyanatobenzyl-desferrioxamine. Nat Protoc 5:739–743

26. Zeglis BM, Lewis JS (2015) The bioconjugation and radiosynthesis of [89]Zr-DFO-labeled antibodies. J Vis Exp 96:e52521. https://doi.org/10.3791/52521

27. Allott L, Da Pieve C, Turton DR et al (2017) A general [^{18}F]AlF radiochemistry procedure on two automated synthesis platforms. React Chem Eng 2:68–74

28. Tshibangu T, Cawthorne C, Serdons K et al (2020) Automated GMP compliant production of [^{18}F]AlF-NOTA-octreotide. EJNMMI Radiopharm Chem 5:4–27

29. McBride WJ, Sharkey RM, Goldenberg DM (2013) Radiofluorination using aluminum-fluoride (Al[18]F). EJNMMI Res 3:36–47

30. Shetty D, Choi SY, Jeong JM et al (2011) Stable aluminium fluoride chelates with triazacyclononane derivatives proved by X-ray crystallography and ^{18}F-labeling study. Chem Commun 47:9732–9734

31. Brom M, Joosten L, Oyen WJ et al (2012) Improved labelling of DTPA- and DOTA-conjugated peptides and antibodies with ^{111}In in HEPES and MES buffer. EJNMMI Res 2:4–15

32. Huang Y, Chai W, Han G et al (2016) Probing acid/base chemistry and adsorption mechanisms of hydrolysable Al(III) species with a clay system in aqueous solution. RSC Adv 6: 114171–114182

33. D'Souza CA, McBride WJ, Sharkey RM et al (2011) High-yielding aqueous ^{18}F-labeling of peptides via Al[18]F chelation. Bioconjug Chem 22:1793–1803

34. Breeman WA, de Jong M, de Blois E et al (2005) Radiolabelling DOTA-peptides with [68]Ga. Eur J Nucl Med Mol Imaging 32:478–485

35. Velikyan I (2015) ^{68}Ga-based radiopharmaceuticals: production and application relationship. Molecules 20:12913–12943

36. Sharma G, Braag MC, Da Pieve C et al (2023) Immuno-PET Imaging of Tumour PD-L1 Expression in Glioblastoma Cancers 15(12) 3131. https://doi.org/10.3390/cancers15123131

37. Kobayashi T, Sasaki T, Takagi I et al (2009) Zirconium solubility in ternary aqueous system of Zr(IV)-OH-carboxylates. J Nucl Sci Technol 46:142–148

Part II

Models and Validation

Chapter 11

Small Animal Multisubject PET/CT Workflow

Alexia Kirby and Adam J. Shuhendler

Abstract

Positron emission tomography (PET) is a highly sensitive molecular imaging technique that uses radioactive tracers to map molecular and metabolic processes in living animals. PET can be performed as a standalone modality but is often combined with CT to provide for objective anatomical localization of PET signals in a multimodality approach. In order to outline the general approach to evaluating four mice simultaneously by dynamic PET imaging, the use of the aldehyde-targeted radiotracer $[^{18}F]NA_3BF_3$ in mouse models of hepatotoxicity will be described. Indeed the production of aldehydes is upregulated in a wide range of disease and injury, making them a suitable biomarker for PET imaging of numerous pathologies.

Key words Positron emission tomography, Aldehydes, In-vivo imaging, PET-CT, hepatotoxicity

1 Introduction

PET is an important preclinical molecular imaging technique that uses radionuclide-labelled molecules to noninvasively map biological processes of interest with high sensitivity and in three dimensions. While PET imaging is an important clinical tool, it is also a powerful preclinical technique that not only leads to the development of clinical tracers but is also used for longitudinal studies in animal models to better understand certain biological processes. While PET provides high sensitivity information about the localization of radiotracers, it does not provide anatomical information about the subject under study. As a result, PET is often combined with computed tomography (CT), an X-ray-based imaging technique that can generate high-resolution images of subject anatomy. This multimodality approach is invaluable for the objective quantitation of radiotracer uptake in tissues and pathologies with a high degree of spatial certainty and accuracy.

In vivo aldehydes are produced and maintained by tightly regulated mechanisms [1]. Disruption of these mechanisms often results in an increase of aldehyde production, creating a tissue

environment with high aldehydic load [2]. This increase in aldehydic load often underlies the early stages of many pathologies, including cancer, cardiovascular disease, and acutely following injury [3–6]. These aldehydes are highly reactive and quickly form adducts with DNA and proteins, which may contribute to the propagation of injury and disease. The diversity of aldehydes with pathogenic potential supports the need for in vivo imaging of aldehydes.

A radiotracer designed to measure aldehydic load is unlike the most common radiotracer, 2-deoxy-2-[^{18}F]fluoro D-glucose (FDG), in that it does not act as a metabolic surrogate. FDG is taken up by glucose transporters, phosphorylated, and, subsequently, trapped intracellularly and, thereby, maps aerobic metabolism. Imaging in vivo aldehydes, however, is more efficient through a substrate-binding mechanism rather than a surrogate mechanism. For a PET radiotracer to work effectively to map aldehydes, the reaction must occur rapidly, without a catalyst, under physiological conditions, and stick to the location where the substrate was bound.

Two radiotracers have been developed for this technique: ^{68}Ga-NODAGA-Indole [7] and ^{18}F-NA$_3$BF$_3$ [8]. The former is an allysine-reactive probe that binds to converted lysine residues of oxidized collagen in fibrotic lung tissue. ^{18}F-NA$_3$BF$_3$ is an anthranilic acid-based probe that reacts with both intra- and extracellular aldehydes to form hydrazones. This tracer represents a first-generation aldehyde PET tracer that can be used to map whole-body in vivo aldehydic load.

Here, aldehyde PET imaging with ^{18}F-NA$_3$BF$_3$ is described in a mouse model of acetaminophen overdose-induced hepatotoxicity. The model involves a single, same-day injection of acetaminophen, which induces lipid peroxidation and aldehyde production, especially in the liver, and has been shown to cause an increase in aldehydic load. The goal of the method is to quantitatively map the in vivo aldehydic load in mice over time and across acetaminophen doses using [^{18}F]-NA$_3$BF$_3$-PET.

2   Materials

2.1   PET/CT Scanner Preparation

1. Small animal PET/CT scanner with heater and integrated animal monitoring system for respiration and temperature
2. Computer station with associated software
3. Multi-mouse imaging bed (*see* **Note 1**)

2.2   Animal Preparation

1. Personal protective equipment (PPE, including, but not limited to, gloves and lab coat)
2. Acetaminophen-injected or sham-injected mice
3. Absorbent pads

4. Heat lamp

5. Water pump heating mat

6. Isoflurane system directed to either induction box or nose cone

7. Isoflurane scavenging system

8. Oxygen tank

9. Small animal anesthesia induction box

10. Preparation table with nose cone

11. 27G or 30G 13mm needles

12. Polyethylene tubing

13. 0.9% saline solution

14. Isopropyl alcohol swabs

15. 1 mL syringes

16. Needle forceps

17. Paper tape (3 M micropore)

18. Surgical plastic tape (3 M transpore)

19. Topical skin adhesive (vetbond)

20. Eye gel

2.3 Radiotracer Preparation and Animal Injection

1. $[^{18}F]NA_3BF_3$ or other nonmetabolic PET radiotracer

2. Lead-lined radioisotope workstation with plexiglass shield (*see* **Note 2**)

3. Contamination monitor (Geiger counter)

4. 0.9% saline solution

5. 1 mL syringes

6. 27G needles

7. Dose calibrator (Capintec)

2.4 Image Analysis

1. Image analysis software (VivoQuant)

3 Methods

3.1 PET/CT Scanner Preparation

1. PET/CT calibration should be performed on a regular schedule based on manufacturer's instructions prior to beginning an imaging study.

2. If CT is to be used, X-ray tube conditioning of the CT scanner should be performed at least 30 min prior to receiving radiotracer.

3. Heat imaging bed to 37 °C.

4. Prepare respiration monitor and rectal temperature probe on PET bed.

3.2 Animal Preparation

1. Create a sterile environment by wiping area with disinfecting spray and placing absorbent padding on bench. Lay out all materials needed to prepare the animals for cannulation.

2. Prepare one tail vain cannula per mouse (Fig. 1). Cut a length of polyethylene tubing long enough to allow access when animals are centered in PET scanner (approx. 10–15 cm for most scanners). Remove a 27G or 30G needle from its hub by breaking the plastic with needle forceps, and secure the blunt end into one end of the tubing. Draw 500 μL saline with a needle attached to a 1 mL syringe, and secure onto the other end of the tube. Push the syringe until the saline exits from the needle end of the cannula, and take note of the volume pushed through. Ensure there are no air bubbles anywhere in the line.

3. Place mouse in induction box on heating pad with 3% isoflurane at 1.5–2 L/min

4. When mouse is anesthetized (unresponsive to touch), remove from box and place head in nose cone on prep table on heating pad.

5. Apply eye gel to the eyes.

6. Place mouse on its side to expose lateral tail vein, located on the left- and right-most aspects of the tail when the mouse is on its side. The vein will be more difficult to see in strains with darker pigmented tails (e.g., C57bl/6, Fig. 1a)

7. Warm tail with heat lamp, taking care not to burn the tail (*see* **Note 3**)

8. Wipe the tail with an alcohol swab.

9. Cannula insertion should be attempted toward the distal end of the tail, with following attempts moving more proximal. In the nondominant hand, either hold the tail between the thumb and index finger or weave the tail under the forefinger, under the third and fourth, and over the fifth finger (Fig. 1a). Bend the tail slightly to expose an area for cannulation (Fig. 1b). Insert the needle of the cannula into the lateral tail vein at a ~5° angle to the tail, ensuring at least half (>6.5 mm) of the needle is in the vein (Fig. 1c).

10. Verify the cannula is in the vein by pushing on the syringe. The vein will visibly flush with saline, and the plunger will have no resistance. If the needle is not in place, the syringe will be difficult to push and the tail will blanche at needle insertion site.

11. Add one drop of skin adhesive where the needle meets the tail and allow to dry for 30 s.

12. Secure the cannula with paper tape (Fig. 1d).

13. Turn on isoflurane to PET/CT bed to 2%.
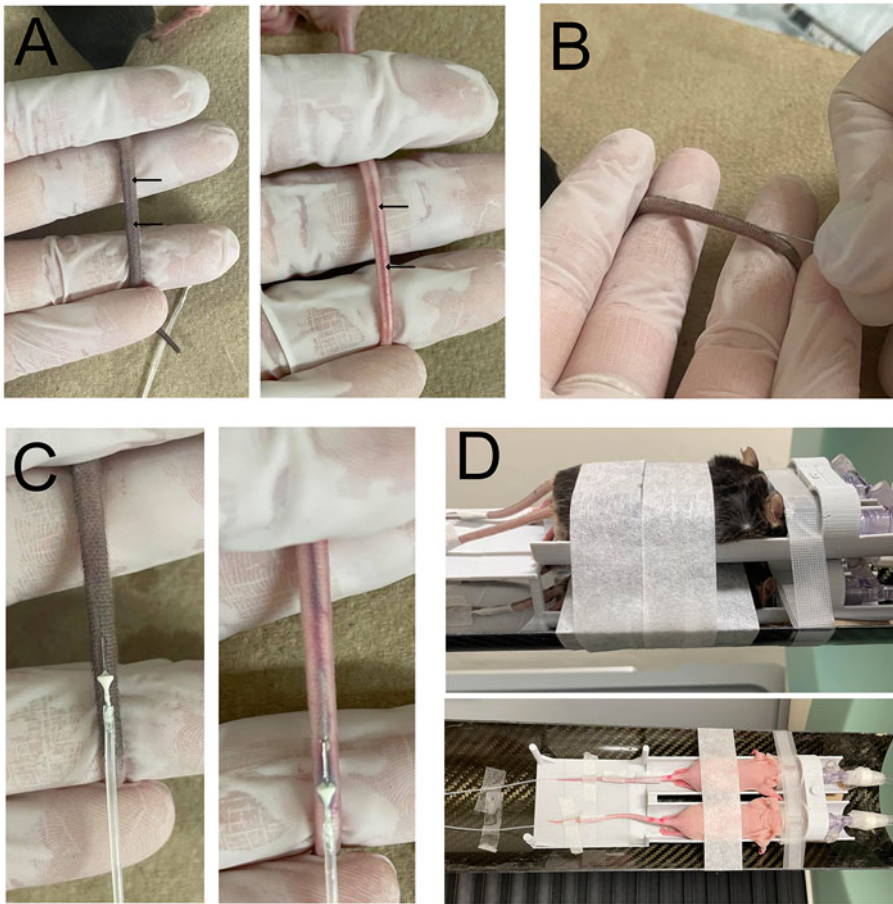
Fig. 1 Animal preparation for PET scan. Before the radiotracer is received, mice are prepared for injection. (**a**) The lateral tail vein is located and dilated with a heat lamp in a C56Bl/6 mouse (left) and nu/nu mouse (right). (**b**) Needle insertion into vein occurs at a ~5° angle to the tail. (**c**) Successful placement of the needle of the cannula is shown in both mice. (**d**) The animals are moved to the PET bed and tape is placed to secure the bodies of the mice, the tails, and the cannulas

14. Move the mouse over to the PET/CT bed, with the mouse in one hand and syringe in the other to avoid displacing the cannula. Place the mouse in a prone position.

15. Secure the body of the mouse, tail, and cannula with tape, and ensure the cannula is in place by pushing the plunger of the syringe (Fig. 1d). This will ensure proper injection of the radiotracer. Insert rectal temperature probe and secure with tape.

16. Verify that temperature and respiration monitors are working and within range. Respiration rate should be maintained at 60–100 breaths per minute, which can be adjusted by increasing or decreasing isoflurane. Body temperature should be maintained at 35–37 °C.

17. Note the position of each mouse in the imaging bed, and ensure the bed is aligned with the imaging field of view (FOV) of the scanner. The specific method for FOV centering will change depending on the vendor. Ensure both PET and CT FOVs are adequate for region of interest of imaging (i.e., whole mouse, head only, abdomen only).

3.3 Radiotracer Preparation

1. Synthesize radiotracer as previously described. Due to the short half-life of ^{18}F, the subsequent steps need to be done quickly.

2. Radiotracer dose preparation is performed behind a lead shield, with one dose prepared for each animal in the immediately following scan. It is recommended to double glove when handling radioactivity so that contaminated PPE can be quickly removed.

3. Measure the total radioactivity obtained in the dose calibrator. Note the time of this measurement to account for decay.

4. Dilute stock radiotracer to ~200 μCi/100 μL. If more than one round of imaging will be done with the same stock, only dilute a portion of the stock.

5. Draw up 150–200 μCi of activity per mouse with 27G insulin syringes, ensuring the volume is a maximum of 10 mL/kg per mouse. If multiple mice are being scanned, mark each syringe with a number corresponding to each mouse ID. Measure each syringe in the dose calibrator and note the activity and time for each syringe.

6. When all doses have been prepared, place in a lead carrier and bring to PET/CT animal bed or cradle.

3.4 Injection and Scanning

1. Attach the radiotracer dose to the tail vein cannula. With a pair of forceps, grasp the end of the cannula and remove the syringe and needle containing saline and place to the side. Carefully insert the needle of the tracer-containing syringe into the cannula. Repeat for all mice.

2. The scan types should be selected and placed in queue. For PET/CT, select the PET scan program desired (e.g., static scan of a given time frame and dynamic scan with preset imaging bins) and the CT program necessary (*see* **Note 4**). Importantly, for dynamic scans, an initial 15–30 s bin should be included to allow delay between scan program initiation and radiotracer injection. This is key for accurate kinetic analyses.

3. On the instrument control station, start the scan and timer simultaneously

4. After the delay set in the first bin of a dynamic scan has passed (15 or 30 s), inject the radiotracer over a period of 3–5 s.

5. Replace the empty radiotracer syringes with the saline-filled syringes, and inject enough volume to simultaneously flush all of the cannulae (~50–100 μL) with saline.

6. Measure the residual radioactivity in each radiotracer syringe and note the time.

7. Monitor respiration rate carefully during the scan, and adjust isoflurane if necessary.

8. If another PET/CT scan is to be performed afterwards, use this time to set up for the next scan. Mice can be cannulated, and doses can be drawn toward the end of the first scan.

9. When imaging is complete, remove all tape securing the cannula to the bed and the tail. Pinch the injection site the with gauze while removing the needle to stop bleeding. Place mouse back in cage on heating pad to recover. The mice should be held in a designated area behind a lead shield overnight or until ready to replace back in housing room, depending on the facility.

3.5 Image Reconstruction

1. Depending on the vendor, there will be a variety of image reconstruction algorithms to choose from. Reconstruction algorithm choice will depend on a balance of resolution, time, and quantitative accuracy required and should be evaluated in a pilot fashion.

2. Reconstruction will necessarily involve data about photon attenuation derived from the CT or an attenuation scan if PET-only imaging is performed.

3.6 Image Analysis

1. The specific workflow for image analysis will depend on the tissue/organ of interest and the disease model utilized, as well as the software package chosen for analysis.

2. For multi-animal scans, each animal should be cropped from the image and analyzed separately so that precise injected dose can be input into time-activity curves or use for radiotracer uptake (either as % injected dose per gram or summed uptake value).

3. Output images should include a standardized scale range and scale unit (either as % injected dose per gram or summed uptake value) to afford comparison across individuals between treatment groups (Fig. 2).

4 Notes

1. Multi-mouse beds are commonly provided by the PET/CT instrument manufacturers and are supplied with anesthesia and heating with proprietary adaptors. If this is not the case, a
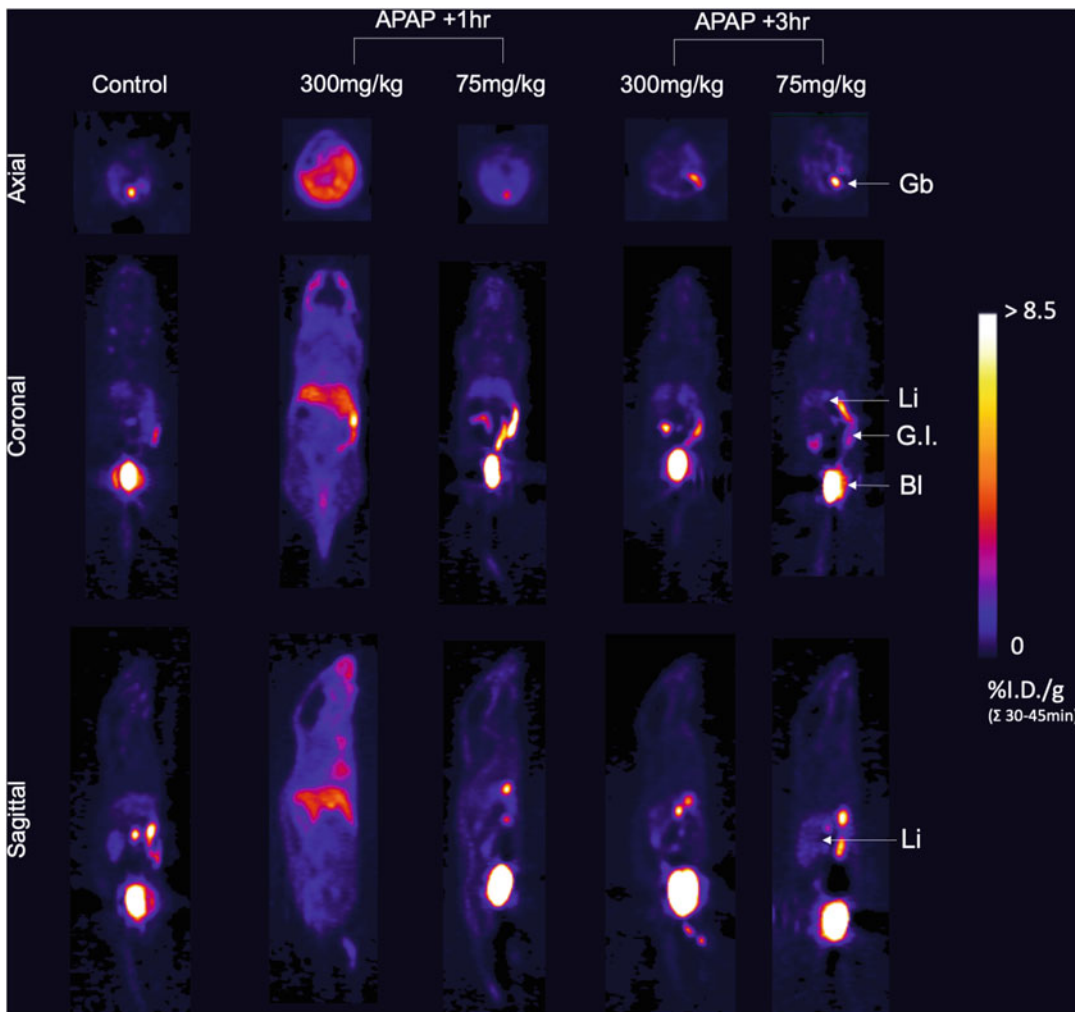
Fig. 2 Distribution of $[^{18}F]$-NA_3BF_3 in mice following acetaminophen dosing by PET imaging. Mice were untreated (left-most), or given an overdose (300 mg/kg) or therapeutic dose (75 mg/kg) acetaminophen i.p. and imaged 1 or 3 h after administration. Images are summed from the time activity curves from 30–45 min after PET scan initiation

multi-mouse bed can be 3-D printed; however, heating and the equal distribution of anesthesia to all positions must be tested prior to implementation on live animals.

2. Use of radioisotopes and radiotracers should comply with institutional and Federal policies for the safe use of radioactivity.

3. Keeping one hand next to mouse under heat lamp will ensure heating does not result in burn.

4. CT program for single mouse and multi-mouse will be different with different total deposited dose. These programs can be found preprogrammed on most scanners and should be evaluated prior to use.

5. Unlike in metabolism-based imaging (e.g., FDG), animals do not need to be fasted overnight to image aldehydes.

6. ^{18}F-NA$_3$BF$_3$ does not cross the blood–brain barrier and, therefore, cannot be used for aldehydes imaging in brain tissue.

7. Animals should always be warmed while under general anaesthesia, as they cannot regulate their body temperature. The effect of body temperature on ^{18}F-NA$_3$BF$_3$ distribution is unknown, but animals should be kept at 37 °C for animal welfare.

8. F18-labelled radiotracers have a half-life of 109.7 min, which makes it possible to perform multiple scans in a day if the production yield is good

9. Always be sure to choose an appropriate mouse model for the pathology of interest

10. Dynamic scans are recommended for novel radiotracers as the optimal time with peak uptake will be unknown. A dynamic scan will capture the tracer's entry into the blood stream and biodistribution, as well as clearance (hepatic or urinary).

11. Position the area of interest (e.g., tumor, organ) to the center of the PET camera, where sensitivity and resolution are highest.

References

1. O'Brien PJ, Siraki AG, Shangari N (2005) Aldehyde sources, metabolism, molecular toxicity mechanisms, and possible effects on human health. Crit Rev Toxicol 35:609–662

2. Wood PL, Khan MA, Moskal JR (2007) The concept of "aldehyde load" in neurodegenerative mechanisms: cytotoxicity of the polyamine degradation products hydrogen peroxide, acrolein, 3-aminopropanal, 3-acetamidopropanal and 4-aminobutanal in a retinal ganglion cell line. Brain Res 1145:150–156

3. Antoniak DT, Duryee MJ, Mikuls TR, Thiele GM, Anderson DR (2015) Aldehyde-modified proteins as mediators of early inflammation in atherosclerotic disease. Free Radic Biol Med 89:409–418

4. Burke WJ, Li SW, Chung HD, Ruggiero DA, Kristal BS, Johnson EM, Lampe P, Kumar VB, Franko M, Williams EA, Zahm DS (2004) Neurotoxicity of MAO metabolites of Catecholamine neurotransmitters: role in neurodegenerative diseases. Neurotoxicology 25:101–115

5. Burke WJ, Kumar VB, Pandey N, Panneton WM, Gan Q, Franko MW, O'Dell M, Li SW, Pan Y, Chung HD (2008) Aggregation of alpha-synuclein by DOPAL, the monoamine oxidase metabolite of dopamine. Acta Neuropathol 115:193–203

6. Cristofori L, Tavazzi B, Gambin R, Vagnozzi R, Signoretti S, Amorini AM, Fazzina G, Lazzarino G (2005) Biochemical analysis of the cerebrospinal fluid: evidence for catastrophic energy failure and oxidative damage preceding brain death in severe head injury: a case report. Clin Biochem 38:97–100

7. Chen HH, Waghorn PA, Wei L, Tapias LF, Schühle DT, Rotile NJ, Jones CM, Looby RJ, Zhao G, Elliott JM, Probst CK, Mino-Kenudson M, Lauwers GY, Tager AM, Tanabe KK, Lanuti M, Fuchs BC, Caravan P (2017) Molecular imaging of oxidized collagen quantifies pulmonary and hepatic fibrogenesis. JCI Insight 2:e91506

8. Kirby A, Suchý M, Brouwer A, Shuhendler A (2019) Mapping aldehydic load *in vivo* by positron emission tomography with [^{18}F]NA$_3$BF$_3$. Chem Commun 55:5371–5374

Chapter 12

The Basics of Visualizing, Analyzing, and Reporting Preclinical PET/CT Imaging Data

Christopher J. Cawthorne, Alessia Volpe, and Gilbert O. Fruhwirth

Abstract

Positron emission tomography (PET) has transformed medical imaging, and while first developed and applied to the human setting, it has found widespread application at the preclinical level over the past two decades. Its strength is that it offers noninvasive 3D tomographic imaging in a quantitative manner at very high sensitivity. Paired with the right molecular probes, invaluable insights into physiology and pathophysiology have been accessible and therapeutic development has been enhanced through preclinical PET imaging. PET imaging is now often routinely combined with either computed tomography (CT) or magnetic resonance imaging (MRI) to provide additional anatomical context. All these developments were accompanied by the provision of ever more complex and powerful analysis software enabling users to visualize and quantify signals from PET imaging data. Aside from experimental complexities, there are also various pitfalls in PET image data analysis, which can negatively impact on reporting and reproducibility.

Here, we provide a protocol intended to guide the inexperienced user through PET/CT data analysis. We describe the general principles and workflows required for PET/CT image data visualization and quantitative analysis using various software packages popular in the field. Moreover, we present recommendations for reporting of preclinical PET/CT data including examples of good and poor practice.

Key words AMIDE, Analysis software, Data sharing, Dynamic PET, PET/CT, PMOD, Preclinical PET imaging, Quantification, VivoQuant

1 Introduction

Positron emission tomography (PET) is now an established and invaluable tool for the quantitative assessment of molecular and physiological biomarkers in many different fields, including oncology [1–5], neurology [6–9], cardiology [10–12], and immunology, [13–15] as well as preclinically and clinically. Moreover, the principles of molecular imaging [16] have been applied for noninvasive whole-body tracking of cells using PET-compatible approaches

---

Christopher J. Cawthorne and Gilbert O. Fruhwirth contributed equally with all other contributors.

[17], for example, to quantify cancer cell spread in preclinical tumor models [18, 19] and the in vivo distribution of stem cells [20–23] or to enhance the development of emerging T cell-based therapies [24–31].

PET images can be considered as space and time integrals of exogenously administered radioactive probe distribution in each timeframe, commonly with units of kBq/cm^3 tissue (radioactivity/volume). Such "dynamic" scans provide time-activity concentration curves (TAC) for each individual voxel in a 3D image. The gold standard for PET quantitation is compartmental tracer kinetic modelling. The standard uptake value (SUV, also known as differential uptake ratio) is a frequently used measure indicating high or low tissue uptake of a PET probe, reflecting the concentration of radioactivity corrected for both the administered dose as well as (commonly) the weight of the subject, although other metrics (body surface area, lean body mass) can be used. Although there are no agreed guidelines for preclinical studies, SUV and %ID/g or %ID/mL are the most common metrics reported. As SUV relies on several assumptions that may not be met [32], as well as standardized conditions, the use of tissue ratios (SUVR) can help control for such variation [33].

PET technology requires signal acquisition, image reconstruction, and further processing steps including frequent overlay with images from other modalities (e.g., computed tomography (CT) or magnetic resonance imaging (MRI)) to visualize and interpret the obtained data reliably (for physics and technical aspects we refer to [7, 8]). The standardization of these processes is key to ensure that the obtained data and interpretations thereof are reproducible, reliable, valid, and comparable between studies and institutions. While much progress has been made in clinical PET, which is often performed now in multi-center studies, preclinical standardization lags behind, with animal studies usually performed only by single sites and not validated across facilities. The apparent lack of standardization in preclinical PET imaging affects study designs (e.g., amount and specific molar radioactivity of administered molecular probe, type of anesthetic agent, and depth of animal anesthesia, etc.), image acquisition (e.g., scanner performance, including limits of detection, resolution, noise equivalent count rate (NECR), and calibration thereof), image reconstruction, image processing (e.g., use of different software packages), and image visualization. Notably, there is currently no uniform way for reporting any of the latter in scientific publications. Several initiatives have been formed to tackle these issues in preclinical PET research, including the European Society of Molecular Imaging Standardization of Small Animal Imaging Working Group and the Euro-BioImaging Medical Node Data Management Working Group, with a small consortia also publishing in this area [34, 35].

In this protocol, we provide guidance on how to use the popular and instrument vendor-neutral software analysis platforms VivoQuant, PMOD, and AMIDE to visualize reconstructed PET/CT data and to ensure appropriate reporting in scientific publications. This includes image segmentation for the extraction of quantitative PET data from images. Moreover, we present recommendations for preclinical PET image reporting as well as illustrations of acceptable and, nowadays, unacceptable procedures.

2 Materials

There are several software packages available to visualize PET/CT images. They include the commercial suites VivoQuant, PMOD, MIM, and OsiriX, as well as free software such as AMIDE, 3D Slicer, or the Beth Israel PET/CT Viewer (a FIJI/ImageJ plugin). Here, we focus on three of the most frequently used software packages in preclinical research, VivoQuant, PMOD, and AMIDE (Fig. 1). General principles and workflows are emphasized over detailed specifics, which may change as software is updated.
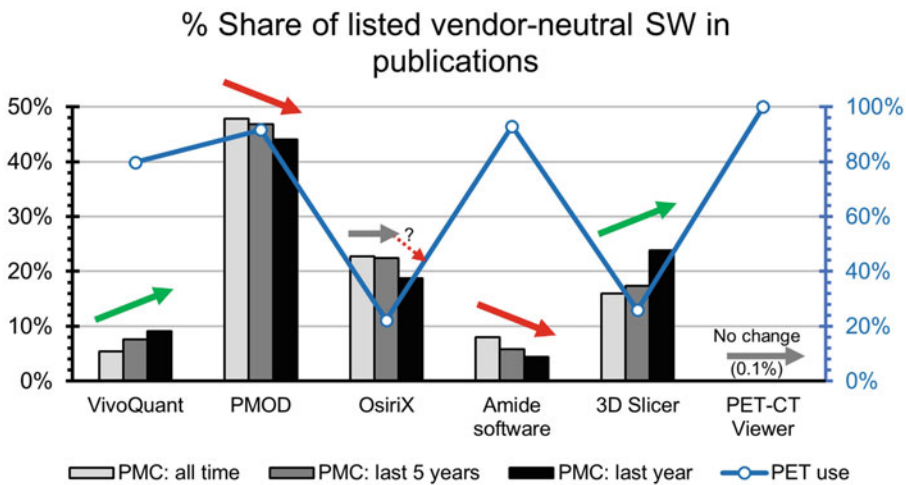
Fig. 1 Usage data for commercial and free image processing and analysis software. Data are derived from the PMC database (*Bars/grey*). Using the search terms "[software] AND [imaging] AND [PET]," the number of publications was extracted from the whole PMC database, publications of the last 5 years, and publications of the last year (search performed on 13 Feb 2021). The share that each software package had in each category as a percentage of the total sum of papers published using these software packages is shown. Arrows indicate if the share of a software package increased, fell, or stayed roughly constant over the years (*Open circles/ blue*). Using the search terms "[software] AND [imaging] AND [PET]," the number of publications was extracted and compared to the number of publications found with the more generic search terms "[software] AND [imaging]," which included all other imaging modalities. The percentage of publications using the shown software is displayed, indicating which software packages were particularly used by the PET, PET/CT, and PET/MRI imaging communities

2.1 VivoQuant
VivoQuant is a commercial postprocessing suite for preclinical images, and its latest release is VivoQuant 2020 (http://www.VivoQuant.com/). It consists of base software with viewing functionality and region of interest analyses, as well as various additional compatible modules, including, for example, a rodent organ atlas. Here, the VivoQuant 2020 version has been used.

2.2 PMOD
PMOD is commercial software and consists of the PBAS basic package, with additional modules available for specialized visualization and analysis. Commonly, PBAS and PFUS are available to allow basic image quantification and coregistration of multimodal datasets, and the workflows described here cover image loading, scaling, coregistration, segmentation, and quantitation. Here, PMOD version 4.2, including the PBAS and PFUS packages, has been used. The PMOD interface does not use the standard filebar/submenu format, but rather there are a few main interface tabs dedicated to particular processing steps, with further tools accessible via a right-hand interface and individual submenus. As such, processing steps are difficult to describe concisely; however, a series of video tutorials for small animal image processing based on PMOD version 4.1 in PBAS and PFUS made by the manufacturer is available on the PMOD website.

2.3 AMIDE
AMIDE is an open-source software and was developed at Stanford University [36] and consists of a single package that enables multimodality image viewing and basic region of interest analyses; although in use at many sites, it is no longer actively maintained or developed.

3 Methods

3.1 Loading Images into VivoQuant and Basic Image Adjustments

1. The [File>Data Browser] menu permits opening imaging data (*see* **Note 1**) from local as well as remote data repositories, such as those stored on acquisition instrument servers (e.g., running Invicro's iPACS software). There are various options to search for data within these repositories, and these include practical features such as place holder characters (e.g., the string *GF* in the fields [Patients Name], [Patient ID], and [Description] preselects data with the character sequence "GF" at any position within these fields), individual dataset selection (select clicking on the arrow, e.g., CT or PET reconstructions separately or combined for overlays), and the option to also append a dataset to already opened data (e.g., add a corresponding CT dataset to an already open PET dataset).

2. The [Tools>Pre-processing] menu enables the setting of desired scale units (see [NM/PT Convert unit] tick box).

Depending on the chosen unit, additional fields for data entry become editable, for example, the fields to enter animal weight and injected dose when converting to SUV scale.

3. Via the menu [Tools], turn on the tabs [View control] to enable manual slice selection with sliders; noting slice numbers defining specific views is recommended. The tab [MIP control] allows adjustment of MIP views and basic visualization toolkit (VTK) functions, and the tab [Data Manager] permits visual adjustment of the scales in individual opened datasets, for example, PET and CT.

4. Each opened dataset is auto-scaled, and a typical example of how a raw PET/CT overlay looks like when a newly acquired dual-mode image is opened is shown in Fig. 2a. Adjust the PET and CT scales taking care that CT signals relevant for anatomical context, the animal bed, and any sensors remain visible with good contrast in the sectional views (*see* Fig. 2b; *see* **Notes 2** and **3**).

5. It is recommended to save the opened session in regular intervals (via [File]>[Session]>[Save]).

3.2 Loading Images into PMOD and Basic Image Adjustments

1. PMOD includes a database functionality where images can be loaded directly, this appears in the [DB Load] tab on the main window, where images can be selected for loading. DICOM data can be loaded via the [DICOM] button at the lower right-hand corner of the [DB Load] tab, while all available image formats can be loaded via the adjacent [AUTODETECT] tab (*see* **Note 1**). In both cases, once selected, the files appear in the [Selected for loading] window and are loaded using the [Open] command. Files are then displayed in the [View] tab (PBAS module) and the [Matching] tab (PFUS module).

2. By default, units are as exported from the scanner. Units can be altered in the [Series Information and Editing Window] if needed; SUV information (isotope, animal weight, injection time and radioactive syringe activities before and after injection) can be added in the [Edit Subject/Study info] tab in this window, allowing the program to calculate SUV. Images can also be converted to SUV scale using the [SUV Image Calculation tool] in the processing tools tab, though here, the ability to display images in both original units (e.g., kBq/cc) and SUV is lost (*see* **Note 4**).

3. Decay correction and unit calibration information can be applied to datasets directly by opening using the [With Operations] button, next to the [Open] command on the [DB Loading] tab and selecting [Normalization] under [Pre-processing Tools] (*see* **Note 5**).
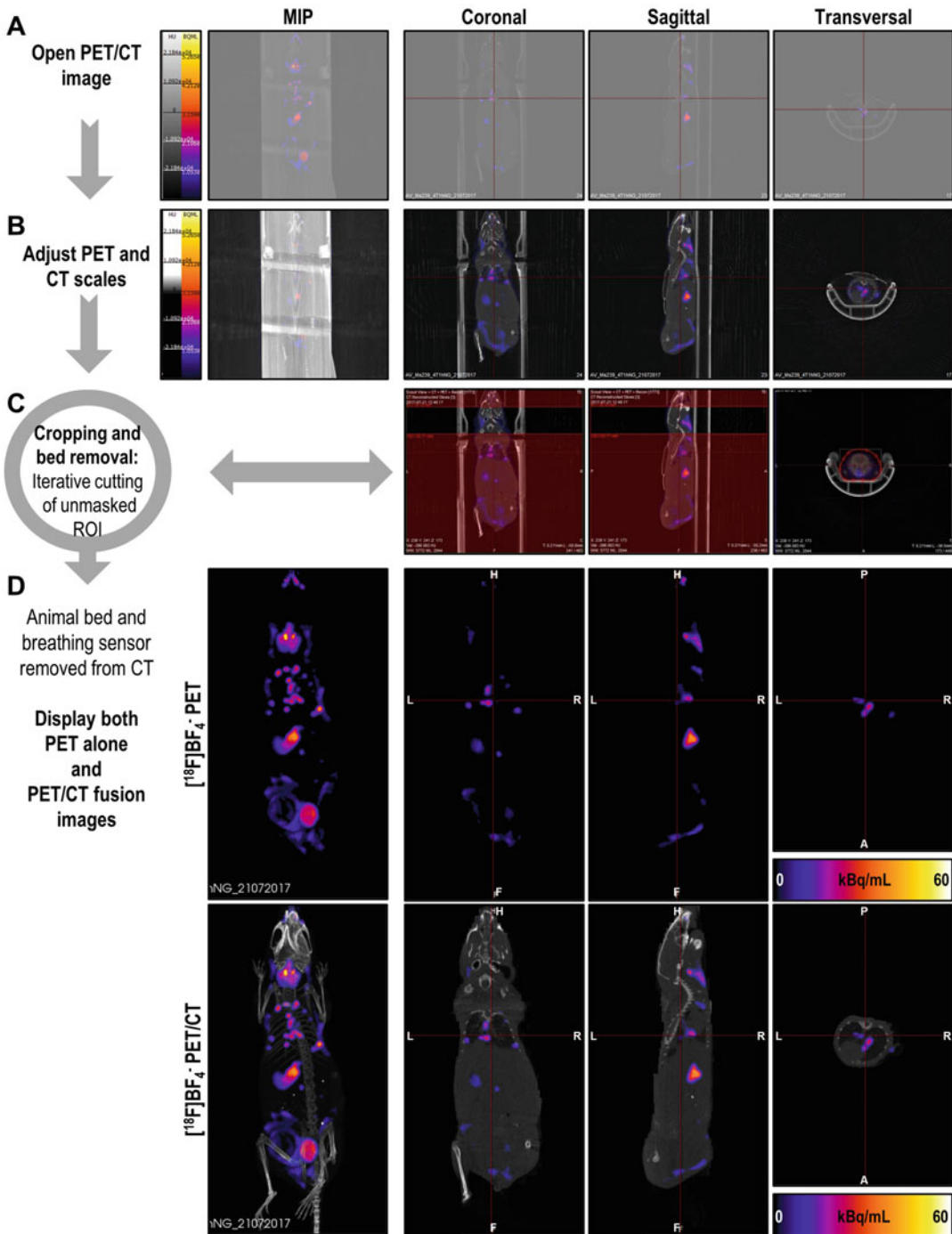
Fig. 2 Basic image processing pipeline for publication quality visualization of preclinical PET/CT data. An example is shown using data from a previously reported non-invasive cancer metastasis tracking experiment [9], in which sodium iodide symporter (NIS)-expressing tumor and metastases were detected alongside endogenously NIS-expressing organs by [^{18}F]BF$_4^-$-PET. (**a**) A PET/CT image in DICOM format was loaded into VivoQuant software, which resulted in auto-scaled images for both PET and CT datasets. After (**b**) CT image scale adjustment, the alignment of PET and CT datasets was confirmed to be sufficient for further processing. (**c**) Removal of the animal support bed and breathing sensor: One iteration of many in a manual process is

4. Slice and frame number are indicated on the upper two sliders in the [General Image Display Control] tab, found on the right-hand side of the main display; information is indicated for the window currently active. The number and type of images displayed can be selected in the adjacent [Display Layouts].

5. Many current instruments provide already decay-corrected data as output. Consequently, care must be taken whether it is appropriate to manually apply decay correction to the datasets.

6. Image scale lookup tables and range can be selected in the [General Image Display Control], with SUV available as an option if the relevant data have been entered. SUV allows consistent scaling within and between studies, while CT windows can be set to standard Hounsfield Unit values (*see* **Note 3**). Scale application to slice/frame/series/user-defined values can be selected via the [Color Table Min/Max].

7. Scales for figure generation can be exported by selecting the [scientific output] option on the [Capture image display] button, found at the lower right-hand corner of the display.

8. Save using the icon on the right-hand toolbar [Save all image results] will save all current image files, transformations, and volume of interest files. For multistep analysis, the workspace can be saved at each stage for easy recall.

3.3 Loading Images into AMIDE and Basic Image Adjustments

1. Files are loaded using [File>Import File (specify)] command, with the datatype for loading being selected.

2. By default, units are as exported from the scanner. Units can be converted to, for example, %ID/g or SUV by right-clicking on the filename in the left-hand window to bring up the [Modification dialog] and entering the required information in the [Basic Info] tab under the [Conversion Type] heading; note that injected dose must reflect activity at the start of the scan period for the data loaded; the cylinder factor is used to convert existing units to those specified in the dropdown menu (*see* **Note 4**).

Fig. 2 (continued) shown with image areas masked (red-shaded) in all sectional images and the areas outside of the mask deleted. (**d**) Resultant images are displayed as *(top)* PET-only data and *(bottom)* appropriate PET/CT fusions. It is good practice to show both panels as the CT can mask some PET signals (*see* Fig. 3). Importantly, an MIP alongside relevant coronal, sagittal, and transversal sections should be shown. A crosshair indicating how the three individual sections fit together should be added. Images must include a scale bar for the PET data, while for CT data, it is not necessary when CT serves only to provide anatomical context (but should be shown if experimentally relevant, for example, when using CT contrast agents). Notably, indicators for orientation are recommended; here they mark (L) left, (R) right, (H) head, (F) foot, (A) anterior, and (P) posterior sides
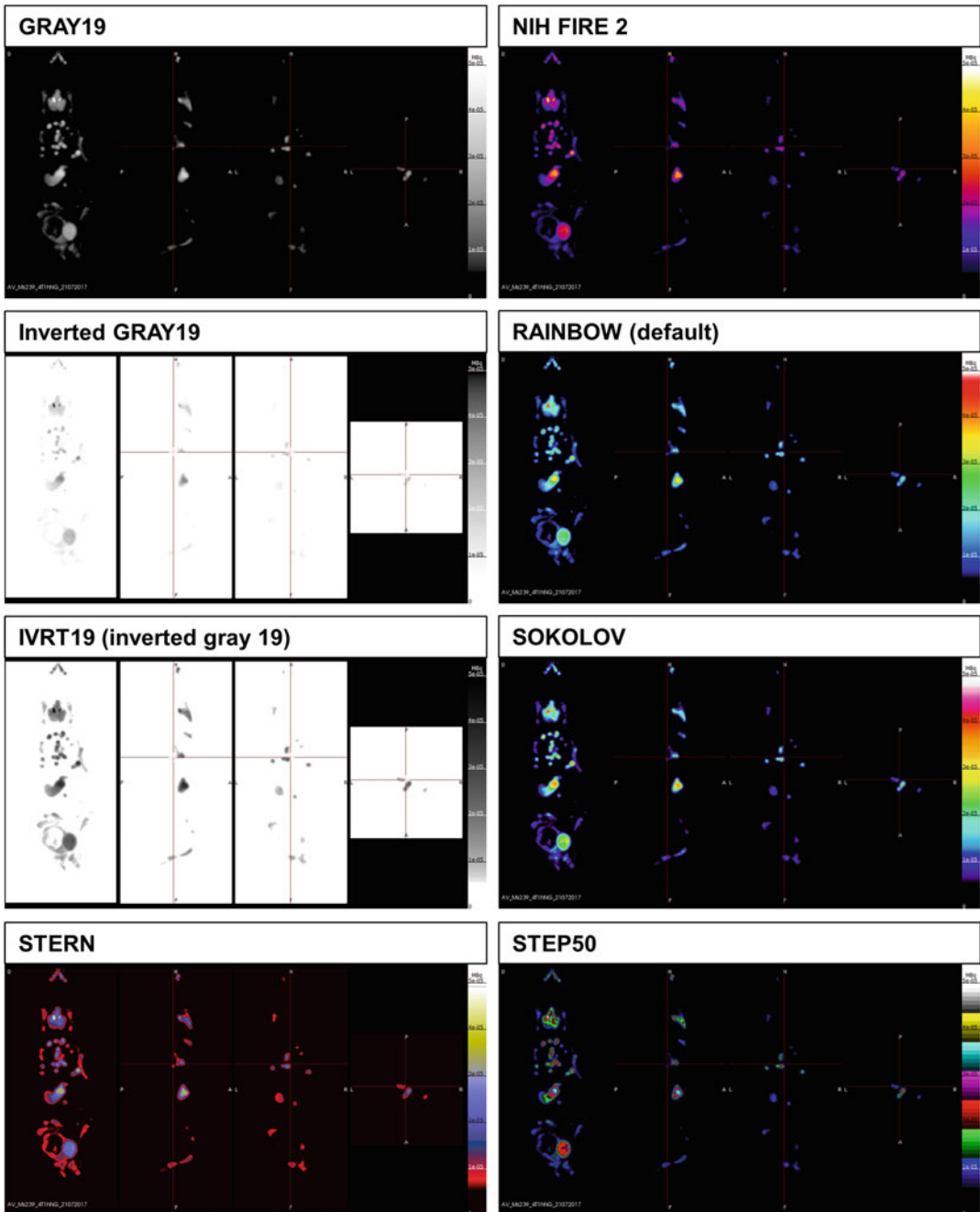
Fig. 3 Impact of different look up tables (LUT) on visualization. PET data from Fig. 2D (upper left-hand panel) are represented using the same scale but different LUTs (as identified). "**GRAY19**' uses bright shades of grey for high signals and dark ones for low signals; this emphasizes high signals but makes low signals difficult to distinguish from one another. "**NIH FIRE 2"** is a LUT with changing colors according to signal levels, which facilitates the differentiation of signal levels compared to "GRAY19" ("NIH FIRE 2" is the standard LUT in VivoQuant for PET data). Rainbow-style LUTs, for example, the default "**RAINBOW**" or "**SOKOLOV,"** remain popular despite being problematic as they result in distorted images as well as images that cannot be accurately interpreted by people with color weaknesses [42]. "**Inverted GRAY19"** is the result of simple scale inversion of "GRAY19," which results in too little contrast. This is caused by most pixel intensities being

3. The current location of the cursor in the x, y, and z planes is indicated in the lower left-hand corner underneath the list of loaded images, while frame number is indicated in the drop-down menu next to [time:] on the far right-hand side of the icon list.

4. Image scale lookup tables, range, and application settings can be selected in the [Colormap/Threshold] tab of the [Modification Dialog], found by right clicking on the dataset.

5. All loaded data can be saved as an AMIDE file (.xif) using [File>Save Study As] command.

3.4 Processing of Combined PET and CT Images in VivoQuant

Coregistration is an optional step for in-line systems and only required if any registration issues are evident. In our example data, there was no need for realignment of datasets, but the procedure is outlined in the following.

1. VivoQuant permits manual as well as automatic realignment of image data via translation, rotation, and flipping. Reference and input data may be changed separately using the [Reorientation/Registration] tool, which is in the [Controls + Operators] toolbar. We recommend saving registration settings locally as they can be useful for applying them to future images in need of realignment.

2. PET and CT voxel sizes differ depending on their acquisition and the voxel size in VivoQuant is set by the first opened "reference" dataset. Automatic coregistration of all opened input datasets to the first opened "reference" dataset is accessible using the Pre-processing tool [Tools>Pre-processing]. If up-/downsampling of one image to match the other for an overlay is required, the Pre-processing tool also permits this alongside specification of the voxel dimensions.

3.5 Processing of Combined PET and CT Images in PMOD

When images are loaded simultaneously, CT and MRI data will be assigned to the reference image.

1. After loading, images can be coregistered in the [Reference and Matching] Tab.

Fig. 3 (continued) represented by shades of grey that differ hardly (cf. concept of gamma in greyscale images [37]). "**IVRT19**" represents a better "inverted" LUT as it aids the recognition of relevant signals and represents the type of LUT used in clinical PET. Notably, detection of signals depends on the LUT used, which is standardized in the clinical setting but not for preclinical experimentation. "**STERN**" is an example of a LUT enabling the appreciation of dim signals as they are presented with high color contrast. This LUT finds utility in thresholding applications. "**STEP50**" is an example for a multicolor multistep LUT and presents data in defined color/saturation bins rather than as a continuum of intensity levels and colors. This can be useful for thresholding applications and illustrating data as contour plots

First, the PET data are manually aligned to the CT/MRI image using the [Manually shift and rotate the input image until it matches the reference image] button, then registration type is selected and activated using the tab above the [Match Current] button (Rigid registration is most applicable for standard coregistration).

2. After coregistration, the transformation matrixes between images can be saved alongside the image for subsequent transformation of re-reconstructed data. For dynamic PET scans, frames can be summed to aid coregistration using the [Avg] tab in the [Tools] Tab.

3. Commonly, the resolution of the CT scanner is higher than that of the PET. To reduce file sizes and the interpolation of PET data, CT images can be downsampled to the resolution of the PET scan using the [Rdc] tab in the [Tools] tab.

3.6 Processing of Combined PET and CT Images in AMIDE

Coregistration is an optional step for in-line systems and only required if any registration issues are evident. In our example data, there was no need for realignment of datasets, but the procedure is outlined in the following.

1. Images can be manually realigned by adjusting the location from the center in each plane using the windows in the [Centre] tab in the [Modification Dialog] window.

2. Alternately, alignment based on fiducial markers can be carried out using [Tools>Alignment wizard].

3.7 Cropping Images in VivoQuant

To further reduce image size, images can be cropped to include only the animal of interest. This is best carried out on the coregistered image (*see* Subheading 3.4).

1. Use the [Cropping] tool, which is in the [Controls + Operators] toolbar.

2. VivoQuant also provides an [Autocrop] function, which is located within the Pre-processing tool; this searches boundaries starting at the end slices and moves toward the center of the dataset until a nonbackground voxel is detected in any of the image faces.

3.8 Cropping Images in PMOD

To further reduce image size, images can be cropped to include only the animal of interest. This is best carried out on the coregistered image (*see* Subheading 3.5).

1. In the [VOI Analysis] tab, a cuboidal VOI on the PET dataset can be created using the [CUBE (Analytic object)] tool and adjusted until the animal is encompassed.

2. The data can then be cropped using the [Crop] tool in the [Data modification] tab, found in the lower right-hand panel; apply this to both images.

3. It is also possible to crop to a cylinder by applying a circular ROI to a slice and clicking "apply to all" in the VOI menu tab, which appears on the right of the VOI list.

4. For multiple animal scans, single animals can be cropped from the main image datasets before checking coregistration and entering SUV information as in Subheading 3.2; they can then be saved as individual coregistered datasets.

3.9   Cropping Images in AMIDE

To further reduce image size, images can be cropped to include only the animal of interest. This is best carried out on the coregistered image (*see* Subheading 3.6).

1. Images can be cropped using the [Tools>Crop Active Data Set] command. Selected images are displayed as MIPs, and a bounding box is defined in each plane by altering the x, y, and z slice numbers indicated (which can also be recorded so bounding boxes can be applied consistently to coregistered datasets).

2. Output datatype can be selected, and the cropped dataset is added to the main data list.

3.10   Removal of the Animal Beds and Sensors from Preclinical PET/CT Images Using VivoQuant

For publication quality images, it is necessary to focus the onlooker's attention onto the relevant image information. Animal beds and any external sensors usually are detected by CT and, hence, need to be removed from these images. Manual bed/sensor removal is the option of choice in most cases, while automatic bed removal is an option if compatible animal beds have been used during image acquisition (e.g., the Minerve beds for mice and rats). Figure 2a–c illustrates the removal of the animal bed as well as the breathing sensor (compare coronal sections between middle and bottom rows).

1. Use the [Cropping] tool, which is in the [Controls + Operators] toolbar, and draw a contour around the animal with either the spline, freehand, or thresholding drawing tools. Red-shaded areas show the selected area (see transversal slice in Fig. 2c).

2. Use the [Cut]>[Outside] tool in the same toolbar to cut voxels outside the contour.

3. Repeat until the animal bed and any sensors are completely removed. Make sure you save repeatedly between cutting steps to be able to return to a partially cut product in case of errors. This is noteworthy as there is no "Undo" function for these steps in VivoQuant.

3.11 Removal of the Animal Beds and Sensors from Preclinical PET/CT Images Using PMOD

1. Go to the [VOI Analysis] tab, and draw a region of interest around the animal using any of the available tools in the left-hand VOI menu.

2. When the VOI is complete, crop the PET and CT images, as described in Subheading 3.8, to remove voxels outside of the VOI. VOIs drawn on each slice should be frequently saved. The [Mask] command can also be used, setting the voxel values outside the VOI to zero rather than deleting them.

3.12 Removal of the Animal Beds and Sensors from Preclinical PET/CT Images Using AMIDE

1. First an ROI is defined using the [Edit>Add ROI] and selecting 2D or 3D freehand or iso-contour. For Iso-contouring, the ROI is named, the threshold defined, the cursor is clicked at the desired starting point, and the desired range is set (voxel values for the current cursor position appear in the lower left-hand corner under the list of loaded images).

2. For manual delineation, the ROI is named and the left mouse button (m1) is used to define the start point. The voxel size is then selected, and the VOI is defined using the mouse, with deletion of selected voxels via right click (m3). ROI drawing mode is exited using the m2 button (wheel click; a 3-button mouse is needed to access these features of the programme). It is worth noting that iso-contouring is difficult to apply to preclinical images due to the lack of space between the bed and the animal, while manual delineation is very time-consuming.

3. When the ROI is complete, voxel values within the ROI can be set to zero using [Control>right click]. This operation is irreversible.

3.13 Reporting Preclinical PET/CT Fusion Images Using VivoQuant

PET signals are not easily attributable to regions of interest without anatomical context. In PET/CT fusion images, quantitative information is contained in the PET image (hue), whereas the CT image (greyscale) provides anatomical context in most cases. Consequently, data visualization requires overlay image. It is, however, highly recommended to show a PET-only image as an additional panel to allow the onlooker to better appreciate the quantitative PET image without potentially distracting CT signals. Ideally, both maximum intensity projections (MIP) and individual slices of areas of interest should be shown (Fig. 2d). A wide variety of different look-up tables (LUT) have been used for PET images (*see* Fig. 3 for selected examples), and it is important that a suitable LUT that avoids data misrepresentation (for details on the impact of the gamma parameter [37]) is used and that the same LUT is used throughout a reported study. The PET image scale should be the same in both the PET and the PET/CT image, while CT images are usually scaled such that the skeleton and body outline are visible
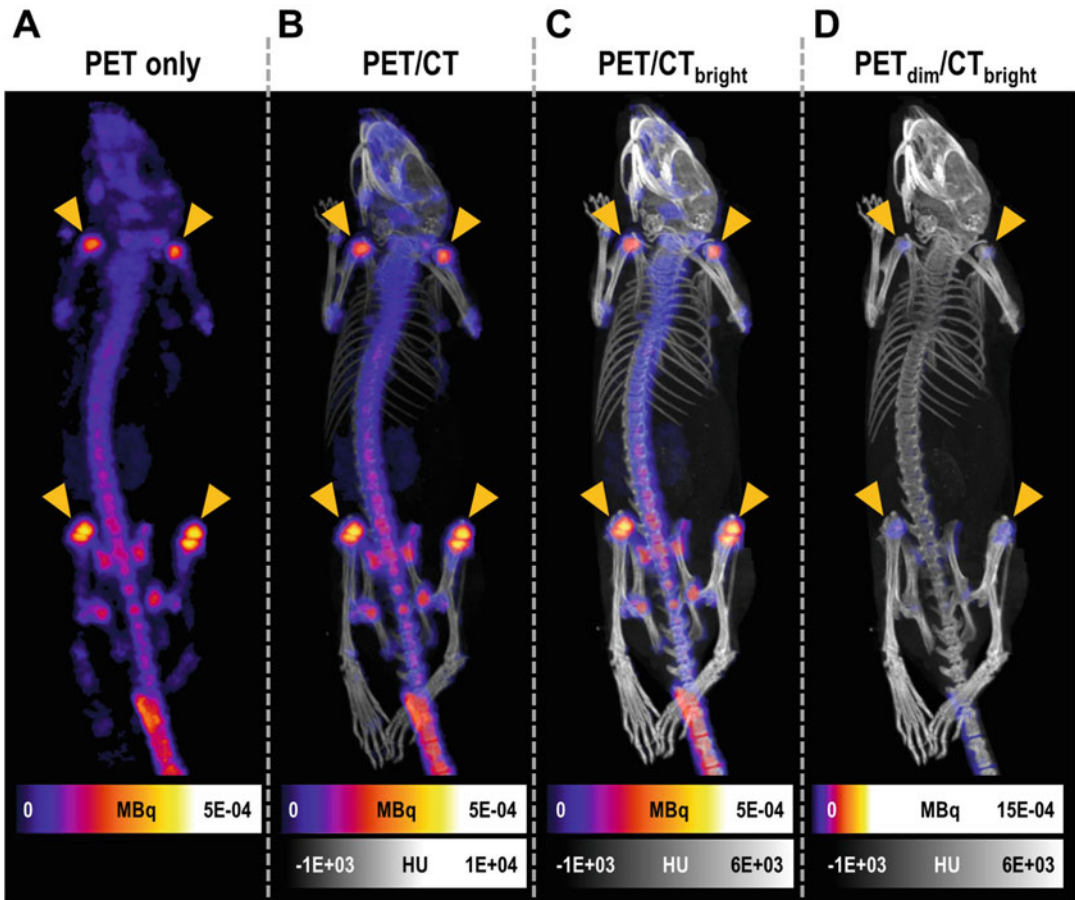
Fig. 4 Impact of scaling individual components in PET/CT fusion images. PET only and various PET/CT fusion overlay images of the same dataset but with differing relative scales for each modality. Data are from a previously reported study using a probe that localizes to the bones [43]. (**a**) The PET-only image provides best visualization of PET signals but lacks anatomical context. (**b**) An appropriate PET/CT overlay in which PET signals remain recognizable in most areas and the CT image provides anatomical context without disturbing PET signal recognition. (**c**) A PET/CT overlay image using a narrower CT scale that results in brighter signals from the skeleton; this results in less recognizable lower bone signals. (**d**) A more extreme scale alteration in which the PET scale was widened resulting in existing signals to be presented dimmer, while the CT scale was kept the same compared to (**c**). Here, the image appears as if there was hardly any bone uptake of the radiotracer despite this being the main target of that radioisotope in this experiment. This illustrates how PET/ CT data could be misrepresented by using inadvertently or deliberately suboptimal image scales; hence, it underlines the need for researchers to provide not only images but also quantitative image analysis data

without generating bright areas in the CT that could interfere with PET signal recognition in the overlays. The latter represent data misrepresentation, and Fig. 4 demonstrates the impact of different relative scales. The PET scale including corresponding units must be added to the presented image, while the CT scale, if just for anatomical context, is frequently omitted.

1. To select a LUT, using the Data Manager [DM] tool, right-click on the shown LUT and select one of the available ones for each dataset. We recommend displaying CT data as greyscale and PET in hue using either "NIH FIRE2" or one of the continuous rainbow LUTs (*see* Figs. 1 and 3).

2. Use the above-described scale adjustment procedure (*see* Subheading 3.1).

3. Use the [File>Save image] export tool to save any individual slice, the MIP, or a combined overview image both. File formats available are png, jpg, bmp, gif, and tif. To coexport the necessary image scales, choose [smart labels] under [colorbar options].

3.14 Reporting Preclinical PET/CT Fusion Images Using PMOD

1. LUTs can be selected in the [General Image Display Control], as described in Subheading 3.13 above; LUT and scale controls are also available in the [MIP] tab. For fused datasets, CT data can be displayed in grayscale, with PET in either "Hot" or "Cold."

2. Use the above-described scale adjustment procedure (*see* Subheading 3.2), scale windows are also available in the [MIP] tab.

3. Displayed images can be exported using the [Capture image display] button found at the lower right-hand corner of the display in each tab; selecting the [scientific output] option includes the current image scale in the exported image.

4. MIP movies (rotating, across timeframes or rotating and across timeframes) can be generated and exported in the dedicated MIP tab using the controls in the lower window to set individual image scales and fusion ratios, as well as movie parameters. MIPs can be saved as Quicktime or MP4 movies.

3.15 Reporting Preclinical PET/CT Fusion Images Using AMIDE

1. LUTs can be selected both using the scale icon on the main icon toolbar or by selecting the [Colormap/Threshold] tab in the [Modification Dialog] window.

2. Coronal, sagittal, and transaxial views can be exported as .jpgs using the [File>Export View] command. MIPs can be generated by altering the thickness sampled in the viewer via the [Thickness] window, with cross sectional pointers expanding to the sampled range so the entire animal can be selected.

3. MIPs can be exported via the [Tools>Generate Flythrough] tool by entering the same location in the dialog box and selecting frames based on frame number or time since the start of acquisition.

3.16 Image Quality Control

Before quantitative analysis of PET data, some image quality control should be performed. For whole body mouse scans, a region of interest encompassing the entire field of view (FOV) can be created using the ROI/VOI tools in VivoQuant/PMOD/AMIDE, respectively. (Such a ROI/VOI can be saved in a convenient location for repeated use.) The total activity in the FOV should be calculated and compared with the actual injected dose the animal received as part of the imaging experiment. Additionally, activity remaining in the tail vein can be assessed (this should be <5%; *see* **Note 6**).

3.17 Image Segmentation for Quantitation in VivoQuant

Outside of the brain, manual delineation of organs/region of interest is in many cases the gold standard; however, automatic segmentation via a range of thresholding techniques is also useful when an organ is sufficiently distinct from its surroundings. Whilst thresholding provides in theory better reproducibility than manual analysis, it is important that the same thresholds are universally applied. Here, we assume that fused images are displayed with the anatomical modality as a reference, such that it can inform the delineation of VOIs.

1. Perform manual delineation of regions of interest using the [3D ROI] tool, accessible via the [Controls + Operators] toolbar. This opens the [Arrow] tab, in which ROIs can be added and deleted and various of their properties set (e.g., ROI colour, name, transparency, and whether they are displayed or hidden). Create an ROI and set its properties.

2. Switch to the [Sphere] tab, in which ROIs can be painted using either "sphere," "cylinder"- or "cube"-style paintbrushes; their size in pixels can be manually set, too. ROIs will be drawn in 3D, extending to multiple slices, unless the [2D mode] is ticked, in which the ROIs are then painted only in one slice. Draw the ROI in each of the available slices.

3. Spline, Freehand, and Bully tools are also available (via the [Spline] tab) for ROI drawing in 2D mode (*see* **Note 7**).

4. Undo/Redo functionality is accessible via the [View>Undo] or [View>Redo] menu (starting with VivoQuant v3.5 and in VivoQuant 2020, which is used here).

5. Alternatively, automatic thresholding algorithms can be used to paint ROIs when switching to the [Magic wand] tab; they include "Global" and "Otsu" thresholding [38], both of which do not requires seeds, as well as "Connected," "Confidence Connected," and "Neighbourhood" thresholding, which require seeds. Use any of these tools to draw the relevant ROIs (*see* **Note 8**).

6. To trigger calculation of quantitative data from ROIs, click on either [Show table] or [Export table] within the [Arrow] tab;
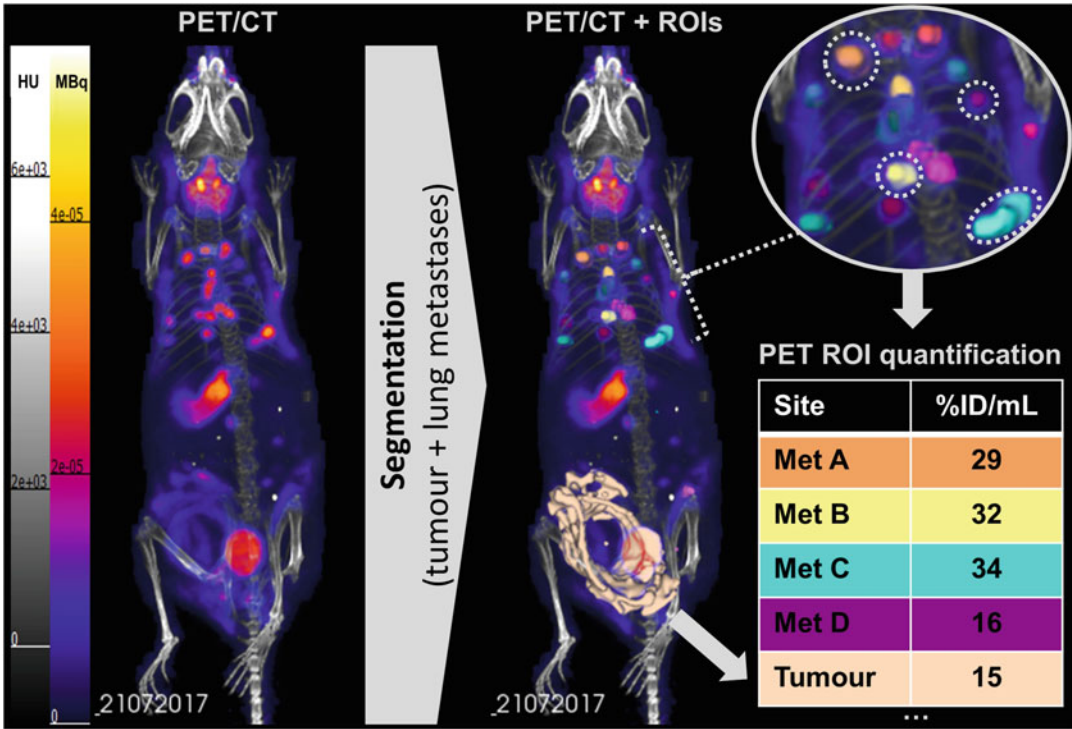
Fig. 5 Workflow for PET signal quantification in ROIs. PET/CT data from Fig. 1 were manually segmented with different ROIs created and individually drawn in VivoQuant's 2D mode in each slice (VivoQuant automatically combined them to volumes of interest). Tissues of interest were the primary tumor (beige) and lung metastases (see inset, each identifiable lesion in a different ROI color). The whole image was calculated and tabulated radioactivity concentrations exported, as described in Methods. Selected ROIs (tumor an encircled metastases) are shown as examples

this will either display or export (csv file format) the results for all ROIs in all overlayed image datasets with export configurable for a variety of relevant read-out parameters. A brief workflow example is shown in Fig. 5 illustrating the PET/CT MIP without and with ROIs drawn, as well as selected examples of ROI quantitation from the shown images.

3.18 Image Segmentation for Quantitation in PMOD PBAS/PFUS

1. Manual delineation of the organ is performed in the [VOI Analysis] tab. Individual contours created on an image slice are linked to give a region of interest, and regions of interest in a slice are linked to give the final volume of interest. Contours can be created manually using the polygon or paint tools and edited with the [eraser] or [bully] tool until the shape is correct in each cross-sectional view displayed in the main window.

2. Further VOI operations (e.g., Union and Intersection) can be implemented in the [Group] tab of the VOI list window (*see* **Note 8**).

3. Importantly, VOI overlap can be set in the [Classification modes, overlap modes, etc.] tab in the lower right-hand window, allowing the user to choose whether new VOIs can include voxels previously assigned to other VOIs. Create contours using either the [Point-to-point vertex] tool or the [Paint] tool. Edit, if necessary, using [Eraser] or [Bully] tools until the volume of interest is correct (*see* **Note 8**).

4. A range of thresholding techniques can be applied to the image using the iso-contouring tools selectable on the left of the VOI list window. 2D and 3D iso-contouring via interactive region growing is available via dedicated buttons, while further contouring options are directly selectable in the [Iso-contouring via region growing] button. Using this control, it is possible to apply user-defined thresholds to previously defined VOIs; in this way, SUV_{peak} metrics can be derived from manually segmented tumors. It is important to apply thresholds consistently across datasets for accurate comparison.

5. VOIs can be quantified using the [Selected Statistics] tab under the graph icon above the main VOI list panel. Selected statistics are chosen from the available list by clicking the adjacent [Select Statistics to be calculated] table A list of the VOI TACs is then presented under the [VOI Statistics] tab, with statistics selected for display in the right-hand window. Selected statistics can be copied to the clipboard or exported as a statistics file that can be exported into, for example, Microsoft Excel for further analysis. Units can also be selected using the [Data Unit] buttons at the top of the window.

3.19 Image Segmentation for Quantitation in AMIDE

1. ROIs are created using the [Edit>Add ROI] dialog described for bed removal in Subheading 3.12.

2. *See* Subheading 3.12 for thresholding techniques for VOI generation. Thresholding and iso-contouring tools are available.

3. ROIs can be quantified using the [Tools>Calculate ROI statistics] command. By default, selected ROIs are applied to selected images, but this is adjustable in the dialog. Results can be copied to the clipboard, or the raw data can be exported directly.

3.20 Double-Check Correct Use of the ROI/ VOI Tools to Avoid Illicit Image Manipulation

ROI/VOI tools are powerful and a prerequisite for image quantification in PET. It is noteworthy, however, that these ROI/VOI tools also empower the user to much more than quantification of a region; they enable the tempted user to treat the selected regions in a different manner compared to other parts of the image. Such unequal treatment of different parts of the same dataset simply constitutes an illicit image manipulation [39, 37]. Among several possible image manipulations accessible through these tools is, for

example, the removal of selected signals from, for example, the PET image. We performed such a procedure to demonstrate how this leads to false interpretations because of image misrepresentation (Fig. 6). As PET data are quantitative, every effort should be made to provide quantitative organ data in addition to the images.

We encourage peer-reviewers to: (i) ask for PET only images alongside fused PET/CT images; (ii) check provided images for image manipulations (e.g., through contrast enhancements or applying appropriate color deconvolution algorithms, such as those available in the free ImageJ software package); and (iii) ask authors for quantitative results rather than be satisfied merely with individual images. If there are space concerns raised, these necessary data can in most journals be deposited as supplemental data.

3.21 Visualization and Quantitation of Dynamic PET/CT Scans in VivoQuant

For quantitative PET and to better assess the biodistribution of novel PET probes over time, dynamic scanning is performed.

1. Dynamic images are loaded as in Subheading 3.1.

2. *See* above Subheading 3.17 for details on segmentations.

3. Dynamic PET images are first rebinned and reconstructed into a desired series of frames. Use the [Time Series] operator to visualize sets of dynamic scans by playing slice views of each image in sequence and navigate there.

4. Right-click on the activity in the ROI quantification table generated following Subheading 3.17, and select the [Plot data] option in the dropdown menu; the software then generates the corresponding time-activity curves (*see* **Note 9**).

3.22 Visualization and Quantitation of Dynamic PET/CT Scans in PMOD/PFUS

Loading of dynamic PET/CT data is essentially the same compared to static images in PMOD, with individual PET frames accessed via the main menu by default.

1. Dynamic PET data are loaded in the same way as static data (*see* Subheading 3.2). For dynamic data, the [Frame] button and scalebar become active in the [General Image Display Control] tab and individual frames can be selected for display. Frame information can be found in the [Edit frame time] tab of the [Series Information and Editing Window] window.

2. Using the [Frame] tab, images can be inspected to detect motion that occurred during the scan period. If this is absent, images can be summed using the [Avg] button on the tools tab.

3. For co-registration, the entire image can be summed as early timeframes provide images more dominated by blood flow and, thus, more information for accurate coregistration; this can also inform segmentation.
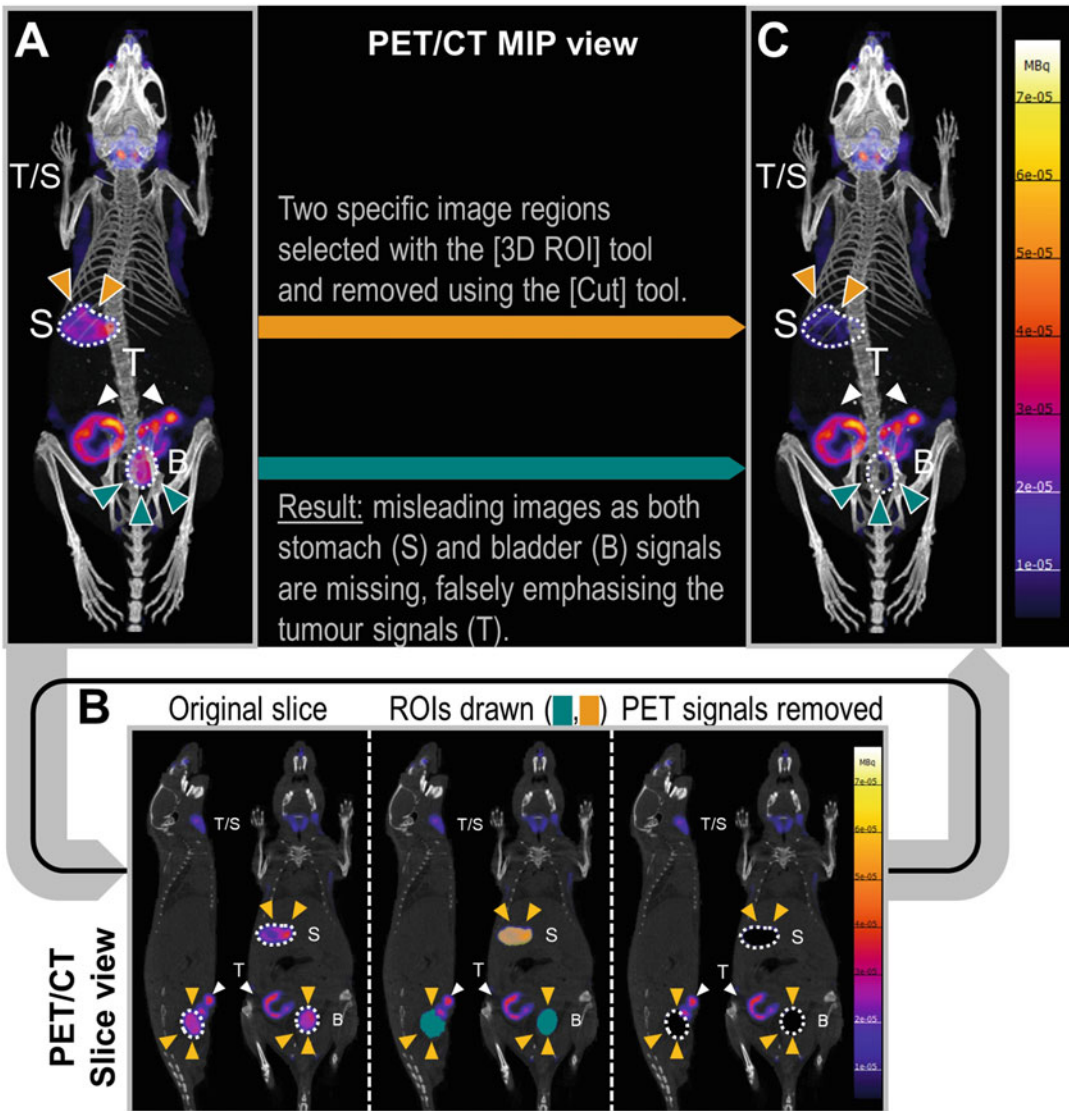
Fig. 6 Example of data misrepresentation by removal of distinct signals. This example demonstrates how straightforward it is using software packages as the described ones to define ROI/VOI and remove signals from images. This constitutes data misrepresentation as not all areas of an image are treated in the same way [37, 39]. Here, cancer cells expressing the radionuclide reporter NIS were tracked by $[^{18}F]BF_4^-$ -PET. (**a**) Visible signals are from organs with endogenous NIS expression (T/S: thyroid and salivary glands; S: stomach), radiotracer excretion (B: bladder), and the in vivo traceable NIS-expressing cancer cells. As it might be not important for the cancer cell tracking experiment to visualize stomach and bladder, (**b**) one might be tempted to remove these signals for better visualization of the cancer cells, generating images like in (**c**) depicting what is deemed experimentally relevant only and omitting other organs that perhaps are irrelevant for the study. Nevertheless, this misrepresents the image and misleads the observer; here, to think the cancer cells take a larger share of the administered radiotracer or to think that images were much "cleaner." In the opinion of the authors, this is unacceptable practice even when mentioned in the figure caption and should be avoided at all costs
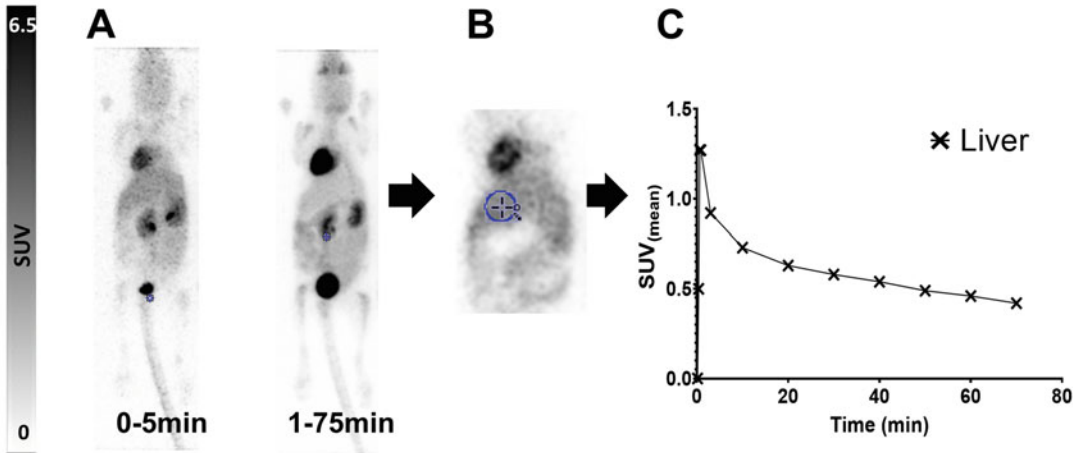
Fig. 7 Summing dynamic data to emphasize blood pool for organ VOI definition. 75-min dynamic [^{18}F]-FDG PET images of a healthy naïve mouse were summed (**a**) between 0 and 5 min and 5 and 75 min. The liver is clearly recognizable in the early summed image. (**b**) This enabled a spherical VOI (blue circle) to be placed within the liver to (**c**) generate a reference Time Activity Curve. Summed images can also aid with coregistration, especially for images acquired on separate instruments

4. Dynamic images are segmented using the same tools described in Subheading 3.18. VOIs can be drawn on individual frames and then applied to all frames using the [Apply to all] button in the VOI menu, or on a summed image for later application to the dynamic dataset; the choice of method depends on the nature of the volume of interest.

5. For illustration of dynamic PET data, a series of slices can be presented over time using the [Image Display Layout Configuration] subtab of the image display layouts tab (Fig. 7).

6. More usefully, MIPs can also be displayed in this window using the [3D] tab; however, the LUT scale must be adjusted to give the correct SUV range for each timeframe (Fig. 8).

7. In addition, MIP movies representing the time course of activity in the animal overlaid onto the anatomical reference can be created in the MIP processing tab, commonly uploaded to supplementary information.

8. Generation of TACs from dynamic data is essentially the same as for static images described in Subheading 3.18; a graph of the VOI TACs rather than a list is then presented under the [VOI Statistics] tab, with statistics selected for display in the right-hand window. Selected statistics can be copied to the clipboard or exported as a statistics file as previously described.
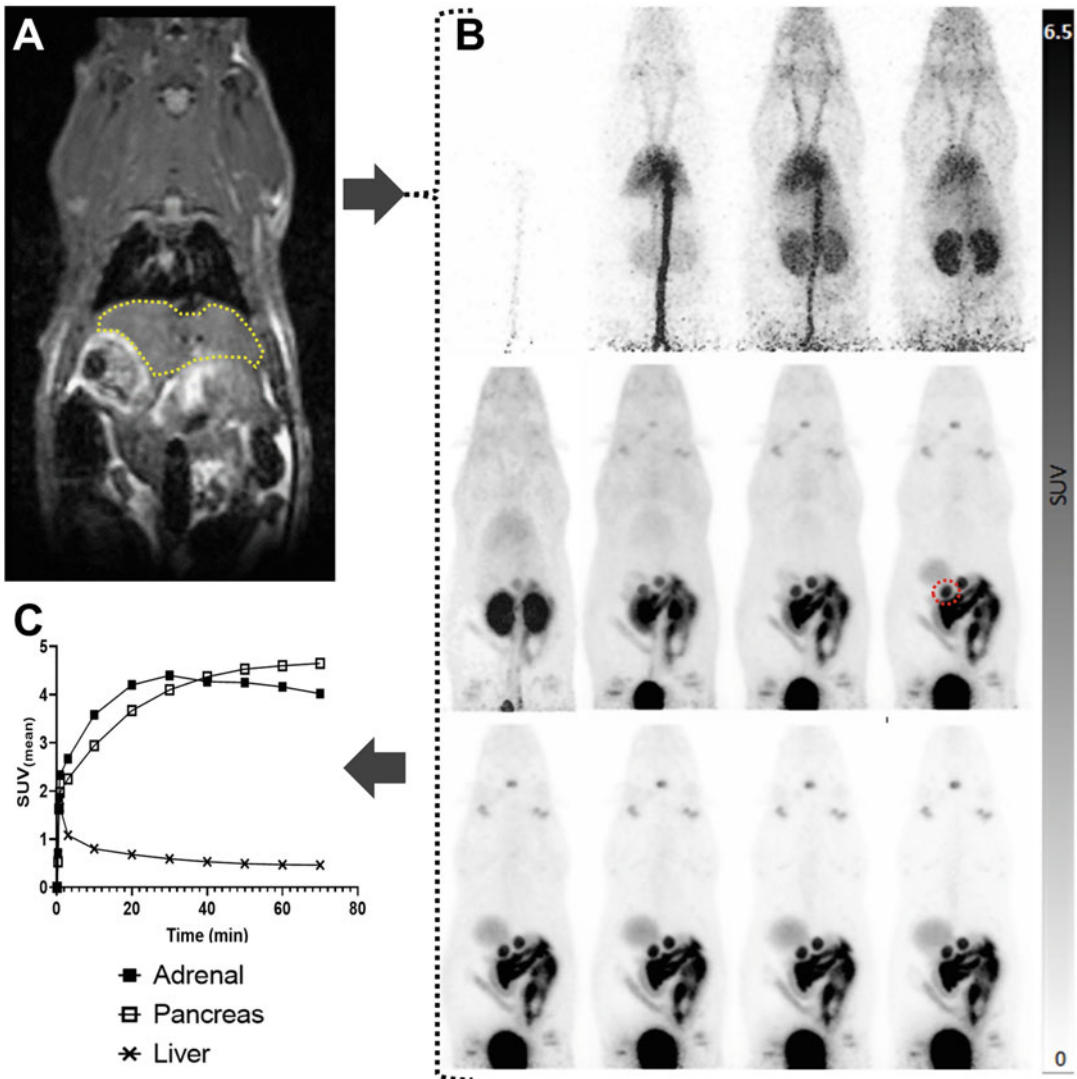
Fig. 8 Workflow for the generation of Time Activity Curves (TAC). (**a**) Organs were manually segmented on the MRI image to create VOIs (e.g., liver illustrated by the yellow-dotted line), which were then in (**b**) applied to a simultaneously acquired PET dataset (e.g., one adrenal gland within the red dotted circle). (**c**) TACs for each organ were generated in the [Statistics tab] of PMOD and graphed using GraphPad Prism

3.23 Visualization and Quantitation of Dynamic PET/CT Scans in AMIDE	Time series of slices can be visualized and analyzed using AMIDE [40]; however, the process is elaborate and not user-friendly. Hence, we do not recommend using AMIDE for this type of analysis.
3.24 Saving/ Exporting Data for Community Sharing Using VivoQuant	The universal file format and protocol for medical imaging data is DICOM (Digital Imaging and Communication in Medicine; *. dcm). This format satisfies the need of a standardized format for transferring and reading medical images, granting access to the data

from any DICOM-compliant device, regardless of the medical system used. DICOM files contain all necessary metadata and can be transferred, loaded, and read fast across different platforms, including all image analysis software described here.

Export data via [File]>[Save data]>[DICOM] or [File]>[Save data]>[Raw] to produce platform independent datasets. We recommend using the DICOM format.

3.25 Saving/ Exporting Data for Community Sharing Using PMOD

Image data can be exported in several image formats using the [Open Dialog Window for Saving Images] menu found under the disk icon on the right-hand tab presented in all windows (*see* **Note 10**).

3.26 Saving/ Exporting Data for Community Sharing Using AMIDE

Image data can be exported in a range of common datasets using the [File>Export Dataset] command.

4 Notes

1. VivoQuant can handle multiple file formats, including DICOM (dcm, dicom), TRaster (ras, res., bin), RAW (raw, zraw), conventional image formats (png, tif, tiff, jpg, jpeg, bmp), plus some more less common ones (img, nii, mhd, mha, fdf, dc3, vol). Notably, VivoQuant also provides the user with a dedicated file format to save the session, that is, the current workspace, including visualization settings, etc. (zipacs). PMOD can handle multiple file formats, and loading via Autodetect can be used in all cases. The main disadvantage of this method is it relies on an intelligible and unchanging file structure, which is handled automatically if the database functionality is used. Use of standard orientation relies on correct position encoding in the input file. If needed, orientation can be adjusted using the information/Edit Subject/Study info/ Subject position tab by selecting the species and correct orientation; orientation markers (e.g., H/F, A/P, and L/R for bipeds; CR/CA, D/V, and LE/RT for quadrupeds) should then be checked in the main study tab. This is especially important for coregistering subjects acquired on separate instruments.

2. Scale adjustment for slices results in unsightly MIPs prior to animal bed removal unless the VTK viewer settings are additionally changed separately.

3. Scaling for CT images will depend on the region of interest to be segmented, with a range typically between −1000 and 3500

Hounsfield Units (HU). For presentation of PET-CT as MIP images, CT images are usually scaled so that the skeleton and body outline are visible.

4. Best practice is to separately calculate injected doses in Excel, such that entries in PMOD can be checked and any issues pertaining to scanner export conventions can be identified. Moreover, check FOV region for ID.

5. Best practice is to keep radiotracer injection records that also include a "traffic light" system to indicate whether the injection was successful, that is, no or only very minor amounts of paravenous leakage observed around the intravenous administration site. Including a small series of Eppendorfs containing a dilution series of the tracer in a standard volume in the FOV allows absolute quantitation to be easily assessed.

6. Rough surfaces from manually created 3D ROIs can be smoothed using the low-pass filter provided. The [3D ROI/2D mode] tool matches the one available within the [Quantification ++] tool of earlier VivoQuant versions.

7. CT does not provide sufficient contrast to segment all organs in the preclinical setting. For the liver, a small sphere can be placed in the left lobe to provide an average value. In dynamic PET studies, it is often possible to segment the left ventricle of the heart or the vena cava from early images and so derive a measure of blood activity; however, this will be affected by both partial volume effect [41] and spill-out/spill-in depending on the radiotracer used. VOIs can also be placed in the thigh muscle.

8. This function can also be applied to study multiple serial scans.

9. This allows saving files in formats suitable for specific imaging analysis programmes, for example, Nifti, Analyze, or interfile. Transfer syntax is also selectable, with FLOAT format data being the most accurate.

References

1. Mankoff DA, Farwell MD, Clark AS, Pryma DA (2017) Making molecular imaging a clinical tool for precision oncology: a review. JAMA Oncol 3(5):695–701. https://doi.org/10.1001/jamaoncol.2016.5084

2. Schwartz LH, Litiere S, de Vries E, Ford R, Gwyther S, Mandrekar S, Shankar L, Bogaerts J, Chen A, Dancey J, Hayes W, Hodi FS, Hoekstra OS, Huang EP, Lin N, Liu Y, Therasse P, Wolchok JD, Seymour L (2016) RECIST 1.1-Update and clarification: from the RECIST committee. Eur J Cancer 62:132–137. https://doi.org/10.1016/j.ejca.2016.03.081

3. Seymour L, Bogaerts J, Perrone A, Ford R, Schwartz LH, Mandrekar S, Lin NU, Litiere S, Dancey J, Chen A, Hodi FS, Therasse P, Hoekstra OS, Shankar LK, Wolchok JD, Ballinger M, Caramella C, de Vries EGE, group Rw (2017) iRECIST: guidelines for response criteria for use in trials testing immunotherapeutics. Lancet Oncol 18(3):e143–e152. https://doi.org/10.1016/S1470-2045(17)30074-8

4. Kircher MF, Hricak H, Larson SM (2012) Molecular imaging for personalized cancer care. Mol Oncol 6(2):182–195. https://doi.org/10.1016/j.molonc.2012.02.005

5. Krekorian M, Fruhwirth GO, Srinivas M, Figdor CG, Heskamp S, Witney TH, Aarntzen E (2019) Imaging of T-cells and their responses during anti-cancer immunotherapy. Theranostics 9(25):7924–7947. https://doi.org/10.7150/thno.37924

6. Beaurain M, Salabert AS, Ribeiro MJ, Arlicot N, Damier P, Le Jeune F, Demonet JF, Payoux P (2019) Innovative molecular imaging for clinical research, therapeutic stratification, and nosography in neuroscience. Front Med (Lausanne) 6:268. https://doi.org/10.3389/fmed.2019.00268

7. Kreisl WC, Kim MJ, Coughlin JM, Henter ID, Owen DR, Innis RB (2020) PET imaging of neuroinflammation in neurological disorders. Lancet Neurol 19(11):940–950. https://doi.org/10.1016/S1474-4422(20)30346-X

8. Henriksen G, Drzezga A (2011) Imaging in neurology research II: PET imaging of CNS disorders. In: Kiessling F, Pichler BJ (eds) Small animal imaging: basics and practical guide. Springer, Berlin, Heidelberg, pp 499–513. https://doi.org/10.1007/978-3-642-12945-2_33

9. Schiffer WK (2011) Imaging in neurology research III: focus on neurotransmitter imaging. In: Kiessling F, Pichler BJ (eds) Small animal imaging: basics and practical guide. Springer, Berlin Heidelberg, pp 515–541. https://doi.org/10.1007/978-3-642-12945-2_34

10. Chen IY, Wu JC (2011) Cardiovascular molecular imaging: focus on clinical translation. Circulation 123(4):425–443. https://doi.org/10.1161/CIRCULATIONAHA.109.916338

11. Bengel FM (2005) Noninvasive imaging of cardiac gene expression and its future implications for molecular therapy. Mol Imaging Biol 7(1):22–29. https://doi.org/10.1007/s11307-005-0923-1

12. Farber G, Boczar KE, Wiefels CC, Zelt JGE, Guler EC, deKemp RA, Beanlands RS, Rotstein BH (2020) The future of cardiac molecular imaging. Semin Nucl Med 50(4):367–385. https://doi.org/10.1053/j.semnuclmed.2020.02.005

13. McCarthy CE, White JM, Viola NT, Gibson HM (2020) In vivo imaging technologies to monitor the immune system. Front Immunol 11:1067. https://doi.org/10.3389/fimmu.2020.01067

14. Signore A, Anzola KL, Auletta S, Varani M, Petitti A, Pacilio M, Galli F, Lauri C (2018) Current status of molecular imaging in inflammatory and autoimmune disorders. Curr Pharm Des 24(7):743–753. https://doi.org/10.2174/1381612824666180130115153

15. Lee JT, Nair-Gill ED, Rabinovich BA, Radu CG, Witte ON (2011) Imaging in immunology research. In: Kiessling F, Pichler BJ (eds) Small animal imaging: basics and practical guide. Springer, Berlin Heidelberg, pp 565–583. https://doi.org/10.1007/978-3-642-12945-2_36

16. Mankoff DA (2007) A definition of molecular imaging. J Nucl Med 48(6):18N, 21N

17. Iafrate M, Fruhwirth GO (2020) How non-invasive in vivo cell tracking supports the development and translation of cancer immunotherapies. Front Physiol 11(154). https://doi.org/10.3389/fphys.2020.00154

18. Diocou S, Volpe A, Jauregui-Osoro M, Boudjemeline M, Chuamsaamarkkee K, Man F, Blower PJ, Ng T, Mullen GED, Fruhwirth GO (2017) [(18)F]tetrafluoroborate-PET/CT enables sensitive tumor and metastasis in vivo imaging in a sodium iodide symporter-expressing tumor model. Sci Rep 7(1):946. https://doi.org/10.1038/s41598-017-01044-4

19. Maiques O, Fanshawe B, Crosas-Molist E, Rodriguez-Hernandez I, Volpe A, Cantelli G, Boehme L, Orgaz JL, Mardakheh FK, Sanz-Moreno V, Fruhwirth GO (2021) A preclinical pipeline to evaluate migrastatics as therapeutic agents in metastatic melanoma. Br J Cancer 125(5):699–713. https://doi.org/10.1038/s41416-021-01442-6

20. Merron A, Peerlinck I, Martin-Duque P, Burnet J, Quintanilla M, Mather S, Hingorani M, Harrington K, Iggo R, Vassaux G (2007) SPECT/CT imaging of oncolytic adenovirus propagation in tumours in vivo using the Na/I symporter as a reporter gene. Gene Ther 14(24):1731–1738. https://doi.org/10.1038/sj.gt.3303043

21. Ashmore-Harris C, Blackford SJ, Grimsdell B, Kurtys E, Glatz MC, Rashid TS, Fruhwirth GO (2019) Reporter gene-engineering of human induced pluripotent stem cells during differentiation renders in vivo traceable hepatocyte-like cells accessible. Stem Cell Res 41:101599. https://doi.org/10.1016/j.scr.2019.101599

22. Terrovitis J, Kwok KF, Lautamaki R, Engles JM, Barth AS, Kizana E, Miake J, Leppo MK, Fox J, Seidel J, Pomper M, Wahl RL, Tsui B, Bengel F, Marban E, Abraham MR (2008) Ectopic expression of the sodium-iodide symporter enables imaging of transplanted cardiac stem cells in vivo by single-photon emission computed tomography or positron emission tomography. J Am Coll Cardiol 52(20):1652–1660. https://doi.org/10.1016/j.jacc.2008.06.051

23. Hung SC, Deng WP, Yang WK, Liu RS, Lee CC, Su TC, Lin RJ, Yang DM, Chang CW, Chen WH, Wei HJ, Gelovani JG (2005) Mesenchymal stem cell targeting of microscopic tumors and tumor stroma development monitored by noninvasive in vivo positron emission tomography imaging. Clin Cancer Res 11(21):7749–7756. https://doi.org/10.1158/1078-0432.CCR-05-0876

24. Ashmore-Harris C, Iafrate M, Saleem A, Fruhwirth GO (2020) Non-invasive reporter gene imaging of cell therapies, including T cells and stem cells. Mol Ther 28(6):1392–1416. https://doi.org/10.1016/j.ymthe.2020.03.016

25. Minn I, Huss DJ, Ahn HH, Chinn TM, Park A, Jones J, Brummet M, Rowe SP, Sysa-Shah P, Du Y, Levitsky HI, Pomper MG (2019) Imaging CAR T cell therapy with PSMA-targeted positron emission tomography. Sci Adv 5 (7):eaaw5096. https://doi.org/10.1126/sciadv.aaw5096

26. Volpe A, Lang C, Lim L, Man F, Kurtys E, Ashmore-Harris C, Johnson P, Skourti E, de Rosales RTM, Fruhwirth GO (2020) Spatiotemporal PET imaging reveals differences in CAR-T tumor retention in triple-negative breast cancer models. Mol Ther 28(10):2271–2285. https://doi.org/10.1016/j.ymthe.2020.06.028

27. Jacob J, Nadkarni S, Volpe A, Peng Q, Tung SL, Hannen RF, Mohseni YR, Scotta C, Marelli-Berg FM, Lechler RI, Smyth LA, Fruhwirth GO, Lombardi G (2021) Spatiotemporal in vivo tracking of polyclonal human regulatory T cells (Tregs) reveals a role for innate immune cells in Treg transplant recruitment. Mol Ther Methods Clin Dev 20:324–336. https://doi.org/10.1016/j.omtm.2020.12.003

28. Keu KV, Witney TH, Yaghoubi S, Rosenberg J, Kurien A, Magnusson R, Williams J, Habte F, Wagner JR, Forman S, Brown C, Allen-Auerbach M, Czernin J, Tang W, Jensen MC, Badie B, Gambhir SS (2017) Reporter gene imaging of targeted T cell immunotherapy in recurrent glioma. Sci Transl Med 9(373). https://doi.org/10.1126/scitranslmed.aag2196

29. Weist MR, Starr R, Aguilar B, Chea J, Miles JK, Poku E, Gerdts E, Yang X, Priceman SJ, Forman SJ, Colcher D, Brown CE, Shively JE (2018) PET of adoptively transferred Chimeric antigen receptor T cells with (89)Zr-Oxine. J Nucl Med 59(10):1531–1537. https://doi.org/10.2967/jnumed.117.206714

30. Man F, Lim L, Volpe A, Gabizon A, Shmeeda H, Draper B, Parente-Pereira AC, Maher J, Blower PJ, Fruhwirth GO, R TMdR (2019) In vivo PET tracking of (89)Zr-labeled Vgamma9Vdelta2 T cells to Mouse Xenograft breast tumors activated with liposomal alendronate. Mol Ther 27(1):219–229. https://doi.org/10.1016/j.ymthe.2018.10.006

31. Jacob J, Volpe A, Peng Q, Lechler RI, Smyth LA, Lombardi G, Fruhwirth GO. Radiolabelling of Polyclonally Expanded

Human Regulatory T Cells (Treg) with 89Zr-oxine for Medium-Term In Vivo Cell Tracking Molecules 2023; 28:1482 https://doi.org/10.3390/molecules28031482

32. Huang SC (2000) Anatomy of SUV. Standardized uptake value. Nucl Med Biol 27(7):643–646. https://doi.org/10.1016/s0969-8051(00)00155-4

33. McCluskey SP, Plisson C, Rabiner EA, Howes O (2020) Advances in CNS PET: the state-of-the-art for new imaging targets for pathophysiology and drug development. Eur J Nucl Med Mol Imaging 47(2):451–489. https://doi.org/10.1007/s00259-019-04488-0

34. McDougald W, Vanhove C, Lehnert A, Lewellen B, Wright J, Mingarelli M, Corral CA, Schneider JE, Plein S, Newby DE, Welch A, Miyaoka R, Vandenberghe S, Tavares AAS (2020) Standardization of preclinical PET/CT imaging to improve quantitative accuracy, precision, and reproducibility: a multicenter study. J Nucl Med 61(3):461–468. https://doi.org/10.2967/jnumed.119.231308

35. Mannheim JG, Mamach M, Reder S, Traxl A, Mucha N, Disselhorst JA, Mittelhauser M, Kuntner C, Thackeray JT, Ziegler S, Wanek T, Bankstahl JP, Pichler BJ (2019) Reproducibility and comparability of preclinical PET imaging data: a multicenter small-animal PET study. J Nucl Med 60(10):1483–1491. https://doi.org/10.2967/jnumed.118.221994

36. Loening AM, Gambhir SS (2003) AMIDE: a free software tool for multimodality medical image analysis. Mol Imaging 2(3):131–137. https://doi.org/10.1162/153535003322556877

37. Cromey DW (2010) Avoiding twisted pixels: ethical guidelines for the appropriate use and manipulation of scientific digital images. Sci Eng Ethics 16(4):639–667. https://doi.org/10.1007/s11948-010-9201-y

38. Otsu N (1979) A threshold selection method from gray-level histograms. IEEE Trans Syst Man Cybern 9(1):62–66. https://doi.org/10.1109/tsmc.1979.4310076

39. Rossner M, Yamada KM (2004) What's in a picture? The temptation of image manipulation. J Cell Biol 166(1):11–15. https://doi.org/10.1083/jcb.200406019

40. Mirrione MM, Ruth N, Alexoff D, Logan J, Fowler J, Kernan M (2014) Positron Emission Tomography (PET) and graphical kinetic data analysis of the Dopamine neurotransmitter system: an exercise for an undergraduate laboratory course. J Undergrad Neurosci Educ 12(2):A114–A122

41. Soret M, Bacharach SL, Buvat I (2007) Partial-volume effect in PET tumor imaging. J Nucl Med 48(6):932–945. https://doi.org/10.2967/jnumed.106.035774

42. Crameri F, Shephard GE, Heron PJ (2020) The misuse of colour in science communication. Nat Commun 11(1):5444. https://doi.org/10.1038/s41467-020-19160-7

43. Edmonds S, Volpe A, Shmeeda H, Parente-Pereira AC, Radia R, Baguna-Torres J, Szanda I, Severin GW, Livieratos L, Blower PJ, Maher J, Fruhwirth GO, Gabizon A, R TMdR (2016) Exploiting the metal-chelating properties of the drug Cargo for in vivo positron emission tomography imaging of liposomal nanomedicines. ACS Nano 10(11):10294–10307. https://doi.org/10.1021/acsnano.6b05935

Chapter 13

Radiosynthesis of [18F]FPenM-C2Am: A PET Imaging Agent for Detecting Cell Death

Flaviu Bulat, André A. A. Neves, and Kevin M. Brindle

Abstract

Imaging agents capable of detecting the extent, timing, and distribution of tumor cell death following treatment could be used in clinical trials of novel cancer therapies to get an early indication of efficacy and subsequently in the clinic to guide treatment in individual patients. We have shown how the C2A domain of synaptotagmin I, which binds the phosphatidylserine exposed by apoptotic and necrotic cells, can be used to image cell death (Bulat et al., EJNMMI Res 10(1):151, 2020; Neves et al. J Nucl Med 58(6):881–887, 2017). We describe here the semi-automated ^{18}F labeling of the single cysteine residue in the protein (C2Am) that had been introduced by site-directed mutagenesis.

Key words apoptosis, necrosis, fluorine-18, PET, early treatment response, radiochemistry, labeling, conjugation

1 Introduction

There is a pressing need for imaging methods capable of detecting the early onset of cell death in tumors following treatment. However, to date, no targeted imaging agent has been approved for routine clinical imaging of cell death. Historically, the major challenge has been to identify relevant hallmarks of cell death with clinical significance, and later to develop and validate novel imaging agents that can be transferred to the clinic as biomarkers of cell death.

Cell death plays a critical role in cell growth and differentiation, tissue homeostasis, and embryonic development and is also an important feature of many diseases, including cancer. In oncology, monitoring early responses to tumor therapy would allow the rapid selection of the most effective treatments and abandonment of ineffective therapies, with reduction of deleterious side effects and therefore more effective patient management.

Several molecular alterations that occur in dying cells have been exploited historically as targets for imaging of cell death. Many of these changes occur during programmed cell death or apoptosis including externalization of phosphatidylserine (PS) from the inner to the outer leaflet of the plasma membrane bilayer; activation of effector caspases; depolarization of the mitochondrial and plasma membranes; and loss of plasma membrane integrity, often a late event that occurs during necrosis, which is an unregulated form of cell death.

The Nomenclature Committee on Cell Death recommended a classification based on molecular events [3]. Apoptosis can be executed in response to either external (death-domain receptor activation) or internal (mitochondrial disruption) stimuli and is noninflammatory. Necrosis is often inflammatory and pathologic, frequently occurring following an extreme physicochemical insult, including non-physiologic pH exposure, osmotic pressure, or temperature. Apoptosis and necrosis are usually seen as two ends of a spectrum and are often inter-connected. For example, late-stage apoptotic cells which are not removed by immune cells frequently undergo a form of secondary necrosis [4]. Several additional forms of regulated cell death have been identified, including necroptosis, pyroptosis, anoikis, entosis, parthanatos, ferroptosis, autophagy, mitotic catastrophe, and lysosomal-mediated programmed cell death [5]. A dynamic response to stress stimuli often results in crosstalk and plasticity between alternative cell death pathways [3]. Importantly, in the context of cancer, apoptosis and necrosis have dynamic roles in the process of carcinogenesis and often mediate the response of malignant tumors to chemo-, radio-, hormonal, and immune-therapy [5].

To date, a wide range of potential radiopharmaceuticals targeting apoptosis have been described for PET imaging [6]. We have described recently ^{99m}Tc- and ^{111}In-labeled derivatives of a phosphatidylserine-binding imaging agent (C2Am) for imaging tumor cell death in vivo, in the form of apoptosis and/or necrosis, using SPECT [2].

More recently [1], we described an ^{18}F-labeled derivative of C2Am ([^{18}F]FPenM-C2Am) for PET imaging which has rapid renal clearance, resulting in good levels of tumor contrast post-therapy (tumor-to-muscle ratios of ~6–10, at 2 h following intravenous administration; Fig. 1).

We describe here the semi-automated protocol used for the production of [^{18}F]FPenM-C2Am. This chapter describes a procedure developed and implemented on a GE TRACERlab™FX$_{FN}$ automated synthesis module which can be adapted to other similar systems.
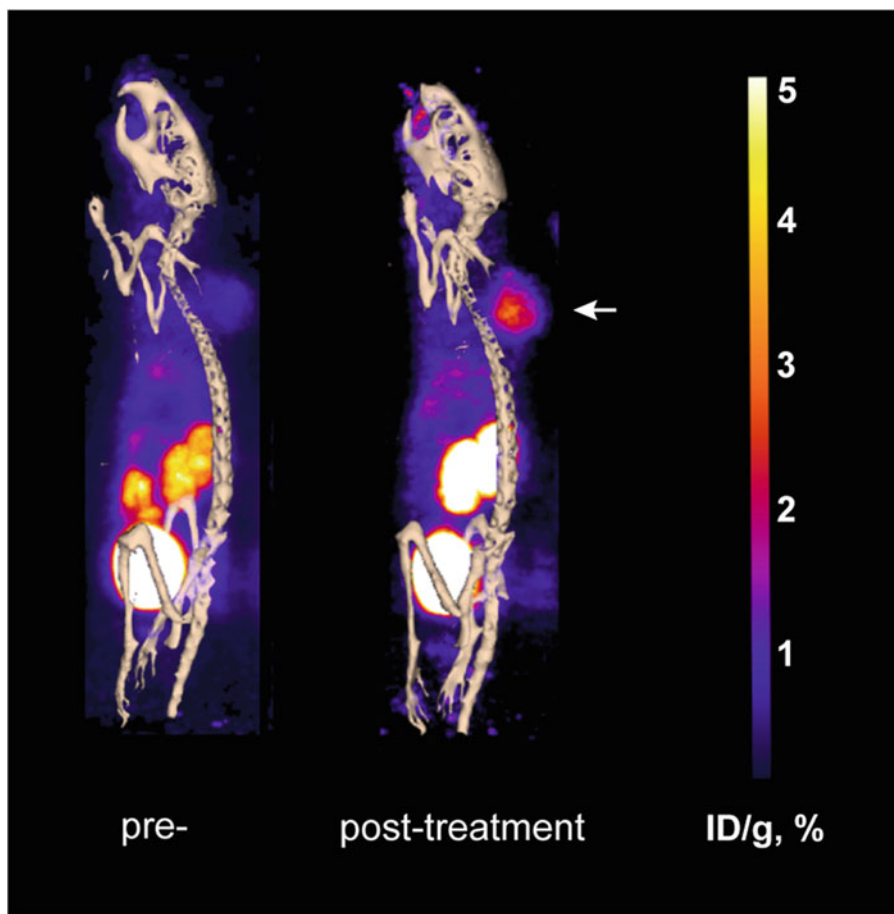
Fig. 1 PET/CT imaging of cell death following treatment of an MDA-MB-231 breast cancer xenograft with a TRAIL-R2 agonist (MEDI3039; 0.4 mg/kg, i.v.) using [^{18}F]FPenM-C2Am (1). Sagittal images showing maximum intensity projections (ID/g, %) before (left) and 24 h post-treatment (right). Skeleton rendered from CT signal using Otsu thresholding. Tumor location is indicated by the arrow

2   Materials

Dry solvents and reagents were purchased from Sigma-Aldrich, Fisher Scientific, and Acros Organics and used without further purification. Prepare all solvents with high resistivity (18.2 MΩ. cm) deionized water. A step-by-step protocol for loading the GE TRACERlab FX$_{FN}$ (Fig. 2) module used in the synthesis of 5-[^{18}F] fluoropentylmaleimide is described below.

2.1 Buffer Preparation (in 500 mL Total)

1. Hepes-buffered saline (HBS): 10 mM Hepes and 150 mM sodium chloride, adjusted to pH 7.4 with 1 M NaOH.
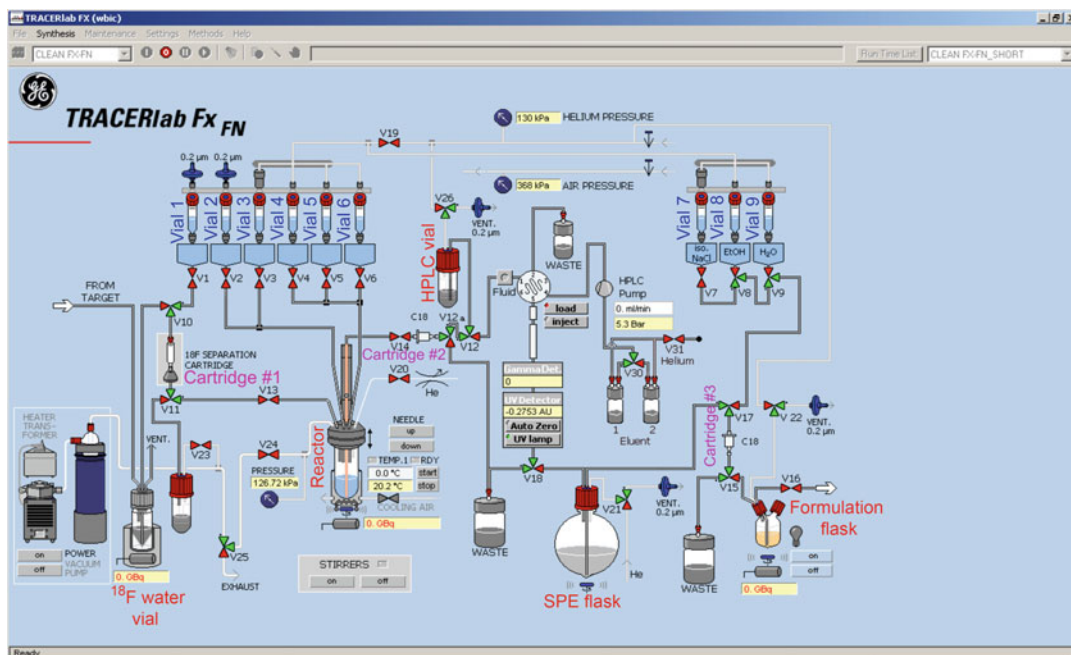
Fig. 2 Screenshot of a TRACERlab FX$_{FN}$ flow diagram user interface showing vial and cartridge setup for the synthesis of 5-[^{18}F]fluoropentylmaleimide

2. Phosphate-buffered saline (PBS): 10 mM sodium phosphate dibasic, 1.9 mM potassium phosphate monobasic, 137 mM sodium chloride, and 2.7 mM potassium chloride, pH 7.4.

3. Ammonium acetate buffer (NH$_4$OAc): 150 mM ammonium acetate, pH 6.8.

4. Kryptofix® 222 elution solution: 2.5 mg K$_2$CO$_3$, 15 mg Kryptofix K$_{222}$, 1.5 mL 95:5 (*v/v*) ACN: H$_2$O.

2.2 Protocol for Loading the Automated Radiosynthesis Module

1. Cartridge #1 QMA: Waters Sep-Pak Accell Plus QMA Carbonate Plus Light cartridge.

2. Cartridge #2 Pre-HPLC vial: Waters Sep-Pak Alumina N Plus Light cartridge.

3. Cartridge #3 C18: Waters Sep-Pak Plus Light C18.

4. Vial 1: 1.5 mL Kryptofix® 222 solution.

5. Vial 2: 2 mL dry acetonitrile.

6. Vial 3: 5 mg, 15.2 μmol, 15.2 mM mesylate precursor in 1 mL dry dimethylsulfoxide (DMSO).

7. Vial 4: 20 μL methanesulfonic acid in 0.5 mL dry DMSO.

8. Vial 5: 0.5 mL DMSO, 1 mL NH$_4$OAc buffer with 2 mg/mL ascorbic acid, and 10 μL AcOH, pH 4.12.

9. HPLC Vial: 2 mL NH_4OAc buffer, 2 mg/mL ascorbic acid, and 20 μL AcOH, pH 4.12.

10. Vial 6 & 7: Not used

11. Vial 8L 0.3 mL EtOH.

12. Vial 9: 1 mL HBS.

13. SPE Flask: 30 mL 50 mM NH_4OAc buffer, pH 6.8, 1 mg/mL ascorbic acid, and 300 μL AcOH, pH 3.65.

14. Formulation flask: 100 μL HBS, pH 7.4, and 1 mg/mL ascorbic acid, pH 4.5.

15. HPLC solvent for isocratic run: 38:62 183 mL ACN: 30 mL 50 mM NH_4OAc buffer, pH 6.8, 0.1 mg/mL ascorbic acid, and 300 μL AcOH, pH 5.6–5.7.

16. Protein vial: 10 μL, 10 mg/mL C2Am protein.

17. Empty product collection vial.

2.3 Radiochemistry

Procedures involving radioisotopes should be risk assessed in accordance with local rules and environmental protection agency permits. A PETtrace 800 cyclotron (16.5 MeV proton energy, General Electric) was originally used for the production of $[^{18}F]$fluoride in ^{18}O-water. Dose calibration should be performed using a CRC-15R (Capintek) system, or similar. Decay correction and decay corrected radiochemical yields can be calculated using an online calculator (RadPro).

A TRACERlab FX_{FN} synthesis rig (General Electric; Fig. 3) was used to run a pre-programmed sequence to produce the maleimide prosthetic group N-5-$[^{18}F]$fluoropentylmaleimide ($[^{18}F]$FPenM). The sequence source used can be found elsewhere [7].

3 Methods

3.1 Radiochemistry

1. Install cartridge #1 without pre-conditioning (*see* **Note 1**).

2. Precondition cartridge #2 with 2 mL DMSO before installation (*see* **Note 2**).

3. Precondition cartridge #3 with 2 mL ethanol followed by 10 mL water before installation (*see* **Note 2**).

4. Prepare and add all the other reagents required in vials 1,2,3,4,5,8,9, SPE flask, HPLC vial, HPLC solvent, product vial, and protein vial as described in Subheading 2.2.

5. Program the automated system to execute the following sequence: Push ~30GBq, ~2.4 mL $[^{18}F]$Fluoride in water obtained from the cyclotron through cartridge #1 (QMA) using an inert gas such as nitrogen or helium to trap the $[^{18}F]$fluoride [7] (*see* **Note 3**).

Fig. 3 GE TRACERlab FX$_{FN}$ automated synthesizer. Reactor is arrowed (red arrow)

6. Flow the Kryptofix solution (vial 1) through cartridge #1 into the reactor. With stirring, heat reactor to 95 °C for 7 min, start the helium flow, and vacuum the reactor (to at least 30 kPa) to initiate evaporation (*see* **Note 5**).

7. Add acetonitrile (vial 2) in 3 portions allowing for azeotropic removal of water (*see* **Note 4**).

8. When the [^{18}F]fluoride is dry, add the precursor solution (vial 3) and heat to 92 °C for 12 min (*see* **Note 6**).

9. Add methanesulfonic acid (vial 4) and heat to 160 °C for 6 min (*see* **Note 7**).

10. Cool the reactor to approximately 30 °C and add the buffered solution from vial 5 (*see* **Note 8**).

11. Flow the reactor contents through cartridge #2 (alumina) into the HPLC vial (*see* **Note 9**).

12. Load 5 mL of solution into the HPLC loop and start the purification (*see* **Note 10**).

13. Cut the product peak and collect it into the SPE flask (*see* **Note 11**).

14. Push the SPE flask contents through cartridge #3 (C18) (*see* **Note 12**).
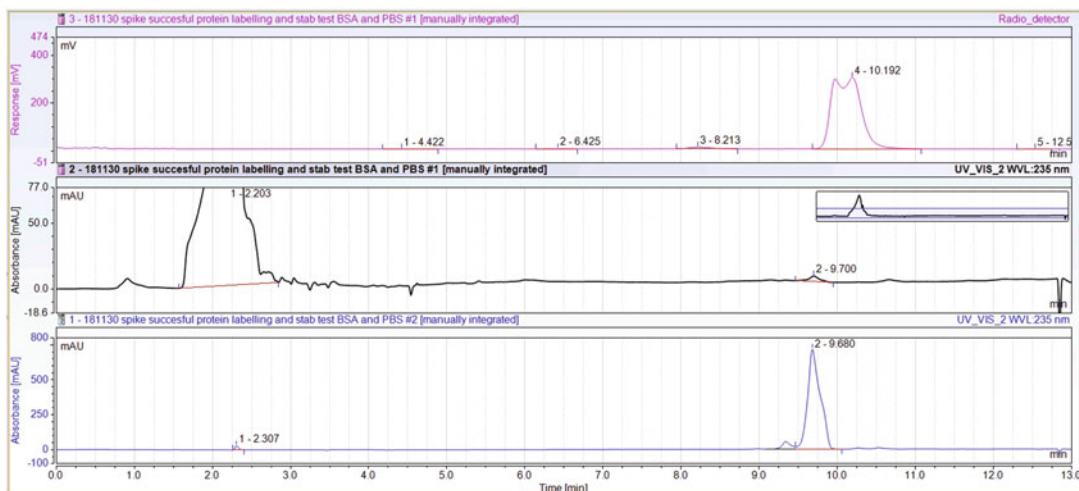
Fig. 4 Analytical RP-HPLC analysis of [^{18}F]FPenM. Top chromatogram shows the radio-peak of [^{18}F]FPenM at 10.2 min**.** The UV chromatogram (middle) shows peaks at 9.7 min from FPenM. UV chromatogram (lower) shows the spiked sample with a FPenM standard added (peak at 9.7 min)

15. Use vial 8 contents to elute [^{18}F]FPenM product off cartridge #3 into the formulation flask. Then elute the cartridge with contents from vial 9 (*see* **Note 13**).

16. Transfer the product into the empty product collection vial situated outside the hot cell.

17. Measure the activity of the [^{18}F]FPenM prosthetic group and perform a QC check to confirm purity (Fig. 3).

18. Aliquot 100 μL of [^{18}F]FPenM into the protein vial containing 100 μg C2Am (*see* **Note 14**).

19. Allow it to react at room temperature for 30 min (*see* **Note 15**).

20. Prime the PD-10 cartridge by flowing through 5 mL of PBS (*see* **Note 16**).

21. Top-load the PD-10 with 110 μL of the C2Am conjugate, allowing it to be adsorbed into the cartridge.

22. Load 350 μL PBS through a PD-10 cartridge, and using gravity, collect fraction 0 in an HPLC vial.

23. Load additional 550 μL PBS through the PD-10 cartridge and collect fraction 1, containing [^{18}F]C2Am, in an HPLC vial.

24. Using a 1 mL syringe, filter the contents of fraction 1 through a 0.22 μm, 13 mm Millex-GV syringe filter.

25. Run QC on fraction 1 to confirm purity (Fig. 4).
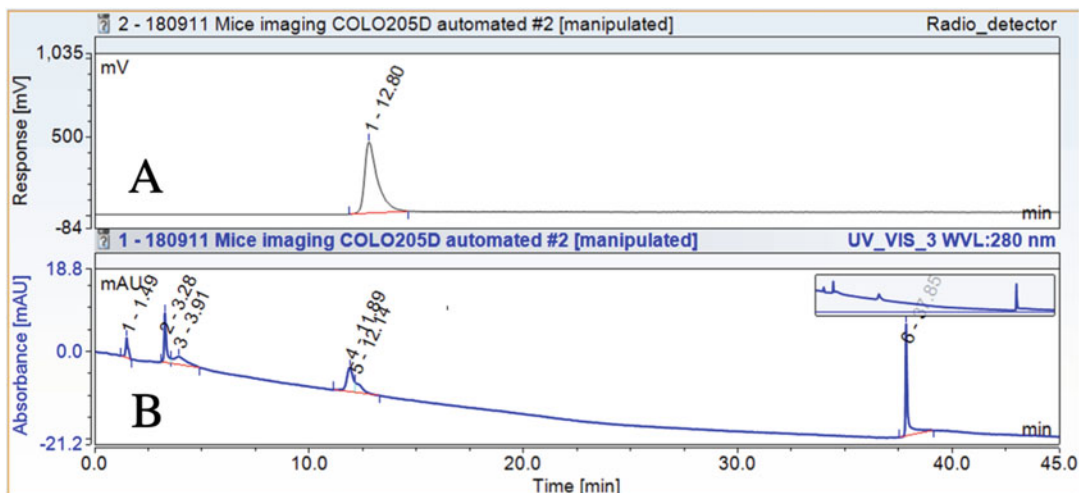
Fig. 5 SEC-HPLC analysis of [¹⁸F]FPenM-C2Am. Chromatogram A represents the radio-detector trace, showing retention time of [¹⁸F]FPenM-C2Am at 12.8 min. Chromatogram B represents the UV (280 nm) trace, showing C2Am at 11.9 min ([¹⁸F]FPenM-C2Am). Peaks 1, 2, and 3 (lower) are likely caused by dimerization of unlabeled C2Am (disulfide bond formation) and aggregation of the dimers. Peak 6 (lower) is likely to be ascorbic acid

26. After 10 half-lives (~20 h), perform the module cleaning program: clean vials 1–6 with 2 mL water, followed by 2 mL acetone. 2 mL of ethanol is required for vials 7–9.

27. Dry the vials and lines in situ using either helium or nitrogen gas.

3.2 Quality Control

1. Perform analytical reverse-phase HPLC. Acquire and analyze data using Chromeleon software, or similar.

2. Use a Primesphere C18-HC 110A (250 × 4.6 mm, 5 μm; Phenomenex) analytical column, or similar (Fig. 4).

3. Use a 10 min long elution with 5–95% ACN:H_2O gradient, running at 1 mL/min, followed by 3 min of 5:95 ACN:H_2O column re-equilibration step.

4. Radioactive species can be detected using a flow-count radio-HPLC system (Eckert & Ziegler) connected in series to the HPLC after the UV detector.

5. Assess the extent and purity of protein radiolabeling using an xBridge BEH 125A (7.8 × 300 mm, 3.5 μm; Waters) size exclusion column (SEC) (Fig. 5).

6. Here, use an isocratic elution method (100% PBS) at 0.7 mL/min for 45 min. An acetonitrile wash between 20 and 40 min is required to elute small organic molecules retained non-specifically by the column resin.

4   Notes

1. Cartridge #1 does not require pre-conditioning; however, performance can be improved if washed with Na_2CO_3 (1 M, 10 mL) followed by water (20 mL).

2. Pre-conditioning requires a slow flow rate of ~1 mL/min. Air bubbles will not disrupt cartridge performance.

3. After loading [^{18}F]fluoride on cartridge #1 (QMA), use nitrogen flow for 20–30 s to remove excess water and thus accelerate the subsequent drying process.

4. Drying process takes approximately 7–8 min by heating to 95 °C using a steady flow of helium and a vacuum of 30 kPa. If this proves insufficient, temperatures up to 120 °C can be used to improve fluoride drying.

5. This is a crucial step that will determine the quality and reactivity of [^{18}F]fluoride. A white crystalline powder/residue is the ideal looking kryptofix-fluoride product. However, a yellow wax can also lead to respectable radiochemical conversion yields.

6. Precursor and the solvent in which it is dissolved must be of highest quality and very dry.

7. Methanesulfonic acid is added to neutralize the carbonate base and stabilize the maleimide during the retro Diels-Alder furan deprotection step.

8. It is important to avoid maleimide hydrolysis; therefore, cool down reactor to less than 35 °C before adding the acetate buffer.

9. Alumina cartridge filters retain any unreacted [^{18}F]fluoride and polar organic compounds. If the product is obtained in a low yield, measuring the radioactivity of the alumina cartridge could provide information about product loss.

10. Use a bubble detector to effectively load product into the HPLC loop with minimal waste.

11. Expect to collect the product peak at around 14 min (Fig. 6) if using the same isocratic solvent mix, a 3 mL/min flow rate, and the same size C18 reverse phase column (250 mm × 100 mm).

12. The product fraction contains acetonitrile, which is diluted by the contents of the SPE flask. This ensures that the product is retained by the C18 cartridge.

13. If eluting the C18 cartridge with ethanol first followed by the HBS buffer, the eluate must not be directed straight into the protein vial as the ethanol can denature the protein.
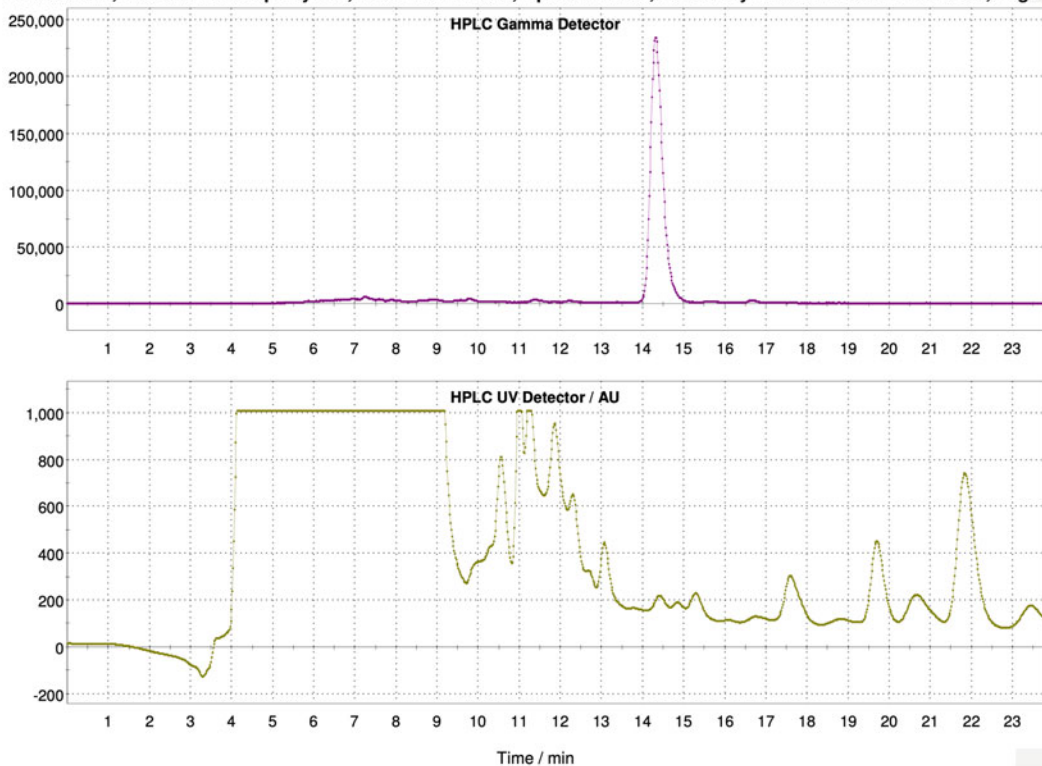
Fig. 6 Preparative HPLC purification of [^{18}F]FPenM showing gamma detector (top) and UV (lower) chromatograms. Collected peak starts at 14 min and ends at 15 min

14. Ensure that the final [^{18}F]FPenM is in the pH range of 6.4–6.7. This pH will ensure that the maleimide prosthetic group is sufficiently stable to hydrolysis while allowing Michael addition to the protein to occur.

15. The conjugation reaction of [^{18}F]FPenM to protein does not require stirring or heating.

16. The PD-10 cartridge storing buffer must be replaced with the buffer used for final formulation of [^{18}F]FPenM-C2Am; therefore, washing with PBS prior to use is required.

References

1. Bulat F, Hesse F, Hu DE, Ros S, Willminton-Holmes C, Xie B, Attili B, Soloviev D, Aigbirhio F, Leeper FJ, Brindle KM, Neves AA (2020) (18)F-C2Am: a targeted imaging agent for detecting tumor cell death in vivo using positron emission tomography. EJNMMI Res 10(1):151. https://doi.org/10.1186/s13550-020-00738-7

2. Neves AA, Xie B, Fawcett S, Alam IS, Witney TH, de Backer MM, Summers J, Hughes W, McGuire S, Soloviev D, Miller J, Howat WJ, Hu DE, Rodrigues TB, Lewis DY, Brindle KM (2017) Rapid imaging of tumor cell death in vivo using the C2A domain of Synaptotagmin-I. J Nucl Med 58(6):881–887. https://doi.org/10.2967/jnumed.116.183004

3. Galluzzi L, Vitale I, Aaronson SA, Abrams JM, Adam D, Agostinis P, Alnemri ES, Altucci L, Amelio I, Andrews DW, Annicchiarico-Petruzzelli M, Antonov AV, Arama E, Baehrecke EH, Barlev NA, Bazan NG, Bernassola F, Bertrand MJM, Bianchi K, Blagosklonny MV, Blomgren K, Borner C, Boya P, Brenner C, Campanella M, Candi E, Carmona-Gutierrez D, Cecconi F, Chan FK, Chandel NS, Cheng EH, Chipuk JE, Cidlowski JA, Ciechanover A, Cohen GM, Conrad M, Cubillos-Ruiz JR, Czabotar PE, D'Angiolella V, Dawson TM, Dawson VL, De Laurenzi V, De Maria R, Debatin KM, DeBerardinis RJ, Deshmukh M, Di Daniele N, Di Virgilio F, Dixit VM, Dixon SJ, Duckett CS, Dynlacht BD, El-Deiry WS, Elrod JW, Fimia GM, Fulda S, Garcia-Saez AJ, Garg AD, Garrido C, Gavathiotis E, Golstein P, Gottlieb E, Green DR, Greene LA, Gronemeyer H, Gross A, Hajnoczky G, Hardwick JM, Harris IS, Hengartner MO, Hetz C, Ichijo H, Jaattela M, Joseph B, Jost PJ, Juin PP, Kaiser WJ, Karin M, Kaufmann T, Kepp O, Kimchi A, Kitsis RN, Klionsky DJ, Knight RA, Kumar S, Lee SW, Lemasters JJ, Levine B, Linkermann A, Lipton SA, Lockshin RA, Lopez-Otin C, Lowe SW, Luedde T, Lugli E, MacFarlane M, Madeo F, Malewicz M, Malorni W, Manic G, Marine JC, Martin SJ, Martinou JC, Medema JP, Mehlen P, Meier P, Melino S, Miao EA, Molkentin JD, Moll UM, Munoz-Pinedo C, Nagata S, Nunez G, Oberst A, Oren M, Overholtzer M, Pagano M, Panaretakis T, Pasparakis M, Penninger JM, Pereira DM, Pervaiz S, Peter ME, Piacentini M, Pinton P, Prehn JHM, Puthalakath H, Rabinovich GA, Rehm M, Rizzuto R, Rodrigues CMP, Rubinsztein DC, Rudel T, Ryan KM, Sayan E, Scorrano L, Shao F, Shi Y, Silke J, Simon HU, Sistigu A, Stockwell BR, Strasser A, Szabadkai G, Tait SWG, Tang D, Tavernarakis N, Thorburn A, Tsujimoto Y, Turk B, Vanden Berghe T, Vandenabeele P, Vander Heiden MG, Villunger A, Virgin HW, Vousden KH, Vucic D, Wagner EF, Walczak H, Wallach D, Wang Y, Wells JA, Wood W, Yuan J, Zakeri Z, Zhivotovsky B, Zitvogel L, Melino G, Kroemer G (2018) Molecular mechanisms of cell death: recommendations of the Nomenclature Committee on Cell Death 2018. Cell Death Differ 25(3):486–541. https://doi.org/10.1038/s41418-017-0012-4

4. Silva MT, do Vale A, dos Santos NM (2008) Secondary necrosis in multicellular animals: an outcome of apoptosis with pathogenic implications. Apoptosis 13(4):463–482. https://doi.org/10.1007/s10495-008-0187-8

5. Rybczynska AA, Boersma HH, de Jong S, Gietema JA, Noordzij W, Dierckx R, Elsinga PH, van Waarde A (2018) Avenues to molecular imaging of dying cells: focus on cancer. Med Res Rev 38(6):1713–1768. https://doi.org/10.1002/med.21495

6. Van de Wiele C, Ustmert S, De Spiegeleer B, De Jonghe PJ, Sathekge M, Alex M (2021) Apoptosis imaging in oncology by means of positron emission tomography: a review. Int J Mol Sci 22(5). https://doi.org/10.3390/ijms22052753

7. Bulat F (2019) Targeted imaging agents for detecting tumour cell death following therapy. *CRUK* Cambridge Institute, Department of Oncology, University of Cambridge, UK PhD Thesis. https://doi.org/10.17863/CAM.54138

Chapter 14

Imaging the Tumor Antioxidant Response with [^{18}F] FSPG PET

Oskar Vilhelmsson Timmermand and Timothy H. Witney

Abstract

(4S)-4-(3-[^{18}F]Fluoropropyl)-L-glutamic acid ([^{18}F]FSPG) is a flourine-18 labeled glutamate analog that enables the noninvasive in vivo imaging of cellular redox status. [^{18}F]FSPG is transported across the cell membrane by the cystine/glutamate antiporter, system x_c^-, whose expression is upregulated in multiple cancer types. The requirement of cystine for the biosynthesis of glutathione, a major antioxidant, connects [^{18}F]FSPG tissue retention to the intracellular redox response via system x_c^- activity. We herein describe the use of [^{18}F]FSPG positron emission tomography (PET) to image the tumor antioxidant response and highlight key methodological considerations.

Key words [^{18}F]FSPG, (4S)-4-(3-[^{18}F]Fluoropropyl)-L-glutamic acid, PET, ROS, x_c^-, Glutathione, Glutamate, Cystine

1 Introduction

An important hallmark of cancer cells is their metabolic reprogramming, which supports a highly proliferative and metastatic phenotype [1]. Aberrant cancer metabolism, however, results in increased levels of intracellular reactive oxygen species (ROS) as a by-product of elevated mitochondrial respiration. To counter the resulting toxicity from high ROS production, key pathways that mediate redox homeostasis are upregulated. One such adaptation in cancer cells is the elevated expression of the transmembrane antiporter, system x_c^- [2]. System x_c^- transports cystine into the cell in exchange for glutamate, the most abundant intracellular amino acid. Through this transport system, system x_c^- is the primary source of intracellular cysteine which in turn is used to synthesize glutathione (GSH), a powerful antioxidant (Fig. 1).

Non-invasive positron emission tomography (PET) imaging of tumor metabolism was established with the development of the radiolabeled glucose analogue [^{18}F]2-fluoro-2-deoxy-D-glucose
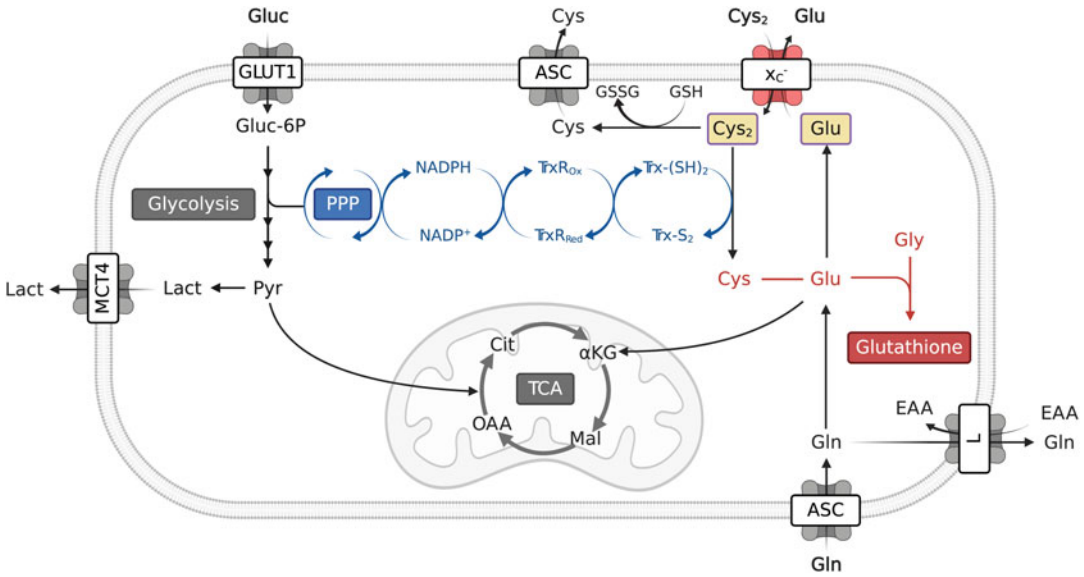
Fig. 1 An overview of the metabolic pathways, substrates, and proteins involved in [^{18}F]FSPG retention, uptake, and efflux. System x_c^- activity is controlled by the extracellular to intracellular concentration gradients of cystine and glutamate. Cystine is reduced to cysteine by the thioredoxin reductase pathway and reduced glutathione. Together, with glycine, these three amino acids form the biosynthetic precursors for glutathione biosynthesis. For clarity, the TCA cycle and glycolysis have been abbreviated. PPP pentose phosphate pathway, TCA tricarboxylic acid cycle, ASC alanine/serine/cysteine transporter subfamily, GLUT1 glucose transporter 1, L system L amino acid transporter, MCT4 monocarboxylate transporter 4, αKG α-ketoglutarate, Cit citrate, Cys cysteine, Cys$_2$ cystine, EAA essential amino acids, Glu glutamine, Gluc glucose, Gluc-6P glucose 6-phosphate, GSH glutathione, GSSG oxidized glutathione (glutathione disulfide), Lact lactate, Mal malate, NADPH reduced nicotinamide adenine dinucleotide phosphate, NADP$^+$ nicotinamide adenine dinucleotide phosphate, OAA oxaloacetate, Pyr pyruvate, TrxR$_{ox}$ oxidized thioredoxin reductase, TrxR$_{Red}$ reduced thioredoxin reductase, Trx-(S$_2$) thioredoxin-disulfide reductase, Trx-(SH$_2$) thioredoxin-dithiol reductase, x_c^- system x_c^-

([^{18}F]FDG), which still remains the most clinically important PET radiotracer for cancer imaging today. In recent years, however, several other PET radiotracers have emerged, designed to image the metabolic rewiring of tumors [3–5]. (4S)-4-(3-[^{18}F]Fluoropropyl)-L-glutamic acid ([^{18}F]FSPG) is a glutamate analog that is bidirectionally transported across the plasma membrane by system x_c^-, acting as a surrogate marker of its activity [6]. In preclinical models of cancer, [^{18}F]FSPG has been shown to be an accurate marker of the tumor antioxidant response and de novo GSH biosynthesis [7], which can be used to monitor the response (Fig. 2) and predict resistance to chemotherapy [7, 8]. Importantly, [^{18}F] FSPG has been used in patients (Fig. 3) to image several different malignancies [9–12], although its ability to image intracellular redox state in humans has yet to be determined.

This chapter describes the use of [^{18}F]FSPG PET imaging as a noninvasive tool to longitudinally follow tumor redox response in a
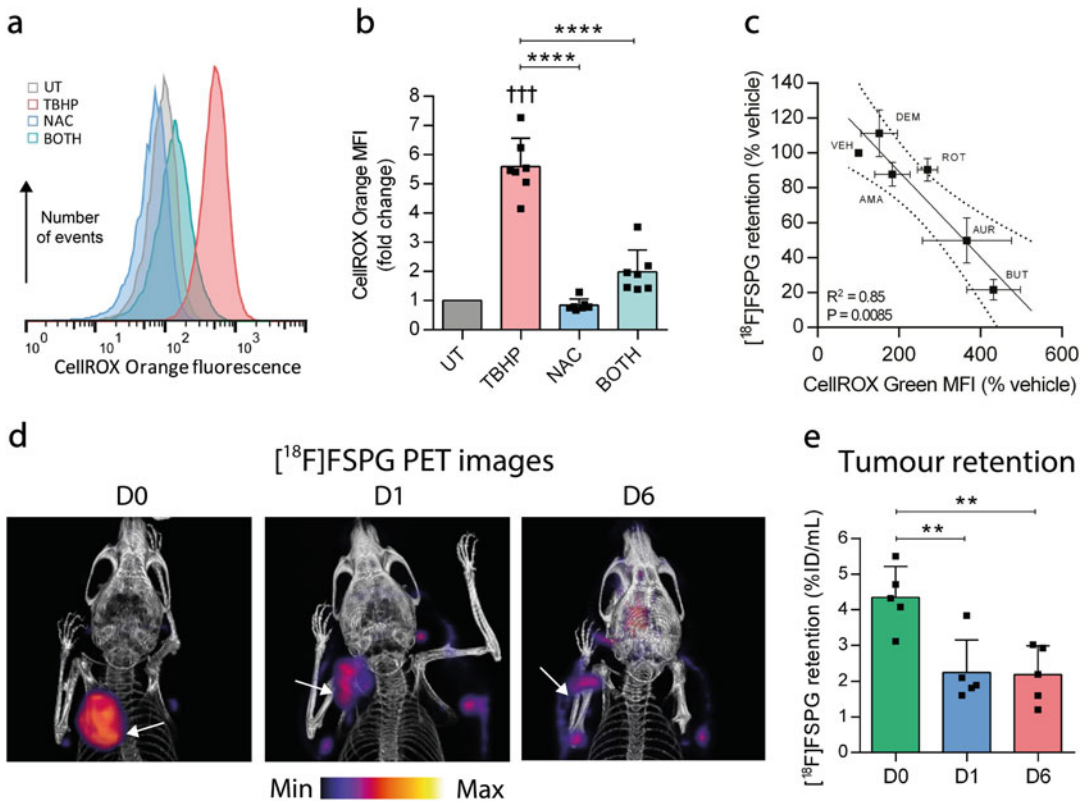
Fig. 2 [^{18}F]FSPG is a surrogate marker of drug-induced oxidative stress. (**a**) Flow cytometric assessment generalized ROS (cellROX Orange) following treatment of ovarian cancer cells with vehicle, TBHP, antioxidant (NAC), or both TBHP and NAC. (**b**) Changes in [^{18}F]FSPG cellular retention following the above treatments. (**c**) Relative [^{18}F]FSPG versus ROS following treatment of ovarian cancer cells with a range of oxidizing therapies. (**d**) Maximum projection images (MIP) showing reduced [^{18}F]FSPG retention following the Doxil-induced oxidative stress in this subcutaneous ovarian cancer model at day 1 (D1) and day 6 (D6) after the start of treatment (D0). (**e**) Quantitative data derived from [^{18}F]FSPG Doxil treatment-response studies. (Images are reproduced from McCormick et al. [7] with the permission of Cancer Research)

preclinical setting and the steps required to validate your findings in cells and ex vivo tissue.

2   Materials

2.1   Induction of Oxidative Stress

1. Complete cell medium (RPMI or equivalent containing 10% fetal calf serum).
2. Tert-butyl hydroperoxide (TBHP).
3. N-acetylcysteine (NAC).

Fig. 3 Example clinical [^{18}F]FSPG image from a patient with hepatocellular carcinoma. In this PET/CT maximum intensity projection (MIP), uptake in two lesions is visible (arrows) [10]. (Images are reproduced with the permission of Molecular Imaging and Biology)

2.2 Quantification of Glutathione in Cells

1. PBS.
2. GSH/GSSG-Glo Assay Kit (Promega).
3. 5 mM glutathione standard in water.
4. GSH lysis buffer: 1 part 5× Passive Lysis Buffer (Promega) with 4 parts distilled water.
5. Oxidized glutathione (GSSG) lysis buffer: 10 parts 5× Passive Lysis Buffer (Promega), 1 part N-ethylmaleimide (25 mM), and 39 parts distilled water.
6. GSH assay buffer: 2 parts Luciferin-NT solution, 20 parts 5× Passive Lysis Buffer, 78 parts water.
7. Luciferin Generation Reagent (Promega)
8. Luminometer.
9. White 96-well plates (or other suitable white well plate for your luminometer).
10. BCA assay kit.

2.3 Flow Cytometry	1. CellROX Green.
	2. Hanks' Balanced Salt solution.
	3. Sytox Red.
	4. Annexin-V.
	5. Hanks' Balanced Salt solution (HBSS) with Mg and Ca^{2+}.

2.4   [^{18}F]FSPG Retention in Cancer Cells

1. [^{18}F]FSPG [13].
2. Complete cell medium (RPMI or equivalent) containing 10% fetal calf serum.
3. Aspirator.
4. Filterless tips for aspirator.
5. Cell scrapers.
6. Microcentrifuge.
7. Trypsin.
8. RIPA buffer: 25 mM Tris–HCl pH 7.6, 150 mM NaCl, 1% NP-40, 1% sodium deoxycholate, 0.1% SDS.
9. PBS.
10. 1.5 mL microcentrifuge tubes.
11. Gamma counter tubes.
12. Gamma counter.
13. BCA assay kit.

2.5   ROS Induction In Vivo with Doxil

1. Caliper.
2. 2 mg/mL Doxil.
3. 26 G needles.
4. 1 mL syringes.

2.6   PET/CT Imaging and Animal Preparation

1. Heating box for mice.
2. Anesthesia box for mice.
3. Heating plate for mice.
4. Infrared heat lamp.
5. Anesthesia rig, i.e., isoflurane evaporator with oxygen.
6. Isoflurane.
7. Preclinical PET/CT system.
8. 30 G needles.
9. 1 mL syringes.
10. Polyethylene tubing (0.28 mm Ø).
11. 0.9% NaCl saline solution in water (bag of 100 mL).

12. Heparin sodium 1000 I.U./mL solution for injection, 5 mL ampoule.

2.7 PET Image Reconstruction and Analysis

1. DICOM database manager.
2. Image analysis software (Vivoquant, PMOD, Inveon Research Workplace, etc.).

2.8 Tissue Collection

1. Liquid nitrogen dewar.
2. Dry ice and insulated container.
3. Microcentrifuge tubes.
4. Forceps.

2.9 Determination of Glutathione Levels in Tissues

1. Tubes containing Lysing Matrix D (MP Biomedicals).
2. GSH/GSSG-Glo Assay Kit (Promega).
3. Homogenizer.
4. Dry ice.
5. Microcentrifuge.
6. White 96-well plate.

3 Methods

3.1 Drug Treatment: Induction of Oxidative Stress with TBHP

1. Seed cells in a suitable format (e.g. 6-well plates) in complete medium at a density that will achieve approximately 70% confluency 24 h prior to start of treatment (e.g., 0.5–2.5×10^6 cells per well in a 6-well plate; *see* **Note 1**).
2. On the day of the experiment, aspirate old medium and add fresh new medium containing 200 μM of TBHP (*see* **Note 2**) 1 h prior to further experimental assays. For a 6-well plate, add 1 mL per well. Include a DMSO vehicle control, a control containing an antioxidant, e.g., 5 mM NAC, and TBHP plus antioxidant for comparison (*see* **Note 3**).

3.2 Quantification of Glutathione Levels in Cells

1. To allow for lower cell densities following drug treatments, seed in 6-well plates to separately collect lysates for analysis.
2. Following drug treatment, place your 6-well plates on ice, remove the medium and wash three times with 2 mL of ice-cold PBS, aspirating the wash solution each time.
3. Keep the 6-well plates on ice and add 300 μL of either GSH or GSSG lysis buffer. Shake on ice for 5–10 min until lysis is visible under a brightfield microscope.
4. Scrape cells thoroughly on ice and transfer the lysates to pre-labeled and pre-chilled 1.5 mL Eppendorf tubes.

5. Spin down using a microcentrifuge at a minimum of $15,000 \times g$ at 4 °C for 10 min to pellet the cell debris. Discard the cell pellet and aliquot the supernatant. Aliquots can be frozen at −80 °C or immediately analyzed for total GSH and GSSG.

6. Make a GSH standard curve using the supplied 5 mM stock solution ranging from 0 to 5 µM no more than 30 min prior to reading your plate in a luminometer.

7. Add 5 µL of cell lysate or standards in triplicate to a white flat-bottom 96-well plate.

8. To all wells, add 50 µL of GSH assay buffer and shake briefly.

9. Additionally, use 10 µL of the lysate to determine the protein concentration using the BCA assay.

10. Add 50 µL of Luciferin Generation Reagent to each well of a 96-well plate and shake briefly. Incubate at room temperature for 30 min, protected from light.

11. Add 100 µL of reconstituted Luciferin Detection Reagent to each well of a 96-well plate. Mix briefly on a plate shaker and incubate for 15 min, protected from light

12. Measure luminescence.

13. With the luminescence readings, calculate the total GSH and GSSG from the GSH standard curve (*see* **Note 4**).

14. Normalize the total GSH and GSSG to the total amount of protein (mg/mL) acquired from the BCA assay to obtain total GSH/mg and GSSG/mg of protein. The amount of reduced GSH/mg is calculated by subtraction of the GSSG content from the total GSH.

3.3 Assessment of Intracellular ROS and Cell Death by Flow Cytometry

1. Seed cells prior to treatment such that, besides the treated and non-treated cell samples, an unstained control can be included (*see* **Note 5**). If cells are stained with >1 fluorophore, make sure that there are control cell samples stained with a single dye for fluorescent compensation. Treat the cells according to 3.1.

2. For ROS determination, add a final concentration of 5 µM of CellROX reagent to the medium of each well (i.e., 2 µL of 2.5 mM CellROX solution to 1 mL medium per well of a 6-well plate). CellROX is a pan-ROS marker (*see* **Note 6**).

3. Incubate for 30 min at 37 °C and remove the medium.

4. On a 6-well plate, wash cells three times with 2 mL warm PBS (37 °C), add 0.3 mL trypsin, and incubate for 5 min at 37 °C.

5. Place the 6-well plate on ice and stop the trypsinization by adding 1 mL complete medium.

6. Collect and spin down the cells in prechilled 1.5 mL Eppendorf tubes at $600 \times g$ and 4 °C.

7. Wash the cells once with 1 mL ice-cold HBSS by centrifugation as above, then resuspend the cells in 0.5 mL ice-cold HBBS, and keep on ice. Proceed to **step 14**.

8. For cell death determination following treatment of cells, remove and collect the medium from each well in 2 mL centrifuge tubes.

9. Wash each well once with PBS prewarmed to 37 °C (700 μL for a 6-well plate), combining the PBS wash with the retained medium. Add preheated trypsin to the cells (200 μL for a 6-well plate at 37 °C) and incubate the well plates for 3–5 min in the incubator.

10. Stop the trypsinization by adding 1 mL of the retained medium into each well from its corresponding tube. Place the entire cell suspension into the 2 mL tubes. Spin down the cells in Eppendorf tubes at $600 \times g$ and discard the supernatant.

11. Wash the cells twice by centrifugation using 1 mL HBSS containing calcium and magnesium (*see* **Note 7**).

12. Incubate the cells at 37 °C in the dark with dyes that stain for cell death. Usually, a cell-impermeable dye that stains the nucleic acids of dead cells, e.g., SytoxRed (final concentration of 5 nM) or 7-AAD (final concentration of 2–20 μM), which detect necrotic cells, is combined with Annexin-V (for final dilution of the stock solution, follow manufacturer's instructions) which is a marker of both apoptosis and necrosis.

13. After a 30 min incubation at 37 °C, place the samples on ice and wash once with ice-cold HBSS by centrifugation (at 4 °C) and resuspend cells in 0.5 mL ice-cold HBSS.

14. Determine the levels of ROS and/or cell death on a flow cytometer according to standard methodology.

3.4 [^{18}F]FSPG Preparation

1. Obtain [^{18}F]FSPG in PBS at high radiochemical purity and molar activity [13].

2. After collection of [^{18}F]FSPG, behind lead shielding in an isotope workstation, calculate the radioactive concentration (MBq/mL or μCi/mL) by measuring the activity with a dose calibrator (*see* **Note 8**).

3.5 [^{18}F]FSPG Retention in Cancer Cells

1. 24 h prior to the [^{18}F]FSPG retention assay, seed a suitable number of cells in each well of a 6-well plate (*see* **Note 9**).

2. Treat the cells according to Subheading 3.1.

3. Label microcentrifuge and gamma counter tubes appropriately.

4. Upon receiving [^{18}F]FSPG, determine the radioactive concentration of the [^{18}F]FSPG stock at the time of experimentation,

taking into account radioactive decay, using the following formula:

$$A_t = A_0 \times e^{-\lambda t} \tag{1}$$

$$\lambda = \ln(2)/t_{1/2} \tag{2}$$

A_t – radioactive dose at time t

A_0 – original radioactive dose at time zero

t – elapsed time from initial radioactivity measurement

λ – decay constant

$t_{1/2}$ – radioactive halflife

5. Approximately 0.185 MBq (5 µCi) of $[^{18}F]$FSPG is needed per well of a 6-well plate in a total of 1 mL complete medium. Calculate the volume of the $[^{18}F]$FSPG stock that should be added per well at the time of experimentation.

6. Incubate cells for 60 min at 37 °C and 5% CO_2. While waiting, prepare ice-cold RIPA buffer and chill PBS.

7. Retain 3 × 10 µL aliquots of the diluted 0.185 MBq/mL $[^{18}F]$ FSPG stock and place in gamma counting tubes for use as standards (1% of the total added activity).

8. To include both attached and floating cells after incubation (*see* **Note 10**), remove and collect the medium from each well in 2 mL tubes before placing on ice. *See* **step 12** below for attached cells only.

9. Wash each well once with PBS pre-warmed to 37 °C (700 µL for a 6-well plate), combining the PBS wash with the retained medium. Add preheated trypsin to the cells (200 µL for a 6-well plate at 37 °C) and incubate the well plates for 3–5 min in the incubator.

10. Stop the trypsinization with the previously retained medium/ PBS solution, collect the cells and spin down at 1,200 × *g* and 4 °C for 3 min. Discard the supernatant and resuspend the pellet in 1 mL ice cold PBS. Wash by centrifugation three times at the same speed.

11. After the last wash, resuspend the cells in 500 µL ice cold RIPA buffer and divide the samples for gamma counting and protein determination with the BCA assay (*see* **steps 14 to 16**).

12. To assay attached cells only, aspirate the medium from each well.

13. Wash the wells three times with 2 mL ice-cold PBS, then lyse the adherent cells through the addition of RIPA buffer (500 µL per well in a 6-plate well). Scrape thoroughly with a cell scraper to collect all the cells.

14. Pipette three-fifth of the volume of each well into a gamma counting tube and count in a gamma counter.

15. For the remaining lysate, collect the supernatant by centrifugation at a minimum of $15,000 \times g$ at 4 °C for 10 min to pellet the cell debris. Determine the protein concentration in the supernatant using a BCA assay.

16. Calculate the percentage added radioactivity per mg protein (% AA/mg) by converting the counts per minute (CPM) to counts per mL (each counting tube contains 0.3 mL). Then normalize each sample with the mg/mL obtained from the BCA assay. Finally convert the fraction to a percentage.

3.6 ROS Induction In Vivo Using Doxil

1. Set up a suitable subcutaneous mouse model by injecting 10^5 to 10^6 tumor cells subcutaneously on either flank of the mouse (*see* **Note 11**). Human or mouse tumor cells are injected subcutaneously on the flank of the mouse by lifting the skin between your thumb and index finger and inserting the needle into the space created. For further details, *see* Fig. 4.

2. Follow tumor growth by measuring the width, height, and depth with a caliper (*see* **Note 12**).

3. Start treatment when the tumor reaches a volume of 100 mm^3 (*see* **Note 13**). Tumor volume is calculated by using the following formula for an ellipsoid:

$$V = \frac{\pi}{6} ABC \qquad (3)$$

Or alternatively, if the width is hard to measure, as:

$$V = \frac{\pi}{6} A^2 C \qquad (4)$$

A = Length (mm)

B = Width (mm)

C = Heigth (mm)

4. Induce a tumor redox response by administering 10 mg/kg of Doxil via intraperitoneal injection (*see* **Note 14**). Treat animals on days zero, two, and five [7].

5. Perform [^{18}F]FSPG PET scan prior to and at timed intervals after treatment, e.g., 1 and 6 days after treatment [7], as described below.

3.7 PET/CT Scanner, Scanning, and Animal Preparation (On Day of Experiment; See Note 15)

1. Make sure that the appropriate quality control of the PET detector has been conducted in advance of the experiment according to the manufacturer's instructions.

2. Prior to use, condition the X-ray tube by running it for at least 30 min.
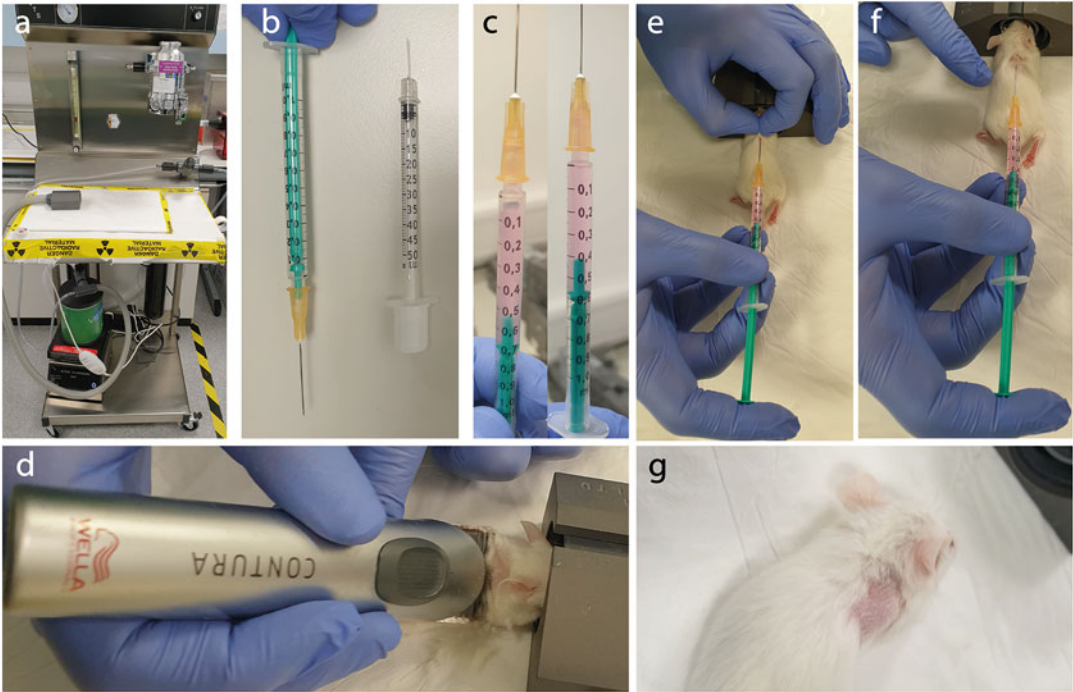
Fig. 4 Mouse subcutaneous tumor inoculation. (**a**) Anesthesia rig with oxygen tubes, oxygen flow meter, isoflurane vaporizer, nose cone, and isoflurane scavenger. (**b**) A 1 mL syringe with a 25G needle (left) with the cutting edge of the bevel at the bottom so that the volume markings on the syringe are visible when injecting subcutaneously. For comparison, a syringe with a 30G needle (right) often used for intravenous or intraperitoneal injections. (**c**) When preparing the syringe with cell suspension, pull up the cells without a needle and then pulldown the suspension with the plunger and attach the needle. Thereafter, gently tap the syringe to move any air bubbles up toward the needle and evacuate the air with the plunger. This can be done similarly when changing the needle between injections. Always prepare more cell solution than what you aim to inject. 25-26G needles have a dead volume of circa 50 μL. (**d**) If necessary, prepare the mouse by shaving the injection site with an electrical shaver for ease of injection and tumor measurements. (**e**) Gently lift the skin of the mouse between your index finger and thumb so that you get a small triangle facing you, with the syringe in the other hand pierce the needle through the skin close to the base of the triangle and into the cavity that has been created. Be careful not to go too deep so that you penetrate the muscle or scratch/damage the dermis. (**f**) One can keep lifting the skin while injecting; however, the skin can be released when the needle is in place as movement is minimized. Usually circa 100 μL of cells are injected. The plunger should move easily without any resistance. Resistance is a sign of the injection not being performed correctly, e.g., intradermally. (**g**) After injection, the cell suspension can often be seen at the injection site, which can persist for hours to days, particularly when the cells require an extracellular matrix (e.g., Matrigel, Cultrex®, Geltrex™) to grow

3. Move the mice for the first scan to a heating box preheated to 37 °C and lined with absorbent paper.

4. Turn on the heating plate where the animals will rest during cannulation and cover with absorbent paper.

5. Check the levels of isoflurane on the anesthesia rig; refill if necessary.

6. Transfer one mouse to an anesthesia box and use a heating lamp at an appropriate distance to maintain body temperature.

7. Set the oxygen flow rate to 0.5–1 L/min. Turn on the isoflurane on the anesthesia rig and make sure there is flow to both the anesthesia box and the nose cone. At induction of anesthesia, keep the isoflurane vaporizer set between 1.5% and 3% (*see* **Note 16**).

8. When anesthetized, move the first mouse onto the heating plate for cannulation and move the second mouse from the heating box and into the anesthesia box if more than one animal is to be imaged in the first scan.

9. Cannulate the tail vein of the first mouse with a syringe attached to the cannula containing sterile 0.9% sodium chloride [14] and proceed until the desired number of animals are cannulated, i.e., four if you are using a mouse hotel for your PET/CT scans [15]. Lower the amount of isoflurane by changing the vaporizer dial between 1 and 2% to maintain anesthesia (*see* **Note 16**).

10. Turn on the anesthesia and oxygen delivery system for the PET/CT scanner.

11. Set up a PET/CT protocol consisting of a scout CT, a 10 min static PET acquisition, followed by a CT scan for anatomical registration and attenuation correction (*see* **Note 17**). The CT scan can be acquired before or after the PET acquisition, depending on the imaging workflow. Additionally, dynamic scans might be necessary to determine [^{18}F]FSPG pharmacokinetics (*see* **Note 18**).

12. Draw four syringes containing 3 MBq of [^{18}F]FSPG each in a volume of 50–150 µL. Move these injection syringes onto the cannula, replacing the syringes containing sterile 0.9% sodium chloride syringes by cutting and reapplying the polyethylene tubing onto the new needle [14]. Measure the activity of the syringe before and after injection with a dose calibrator and take note of the time of each measurement. Use this together with the time of injection to correct for radiotracer decay and calculate the injected activity using the formula described in Subheading 3.5.

13. Inject the animals with [^{18}F]FSPG and move the mice onto the PET/CT animal bed. Alternatively, the mice can be injected when located on the camera.

14. Run the scout CT.

15. Use the image from the scout CT to determine the field of view for the PET and set CT coordinates to match the PET field of view.

16. Start the PET acquisition for 10 min at 50 min post-injection if performing a static scan. Otherwise, simultaneously start the scanner and inject the radioactivity when the mice are located in the acquisition field of view after running the scout CT.

17. After the imaging session, return the mice to their cages and monitor them while they fully recover, or at the experimental end point, cull the mice and collect the required tissue (*see* Subheading 3.9).

3.8 PET Image Reconstruction and Image Analysis

1. PET reconstruction varies depending on the PET/CT manufacturer. The reconstruction is usually performed on a dedicated computer and the parameters are often specific for the application, i.e., dynamic or static scan. It is highly recommended to correct for decay, scatter, and attenuation, which can be done with a CT image as a reference.

2. Transfer the reconstructed data, i.e., digital imaging and communications in medicine (DICOM) files, to a computer containing your analysis software.

3. In the software, perform bed removal, preprocess the images, and draw region of interests (ROIs) to obtain quantitative data from the images [14].

3.9 Tissue Collection

1. Collect liquid nitrogen in a dewar and collect dry ice in an insulated container suitable for storing tissues samples. Label microcentrifuge tubes for each planned necropsy with experimental details.

2. Immediately after tissue excision, move the required tissue into the appropriate tube and snap-freeze in liquid nitrogen. Wait 3–4 min, then move the sample to dry ice with long forceps (*see* **Note 19**).

3.10 Determination of GSH Levels in Tissues

1. After the imaging session, return the mice to their cages and monitor them while they fully recover, or at the experimental end point, cull the mice and collect the required tissue (*see* Subheading 3.9).

2. Prepare your homogenizer prior to start according to manufacturer's instructions as the tissue needs to be lysed with the use of a cooling system which may require dry ice to maintain the desired temperature. Alternatively, homogenization can be performed in a cold room.

3. Add up to 0.2 g or 0.2 mL of frozen or fresh tissue to 2 mL tubes suitable for your homogenizer containing lysis beads, e.g., impact-resistant tubes with Lysing Matrix D.

4. Add 1 mL ice-cold GSH lysis buffer to the lysate. To a separate sample, use the GSSG lysis buffer to determine GSSG.

5. Run the homogenizer at 4 °C for 15 s to lyse the tissue.

6. Centrifuge the tubes at $15{,}000 \times g$ and 4 °C for 10 min to remove any debris from the solution and collect the supernatant.

7. The supernatant can then be processed similarly to Subheading 3.2. to determine total GSH, reduced GSH, and GSSG tumor tissue concentrations per mg protein.

4   Notes

1. Seeding density is dependent on the choice of cell line and should be experimentally determined in advance.

2. A 200 µM concentration of TBHP is likely to induce high levels of oxidative stress at early (1–2 h) timepoints prior to cell death. The optimal TBHP concentration for individual cells can be experimentally determined using CellROX. Alternatively, other drugs that induce high levels of ROS following 24 h treatment can be used: rotenone (50 mmol/L), auranofin (50 mmol/L), antimycin A (1.10 mg/mL), diethyl maleate (100 mmol/L), Doxil (200 nmol/L) [7].

3. Antioxidants can include NAC (5 mM; 2 h) or Butein (100 mM; 24 h) [7]. Caution should be applied with the use of NAC as free intra- and extracellular cysteine is liberated, which may affect system x_c^- activity irrespective of NAC's antioxidant properties.

4. Note that two moles of GSH is produced for every reduced mole of GSSG.

5. To set up the compensation of the dyes for the flow cytometer protocol, the following samples are needed: unstained control, untreated stained control, and treated stained control. The untreated and the treated population of cells can then be mixed in a 50:50 ratio to make a sample containing both a positive and a negative population.

6. To determine generalized intracellular ROS, cell permeant probes, such as the CellROX reagents, which fluoresce upon oxidation, can be used. Alternatively, a range of fluorescent probes are available for the selective assessment of different reactive oxygen species (e.g., MitoSOX Red Superoxide Indicator for mitochondrial superoxide), lipid peroxidation (e.g., BODIPY® 581/591 C11), or GSH (e.g., ThiolTracker).

7. Annexin-V binding to phosphatidylserine exposed during apoptosis is calcium-dependent. It is therefore important to keep the cell in a buffer-containing calcium.

8. For accuracy, when using highly concentrated preps, dilute the [^{18}F]FSPG stock to 9.25 MBq/mL, adding 20 μL of this diluted [^{18}F]FSPG solution to each well. This procedure is necessary when collecting both floating and attached cells. Alternatively, when collecting only the attached cells, [^{18}F] FSPG can be diluted to 0.185 MBq/mL in cell culture medium and directly added to cells following aspiration of the old medium. Special care should be applied in this situation to make sure that drug is also supplemented to the culture medium (if required) and that an excess volume is prepared for all treatment conditions to account for any potential losses.

9. The extent of drug-induced oxidative stress, cell death, and [^{18}F]FSPG retention can be cell seeding density-dependent. Cell seeding density optimization is therefore crucial.

10. The decision to assay attached cells or to include both attached and floating cells, that is dead or dying cells, can be a crucial consideration that one needs to make. If interest is only in biochemical changes (e.g., upon sublethal oxidative damage), the straightforward approach would be to only assay the attached cells. If cell death or biochemical changes closely connected to cell death are to be investigated, including all cells in the analysis is most likely to be the best approach.

11. The number of cells used at implantation might have to be titrated, as given in the literature. Further, in preclinical molecular imaging, it is common to start with a syngeneic or immunocompromised subcutaneous xenograft model, based on an established cell line, for proof of concept. However, these are rarely good models of the disease as their growth, microenvironment, and extent of genetic heterogeneity differ from the human disease. There is a large variety of other types of models such as patient-derived xenografts (PDX), orthotopic (where cells are inoculated in tissue of origin), or genetically engineered mouse models (GEMM) with a phenotype and behavior more similar to human disease [16].

12. Monitoring the tumor growth of non-subcutaneous models can be challenging. Often these models need to be thoroughly characterized so that tumor burden over time can be determined. There are alternative ways of monitoring tumor growth such as bioluminescence imaging of tumor cells transduced with luciferase and CT imaging using contrast agents, e.g., in models of abdominal and hepatic tumors. Combinations of different techniques can make it easier to detect and provide a more accurate estimation of the tumor burden. For example, [^{18}F]FDG PET imaging has been used to follow tumor growth preclinically, together with anatomical imaging such as CT or

magnetic resonance. Here, the [^{18}F]FDG signal helps with tumor localization.

13. A tumor xenograft size of 100 mm^3 is commonly seen as the ideal volume for PET imaging studies. At this size, tumors are a solid mass and are vascularized, while not too large that they have become necrotic. The vascularization of the tumor can differ between different cell lines. Further, measuring tumor size using calipers has some known pitfalls, including lack of accuracy and interpersonal variations in measurements.

14. There are several routes to administer drugs. Four commonly used routes in rodents are intravenous injection, intraperitoneal injection, subcutaneous injection, and oral gavage. The route of administration will determine the drug's pharmacokinetics, efficacy, and off-target toxicity profile.

15. For a thorough description of how to set up and conduct a PET/CT scan, *see* "Imaging Cancer Metabolism with Positron Emission Tomography (PET)" [14].

16. The concentration of isoflurane on induction of anesthesia is usually between 2% and 3%. This is lowered to 1–2% during maintenance of anesthesia. Different strains of mice have different tolerance to isoflurane, which is further influenced by their general health condition, e.g., disease model, ongoing treatments, and the volume of injections during anesthesia can lead to lowered tolerance. It is therefore important to carefully monitor the mice when anesthetized.

17. The time it takes to perform a CT scan is usually around 10 min.

18. Initially a dynamic scan with injections directly on the animal bed of the PET camera at the beginning of the acquisition is preferable as this could be used to determine the uptake, retention, and efflux (i.e., the kinetics) of [^{18}F]FSPG in the model system. When the pharmacokinetics have been established, static PET scans of approximately 10 min at a predetermined timepoint after [^{18}F]FSPG injection leads to a faster and more manageable workflow as there is no need to perform long scans and injections directly on the camera.

19. Detailed descriptions of routine necropsy and specific necropsy protocols for different purposes, such as fixing tissue for staining or isolating mRNA, can be found elsewhere [17].

References

1. Faubert B, Solmonson A, DeBerardinis RJ (2020) Metabolic reprogramming and cancer progression. Science 368(6487). https://doi.org/10.1126/science.aaw5473

2. Liu JY, Xia XJ, Huang P (2020) xCT: a critical molecule that links cancer metabolism to redox signaling. Mol Ther 28(11):2358–2366.

https://doi.org/10.1016/j.ymthe.2020.08.021

3. Oyama N, Akino H, Kanamaru H, Suzuki Y, Muramoto S, Yonekura Y, Sadato N, Yamamoto K, Okada K (2002) 11C-acetate PET imaging of prostate cancer. J Nucl Med 43(2):181–186

4. Qu W, Oya S, Lieberman BP, Ploessl K, Wang L, Wise DR, Divgi CR, Chodosh LA, Thompson CB, Kung HF (2012) Preparation and characterization of L-[5-11C]-glutamine for metabolic imaging of tumors. J Nucl Med 53(1):98–105. https://doi.org/10.2967/jnumed.111.093831

5. Farsad M, Schiavina R, Castellucci P, Nanni C, Corti B, Martorana G, Canini R, Grigioni W, Boschi S, Marengo M, Pettinato C, Salizzoni E, Monetti N, Franchi R, Fanti S (2005) Detection and localization of prostate cancer: correlation of (11)C-choline PET/CT with histopathologic step-section analysis. J Nucl Med 46(10):1642–1649

6. Koglin N, Mueller A, Berndt M, Schmitt-Willich H, Toschi L, Stephens AW, Gekeler V, Friebe M, Dinkelborg LM (2011) Specific PET imaging of xC- transporter activity using a (1)(8)F-labeled glutamate derivative reveals a dominant pathway in tumor metabolism. Clin Cancer Res 17(18):6000–6011. https://doi.org/10.1158/1078-0432.CCR-11-0687

7. McCormick PN, Greenwood HE, Glaser M, Maddocks ODK, Gendron T, Sander K, Gowrishankar G, Hoehne A, Zhang T, Shuhendler AJ, Lewis DY, Berndt M, Koglin N, Lythgoe MF, Gambhir SS, Arstad E, Witney TH (2019) Assessment of tumor redox status through (S)-4-(3-[F-18] fluoropropyl)-L-glutamic acid PET imaging of system x(c)(-) activity. Cancer Res 79(4):853–863. https://doi.org/10.1158/0008-5472.Can-18-2634

8. Greenwood HE, McCormick PN, Gendron T, Glaser M, Pereira R, Maddocks ODK, Sander K, Zhang T, Koglin N, Lythgoe MF, Arstad E, Hochhauser D, Witney TH (2019) Measurement of tumor antioxidant capacity and prediction of chemotherapy resistance in preclinical models of ovarian cancer by positron emission tomography. Clin Cancer Res 25(8):2471–2482. https://doi.org/10.1158/1078-0432.CCR-18-3423

9. Park SY, Na SJ, Kumar M, Mosci C, Wardak M, Koglin N, Bullich S, Mueller A, Berndt M, Stephens AW, Cho YM, Ahn H, Chae SY, Kim HO, Moon DH, Gambhir SS, Mittra ES (2020) Clinical evaluation of (4S)-4-(3-[(18)F]Fluoropropyl)-L-glutamate ((18)F-FSPG) for PET/CT imaging in patients with newly diagnosed and recurrent prostate cancer. Clin Cancer Res 26(20):5380–5387. https://doi.org/10.1158/1078-0432.CCR-20-0644

10. Kavanaugh G, Williams J, Morris AS, Nickels ML, Walker R, Koglin N, Stephens AW, Washington MK, Geevarghese SK, Liu Q, Ayers D, Shyr Y, Manning HC (2016) Utility of [(18)F]FSPG PET to image hepatocellular carcinoma: first clinical evaluation in a US population. Mol Imaging Biol 18(6):924–934. https://doi.org/10.1007/s11307-016-1007-0

11. Magarik MA, Walker RC, Gilbert J, Manning HC, Massion PP (2018) Intracardiac metastases detected by 18F-FSPG PET/CT. Clin Nucl Med 43(1):28–30. https://doi.org/10.1097/RLU.0000000000001883

12. Mittra ES, Koglin N, Mosci C, Kumar M, Hoehne A, Keu KV, Iagaru AH, Mueller A, Berndt M, Bullich S, Friebe M, Schmitt-Willich H, Gekeler V, Fels LM, Bacher-Stier C, Moon DH, Chin FT, Stephens AW, Dinkelborg LM, Gambhir SS (2016) Pilot preclinical and clinical evaluation of (4S)-4-(3-[18F]Fluoropropyl)-L-glutamate (18F-FSPG) for PET/CT imaging of intracranial malignancies. PLoS One 11(2):e0148628. https://doi.org/10.1371/journal.pone.0148628

13. Edwards R, Greenwood H, Witney T (2020) Robust and facile automated radiosynthesis of [18F]FSPG on the GE FASTlab. https://doi.org/10.26434/chemrxiv.13434143.v2

14. Witney TH, Lewis DY (2019) Imaging cancer metabolism with positron emission tomography (PET). Methods Mol Biol 1928:29–44. https://doi.org/10.1007/978-1-4939-9027-6_2

15. Greenwood HE, Nyitrai Z, Mocsai G, Hobor S, Witney TH (2020) High-throughput PET/CT imaging using a multiple-mouse imaging system. J Nucl Med 61(2):292–297. https://doi.org/10.2967/jnumed.119.228692

16. Gengenbacher N, Singhal M, Augustin HG (2017) Preclinical mouse solid tumour models: status quo, challenges and perspectives. Nat Rev Cancer 17(12):751–765. https://doi.org/10.1038/nrc.2017.92

17. Golubeva Y, Rogers K (2009) Collection and preparation of rodent tissue samples for histopathological and molecular studies in carcinogenesis. Methods Mol Biol 511:3–60. https://doi.org/10.1007/978-1-59745-447-6_1

Characterization and Validation of Radiotracer Kinetics Using the Langendorff Isolated Perfused Heart

Friedrich Baark, Edward C. T. Waters, Thomas R. Eykyn, and Richard Southworth

Abstract

The Langendorff isolated perfused heart is a physiologically relevant and controllable ex vivo model well suited to characterizing and validating novel radiotracers for a wide range of molecular imaging applications. It allows the monitoring of first pass tracer uptake kinetics either as a bolus injection or as a continuous infusion in beating myocardial tissue with a high degree of experimental control in terms of cardiac workload, perfusion, energy substrate delivery and composition, and drug co-administration. The radiotracer pharmacokinetic data that it provides is not contaminated by confounding factors such as off-target tracer metabolism, and as a non-imaging technique, time activity curves can be acquired with very high temporal resolution. In this chapter, we describe the basic principles and practice for setting up and using Langendorff isolated perfused hearts for the assessment of novel radiotracers and outline their potential for modeling pathophysiological conditions relevant to cardiovascular disease.

Key words Langendorff, Cardiovascular, PET, SPECT, Perfusion, Hypoxia, ROS, Molecular Imaging

1 Introduction

While the initial screening of novel radiotracers is traditionally performed in cultured cells as a high throughput and relatively inexpensive approach, in vitro assessment can only provide limited insight into how radiotracers might behave in vivo. Conversely, while the pharmacokinetics and targeting of radiotracers can be evaluated in vivo using positron emission tomography (PET) and single-photon emission computed tomography (SPECT), the level of experimental control possible in vivo is often limited, and it is difficult to exclude confounders such as tracer metabolism or regional variations in perfusion to confirm a radiotracer's trapping mechanism. To bridge this translational gap, ex vivo–isolated perfused organ systems are a useful intermediate step: recapitulating
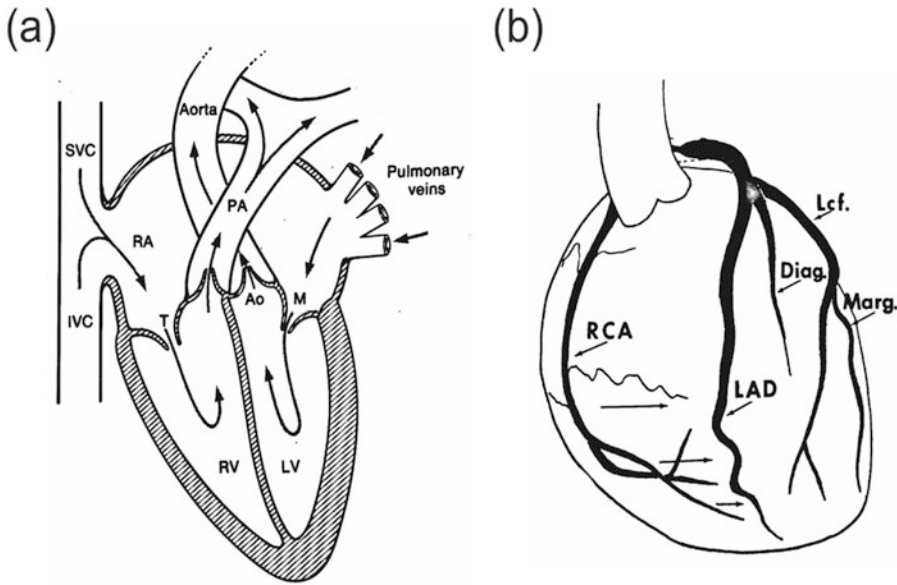
Fig. 1 Cardiac anatomy relevant to Langendorff perfusion. (**a**) Gross cardiac anatomy showing the position of the aorta relative to the rest of the cardiac structures. (**b**) The coronary ostea arises at the base of the ascending aorta just above the aortic valve. Buffer introduced retrogradely by the perfusion cannula into the aorta forces the aortic valve closed and diverts buffer into the coronary arteries to perfuse the myocardium. LAD left anterior descending coronary artery, RCA right coronary artery, LCF left circumflex coronary artery [25]

the in vivo environment, but gaining the experimental control and access required for radiotracer characterization and validation.

Since its first description in 1895, Oskar Langendorff's isolated perfused heart technique has been the cornerstone of basic science in cardiovascular physiology and biochemistry [1, 2]. By excising the heart and cannulating the ascending aorta, it is possible to retrogradely perfuse the myocardium under pressure with a warmed oxygenated perfusion buffer via coronary ostia and the coronary arteries (Fig. 1) to maintain the heart in a viable contractile state for 1–2 h (*see* **Note 1**). Typically, perfusion buffers are delivered under gravity at the arterial pressure appropriate for the animal species being used (*see* **Note 2**). However, when evaluating radiotracer pharmacokinetics, we have found that it is advantageous to deliver perfusate at a constant flow using a peristaltic pump rather than constant pressure because it allows the delivery of radiotracer at a constant rate, which greatly simplifies pharmacokinetic modeling and eliminates the potential confounding effects of variations in coronary perfusion and radiotracer delivery [3]. Thus, rather than maintaining pressure constant and monitoring coronary flow as an indication of preparation stability as is usually done, we maintain perfusion constant and monitor changes in perfusion pressure with an in-line transducer (Fig. 2, *see* **Note 3**).
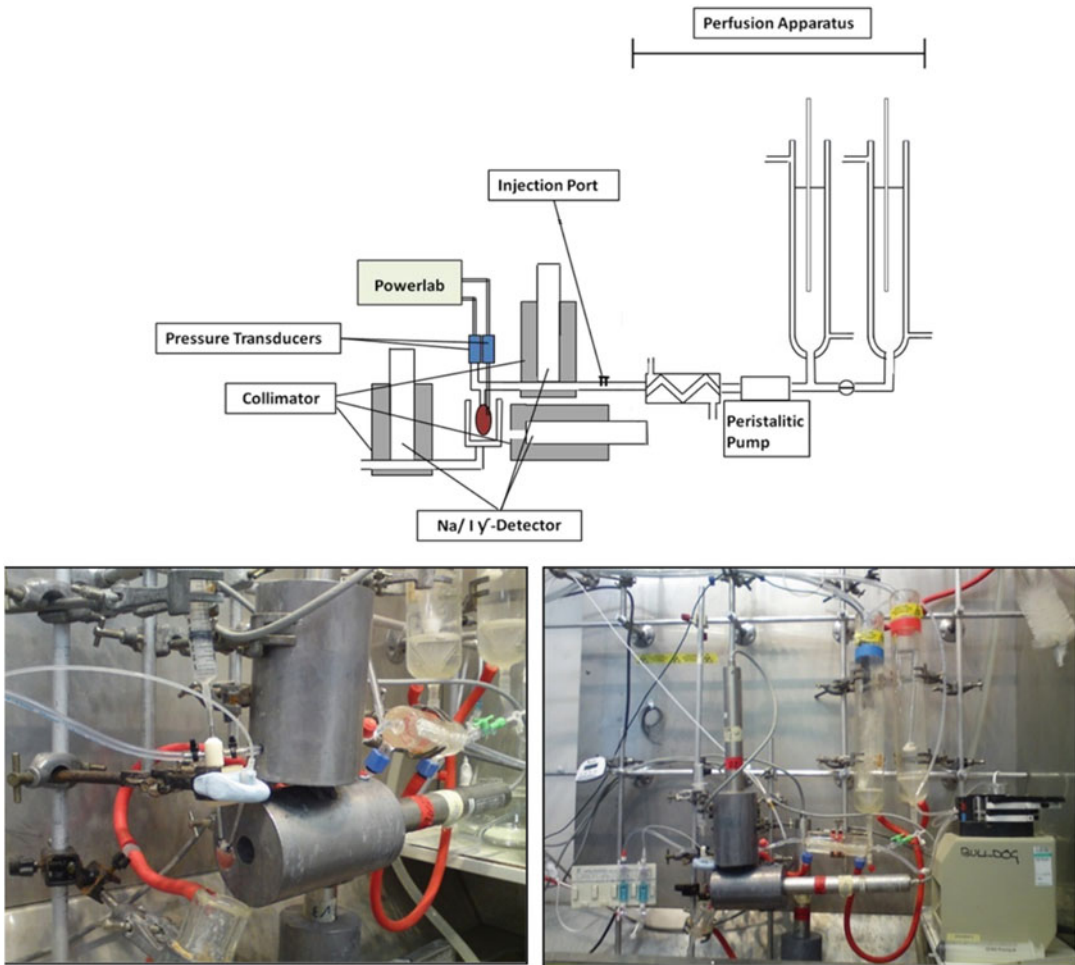
Fig. 2 The triple γ-detection apparatus for radiotracer evaluation in the isolated perfused heart. Schematic (top) shows the basic architecture and the positioning of the detectors relative to the perfusion apparatus. Photograph (right) shows the perfusion rig secured to a lead-lined backing plate which supports a custom-built scaffold. Photograph (left) shows the heart instrumented with the intraventricular balloon, with a horizontally mounted γ-detector interrogating the heart via a collimated lead shield

While we describe here a simple approach using a Krebs-Henseleit buffer perfusate containing glucose as the sole energy substrate, it is also possible to better recapitulate the in vivo situation by employing more complicated perfusates, variously incorporating fatty acids and ketones as additional energy substrates [4], perfluorocarbons to enhance oxygen carrying capacity [5], or even washed blood [6] or erythrocyte suspensions [7, 8] (*see* **Note 4**). It is also possible to independently perfuse the left and right sides of the heart using a dual-perfusion cannula to enable one side of the heart to be used as a control for the other when modeling regional low-flow ischemia [9]. The interested reader is directed to the following excellent reviews on these topics [10, 11].

To characterize and assess the uptake kinetics of radiotracers in the ex vivo isolated heart, we have built a system comprising three Na/I detectors placed (i) on the arterial input line above the heart, (ii) directly adjacent to the heart recording the myocardium, and (iii) on the coronary effluent line. The detectors are collimated with lead shields and arranged orthogonally to minimize shine through from radioactivity in neighboring parts of the apparatus. This enables the simultaneous acquisition of time activity curves for the radiotracer input functions, cardiac uptake kinetics, and output function (efflux) [12].

In this chapter, we describe this adaptation of Langendorff's original method to enable the characterization and validation of radiotracers in a system which allows the modulation of perfusion pressure, coronary flow, heart rate, energy substrate delivery, buffer oxygenation, and co-administration of drugs as required, while simultaneously evaluating radiotracer kinetics when delivered either as a bolus or as a constant infusion.

2   Materials

1. 8-channel PowerLab 8/35.

2. Laptop computer running LabChart software.

3. Two physiological pressure transducers.

4. Medical grade perfusion tubing. Tubing should be sufficiently thick to minimize heat loss and gas exchange, but sufficiently thin to be easily manipulable and flexible to fit onto perfusion glassware.

5. Multichannel peristaltic pump and tubing. Multiple roller pump heads are recommended to minimize pulsatile flow.

6. A bench-top general-purpose thermal bath/circulator that allows temperature control in the range from ambient temperature to 120 °C. Closed systems are recommended for long-term use.

7. Appropriate cannula for animal species of choice. Surgical steel recommended. Cannula should have sufficient external diameter to stretch the aorta to achieve a good seal. It is advisable to score a series of horizontal grooves into the cannula exterior near the tip to increase friction and prevent the heart slipping off during cannulation and ensure a watertight seal under pressure.

8. An in-line bubble trap/compliance chamber. This can be constructed from an inverted 10 mL syringe with the plunger locked in place using a split pin.

9. A sturdy lab stand assembly and all associated clamp hardware.

10. Luer adapter and connection kit for connecting tubing.

11. Luer-lock three-way taps to allow changes in flow at points along the perfusion apparatus.

12. Two 0.5 L borosilicate water-jacketed glassware buffer reservoirs to enable switching between oxygenated and hypoxic buffers (O_2 titrated using a programmable gas mixer), or control and treated, but any number of reservoirs can be used to enable substrate switching/drug administration, with flow switched between them using 3-way taps and additional peristaltic pumps (*see* **Note 5**).

13. Heat exchanger.

14. Heart perfusate cup.

15. Two sintered-glass gassing sticks for buffer oxygenation.

16. Three Na/I detectors and lead collimators.

17. γ-detector acquisition system software and hardware.

18. Syringe infusion pump.

19. Precision seal rubber septa.

20. Software controlled stimulator unit, connector leads, and silver wire (AD Instruments, UK).

21. *Optional:* GSM-3 Programmable Gas Mixer.

22. *Optional:* In-line dissolved oxygen sensor.

2.1 Preparation of Krebs-Henseleit Buffer (KHB)

All reagents were supplied by Sigma Aldrich Ltd., UK, unless otherwise stated. Prepare all solutions and buffers using ultrapure deionized water (18 MΩ) and analytical grade reagents. Prepare and store all reagents at room temperature (*see* **Note 6**).

1. Krebs-Henseleit Buffer: 0.5 mM NaEDTA, 118.5 mM NaCl, 11 mM glucose, 6 mM KCl, 1.2 mM $MgSO_4$, 25 mM $NaHCO_3$, 2 mM $CaCl_2$, pH 7.4. Dissolve all reagents in 5 L ultrapure water previously saturated with 95% O_2/5% CO_2 by continuously gassing via a sintered glass bubble stick for 15 min (*see* **Note 4**).

2. Filter using 0.2 μM pore size vacuum filtration system.

3. Each batch of KHB can be stored at 4 °C for a maximum of 3 days. Glucose and calcium-free stock solutions (stable for 1 month) can be made and kept at 4 °C to minimize preparation time.

2.2 Construction of an Intraventricular Balloon

While latex balloons for measuring intraventricular pressure are commercially available, we find them too thick-walled and compliant to reliably and sensitively transduce pressure changes down the pressure line to the transducer.

1. Wrap clingfilm around the tip of a plastic Luer-tip catheter, and tie it securely in place with suture using a long knot such as a heaving line to minimize the chance of leakage [13].

2. Connect the catheter to a water-filled 1 mL syringe, which is slowly inflated to stretch the clingfilm until the balloon is slightly larger than the internal volume of the left ventricle.

3. Slowly depress the plunger and reverse it to remove air bubbles from the balloon.

4. Connect the water-filled bubble-free balloon to a fine hard plastic tube and pressure transducer via a Luer-lock 3-way tap.

3 Methods

3.1 Perfusion Rig/ Triple-γ-Detector System

A schematic representation and photographs of the isolated heart perfusion rig are shown in Fig. 2 (*see* **Note** 7).

1. Secure glass reservoirs, heat exchanger, and cannula block to the lab stand assembly using retort clamps. The rig is designed to be as compact as possible to minimize heat loss. All tubing runs are insulated and water-jacketed wherever possible.

2. Connect perfusion between the glassware components and dedicated peristaltic pump tubing around the pump head. Insert 3-way taps under each perfusion reservoir to enable purging of bubbles with a 50 mL syringe as necessary.

3. Position a multi-way connector above the perfusion cannula, connected to the bubble trap directly above the cannula. The side arms are connected to the arterial input line and the arterial line pressure transducer.

4. Connect water-jacketed glassware to the thermal circulator unit (*see* **Note 8**).

5. Both physiological pressure transducers should be clamped onto the lab stand, positioned at the same height as the heart.

6. Insert an injection port between the heat exchanger and cannula block. This can either be a T-piece with a rubber septum cover for bolus radiotracer injections or tubing running to a syringe pump for administration by infusion. A further T-piece infusion line can be inserted for parallel drug administration if necessary.

7. The three lead collimated gamma detectors are arranged around the perfusion rig, supported using retort clamps to measure (i) in the arterial line above the heart, (ii) the heart itself, and (iii) the coronary effluent line. The detectors are housed in lead collimators, and the apparatus geometry fine-tuned to ensure minimal shine-through from distal perfusion

lines using a sealed radioactive source. Each collimator has a detection hole drilled in the base and 2 orthogonal holes drilled through the sides to allow the routing of the arterial and venous perfusion lines, respectively.

8. Equip a pressure transducer with a 3-way Luer-lock tap at either end. Connect a 1 mL syringe to one tap and fit a pressure balloon to the other port on the tap via a long, thin non-distensible plastic pressure line. Fill the system with water, allowing the balloon to be inflated and deflated remotely. Actuate the syringe and tap the tubing to bleed all further air from the system, topping up with water as necessary.

3.2 Perfusion Rig Setup and Calibration

1. Fill the reservoir(s) with boiling water and flush the entire volume through the perfusion rig to ensure it is clean before use. If the perfusion rig has been unused for an extended period, flush with 70% ethanol prior to flushing with boiling water.

2. Turn on the circulator and allow rig to warm for 15 min prior to filling the reservoirs with KHB (*see* **Note 9**).

3. Allow warmed and gassed KHB to fill the rest of the perfusion rig by opening the 3-way tap at the base of each reservoir.

4. Fill the bubble trap/compliance chamber, ensuring 2–3 mL of air is retained at the top for elasticity within the perfusion system (*see* **Note 10**).

5. Adjust the peristaltic pump speed to deliver 14 mL/min (for adult rat heart perfusion) by measuring effluent flow at the cannula over a 1-min period (*see* **Note 11**).

6. Calibrate both pressure transducers using a sphygmomanometer (*see* **Note 12**).

7. Perform a final check on the perfusion rig including checking the ventricular balloon and the rest of the rig for air bubbles. Confirm that the perfusate temperature at the cannula is 37 °C when running at the prescribed flow rate.

8. When the final checks on the rig have been performed, lower the flow rate to a very slow speed (~1 drip every 5 s) to allow heart cannulation (*see* **Note 13**).

3.3 Heart Excision

1. Anesthetize rats via intraperitoneal (I.P.) injection with sodium pentobarbital (1 mL/kg) in combination with 800 IU/kg heparin to prevent blood clotting in the excised heart.

2. Once animals are sedated and no longer responding to reflex tests (blinking test and pedal withdrawal test), access the diaphragm by transabdominal incision and carefully expose the thoracic cavity.

3. Perform a thoracotomy by a bilateral incision along the lower margin of the last to first ribs, then lift the thoracic bib to expose the heart.

4. Swiftly excise the heart, keeping the scissors aligned along the spine to ensure as much of the aortic arch as possible is retained, lift it clear, and immediately immerse in ice-cold (4 °C) KHB.

3.4 Heart Cannulation and Perfusion

1. Ensuring that the heart is kept immersed in ice-cold KHB, and working quickly, carefully dissect away any excess connective and lung tissue.

2. Make a diagonal cut across the aortic arch at the level of the brachiocephalic artery to create an oval cross-section at the end of the aorta to facilitate cannulation.

3. Using two pairs of curved forceps, stretch the aortic arch laterally and feed it onto the cannula, alternately advancing one side and then the other (much like you would pull on a sock). Temporarily hold the aorta in place using an artery clip prior to tightly securing it with a suture, located into one of the lateral grooves on the cannula to ensure a good seal (*see* **Note 14**). Correct cannulation of the aorta can be confirmed by wash-through of residual blood in the effluent immediately following cannulation.

4. Using the peristatic pump, increase the coronary flow rate to 14 mL/min (*see* **Note 11**).

5. Cut a small incision in the pulmonary artery to allow outflow of buffer.

6. Carefully remove the left atrial appendage to allow the deflated intraventricular balloon to be inserted into the left ventricle.

7. Using the 1 mL syringe, slowly inflate the intraventricular balloon while monitoring the left ventricular developed pressure recorded by the pressure transducer to achieve an end diastolic pressure of 4–6 mm Hg. Secure the balloon catheter in place with modeling clay and a rubber band if necessary.

8. Pierce the right atrial appendage with the tip of the silver pacing wire, pull it through and bend the wire through 90° with forceps to hold it in place. Wrap the second cable around the cannula and connect both wires to the stimulator unit.

9. Initiate electric pacing, slowly increasing the voltage until electrical capture is achieved, as denoted by regularization of heart rate in the left ventricular pressure readout or widening of the QRS complex if using ECG monitoring.

10. Monitor cardiac hemodynamic parameters to ensure preparation viability and stability for 10 min prior to initiating any experiment (*see* **Note 15**).

3.5 Radiotracer Administration by Bolus

For illustration, we describe a typical protocol for a PET hypoxia tracer, although the approach is entirely flexible and amenable to any number of other applications [3, 9, 12, 14–23]. A typical dataset for this protocol is shown in Fig. 3, allowing the direct comparison of a hypoxia probe library, as shown in Fig. 4.

1. Fill both 0.5 L glass reservoirs with KHB during perfusion rig setup. Gas one reservoir with 95% O_2/5% CO_2, with the other reservoir gassed with a lower O_2 concentration to investigate hypoxia by mixing N_2, O_2, and 5% CO_2 (for pH buffering), delivered using a GSM-3 gas mixer.

2. Initiate monitoring of the arterial O_2 partial pressure using the in-line Oxylite oxygen probe (*see* **Note 16**).

3. Acquire radioactive counts at the start of the stability period of each perfusion experiment with a temporal resolution of 5 Hz.
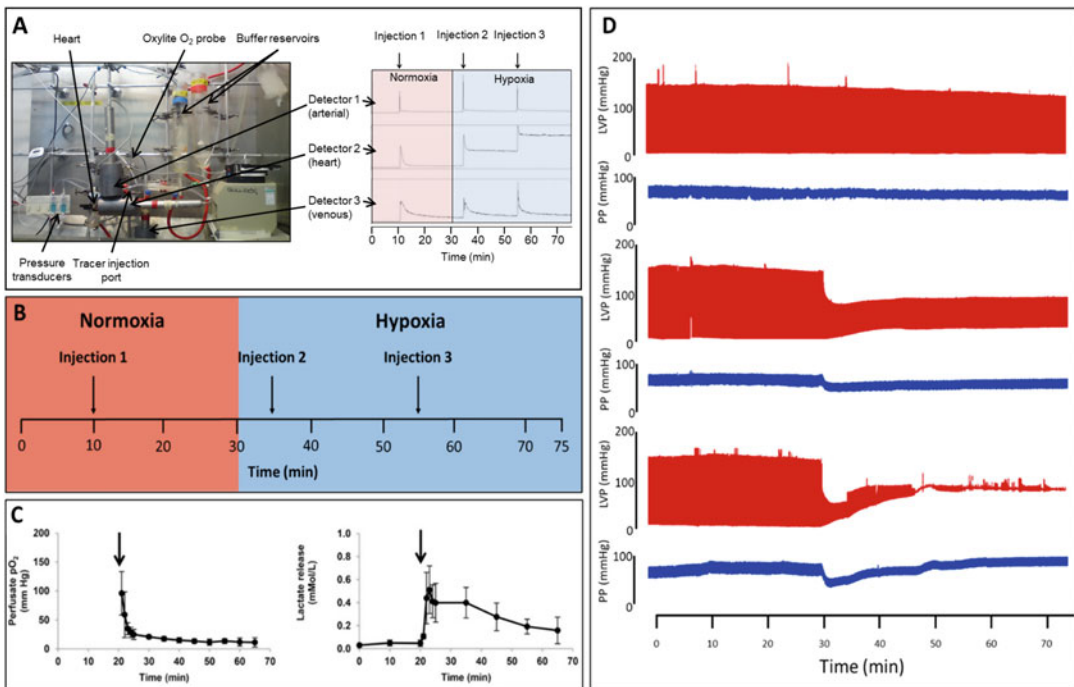
Fig. 3 The outputs derived from the respective detectors in the triple-γ-detector system. (**a**) Representative time–activity curves are shown using the hypoxia-selective PET probe ^{64}Cu-ATSM displaying input function in arterial line (detector 1), retention/washout through heart (detector 2), and washout (detector 3). (**b**) The experimental protocol. (**c**) Changes in perfusate partial pressure of O_2 (left) and lactate washout (right) measured in parallel during the experiment. (**d**) Concurrent real-time measurements of cardiac contractile function (red) and perfusion pressure (blue) data for hearts perfused with buffers saturated with 95% (top), 30% (middle), and 0% (bottom) O_2 respectively
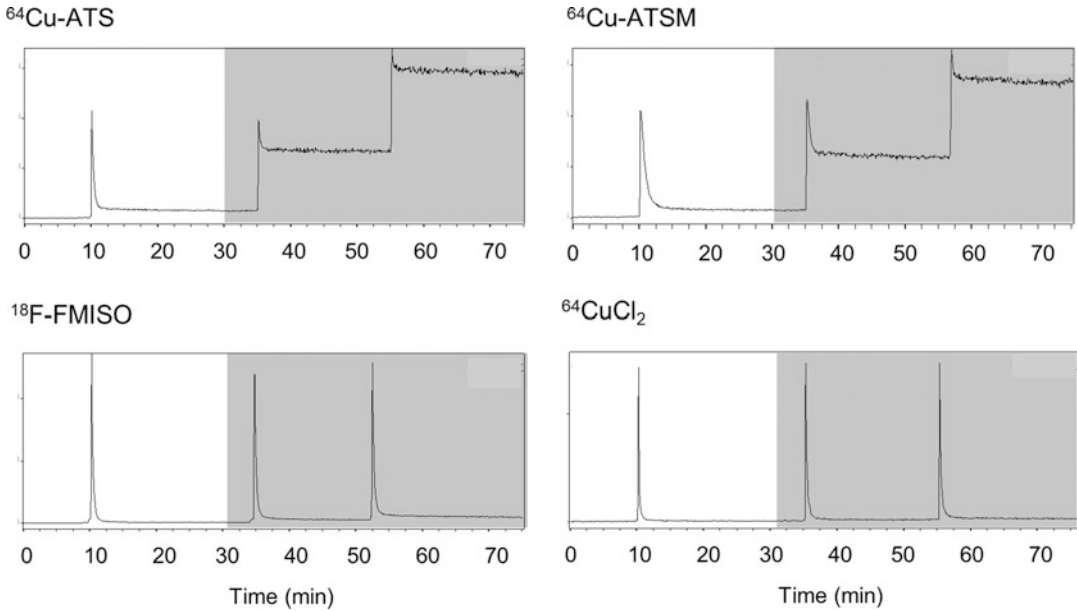
Fig. 4 Representative time–activity curves from serial bolus injections of PET hypoxia probes. Showing the hypoxia-dependent myocardial accumulation of the most clinically evaluated bisthisemicarbazone complex ^{64}Cu-ATSM, the next generation complex ^{64}Cu-ATS which exhibits greater hypoxia selectivity, the clinical gold standard ^{18}F-fluoromisonidazole (FMISO) which displays significantly slower pharmacokinetics and lower tissue uptake, and ^{64}CuCl$_2$ as a non-hypoxia selective control. Perfusion with normoxic (white background) and hypoxic buffer (grey background). Each spike represents a 1 MBq bolus

4. Once cannulation and manipulations such as balloon and pacing wire insertion have been completed, a 20 min stabilization period is used to ensure contractile function and perfusion pressure meet predetermined exclusion criteria (*see* **Note 15**).

5. Following the stability period, determine baseline normoxic cardiac trapping and pharmacokinetics using a bolus injection of radiotracer (typically 1–5 MBq in 100 μL), using a Hamilton syringe into the injection port (*see* **Note 17**).

6. 20 min after the first bolus injection, switch the perfusion to the second reservoir containing hypoxic buffer.

7. After 5 min of hypoxic buffer perfusion, administer a second bolus injection of radiotracer (1–5 MBq in 100 μL) to obtain an index of cardiac retention during early hypoxia.

8. Administer a final bolus injection of radiotracer 20 min after the previous one to obtain an index of cardiac retention during prolonged hypoxia.

9. Terminate experiments 20 min after the final bolus injection.

3.6 Radiotracer Administration by Continuous Infusion

1. Initiate the acquisition of the radioactivity data at the start of the stability period of each perfusion experiment to record background activity (determined by averaging the background radioactivity counts over a 5-min period immediately before the introduction of radioactivity). Subtract these background counts from all measurements recorded in the rest of the experiment. All data are then corrected for radioactive decay, with time zero taken as the time that the first bolus was injected.

2. At the end of the stability period, initiate a constant infusion of radiotracer via a side arm to the perfusate line by syringe pump (*see* **Note 18**).

3. Continue the infusion for 20 min to establish a baseline rate of radiotracer uptake (*see* **Note 15**).

4. After the baseline uptake has been established, the experimental intervention can then be performed (be it induction of ischemia, hypoxia, drug administration, modification of energy substrate delivery, etc.), and the resultant change in radiotracer uptake or washout rate recorded. Parallel time-matched control groups should be included wherever possible, typically switching to a reservoir containing vehicle.

5. Calculate the effect of an intervention on radiotracer accumulation as a ratio between the rates pre-and post-intervention. By taking a ratio between these two rates, the units cancel out and the ratio is unitless. Decay correct the counts to time zero, and differences in the amount of activity infused will not prevent direct comparison between experiments [3].

3.7 Radiotracer Retention Calculation

A typical kinetic profile of a radiotracer moving through the heart is shown in Fig. 5. This can be used as a guide profile for the tracer retention calculation used in this section. The pharmacokinetics can be interpreted using simple compartmental models (*see* **Note 19**).

1. Use a simple ratiometric approach to assess the degree of trapping by calculating the ratio of the plateau phase (trapped component) to the peak activity (dominated by the radioactivity from the bolus).

2. The percentage tracer retention for each bolus injection is calculated using the following equation:

$$TR\ (\%) = \left(\frac{RCPS}{MCPS} \right) \times 100$$

Where TR is the tracer retention, RCPS is the residual count per seconds, and MCPS is the maximal count per second. RCPS is measured by taking a 2-min average of cps 15 min post-tracer injection. MCPS is equal to the maximum recorded activity after tracer injection, averaged over 1 s.
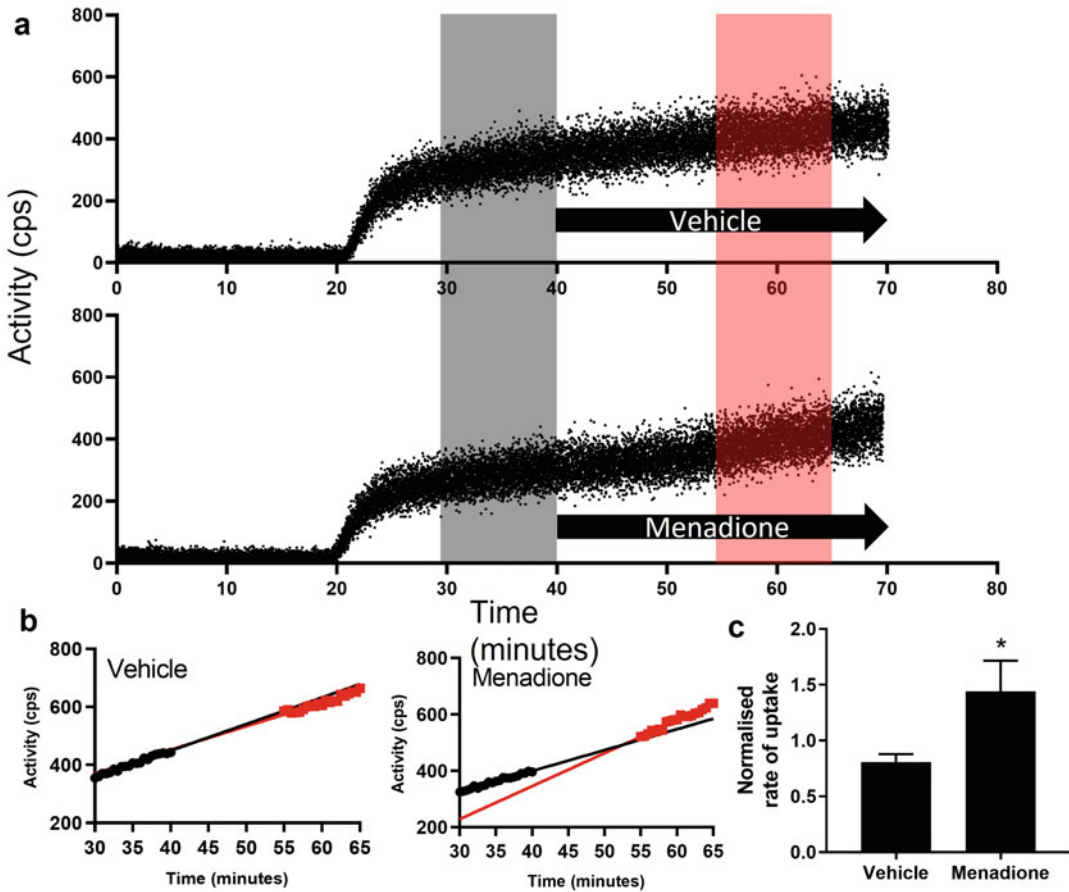
Fig. 5 Representative time-activity curves from the infusion of a ROS-sensing PET probe. (**a**) Representative time-activity curves demonstrating the cardiac uptake of [^{18}F]dihydroethidine ([^{18}F] DHE) uptake in hearts perfused with vehicle or menadione (50 μM). Black arrow represents treatment, gray shows the baseline rate of uptake, and red shows the rate of uptake during treatment. (**b**) Representative trace of data used to normalize uptake of [^{18}F]DHE over time during control conditions (30–40 min, black) versus vehicle (55–65 min, red). (**c**) Summarized data comparing [^{18}F]DHE uptake rate during control conditions and 50 μM menadione infusion ($n = 4$, ± SD, * = $p < 0.05$) [3]

> 3. Tracer retention of subsequent boli should be calculated in the same way, except that an average of cps is taken for 1 min before injection, and that as well as background is subtracted from that measurement to correct for residual activity left from the previous injection.

4   Notes

> 1. It must be appreciated that because of its retrograde nature, the Langendorff heart is beating but not performing active work (i.e., pumping liquid) against an afterload and is, therefore, in a less energetically demanding state compared to the in vivo situation.

2. We typically perfuse our rat hearts (from 220 to 240 g rats) at 14 mL/min constant flow, which is the average coronary flow that results when hearts of this size are perfused under 100 cm H_2O (74 mm Hg) constant pressure, which is the normal arterial pressure in an adult rat [24].

3. More elaborate and physiologically relevant models are available, but each comes with additional cost in terms of requisite expertise and throughput, and a pragmatic approach is recommended to balance the degree of physiological relevance (and practical difficulty) to the scientific requirement. In "working heart" mode, all four chambers are cannulated, and the heart is perfused via the right atrium as it would be in vivo, with the ventricles performing active work by pumping against columns of liquid in a recirculating manner via a large surface area counter-current glass column to replicate lung function and resistance.

4. Perfusion buffers containing proteins and fatty acids tend to froth when directly oxygenated by gassing. More elaborate perfusion rigs which incorporate membrane oxygenator systems are required for such work.

5. Historically, these items have been constructed in-house by university glassblowers, but heart perfusion systems and accessories are also commercially available.

6. To prevent $CaCl_2$ from crashing out of solution, dissolve it in ~20 mL deionized water and add it to the main volume once all other reagents have been dissolved.

7. Careful consideration should be given to the physical location of the perfusion apparatus. Ideally it should be placed in an area with minimal through traffic, away from potential draughts and direct sunlight which may cause temperature fluctuations. Our custom-built frames feature a drip tray which feeds directly into a drain designated for radioactive waste to facilitate cleaning and drainage with minimal risk of personal exposure. The aluminum back plate to the frame is also filled with lead shot to minimize potential radiation exposure into the corridor behind our laboratory.

8. Water-jacketed glassware is connected to the bench-top circulator (positioned above the perfusion rig) with thick-walled tubing and routed to ensure that it fills from the circulator outlet port to the lowest point of the perfusion rig first. The perfusion apparatus is connected in parallel circuits using Y-pieces, progressing to the top of the perfusion rig where each parallel circuit is then connected to a common outflow tube which returns to the circulator. This design ensures even heating throughout the rig, minimizes the potential for air pockets, and allows the most accurate control of buffer temperature at the perfusion cannula.

9. Initiate gas flow *before* filling the reservoirs with KHB to minimize buffer ingress into the gassing sticks (which is difficult to clean subsequently and can become a problematic reservoir for bacterial/fungal growth).

10. This compliance chamber/bubble trap is a crucial component of the perfusion rig. Although the heart is not actively pumping liquid via the left ventricle, the coronary circulation is under pressure. The elasticity within the system that the bubble in the compliance chamber affords prevents vascular damage which would otherwise result from the heart working directly against the peristaltic pump. Furthermore, the KHB is saturated with oxygen, meaning that bubbles can periodically seed from scratches and imperfections in glassware and tubing, even if the perfusion rig is carefully bled for bubbles each time it is filled. Positioning the bubble trap directly above the perfusion cannula diverts those bubbles upward, preventing them from being forced into the coronary vasculature, which is catastrophic for the heart preparation, and can necessitate premature termination of an experiment.

11. Since it is being perfused with a crystalloid solution which does not have the same oxygen-carrying capacity as blood, the heart is nearly maximally vasodilated, meaning that coronary flow is significantly greater than would be observed in vivo [5]. This flow rate is defined as that required to achieve the mean arterial pressure for the animal species/size being used, and should be determined experimentally for every perfusion rig, as part of each investigator's establishing work. The actual flow rate should be measured as mL/min pumped from the cannula, and not merely by reading from the digital readout on the pump. Delivery by peristaltic pumps is highly dependent on the compliance of the pump tubing, and the compression that the tubing is under, governed by the tightness of the tensioning screw on the pump head (which can change as the tubing ages). The digital readout should therefore be calibrated against *actual* flow rate each day.

12. The pressure transducers and recording system are set up using a two-point calibration. A zero baseline is set with the 3-way tap open to atmosphere. To set the second calibration point, the sphygmomanometer is connected, 3-way tap is closed to atmosphere, and the system is pressurized to 100 mmHg.

13. This should be the minimum required to ensure that no bubbles are introduced into the aorta during cannulation. Introducing buffer into the heart too fast during cannulation will enable it to start beating, which will make securing it onto the cannula significantly more difficult.

14. Maintain tension between the suture and the back of the cannula as the knot is being tied by locating the suture in one of the cannula grooves and pulling it the knot toward you as it is tied. This ensures that the suture will not slip off the cannula as it is being tightened, which frequently causes the aorta to be accidentally tied shut.

15. We would recommend that any trainee perfusionist should establish exclusion criteria against which to compare each preparation, which includes ranges of ideal left ventricular end diastolic and developed pressures and perfusion pressures, and to use them as a go/no go checklist for whether to proceed with or discard each preparation. We would recommend the following: (i) heart excision to stable perfusion with inserted balloon should be achieved in less than 5 min, (ii) end diastolic pressure should be 4–8 mm Hg, (iii) LV-developed pressure should be >120 mm Hg, (iv) initial perfusion pressure should be no more than ± 10% of that measured in vivo for that species, and (v) successful electric pacing capture.

16. Fully oxygenated KHB has a pO_2 of approximately 500 mm Hg, which saturates the probe during normoxia (they have an operating maximum of 150 mm Hg), but pO_2 decreases to measurable levels within a minute of switching to hypoxic buffer.

17. Wherever possible, radiotracers should be dissolved in the perfusion medium being used. Volumes of radiotracer injections are kept below 150 μL to avoid any increases in coronary perfusion pressure.

18. Perfusate flow rate from the peristaltic pump should be adjusted to account for the additional flow from the side arm. The maximum injection rate from the sidearm should not exceed 5% of total flow to minimize temperature and buffer oxygen fluctuations.

19. The bolus delivery can be modeled as an instantaneous delivery of radioactivity at $t = 0$ or as a gamma variate function to allow modeling of the duration and potential dispersion of the injection bolus. The activity is then delivered to the heart at a constant rate due to flow and perfusion within the extracellular space. The tracer can then either exit the heart due to efflux or be taken up by cardiomyocytes through passive diffusion, permeability, or active transport processes. Trapping mechanisms can then be modeled as either a reversible or an irreversible process.

20. The first 10 min typically exhibit a rapid myocardial loading of the vascular space, interstitium, and myocardium, which declines to a constant rate of accumulation as the system reaches equilibrium.

Acknowledgments

References

1. Langendorff O (1895) Untersuchungen am überlebenden Säugethierherzen. Archiv für die gesamte Physiologie des Menschen und der Tiere 61(6):291–332. https://doi.org/10.1007/BF01812150

2. Döring HJ (1990) The isolated perfused heart according to Langendorff technique--function--application. Physiol Bohemoslov 39(6):481–504

3. Waters ECT, Baark F, Yu Z, Mota F, Eykyn TR, Yan R, Southworth R (2021) Detecting validated intracellular ROS generation with 18F-dihydroethidine-based PET. Mol Imaging Biol. https://doi.org/10.1007/s11307-021-01683-0

4. Southworth R, Davey KAB, Warley A, Garlick PB (2007) A reevaluation of the roles of hexokinase I and II in the heart. Am J Phys Heart Circ Phys 292(1):H378–H386. https://doi.org/10.1152/ajpheart.00664.2006

5. Southworth R, Blackburn SC, Davey KA, Sharland GK, Garlick PB (2005) The low oxygen-carrying capacity of Krebs buffer causes a doubling in ventricular wall thickness in the isolated heart. Can J Physiol Pharmacol 83(2):174–182. https://doi.org/10.1139/y04-138

6. Schuster A, Grünwald I, Chiribiri A, Southworth R, Ishida M, Hay G, Neumann N, Morton G, Perera D, Schaeffter T, Nagel E (2010) An isolated perfused pig heart model for the development, validation and translation of novel cardiovascular magnetic resonance techniques. J Cardiovasc Magn Reson 12(1):53. https://doi.org/10.1186/1532-429x-12-53

7. Galiñanes M, Lawson CS, Ferrari R, Limb GA, Derias NW, Hearse DJ (1993) Early and late effects of leukopenic reperfusion on the recovery of cardiac contractile function. Studies in the transplanted and isolated blood-perfused rat heart. Circulation 88(2):673–683. https://doi.org/10.1161/01.cir.88.2.673

8. Kolocassides KG, Galiñanes M, Hearse DJ (1995) Preconditioning accelerates contracture and ATP depletion in blood-perfused rat hearts. Am J Phys 269(4 Pt 2):H1415–H1420. https://doi.org/10.1152/ajpheart.1995.269.4.H1415

9. Southworth R, Dearling JL, Medina RA, Flynn AA, Pedley BR, Garlick PB (2002) Dissociation of glucose tracer uptake and glucose transporter distribution in the regionally ischaemic isolated rat heart: application of a new autoradiographic technique. Eur J Nucl Med Mol Imaging 29(10):1334–1341. https://doi.org/10.1007/s00259-002-0922-2

10. Bell RM, Mocanu MM, Yellon DM (2011) Retrograde heart perfusion: the Langendorff technique of isolated heart perfusion. J Mol Cell Cardiol 50(6):940–950. https://doi.org/10.1016/j.yjmcc.2011.02.018

11. Sutherland FJ, Hearse DJ (2000) The isolated blood and perfusion fluid perfused heart. Pharmacol Res 41(6):613–627. https://doi.org/10.1006/phrs.1999.0653

12. Handley MG, Medina RA, Mariotti E, Kenny GD, Shaw KP, Yan R, Eykyn TR, Blower PJ,

Southworth R (2014) Cardiac hypoxia imaging: second-generation analogues of 64Cu-ATSM. J Nucl Med 55(3):488–494. https://doi.org/10.2967/jnumed.113.129015

13. Miller A, Wright GL (2011) Fabrication of murine ventricular balloons for the Langendorff heart preparation. J Biotechnol Biomater 1(101):1000101. https://doi.org/10.4172/2155-952x.1000101

14. Carvalho PA, Chiu ML, Kronauge JF, Kawamura M, Jones AG, Holman BL, Piwnica-Worms D (1992) Subcellular distribution and analysis of technetium-99m-MIBI in isolated perfused rat hearts. J Nucl Med 33(8):1516–1522

15. Garlick PB, Medina RA, Southworth R, Marsden PK (1999) Differential uptake of FDG and DG during post-ischaemic reperfusion in the isolated, perfused rat heart. Eur J Nucl Med 26(10):1353–1358. https://doi.org/10.1007/s002590050595

16. Smith AJ, Osborne BE, Keeling GP, Blower PJ, Southworth R, Long NJ (2020) DO2A-based ligands for gallium-68 chelation: synthesis, radiochemistry and ex vivo cardiac uptake. Dalton Trans 49(4):1097–1106. https://doi.org/10.1039/C9DT02354B

17. McCluskey SP, Haslop A, Coello C, Gunn RN, Tate EW, Southworth R, Plisson C, Long NJ, Wells LA (2019) Imaging of chemotherapy-induced acute cardiotoxicity with ^{18}F-labeled lipophilic cations. J Nucl Med 60(12):1750–1756. https://doi.org/10.2967/jnumed.119.226787

18. Baark F, Shaughnessy F, Pell VR, Clark JE, Eykyn TR, Blower P, Southworth R (2019) Tissue acidosis does not mediate the hypoxia selectivity of [(64)Cu][Cu(ATSM)] in the isolated perfused rat heart. Sci Rep 9(1):499. https://doi.org/10.1038/s41598-018-36145-1

19. Safee ZM, Baark F, Waters ECT, Veronese M, Pell VR, Clark JE, Mota F, Livieratos L, Eykyn TR, Blower PJ, Southworth R (2019) Detection of anthracycline-induced cardiotoxicity using perfusion-corrected 99mTc sestamibi SPECT. Sci Rep 9(1):216. https://doi.org/10.1038/s41598-018-36721-5

20. Medina RA, Mariotti E, Pavlovic D, Shaw KP, Eykyn TR, Blower PJ, Southworth R (2015) 64Cu-CTS: a promising radiopharmaceutical for the identification of low-grade cardiac hypoxia by PET. J Nucl Med 56(6):921–926. https://doi.org/10.2967/jnumed.114.148353

21. Shaughnessy F, Mariotti E, Shaw KP, Eykyn TR, Blower PJ, Siow R, Southworth R (2014) Modification of intracellular glutathione status does not change the cardiac trapping of 64Cu (ATSM). EJNMMI Res 4(1):40. https://doi.org/10.1186/s13550-014-0040-8

22. Mariotti E, Veronese M, Dunn JT, Medina RA, Blower PJ, Southworth R, Eykyn TR (2013) Assessing radiotracer kinetics in the Langendorff perfused heart. EJNMMI Res 3(1):74–74. https://doi.org/10.1186/2191-219X-3-74

23. Southworth R, Garlick PB (2003) Dobutamine responsiveness, PET mismatch, and lack of necrosis in low-flow ischemia: is this hibernation in the isolated rat heart? Am J Phys Heart Circ Phys 285(1):H316–H324. https://doi.org/10.1152/ajpheart.00906.2002

24. Southworth R, Shattock MJ, Hearse DJ, Kelly FJ (1998) Developmental differences in superoxide production in isolated Guinea-pig hearts during reperfusion. J Mol Cell Cardiol 30(7):1391–1399. https://doi.org/10.1006/jmcc.1998.0707

25. Garlick PB (1979) Molecular studies of cardiac metabolism (PhD thesis). Oxford University

Chapter 16

Brain PET Imaging in Small Animals: Tracer Formulation, Data Acquisition, Image Reconstruction, and Data Analysis

Hussein Bdair, Min Su Kang, Julie Ottoy, Arturo Aliaga, Peter Kunach, Thomas A. Singleton, Stephan Blinder, Jean-Paul Soucy, Marco Leyton, Pedro Rosa-Neto, and Alexey Kostikov

Abstract

Positron emission tomography (PET) is a noninvasive functional imaging modality that involves in vivo detection of spatiotemporal changes in the binding of radioactive pharmaceuticals (a.k.a. PET tracers) to their target sites in different organs. The development of new PET tracers commonly involves their preclinical evaluation in small rodents. Moreover, laboratory animal PET research is now being used with progressively greater frequency to complement human PET studies, to investigate in greater depth the underlying pathophysiology of human diseases, and to monitor the efficiency of novel therapeutic interventions. Here we describe the steps toward a successful small animal PET study, from tracer formulation and image acquisition to data reconstruction and analysis of the acquired scans, with a particular focus on its utility for the brain.

Key words Positron emission tomography, Preclinical imaging, PET tracers, PET image acquisition, PET image reconstruction, PET image analysis

1 Introduction

Positron emission tomography (PET) enables detection and mapping of discrete physiological processes implicated in cancers, heart, and brain diseases. PET radiotracers—radioisotopically labeled molecules targeting specific biomarkers—are administered to living subjects via intravenous bolus, infusion, bolus and constant infusion, or inhalation. Following beta-plus decay of the radioisotope, a positron (e^+ or β^+) is emitted from the radiotracer and, upon colliding with an electron (e^-), the two particles annihilate to emit two gamma (γ) photons traveling in the opposite directions near the speed of light. These γ photons are then simultaneously captured by the opposite scintillation detectors located in the scanner bore and reconstructed to generate a three-dimensional

image of the radiotracer biodistribution over time and, by extension, expression of the targeted biomarker.

[^{18}F]Fluorodeoxyglucose ([^{18}F]FDG) has been a valuable diagnostic PET tool in detecting tumors and their metastases for several decades and is now considered the gold standard radiotracer in diagnosing and staging various cancers. More recently, PET has been rapidly evolving beyond [^{18}F]FDG, thanks to the development of the target-specific radiotracers for imaging amyloid load [1], tau protein aggregates [2], and amino acid decarboxylase [3] in neurodegenerative diseases as well as neuroendocrine [4] and prostate tumors [5], to name a few. Validation of all novel PET tracers involves their preclinical evaluation in various animal species and often begins with imaging of the small rodents. While mice are perfectly suited for the evaluation of cancer-targeting onco-radiotracers due to the abundance of genetic and xenograft models, the small anatomical size of their brains makes the mice models suboptimal for preliminary studies of the neuro radiotracers. Rats are therefore preferred for brain radiotracer development workflow since they offer a good compromise between brain size, affordability, abundant disease models, and translational potential toward human studies. Here we present our standard procedures which we commonly deploy for brain PET imaging studies in rodents at the McConnell Brain Imaging Center (BIC) of the Montreal Neurological Institute (The Neuro). This general imaging protocol allowed us to evaluate numerous PET radiotracer candidates for imaging melatonin receptors [6], p75 neurotrophin receptors [7], and tropomyosin receptor kinase [8]; characterize animal models of human diseases [9]; and follow up the therapeutic effect of experimental drugs [10]. While the BIC at the Neuro is equipped with Siemens Concordia microPET R4 scanner [11], these general procedures can be employed with other commercial small animal PET scanners.

2   Materials

Prepare all solutions using sterile water and USP-grade reagents. All reagents can be prepared and stored at room temperature. Diligently follow all radiation safety regulations when handling radioactive materials. Diligently follow standard operating procedures and protocols approved by the local animal care committee when handling live animals.

2.1   Tracer Formulation and Quality Control (QC)

1. Sterile water.

2. Ethanol.

3. Disposable reversed phase cartridge (Waters C18, tC18 or Oasis), up to 135 mg load of resin.

4. Sterile vials.

5. Sterile syringes.

6. Sterile needles.

7. Analytical high performance liquid chromatography (HPLC) equipped with a radioactivity detector.

8. Gas chromatograph (GC).

9. pH paper or pH meter.

2.2 Animal Handling

1. Animals: usually purchased from a reputable source (e.g., Charles River) or bred in-house.

2. Isoflurane, USP inhalation anesthetic.

3. Isoflurane vaporizer, along with tubes and a nose cone.

4. Induction chamber.

5. Medical air.

6. Rectal temperature probe.

7. Respiration probe.

8. Isotonic saline (0.9% NaCl).

9. Gauze.

10. Alcohol swabs.

11. IV catheters.

12. Heated pad and/or infrared lamp.

13. Ophthalmic ointment (Natural tears).

14. Scale.

2.3 PET Image Acquisition

1. Sterile syringe.

2. Dose calibrator.

3. microPET scanner.

4. ^{57}Co point-source for the transmission scan and blank scans (*see* **Note 1**).

5. Computer with proprietary microPET software.

2.4 PET Image Reconstruction

1. Scanner proprietary software (e.g., Siemens microPET suite, including microPET Manager software, microPET SSD software, microQ, microQView, microPET MAP Files, and ASI-Pro VM software).

2.5 PET Image Analysis

1. MINC Toolkit software (http://bic-mni.github.io).

2. Computer with a Linux-based operating system (e.g., Ubuntu, MacOS X or similar) or a Unix-like environment and command-line interface for Microsoft Windows (e.g., Cygwin).

3   Methods

3.1   Tracer Formulation

This section discusses the formulation for administering living animals a typical ^{18}F- or ^{11}C-labeled radiotracer purified by semi-preparative reversed phase HPLC using typical organic solvents (acetonitrile, methanol, tetrahydrofuran, etc.). We do not discuss the radiosynthesis of those radiotracers due to the large variability of the labeling conditions.

1. Precondition a suitable disposable reversed phase cartridge, such as Waters Sep-Pak® C18, Sep-Pak® tC18, or Oasis® HLB with ethanol (minimum 5 mL) followed by water (minimum 10 mL). The choice of cartridge is radiotracer-specific and might require optimization. Most radiotracers, however, are efficiently trapped and released on the standard Waters Sep-Pak C18 Plus Light Cartridge (130 mg sorbent per cartridge).

2. Collect the fraction containing purified radiotracer from semi-preparative HPLC in a vial or flask prefilled with sterile water, minimum 5 times the volume of the HPLC eluate.

3. Pass the dilute aqueous solution of radiotracer through a pre-conditioned cartridge (*see* **Note 2**).

4. Wash the cartridge with sterile water (minimum 10 mL) to remove the traces of HPLC solvents and possible other polar impurities (*see* **Note 3**).

5. Elute the radiotracer trapped on the cartridge with ethanol (up to 1 mL) into the sterile vial equipped with a vent filter (*see* **Note 4**).

6. Optionally, attach a sterile filter between the cartridge and the sterile vial to ensure the sterility of the final formulation (*see* **Note 5**).

7. Pass sterile saline or phosphate-buffered solution (PBS) solution (up to 10 mL) along the same liquid path into the same sterile vial (*see* **Note 6**).

8. Withdraw a small aliquot of the formulated radiotracer for a quality control (QC) analysis.

9. Inject the portion of QC sample on an analytical HPLC equipped with the radioactivity detector to ensure:

   - Radiochemical identity by comparing the retention time of the radiotracer to that of the non-radioactive standard, taking into account the delay between the 2 detectors along the liquid path.

   - Radiochemical purity (RCP) by ensuring that the peak of radiotracer on radioactivity chromatogram accounts for ≥95% of the total counts.

- Chemical purity, by ensuring there are no other major peaks on the UV chromatogram.

- Calculate the molar activity (A_m) by quantifying the amount of non-radioactive standard in the sample (*see* **Note 7**).

10. Inject the portion of QC sample on GC system to ensure that the concentrations of the toxic organic solvents used in the radiosynthesis and semi-preparative HPLC are below the corresponding limits (*see* **Note 8**).

11. Measure the pH of the QC sample using calibrated pH-meter or validated pH paper to ensure it is in the physiological range of 4–8 (*see* **Note 9**).

3.2 Animal Handling and Preparation

1. Induce anesthesia in the animal by placing it in an induction chamber and then fill the chamber with isoflurane gas at a concentration of 5% with a flow rate of 2–3 L/min of medical air (*see* **Note 10**).

2. Following anesthesia induction, weigh the animal, transfer it to the scanner bed, and place it on top of a heating pad to maintain their body temperature. Maintain the anesthesia for the duration of the scan at 1.0–2.5% isoflurane with a 0.8 L/min medical air flow, delivered to the animal via a nose cone or a mask (*see* **Note 11**).

3. Apply an ophthalmic ointment (natural tears) to both eyes to prevent dryness and damage to the cornea. Reapply as needed.

4. Monitor body temperature of the animal by inserting the temperature probe in the rectum. Observe breathing rate of the animal by placing the respiration probe underneath the animal chest.

5. Clean the animal tail with a wet piece of gauze from any debris, then sanitize the injection site with an alcohol swab. Insert a catheter in the tail vein of the animal for later intravenous injection of the tracer.

6. Position the animal head in the center of the field of view (FOV) of the scanner.

3.3 PET Image Acquisition

This section will be limited to image acquisition of PET tracers that bind reversibly to their targets and are administered by intravenous bolus injection.

1. Withdraw a dose of the radiotracer (typically 10–30 MBq, depending on the animal weight, molar activity of the radiotracer, and scanner sensitivity) into a 1 mL (or exceptionally 3 mL) syringe (*see* **Note 12**).

2. Administer the entire content of the syringe as a bolus injection intravenously in the tail vein via the pre-installed tail vein cannula and concomitantly initiate the emission scan from the software.

3. Immediately remove the syringe and cannula altogether and measure the remaining radioactivity to account for the dead volume and the tracer retention on the plastic surfaces (*see* **Note 13**).

4. Cover the injection site on the animal's tail with sterile gauze and apply a light pressure for 1 min to stop bleeding.

5. Continue scan acquisition for the desired duration, typically 1 h (*see* **Note 14**).

6. Perform a 9 min transmission scan with the [57]Co point-source before or after the emission scan to correct for attenuation and scatter (*see* **Note 15**).

7. After the scan conclusion, turn off the isoflurane vaporizer and place the animal back into their enclosure. Keep the animal warm by using an infrared lamp or heated pad. Hydrate the animal with 0.2–0.5 mL per 10 g body weight of 0.9% NaCl, subcutaneously.

8. Acquire a 1 h blank transmission scan with the [57]Co point source (*see* **Note 16**).

3.4   PET Image Reconstruction

The section will be limited to image reconstruction of PET scans conducted with Siemens Concord microPET R4 scanner.

1. On the computer that operates the scanner, open the scheduler microQView and the microPET Manager (if not previously launched for the scan acquisition).

2. Generate the blank and transmission sinograms from the list-mode data by setting a histogram configuration file if not already defined. When launching this latter, select all the required files (*see* **Note 17**).

3. Generate the emission sinogram by also setting and launching a histogram configuration file (*see* **Note 18**).

4. Reconstruct the attenuation map from the attenuation sinogram by setting a reconstruction configuration file if not already defined. Then launch this latter script and select the attenuation sinogram to be reconstructed (file with an .atn extension) (*see* **Notes 19** and **20**).

5. Reconstruct the final image (for a static study) or images (for a dynamic study) of the 3D activity concentration distribution from the emission sinogram by setting a reconstruction configuration file if not already defined. Then launch this latter script and select the emission sinogram to be reconstructed (file with a .scn extension). Select the attenuation file or the manually segmented attenuation file previously described. The normalization file is automatically selected. Ensure it is the correct calibrated normalization (*see* **Note 21**).

3.5 PET Image Analysis

The step-by-step descriptions of various PET quantification methods and image analyses are too extensive to cover in this chapter. Instead, this section will focus on general PET image processing steps that can be used together with more advanced full- or semi-quantification methods. Specifically, we will describe the steps for manual registration and segmentation, quantification of standardized uptake value (SUV) and standardized uptake value ratio (SUVR), and generation of a time-activity curve (TAC). While there are numerous open-source libraries or software available to do image processing and analyses, we will use MINC Toolkit software as an example. We will use minimal command options as examples, but it does not showcase all usage examples of the MINC Toolkit.

Please note that for the accurate regional quantification of the brain PET images acquired using a standalone PET camera, a structural MR image must be acquired in the same study subject. The MRI acquisition sequence and detailed procedures may vary and they are not covered in this chapter. Depending on the study design, the PET and MR images may be acquired in any order, but in a relatively short timeframe, typically within 1 week. The steps below describe coregistration (overlapping) of the PET and MR images with consequent regional analysis of the former.

1. Download MINC Toolkit software that is developed at the McConnell Brain Imaging Centre, Montreal Neurological Institute from the following link: http://bic-mni.github.io

2. Convert the raw PET image with the header information to the minc format using the *upet2mnc* tool: **upet2mnc** <dynamic_PET_image.img.hdr> <dynamic_PET_image.mnc>.

3. Check if the output MINC image is working by using the *Display* tool: **Display** <dynamic_PET_image.mnc>.

4. Check if the output MINC image dimensions are correct by using *mincinfo* tool:**mincinfo** <dynamic_PET_image.mnc> (*see* **Note 22**).

5. Blur the PET image by using the *mincblur* tool: **mincblur** -fwhm <blurring_kernel> <PET_imgae.mnc> <blurred_PET_image.mnc> (*see* **Note 23**).

6. Coregister the PET image to the corresponding MR image. To do so:

   • Average the frames in the dynamic PET image by using the *mincaverage* tool: **mincaverage** -avgdim time -width_weighted <dynamic_PET_image.mnc> <averaged_PET_image.mnc>.

   • View the averaged reshaped PET and the MR images side-by-side via using the *register* tool: **register** <MRI_image.mnc> <averaged_reshaped_PET_image.mnc> (*see* Fig. 1 *and* **Note 24**).
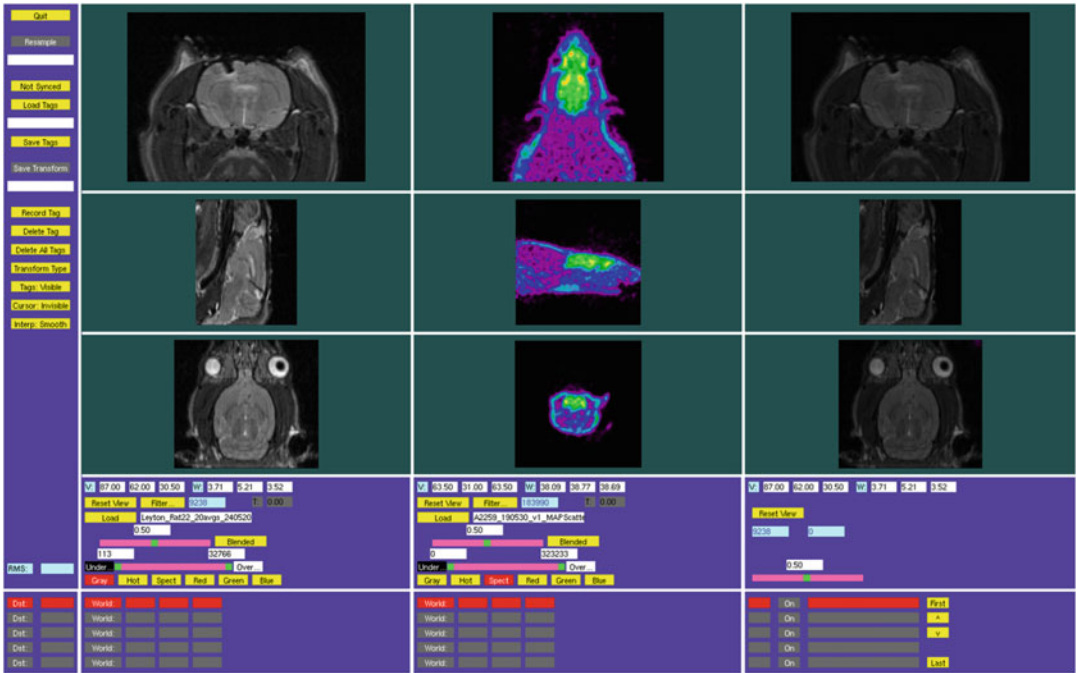
Fig. 1 Side-by-side view of the MR (left column) and PET (middle column) images prior to coregistration, using the *register* tool of the MINC Toolkit software

- Select a minimum of 4 landmarks (e.g., both eyes, the nose bone, the base of the skull) in both the PET and corresponding MR images (*see* Fig. 2 *and* **Note 25**).

- Coregister the original dynamic PET image to the space of the MR image by using the *mincresample* tool: **mincresample** <dynamic_PET_image.mnc> -transform <transformation_file.xfm> -like <MRI_image.mnc> <transformed_dynamic_PET_image.mnc>.

7. Create masks/labels of the regions of interest (ROIs). To do so:

- Open the image for the ROI analysis by using the *Display* tool: **Display** <MRI_image.mnc> (*see* Fig. 3 *and* **Note 26**).

- Using mouse or trackpad, manually draw or color the ROIs to be analyzed and saved (*see* Fig. 4 *and* **Note 27**).

- Once the new masks/labels are finished, save the files (*see* **Note 28**).

8. Create SUV or SUVR images. To do so:

- Select the time windows to be averaged together by using the *mincreshape* tool: **mincreshape** -dimrange time=<−start_frame>,<end_frame> <dynamic_PET_image.mnc> <reshaped_dynamic_PET_image.mnc>.
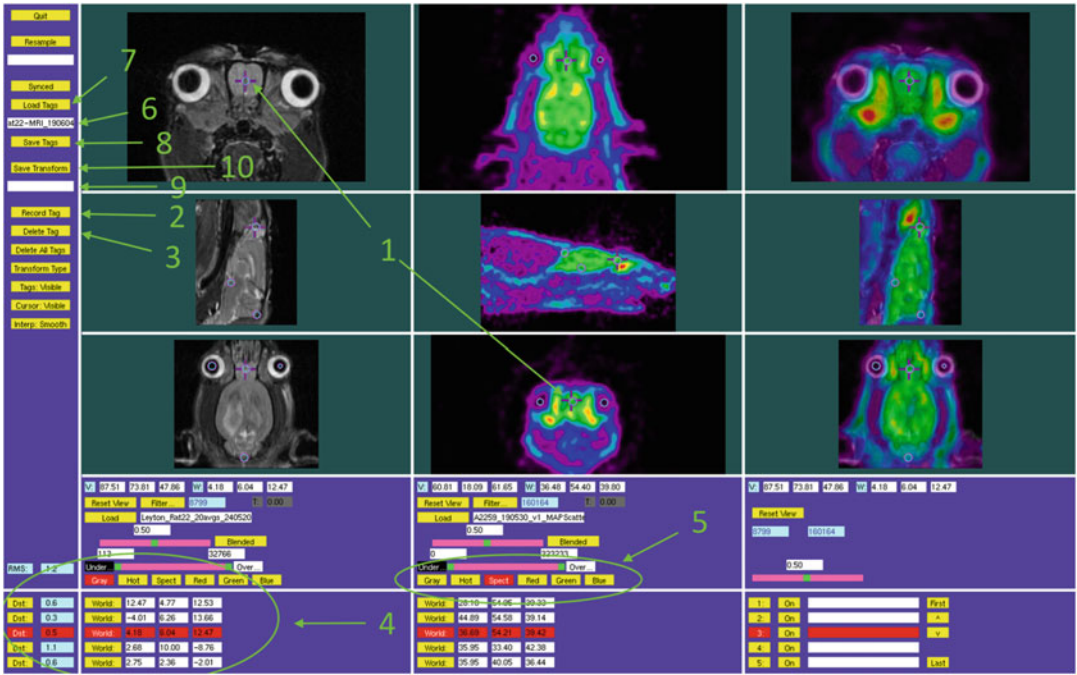
Fig. 2 Coregistration of the PET and corresponding MR images using the *register* tool. Left column: MR images; middle column: PET images; right column: overlapped images. (1) A tag of the nose as a representative landmark. (2) *Record Tag* button. (3) *Delete Tag* button. (4) A list of tags. (5) Image colormaps. (6) Box of the name of a .tag file. (7) *Load Tag* button. (8) *Save Tag* button. (9) Box of the name of an .xfm file. (10) *Save Transform* button
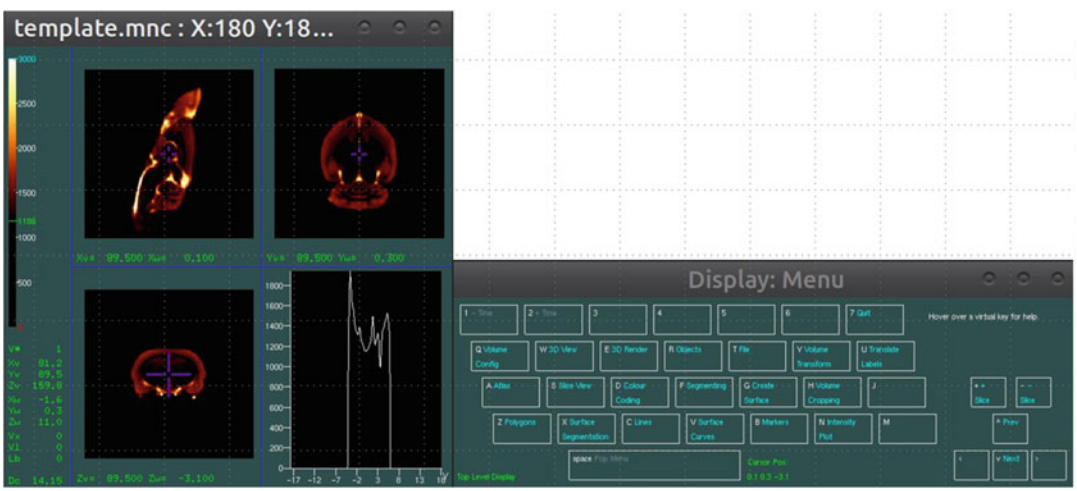
Fig. 3 First view of the windows opened using Display command. Left window: brain images; right window: *Display* menu
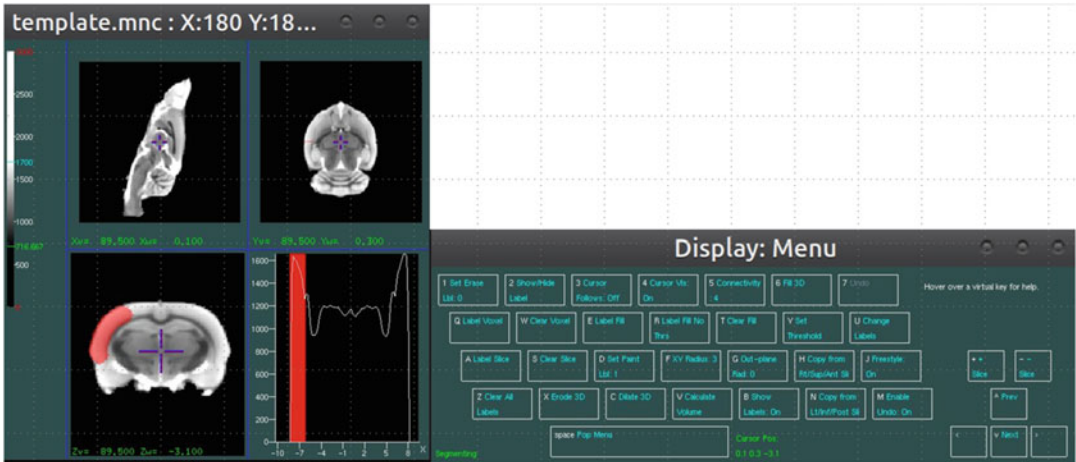
Fig. 4 Segmentation of a brain region manually using the Display tool using part of the cortex as an example

- Average the frames together by using the *mincaverage* tool: **mincaverage** -avgdim time -width_weighted <reshaped_-dynamic_PET_image.mnc>   <averaged_   PET_image.mnc>.

- To calculate SUV, normalize the image by the injected dose and body weight ratio by using the *mincmath* tool: **mincmath** -mult –const <body_weight>/<injected_dose> <averaged_ PET_image.mnc> <SUV_PET_image.mnc> (*see* **Note 29**).

- To calculate SUVR, get a reference region value by using the *mincstats* tool: **mincstats** -mask <reference_region.mnc> -mask_binvalue <your_ROI_label_number> -mean <averaged_PET_image.mnc>.

- Then, normalize the averaged PET image to the reference region value by using the *mincmath* tool: **mincmath** -div -const <reference_region_mean_value> <averaged_PET_-image.mnc> <SUV_PET_image.mnc>.

9. Create a time-activity curve. To do so,

- Select individual time frames by using the *mincreshape* tool: **mincreshape** -dimrange time=<start_frame>,<end_-frame> <dynamic_PET_image.mnc> <reshaped_dyna-mic_PET_image.mnc>.

- Get the ROI value by using the *mincstats* tool: **mincstats** -mask <ROI.mnc> -mask_bonvalue <your_ROI_label_-number> -mean <individual_frame_PET_image.mnc>.

- Repeat these steps until all of the frames have been calculated for each ROI value.

- Plot these values against the time information of the PET scan per frame.

4   Notes

1. A ^{68}Ge point source and ^{68}Ge cylinder are needed to produce a calibrated normalization file which is required for the reconstruction of images. This file is generated only once, after a system setup, or an intervention on a detector module, or when the daily quality control test fails. The generation of the calibrated normalization file lies beyond the scope of this chapter.

2. This can be done either manually by withdrawing the dilute HPLC eluate into a large syringe (e.g., 50 mL) and passing it through a cartridge or semi-automatically by either using a syringe dispenser (withdraw and push through method) or applying a vacuum (pull method). In case of manual formulation, seek approval of the local radiation safety officer (RSO) and make sure you are not exceeding the maximum radioactivity dose that can be handled manually.

3. Consider placing a stopcock upstream of the cartridge to rapidly and conveniently switch the input to the cartridge between the dilute HPLC eluate and the sterile water to wash the cartridge.

4. Consider placing a stopcock downstream of the cartridge to rapidly and conveniently switch the output from the cartridge between the waste and the sterile vial.

5. Make sure the casing and the membrane of the sterile filter are resistant to neat ethanol. Some filters with polycarbonate casings crack and leak when used with ethanol.

6. PET tracers for brain imaging are typically lipophilic small molecules, which require ethanol content in the formulation to prevent precipitation and absorption to plastic syringes and catheters. The maximum ethanol concentration for animal injection is 10% aqueous solution.

7. Prepare the calibration curve (amount of standard vs. the UV area peak) in advance of the PET imaging experiment to quantify the molar amount of tracer. The A_m equals the radioactivity of the sample divided by the molar amount of the non-radioactive compound and is typically measured in mCi/μmol or GBq/μmol.

8. Limits for the most commonly used organic solvents used in radiosynthesis and HPLC are acetonitrile, 410 ppm; methanol, 3000 ppm; tetrahydrofuran, 720 ppm; *N*,*N*-dimethylformamide, 880 ppm; *N*,*N*-dimethylacetamide, 1090 ppm. For more information, refer to USP documents, e.g., https://www.uspnf.com/sites/default/files/usp_pdf/EN/USPNF/generalChapter467Current.pdf

9. pH lower than 4 might cause itching or even burning at the injection site that will result in twitching of the animal after administration.

10. Take the animal out of the incubation chamber once their respiration rate is relatively slower (typically 1–2 min after inducing anesthesia).

11. This step needs to be performed in a timely manner to avoid the animal recovering from anesthesia. In case the same isoflurane vaporizer is being used for anesthesia induction and maintenance, ensure to connect the tubing of the nose cone and disconnect the tubing of the induction chamber from the vaporizer upon transferring the animal to the scanner bed.

12. The total injected volume should never exceed 5 mL/kg. Therefore, for a typical rat weighing 300–500 g, a 1 mL syringe should be sufficient. In terms of the injected activity per body weight, the dose largely depends on the sensitivity of the PET camera. In our experience, the optimal dose for Siemens Concord microPET R4 camera is about 1 μCi/g (37 kBq/g). Also for the baseline scan, the target occupancy by the injected molar amount of the ligand ideally should not exceed 1%.

13. If the time between measurements is longer than 1 min, the residual activity measured in the syringe and catheter should be corrected for decay to the time of injection using the half-life of the PET isotope to accurately calculate the injected dose of activity.

14. Avoid maintaining the anesthesia for longer than 60 min, at most 90 min.

15. Ideally, conduct the transmission scan prior to tracer injection if this can be done (make sure the animal is already positioned inside the bore of the camera and there is sufficient radioactivity available). However, if the transmission scan cannot be performed before tracer injection (e.g., when limited radioactivity of the tracer necessitates immediate injection), conduct it after the emission scan. Note that there is almost no cross contamination of the transmission scan by the tracer since their respective energy windows are well apart.

16. This is done once a day at any time by leaving the FOV empty.

17. In the "Acquisition Mode" field, select "Blank Singles" and "Transmission Singles" for the blank and transmission scans, respectively. Set the "Histogram Type" as single-slice rebinning (SSRB). Keep the default values for all the other fields. Note that blank and transmission scans must be histogrammed with the same parameters (only "Acquisition Mode" differs). The blank sinogram should be generated first since it will be automatically selected to histogram the transmission scan.

18. In the "Acquisition mode" field, select "Emission" and define the "Dynamic Framing" according to the protocol parameters (in seconds). For the "Data Format" field, avoid the default value (2-byte integer), especially for the long scans or when high activity is injected. Keep the default value for the remaining fields.

19. Set the "Reconstruction Algorithm" to "2D FBP" for faster reconstructions or to "MAP TR" for higher quality segmented reconstructions. Set the desired "Image Zoom" and "Image Size" (defaults are 1 and 128, respectively). The other fields should remain with their default values.

20. The reconstruction of the attenuation map is not a required step to generate the final emission image. It is a quality control step before performing the attenuation and scatter corrections for the reconstruction of the emission data. If the map is not satisfactory (too noisy or wrong values), one can use the segmentation tool accessible from ASIPro to correct the map. From ASIPro menu, select "Tools" > "mu-Map Calibration and Segmentation," choose the attenuation map to be corrected (or a smoothed version of it) and click on "Skip Calibration." A segmented map with 5 segments is then displayed beside the spectrum of the attenuation values (mu-values) and the visualization of the segments. Boundaries and mu-values of each segment can be tuned until the obtention of a satisfactory segmented map. Then click on "Segment" to segment the attenuation map and proceed to the final projection step of the newly segmented map. Click "OK" to obtain a new segmented attenuation sinogram (file with an .atn extension) and exit the procedure.

21. Choose a "Reconstruction Algorithm" between "2D FBP" and "3DRP," which are fast analytical algorithms, or "OSEM2D," "OSEM3D," and "MAP," which are iterative methods providing better images at the cost of a slower reconstruction process. For higher image quality, OSEM3D/MAP option should be chosen. Set "Image Zoom" and "Image Size" as desired. "Scatter Correction" should be checked and "Image Data Type" set to 4-byte float. For OSEM3D algorithm, set "OSEM 3D Iterations" to 12, "MAP Iterations" to 0. "Resolution" is ignored. For the "Uniform" field, check Resolution and uncheck "Use FastMAP." For MAP algorithm, set "OSEM 3D Iterations" to 0, "MAP Iterations" to 18, "Resolution" to 1.8. Check Resolution for the "Uniform" field and uncheck "Use FastMAP." The authors recommend the MAP algorithm, which generally provides the best image quality. Note that the optimal number of iterations for MAP or OSEM3D depends on the type of study, more specifically on

the characteristics of the activity concentration distribution inside the scanned animal. The numbers mentioned above are generic.

22. **mincinfo** <dynamic_PET_image.mnc> will show the dimension information of the dynamic PET file. There are length, step, and start columns describing each dimension in time: zspace, yspace, and xspace. Here, the step and start in the time dimension could say *unknown* for a dynamic PET file because the information can be irregular or arbitrary. For example, typically PET scans have increasing time in each frame (9 × 30 s, 6 × 1 min, 5 × 2 min, 7 × 5 min) and this will be considered irregular time spacing. More detailed information can be found in the minc file header by **mincheader** <file.mnc>. The length of time refers to the number of frames.

23. This step can be performed to improve the signal-to-noise ratio (SNR) either prior to the PET image coregistration to the MRI space or just before calculating SUV. The recommended size of a blurring kernel for brain PET images in rodents is twice the size of the pixel.

24. If the MR image is in NIFTI format, convert it to the MINC format by using the *nii2mnc* tool: **nii2mnc** <MRI_image.nii> <MRI_image.mnc>. If the MR image is in DICOM format, convert it to the MINC format by using the *dcm2mnc* tool: **dcm2mnc** <MRI_image.dcm> <MRI_image.mnc>. For optimal visualization, change the colormap of the PET and MRI images to *spectral* and *gray*, respectively.

25. It is important to note that the first image column is the target space and the second image column is the source space. Thus, the transformation generated from this step should be applied to the second image in forward transformation. To select the landmarks, place the cursor at the same landmark in both the PET and MR images and then tag them by clicking on *Record Tag* in the left panel. To remove a tag, select it from the list of tags at the bottom of the image click on *Delete Tag* in the left panel. Save the tags in a .tag file by naming the file in the box in left panel, between *Load Tags* and *Save Tags*, then click on *Save Tags*. Tags can be later recalled by typing the name of the .tag file in the same box and then clicking on *Load Tags*. Save the transformation (.xfm) file by naming it in the box in the left panel below *Save Transform*, then click on *Save Transform*. Both the .tag and .xfm files are saved in the same directory of the PET image where *register* was opened.

26. Both windows are interactive. For example, the color scale can be adjusted manually by dragging the top (blue) and bottom value (green) lines. Furthermore, the Menu functions have

hierarchies. Enter by clicking on the menu and go back to the previous menu by clicking *Pop Menu*. The Menu function can also be controlled by using the computer keyboard as indicated on the Menu window. Hover over the Menu key to get the virtual help description on the Menu window.

27. To segment, click on *segmenting* from the Menu. Start segmenting or drawing the mask/label by clicking and holding the right-click on the mouse. The size of the paintbrush can be changed by clicking *XY Radius* and putting the appropriate size and clicking *Enter*. The label number can be changed by clicking *Set Paint Lbl:* # and putting in the new label number and clicking enter. To delete the segmentation to edit, do the same procedure as drawing except also holding the *Shift* button on the keyboard. Repeat the process until the 3D region is completed. The next slice of the volume is controlled by the $+/-$ keyboard buttons.

28. To save the ROIs, click on *File* and click on *Save Labels.mnc* from the Menu. Then a new pop-up window will appear to navigate where to save the file with a specific name.

29. To correctly calculate SUV as a unitless value, note the units of the raw PET image after the reconstruction. In the example above, the units are becquerel per cubic centimeter (Bq/cc). Thus, the body weight and injected dose should be converted to the same units before normalizing. To convert the body weight to liters, assume the density of the tissues to be 1 kg/L. The general formula to calculate the SUV is: $SUV_{ROI} = (C_{img} \times BW) \div ID$, where C_{img} is the image-derived radioactivity concentration in the ROI in Bq/cc, BW is the body weight in grams, and ID is the injected dose in Bq.

References

1. Garber K (2012) First FDA-approved beta-amyloid diagnostic hits the market. Nat Biotechnol 30(7):575

2. Barthel H (2020) First tau PET tracer approved: toward accurate in vivo diagnosis of Alzheimer disease. J Nucl Med 61(10):1409–1410

3. Dhawan V et al (2020) Prospective FDOPA PET imaging study in human PD: our final step towards NDA approval. J Nucl Med 61 (supplement 1):1565

4. Hennrich U, Kopka K (2019) Lutathera®: the first FDA- and EMA-approved radiopharmaceutical for peptide receptor radionuclide therapy. Pharmaceuticals 12(3):114

5. Wurzer A et al (2021) Automated synthesis of [^{18}F]Ga-rhPSMA-7/−7.3: results, quality control and experience from more than 200 routine productions. EJNMMI Radiopharm Chem 6(1):4

6. Bdair H et al (2022) Radiosynthesis and in vivo evaluation of four positron emission tomography tracer candidates for imaging of melatonin receptors. ACS Chem Neurosci 13(9):1382–1394

7. Gibon J et al (2016) Towards the PET radiotracer for p75 neurotrophin receptor: [^{11}C] LM11A-24 shows biological activity in vitro, but unfavorable ex vivo and in vivo profile. Bioorg Med Chem 24(19):4759–4765

8. Singleton TA et al (2020) Efficient radiosynthesis and preclinical evaluation of [^{18}F]FOM-PyD as a positron emission tomography tracer candidate for TrkB/C receptor imaging. J Labelled Comp Radiopharm 63(3):144–150

9. Parent MJ et al (2017) Multimodal imaging in rat model recapitulates Alzheimer's disease biomarkers abnormalities. J Neurosci 37(50):12263–12271

10. Kang MS et al (2020) A novel p75-neurotrophin receptor antagonist, EVT901, reduces neuroinflammation in the TgFAD344 rat model of Alzheimer's disease. Alzheimers Dement 16(S9):e046697

11. Knoess C et al (2003) Performance evaluation of the microPET R4 PET scanner for rodents. Eur J Nucl Med Mol Imaging 30(5):737–747

Chapter 17

CRISPR/Cas for PET Reporter Gene Engineering

Taemoon Chung, Joseph R. Merrill, and Scott K. Lyons

Abstract

The relatively recent discovery of CRISPR/Cas has led to a revolution in our ability to efficiently manipulate the genome of eukaryotic cells. We describe here a protocol that employs CRISPR technology to precisely knock-in a PET imaging reporter transgene into a specific genetic locus of interest. Resulting transcription of the targeted reporter will more accurately mimic physiologic expression of the endogenous allele than conventional approaches, and so this method has the potential to become an efficient way to generate a new generation of "gold-standard" reporter transgenes. We break down the protocol into three experimental stages: how to identify the genomic location that the reporter transgene will be inserted, how to practically insert the reporter transgene into the genome, and how to screen resultant clones for the correct targeted event.

Key words CRISPR, Reporter transgene, Imaging, PET, Cas9, Knock-in, Double-strand break, DNA repair, Non-homologous end joining

1 Introduction

Reporter transgenes (RTs) have been used for many years as a proxy readout for the expression of a gene or the activity of a biological process of interest. Cells "light up" when a gene is expressed or a molecular pathway is active, and so specific aspects of cellular biology can be readily and non-destructively assessed in vivo during development, disease, or following experimental perturbation.

Frequently, a short piece of relevant promoter sequence (<1 kb) is cloned upstream of the RT to regulate its transcription and achieve this kind of imaging readout [1, 2]. Although relatively quick to make and use, such constructs have several significant limitations that can ultimately make them misleading. First, not all relevant regulatory elements are necessarily present within the short promoter fragment employed, and second, the genomic integration site of stable expressing cells is random, and so expression of the reporter can be influenced by neighboring genomic sequences or by epigenetic modification of the integration site

(the position effect). Other methods have been developed to try to counter these limitations (e.g., "safe-harbor" cloning at the ROSA locus [3], BAC cloning [4], or gene targeting via homologous recombination [5]), but these either do not address all issues or can be significantly more technically challenging and time-consuming to employ.

Since the first reports of its ability to efficiently cleave double-stranded DNA with precision in 2012 [6], CRISPR technology has advanced at a terrific pace, completely revolutionizing molecular biology [7]. Although frequently used to knock-out the expression of specific genes, CRISPR can also be used to precisely introduce (or "knock-in") a reporter transgene at a defined location of the genome in practically any eukaryotic cell type of interest. Using an approach previously described by others [8, 9], we present here a detailed description of the practical steps needed to insert a RT into a defined genomic location by this method. Resulting knock-in reporters transcribe as the targeted endogenous allele, largely obviating the limitations of conventional approaches and giving rise to a new gold standard of reporter. With care, reporters can be knocked-in in such a manner as to minimally affect the expression or function of the endogenous allele, which in some cases could inadvertently give rise to a cellular phenotype.

The approach relies upon the transfection of two plasmids into the cell line of interest (Fig. 1). One plasmid (which we refer to as plasmid A) expresses Cas9 and a guide RNA (gRNA) that is specific to the knock-in site in the recipient cell genome. The other plasmid (denoted here plasmid B) is the donor vector and contains the RT expression cassette flanked by short sequences of DNA that do not arise in the mammalian genome [8, 9]. Plasmid B also expresses a
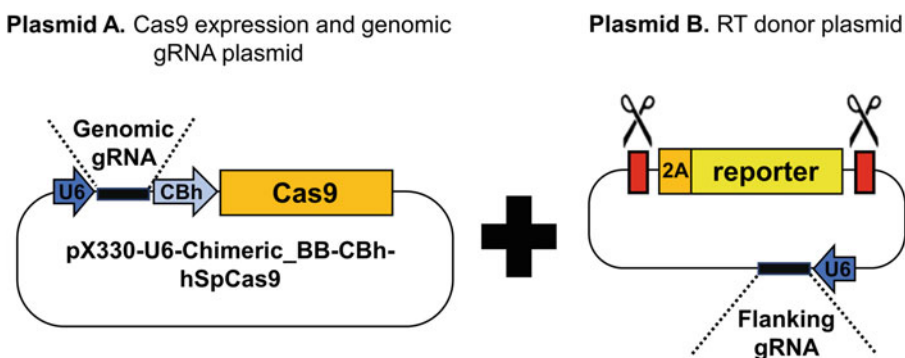
Fig. 1 Two plasmid system. This knock-in approach relies upon the co-transfection of two plasmids (denoted here as A and B) into the cell line of interest. Plasmid A expresses both the Cas9 enzyme and a gRNA specific to the location in the genome where the RT will be inserted. Plasmid B contains the RT donor sequence that will be inserted into the genome, flanked by non-mammalian sequences and a gRNA specific to that flanking sequence

gRNA specific to those flanking sequences. Upon transfection of both plasmids, Cas9 protein and the two gRNAs are expressed. Cas9 and the genomic gRNA make a double-strand break (DSB) in the genome, and this governs the site of RT insertion. Cas9 and the non-mammalian gRNA make DSBs on either side of the RT donor sequence, effectively dropping it out from its plasmid backbone as a linear piece of DNA. Lackner et al. [8] demonstrated that this linear piece of DNA can be incorporated into the genomic DSB by a DNA repair process called non-homologous end joining (NHEJ) at a practically useful frequency. When inserted in-frame and either between the promoter of the gene of interest and its coding sequence (5′ knock-in) or just before the stop codon (3′ knock-in), the RT donor sequence will transcribe as the endogenous targeted allele with minimal disruption (Fig. 2). Any genetically encoded RT can be knocked in by this method, but as exemplified by this issue dedicated to in vivo PET imaging methods, the use of a PET RT (Table 1) would afford the researcher certain unique experimental advantages, such as highly sensitive tomographic in vivo images of gene expression.
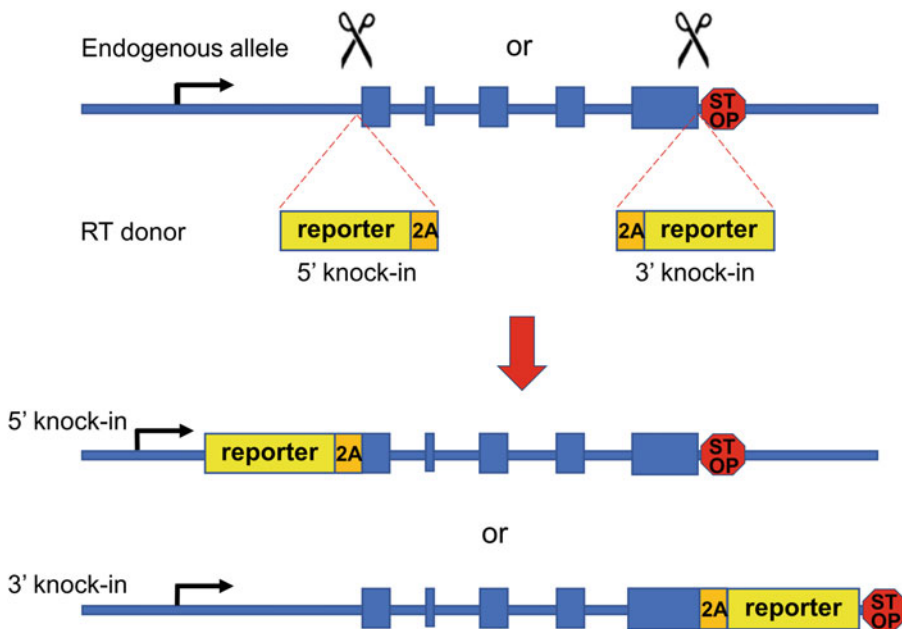
Fig. 2 An overview of how a reporter transgene can be inserted into the genome and minimally affect the expression of the targeted endogenous allele. RTs can be inserted at either the 5′ end of the gene of interest, immediately upstream of the endogenous ATG start codon, or at the 3′ end, immediately upstream of the stop codon. To ensure co-expression, a 2A sequence [12] can be employed between and in the same reading frame as both genes. It is also important to ensure that no stop codons are inadvertently introduced between the endogenous gene, RT, and 2A sequence during cloning

Table 1
Commonly used PET reporter transgenes and their tracers

Class	Gene	PET tracer(s)	References
(Transmembrane) Transporter	Sodium iodide symporter (NIS)	^{18}F-TFB; [124]I-NaI	[20]
	Organic anion transporting protein 1a1 (Oatp1a1)	^{68}Ga-EOB-DTPA	
(Extracellular) Receptor	Somatostatin receptor type 2 (SSTR2)	^{68}Ga-DOTATOC; ^{68}Ga-DOTATATE	[21]
	Dopamine 2 receptor (D2R)	^{18}F-FESP; ^{11}C-raclopride; ^{18}F-fallypride	
	Glutamate carboxypeptidase II (GCPII), i.e., prostate-specific membrane antigen (PSMA)	^{68}Ga-PSMA-11; ^{18}F-PSMA-1007; ^{18}F-DCFPyL	
(Intracellular) Kinase	Herpes simplex virus type 1—tyrosine kinase (HSV1-tk)	[124]I-/^{18}F-FIAU; [124]I-/^{18}F-FEAU; ^{18}F-FHBG	[22]
	Pyruvate kinase M2 (PKM2)	^{18}F-DASA-23	

We break the overall protocol down into three main parts. First, how to identify a specific gRNA sequence and define the precise location of RT insertion into the host cell genome. Second, we discuss design considerations for the RT donor sequence and how to practically achieve targeting in a cell line of interest. Third, how to screen resulting clones for correctly targeted insertion of the reporter transgene into the genome. Finally, to aid visualization, we illustrate the success of this method with the targeted insertion of a fluorescent RT donor sequence to the 5′ end of a gene called NQO1, the expression of which indicates that a cell is experiencing oxidative stress.

We assume prior knowledge of basic molecular biology and in vitro tissue culture techniques. However, we appreciate that CRISPR biology may not be completely familiar to all within the molecular imaging research community and have attempted to clearly explain the reasoning behind each step. Should further background information on CRISPR technology or its many applications be needed, several excellent general review articles have been published recently [7, 10].

2 Materials

2.1 Plasmid Vector Construction

1. pX330-U6-Chimeric_BB-CBh-hSpCas9 (Addgene; #42230), or equivalent plasmid for Cas9 and genomic gRNA expression (plasmid A; *see* **Note 1**).

2. Tia1L-MCS plasmid (available upon request [8], or equivalent "double-cut NH-donor" plasmid (Addgene; #83576) [9] for RT donor sequence (plasmid B).

3. DNA oligonucleotides: 0.025 μM, unmodified and desalt purification.

4. Gene synthesis of RT donor sequence (*see* **Note 2**).

5. TNE buffer: 10 mM Tris-HCl pH 7.5, 1 mM EDTA, 50 mM NaCl.

6. TE buffer: 10 mM Tris-HCl pH 7.5, 1 mM EDTA.

7. T4 DNA ligase.

8. Top10F competent bacteria, liquid LB and LB-ampicillin broth, and LB-ampicillin agarose plates.

9. Restriction enzymes.

10. TAE buffer (1×): 40 mM Tris-HCl, 20 mM glacial acetic acid, 1 mM EDTA pH 8.0.

11. 0.8% Agarose gel: 0.8 g Agarose, 100 mL TAE buffer, 10 μL SYBR Green (or equivalent DNA stain).

12. 1 kb DNA ladder.

13. DNA gel extraction kit.

14. Plasmid DNA miniprep and maxiprep kits.

2.2 Co-transfection of Cell Line and Selection of Clones

1. Cell line of interest (e.g., MIA PaCa-2 cells or HEK293T cells).

2. Lipofectamine 3000.

3. Opti-MEM reduced serum media.

4. DMEM medium: containing 10% fetal bovine serum (FBS) or equivalent routine cell culture media.

5. Phosphate Buffered Saline (PBS).

6. Trypsin.

7. 24-well plate and 10 cm dish.

8. Antibiotic for positive selection of stably integrated clones (e.g., puromycin or hygromycin).

9. Adeno-FlpO (Vector Biolabs; #1775); optional.

2.3 Analysis of Targeted Clones

1. Genomic DNA extraction and gel purification kits.

2. PCR reagents.

3. Knock-in locus-specific and internal RT-specific DNA oligonucleotides 0.025 μM, unmodified and desalt purification.

4. 0.8% Agarose gel: 0.8 g Agarose, 100 mL TAE buffer, 10 μL SYBR Green (or equivalent DNA stain).

5. Sanger DNA sequencing from preferred supplier.

3   Methods

3.1   Identify a gRNA to Specify the Genomic Location of the RT Knock-In

The reporter transgene will be inserted into the genome at the site of a CRISPR-mediated double-strand break (DSB). It is therefore important to identify a genomic gRNA that is specific to the locus being targeted and with the least potential for off-target activity (i.e., with the least number of closely related sequences spread throughout the genome). Multiple software programs have been developed to identify and rank the specificity of gRNA sequences, such as CHOPCHOP (http://chopchop.cbu.uib.no/) or CRIS-Pick at the Broad Institute (https://portals.broadinstitute.org/gppx/crispick/public). The key practical steps are illustrated by Figs. 3 and 4.

1. Using the open access "Gene" program from the NCBI (https://www.ncbi.nlm.nih.gov/gene/), select the relevant species and gene of interest. As shown by Fig. 3a, a software viewer then displays the genomic organization of that gene (the exon and intron boundaries), as well as translated and untranslated sequence of the mRNA transcript. By using the magnifying glass tool, it is possible to zoom in and view the region of interest at the single nucleotide level (Fig. 3b).

2. Select approximately 200 base pairs (bp) of genomic sequence for analysis to identify a specific gRNA. If planning to insert the RT donor sequence upstream of the gene of interest, select approximately 200 bp of genomic sequence immediately upstream and including the ATG start codon. If targeting the 3′ end of the gene, select approximately 200 bp of sequence just before and including the stop codon for gRNA analysis (Fig. 2, also *see* **Note 3**).

3. The best genomic gRNA will have low potential for off-target activity and be close to either the ATG or stop codon of the gene of interest. As shown by Fig. 4, order complementary oligonucleotides with the appropriate overhangs to enable efficient cloning into pX330. Alternative Cas9 and genomic gRNA expression plasmids will also work with this protocol, but the precise gRNA cloning strategy as detailed here will likely be different.

3.2   Clone Genomic gRNA into Plasmid A

1. Using the results from Subheading 3.1, order sense and antisense oligonucleotides (as illustrated in Fig. 4) and resuspend to 10 μM in TNE buffer.

2. To anneal the complementary oligos, mix 10 μL of both resuspended oligos in a 0.5 mL Eppendorf tube. Incubate at 95 °C for 5 min and allow tube to slowly cool back to room temperature (25 °C) over 45–60 min. Take 1 μL of annealed oligo and dilute 1:50 in TE buffer.
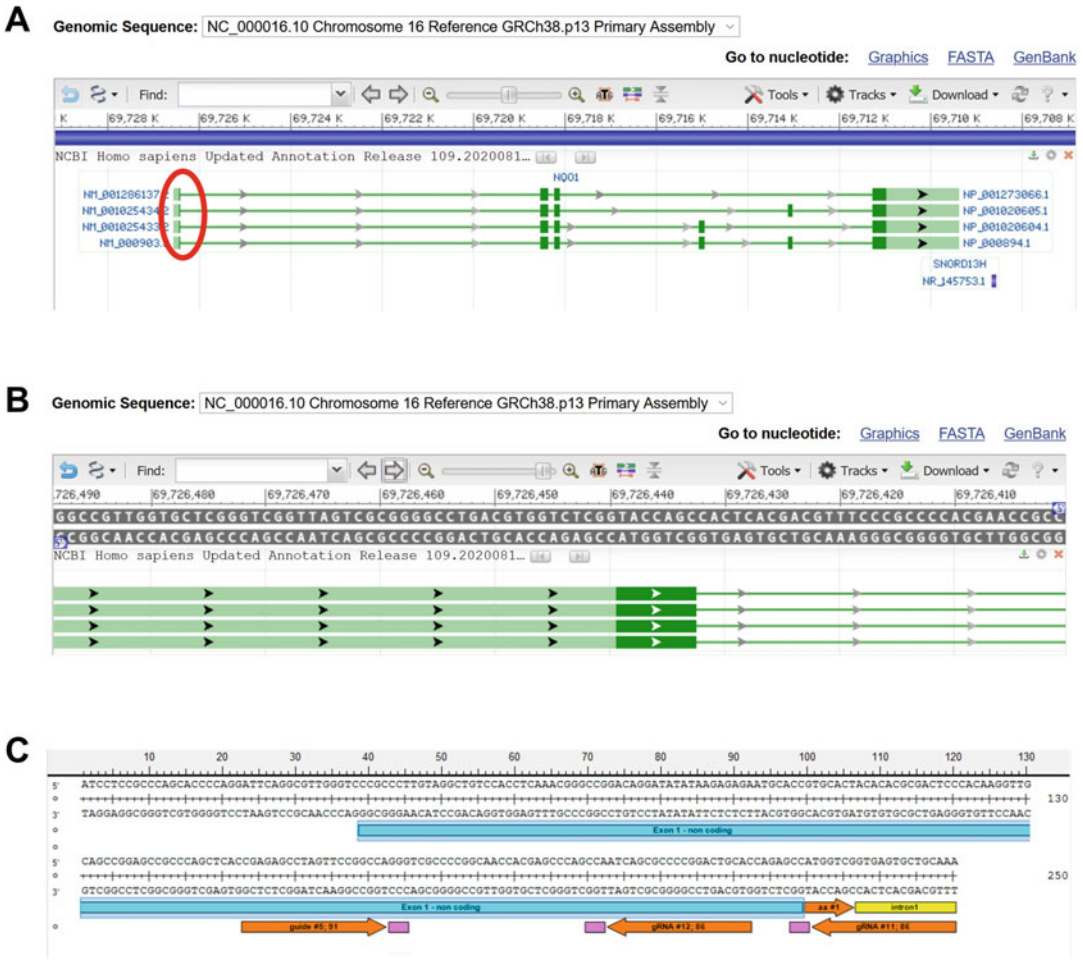
Fig. 3 How to identify a specific genomic gRNA to insert the RT into the genome. (**a**) The browser view of the NCBI program "Gene" and the genomic organization of the gene of interest in the relevant species; in this instance, the human NQO1 locus. Four splice isoforms are noted here; dark green boxes indicate coding exons, light green boxes denote non-coding exons. (**b**) A zoomed-in sequence level view of NQO1 exon 1 (the region within the red oval in A). Once this sequence is analyzed, (**c**) depicts genomic NQO1 sequence with three highly ranked candidate gRNA sequences and locus features manually annotated (Seqbuilder, Lazergene). Note that the PAM sequence (NGG, pink box, where N is A, T, C, or G) immediately follows the 20mer sequence of the gRNA. This is helpful for correct orientation and cloning of the gRNA that will ultimately make the DSB in the genome

3. Cut pX330 plasmid with BbsI restriction enzyme as instructed by supplier and run on a 0.8% TAE agarose gel. Cut out corresponding DNA band and gel purify with a DNA gel extraction kit.

4. Set up a 20 μL ligation reaction. To 2 μL of 10× DNA ligation buffer (supplied with enzyme) add 50 ng of BbsI cut pX330 vector (not dephosphorylated), 1 μL of annealed oligo and
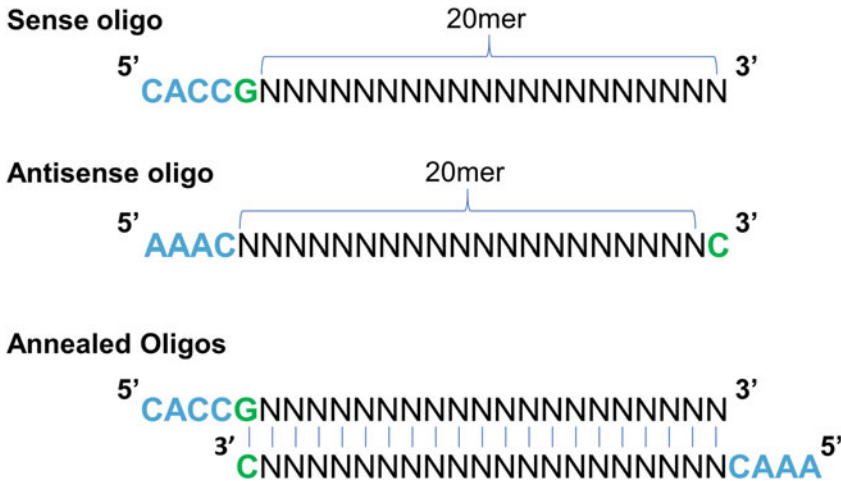
Fig. 4 How to clone a genomic gRNA into plasmid A. Note that the sense oligo is identical to the sequence returned by the gRNA analysis program. When looking at the genomic sequence, the 3 nucleotides that immediately follow the sense oligo will be the 'NGG' PAM sequence. The antisense oligo is complementary to the sense oligo. The blue bases denote the 5′ overhangs that are complementary to BbsI cut pX330. The green base is optional, but it has been suggested that a G residue at +1 is required to efficiently initiate transcription from the U6 promoter, a RNA polymerase III promoter [19]

nuclease-free dH$_2$O to 19 μL. Mix gently with a pipette tip, then add 1 μL T4 DNA ligase and incubate at room temperature for 1 h.

5. Transform competent bacteria with ligated DNA. Take 2 μL of ligation reaction and add to 25 μL of competent bacteria (e.g., Top10F cells) defrosted on ice, gently stirring with pipette tip. Keep tube on ice for 30 min, then heat shock in a 42 °C water bath for 45 s and place back on ice for 2 min. Add 1 mL of LB broth (no antibiotic) and incubate on a 37 °C shaker for 1 h.

6. Plate out 100–200 μL of transformed bacteria on a LB-ampicillin agarose plate and grow colonies overnight at 37 °C. The next day, pick 12 colonies to grow overnight in 5 mL liquid cultures at 37 °C in LB-ampicillin broth. The day after that, take 1.5 mL of turbid liquid culture and purify plasmid DNA as per the manufacturer's instructions of a plasmid miniprep kit.

7. Quick confirmation of gRNA cloning can be made by running an AgeI/BbsI restriction digest of miniprepped plasmid DNA on 0.8% agarose gel. The BbsI site is destroyed by successful gRNA cloning, and positive clones produce a single 8.5 kb band, whereas empty self-ligated plasmid will produce 1 kb and 7.5 kb bands.

8. Successful clones should be further verified by Sanger DNA sequencing with primer U6F1: TACGATACAAGGCTGTTA GAGAG.
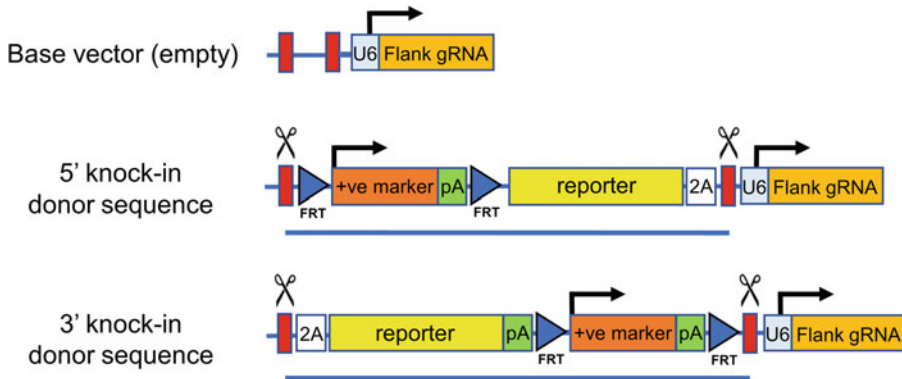
Fig. 5 Key features and organization of possible RT donor sequences (for plasmid B) for 5′ or 3′ CRISPR-mediated knock-in. To ensure co-expression of the endogenous allele and RT, it is critical that the inserted RT donor and 2A sequences are in the same reading frame as the endogenous allele with no intervening stop codons. Key: *+ve marker*, positive antibiotic selection marker; *Reporter*, PET and/or fluorescent RT of choice; *2A*, a 2A cassette; *Red box*, non-mammalian flanking DNA sequence (e.g., Tia1L or Sg-A), and the site of CRISPR dependent DSBs to linearize RT donor; *pA*, poly A sequence; *FRT*, FRT site for FlpO recombinase-mediated deletion of positive selection marker (optional for 3′ knock-in, essential for 5′ knock-in, (*see* **Note 12**); *U6*, RNA pol III promoter to drive expression of *Flank gRNA*, which will induce Cas9-dependent DSB's in flanking red box sequences. The sequence between red boxes (underlined) will be inserted in the genome

3.3 Design Considerations for the Donor RT Sequence in Plasmid B

The base vector for plasmid B (*see* Fig. 1) ensures effective CRISPR-mediated linearization of the RT donor cassette for insertion at the site of the genomic DSB. The RT donor sequence should be positioned between the two flanking non-mammalian sequences (e.g., between the red boxes depicted in Fig. 1) by standard plasmid cloning methods. We have had success with targeting donor sequences >5 kb in total size via this method.

The RT donor sequence could be as simple as the reporter transgene coding sequence itself. However, as shown in Fig. 5, we include additional features that significantly enhance the resulting knock-in allele. Please *see* **Notes 4** and **5** for an explanation of the rationale for including these features. Also *see* **Note 2** for a comment on how to efficiently incorporate these elements in plasmid B. Overall, an advantage of this gene targeting approach is that it is homology-free (*see* **Notes 6** and **7**) and so in principle once built, plasmid B can be used to target other genomic loci with little to no further modification required (the genomic location of RT donor sequence integration being specified by the gRNA identified and cloned into plasmid A in Subheading 3.1).

3.4 Co-transfection Protocol and Selection of Targeted Clones

We illustrate this step of the protocol with the transfection of MIA PaCa-2 cells (human pancreatic carcinoma cells) by Lipofectamine. DNA amounts, cell numbers, and plate surface area are scalable, but we find the numbers detailed here ultimately produce a practicable

number of well-isolated antibiotic-resistant clones. Transfection conditions will be largely equivalent for many cell types, but may need optimization in certain cases.

1. On day 0, seed 5×10^3 MIA PaCa-2 cells onto wells of a 24-well culture plate. Always plate one extra well of non-transfected cells as a selection control. All the cells in this control well should die after the addition of antibiotic selection media, confirming that the selection of stable clones has been effective.

2. On day 1, label two microcentrifuge tubes 1 and 2 for each well to be transfected. In tube 1, add 1 μL Lipofectamine 3000 to 49 μL of Opti-MEM reduced serum media. In tube 2, add a total of 1 μg of plasmid DNA (a 1:1 molar ratio of plasmids A and B; *see* **Note 8**) and 1 μL of p3000 reagent, made up to a total volume of 50 μL with Opti-MEM reduced serum media.

3. To prepare the lipid-DNA complex, slowly add the contents of tube 2 to tube 1 and gently mix.

4. Incubate for 15 min at room temperature, then add the total 100 μL volume to one well of the cells plated the day before.

5. Incubate transfected plates for 24 h at 37 °C, 5% CO_2.

6. On day 2, 24 h after transfection, trypsinize cells and plate each well on a 10 cm dish. Add antibiotic to the culture media to positively select for clones that have stably integrated the RT donor.

7. Surviving clones should become visible 7 to 10 days after selection media is added. All cells should be dead in the untransfected selection control well.

8. Pick clones to a 24-well plate. We recommend picking at least 24 clones and typically observe an approximate 10% gene targeting success rate after antibiotic selection (the success rate will vary according to the target gene and the cell line employed).

9. Continue to grow and expand selected clones for around another week. Once at 50–70% confluency, trypsinize the cells and use half for continued propagation. Isolate genomic DNA from the other half for analysis.

3.5 Validation of Targeted RT Donor Knock-In by PCR

Cells that have stably integrated the RT donor sequence in their genome will grow out as antibiotic-resistant clones during selection. We employ a triple PCR screening strategy (Fig. 6) to efficiently identify which clones have correct on-target integration of the RT donor sequence versus random off-target integration. Please *see* **Note 9** for an important recommendation about PCR reaction optimization and **Note 10** for a deeper explanation of the rationale for the assay.
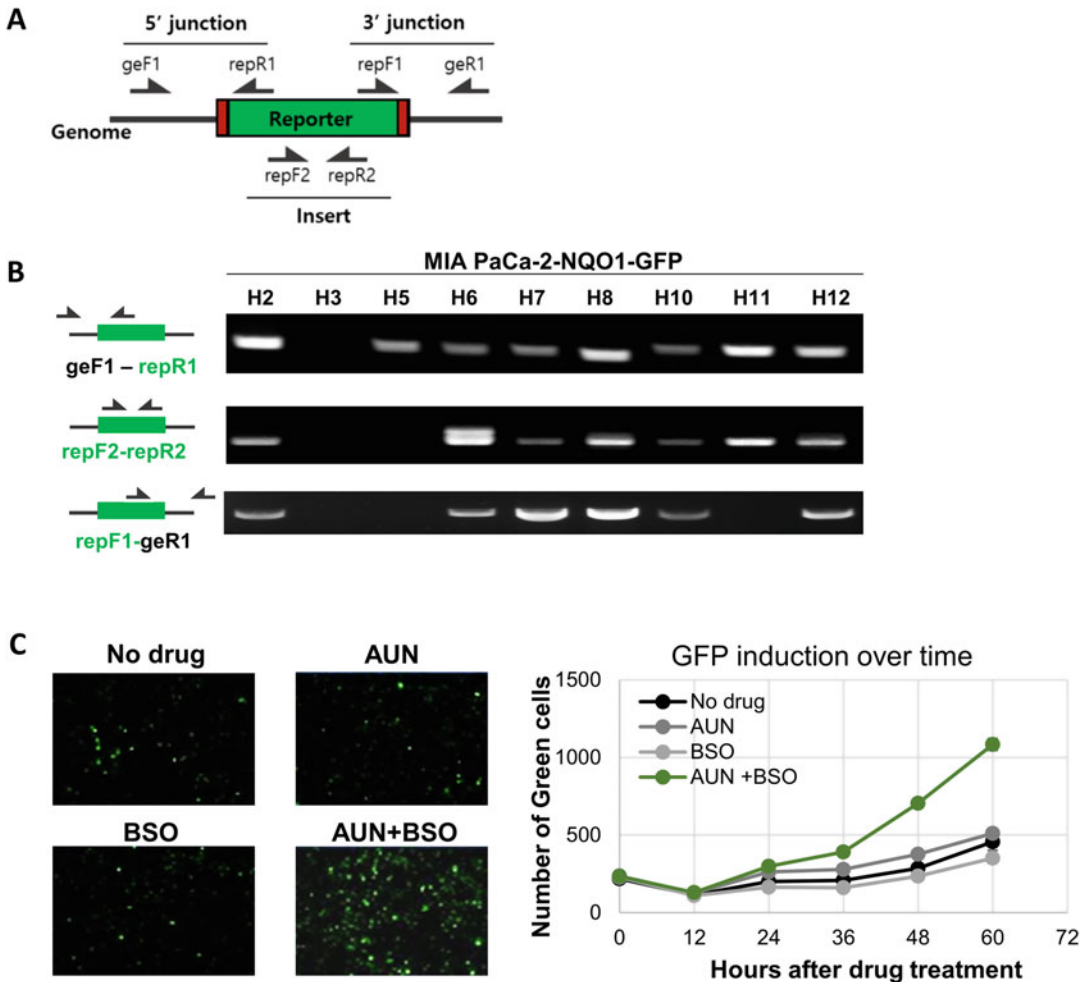
Fig. 6 Triple PCR strategy to identify RT knock-in alleles and functional validation. (**a**) Three PCR primer pairs are employed to screen antibiotic-resistant clones for successful insertion of the RT donor sequence (ge—genome specific, rep—donor sequence specific, F1 or F2—forward primer, R1 or R2—reverse primer). The majority of clones surviving antibiotic selection should be PCR positive for the internal primer pair, but the 5′ and 3′ junction products can only amplify in correctly targeted clones. (**b**) The results of a triplePCR screen of antibiotic-resistant clones on an agarose gel following the targeting of a GFP cassette to the 5′ end of NQO1 in the human pancreatic tumor cell line MIA PaCa-2. (**c**) Preliminary functional validation of a targeted clone after the administration of two therapeutics (auranofin and buthionine sulfoximine) that induce oxidative stress and GFP expression in this NQO1 targeted clone. The number of green cells was quantified over time with an IncuCyte Live-Cell analysis system

1. Isolate genomic DNA from antibiotic-resistant cell clones using an appropriate genomic DNA isolation kit.

2. Use the following standard PCR reaction conditions to analyze clones for targeted integration of the RT (note that primer sequences, annealing temperature, or $MgCl_2$ concentration may require optimization): 2 μL 10× PCR reaction buffer,

1 μL 4 mM dNTP mixture, 1.5 mM MgCl₂, 1 μL 10 μM sense primer, 1 μL 10 μM antisense primer, 1 μL DNA template, nuclease-free dH₂O to 19 μL, then 1 μL Taq DNA polymerase (20 μL final volume).

3. Run the samples on a PCR thermocycler, initially for 2 min at 94 °C, then 32 cycles of 94 °C for 30 s, 58 °C for 30 s, and 72 °C for 30 s, then finally 72 °C for 2 min.

4. Run out the PCR reaction products on a 0.8% agarose gel. A triple-positive PCR sample indicates that the RT donor has been targeted to the desired genomic locus. To confirm that the inserted RT and endogenous targeted allele share the same reading frame, it is essential to next sequence the 5′ or 3′ junction PCR product.

5. Cut out the appropriate flanking PCR amplicon from the 0.8% agarose gel and purify DNA with an appropriate gel purification kit.

6. Submit recovered DNA and a sequencing primer to preferred vendor for Sanger DNA sequencing. A DNA concentration between 10 and 20 ng/μL is recommended for sequencing a PCR product less than 500 bp in size, 20 ~ 50 ng/μL for sizes above 500 bp.

As a rough estimate, we expect around 10% of all antibiotic-resistant clones to be on-target and in-frame per experiment. *See* **Note 11** about an optional assay to identify additional off-target insertions.

Once successfully targeted clones have been identified, they can be expanded for further experimentation and frozen down as aliquots for stock. The positive selection cassette may be removed if necessary (*see* **Note 12**). To aid visualization of successful targeting, Fig. 6b, c shows MIA PaCa-2 cells with a GFP RT targeted to the NQO1 locus. In this specific case, these targeted pancreatic cancer cells now express GFP upon the induction of oxidative stress. The application of a RT from Table 1 would confer uptake of its respective tracer and positive contrast on a PET scan.

4   Notes

1. This protocol employs the plasmid pX330 as "plasmid A" to express the Cas9 enzyme and the genome-specific gRNA. Other Cas9 mutant enzymes have been described with a lower frequency of off-target activity [11] and could equally be employed here.

2. To rapidly generate RT donor sequences with multiple features (as shown in Fig. 5), we recommend commercial gene synthesis as a time- and cost-efficient option. At a minimum, ensure that

the synthesized fragment of DNA can be readily cloned into the empty base vector. The overall size and cost of the synthesized fragment can be reduced by including unique restriction sites to incorporate the RT or antibiotic selection cassette as one additional cloning step. Correspondingly, the versatility of the vector can be increased by ensuring that suitable restriction sites are positioned on either side of the RT or antibiotic selection cassette, enabling efficient substitution of alternative sequences.

3. DSBs in DNA mediated by CRISPR are reliant upon the presence of a protospacer adjacent motif (PAM) sequence in the genome immediately adjacent to the identified gRNA sequence. NGG (where N is A, T, C, or G) is the PAM sequence for Cas9, and this requirement may limit the total number of places that a RT can be inserted into the host cell genome. In addition to selecting a gRNA with a predicted low rate of off-target activity, it is ideal to make the genomic DSB upstream and as close as possible to either the endogenous ATG or the stop codon to minimize the amount of coding sequence added to or deleted from the endogenous allele.

4. An explanation of useful genetic and design elements of the RT donor sequence in plasmid B (Fig. 5): (1) The base vector for plasmid B should either be available upon request (pTia1L-MCS, Lackner et al. [8]) or from Addgene (e.g., #83576) and will ensure effective CRISPR-mediated linearization of the RT donor cassette for insertion at the site of the genomic DSB. (2) Any genetically encoded RT will work with this protocol, but the inclusion of a PET RT (Table 1) will afford the researcher several unique experimental advantages for in vivo imaging. (3) 2A sequence; to best ensure that the expression level of the RT is reflective of the targeted endogenous allele [12] (also *see* **Note 5**). The decision to make a 5′ or 3′ RT knock-in depends largely upon the nature of the targeted endogenous allele and whether it will tolerate minor amino acid additions or deletions at its N- or C-terminus. An IRES (internal ribosome entry sequence) [13] could be employed here instead to co-express both genes without any residual amino acid tag, but the expression level of the RT may not reflect the expression level of the endogenous gene. Equally, a fusion protein of the endogenous targeted allele and the RT could be achieved by employing a peptide linker [14] in place of the 2A sequence. (4) Positive selection marker; to confer antibiotic resistance and allow for the positive selection of cells with a stably integrated RT donor sequence. Such a positive selection strategy does not discriminate between on- and off-target genomic integrations (*see* Subheading 3.5) but is very useful for improving the overall observed frequency of

correctly targeted clones by removing all cells without stable integration of the RT donor sequence. (5) FRT sites; used to flank the positive selection marker and enable its removal in correctly targeted clones by in vitro infection of an adeno-FlpO vector (*see* **Note 12**). After identification of a correctly targeted clone, the removal of this sequence is optional for 3′ RT knock-ins, but essential for 5′ RT knock-ins, as the selection cassette will be positioned between the endogenous promoter and the RT and endogenous gene, blocking their expression.

5. 2A sequences are around 18–20 amino acids long and during translation, a peptide bond fails to form between the terminal G and P amino acid residues. This means that when a 2A sequence is positioned in-frame between two genes, both co-express in equimolar amounts as two separate entities from the same mRNA [12]. It is essential that both genes and the 2A sequence all share the same reading frame and that no stop codons are inadvertently introduced between them. Also of note, the upstream gene will have the majority of the amino acids encoded by the 2A fused to its C-terminus. The downstream gene will have a single proline residue fused to its N-terminus. These extra amino acids are therefore a consideration when deciding whether to target the 5′ or 3′ end of the endogenous gene to best preserve its function.

6. This gene targeting approach relies upon a DNA repair process termed non-homologous end joining (NHEJ). NHEJ is considered error prone and frequently results in microdeletion of one or more DNA nucleotides at the site of the DSB. DNA repair by NHEJ can therefore be frameshifting. To co-express the reporter transgene as the targeted allele, it is essential that the RT donor sequence is inserted in the same reading frame as the endogenous allele. The DSB in the genome typically occurs 3 nucleotides from the PAM sequence. It is possible that pairing of the predicted genomic DSB with RT donor sequences in the relevant 0, +1, and +2 reading frames may increase the frequency of successfully targeted clones in the desired reading frame. Given the high frequency of genomic sequence microdeletion at the DSB however, we routinely use the same donor for all our knock-in experiments.

7. Others have described an alternative CRISPR knock-in approach that similarly employs Cas9 to make a specific DSB in the host cell genome, but uses homologous sequence and a DNA repair process called homology directed repair (HDR) to insert the RT donor sequence into the host cell genome [15]. We note that HDR is significantly less prone to error or microdeletion than the NHEJ repair employed by this approach. However, HDR is less efficient than NHEJ and only occurs in dividing cells. Moreover, HDR targeting needs

homologous sequence specific to each targeted locus added to plasmid B, whereas the approach described here is homology free and employs a universal donor sequence that can in principal be targeted to any location in the genome. We reason that the approach described here may be most useful to efficiently generate targeted cell lines, whereas an HDR-based approach may be better suited for more precision targeting of murine embryonic stem (ES) cells and the generation of transgenic mice.

8. Plasmids A and B will typically be different sizes in terms of DNA base pair number. If 0.5 μg of each plasmid were mixed for a total transfection amount of 1 μg DNA, there would be fewer physical copies of the larger construct relative to the shorter construct. Instead, to ensure an equal number of plasmid copies in the transfection mix (i.e., a 1:1 molar ratio), it is necessary to incorporate the base pair size of the plasmids into the calculation. For example, if we wanted to transfect a total of 1 μg DNA in a 1:1 molar ratio of plasmid A (5 kb) and plasmid B (4 kb), we would need to transfect $5/9 \times 1$ for the μg amount plasmid A and $4/9 \times 1$ for the μg amount of plasmid B (i.e., number of kb plasmid A divided by the total plasmid kb transfected, multiplied by the total microgram amount to be transfected). In this hypothetical case, we would transfect a mix of 0.56 μg plasmid A and 0.44 μg plasmid B to achieve a 1:1 molar ratio.

9. For every targeted locus, it is essential that all three PCR reactions are first optimized to have confidence in the triple PCR screen. Failure to adequately optimize the flanking PCR reactions may lead to the erroneous conclusion that targeting of the RT donor has been unsuccessful. Accordingly, we first pilot the targeting of the RT donor with an easy-to-transfect cell line from the same species as being targeted. After antibiotic selection, we pool all surviving clones and extract DNA for PCR analysis. This polyclonal DNA mix will comprise a mixture of on- and off-target RT donor integrants, but importantly will contain template DNA to optimize the 5′ and 3′ flanking PCR reactions.

10. For the triple PCR assay depicted in Fig. 6, one PCR amplicon is completely internal within the RT donor sequence itself and so confirms that the RT donor has stably integrated in the host cell genome. All antibiotic-resistant clones should be positive for this PCR product, and so this is a useful positive control that the DNA being analyzed is of sufficient quality for PCR amplification. The other two reactions confirm correct targeting, with one primer annealing to adjacent genomic sequence, the other internal to the RT donor. It is extremely unlikely that an amplicon of the predicted size can arise from these primer

pairs unless the RT donor has correctly integrated into the genome. Amplicon size is typically <500 bp to maximize the efficiency of PCR amplification from a complex genomic DNA template.

11. The triple PCR assay does not determine if additional off-target insertions of the RT donor have also occurred in a correctly targeted cell. This is typically of minor concern to us as we functionally validate the biological readout of correctly targeted cells. If the ultimate goal is to produce a transgenic mouse, however, we would recommend testing this in the context of targeted mouse ES cells. RT copy number can be determined accurately by Southern blot or by droplet digital PCR [16, 17].

12. The inclusion of an antibiotic selection marker in the RT donor sequence greatly increases the likelihood of identifying correctly targeted clones by this method. As shown in Fig. 5, however, when targeting the 5′ end of genes, the position of the antibiotic selection cassette will block expression of the RT and endogenous gene from the endogenous promoter. As shown in Fig. 5, we flank the selection cassette with FRT sites, such that it can be readily removed from correctly targeted cells by in vitro infection with Adenoviral-FlpO [18], at a multiplicity of infection (MOI; the ratio of infectious units to cells) of 20–200 for 24 h, or as determined empirically for the cell line of interest. Removal of the antibiotic selection marker is optional when targeting the 3′ end of genes.

Acknowledgments

References

1. Vooijs M, Jonkers J, Lyons S, Berns A (2002) Noninvasive imaging of spontaneous retinoblastoma pathway-dependent tumors in mice. Cancer Res 62(6):1862–1867

2. Bharti SK, Kakkad S, Danhier P, Wildes F, Penet MF, Krishnamachary B, Bhujwalla ZM (2019) Hypoxia patterns in primary and metastatic prostate cancer environments. Neoplasia 21(2):239–246. https://doi.org/10.1016/j.neo.2018.12.004

3. Strathdee D, Ibbotson H, Grant SG (2006) Expression of transgenes targeted to the Gt (ROSA)26Sor locus is orientation dependent.

PLoS One 1:e4. https://doi.org/10.1371/journal.pone.0000004

4. Roberts EW, Deonarine A, Jones JO, Denton AE, Feig C, Lyons SK, Espeli M, Kraman M, McKenna B, Wells RJ, Zhao Q, Caballero OL, Larder R, Coll AP, O'Rahilly S, Brindle KM, Teichmann SA, Tuveson DA, Fearon DT (2013) Depletion of stromal cells expressing fibroblast activation protein-alpha from skeletal muscle and bone marrow results in cachexia and anemia. J Exp Med 210(6):1137–1151. https://doi.org/10.1084/jem.20122344

5. Burd CE, Sorrentino JA, Clark KS, Darr DB, Krishnamurthy J, Deal AM, Bardeesy N, Castrillon DH, Beach DH, Sharpless NE (2013) Monitoring tumorigenesis and senescence in vivo with a p16(INK4a)-luciferase model. Cell 152(1–2):340–351. https://doi.org/10.1016/j.cell.2012.12.010

6. Jinek M, Chylinski K, Fonfara I, Hauer M, Doudna JA, Charpentier E (2012) A programmable dual-RNA-guided DNA endonuclease in adaptive bacterial immunity. Science 337(6096):816–821. https://doi.org/10.1126/science.1225829

7. Adli M (2018) The CRISPR tool kit for genome editing and beyond. Nat Commun 9(1):1911. https://doi.org/10.1038/s41467-018-04252-2

8. Lackner DH, Carre A, Guzzardo PM, Banning C, Mangena R, Henley T, Oberndorfer S, Gapp BV, Nijman SMB, Brummelkamp TR, Burckstummer T (2015) A generic strategy for CRISPR-Cas9-mediated gene tagging. Nat Commun 6:10237. https://doi.org/10.1038/ncomms10237

9. He X, Tan C, Wang F, Wang Y, Zhou R, Cui D, You W, Zhao H, Ren J, Feng B (2016) Knock-in of large reporter genes in human cells via CRISPR/Cas9-induced homology-dependent and independent DNA repair. Nucleic Acids Res 44(9):e85. https://doi.org/10.1093/nar/gkw064

10. Hille F, Richter H, Wong SP, Bratovic M, Ressel S, Charpentier E (2018) The biology of CRISPR-Cas: backward and forward. Cell 172(6):1239–1259. https://doi.org/10.1016/j.cell.2017.11.032

11. Chen JS, Dagdas YS, Kleinstiver BP, Welch MM, Sousa AA, Harrington LB, Sternberg SH, Joung JK, Yildiz A, Doudna JA (2017) Enhanced proofreading governs CRISPR-Cas9 targeting accuracy. Nature 550(7676):407–410. https://doi.org/10.1038/nature24268

12. Szymczak-Workman AL, Vignali KM, Vignali DA (2012) Design and construction of 2A peptide-linked multicistronic vectors. Cold Spring Harb Protoc (2):199–204. https://doi.org/10.1101/pdb.ip067876

13. Ngoi SM, Chien AC, Lee CG (2004) Exploiting internal ribosome entry sites in gene therapy vector design. Curr Gene Ther 4(1):15–31. https://doi.org/10.2174/1566523044578095

14. Chen X, Zaro JL, Shen WC (2013) Fusion protein linkers: property, design and functionality. Adv Drug Deliv Rev 65(10):1357–1369. https://doi.org/10.1016/j.addr.2012.09.039

15. Zhang JP, Li XL, Li GH, Chen W, Arakaki C, Botimer GD, Baylink D, Zhang L, Wen W, Fu YW, Xu J, Chun N, Yuan W, Cheng T, Zhang XB (2017) Efficient precise knockin with a double cut HDR donor after CRISPR/Cas9-mediated double-stranded DNA cleavage. Genome Biol 18(1):35. https://doi.org/10.1186/s13059-017-1164-8

16. Codner GF, Erbs V, Loeffler J, Chessum L, Caulder A, Jullien N, Wells S, Birling MC, Teboul L (2020) Universal Southern blot protocol with cold or radioactive probes for the validation of alleles obtained by homologous recombination. Methods. https://doi.org/10.1016/j.ymeth.2020.06.011

17. Vossen RH, White SJ (2017) Quantitative DNA analysis using droplet digital PCR. Methods Mol Biol 1492:167–177. https://doi.org/10.1007/978-1-4939-6442-0_11

18. Kondo S, Takata Y, Nakano M, Saito I, Kanegae Y (2009) Activities of various FLP recombinases expressed by adenovirus vectors in mammalian cells. J Mol Biol 390(2):221–230. https://doi.org/10.1016/j.jmb.2009.04.057

19. Gao Z, Harwig A, Berkhout B, Herrera-Carrillo E (2017) Mutation of nucleotides around the +1 position of type 3 polymerase III promoters: the effect on transcriptional activity and start site usage. Transcription 8(5):275–287. https://doi.org/10.1080/21541264.2017.1322170

20. Diocou S, Volpe A, Jauregui-Osoro M, Boudjemeline M, Chuamsaamarkkee K, Man F, Blower PJ, Ng T, Mullen GED, Fruhwirth GO (2017) [(18)F]tetrafluoroborate-PET/CT enables sensitive tumor and metastasis in vivo imaging in a sodium iodide symporter-expressing tumor model. Sci Rep 7(1):946. https://doi.org/10.1038/s41598-017-01044-4

21. Castanares MA, Mukherjee A, Chowdhury WH, Liu M, Chen Y, Mease RC, Wang Y, Rodriguez R, Lupold SE, Pomper MG (2014) Evaluation of prostate-specific membrane antigen as an imaging reporter. J Nucl Med 55(5):805–811. https://doi.org/10.2967/jnumed.113.134031

22. Haywood T, Beinat C, Gowrishankar G, Patel CB, Alam IS, Murty S, Gambhir SS (2019) Positron emission tomography reporter gene strategy for use in the central nervous system. Proc Natl Acad Sci U S A 116(23):11402–11407. https://doi.org/10.1073/pnas.1901645116

Chapter 18

Genetic Engineering of Therapeutic Cells with the Sodium Iodide Symporter (NIS) to Enable Noninvasive In Vivo Therapy Tracking

Ben Grimsdell, Adeel Saleem, Alessia Volpe, and Gilbert O. Fruhwirth

Abstract

Noninvasive long-term imaging of therapeutic cells in preclinical models can be achieved through introducing a reporter gene into the cells of interest. Despite important recent developments such as gene editing, cell engineering based on lentiviruses remains a mainstream tool for gene transfer applicable to a variety of different cell types.

In this chapter, we describe how to use lentivirus-based genetic engineering to render different candidate cell therapies in vivo traceable by radionuclide imaging. We illustrate this reporter gene technology using the sodium iodide symporter (NIS), which is compatible with both positron emission tomography (PET) and single-photon emission computed tomography (SPECT). For preclinical experimentation, we fused NIS with a suitable fluorescent protein such as monomeric GFP or RFP to streamline cell line generation and downstream analyses of ex vivo tissue samples. We present protocols for reporter gene engineering of human cardiac progenitor cells, regulatory T cells, and effector T cells as well as for the characterization experiments required to validate NIS-fluorescent protein reporter function in these candidate therapeutic cells.

Key words Cell therapy, Cell tracking, Cardiac progenitor cells, Effector T cells, PET, Radionuclide imaging, Regulatory T cells, Sodium iodide symporter

1 Introduction

Cell-based therapies represent a rapidly emerging class of promising therapeutics. They are developed for the treatment of some of the most prevalent human diseases, including cancer and diabetes, and have applications for regenerative medicine. Cell-based therapies use either cells isolated from the patient (autologous) or those from a donor (allogeneic). The type of therapeutic cell used varies widely, with clinical trials currently dominated by hematopoietic cells,

---

Adeel Saleem and Alessia Volpe contributed equally with all other contributors.

mesenchymal signaling cells [1], and lymphocytes, but also, at a lesser frequency, dendritic cells, hepatocytes, epithelial cells with various others also under investigation [2, 3]. Currently, they are largely developed without precise assessment of their in vivo distribution, efficacy, or survival. It would be highly beneficial for both preclinical development and subsequent clinical use to assess these parameters in situ to enable enhancements in efficacy, applicability, and safety [4, 5]. In vivo cell tracking rests on the principles and mechanisms of molecular imaging to achieve contrast between cells of interest and the other cells of the organism. In some cases, there are intrinsic features of the cells of interest that can be exploited for the generating of contrast, for example, when cells produce targetable molecules that show low or no expression in other tissues. Under these circumstances, conventional molecular imaging offers cell tracking possibilities both preclinically and clinically. However, in most in vivo cell tracking scenarios, including all reported cases of cell-based immunotherapy, molecular probes, or contrast-generating features must be introduced to the cells of interest.

Labels can be introduced into cells via two different methodologies, direct or indirect cell labeling [4, 6]. When long-term cell tracking (e.g., beyond 1 week) is desired or fast-expanding cell types (e.g., proliferating T cells), indirect cell labeling is considered the best option [7]. Indirect labeling requires genetic engineering to ectopically express a reporter gene, rendering the traceable cells different from the surrounding cells in vivo. The reporter must allow the cells to be visualized by molecular imaging in vivo following administration of a suitable labeling agent. Therefore, the relatively simple process of molecular imaging can be performed repeatedly allowing the genetically modified cells to be tracked noninvasively over time. Currently, the most promising clinically compatible imaging technology for this purpose is positron emission tomography (PET) [4].

First proof-of-principle for clinical reporter gene-afforded cell tracking has already been demonstrated using a viral reporter and PET imaging [8]. In contrast to foreign reporter genes, host reporter genes are endogenous proteins. Importantly, host reporters should be endogenously expressed only in a very limited number of host tissues to ensure favorable contrast and overcome any immunogenicity issues intrinsic to foreign reporters [4]. One of the most promising host radionuclide reporter genes is the human sodium iodide symporter (NIS), which has been shown to be well tolerated in different cell types including cancer cells, cardiomyocytes, stem cells as well as effector and regulatory T cells [9–14]. Importantly, it was also shown that the radioactivity levels, which can be expected to be taken up into T cells through NIS use, during imaging, did not cause lasting DNA damage in T cells [14]. Moreover, the matching radiotracers required for NIS imaging have already been translated to humans for thyroid imaging

[15, 16]. Together, these features render NIS a well-established host reporter gene suitable for preclinical long-term cell tracking and a candidate reporter for the clinical setting.

Genetic engineering of cells to introduce reporter genes into their genomes is most frequently performed using viral vectors (e.g., γ-retroviruses, lentiviruses), which integrate the transgenes into the genome without stringent positional control [17]. Lentiviruses are capable of efficiently transducing both actively dividing and non-dividing cell types, making them particularly valuable for stable gene transfer of mature somatic cells and lineage-committed, non-proliferating cells (i.e., differentiated from stem cells). In contrast, γ-retroviruses efficiently transduce only actively dividing cells. Both have been approved and are in commercial use in gene therapy applications for ex vivo modification of T cells and hematopoietic stem cells [18]. Random genomic integration is associated with the risk of altering normal gene function at or around the integration site. Effects on the inserted reporter cannot be ruled out as well as epigenetic silencing. To mitigate this, episomal plasmids, which can also yield stable transgene expression, have been suggested [19, 20]. A recent development is gene editing, which offers a much more specific way of integrating the desired reporter gene at a distinct location into the genome of target cells [21, 22]. This is of utility in the context of stem cell therapies, where random integration of therapeutic, reporter, and suicide genes would pose risks of both insertional mutagenesis and downstream silencing. In fact, gene editing is emerging also clinically for a range of cell-based therapies [23]. Nevertheless, γ-retrovirus- and lentivirus-based technologies currently remain the state of the art for cell engineering as is evidenced by currently approved chimeric antigen receptor T cell therapies (CAR-T) [24]. Genetic engineering to implement additional payloads (e.g., reporter genes for imaging, suicide genes) into immune cell therapies such as CAR-Ts is less of a regulatory concern compared to genetic engineering of stem cell therapies, given that CAR expression is enabled by genetic engineering and therefore a prerequisite for therapy efficacy. In contrast, the clinical use of genetically modified stem cell therapies is not yet widespread [23, 25].

In this protocol, we describe how to use lentivirus-based engineering to render different candidate cell therapies in vivo traceable by radionuclide imaging using NIS as a reporter. For preclinical experimentation only, we fused NIS with a fluorescent protein to streamline cell line production and ex vivo downstream analyses [9–11, 13, 14, 26]. We detail the procedures involved using three cell therapy examples including human cardiac progenitor cells (CPC), effector T cells, and regulatory T cells.

2 Materials

2.1 Virus Production

1. HEK293T cells (*see* **Notes 1** and **2**).

2. HEK293T culture medium: Dulbecco's Modified Eagle's Medium supplemented with 10% (v/v) fetal bovine serum (FBS; heat inactivated) and 2 mM *L*-glutamine.

3. Cell counter (automated cell counter or hematocytometer according to user preference).

4. Cell culture flasks with 25 cm^2 surface area for growth ("T25"), sterile.

5. 15 mL Falcon tubes, sterile.

6. 1.5 mL Eppendorf tubes, sterile.

7. Phosphate buffered saline (PBS): aqueous solution of 137 mM NaCl, 2.7 mM KCl, 10 mM Na_2HPO_4, and 1.8 mM KH_2PO_4.

8. PBS^{CaMg}: PBS containing 0.5 mM Mg^{2+} and 0.9 mM Ca^{2+}.

9. Transgene plasmid: pLNT SFFV>NIS-GFP or pLNT SFFV>NIS-RFP (available from the authors; [10]).

10. Viral packaging plasmid: pCMV ΔR8.91 (available from authors of [27]).

11. Viral envelope plasmid: pCMV VSV-G (Addgene).

12. Polyethylenimine transfection reagent: dissolve polyethylenimine (PEI, 25kD, linear; Polysciences) in deionized water at a final concentration of 1 μg/μL. Aliquot and freeze at −20 °C until use.

13. 10 mL sterile syringes.

14. 0.45 μm filters made from surfactant-free cellulose acetate (SCFA).

15. Cryo tubes for storing aliquots of the lentivirus-containing product at −80 °C.

16. Virkon or similar bleach reagent to decontaminate all materials that encountered viruses.

2.2 CPC Transduction

1. CELLstart™ (Gibco) is a defined substrate that allows the growth of undifferentiated human stem cells without the need for feeder cells.

2. CPC growth media: 45% Dulbecco's Modified Eagle's Medium F-12 Ham.

3. 45% Neurobasal™ A Medium (Thermofisher).

4. 10% Stemulate serum (Sexton Biotechnologies).

5. B27 and N2 Supplements (1×, both Thermofisher).

6. 10 ng/mL Leukemia inhibitory factor (LIF; Millipore).

7. 10 ng/mL bFGF.

8. 20 ng/mL EGF.

9. 100× Insulin-transferrin-selenite (ITS).

10. 1% PenStrep, 0.1% gentamicin.

11. GlutaMAX™ Supplement. Store at 4 °C.

12. Accutase.

13. Phosphate buffered saline (PBS): aqueous solution of 137 mM NaCl, 2.7 mM KCl, 10 mM Na_2HPO_4, and 1.8 mM KH_2PO_4.

14. Cardiac progenitor cells (for isolation *see* [28, 29]).

15. Cell culture vessel: Tissue culture-treated 24-well plate.

16. Dulbecco's Modified Eagle's Medium F-12 Ham.

17. Embryonic stem cell qualified fetal bovine serum (ESQ; Gibco™ #11500526).

18. CPC passage media (*see* **Note 3**).

19. Cell counter (automated cell counter or hematocytometer according to user preference).

2.3 Treg Transduction

1. T cells culture medium: X-VIVO 15 medium supplemented with 5% normal human AB serum, 2 mM *L*-glutamine.

2. Interleukin-2 cytokine (IL-2).

3. Rapamycin.

4. PBS.

5. Regulatory T cells isolated as previously described [13, 30–32].

6. Cell culture flask, e.g., suitable T cell culture tube or a "T25" flask.

7. Retronectin reagent (recombinant human fibronectin fragment, also referred to as rFN-CH-296, TakaraBio) diluted 1 in 20 into PBS.

8. Non-tissue culture-treated 24-well plate (*see* **Note 4**).

9. Lentivirus particles (prepared as described below).

10. 15 mL Falcon tubes.

11. Cell counter (automated cell counter or hematocytometer according to user preference).

2.4 Teff Transduction

1. Growth medium: RPMI 1640 containing 5% (v/v) human serum (HS, BioSera), 2 mM *L*-glutamine, and 100 IU/mL sterile-filtered penicillin/streptomycin. Stored at 4 °C.

2. IL-2 (use at 100 IU/mL) or IL-15 (use at 10 ng/mL).

3. PBS, pH 7.4, sterile-filtered, and without calcium chloride and magnesium chloride.

4. Effector T cells, either cryopreserved or thawed followed by 1–2 days of culture or freshly isolated as described.

5. Cell culture flask, e.g., suitable T cell culture tube or a "T25" flask.

6. 50 μg/μL retronectin reagent in PBS (recombinant human fibronectin fragment, also referred to as rFN-CH-296; TakaraBio).

7. Non-tissue culture-treated 6-well plate.

8. Lentivirus particles (prepared as described below).

9. 15 mL Falcon tubes.

10. Cell counter (automated cell counter or hematocytometer according to user preference).

11. DMSO.

12. Pentastarch.

13. Human serum albumin.

2.5 Materials for Characterization Assays

1. Flow cytometer.

2. Round-bottom flow cytometry tubes.

3. PBS, pH 7.4, sterile-filtered, and without calcium chloride and magnesium chloride (PBS^{CaMg}).

4. Stemulate serum (Sexton Biotechnologies).

5. Bovine serum albumin.

6. A fluorescence wide-field microscope equipped with fluorescence cubes compatible with the observation of the desired fluorescent proteins. An objective with a minimum of 20× magnification is recommended as well as a camera attached to acquire images.

7. Round cover glasses (No.1 or No.1.5; 13 mM diameter).

8. 0.01% Poly-L-Lysin solution (MW 70,000–120,000).

9. 4% (w/v) paraformaldehyde solution in PBS.

10. 1.0 mg/mL wheat germ agglutinin-AlexaFluor633 labeling solution (stored at −20 °C; *see* **Note 5**).

11. 2.5 μg/mL DAPI or 25 μg/mL Hoechst solution.

12. CFM-3 (Citifluor), a mounting medium with a high refractive index of ~1.52 that also contains an anti-fade agent.

13. Cell culture vessel: Tissue culture-treated 12-well plate.

14. 1.5 mL Eppendorf tubes.

15. Laboratory radiation counter for Falcon-type tubes, required for the preparation of the radioactive working solutions.

16. Radiotracer working solution: use $[^{99m}Tc]TcO_4^-$ within 6 h of its elution from the generator; diluted as needed with PBS^{CaMg} to the working concentration of 50 kBq/mL.

17. 12.5 μM $NaClO_4^-$ solution as a competitive substrate of NIS.

18. Gamma counter.

19. Radiation monitoring and safety equipment as required by institutional regulations.

3   Methods

3.1 Production of Lentivirus Particles for Engineering Cells to Express Reporter Genes

1. Seed 293T cells ("virus producer cells") at a density of 5×10^4 cells/cm² into tissue culture-treated plastic flasks using the appropriate growth medium (cf. Materials).

2. 24 h later, prepare for transfection. Therefore, bring all transfection reagents to room temperature (RT) within a cell culture hood.

3. Prepare the transfection mix under sterile conditions by diluting the combined amounts of required plasmid DNA into base DMEM in an Eppendorf tube (*see* **Note 6**). In the following, we describe the procedure for a second-generation lentivirus and on a final production volume of ~2.5 mL using a 25 cm² cell culture flask for production. Production can be scaled up or down for different culture vessels sizes. Mix 3.75 μg of the reporter gene plasmid pLNT SFFV>NIS-GFP or pLNT SFFV>NIS-RFP (*see* **Note 7**) with 2.81 μg of the packaging plasmid pCMV ΔR8.91 [27] and 0.94 μg of the envelope plasmid pCMV VSV-G and dilute this pre-mixed total amount of 7.5 μg plasmid DNA into 0.5 mL base DMEM. The relative mass ratio of plasmids is 4:3:1 in this case.

4. Add the Polyethylenimine (PEI) transfection reagent to the diluted DNA on a 3:1 mass ratio of PEI:total DNA. Here, add 22.5 μg PEI transfection reagent to the diluted plasmid mix from **step 3**. This solution is termed the "transfection mix." The PEI is prepared by pre-dissolving it in endotoxin-free water and heated to ~80 °C, neutralized to pH 7.0, sterile-filtered and stored at 4 °C,

5. Incubate the transfection mix for 15 min at RT.

6. Replace growth medium of the 293T cells; use 80 μL/cm², which amounts to 2 mL at the scale used here.

7. Slowly add the transfection mix dropwise to the virus producer cells.

8. After 18–24 h, inspect the virus producer cells using a tissue culture fluorescence microscope (*see* **Note 8**). If fluorescence signals are observed, discard cell supernatant and add fresh medium (into which transfected cells will continue to release virus particles).

9. After a further 24 h, harvest the first lentivirus-containing solution, i.e., the culture supernatant, and filter through a 0.45 μM filter to remove any producer cells and large cell debris (*see* **Note 9**). Store the harvested virus particle solution at 4 °C. Add fresh medium to the cells for further virus production.

10. After another 24 h, again harvest the lentivirus-containing supernatant, filter through a 0.45 μM filter, and combine it with the harvested lentivirus solution from the previous day. Destroy the virus producer cells by addition of bleach and discard after bleach action.

11. Concentrate lentivirus particles if desired. Several methods can be used including commercial products (*see* **Note 10**).

12. Optional virus concentration by sedimentation centrifugation (**steps 12–14**). Using an ultracentrifuge, spin the combined harvested virus batches at $50,000 \times g$ for 2 h at 4 °C.

13. Carefully decant the supernatant by inversion, let the tube dry for approximately 3 min at RT. Do not let completely dry the tube as the always remaining remnant (~10–15 μL) provides some proteins that are important for virus stabilization when subsequently resuspending the virus particles.

14. Resuspend the viral pellet in the culture medium compatible with the cell type to be transduced. Therefore, add first a small amount of resuspension solution (i.e., 15–20 μL desired culture medium) and pipet up and down about a dozen times. Avoid air bubble generation during this process as they reduce the available product volume and thus yield.

15. Use lentiviral particles for transduction or store them in aliquots at −80 °C for future transduction experiments (*see* **Notes 11** and **12**). Virus titer determination is recommended using either a physical or functional titration approach [33].

3.2 Transduction of Human Cardiac Progenitor Cells (CPC)

1. Culture of CPCs requires specially pre-coated culture vessels. To prepare them add a 1:50 dilution of CELLstart in PBS and incubate the vessel in a humidified hypoxia incubator in an atmosphere containing 2% (v/v) O_2 and 5% (v/v) CO_2 at 37 °C for 30–45 min. Prepare a 24-well plate in this manner.

2. Remove coating mix and, without washing the 24-well plate, seed 2×10^5 CPCs per well (1×10^5 cells/cm^2).

3. Place plate back in a humidified hypoxia incubator (cf. atmosphere in **step 1**) and incubate for 18–24 h.

4. Wash CPCs twice with PBS pre-warmed to 37 °C.

5. Add either fresh or thawed lentivirus particle solution to the cells. To ensure optimal transduction, we recommend optimizing the MOI (starting range 1–5; *see* **Note 13**).

6. Incubate the cells with lentivirus particles in a humidified hypoxia incubator (cf. atmosphere in **step 1**) for 48 h.

7. Remove supernatant and wash cells twice with fresh growth medium and add fresh growth media.

8. Continue CPC culture until 70–80% confluency is reached (as determined by user estimation employing brightfield microscopy).

9. Aspirate media and wash the cells twice with PBS.

10. Add Accutase at 80 μL/cm^2 and place flask in the humidified hypoxia incubator for 3 min to lift CPCs.

11. Neutralize the Accutase-containing CPC suspension by adding two additional volumes of CPC Passage medium, e.g., 4 mL of Passage medium to neutralize 2 mL of Accutase-containing cell suspension.

12. Transfer the neutralized cell suspension into a Falcon tube and centrifuge at 300 × *g* for 5 min at RT.

13. Discard the supernatant and resuspend the CPC cell pellet in growth medium and reseed cells at 2 × 10^4 cells/cm^2 for transduction into a pre-coated culture flask (cf. **step 1**).

14. Continue to expand transduced CPC cells (**steps 8–13**) and/or start characterization (*see* Subheadings 3.5, 3.6, and 3.7) depending on available cell amounts. Accompany culture with tissue culture fluorescence microscopy to crudely assess transduction success based on NIS-GFP expression (use untransduced cells as controls).

3.3 Transduction of Human Regulatory T Cells

Tregs grow in suspension and to transduce them culture vessels are used that were not pre-treated for tissue culture use but instead were pre-coated with retronectin. Here, transduction is performed in a 24-well format, but this can be scaled up or down as desired. The range of cells to be transduced in a 24-well format spans 0.25 × 10^6 to 1 × 10^6 cells.

1. To pre-coat the culture vessel with retronectin, completely cover each well with the retronectin working solution and incubate for 2 h at RT; for a 24-well, 200 μL is sufficient (*see* **Note 14**).

2. Aspirate the retronectin solution and carefully wash the well with 1 mL PBS.

3. To prepare Tregs for transduction, collect them from their culture flask into a 15 mL Falcon tube and count the cells using either an automated cell counter or a hematocytometer (*see* **Note 15**).

4. Take the aliquot for the desired cell number and transfer into a new Flacon tube and centrifuge at $350 \times g$ for 10 min to pellet the cells.

5. Wash the cells twice with PBS (spin at $350 \times g$ for 10 min each time), resuspend at 5×10^6 cells/mL growth medium.

6. Add the desired aliquots of lentivirus to each retronectin pre-coated well. To ensure optimal transduction, we recommend optimizing the MOI (starting range 1–5).

7. Incubate virus for 15 min at RT.

8. Add the desired amount of Tregs to each well. Keep within the optimal range of $0.25–1 \times 10^6$ Tregs/24-well.

9. Add IL-2 to a final concentration of 1000 IU/mL.

10. Perform "spin inoculation" by centrifuging the plate containing the 24-wells for at $600 \times g$ for 1 h at 40 °C (*see* **Note 16**).

11. Transfer plate in an incubator and leave in a humidified atmosphere containing 5% (*v/v*) CO_2 at 37 °C for 48–72 h.

12. Resuspend well contents and transfer into an Eppendorf tube and centrifuge at $350 \times g$ for 10 min to collect cells.

13. Wash cells twice in growth medium and resuspend for further culture.

14. Expand the newly generated NIS-xFP⁺ Treg cells for further experiments including in vitro characterization (alongside untransduced Tregs as controls). Therefore, activate the cells with anti-CD3/CD28 beads (1:1 bead:cell ratio) in their normal growth medium (ensure both 1000 IU/mL IL-2 and 100 nM rapamycin have been added), monitor cell numbers, and replace media as previously described [13, 30–32].

3.4 Transduction of Human Effector T Cells

Teffs grow in suspension. To transduce them, culture vessels are used that were not pre-treated for tissue culture use but instead are pre-coated with retronectin. Here, transduction is performed in a 6-well format, but this can be scaled up or down as desired. The number of cells to be transduced in a 6-well format is 10^6 cells.

1. Activate fresh or cryopreserved primary human T cells by addition of anti CD3/CD28 magnetic beads at a ratio of 3:1 for beads:T cells in 6-well cell culture plates. Maintain T cells at a concentration of 10^6 T cells/mL during expansion.

2. Pre-coat a different 6-well culture plate with retronectin. Therefore, completely cover each well with the retronectin working solution overnight, seal it using parafilm, and store overnight at 4 °C (*see* **Note 17**); for a 6-well, 1 mL is sufficient to ensure surface area coverage.

3. On the day of the transduction, remove CD3/CD28 magnetic beads from the T cells by transferring them into a 15 mL Falcon tube and collecting the beads using a permanent magnet fitting the tube between its poles (field strength ~0.5 T between the poles). Gently collect the supernatant containing the T cells in a separate 15 mL Falcon tube and determine cell concentration (using an automated cell counter or hematocytometer).

4. Take an aliquot amounting for the desired cell number, transfer it to a new Falcon tube, and pellet the cells (i.e., centrifuge at $350 \times g$ for 10 min).

5. During centrifugation, aspirate retronectin solution from the pre-coated plate and carefully wash the well with 1 mL PBS. After that, leave 1 mL PBS in each well until use.

6. Resuspend T cells and add the desired aliquot of lentivirus particles to the T cells. To ensure optimal transduction, we recommend optimizing the MOI, whereby values of 1–5 constitute a good starting range. The optimal cell concentration is 5×10^5 T cells per mL (with a total volume of 3 mL for the 6-well scale described herein).

7. Add IL-2 to a final concentration of 100 IU/mL to the T cell suspension containing the lentivirus particles and resuspend (*see* **Note 18**).

8. Add the mix from **step 7** to the retronectin-coated and pre-washed 6-well plate from **step 5**.

9. Perform "spin inoculation" by centrifuging the 6-well plate at $300 \times g$ for 1 h at RT.

10. Transfer plate in the incubator and leave in a humidified atmosphere containing 5% (*v/v*) CO_2 at 37 °C for 48 h.

11. 48 h post-transduction, centrifuge the 6-well plate at $300 \times g$ for 5 min and gently remove supernatant containing lentiviral particles. Wash the cells once with growth medium and spin again.

12. Resuspend cells in fresh medium containing the appropriate cytokine (*see* **Note 18**) and transfer them into a tissue-culture flask. Keep the cells at a concentration of 10^6/mL.

13. Culture the newly generated NIS-xFP+ T cells for further experiments including in vitro characterization (alongside untransduced T cells as controls; *see* Subheadings 3.5, 3.6, and 3.7).

14. Optionally, T cells can also be cryopreserved (**steps 14–19**). Therefore, collect a representative aliquot of cells and remove any magnetic beads from stimulation steps.

15. Make freezing medium containing base medium supplemented with 5% (v/v) DMSO, 6% pentastarch, and 4% (v/v) human serum albumin and cool to 4 °C until use (*see* **Note 19**).

16. Centrifuge T cells at $300 \times g$ for 5 min, discard the supernatant.

17. Wash T cells once with 5 mL PBS followed by centrifugation ($300 \times g$ for 5 min) and discard supernatant.

18. Resuspend pellet in 1 mL of cold freezing medium.

19. Freeze T cells in a freezing container offering controlled-temperature cooling and store at $-80\ °C$ for 48 h and then transfer the frozen cells into liquid nitrogen for storage .

3.5 Determination of NIS-Fluorescent Protein Reporter Expression in Transduced Cells

The expression of NIS-xFP can be directly assessed by fluorescence methodology. While reporter expression in adherent cells is readily accessible by fluorescence microscopy of cells in their culture vessels, and this is sufficient for the confirmation of transduction success, we recommend using analytical flow cytometry to obtain quantitative reporter expression data. The xFP offers a directly detectable marker for quantification of the percentage of positively transduced cells and, if desired, for preparative isolation of transduced cells using fluorescence-assisted cell sorting (FACS) technology. Here, we describe basic reporter expression analysis in live cells by analytical flow cytometry (*see* **Notes 20** and **21**).

1. To analyze reporter-transduced CPCs, lift and pellet aliquots of $1–2 \times 10^5$ cells as described in Subheading 3.2 (Subheading 3.2, **steps 9–12**). Resuspend cells in 500 µL PBS containing 2% (*v/v*) Stemulate serum and transfer to a round-bottom flow cytometry tube.

2. To analyze reporter-transduced Tregs or Teffs, count cell suspensions and take aliquots of $1–2 \times 10^5$ cells, wash with PBS, resuspend in 500 µL PBS containing 2% (*v/v*) BSA, and transfer to a round-bottom flow cytometry tube.

3. Always prepare in the same way as described in **step 1** untransduced cells (best to use parental cells that were grown alongside the transduced ones), which serve as negative controls for determining the flow cytometer settings. If available, also use positive control cells, e.g., the same cell type or similar cells transduced with the same construct or a construct that also offers expression of the same xFP.

4. Use a flow cytometer suitable for the chosen reporter fluorophore and acquire FSC, SSC, and xFP channel data. Analyze by gating on intact cells using FSC/SSC and produce xFP channel histograms as shown in Fig. 1 for NIS-GFP[+] CPCs, in Fig. 2 for NIS-RFP[+] Tregs, and in Fig. 3 for or NIS-RFP[+] Teffs. Quantitative analysis comparing untransduced and transduced cells reveals the percentage of transduced cells.
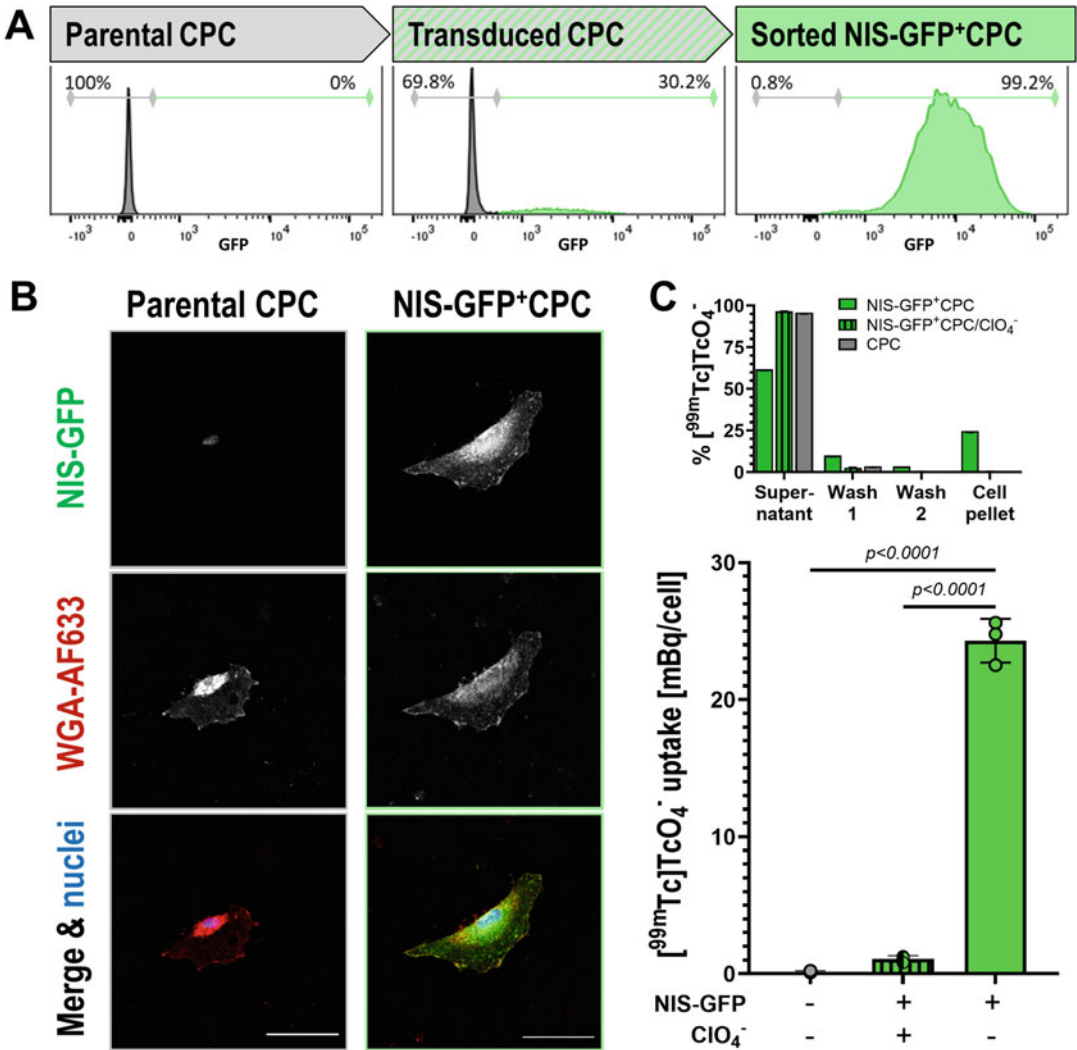
Fig. 1 Reporter gene engineering of cardiac progenitor cells. (**a**) Analysis of reporter expression: comparative flow cytometric analysis of parental cardiac progenitor cells (CPCs), transduced CPCs (transduction efficiency was ~30%), and final FACS-purified NIS-GFP$^+$ CPC. Representative histograms are shown. (**b**) Analysis of subcellular reporter localization: plasma membranes were visualized with wheat germ agglutinin (WGA) conjugated to the AlexaFluor633 dye and NIS-GFP by its intrinsic fluorescence. Areas of overlap indicate NIS-GFP reporter plasma membrane localization, which is a prerequisite for its function. Representative micrographs of untransduced parental and purified NIS-GFP$^+$ CPCs are shown. (**c**) Analysis of reporter function: (*Top*) The ability to take up [^{99m}Tc]TcO$_4^-$ is conferred to CPCs by the NIS part of the fusion reporter NIS-GFP. Distribution of added radiotracer between indicated assay fractions showing NIS-GFP$^+$ CPCs took up radiotracer while the ability to take up the radiotracer while untransduced CPCs did not. Perchlorate is a competitive co-substrate and when present reduced radiotracer uptake, thereby demonstrating radiotracer uptake to specific to NIS-GFP expression in cells. Radioactivity in fractions was determined by gamma counting of fractions. (*Bottom*) From directly quantified assay fractions in the top panel, the cellular radioactivity was calculated, which is the usual form of presenting this data. Cumulative data from three independent batches are shown with error bars representing SD.
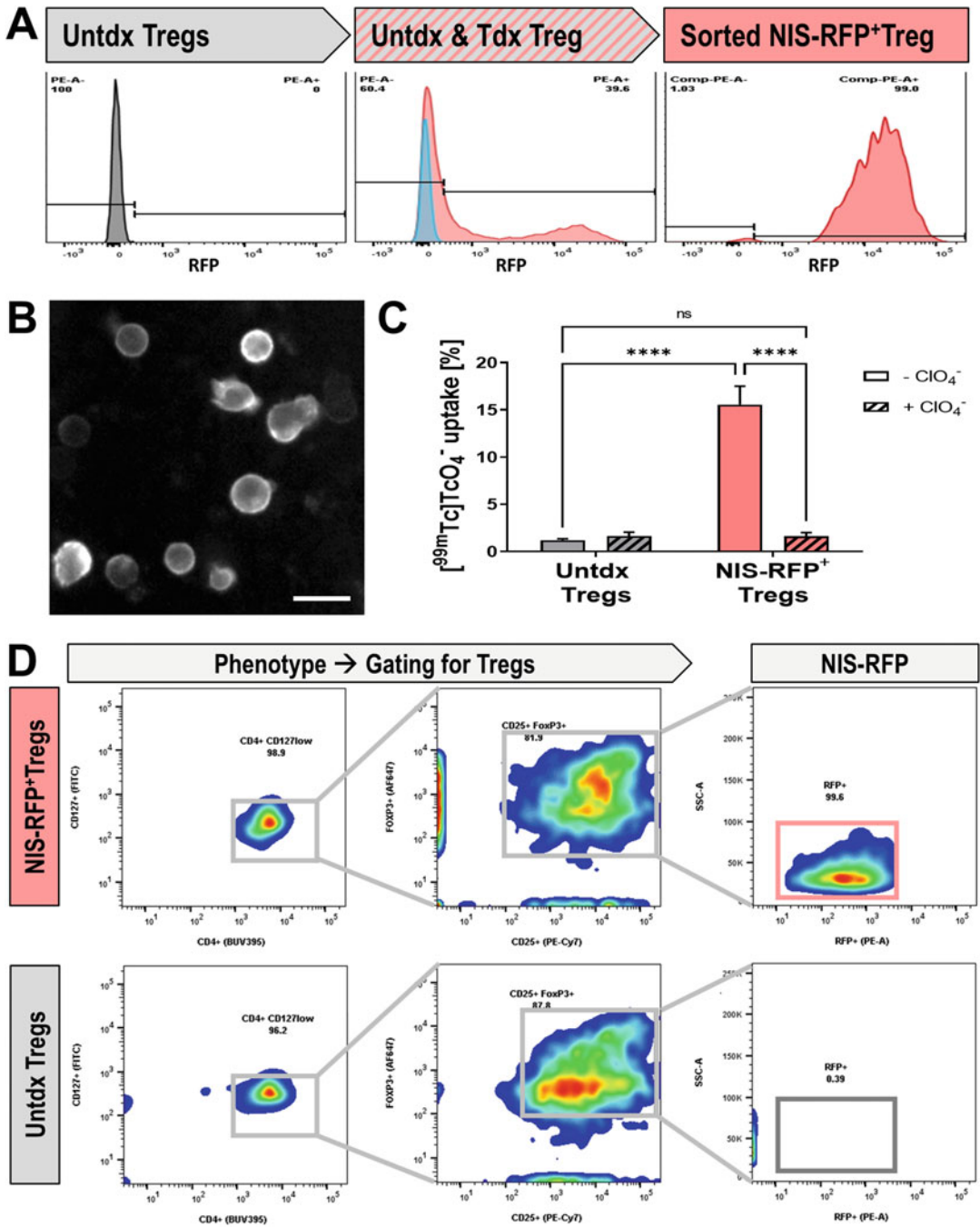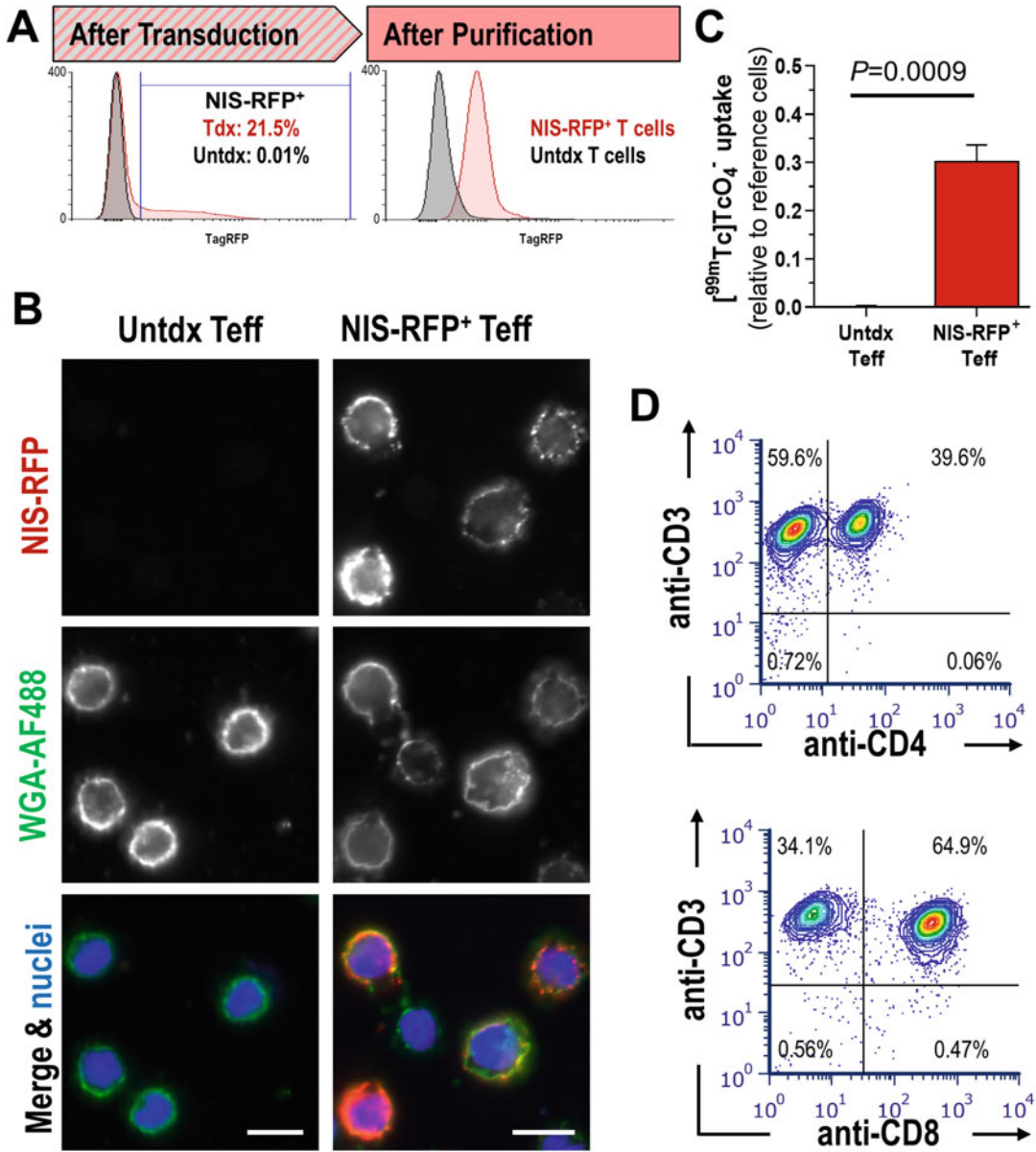
Fig. 2 Reporter gene engineering of regulatory T cells. (**a**) Analysis of reporter expression: comparative flow cytometric analysis of untransduced (untdx) Tregs, transduced Tregs (red), and untdx Tregs (gray), and final FACS-purified NIS-RFP+ Tregs. Representative histograms are shown. (**b**) Sorted NIS-RFP+ Tregs were attached to retronectin-coated glass-bottom 96-wells and imaged live by wide-field fluorescence microscopy; scale bar is 10 μm. (**c**) Analysis of reporter function by uptake of the NIS radiotracer $[^{99m}Tc]TcO_4^-$. Perchlorate is a competitive co-substrate and when present reduced radiotracer uptake, thereby demonstrating radio-tracer uptake being specific to NIS-RGFP expression in Tregs. Cumulative data from three independent batches are shown with error bars representing SD. (**d**) Phenotypic analysis of untdx and NIS-RFP+ Tregs by

3.6 Determination of Reporter Localization in Transduced Cells

The plasma membrane localization of NIS-xFP fusion reporters is crucial for reporter function (*see* **Note 22**) and can be directly observed by counterstaining the plasma membrane with suitable agents. Here, we describe the staining of NIS-GFP⁺ CPC plasma membranes with wheat germ agglutinin (WGA) conjugated to the AlexaFluor 633 dye and thereby demonstrating NIS-GFP plasma membrane localization. The same protocol can be used for suspension cells such as Tregs or Teffs after they have been attached to the glass surface of a coverslip (e.g., using either poly-*L*-lysine or retronectin-coated glass coverslips or cytocentrifugation [34]).

1. Prepare cover glasses to subsequently seed cells onto them: Incubate cover glasses in 40% (v/v) conc. HCl with 60% (v/v) EtOH for 2 h using a porcelain/glass petri dish. Then wash twice with 70% (v/v) ethanol solution, wash twice with methanol, wash once with acetone (all at RT), and let cover glasses dry on filter paper. Place cover glasses into a glass petri dish containing one layer of filter paper and autoclave the vessel to sterilize it. Subsequently, open only under sterile conditions using sterile forceps to handle cover glasses.

2. Pre-coat sterile cover glasses with poly-L-lysine. Therefore, add one cover glass into a well of a 24-well or 4-well plate and 250 μL poly-L-lysine stock solution; close plate and leave for 15 min at room temperature, then wash thrice with sterile water and let dry within the tissue culture hood.

3. Seed NIS-GFP⁺ CPCs and untransduced CPCs, respectively, onto sterile poly-L-lysine-coated glass coverslips at a density of 0.15×10^5 cells/cm² (*see* CPC culture in Subheading 3.2, **steps 8–13**). For Tregs and Teffs, seed 3×10^4 cells/cm² on CELL-Start pre-coated glass coverslips.

4. After 24 h, aspirate the media and carefully wash the cells twice with 500 μL PBS (*see* **Note 23**).

5. Add 500 μL 4% paraformaldehyde solution and incubate for 10 min at RT (*see* **Note 24**).

6. Aspirate fixative and wash cells twice with PBS (*see* **Note 23**).

7. Add 200 μL of WGA-633 working solution (2 μg/mL in PBS) and incubate for 10 min at RT in the dark.

8. Wash cells twice with PBS (leave PBS on cells for ~5 min per wash step).

Fig. 2 (continued) flow cytometry: Cells were stained with antibodies specific to CD127, CD4, CD25, and Foxp3 to identify Tregs, which were then analyzed for RFP expression. Human Tregs are generally defined as CD4⁺CD25⁺CD127^low FoxP3⁺ cells and data reveal not only that transduced and sorted NIS-RFP⁺ Tregs are >99% positive for the reporter after purification and expansion for 10 days, but also that their phenotype is unchanged to untransduced Tregs.

Fig. 3 Reporter gene engineering of effector T cells. (**a**) Analysis of reporter expression: lentivirus particles encoding the NIS-RFP reporter were used to transduce primary human T cells. (*Left*) Transduction was analyzed 3 days later by flow cytometry (red) and compared to untransduced cells (gray). (*Right*) Transduced T cells were FACS-sorted for RFP-positive cells and subsequently expanded and analyzed by flow cytometry (red) in comparison to untransduced controls (gray). Representative histograms are shown. (**b**) Analysis of subcellular reporter localization after attaching transduced Teffs to retronectin-coated coverglasses: plasma membranes were visualized with wheat germ agglutinin (WGA) conjugated to the AlexaFluor488 dye and NIS-RFP by its intrinsic fluorescence. Areas of overlap indicate NIS-RFP reporter plasma membrane localization, which is a prerequisite for its function. Representative micrographs of untransduced parental and purified NIS-GFP[+] CPCs are shown. Scale bars are 10 μM. (**c**) Analysis of reporter function: Comparative radiotracer uptake in untransduced and sorted NIS-RFP[+] Teffs. Cumulative data from three independent batches are shown with error bars representing SD. (**d**) Phenotype analysis: sorted NIS-RFP[+] Teffs were analyzed for T cell markers using indicated marker antibodies and flow cytometry.

9. Add 200 µL Hoechst 33342 working solution (4 µg/mL in PBS) as a nuclear counterstain (*see* **Note 25**) and incubate for 10 min at RT in the dark.

10. Wash cells twice with PBS (leave PBS on cells for ~5 min per wash step).

11. Rinse cells twice with deionized water (leave water on cells for ~5 min per wash step) and then fill the well with 1 mL deionized water (*see* **Note 26**).

12. Pipette 12 µL CFM-3 mounting solution onto microscope slides.

13. Use pointed forceps to carefully remove cover glasses from the wells (*see* **Note 27**), dip them carefully with a corner onto filter paper to suck off most of the water, and then mount them with the cells facing the microscope slide by placing them on top of the CFM-3 drop prepared in **step 12**.

14. Leave the samples to dry for 24 h at RT in the dark. Samples can be stored for days at RT or for months at −20 °C.

15. Image samples using a confocal fluorescence microscope equipped with lasers and filters appropriate for the chosen fluorophores. Here, we used one equipped to image DAPI/Hoechst 33342, FITC/GFP, and Cy5/AlexaFluor633 in the case of CPCs (Fig. 1b) and DAPI/Hoechst 33342, FITC/AlexaFluor488, and Cy3/TagRFP in the case of Teffs (Fig. 3b).

3.7 Reporter Function

Functional considerations of NIS-xFP reporters include both NIS-substrate transport and fluorescence properties. Assessment of fluorescence properties has been described above and serves as a prerequisite for the subsequent use of radioisotopes to determine NIS transport activity (*see* **Note 28**). Here, we describe the determination of NIS function through its uptake of the radiotracer $[^{99m}\text{Tc}]\text{TcO}_4{}^-$, which is a generator-produced and readily available radiotracer. We describe it for adherent CPC (**steps 1–10**) as well as for suspension cells using Teffs (**steps 11–20**) as an example; the handling steps for Tregs would be identical.

1. For adherent cells (here CPCs): Seed 2×10^5 purified NIS-GFP$^+$ CPCs cells in 12-well plates (pre-coated as described in Subheading 3.2, **steps 1** and **2**) 1 day prior to the experiment. Prepare all samples in triplicate and include control samples: "specificity controls," i.e., NIS-GFP expressing CPCs that will be pre-incubated with a competitive NIS substrate to test uptake specificity, and "untransduced cell controls," i.e., parental CPCs that will receive the radiotracer substrate to determine potential basal cell-intrinsic uptake (*see* **Note 29**).

2. On the next morning, wash cells twice with serum-free growth medium.

3. For specificity controls, pre-incubate the cells for 20 min with 12.5 μM of the competitive substrate $NaClO_4^-$. Keep the competitive substrate concentration constant throughout the experiment in all subsequent incubation steps involving these controls.

4. Incubate cells in serum-free growth medium in the presence of 1 mL of 50 kBq/mL $[^{99m}Tc]TcO_4^-$ for 30 min in the cell culture incubator as for normal cell culture.

5. Collect the supernatant and transfer 100 μL of it to a prepared collection tube labeled "Supernatant" (*see* **Note 30**).

6. Wash the cells twice with 1 mL ice-cold PBS^{CaMg}. Collect each wash solution and transfer 100 μL of each into a prepared collection tube labeled "Wash 1" or "Wash 2," respectively (*see* **Note 31**).

7. Lift the cells by adding 500 μL accutase to each sample, incubate for 3 min in the cell incubator, check cell detachment, and collect the cell suspension in a tube labeled "Cells." Wash the wells with 500 μL ice-cold PBS^{CaMg} to collect remaining cells and add to the tube "Cells." Pellet the cells by centrifugation ($250 \times g$, 4 min). In some cases, re-seeding of the radiolabeled cells might be desired (*see* **Note 32**).

8. Measure the counts per minute (CPM) of all four tubes per samples using a γ-counter set to the energy window of the chosen radiotracer (i.e., ^{99m}Tc (140.5 KeV)).

9. Analyze data by summing obtained γ-counts in CPM from each well to determine a total radioactivity count per well. Take aliquoting in **steps 5** and **6** into account by multiplying numbers by a factor of 10 for "Supernatant," "Wash 1," and "Wash 2" tubes.

10. Express the cellular radiotracer uptake as %Uptake as indicated in Eq. 1. Calculate averages and standard deviations from triplicate experiments. Typical results are shown in Fig. 1c.

$$\%\text{Uptake} = \frac{\text{CPM (Cells)}}{\text{CPM (Cells)} + \text{CPM (Wash 1)} + \text{CPM (Wash 2)} + \text{CPM (Supernatant)}} \times 100 \qquad (1)$$

11. For suspension cells (here Teffs): Aliquot 1×10^6 NIS-GFP$^+$ T cells in Eppendorf tubes on the day of the experiment. Prepare all samples in triplicate and include control samples: "specificity controls," i.e., NIS-GFP$^+$ T cells that will be pre-incubated with a competitive NIS substrate to test uptake specificity, and "untransduced cell controls," i.e., parental T cells that will receive the radiotracer substrate to determine potential basal cell-intrinsic uptake.

12. Wash cells twice with ice-cold PBS^{CaMg}.

13. For specificity controls, pre-incubate the cells for 20 min with 12.5 μM of the competitive substrate NaClO$_4^-$. Keep the competitive substrate concentration constant throughout the experiment in all subsequent incubation steps involving these controls.

14. Incubate cells in PBS^{CaMg} in the presence of 1000 μL of 50 kBq/mL [^{99m}Tc]TcO$_4^-$ for 30 min in the cell culture incubator as for normal T cell culture.

15. After sample centrifugation (300 × g, 5 min), collect the supernatant and transfer 100 μL of it to a prepared collection tube labeled "Supernatant" (*see* **Note 30**).

16. Wash the cells twice with 1000 μL ice-cold PBS^{CaMg} followed by a centrifuging step each (300 × g, 5 min). Collect each wash solution and transfer 100 μL of each into a prepared collection tube labeled "Wash 1" or "Wash 2," respectively (*see* **Note 31**).

17. Label the Eppendorf tube containing the cell pellet "Cells" and resuspend T cells in their growth medium. In some cases, re-seeding of the radiolabeled cells might be desired (*see* **Note 32**).

18. Measure the CPM of all four tubes per samples using a gamma counter set to the energy window of the chosen radiotracer (i.e., ^{99m}Tc (140.5 KeV)).

19. Analyze data by summing obtained CPM from each well to determine a total radioactivity count per well. Take aliquoting in **steps 15** and **16** into account by multiplying numbers by a factor of 10 for "Supernatant," "Wash 1," and "Wash 2" tubes.

20. Express the cellular radiotracer uptake as %Uptake as indicated in Eq. (1). Calculate averages and standard deviations from triplicate experiments. Typical results for Tregs and Teffs are shown in Figs. 2c and 3c, respectively.

4   Notes

1. All solutions that encounter living cells must be sterilized or purchased sterile and kept sterile. All handling of cells must be done in a suitable cell culture hood with appropriate personal protection equipment. Primary human cells need to be handled according to biosafety class 2 regulations. All items that encounter live lentivirus particles must be disinfected using bleach.

2. As virus producer cells, we use the HEK 293T cell line, originally referred as 293tsA1609neo, which is a highly transfectable derivative of human embryonic kidney 293 cells and

contains the SV40 T-antigen. It gives high titers when used to produce retroviruses. It has been widely used for retroviral production, gene expression, and protein production. These cells can be grown in the presence of 100 IU penicillin/streptomycin (PenStrep) if desired. Subcultivation ratios range from 1:3 to 1:8 and 0.05% (w/v). Trypsin containing 0.53 mM EDTA can be used.

3. Dulbecco's Modified Eagle's Medium F-12 Ham supplemented with 10% ESQ; 1% PenStrep can be added if desired. This medium is used as a quenching solution to the lifting agent, containing Accutase, during CPC cell culture.

4. Non-tissue culture plates must be used as tissue culture-treated plates would give lower transduction efficiencies and lower recovery of Tregs from the plates.

5. Similarly, WGA conjugated to other fluorophores can be used as long as the organic dye does not impede observation of the fluorescent protein.

6. The total amount of plasmid DNA consists of a mixture of various DNA plasmids that together encode all parts necessary to form the virus and the reporter gene transfer vector. This includes the reporter gene encoding plasmid, second- or third-generation lentiviral packaging plasmids, and a plasmid encoding the desired virus envelope. Depending on the precise lentivirus to be produced, the plasmids used for its production vary and consequently also the relative mass ratios as the plasmid sizes differ. For example, the second-generation lentivirus system in our example above uses the mass ratio 4:3:1 for the reporter gene encoding plasmid, the required packaging plasmid, and the envelope plasmid, respectively. A different non-commercial third-generation lentivirus system employs the two packaging plasmids pMDL g/p RRE (Addgene #12251) and pRSV-Rev (Addgene #12253) and pMD2.G as an envelope plasmid (Addgene #12259) encoding for VSV-G. The ratio of these plasmids (assuming the target plasmid is similar in size to our reporter gene plasmid) is 4:2:2:1.To alter the lentivirus tropism, the VSV-G encoding envelop plasmid can be replaced by others that result in the lentiviral particles to be pseudotyped as desired [35].

7. The plasmids referred to here as pLNT SFFV>NIS-GFP or pLNT SFFV>NIS-RFP both encode for the radionuclide reporter NIS which is fused on its C-terminus to a fluorescent protein [9, 10]. In both reporter plasmids, monomeric variants of the fluorescent proteins are used such as the GFP mutant mEGFP A206K [36, 37] or mTagRFP [38], which are used in the NIS-GFP and NIS-RFP reporters, respectively, in this protocol. This is important to avoid artificial clustering of the plasma membrane-localized radionuclide reporter NIS.

8. Fluorescence signals from the NIS-GFP or NIS-RFP reporters can be seen in producer cells and are indicative of successful reporter gene transfection. But it is important to appreciate that they are only a surrogate for successful co-transfection and not an indicator of successful virus production (e.g., they would also be observed if reporter gene plasmids were wrongly transfected without any other relevant components for virus production). If there are no fluorescence signals detected, either there is a problem with the reporter plasmid or transfection failed and the experiment should be terminated and re-started.

9. The filter used in this step is not the conventional 0.22 μm sterile filtration device. While lentiviruses are in the range of 80–100 nm in diameter, it is safer to use a filter pore size of 0.45 μm to ensure virus particles are not damaged. Virus aggregation plays a minor role at this stage but can become relevant at high virus particle concentrations ($\sim 10^8$ TU/mL) and presents a major downstream processing caveat for industrial virus manufacturing.

10. Lentiviral particles can be concentrated either by ultracentrifugation or by using commercial kits involving proprietary materials and intended to avoid long-term centrifugation. An example of the latter and which we have successfully used in the past are Speedy Lentivirus Purification (Abmgood, #LV999), Lentivirus Concentration Solution (Origene, #TR30025), and Lenti-X™ Maxi purification kit (Takara, #631234). As for ultracentrifugation, the standard protocol involves sedimentation centrifugation. Alternatively, centrifugation in a 10% sucrose gradient with a relatively low speed ($\leq 10{,}000 \times g$) has also been shown to result high-titer virus preparation (up to 2×10^8 TU/mL) [39].

11. The viral supernatant can be stored at 4 °C for around 2 days without significant losses in titer but should be aliquoted and snap frozen in liquid nitrogen for storage at $-70/-80$ °C as soon as if longer storage is required.

12. Consideration of practical aliquot sizes is paramount as lentivirus titers decrease about twofold with each freeze-thaw cycle. Virus titer determination via standard methods is recommended when larger virus batches are produced intended for several or comparative transductions and is required when the multiplicity of infection is of importance for experimental success.

13. MOI is an important aspect in viral transduction (infection) of cells. In this context, it is the ratio of infecting agents (i.e., virus particles) to susceptible targets (i.e., target cells). A MOI of one means that on an average there is one virus particle for one

target cell. However, multiple virus particles can infect a single target cell, while some of the target cells might remain unaffected. The infection of a target cell is a chance event and can be described by the Poisson distribution. At a set MOI, the probability of a target cell to be infected by ν virus particles is given by Eq. 2:

$$P(\nu) = \frac{MOI^{\nu} e^{-MOI}}{\nu!} \tag{2}$$

For example, at an MOI of 1, the probability that a target cell will not get infected is $P(\nu = 0) = 36.8\%$ and the probability that it will be infected by a single particle is also $P(\nu = 1) = 36.8\%$, while the probabilities that a target cell is infected by two or three virus particles are $P(\nu = 2) = 18.4\%$ and $P(\nu = 3) = 6.13\%$, respectively. Cumulatively viewed, the probability that a target cell is infected by at least one virus particle is $P(\nu > 0) = 63.2\%$. If the MOI is increased to 3 or 5, $P(\nu > 0)$ increases to 95.0% and 99.3%, respectively. It is important to remember that the MOI is also affected by virus' abilities to infect target cells (cf. tropism), the attachment to the target cells, how much time is allowed for attachment, and also the target cell status (e.g., lentiviruses infecting resting and growing cells, while several retroviruses can only infect growing cells). Hence, it is also recommended to observe actually achieved transduction efficiencies (e.g. here by flow cytometry based on NIS-xFP expression) as a function of input MOIs. These relationships vary between the different cell types used in this protocol.

14. Retronectin coating of plates may be performed overnight, whereby it must be ensured that the solution does not dry out in the well. Coated plates can be sealed using parafilm and stored at 4 °C for up to a week.

15. Prior to transduction, Tregs may or may not be stimulated. Better results may be achieved if they have been stimulated 2–3 days prior to transduction. If stimulation is performed using CD3/CD28 beads, it is not necessary to remove beads before transduction.

16. Centrifuge speed may be increased to up to $1000 \times g$ using compatible cell culture plates to improve transduction efficiency. Risk of producing aerosols increases at higher speeds and Treg viability may be negatively affected.

17. Retronectin-coated plates can be stored at 4 °C for up to one week. The parafilm sealing will prevent evaporation while maintaining sterility.

18. IL-2 is used in the initial phase of T cell expansion and can be replaced by IL-15 three days after transduction. This has been

reported to preserve a less-differentiated stem cell memory phenotype, result in less expression of exhaustion markers, and improve anti-tumor activity [40–42]. Notably, selective expansion strategies have also been reported. For example, one based on a co-transduced IL-4Rα—IL-2/15Rβ chimera permitting the use of IL-4 to transmit an IL-2/15-like signal in the absence of either IL-2 or IL-15, thereby selectively expanding transduced cells only by administration of IL-4 [43]. The latter strategy has recently been used in combination with a NIS-RFP reporter to produce traceable T cells [14].

19. Alternatively, freezing media without animal products are commercially available. Notably, freezing media containing 10% DMSO results in lower T cell recovery rates upon thawing.

20. Characterization of reporter gene-engineered cells must include the validation of the reporters. Importantly, validation must also entail other cellular aspects to ensure the genetic engineering did not impair other relevant cellular behaviors and functions. This can mean a large variety of experiments are required to compare untransduced and reporter-expressing cells [4, 10, 11, 13, 14]. Here, we describe only the experiments necessary to validate reporter function, as others are cell type-dependent and application-specific. Typical results for CPC, Treg, and Teff cells are depicted for each cell type in Figs. 1, 2, and 3, respectively.

21. As an alternative to live cell-based flow cytometry, cells can be fixed and stained with DNA dyes (to discriminate intact cell from dead cells or debris). If required by experimental scheduling, this approach can also introduce a "breaking point" as fixed cells could be kept refrigerated for a few days prior to staining and analysis by flow cytometry.

22. NIS is a transport protein and only functional if correctly inserted into the plasma membrane of a cell. NIS is normally expressed in thyroid follicular cells and cells of the stomach lining and at much lower levels in salivary glands, lactating mammary glands, and testes [44]. While this makes it an excellent host reporter gene for PET and SPECT imaging [4], it also means that it is not normally expressed in the cells one wishes to track. While NIS has been shown to be sensitive to N-terminal modification [14], it is permissive to C-terminal modification with xFP [9, 10] enabling NIS-xFP fusion proteins to be used for preclinical research. Consequently, it is necessary to assess its correct localization in transduced cells to confirm localization to the plasma membrane in the cells of interest.

23. Relative to other cell types, these cells can easily detach from the surface of the coverslip, hence add the PBS slowly via the wall of the well to reduce the shear force on the cells.

24. The fixation time varies depending on the cell type, usually fix between 7 and 15 min. Do not use any fixative that contains permeabilizing agents (e.g., Triton X-100) as the aim here is to leave the plasma membrane intact. This also means that "over-fixing" should be avoided (e.g., excessive paraformaldehyde fixation can lead to pores in cells). WGA bind to glycosylated proteins and should not gain entry into cells as it would stain, for example, the Golgi apparatus to a heavy extent, thereby WGA-633 signals would no longer be exclusive to the plasma membranes and results become difficult to interpret. We recommend optimizing fixatives and fixing conditions before experimentation with new or different cell types.

25. Any nuclear stain that is not interfering in its fluorophore properties with both the used reporter fluorophore and WGA-633 can be used.

26. To reduce background, we recommend observing the timings during the washing steps.

27. Removing the cover glasses from the wells represents a delicate handling step. Using filled wells to remove the cover glasses reduces the force necessary to do so and thereby the likelihood to break the thin cover glasses. We also recommend using a "customized" pair of pointed forceps in which one tip is shortened by ~2 mm and the second bent toward the other tip.

28. NIS is very selective in cation transport and requires the cellular Na^+/K^+ gradient to be intact to function. In contrast, it is very unselective in anion transport, which has been exploited for nuclear medicine and cell tracking applications. There are several anions that can be transported by NIS [26, 44, 45] and consequently could be used for radioactive uptake assays; practical radioactive substrates include the iodide isotopes $^{123}I^-$, $^{124}I^-$, $^{125}I^-$, and $^{131}I^-$, and the tetrahedral pertechnetate analogs $^{188}ReO_4^-$ and $[^{18}F]BF_4^-$. When choosing a radiotracer, several properties must be considered, including a practical half-life, compatibility of the emitted radiation energy with the available detection instrumentation, potential radiodamage to the cells if they were to be kept for longer, radiotracer cost, radiotracer disposal, and available personal protection equipment.

29. For fast growing cells, it is necessary to seed an extra number of wells (not to be incubated with the radiotracer), harvest, and count cells to obtain a reading for the actual number of cells in the seeded wells at the time of the radiotracer uptake experiment.

30. Due to the large number of samples each requiring several collection tubes, it is highly recommended to pre-label all tubes before the start of the experiment, and to use an automated gamma counter capable of automatic decay correction.

31. Two wash steps are usually sufficient; however, if the media supernatant cannot be efficiently removed without disturbing the cell pellet, an extra wash step can be performed.

32. Re-seeding of radiolabeled cells might be required to study radiotracer efflux as well as radiodamage overtime. Therefore, it is recommended to perform the gamma counting as fast as possible to reduce the time cells experience suboptimal conditions by being outside of the incubator. It is also recommended to note all relevant absolute times (radiotracer administration and time of cell pellet resuspension prior to gamma counting as the beginning of a potential efflux experiment, etc.).

Acknowledgments

References

1. Caplan AI (2017) Mesenchymal stem cells: time to change the name! Stem Cells Transl Med 6(6):1445–1451. https://doi.org/10.1002/sctm.17-0051

2. Heathman TR, Nienow AW, McCall MJ, Coopman K, Kara B, Hewitt CJ (2015) The translation of cell-based therapies: clinical landscape and manufacturing challenges. Regen Med 10(1):49–64. https://doi.org/10.2217/rme.14.73

3. Bioinformant (2019) Bioinformant cell therapy industry database. BioInformant. https://

bioinformant.com/product/cell-therapy-industry-database/. Accessed 3 Oct 2019

4. Ashmore-Harris C, Iafrate M, Saleem A, Fruhwirth GO (2020) Non-invasive reporter gene imaging of cell therapies, including T cells and stem cells. Mol Ther. https://doi.org/10.1016/j.ymthe.2020.03.016

5. Krekorian M, Fruhwirth GO, Srinivas M, Figdor CG, Heskamp S, Witney TH, Aarntzen E (2019) Imaging of T-cells and their responses during anti-cancer immunotherapy. Theranostics 9(25):7924–7947. https://doi.org/10.7150/thno.37924

6. Iafrate M, Fruhwirth GO (2020) How non-invasive in vivo cell tracking supports the development and translation of cancer immunotherapies. Front Physiol 11:154. https://doi.org/10.3389/fphys.2020.00154

7. Jacob J, Volpe A, Peng Q, Lechler RI, Smyth LA, Lombardi G, Fruhwirth GO (2023) Radiolabelling of Polyclonally Expanded Human Regulatory T Cells (Treg) with 89Zr-oxine for Medium-Term In Vivo Cell Tracking Molecules 28:1482. https://doi.org/10.3390/molecules28031482

8. Keu KV, Witney TH, Yaghoubi S, Rosenberg J, Kurien A, Magnusson R, Williams J, Habte F, Wagner JR, Forman S, Brown C, Allen-Auerbach M, Czernin J, Tang W, Jensen MC, Badie B, Gambhir SS (2017) Reporter gene imaging of targeted T cell immunotherapy in recurrent glioma. Sci Transl Med 9(373). https://doi.org/10.1126/scitranslmed.aag2196

9. Fruhwirth GO, Diocou S, Blower PJ, Ng T, Mullen GE (2014) A whole-body dual-modality radionuclide optical strategy for preclinical imaging of metastasis and heterogeneous treatment response in different microenvironments. J Nucl Med 55(4):686–694. https://doi.org/10.2967/jnumed.113.127480

10. Volpe A, Man F, Lim L, Khoshnevisan A, Blower J, Blower PJ, Fruhwirth GO (2018) Radionuclide-fluorescence reporter gene imaging to track tumor progression in rodent tumor models. J Vis Exp 133(133):e57088. https://doi.org/10.3791/57088

11. Ashmore-Harris C, Blackford SJ, Grimsdell B, Kurtys E, Glatz MC, Rashid TS, Fruhwirth GO (2019) Reporter gene-engineering of human induced pluripotent stem cells during differentiation renders in vivo traceable hepatocyte-like cells accessible. Stem Cell Res 41:101599. https://doi.org/10.1016/j.scr.2019.101599

12. Kang JH, Lee DS, Paeng JC, Lee JS, Kim YH, Lee YJ, Hwang DW, Jeong JM, Lim SM, Chung JK, Lee MC (2005) Development of a sodium/iodide symporter (NIS)-transgenic mouse for imaging of cardiomyocyte-specific reporter gene expression. J Nucl Med 46(3):479–483

13. Jacob J, Nadkarni S, Volpe A, Peng Q, Tung SL, Hannen RF, Mohseni YR, Scotta C, Marelli-Berg FM, Lechler RI, Smyth LA, Fruhwirth GO, Lombardi G (2020) Spatiotemporal in vivo tracking of polyclonal human regulatory T cells (Treg) reveals a role for innate immune cells in Treg transplant recruitment. Mol Ther – Methods Clin Dev 20:324–336. https://doi.org/10.1016/j.omtm.2020.12.003

14. Volpe A, Lang C, Lim L, Man F, Kurtys E, Ashmore-Harris C, Johnson P, Skourti E, de Rosales RTM, Fruhwirth GO (2020) Spatiotemporal PET imaging reveals differences in CAR-T tumor retention in triple-negative breast cancer models. Mol Ther 28(10):2271–2285. https://doi.org/10.1016/j.ymthe.2020.06.028

15. O'Doherty J, Jauregui-Osoro M, Brothwood T, Szyszko T, Marsden PK, O'Doherty MJ, Cook GJR, Blower PJ, Lewington V (2017) (18)F-Tetrafluoroborate, a PET probe for imaging sodium/iodide symporter expression: whole-body biodistribution, safety, and radiation dosimetry in thyroid cancer patients. J Nucl Med 58(10):1666–1671. https://doi.org/10.2967/jnumed.117.192252

16. Meller J, Becker W (2002) The continuing importance of thyroid scintigraphy in the era of high-resolution ultrasound. Eur J Nucl Med Mol Imaging 29(Suppl 2):S425–S438. https://doi.org/10.1007/s00259-002-0811-8

17. Goswami R, Subramanian G, Silayeva L, Newkirk I, Doctor D, Chawla K, Chattopadhyay S, Chandra D, Chilukuri N, Betapudi V (2019) Gene therapy leaves a vicious cycle. Front Oncol 9:297. https://doi.org/10.3389/fonc.2019.00297

18. Ghani K, Boivin-Welch M, Roy S, Dakiw-Piaceski A, Barbier M, Pope E, Germain L, Caruso M (2019) Generation of high-titer self-inactivated gamma-retroviral vector producer cells. Mol Ther Methods Clin Dev 14:90–99. https://doi.org/10.1016/j.omtm.2019.05.013

19. Ronald JA, Cusso L, Chuang HY, Yan X, Dragulescu-Andrasi A, Gambhir SS (2013) Development and validation of non-integrative, self-limited, and replicating minicircles for safe reporter gene imaging of cell-based therapies. PLoS One 8(8):e73138. https://doi.org/10.1371/journal.pone.0073138

20. Lufino MM, Edser PA, Wade-Martins R (2008) Advances in high-capacity extrachromosomal vector technology: episomal maintenance, vector delivery, and transgene expression. Mol Ther 16(9):1525–1538. https://doi.org/10.1038/mt.2008.156

21. Maggio I, Goncalves MA (2015) Genome editing at the crossroads of delivery, specificity, and fidelity. Trends Biotechnol 33(5):280–291. https://doi.org/10.1016/j.tibtech.2015.02.011

22. Bressan RB, Dewari PS, Kalantzaki M, Gangoso E, Matjusaitis M, Garcia-Diaz C, Blin C, Grant V, Bulstrode H, Gogolok S, Skarnes WC, Pollard SM (2017) Efficient CRISPR/Cas9-assisted gene targeting enables rapid and precise genetic manipulation of mammalian neural stem cells. Development 144(4):635–648. https://doi.org/10.1242/dev.140855

23. Ashmore-Harris C, Fruhwirth GO (2020) The clinical potential of gene editing as a tool to engineer cell-based therapeutics. Clin Transl Med 9(1):15. https://doi.org/10.1186/s40169-020-0268-z

24. US Food & Drug Administration (2017) FDA approval brings first gene therapy to the United States. https://www.fda.gov/newsevents/newsroom/pressannouncements/ucm574058.htm. Accessed 25 Feb 2018

25. Abou-El-Enein M, Bauer G, Reinke P, Renner M, Schneider CK (2014) A roadmap toward clinical translation of genetically-modified stem cells for treatment of HIV. Trends Mol Med 20(11):632–642. https://doi.org/10.1016/j.molmed.2014.08.004

26. Diocou S, Volpe A, Jauregui-Osoro M, Boudjemeline M, Chuamsaamarkkee K, Man F, Blower PJ, Ng T, Mullen GED, Fruhwirth GO (2017) [(18)F]tetrafluoroborate-PET/CT enables sensitive tumor and metastasis in vivo imaging in a sodium iodide symporter-expressing tumor model. Sci Rep 7(1):946. https://doi.org/10.1038/s41598-017-01044-4

27. Zufferey R, Nagy D, Mandel RJ, Naldini L, Trono D (1997) Multiply attenuated lentiviral vector achieves efficient gene delivery in vivo. Nat Biotechnol 15(9):871–875. https://doi.org/10.1038/nbt0997-871

28. Lewis-McDougall FC, Ruchaya PJ, Domenjo-Vila E, Shin Teoh T, Prata L, Cottle BJ, Clark JE, Punjabi PP, Awad W, Torella D, Tchkonia T, Kirkland JL, Ellison-Hughes GM (2019) Aged-senescent cells contribute to impaired heart regeneration. Aging Cell 18(3):e12931. https://doi.org/10.1111/acel.12931

29. Scalise M, Torella M, Marino F, Ravo M, Giurato G, Vicinanza C, Cianflone E, Mancuso T, Aquila I, Salerno L, Nassa G, Agosti V, De Angelis A, Urbanek K, Berrino L, Veltri P, Paolino D, Mastroroberto P, De Feo M, Viglietto G, Weisz A, Nadal-Ginard B, Ellison-Hughes GM, Torella D (2020) Atrial myxomas arise from multipotent cardiac stem cells. Eur Heart J 41(45):4332–4345. https://doi.org/10.1093/eurheartj/ehaa156

30. Boardman DA, Philippeos C, Fruhwirth GO, Ibrahim MA, Hannen RF, Cooper D, Marelli-Berg FM, Watt FM, Lechler RI, Maher J, Smyth LA, Lombardi G (2017) Expression of a chimeric antigen receptor specific for donor HLA class I enhances the potency of human regulatory T cells in preventing human skin transplant rejection. Am J Transplant 17(4):931–943. https://doi.org/10.1111/ajt.14185

31. Fraser H, Safinia N, Grageda N, Thirkell S, Lowe K, Fry LJ, Scotta C, Hope A, Fisher C, Hilton R, Game D, Harden P, Bushell A, Wood K, Lechler RI, Lombardi G (2018) A rapamycin-based GMP-compatible process for the isolation and expansion of regulatory T cells for clinical trials. Mol Ther Methods Clin Dev 8:198–209. https://doi.org/10.1016/j.omtm.2018.01.006

32. Safinia N, Vaikunthanathan T, Fraser H, Thirkell S, Lowe K, Blackmore L, Whitehouse G, Martinez-Llordella M, Jassem W, Sanchez-Fueyo A, Lechler RI, Lombardi G (2016) Successful expansion of functional and stable regulatory T cells for immunotherapy in liver transplantation. Oncotarget 7(7):7563–7577. https://doi.org/10.18632/oncotarget.6927

33. Kutner RH, Zhang XY, Reiser J (2009) Production, concentration and titration of pseudotyped HIV-1-based lentiviral vectors. Nat Protoc 4(4):495–505. https://doi.org/10.1038/nprot.2009.22

34. Harlow E, Lane D (2006) Attaching suspension cells to slides using a cytocentrifuge. CSH Protoc 2006(3). https://doi.org/10.1101/pdb.prot4291

35. Cronin J, Zhang XY, Reiser J (2005) Altering the tropism of lentiviral vectors through pseudotyping. Curr Gene Ther 5(4):387–398. https://doi.org/10.2174/1566523054546224

36. Zacharias DA, Violin JD, Newton AC, Tsien RY (2002) Partitioning of lipid-modified monomeric GFPs into membrane microdomains of live cells. Science 296(5569):

913–916. https://doi.org/10.1126/science.1068539

37. Snapp EL, Hegde RS, Francolini M, Lombardo F, Colombo S, Pedrazzini E, Borgese N, Lippincott-Schwartz J (2003) Formation of stacked ER cisternae by low affinity protein interactions. J Cell Biol 163(2):257–269. https://doi.org/10.1083/jcb.200306020

38. Merzlyak EM, Goedhart J, Shcherbo D, Bulina ME, Shcheglov AS, Fradkov AF, Gaintzeva A, Lukyanov KA, Lukyanov S, Gadella TW, Chudakov DM (2007) Bright monomeric red fluorescent protein with an extended fluorescence lifetime. Nat Methods 4(7):555–557. https://doi.org/10.1038/nmeth1062

39. Jiang W, Hua R, Wei M, Li C, Qiu Z, Yang X, Zhang C (2015) An optimized method for high-titer lentivirus preparations without ultracentrifugation. Sci Rep 5:13875. https://doi.org/10.1038/srep13875

40. Hasan AN, Selvakumar A, Shabrova E, Liu XR, Afridi F, Heller G, Riviere I, Sadelain M, Dupont B, O'Reilly RJ (2016) Soluble and membrane-bound interleukin (IL)-15 Ralpha/IL-15 complexes mediate proliferation of high-avidity central memory CD8(+) T cells for adoptive immunotherapy of cancer and infections. Clin Exp Immunol 186(2):249–265. https://doi.org/10.1111/cei.12816

41. Zhou J, Jin L, Wang F, Zhang Y, Liu B, Zhao T (2019) Chimeric antigen receptor T (CAR-T) cells expanded with IL-7/IL-15 mediate superior antitumor effects. Protein Cell 10(10):764–769. https://doi.org/10.1007/s13238-019-0643-y

42. Alizadeh D, Wong RA, Yang X, Wang D, Pecoraro JR, Kuo CF, Aguilar B, Qi Y, Ann DK, Starr R, Urak R, Wang X, Forman SJ, Brown CE (2019) IL15 enhances CAR-T cell antitumor activity by reducing mTORC1 activity and preserving their stem cell memory phenotype. Cancer Immunol Res 7(5):759–772. https://doi.org/10.1158/2326-6066.CIR-18-0466

43. Wilkie S, Burbridge SE, Chiapero-Stanke L, Pereira AC, Cleary S, van der Stegen SJ, Spicer JF, Davies DM, Maher J (2010) Selective expansion of chimeric antigen receptor-targeted T-cells with potent effector function using interleukin-4. J Biol Chem 285(33):25538–25544. https://doi.org/10.1074/jbc.M110.127951

44. Portulano C, Paroder-Belenitsky M, Carrasco N (2014) The Na+/I- symporter (NIS): mechanism and medical impact. Endocr Rev 35(1):106–149. https://doi.org/10.1210/er.2012-1036

45. Khoshnevisan A, Chuamsaamarkkee K, Boudjemeline M, Jackson A, Smith GE, Gee AD, Fruhwirth GO, Blower PJ (2017) 18F-Fluorosulfate for PET imaging of the sodium-iodide symporter: synthesis and biologic evaluation in vitro and in vivo. J Nucl Med 58(1):156–161. https://doi.org/10.2967/jnumed.116.177519

Chapter 19

Single-Cell PET Imaging and Tracking

Kyung Oh. Jung and Guillem Pratx

Abstract

Positron emission tomography (PET) is one of the most sensitive whole-body molecular imaging techniques available in the clinic, able to detect picomolar levels of probe. As such, it was recently demonstrated that PET could also be used to track single radiolabeled cells in small animals. In this protocol, we present detailed procedures for radiolabeling cells using mesoporous silica nanoparticles (MSNs) and for tracking these cells in real time using in vivo PET. This includes static imaging of single cells as well as dynamic tracking of moving cells directly from the list-mode data. The protocol provides detailed instructions and examples for each step.

Key words Positron emission tomography, Cell tracking, Cancer metastasis, Nanotechnology

1 Introduction

Positron emission tomography (PET) is the only in vivo imaging modality capable of detecting picomolar levels of probe at the whole-body level in humans [1, 2]. Previously, we demonstrated that this high sensitivity could be harnessed to image and track single cells in small-animal models. To achieve this goal, we developed and tested a novel trajectory reconstruction algorithm that uses the list-mode data produced by the scanner to localize single moving sources (such as cells) in 3D and in real time [3, 4].

To translate this concept for in vivo applications, we then investigated and optimized a method for labeling cells with >20 Bq per cell, which is the minimum amount of radioactivity required for accurate tracking. This amount of radioactivity can vary based on several factors. The best tracking performance will be achieved for scanners with high coincidence detection sensitivity (7–14% for preclinical scanners) and low intrinsic background. In addition, due to the very low activity, it is also critical to minimize

background contamination within the room (including any radio-activity stored near the scanner or radioactivity on the scanner bed from a previous experiment). Finally, fast moving cells are more challenging to track and typically require a higher count rate for accurate tracking. A basic rule of thumb [3] is that a tracked cell should be labeled with an amount of radioactivity (in Bq) equal to at least four times its velocity (in mm/s). This is equivalent to say that a tracked cell should emit, on average, four positrons for every 1 mm travelled.

To achieve such high radioactivity per cell, our method uses mesoporous silica nanoparticles (MSNs), a type of nanomaterial that has received considerable attention due to its high surface area and large pore volume [5]. The properties of MSNs make them well suited for carrying specific cargo efficiently into single cells [6]. An additional property of these nanoparticles is that radiometals such as ^{68}Ga and ^{89}Zr naturally form complexes with their silica surface, which provides a straightforward method for radiolabeling MSNs with upwards of 0.5 Bq per single nanoparti-cle. Cells are then labeled through passive incubation with the treated MSNs. Given the high radioactivity per nanoparticles, only ~100 nanoparticles are needed to label cells with sufficient radioactivity for this protocol. Following that, single cells are isolated and administered through an intravenous (IV) catheter into live individuals. Gamma rays emitted from the single cells are captured by a PET scanner and processed by a special-purpose reconstruction algorithm to estimate, in real time, the location of the moving cell.

Single-cell tracking using PET may have a number of applica-tions. For instance, we are interested in applying this technique to understand the migration of immunotherapeutic cells in cancer patients. Being able to identify the migration routes and kinetics of therapeutic cells would enable more efficient delivery of these precious cells toward the solid tumors they are intended to treat. Highly sensitive PET scanners with long axial field of view are being developed that could be used to sensitively detect the dim signals emanating from single cells [7]. In addition, in the preclinical setting, the approach could be useful to better understand the early stage of metastasis, a stage during which cells shed by the tumor circulate in the blood before arresting in a remote organ. Finally, research is ongoing to improve the throughput of the method and enable tracking of multiple cells in parallel in the same individual. This protocol provides a detailed description of the techniques employed for labeling nanoparticles with radioiso-tope, isolating highly radioactive single cells, and tracking these cells in real time and in vivo using PET (Fig. 1).
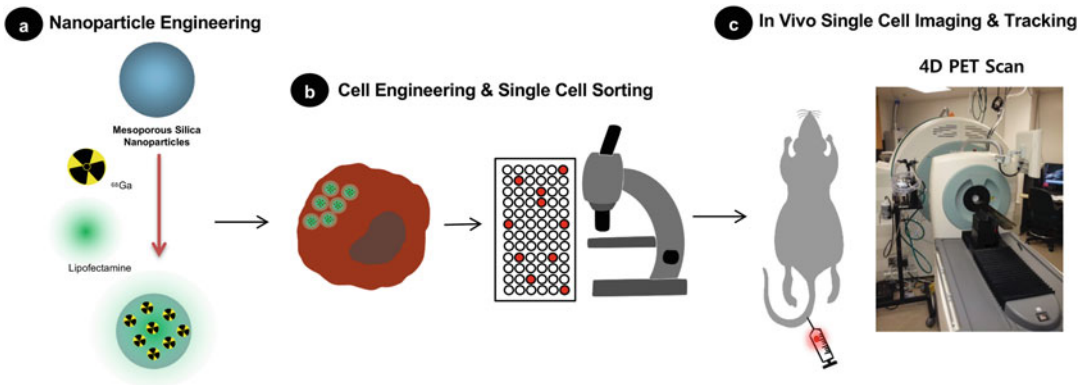
Fig. 1 Overview of the protocol for in vivo single cell tracking. (**a**) Mesoporous silica nanoparticles (MSNs) are labeled with ^{68}Ga or [89]Zr and then coated with lipid bilayer for cell uptake. (**b**) The radiolabeled nanoparticles are transferred to cells, and radioactive single cells (containing >20 Bq) are sorted and isolated. (**c**) The single cells are administered into a subject and then imaged using a small-animal PET scanner and processed by our reconstruction algorithm to obtain either static or dynamic localization information

2   Materials

1. Personal radiation dosimeter badge and ring.
2. Portable radiation survey meter (e.g., Geiger–Mueller detector such as Ludlum model 44-9).
3. Mesoporous silica nanoparticles (Sigma-Aldrich, catalogue #: 749265).
4. Ethanol.
5. Radioisotope (^{68}Ga or [89]Zr; ~600 MBq per run).
6. 0.1 M MES buffer, pH 7.3.
7. 0.1 M HEPES buffer.
8. 0.1 N HCl.
9. 0.9 g/mL ammonium hydroxide solution.
10. 2 M Na_2CO_3 solution.
11. iTLC-SG paper.
12. 50 mM EDTA, pH 5.
13. Radio-TLC scanner (Bioscan AR-2000).
14. MDA-MB-231 cell line (or other suitable cell line).
15. Cell culture medium: Dulbecco's modified Eagle medium with 584.0 mg/l of l-glutamine and 1000.0 mg/l of d-glucose, supplemented with 10% fetal bovine serum (FBS) and 1% antibiotic–antimycotic mix.
16. Liposome transfection agent (Lipofectamine 2000).
17. Opti-MEM cell culture medium.

18. Nuclear fluorescent stain (e.g., 1 μM Hoechst 33342).

19. Fluorescence microscope (e.g., EVOS).

20. Gamma counter (e.g., HIDEX).

21. PET or PET/CT scanner (e.g., Siemens Inveon or Sofie Biosciences GNEXT).

22. Female athymic nude mice (aged 6 weeks; average weight, 20 g).

23. Isoflurane anesthesia system.

24. Butterfly-type catheter.

25. Image analysis software (e.g., Inveon Research Workplace).

26. MATLAB software and CellGPS code (*see* **Note 1**).

3   Methods

3.1   Radiolabeling of MSNs

1. One day before experiment, activate MSNs by overnight incubation in ethanol.

2. All personnel working with radioactive materials should wear proper personal protective equipment (PPE) and personal dosimeters (body and ring).

3. Add 4.5 μg of MSNs to 1.5 mL tube containing, for ^{68}Ga, 100 μL of MES buffer or, for ^{89}Zr, 1 mL of HEPES buffer.

4. Label the MSNs with ^{68}Ga by adding 1.5 mL of ^{68}GaCl$_3$ solution (~600 MBq) eluted with HCl from a clinical-grade generator or with ^{89}Zr by adding ^{89}Zr oxalic acid (93 MBq in 100 μL).

5. For ^{68}Ga, set reaction pH to ~7.3 by adding 30 μL of ammonium hydroxide solution and then incubate mixture at 75 °C for 15 min (*see* **Note 2**). Alternatively, for ^{89}Zr, add Na$_2$CO$_3$ solution to achieve pH of 8–9 and then incubate mixture at 75 °C for 2 h (*see* **Note 3**).

6. Wash the nanoparticles three times with PBS by centrifugation at $16,000 \times g$ for 1 min to remove any residual radioisotope.

7. To validate radiolabeling purity, deposit 1.5 μL of the radiolabeled MSNs onto silica-gel impregnated iTLC-SG paper. Use EDTA as the elution solvent, and analyze the samples using radio-iTLC.

3.2   Lipid Coating of MSN

1. To coat MSN with a lipid bilayer (*see* **Note 4**), prepare two separate solutions: one containing a mixture of 4.5 μg of MSNs in 500 μL of Opti-MEM and the other containing a mixture of 20 μL of Lipofectamine diluted in 500 μL of Opti-MEM.

2. Incubate the two mixtures for 5 min at room temperature.

3. Combine the two solutions and incubate for an additional 15 min at room temperature.

4. Centrifuge at $16,000 \times g$ for 1 min to isolate the coated MSNs.

3.3 In Vitro Cell Uptake and Radioactivity Measurements

1. Culture MDA-MB-231 cells (human invasive ductal carcinoma) in cell culture media. Follow standard culture protocol.

2. Seed MDA-MB-231 cells (5×10^5 cells/well) in 24-well plates and incubate in a CO_2 incubator for 24 h at 37 °C.

3. Add lipid-coated ^{68}Ga/^{89}Zr-MSNs in 3 mL cell culture medium and incubate for 40 min at 37 °C.

4. Rinse the cells three times with 1 mL PBS to remove residual MSNs.

5. Optionally, incubate the cells with a nuclear fluorescent stain according to the manufacturer's instructions and then wash the cells three times by pipetting 1 mL PBS.

6. Prepare a suspension of MDA-MB-231 cells and manually dispense the cells into Terasaki plates [8]. The cell concentration should be adjusted to achieve about 1 cell per 10 μL well on average (about 100 cells per mL). Due to Poisson statistics, the number of cells per well will fluctuate from 0 to more than 1.

7. Use fluorescence microscopy to count the number of cells per well. Identify wells containing various numbers of cells and transfer their contents to a 96-well plate for PET imaging (Inveon D-PET, 425–650 keV energy window, 10 min acquisition time). Assess the sensitivity of the imaging setup by visualizing the reconstructed images for different numbers of cells and performing region of interest analysis using the imaging software.

8. Alternatively, measure the radioactivity of different numbers of cells using gamma counting (counting time of 30–60 s per sample; *see* **Note 5**).

3.4 Static In Vivo Cell Imaging Using PET/CT

1. Static imaging of single cells in mice assumes that the cells are immobile over the duration of the scan. Cell motion will result in incorrect reconstruction of the tracer distribution. This method can be used to reconstruct either a single cell or a small number of cells in the same individual.

2. All animal experiments should be conducted under oversight from an institutional animal use panel.

3. Screen single cells from Terasaki plates and select those with higher count rate (*see* **Note 6**). It is important to note that MSN uptake can be heterogeneous; thus, preselecting cells on the basis of uptake will increase the likelihood of success. This

can be done by pipetting a single cell and then placing the pipet tip next to the survey meter set to 1X setting. Geiger–Mueller detectors are sensitive enough to respond to the radioactivity of single cells loaded with >20 Bq.

4. Load a small number of cells (1–100) into a syringe (100 μL of the injection volume).

5. Anesthetize the mouse using 1–2% isoflurane concentration and 0.5 L/min oxygen flow rate.

6. Inject the cell(s) through desired route of administration (intravenous, etc.).

7. At the desired time point, place the mouse in the scanner, resume gas anesthesia administration, and run a static PET acquisition. The optimal time point will be based on the application, the question of interest, and the half-life of the radionuclide. Imaging can be performed as soon as the cells have been administered or at later time points to provide information regarding the dissemination of cells at different time points. It is important to pay attention to the energy window to minimize the contribution of intrinsic scintillator background to the measured signal. For the Inveon PET/CT, an energy window of 425–650 keV and an acquisition of 10 min yield suitable sensitivity for single cells (*see* **Note 7**). Other scanners may have different optimal settings. Optionally, a normalization scan can be performed with the modified energy window to obtain quantitative images in units of kB/cc. If the normalization step is not performed, only relative activity measurements can be obtained, which is suitable for localizing single cells but not for assessing their radioactivity in vivo. Normalization is a standard procedure performed once a month on most scanners; it requires placing a standard phantom in the bore of the scanner and running a long acquisition overnight.

8. After PET imaging, acquire X-ray CT images with standard settings (80 kVp, 500 μA). Alternatively, an anatomical reference can be obtained by acquiring a transmission scan, according to the ability of the scanner. Either set of images can be used for attenuation and scatter correction.

9. Reconstruct static PET images using the standard algorithm that is available on the scanner, such as OSEM or similar iterative algorithm. A typical example of images reconstructed with this method is shown in Fig. 2.

10. For cells labeled with long-lived ^{89}Zr-MSNs, multiple time points can be acquired for longitudinal imaging up to 48 h (*see* **Note 8**).
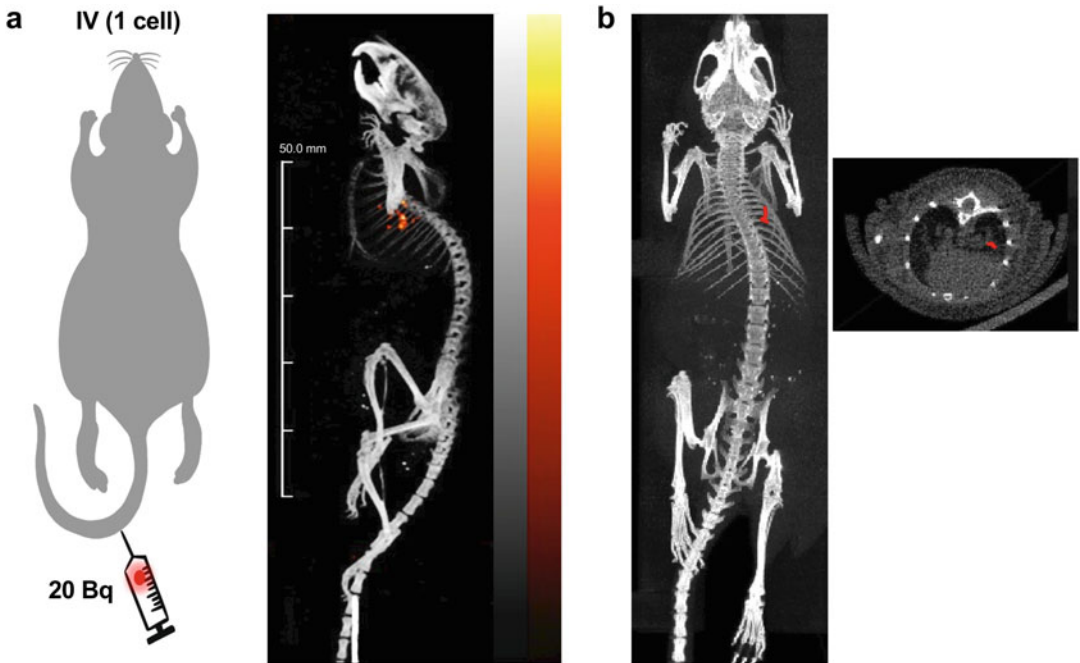
Fig. 2 PET tracking of single IV-injected cell. (**a**) A radiolabeled single MDA-MB-231 cell (22 Bq) was injected IV, and then a PET scan was acquired using PET/CT (425-50 keV energy window, 10 min acquisition, 2 min postinjection). Conventional reconstruction (2D-OSEM) shows focal uptake in the lung area, a likely site of arrest for cancer cells. The noise in the PET image is due to the low radioactivity of the cell (22 Bq), which is barely above the detection threshold (20 Bq). (**b**) The list-mode data was processed using a dynamic trajectory reconstruction algorithm. The result shows that the cell remains essentially at the same position during the 10-min-long scan

3.5 Dynamic Cell Tracking Using PET/CT

1. Dynamic tracking follows in real time the motion of moving cells. In its present implementation, dynamic tracking can only be applied to a single injected cell.

2. For dynamic tracking in mice, the cell should be injected into the subject while inside the scanner bore. One solution is to cannulate the tail vein using a butterfly catheter. Connect an insulin syringe containing the radiolabeled cell (>50 Bq) to the distal end of the tubing, and then depress the plunger slightly until the catheter tubing and needle are filled with the solution. Insert the needle into the lateral tail vein. The animal is now ready to be moved to the scanner bed. Maintain gas anesthesia (1–2% isoflurane and 0.5 l/min oxygen flow).

3. Initiate list-mode PET acquisition. The acquisition should last long enough to observe cell migration. Initial migration will be observed within seconds of administering the cell; subsequent migration may be observed within the next hour or so based on the type of cell and administration route.

4. Slowly depress the plunger to inject the sample. You may place a radiation survey meter near the tail to audibly detect the passage of the radioactive cell.

5. Once the acquisition is complete, import the list-mode data file into MATLAB. Based on the scanner, this may require converting the data from a vendor-specific machine format into a MATLAB-interpretable format. The scanner manufacturer may provide information regarding this step.

6. It is important to identify the exact time at which the cell entered the field of view of the scanner. Prior to that time, the only detected counts are noise and background radioactivity; thus, the reconstruction should start only once the cell has entered the field of view. The arrival of the cell is marked by a marked increase in the event count rate, which can be computed form the list-mode data.

7. Run the CellGPS code according to the package instructions. The package can be downloaded online (*see* **Note 1**). Several parameters should be adjusted by the user. First, set the tracking start time to the value obtained in the previous step. Second, based on the activity and velocity of the cell, the number of spline knots should be adjusted to achieve a good trade-off between the flexibility of the trajectory (how easily it will conform to the path of the cell) and noise rejection. As a rule of thumb, the reconstructed trajectory should have 1 knot for every 50 detected counts. This number may be adjusted until a suitable result is obtained. If too many knots are used in the reconstruction relative to the number of counts available, the reconstructed trajectory will appear noisy. On the other hand, if too few counts are used, the full range of motion of the cell may not be captured. This effect is demonstrated in Fig. 3.

8. Visualize the reconstructed trajectory, which can be superimposed over CT scan of the same subject.

4   Notes

1. Reconstruction code for dynamic cell tracking is available online as a Code Ocean capsule at https://doi.org/10.24433/CO.5746631.v1. A detailed description and evaluation of the algorithm has been reported [3].

2. The entire cell labeling procedure using radiolabeled MSN takes approximately 90 min, which is the equivalent of ~1.5 half-lives for ^{68}Ga (half-life 67 min). Additional time is needed afterward for isolating and selecting a suitable number of single cells. In addition, radiotracer efflux from cells, which can reach 50% after 2 h, is another factor that can reduce radioactivity of
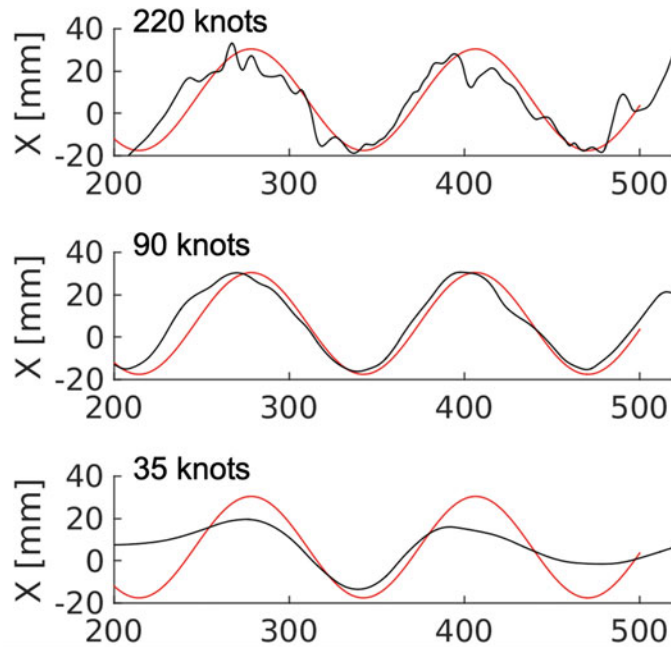
Fig. 3 Example of trajectories reconstructed using different numbers of knots, for a single cell moving along a helical trajectory inside a phantom (2168 counts). Only the *x* coordinate is shown here for simplicity. The black and red lines represent the reconstructed and ground truth trajectories, respectively

labeled cells. Therefore, when using short-lived ^{68}Ga, it is important to plan experiment carefully in view of the time required for each experimental step.

3. For radiolabeling of MSNs, the efficiency depends on reaction temperature, reaction time, and reaction pH. These factors can be optimized for best results.

4. To enhance cellular uptake of radiolabeled MSNs, the nanoparticles should be fused with a liposome-based transfection reagent to coat their surface with a lipid bilayer. This coating also helps achieve high biocompatibility.

5. The most crucial step for successful tracking of single cells in vivo is to prepare single cells with sufficient levels of radioactivity. On the Inveon PET scanner, cells should have at least 20 Bq of radioactivity to be detected in static scans or 50 Bq to be tracked dynamically while moving. However, these values may vary based on the PET scanner being used. Scanners built from BGO detectors (e.g., Sofie Biosciences G4 or G8) have almost no intrinsic radioactivity background, and, therefore, they are able to detect lower amounts of radioactivity [4].

6. Identifying cells with high radioactivity can be challenging. Using serial dilution in Terasaki plate, you should isolate single

cells stained with Hoechst 33342 using fluorescence microscopy, and then quickly confirm the radioactivity of single cell using a portable radiation survey meter. Gamma counting may be used subsequently to quantify the radioactivity of individual cells.

7. Due to naturally occurring radioactivity from ^{176}Lu present in the LSO scintillators of PET detectors, the acquisition protocol should include a lower energy discriminator of 425 keV to minimize background and detect the weak signals of radiolabeled single cells. This value may vary based on the PET scanner being used.

8. For long-term tracking experiments using ^{89}Zr-MSNs, it is important to consider the potential toxicity due to prolonged exposure of labeled cells to ionizing radiation.

References

1. Kircher MF, Gambhir SS, Grimm J (2011) Noninvasive cell-tracking methods. Nat Rev Clin Oncol 8(11):677–688

2. Jung KO, Kim TJ, Jung HY, Rhee S, Zhao W, Ha B, Red-Horse K, Gambhir SS, Pratx G (2020) Whole-body tracking of single cells via positron emission tomography. Nat Biomed Eng 4(8):835–844

3. Lee K, Kim TJ, Pratx G (2015) Single-cell tracking with PET using a novel trajectory reconstruction algorithm. IEEE Trans Med Imaging 34(4):994–1003

4. Ouyang Y, Kim TJ, Pratx G (2016) Evaluation of a BGO-based PET system for single-cell tracking performance by simulation and phantom studies. Mol Imaging 15:1536012116646489

5. Tang F, Li L, Chen D (2012) Mesoporous silica nanoparticles: synthesis, biocompatibility and drug delivery. Adv Mater 24(12):1504–1534

6. Shaffer TM, Wall MA, Harmsen S, Longo VA, Drain CM, Kircher MF, Grimm J (2015) Silica nanoparticles as substrates for chelator-free labeling of oxophilic radioisotopes. Nano Lett 15(2):864–868

7. Cherry SR, Jones T, Karp JS, Qi J, Moses WW, Badawi RD (2018) Total-body PET: maximizing sensitivity to create new opportunities for clinical research and patient care. J Nucl Med 59(1):3–12

8. Yaron JR, Ziegler CP, Tran TH, Glenn HL, Meldrum DR (2014) A convenient, optimized pipeline for isolation, fluorescence microscopy and molecular analysis of live single cells. Biological procedures online 16:9

Part III

PET Technology

Chapter 20

PET System Technology: Theoretical Aspects and Experimental Methodology

Andrea Gonzalez-Montoro and Craig S. Levin

Abstract

Positron emission tomography (PET) imaging provides unique information of the cellular and molecular pathways of disease occurring within the human body, using measurements made from outside the body, which has shown utility in a variety of studies from basic research to clinical applications. This chapter describes some of the most relevant PET system parameters that impact its imaging performance such as 3D spatial, energy, and coincidence timing resolutions and the methodology typically used to evaluate those parameters. In addition, the physical principles underlying PET imaging, PET photon detector technology, and coincidence detection are also described. As a closing remark, the future perspectives of PET imaging and its simultaneous use with anatomical imaging techniques (e.g., computed tomography [CT] and magnetic resonance imaging [MRI]) are outlined.

Key words Positron emission tomography, Silicon photomultipliers, Spatial resolution, Depth of interaction, Energy resolution, Coincidence time resolution

1 Introduction

Positron emission tomography (PET) imaging uses radioactive contrast agents, known as *radiotracers*, for the detection, diagnosis, monitoring, and therapy assessment of a variety of medical conditions. It constitutes the most used molecular imaging technique in the clinic as well as in preclinical research [1–4].

The historical breakthroughs contributing to the development of PET imaging started with the prediction of the positron by Dirac in 1929 [5] and its experimental discovery by Anderson in 1933 [6]. During the next years, other milestones were achieved such as the discovery of radioactive elements by Curie and Joliot, the use of a cyclotron for the artificial production of positron-emitting radionuclides at the University of California in Berkeley [7], and the development of the scintillator [8] and photomultiplier tube (PMT) used for the detection of 511 kilo-electron-volt (keV)
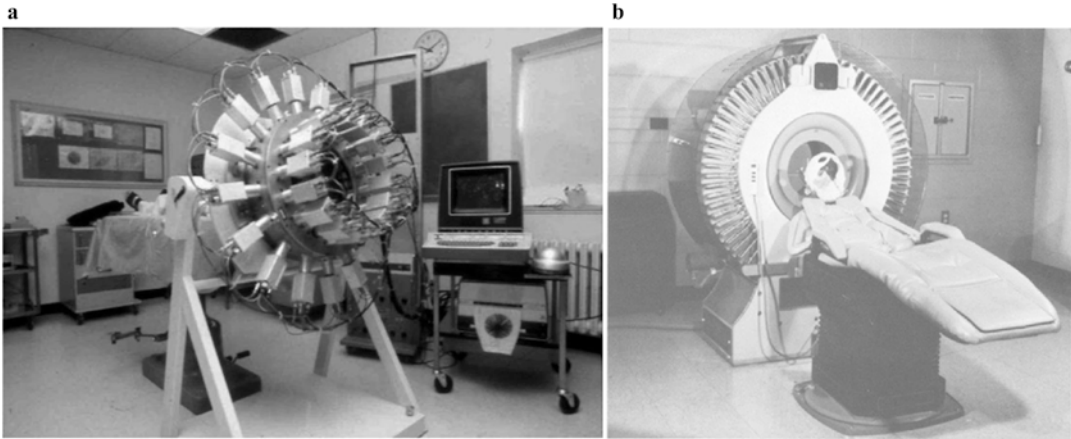
Fig. 1 Photographs of (**a**) the original Positome developed by Thompson and collaborators at Montreal Neurological Institute; original figure extracted from Ref. [29]; (**b**) the PETT VI, developed at the Mallinckrodt Institute of Radiology, Washington University School of Medicine; original figure extracted from Ref. [30]

photons that result from the annihilation of positrons with electrons in the subject tissues [9].

Motivated by these technological breakthroughs, in 1951, Wren, Good, and Handler first reported on the possible use of coincidence detection to generate medical images [10], and, only 2 years later, Brownell and Sweet built the first positron imaging device for the detection of brain tumors [11]. During the next years, Rankowitz and his team designed the first operative positron scanner that was based on NaI(Tl) cylindrical detectors assembled in a ring geometry [12], and Anger and Gottschalk reported on the design of a full positron camera [13]. Finally, in the 1970s, Robertson and Thompson built the so-called Positome [14] (*see* Fig. 1a), and, contemporaneously, Phelps, Hoffman, Mullani, and Ter-Pogossian built the so-called PETT [15, 16] (Fig. 1b) starting a collaboration with EG&G ORTEC to build the first commercial PET scanner known as ECAT I [17].

Over the next years, advancements on both the synthesis of radiotracers for clinical use [18] and on the PET scintillation detector array manufacturing process [19] were achieved. The photodetector technology also evolved and solid-state photodetectors appeared, i.e., avalanche photodiodes (APDs) [20] and later silicon photomultipliers (SiPMs) [21, 22]. Since then, PET detector technology has continuously improved, and, nowadays, commercially available clinical PET scanners offer spatial resolutions of ~4 mm at the system center [23] and 214 ps coincidence time resolution (CTR) [24], which defines the system's ability to estimate the arrival time difference of the annihilation photons into two coincident detectors. Although improvements over previous generation PET systems have been accomplished, 4 mm resolution, still is

often inadequate for visualizing small lesions important for early detection of disease. In addition, state-of-the-art PET scanners report relatively low photon sensitivity, requiring high tracer dose and long scanning times (reduced patient throughput). To enhance resolution and increase system photon sensitivity, specially designed PET systems that may be placed close to the organ of interest have been developed [25]. Moreover, methods to include information on the photon depth of interactions (DOI) in the scintillation crystals is an important factor that PET system designers have studied to preserve resolution uniformity throughout the useful field of view (FOV) in the detection of highly penetrating 511 keV photons. Another approach to improve 511 keV photon detection sensitivity is to increase the axial FOV (length) of PET scanners [26–28]. However, these long axial FOV scanners are much more expensive and require large hospital footprints.

2 Physical Principles of PET

### 2.1 Positron Emission and Annihilation

PET imaging relies on the simultaneous detection of millions of oppositely directed 511 keV photon pairs that result from the annihilation of a positron (e^+) with its antiparticle, the electron (e^-). Positrons are emitted from proton-rich nuclei—which are unstable for positron decay—and travel a short but variable range in the patient body, causing excitation and ionization of the atoms they traverse before they slow down enough to annihilate with nearby electrons [31, 32].

2.2 Photon Interaction with Matter

The two 511 keV annihilation photons generated in the $e^+ - e^-$ annihilation are detected using a high-density scintillation material. The probability of detection, known as detection efficiency, depends on the scintillator material thickness and linear attenuation coefficient (μ), which in turn depends on the effective atomic number and density of the material and the photon energy.

Photon–matter interactions can be described in terms of particle collisions, where the energy of the incident photon is partially or completely transferred to the electrons or to the atomic nuclei in the scintillation material via:

1. The photoelectric effect, in which the incident photon transfers all its energy to an inner-shell electron of one of the scintillator material atoms. The probability of photoelectric interactions increases with the atomic number of the scintillator (Z_{eff}) and its density (ρ) and decreases with increasing photon energy [32] (see Fig. 2a);

2. Compton scattering, in which the incident photon interacts with an outer electron of the scintillation material atoms, transferring only a portion of its energy and thus being deviated
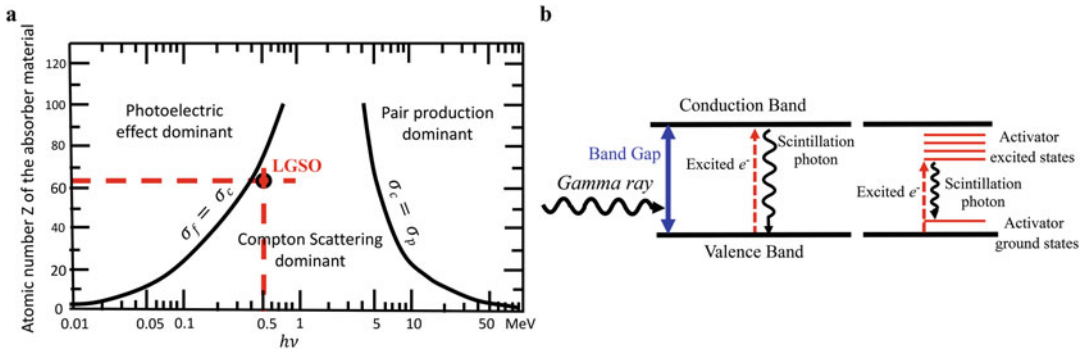
Fig. 2 Theoretical descriptions of (**a**) predominant regions for the photon–matter interaction processes. The lines indicate where the cross section for two processes is equal. As an example, in a *LGSO* scintillator ($Z_{eff} \approx 63$), the most probable interaction for 511 keV photons is Compton scatter, although photoelectric absorption is non-negligible; (**b**) energy band structure of an inorganic scintillator. Left side, pure scintillator. Right side, activated scintillator

from its original direction [33, 34]. Its probability reduces with the incident photon energy, depends on the material density, and is almost independent of Z_{eff} (*see* Fig. 2a);

3. Pair production, in which the photon interacts with the atomic nucleus in such a manner that its energy is converted into matter, producing a pair of particles ($e^+ - e^-$) [35]. This process requires photons with energies >1.02 MeV (combined rest mass of the electron plus positron); thus, it is not encountered in PET.

The photoelectric and Compton interactions both result in the ejection of a fast recoil electron, which interacts with the medium traversed, resulting in a track of low-energy ionization electrons. Note that photoelectric interactions are preferred in PET imaging since all the energy is deposited in one interaction location, and it generates a larger electric signal compared to Compton interactions, thus producing better detector signal-to-noise ratio (SNR), and the single interaction also simplifies positioning of the photon interaction point within the scintillator, thus providing better reconstructed image quality. Algorithms that exploit the kinematics of Compton scatter in order to better estimate the first interaction location (in 3D) of Compton interactions in the detector crystal are under study by several groups [36].

2.3 Scintillation Mechanism in Inorganic Scintillators

The scintillation material in a PET detector is responsible for converting each incident 511 keV photon into lower-energy optical photons (eV range) that are subsequently collected by photodetector elements and converted into measurable electrical pulses which represent the photon energy and arrival time.

The detection efficiency of the scintillator depends on Z_{eff}; thus, inorganic scintillators (high Z_{eff}) are the most commonly

Table 1
Properties of common inorganic scintillator materials used in PET

	NaI(Tl)	BGO	GSO	LaBr$_3$	LSO	LYSO	LGSO
Z_{eff}	51	74	59	46.9	66	63	63
Refractive index	1.85	2.15	1.89	1.9	1.81	1.82	1.81
ρ (g/cm^3)	3.7	7.13	6.7	5.06	7.4	7.1	7.3
LY (ph/MeV)	41,000	9000	9000	42,500	29,000	32,000	30,000
Decay time (ns)	230	300	56	16	40	41	31–47
μ (cm^{-1}) @511 keV	0.35	0.95	0.698	0.476	0.866	0.83	0.80
Wavelength (nm)	410	480	440	380	420	420	410–430
Activator	Thallium	None	Cerium	Cerium	Cerium	Cerium	Cerium

used detector materials in PET scanners [8]; *see* Table 1. The scintillation mechanism in inorganic scintillators depends on the electronic band structure of the crystal lattice of the material; there are two quantized energy bands of closely spaced electronic energy levels, called the valence and conduction bands, and the energy difference between the two bands is known as the bandgap [37]. When a 511 keV photon interacts with the scintillation material (*see* Subheading 2.2) via photoelectric or Compton interactions, the resulting ionization electrons are liberated from the valence band to the conduction band, creating a track of electron–hole (*e-h*) pairs. After a period of time, these electrons return to the valence band emitting light photons with an energy determined by the bandgap. In a pure scintillator, the bandgap is large, and thus the emitted light has a higher frequency (in the ultraviolet [UV] range) which is difficult to detect by standard photodetectors, and the decay rate (i.e., *decay time*) tends to be slower. To promote the generation of visible light photons (e.g., peaked in blue wavelengths), small amounts of impurities, called activators, are added to the crystal, creating special sites in the lattice and modifying the bandgap structure. The energy of the released photons is in the visible regime which is good for photodetection (Fig. 2b), and the decay rate is increased (decay time is decreased).

3 PET Detector Technology

The most common PET photon detector modules are mainly composed of arrays of scintillation crystal elements coupled at its ends to photodetector arrays, which is coupled to readout electronics.
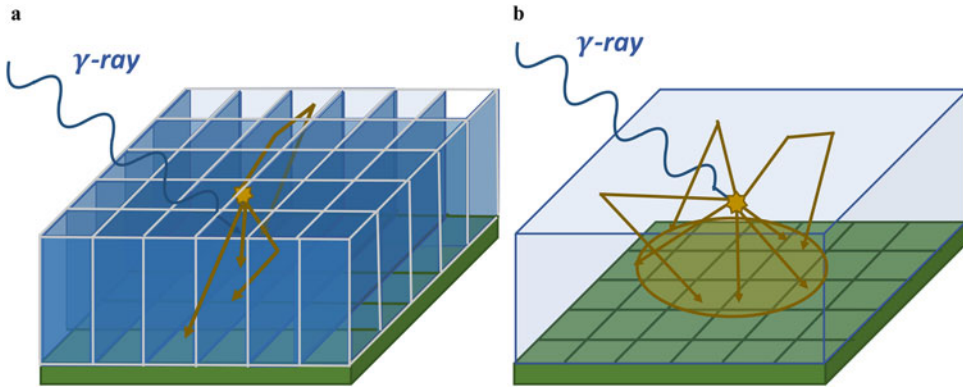
Fig. 3 Drawing of a (**a**) pixel array and (**b**) a monolithic crystal

3.1 Scintillator Elements

Each incoming 511 keV annihilation photon should efficiently interact with the scintillation array and be converted into low-energy scintillation photons as described in Subheading 2.3. The ideal PET scintillator should possess the following properties [38]: (1) high light yield (LY), which is the number of optical photons generated per unit of deposited energy; (2) linearity, which means the number of generated optical photons must be proportional to the energy deposited by the incident radiation, which, among other benefits, allows one to distinguish photoelectric and Compton interactions in the detector; (3) clear and transparent to the wavelength of its own emission spectra; (4) high Z_{eff} to increase the probability of photoelectric interactions; (5) fast decay time of the induced luminescence to avoid pileup events, hence minimizing the dead time and improving system CTR; and (6) a refraction index as close as possible to that of the photodetector, maximizing the light transmission into the photodetector.

There are two main scintillation configurations used in PET detectors, namely, pixel arrays and monolithic crystals; *see* Fig. 3a, b, respectively. Pixelated crystal arrays comprise a matrix of individual small scintillation rod elements [39], while monolithic scintillators consist of a large single piece of scintillation material [40, 41], and therefore there are no inter-element gaps. Advantages and disadvantages of each configuration can be found in [40].

Subheading 5 of this chapter describes the spatial, DOI, energy, and timing resolution of pixelated-based detectors since they are the ones commonly used in commercial PET scanners.

3.2 Photodetector: PMTs and SiPMs

A photodetector suitable for PET imaging has to efficiently convert the scintillation photons into electric signals while ensuring both high photon detection efficiency ($PDE(\lambda,V)$), which, for SiPMs, is a product of the quantum efficiency ($QE(\lambda)$), and the fill factor of the sensor microcells. Moreover, the photodetector has to be compact,

insensitive to temperature fluctuations, and detect photons with low time jitter, thus providing a low variance and short response time between the arrival of the photons and the signal generation.

Since the earliest days of PET imaging, PMTs [42] have been used to collect scintillation photons. PMTs have high gain and low noise and are sensitive for light in the UV, visible, and near-infrared ranges of the electromagnetic spectra. However, they are affected by magnetic fields, making it impossible to be used in PET/MRI systems. During the last decade, a majority of the newer generation PET systems employ SiPMs instead of PMTs; SiPMs are semiconductor (solid-state) detectors composed of thousands of micronsize single-photon avalanche diode (SPAD) cells connected in parallel to common readout contacts [43]. Each SPAD microcell operates in the *Geiger* mode, which means they are biased at a voltage value that is over the breakdown voltage, and thus they have a very high gain. They also have the properties of very low temperature drift, low operating voltage, and excellent temporal response and are insensitive to magnetic fields. In addition, they are much more compact than PMTs allowing for complex and mechanically robust system configuration while reducing dead spaces. However, factors contributing to the SiPM noise and timing jitter are dark count rates (DCR), optical cross talk, afterpulsing, and dead time that have to be addressed to provide accurate information on the incoming annihilation photon interaction location, energy, and arrival time [44]. Depending on whether readout electronics are external to the devices or integrated within the sensor technology, SiPMs can be classified as either analog or digital (dSiPMs), respectively [45, 46].

3.3 Front-End Readout Electronics

The final elements of PET detector modules are the front-end readout electronics, which are responsible for processing and digitizing the photodetector output signals for the data acquisition system (DAQ), which sends those signals to a workstation (PC) for further processing. When using SiPMs, the digital control and processing of the output of analog-to-digital conversion (ADC) boards are usually accomplished using a field-programmable gate array (FPGA).

The best approach to provide good photon positioning accuracy and CTR performance is to read out every pixel of the photodetector array, but this implies digitizing a huge number of signals, which is typically challenging. To diminish the problem, many techniques might be used to reduce the number of signals such as electronic multiplexing schemes [47]. However, these approaches may degrade timing information. An alternative is the use of fast integrated circuits such as application-specific integrated circuits (ASICs) customized for a particular use, i.e., reading out each SiPM signal.

4   Coincidence Detection

As briefly described in Subheadings 2 and 3, each radiotracer decay emits a positron that slows down by colliding with atoms in its path in the surrounding tissue. Near the end of its trajectory, the positron combines (annihilates) with an electron, resulting in the emission of two oppositely directed annihilation photons that are emitted from the body. If both emitted photons are directed toward the PET system, they will likely interact in two opposing detectors of the PET scanner, generating two sets of electric signals from each detector. Sometimes one or both of the annihilation photons suffer Compton scattering, leaving energy in the patient tissue before exiting the body; such events should be rejected during the data processing.

To ensure the collection of events resulting only from annihilation processes, a coincidence time window (CTW), usually in the range of few nanoseconds, is defined in the PET coincidence processing, and only those events detected within the same CTW are recorded and labeled as a coincidence event. There is also an energy window applied to each photon event; if the measured energy is significantly less than 511 keV, it is assumed that the photon is scattered, and that event is rejected. Events that pass the energy and coincidence time window filters will then be assigned to a system line of response (LOR) that connects the two detector elements that were hit by the good annihilation photon event. In PET, it is assumed that this line passes through the precise location of the positron decay.

Note however that sometimes the assigned LOR may not pass through the point of the actual positron decay, and therefore the image quality is degraded, as described in Subheadings 4.1 and 4.2. As a final step, data correction methods and reconstruction algorithms are applied to the collected coincidence events to generate 3D images providing detailed visual representations of the 3D radiotracer biodistribution within a patient's body. The radiotracer selection depends on the study to be carried out [48–51]. Figure 4a shows a schematic of the PET imaging formation process.

4.1   Image Degradation Caused by Physical Effects

The quality and accuracy of the reconstructed PET image is affected by several physical factors such as:

1. The variation in positron range, defined as the average distance from the point of positron decay to the end of the positron track where the annihilation photons are created. This factor depends on the emitted positron energies, which depends on the radionuclide label of the tracer and directly affects the spatial resolution [31, 33];
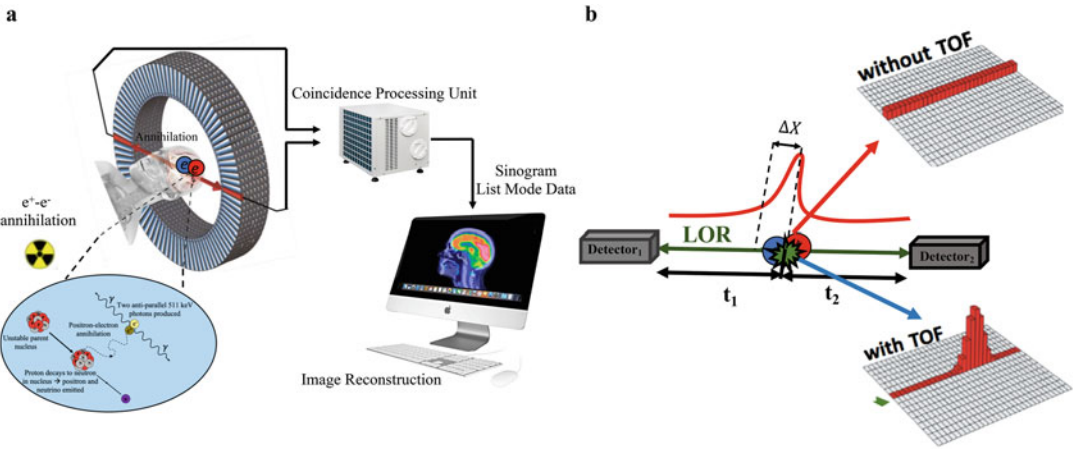
Fig. 4 Schematic of (**a**) operation principle of a PET scanner; (**b**) TOF-PET technique, the red arrow represents the event spread across the entire assigned LOR and the blue one the portion of that LOR where events are concentrated after applying the TOF constraint

2. The crystal element width introduces a variation in annihilation photon interaction location and thus affects the spatial resolution but also the CTR performance;

3. 511 keV photon pair acolinearity, which occurs when the positron and electron are not at rest when they annihilate, resulting in a small deviation from 180° in the angle between the two annihilation photons [52], and leads to incorrect LOR assignment, and thus spatial resolution degradation, depending on the PET system diameter;

4. Parallax error, related to the uncertainty in the annihilation photon interaction depth coordinate (the DOI) within the detector element. This effect produces an error in LOR assignment, and thus spatial resolution degradation, that gets worse with radial coordinate from the system center. If the detector design provides DOI information, then this factor may be compensated. For this reason, the development of DOI-encoding detectors is an ongoing research topic in PET instrumentation [53];

5. Event statistics and the image reconstruction process.

4.2 Degradation Caused by Coincidence Detection Type

There are four types of coincidence events recorded in a PET scan [52], namely:

1. Trues, where the assigned LOR for an event passes through the point of positron annihilation;

2. Scattered, when one or both detected annihilation photons have undergone at least one Compton scatter in the patient and its direction has changed; thus, the assigned LOR does not
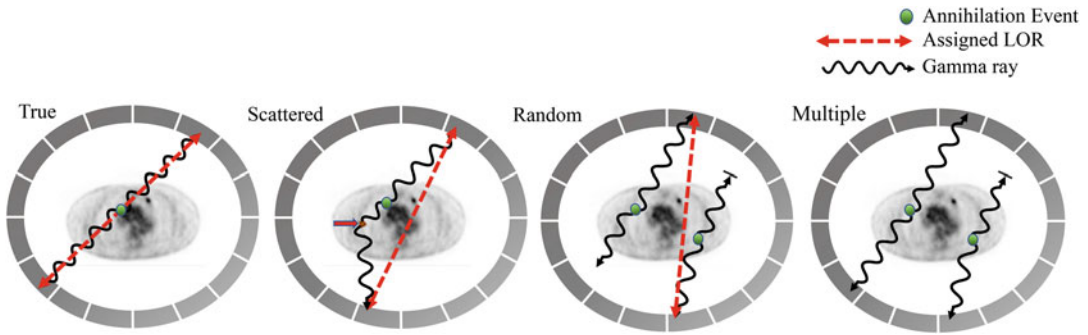
Fig. 5 From left to right, representation of true, scattered, random, and multiple events

pass through the point of positron annihilation, degrading image contrast and accuracy;

3. Randoms, when two photons from different annihilation events are detected within the CTW, which also degrades image contrast and accuracy. The distribution of random coincidences is almost uniform across the FOV, and its rate increases with the square of the activity in the FOV;

4. Multiples, when more than two annihilation photons are detected within the CTW, making impossible to determine the correct LOR; thus, these multiple coincidences are rejected from the dataset.

Figure 5 provides an example of each type of coincident events encountered in PET. Note that only true coincidences provide accurate information about the radiotracer deposition in the subject. Several methods are used to compensate for scatter and random coincidences [54].

5   PET Detector Performance Parameters

The main parameters that are considered when designing a typical PET scanner are the spatial, energy, and coincidence time resolutions. The methodology usually employed to evaluate those parameters is outlined in Subheading 6.

5.1 Spatial Resolution

There are two types of resolution measures in PET, intrinsic and reconstructed. Intrinsic refers to the spatial resolution limit imposed by the detector element dimensions, as well as positron range and annihilation photon acolinearity variations, which can be assessed with coincidence measurements between two detector elements or modules by measuring a distribution known as the point spread function (PSF). Reconstructed PET resolution refers to that measured after the image reconstruction process and may be assessed, for example, by determining how close two-point sources

can be placed together while still distinguishing them in an image. Note that as explained in Subheading 4.1, PET system resolution is strongly determined by the intrinsic resolution, but it also is affected by the image reconstruction process.

In the case of detector modules based on pixelated crystals, the intrinsic resolution of a pair of pixelated PET detectors determined from a PSF measurement can be estimated as [55]:

$$R_{\text{int}} = \sqrt{R_{\text{det}}^2 + R_{\text{range}}^2 + R_{180^\circ}^2} \tag{1}$$

where R_{det}, R_{range}, and R_{180° are the detector resolution, positron range, and the acolinearity effect contributions to resolution, respectively. In pixelated-based detector designs without signal multiplexing, R_{det} is roughly ½ the width of the crystal element width; with multiplexing, an additional decoding term should be applied [55]. For the overall PET system spatial resolution, one would multiply R_{int} by an addition factor due to imperfections of the image reconstruction process due to factors such as the count statistics (i.e., noise level) of the study, linear and angular sampling deficiencies, and image reconstruction characteristics such as the effective degree of smoothing.

5.2 DOI Resolution

The DOI resolution (a type of spatial resolution) is the precision to which the third spatial coordinate (z coordinate or the photon interaction depth within the scintillator element) may be determined. DOI information can be continuous or discrete and helps to reduce the parallax error in order to preserve uniformity of the resolution in the radial direction; *see* Subheading 4.1.

For pixelated-based detectors, retrieving DOI information is not straightforward and usually requires the use of additional scintillator layers and photodetector elements [56] and/or special crystal surface treatments and reflectors [57], compact front-end electronics, and additional readout channels [58], thus increasing manufacturing cost and system complexity. However, drawbacks of most of these DOI methods are that they (1) can only determine one DOI, which is a problem when the photon interacts more than once, which is roughly threefold more likely to occur than single interactions, and (2) usually degrade detector SNR, worsening detector energy resolution and CTR.

5.3 Energy Resolution

The energy resolution (ER) represents the precision to which a PET detector can measure the deposited energy of the photon interaction, which, as described in Subheading 2.2, helps to filter out photons that have undergone Compton scatter in the patient tissues before being detected. In a pixelated detector design, ER depends on the scintillator light yield, the crystal element dimensions, optical coupling to the photodetector, properties of the latter such as PDE and noise, and the noise level of the electronic

readout. The energy resolution is usually evaluated as the ratio of the full-width-half-maximum (FWHM) of the 511 keV photopeak in the pulse height spectrum to its centroid [57].

5.4   CTR   The CTR of a PET system defines the uncertainty on detecting the arrival time difference between each pair of annihilation photons in a coincidence event, over many events, and is determined by several factors including properties of the scintillation crystal (rise and decay times), number of scintillation photons collected by the photodetector, photodetector PDE and noise properties, crystal-to-photodetector coupling configurations, reflective materials, and the readout electronic chain. Achieving accurate CTR allows one to constrain the location of the annihilation point along the LOR (Eq. 2) [59]; since more events are placed closer to the true location along the LOR during the image reconstruction process, the statistical noise levels are reduced, improving the reconstructed image SNR (Eq. 3):

$$\Delta X = \frac{c \cdot \Delta T}{2} \tag{2}$$

$$\text{Gain in SNR} = \left(\frac{D}{\Delta X}\right)^{1/2} = \left(\frac{2 \cdot D}{c \cdot \Delta T}\right)^{1/2} \tag{3}$$

where ΔX is the uncertainty of the annihilation event location along each system LOR, c is the speed of the light, $\Delta T = CTR$ of the system, and D is the patient diameter. Including temporal information on the photon arrival is known as time of flight (TOF)-PET. Figure 4b shows a sketch of the conceptual principle. As an example, if the CTR improves from 600 ps to 100 ps, a gain in reconstructed image SNR of a factor of $\sqrt{6}$ is expected. This increase in SNR can be exploited to enhance lesion visualization and quantification or, alternatively, decrease the injected radiation dose or patient scanning time, or a mixture of these. Moreover, including this information can be useful for systems with nonstandard (e.g., panel or partial ring geometries) since the number of angular views necessary for an artifact-free image reconstruction is reduced as CTR improves [60, 61].

Presently, the best of the state-of-the-art PET systems achieves 214 ps FWHM CTR [62]. However, with progress in the development SiPMs, a CTR well below 100 ps FWHM may be easily achievable in single-pixel, benchtop setups using long scintillators [63–68].

5.5   Other Considerations   To maximize spatial, DOI, energy, and CTR performance of a PET detector, important aspects to consider are the reflector applied to the scintillator crystal element surfaces, the crystal surface roughness, and the scintillator–photodetector coupling media. These factors determine the amount of light reflections on the crystal surfaces, the light transport within the crystal, and the collected LD profiles.

There are many different crystal reflectors and surface conditions described in the literature that focus on reducing reflections to preserve LD profiles (e.g., absorbent black paint and retroreflector layers) [69] or on increasing those reflections to increase the amount of light reaching the photodetector (Teflon, white paints, and enhanced specular reflectors [ESR]). Regarding scintillator–photodetector coupling, silicone or optical grease is most commonly used for prototyping and optical epoxy for production. It is better to use coupling medias with refractive indices somewhere in between that of the photodetector surface (e.g., glass) and that of the scintillator crystal to reduce light transmission losses [70].

6   Experimental Methodology to Evaluate PET Performance Parameters

There are two evaluation stages when designing a PET scanner, namely, detector level, which accounts for the intrinsic performance of one or more detector elements or detector modules comprising arrays of detector elements, and system level, which focuses on the global performance of the scanner (e.g., reconstructed image quality and accuracy) as a research or diagnostic tool.

In the following, the most commonly used approaches to evaluate both detector and system performance are described, using as an example the methodology followed in our lab to characterize energy resolution and CTR performance of TOF-PET detectors based on arrays of discrete scintillation detector elements coupled to photodetectors.

6.1   Detector Level

Performance evaluation of PET detectors involves the characterization of the intrinsic properties of each element building the detector module, namely, scintillation crystal (including reflector and surface condition), photodetectors (including coupling media to the crystal), and electronic readout chain (Subheading 3). Each one of those elements needs to be first characterized individually, to ensure optimal performance, and then in combination to characterize the final detector design for spatial, energy, and temporal information.

Regarding the scintillation crystal, its dimension, geometry, and intrinsic scintillation properties affect the photoemission efficiency of the detector, while the crystal surface treatment, reflector, and crystal–photodetector coupling medium affect the light transferring to the photodetector [70]. Note that reflector materials and optical coupling components only affect the light transferring to the photodetector and thus the number and temporal spread of collected scintillation photons. LY and rise and decay times are not affected since those are intrinsic parameters of the scintillator. For their evaluation, it is common to couple the scintillation crystal to a PMT, as shown in Fig. 6a. Usually, only those events that have pulse
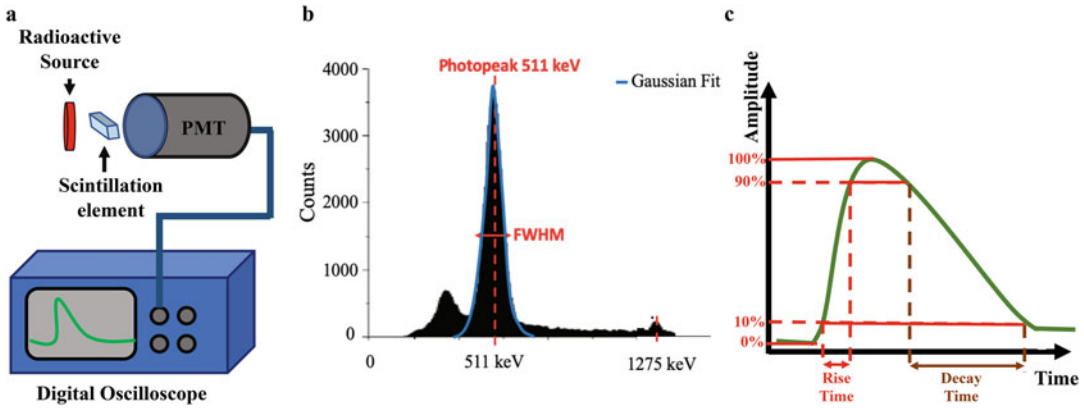
Fig. 6 Sketch of a typical experimental setup, including acquired data. (**a**) Sketch of the experimental setup used to evaluate LY, decay, and rise time of the scintillation crystal element. The scintillation crystal element is attached to a PMT and connected to a digital oscilloscope to acquire waveforms; (**b**) example energy spectrum acquired in single mode using a ^{22}Na source. The plot shows in blue the Gaussian fit to the photopeak and in red the FWHM and FWTM of the photopeak. Note that the second photopeak of the 1275 keV gamma ray emission, which occurs a fraction of the time, is also shown; (**c**) example of the acquired waveforms, indicating the ranges considered for the estimation of the rise and decay times

heights within the FWTM of 511 keV photopeak are processed; *see* Fig. 6b. The decay time of the scintillator is estimated by exponentially fitting the tail of pulses within the range from 90% to 10% of the maximum pulse height. Similarly, the rise time is measured by exponentially fitting the rising edge of pulses but within the range from 10% to 90% (Fig. 6c).

The next element that needs to be studied in isolation is the photodetector. When working with SiPMs, the parameters that are usually evaluated are [43]: the breakdown voltage, which is the bias point that needs to be reached to initiate a Geiger discharge; the gain, which refers to the average amount of charge created for each detected photon; the PDE(λ,V), which refers to the sensitivity of the photodetector; the DCR, which is the main source of noise in an SiPM and is primarily due to the generation of thermal electrons in the active volume; the optical cross talk between single cells; the afterpulsing due to the charge that gets trapped in a cell and is released after some time generating a secondary discharge; and the dynamic range.

Finally, the readout electronic chain (*see* Subheading 3.3) must be also designed and studied in detail. The selection of the components (i.e., capacitor, resistors, RF amplifiers, ASICs, etc.) comprising the electronic chain is the most relevant factor affecting CTR performance. The main parameters to consider when designing the electronic chain are: the inherent electronic noise (σ_{noise}), the transit transfer time (TTS) of the pulses from the photodetector to the electronic components (σ_{TTS}), and the signal slope (dV/dt) which is a combination of both the detector signal and time response

[71]. The combination of these parameters determines the temporal variance, or jitter, (σ_{time}) in the photodetector response and can be estimated as:

$$\sigma_{\text{time}}^2 \approx \left(\frac{\sigma_{\text{noise}}^2}{dV/dt}\right)^2 + \sigma_{\text{TTS}}^2 \tag{4}$$

Once the scintillator, photodetector, and electronic chain have been individually studied and optimized, the final PET detector module can be assembled. Then, the evaluation focuses on the spatial, DOI, energy resolutions, and CTR of the detector. To study these parameters, two identical PET detector elements are used, and coincidence data are acquired. The experiments are repeated several times to ensure truthfulness of the data using different scintillation elements and photodetectors. In addition, the influence of different bias voltages, threshold levels, temperature drifts, and other factors is also evaluated.

In the following, examples of the methodology usually used to evaluate those parameters are outlined.

6.2 Detector Spatial Resolution

The spatial resolution of a PET detector is usually estimated as the average FWHM and FWTM of the Gaussian fit applied to the LD profiles obtained by acquiring data using radioactive sources. In the case of pixelated-based detectors, the source is placed in between the two detector elements being characterized to ensure a homogeneous irradiation of the entire pixelated matrix. Coincidence data is acquired, and after applying positioning algorithms, 2D flood maps are generated. These flood maps are visual representations of the light collected by each individual pixel element; *see* Fig. 7a, b. Pixel profiles are extracted, and Gaussian fitting is applied; the average FWHM of the fitting is considered as the detector spatial
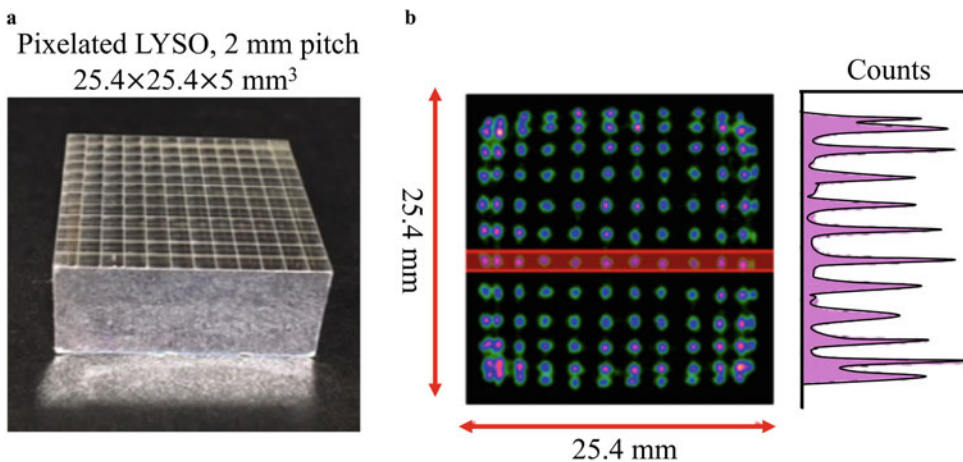
Fig. 7 Illustrations of (**a**) a pixelated LYSO crystal with dimension of 25.4 × 25.4 × 5 mm³; (**b**) a 2D map of the pixel distribution showing extracted profiles for the column highlighted in red
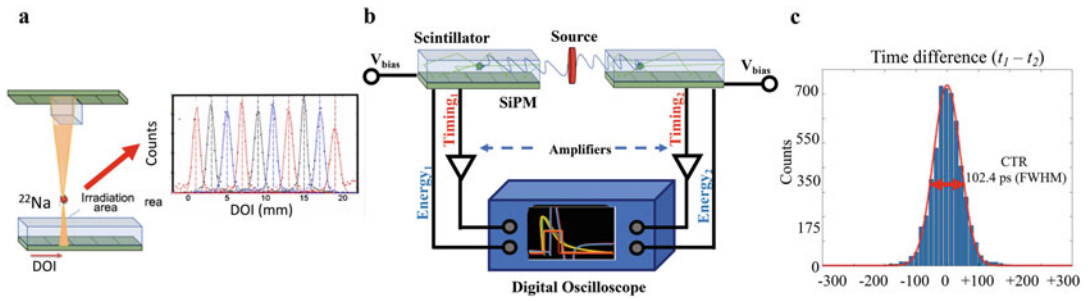
Fig. 8 Sketches of experimental setups used to evaluate (**a**) the DOI resolution and source profiles measured across several depths, (**b**) the CTR of scintillation detectors used in PET, and (**c**) temporal difference histogram between two detector elements

resolution. The peak to valley (P/V) of the profiles is also a good estimator of the spatial resolution; the more accused the valley, the better the pixel discrimination and thus the better the spatial resolution. Note that, as described in Subheading 5.1, the spatial resolution is mainly limited by the individual scintillator pixel size. Usually, for the spatial resolution evaluation in order to avoid undesired scattered events that worsen the average resolution value, only events that fall within the FWTM of the 511 keV photopeak are considered.

6.3 Detector DOI Resolution

The evaluation of the photon DOI resolution of a PET detector is usually performed through side beam illumination experiment in which a radioactive source is placed in such a way that impinges perpendicularly to one detector. The source is displaced (together with the coincidence detector) across the z axis, illuminating different known depths across the scintillation element. Coincidence data is acquired and processed, and then histograms showing the number of counts vs depth are generated (Fig. 8a), and the DOI resolution is estimated as the FWHM of the Gaussian fit applied to those profiles.

6.4 Detector Energy Resolution

To evaluate the energy resolution of a PET detector, a non-collimated radioactive source is used to homogeneously irradiate the detector under evaluation. Then waveforms are acquired, and energy histograms are usually generated considering the waveform area above a certain threshold value. Note that PET detectors usually provide data in arbitrary units (channels, voltage, etc.); thus, the first step is to calibrate the output value into energy units, usually keV. For this purpose, different isotopes (with different energy peaks) are used to acquire data, and the measured centroid of each photopeak is plotted against the theoretical energy value of the corresponding isotope. Then, the data is fitted using an exponential function that provides the calibration curve, which allows conversion of the x-axis of the pulse height histogram into energy

units (Fig. 6b). Then, regions of interest (ROIs) across the 2D flood maps are selected, and the resulting spectra are fitted using a Gaussian function. The energy resolution is finally estimated as $\Delta E/E \times 100\%$ where ΔE is the FWHM and E the centroid (detector Gain) of the 511 keV photopeak. Note that these experiments are also used to evaluate the different gain values (affected by, e.g., scintillator uniformities, photodetector variances, or coupling materials) across the scintillator surface.

6.5 Detector CTR

To evaluate the CTR performance of a pair of detector elements, coincidence measurements are performed by placing a radioactive source in between the detectors (Fig. 8b). Waveforms are acquired, and the photon arrival time (time stamp) of each photon to the detector is recorded. Note that the method employed for the timing pickoff in the rising edge of the signal has a large impact on CTR performance. Several methods can be applied; usually a threshold value is selected, and the arrival time of the photon is considered as the time at which the signal crosses that threshold. In addition, baseline and time-walk corrections are usually applied to enhance CTR performance [65].

Finally, the temporal differences between the two detector elements for every annihilation pair coincidence event are histogramed, and Gaussian fitting is applied. The FWHM of the fit represents the CTR of the detector pair; *see* Fig. 8c. Note that scintillation light sharing or photodetector signal multiplexing schemes that are often employed to reduce the number of photodetectors or readout channels severely affect CTR performance; the best approach is to couple every individual scintillation pixel element one-to-one to a single photodetector, a.k.a. "one-to-one coupling," to avoid dealing with variances among individual detector elements. But this approach will also lead to the largest number of photodetectors and associated electronic readout channels.

6.6 Other Evaluations

In addition to the parameters described before, there are other factors affecting performance that need to be evaluated, such as the scintillator material and surface treatment, scintillator–photodetector coupling media, photodetector arrangement, temperature, bias voltage applied to the SiPMs, or electronic components, to mention but a few. To do so, several measurements (spatial, DOI, energy resolution, and CTR) are performed after modifying those elements. The outputs are compared to ground-truth measurements, and the final selection of these features depends on the parameters that are selected for optimization, often leading to a trade-off between the different properties.

The next step is to combine the already characterized individual detector elements and scale up the design into detector module arrays. At this stage, critical factors to consider are the number of elements comprising one detector module; their arrangement to

minimize gaps between individual elements, thus providing high packing fraction and good sensitivity; and the electronic readout schematics in which design is a trade-off between performance, power consumption, and number of output signals. Once carefully ensembled, the detector module arrays are characterized by usually using a homogeneous source that irradiates the whole detector surface. The detector spatial, energy, and CTR performances are then evaluated, with Fig. 7b illustrating a flood map typically used for the detector characterization. In addition, detector calibration procedures are required at this stage to correct for nonuniformities, mainly produced by light yield differences across the scintillation volume or by gain differences in the photodetector response that will increase the statistical variations of the output information, thus generating image inhomogeneities. The energy response of the detectors is calibrated into keV values, and detector parameters such as cooling requirements or count rate capabilities are also considered.

Once the performance evaluation of the PET detector module is finished and all parameters have been optimized to ensure best performance, the scaling-up process begins. More layers of scintillations and next steps in the electronic chain are included. Finally, more detectors are built and assembled, usually, in a ring geometry, composing the final PET scanner.

7   Tutorial of Experimental Methodology

In the following, a description of the approach typically followed in the evaluation of PET detector elements and PET systems is provided.

7.1   PET Detector Element Evaluation

An example of the methodology used in our lab to evaluate energy resolution and CTR performance of two PET detector elements based on pixelated crystals is detailed below:

1. Select the scintillator material, for example, $3 \times 3 \times 10$ mm^3 LGSO crystals ($\tau_d \sim 34.5$ ns), and gently clean all crystal surfaces using a noncorrosive material, i.e., isopropanol, and let it dry.

2. Apply a reflective material to the crystal surface (except to the face in contact to the photodetector), avoiding the generation of air bubbles or the inclusion of dust. The reflective material has to be previously tested to ensure optimal performance [64]. In our design, we are using reflective white paints.

3. Gently clean the photodetector elements and apply an optical coupling media. For our evaluation, we connected an array of 7 SiPMs (3×3 mm^2 active area, J-Series from SensL) to a
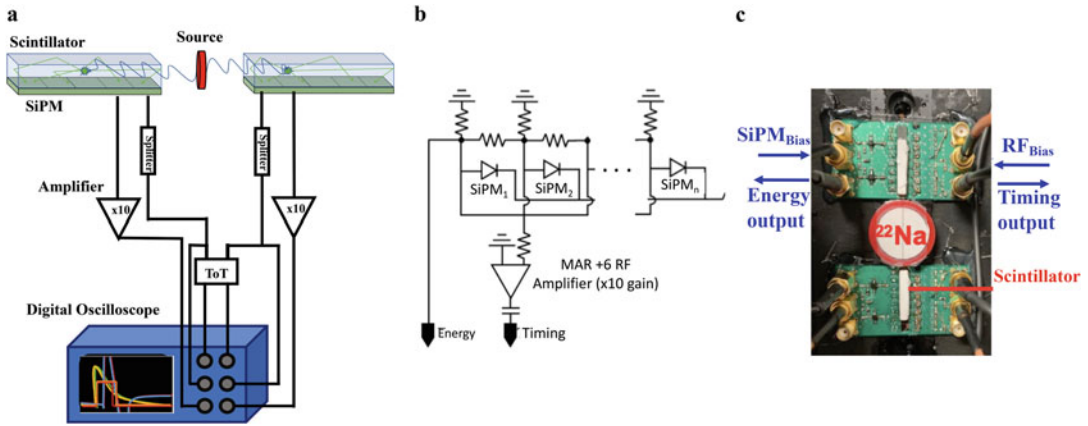
**Fig. 9** Schematics of (**a**) the experimental setup used to evaluate energy resolution and CTR performance, (**b**) the electronic chain of our detectors [64], and (**c**) photograph of the board used to perform coincidence acquisitions

custom-designed RF board, using optical grease (BC-630, Saint-Gobain) as coupling media.

4. Couple the scintillator to the photodetector ensuring perfect alignment; this step is critical to achieve good CTR performance. It may be convenient to use a microscope to guarantee perfect alignment of the components. Traditionally, the scintillator elements were connected to the photodetectors by their end. However, in our setup, we are using a novel side-readout approach, as depicted in Fig. 9a, that has proven to provide high performance when using high aspect ratio scintillators (i.e., >20 mm long), such as the ones required to provide high sensitivity in the final scanner [66].

5. Connect the photodetector board to the data acquisition system. The standard output of the SiPMs was connected to a digital oscilloscope, and waveforms were acquired placing different non-collimated sources between the two detector elements; *see* Fig. 9b. Energy histograms are generated using a single time-over-threshold (ToT) circuit [76] in which the energy value associated with an event is calculated as the amplitude of the signal above a certain threshold value (previously optimized).

6. The "fast outputs" of the SiPMs are connected to a high-bandwidth monolithic RF amplifier (MAR-6+, Minicircuits) and used as the timing signal as shown in the schematic in Fig. 9c. Waveforms are acquired placing a non-collimated ^{22}Na source between the detectors. The amplified timing signal is fed into the digital oscilloscope, and leading threshold (LED) method is applied (in MATLAB) on the rising edge of the digitized scintillation pulse for timing pickoff (Fig. 10a).
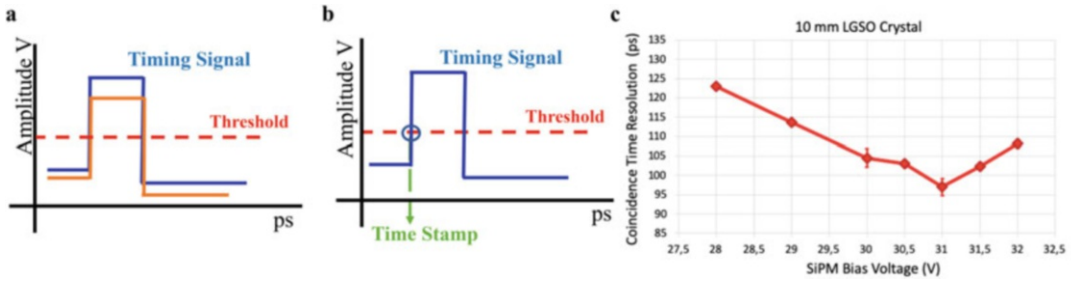
Fig. 10 Schemes showing (**a**) the baseline shift between two coincidence signals, (**b**) the LED threshold method after correcting baseline shifts, and (**c**) example of the achieved CTR performance using two PET detector elements as the one described in the methodology as a function of SiPM bias voltage [65]

Before applying the LED technique, a baseline correction is also applied to define a reference point for all threshold levels among coincidence signals (Fig. 10b).

7. For energy measurements, different isotopes are used to calibrate the detector response into keV units. Once calibrated, the energy resolution is calculated as $\Delta E/E$ using the 511 keV photopeak measured using the ^{22}Na source. Single measurements are also acquired to confirm linearity by calculating the ratio of the second (1024 keV) and first (511 keV) ^{22}Na peaks.

8. For CTR evaluation, the time difference between the time stamps of the two detector elements involved in the coincidence is computed, and a histogram is generated. The FWHM of the time difference profile is considered as the CTR of the detector pair [65]. It is usual to select events with amplitudes that fall within the FWTM of the 511 keV photopeak to avoid undesired scattered events that worsen the average CTR. Figure 10c shows an example of the CTR values achieved using the described methodology for a pair of $3 \times 3 \times 10$ mm^3 LGSO crystals, as a function of different SiPM bias voltages.

9. Repeat **steps 1–8** several times to account for variances. Each time the experiments are repeated, both the crystals and photodetector have to be cleaned and recoupled. The temperature is also monitored during the acquisitions to account for possible fluctuations.

Note that in this evaluation we are using a digital scope to avoid including the electronic chain noise, so we characterize only the detector element (ground-truth measurements). Next steps are therefore to characterize the DAQ system, in our case, a time to digital converters (TDC)-FPGA, with very precise timing information (low jitter). To do so, the output signal of the SiPMs is connected to the FPGA using a custom-designed add-on board.
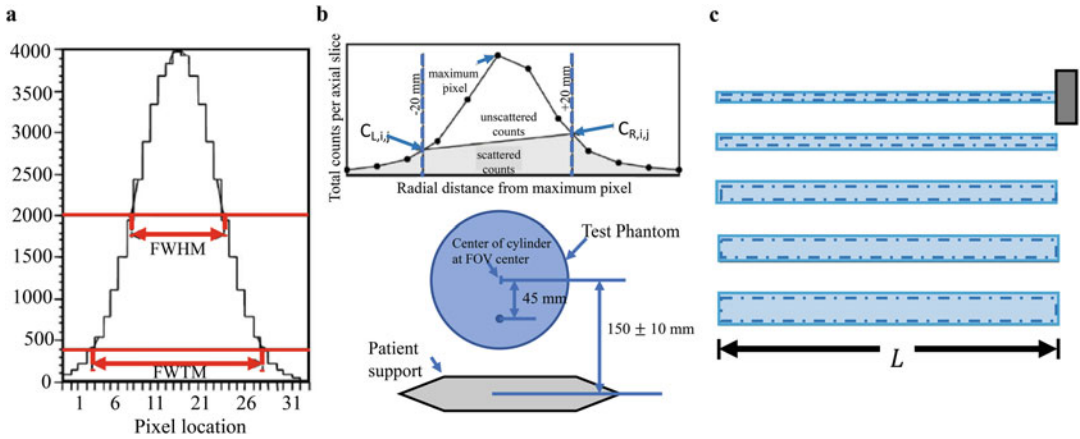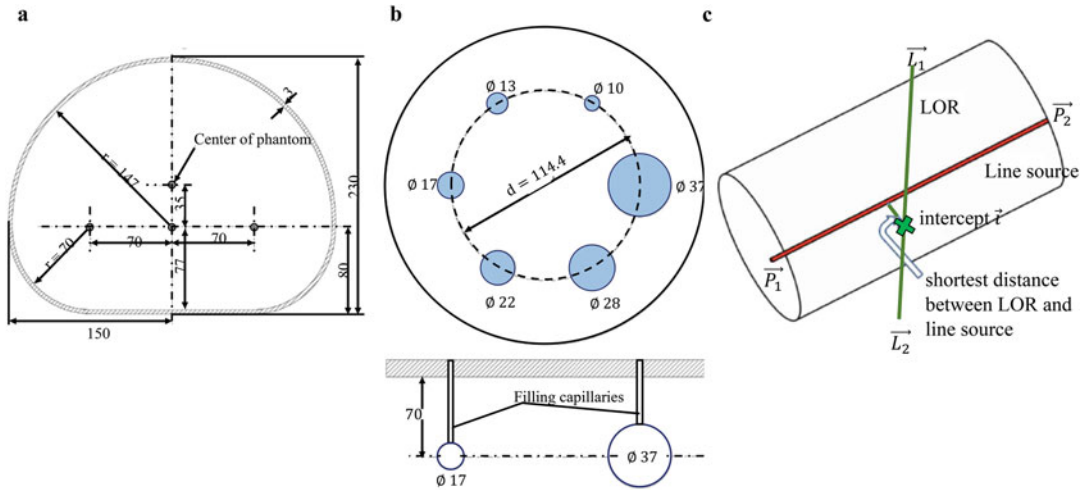
Fig. 11 Adaptation of the NEMA Standards illustrations [72] of the (**a**) typical spatial response function with FWHM and FWTM determined graphically by interpolation, (**b**) plot of background counts and test phantom which is placed parallel to the scanner's axis and centered in the transverse and axial FOV within 5 mm, (**c**) sensitivity phantom comprising five fillable aluminum tubes with different inner and outer diameters

The results are compared with the ones obtained following **steps 1–8**.

7.2 PET System Evaluation

Once the PET scanner has been assembled, several parameters are evaluated following protocols developed to provide fair comparisons between different scanners. These protocols are summarized in the NEMA Standards Publication (Performance Measurements of Positron Emission Tomographs [PET]) published by the National Electrical Manufacturers Association [72]. A brief description of the NEMA protocol for the evaluation of PET systems is outlined below:

1. Spatial resolution, measured in the axial direction and in two directions of the transverse slice (e.g., radially and tangentially) using ^{18}F or ^{22}Na sources located at six points across the FOV. Acquisitions are reconstructed using the filtered-back-projection (FBP) algorithm [73]. The spatial resolution is determined as the FWHM and FWTM of the reconstructed source profiles; *see* Fig. 11a.

2. Scatter fraction, count losses, and random coincidences are used to evaluate the system's ability to mitigate background coincidence events as well as measure high activity within the system FOV. Acquisitions are performed using a cylinder phantom with a drilled hole parallel to the central axis (*see* Fig. 11b [bottom]), filled with a high activity tracer, and measurements are acquired until the isotope has completely decayed. The Noise Equivalent Count Rate (NECR) is estimated by plotting the measured coincidence count rate vs the activity concentration [74], Fig. 11b (top).

Fig. 12 Adaptation of the NEMA Standards illustrations [72] for the (**a**) cross section of body phantom, (**b**) phantom insert with hollow spheres, (**c**) sketch of the determination of LOR distance from a line source

3. Sensitivity evaluates the scanner's coincidence photon detection efficiency and is expressed as the true coincidence events detected versus source strength. ^{18}F mixed with water is used to fill the sensitivity phantom which comprises five concentric aluminum tubes, all 700 mm in length. The innermost tubes are fillable polyethylene tubes with inner diameters of 3.9, 7.0, 10.2, 13.4, and 16.6 mm and outer diameters of 6.4, 9.5, 12.7, 15.9, and 19.2 mm (Fig. 11c). Successive measurements are performed with the line source surrounded by known absorbers, until arriving at an attenuation-free measurement which is used to also extrapolate the sensitivity with no absorber.

4. To obtain quantitative measurements of source activity distributions under widely varying conditions, PET usually compensates for dead time losses and random events [75]. The accuracy of these corrections is evaluated by using a body phantom (Fig. 12a) reconstructed applying corrections used for total body PET imaging.

5. Images simulating those that would be acquired in a total body study are generated using a phantom with hot lesions to determine image quality and for accuracy corrections. The imaging phantom consists of a body phantom, six spheres filled with ^{18}F, a cylindrical insert filled with low atomic material to simulate lung attenuation, and a test line source in a polyethylene cylinder for scatter fraction count losses and randoms (Fig. 12b). Data are collected and reconstructed using the standard parameters for total body imaging (e.g., image matrix size, pixel size, slice thickness, filters, etc.) as recommended by the manufacturer. For data analysis, a transverse image centered

on the hot spheres is used, and ROIs are drawn both at the center of each reconstructed sphere and in the background of the phantom at different positions, and the contrast ratio is estimated.

6. CTR measurement is performed by analyzing the spread of the line source in TOF dimension using the same phantom as for the scatter fraction evaluation. The measured timing difference for each coincidence event used in the TOF measurement is corrected by its expected value based on the measured geometry of the phantom filled with ^{18}F. For each coincidence event in the dataset, the timing difference error is computed as the distance between the detected locations of the coincidence photons in the PET coordinate system and the true location; *see* Fig. 12c. Each event is accumulated into a 2D histogram, and the TOF resolution is estimated as the FWHM of the profile.

To assess PET-CT coregistration accuracy, the alignment between PET and CT images is evaluated by using fiducial markers in the images at six know positions. The coregistration error is determined by *calculating* the distance between the centroids of the markers between the PET and CT image.

8 Future Prospective of PET Imaging and Clinical Translation of Novel Instrumentation

During the last decades, PET imaging has emerged as the clinical molecular imaging technique of choice, especially for evaluating cancer, and constitutes one of the main diagnostic tools used clinically to generate patient-specific images that yield tailored diagnostic, therapeutic, and prognostic information. However, present available commercial PET scanners still offer limited spatial resolution (~4 mm at the system center) and have relatively low sensitivity. Thus, to further extend its clinical and research applications, technological improvements in PET instrumentation are required. Toward improving PET detector performance, it has been proposed to use enhanced scintillators [77] (i.e., photonic crystals, metamaterials, improved reflectors, etc.) in combination with high efficiency and compact SiPMs and accurate 3D positioning algorithms (to address DOI-related problems and boost spatial resolution toward the edges of the scanner FOV). In this regard, artificial intelligence (AI) algorithms have been proposed and tested as methods to achieve homogeneous sub-millimetric resolution in the entire FOV [78, 79].

Enhancing detector performance, in particular CTR, may help to overcome the low sensitivity problem, since information regarding the photon arrival time to the detector could be included

during the reconstruction process. High-resolution TOF-PET imaging would allow for real-time access to dynamic information, one order of magnitude sensitivity increase, and corresponding dose reduction [80]. A main challenge associated to the translation of TOF-PET technology to full scanners is the multiplexing of the large number of SiPMs composing the detectors that deteriorates CTR. TOF-PET technology has been one of the main lines of research in PET instrumentation during the last year, and the best state-of-the-art scanners already reach ~214 ps FWHM CTR [24]. Another approach to boost system sensitivity is building large axial FOV scanners. Following this idea, the first total body scanner was recently developed, the so-called EXPLORER, with 195 cm total axial FOV, which allows one to reduce scanning time to seconds [28]. However, its high price and the requirement for large hospital footprints is a challenge for its clinical deployment as well as research use.

Additionally, beyond instrumentation challenges, to further extend the clinical use of PET, it is important to consider that, while PET provides highly quantitative images for the study of biochemical and functional abnormalities, the absence of background anatomical information makes it difficult to interpret the radiotracer distribution, leading sometimes to misinterpretations of the images. To deal with this problem, PET functional images are coregistered with anatomical images provided by CT or MRI systems [81].

Acknowledgments

References

1. Phelps ME (2000) Positron emission tomography provides molecular imaging of biological processes. Proc Nat Acad Sci 97(16): 9226–9233

2. Rich DA (1997) A brief history of positron emission tomography. J Nucl Med Technol 25(1):4–11

3. Brownel GA (1999) A history of positron imaging. Phys Research Laboratory Massachusetts General Hospital

4. Jones T, Townsend D (2017) History and future technical innovation in positron emission tomography. J Med Imaging 4(1):011013

5. Dirac PAM (1929) A theory of electrons and protons. Proc Camb Soc 126(801). https://doi.org/10.1098/rspa.1930.0013

6. Anderson CD (1933) The positive electron. Phys Rev 43(491). https://doi.org/10.1103/PhysRev.43.491

7. Ruben S, Kamen MD, Hassid WZ (1940) Photosynthesis with radioactive carbon: II. Chemical properties of the intermediates. Jam Chern Soc 62(12):3443–3450

8. Melcher CL (2000) Scintillation crystals for PET*. J Nucl Med 41(6):1051–1055

9. Croll MN (1994) Nuclear medicine instrumentation. Historic perspective. Semin Nucl Med 24(1):3–10. https://doi.org/10.1016/s0001-2998(05)80245-4

10. Wrenn FR, Good ML, Handler P (1951) The use of positron-emitting radioisotopes for the localization of brain tumors. Science 19(2940): 525–527. https://doi.org/10.1126/science.113.2940.525

11. Brownell GL, Sweet WH (1955) Localization of brain tumors with positron emitters. Nucleonics 4:326–330

12. Rankowitz S, Robertson JS, Higinbotham WA, Rosenblum MJ (1962) Positron scanner for locating brain tumors, vol 9. Proceeding of the Institute of Radio Engineers, Brookhaven National Lab., (BNL), Upton, pp 49–56

13. Anger HO, Gottschalk A (1963) Localization of brain tumors with the positron scintillation camera. J Nucl Med 4:326–330

14. Thompson CJ, Yamamoto YL, Meyer E (1976) A position imaging system for the measurement of regional cerebral blood flow, vol 96. Application of Optical Instrumentation in Medicine V, SPIE Proceedings. https://doi.org/10.1117/12.965421

15. Phelps ME, Hoffman EJ, Mullani NA, Ter-Pogossian MM (1975) Application of annihilation coincidence detection to transaxial reconstruction tomography. J Nucl Med 16(3): 210–224

16. Williams CW, Crabtree MC, Burgiss SG (1979) Design and performance characteristics of a positron emission computed axial tomograph—ECAT®-II. IEEE Trans Nucl Sci 26(1):619–627

17. Hoffman EJ, Ricci AR, van der Stee LMAM, Phelps ME (1983) ECAT III—basic design considerations. IEEE Trans Nucl Sci 30(1): 729–733

18. Ido T, Wan CN, Casella V, Fowler JS et al (1978) Labeled 2-deoxy-D-glucose analogs. Fluorine-18-labeled 2-deoxy-2-fluoro-D-glucose. 2-deoxy- 2-fluoro-D-man- nose, and C-14-2-fluoro-D-glucose. J Lab Compd Radiopharm 14(2):175–183

19. Townsend DW, Wensveen M, Byars LG, Geissbuhler A et al (1933) A rotating PET scanner using BGO block detectors: design, performance and applications. J Nucl Med 34(8): 1367–1376

20. Capasso F (1985) Chapter 1 physics of avalanche photodiodes. Semiconductors and Semimetals. Vol 22. Part D, pp 1–172

21. Bloomfield PM, Myers R, Hume SP et al (1997) Three-dimensional performance of a small-diameter positron emission tomograph. Phys Med Biol 42(2):389–400

22. Cherry SR, Shao Y, Silverman RW, Meadors K et al (1997) MicroPET: a high resolution PET scanner for imaging small animals. IEEE Trans Nucl Sci 3:1161–1166

23. Miller M, Zhang J, Binzel K, Griesmer J et al (2015) Characterization of the Vereos digital photon counting PET system. J Nucl Med 56(3):434

24. Siemens Biograph Vision Technical Sheet, retrieved April (2019). www.siemens-healthineers.com

25. Gonzalez AJ, Sanchez F, Benlloch JM (2018) Organ-dedicated molecular imaging systems. IEEE Trans Rad Plasma Med Sci 2(5):388–403

26. Mullani NA, Gaeta J, Yerian K, Wong WH et al (1984) Dynamic imaging with high resolution time-of-flight PET camera-TOFPET I. IEEE Trans Nucl Sci 31(1):609–613

27. Ter-Pogossian MM, Mullani NA, Ficke DC et al (1981) Photon time-of-flight assisted positron emission tomography. J Comput Assist Tomogr 5(2):227–239

28. Cherry SR, Jones T, Karp JS, Qi J et al (2018) Total-body PET: maximizing sensitivity to create new opportunities for clinical research and patient care. J Nucl Med 59(1):3–12

29. del Guerra A, Belcari N, Bisogni M (2016) Positron emission tomography: its 65 years. Rivista del nuovo cimento 39(4). https://doi.org/10.1393/ncr/i2016-10122-6

30. Ter-Pogossian MM, Raichle ME, Sobel BE (1980) Positron emission tomography (PET). Sci Am 243(4):170–181

31. Levin CS, Hoffman EJ (1999) Calculation of positron range and its effect on the fundamental limit of positron emission tomography system spatial resolution. Phys Med Biol 44(3): 781–799

32. Evans RD (1955) The atomic nucleus. McGraw-Hill, New York, LCCCN, pp 55–7275

33. Krane KS (1995) Introductory Nuclear Physics. Wiley, New York

34. Compton AH (1923) A quantum theory of the scattering of X-rays by light elements. Phys Rev 21(5):483

35. Ford RL, Nelson W (1978) The EGS code system: computer programs for the Monte Carlo simulations of electromagnetic cascade showers. SLAC-210, UC-32, Stanford

36. Decuyper M, Stockhoff M, Vandenberghe S, Van Holen R (2021) Artificial neural networks for positioning of gamma interactions in

monolithic PET detectors. Phys Med Biol 66(7):075001

37. Fleming O (1999) Radioisotopes and radiation methodology: chapter 4 scintillation detectors. John Wiley & Sons, Inc. Med Phys 4R06/6R03, pp 4–10

38. Knoll GF (2010) Radiation detection and measurement. John Wiley and sons. Inc, New York

39. Sabet H, Bläckberg L, Uzun-Ozsahin D, El-Fakhri G (2016) Novel laser-processed-CsI:Tl detector for SPECT. Med Phys 43(5):2630

40. Gonzalez-Montoro A, Gonzalez AJ, Pourashraf S, Miyaoka RS et al (2021) Evolution of PET detectors and event positioning algorithms using monolithic scintillation crystals. IEEE Trans Rad Plasma Med Sciences 5(3):282–305

41. Levin CS (2003) Detector design issues for compact nuclear emission cameras dedicated to breast imaging. Nucl Instrum Methods Phys Res A 497(1):60–74

42. Flyckt S-O, Marmonier C (2002) Photomultiplier tubes principles & applications. Phonis Brive, France. https://www2.pv.infn.it/~debari/doc/Flyckt_Marmonier.pdf

43. Dinu N (2013) Instrumentation on silicon detectors: from properties characterization to applications. Université Paris Sud-Paris XI. http://tel.archives-ouvertes.fr/tel-00872318

44. González AJ, Conde P, Hernandez L, Herrero V et al (2013) Design of the PET-MR system for head imaging of the DREAM project. Nucl Instrum Methods Phys Res A 702:94–97

45. Motoyoshi M (2009) Through-Silicon Via (TSV). IEEE Proceeding 97(1):43–48

46. Schaart DR, Charbon E, Frach T, Schulz V (2015) Advances in digital dSiPMs and their application in biomedical imaging. Nucl Instrum Methods Phys Res A 809:31–52

47. Stolin V, Majewski S, Jaliparthi G, Raylman RR, Proffit J (2013) Evaluation of imaging modules based on SensL array SB-8 for nuclear medicine applications. 2013 IEEE Nuclear Science Symposium and Medical Imaging Conference. https://doi.org/10.1109/NSSMIC.2013.6829079

48. Kanno I, Lammertsma AA, Heather JD, Gibbs JM et al (1984) Measurements of cerebral blood flow using bolus inhalation of C15O2 and positron emission tomography: description of the method and comparison with C15O2 continuous inhalation method. J Cereb Blood Flow Metab 4(2):224–234

49. Warburg O (1931) The metabolism of tumors. Richard Smith, New York, pp 129–161

50. Huang SC, Carson RE, Hoffman EJ, Carson J et al (1983) Quantitative measurement of local cerebral blood flow in humans by positron emission tomography and 15O-water. J Cereb Blood Flow Metab 3(2):141–153

51. Fendler WP, Calais J, Eiber M, Flavell RR et al (2019) Assessment of 68Ga-PSMA-11 PET accuracy in localizing recurrent prostate cancer a prospective single-arm clinical trial. JAMA Oncol 5(6):856–863

52. Gopal BS (2010) Basics of PET imaging. Physics, chemistry, and regulations. Springer. ISBN: 978-3-319-16422-9

53. Wernick MN, Aarsvold JN (2004) Emission tomography: the fundamentals of PET and SPECT. Elsevier, Imprint: Academic Press, Inc. ISBN: 0-12-744482-3, 576

54. Kinahan PE, Rogers JG (1989) Analytic 3D image reconstruction using all detected events. IEEE Trans Nucl Sci 36(1):964–968

55. Cherry SR, Sorenson JA, Phelps ME (2003) Physics in nuclear medicine. Saunders/Elsevier Science, Philadelphia. ISBN 0-7216-8341-X

56. Du H, Yang Y, Glodo J, Wu Y et al (2009) Continuous depth-of-interaction encoding using phosphor-coated scintillators. Phys Med Biol 54(6):1757–1771

57. Son JW, Lee MS, Lee JS (2017) A depth-of-interaction PET detector using a stair-shaped reflector arrangement and a single-ended scintillation light readout. Phys Med Biol 62(2):465–483

58. Kuang Z, Sang Z, Wang X, Fu X et al (2018) Development of depth encoding small animal PET detectors using dual-ended readout of pixelated scintillator arrays with SiPMs. Med Phys 45(2):613–621

59. Zen G (2010) Medical image reconstruction. Springer. ISBN-10: 364205367X

60. Surti S, Karp JS (2008) Design considerations for a limited-angle, dedicated breast, TOF PET scanner. Phys Med Biol 53(11):2911–2921

61. Karp JS, Surti S, Daube-Witherspoon ME, Muehllehner G (2008) Benefit of time-of-flight in PET: experimental and clinical results. J Nucl Med 49(3):462–470

62. Vanderberghe S, Mikhaylova E, D'Hoe E, Mollet P, Karp JS (2016) Recent developments in time-of-flight PET. Eur J Nucl Mol Med Imag 3(3). https://doi.org/10.1186/s40658-016-0138-3

63. Gundacker S, Auffray E, Pauwels K, Lecoq P (2016) Measurement of intrinsic rise times for various L(Y)SO and LuAG scintillators with a general study of prompt photons to achieve 10 ps in TOF-PET. Phys Med Biol 61(7):2802–2837

64. Gonzalez-Montoro A, Pourashraf S, Lee MS, Cates JW, Levin CS (2021) Study of optical reflectors used in scintillation detectors that achieve 100 ps coincidence time resolution for TOF-PET. Biomed Phys Eng Express 7(6). https://doi.org/10.1088/2057-1976/ac240e

65. Pourashraf S, Gonzalez-Montoro A, Won JY, Lee MS et al (2021) Scalable electronic readout design for a 100 ps coincidence time resolution TOF-PET system. Phys Med Biol 66(8): 095005. https://doi.org/10.1088/1361-6560/abf1bc

66. Cates JW, Levin CS (2018) Evaluation of a clinical TOF-PET detector design that achieves ≤100 ps coincidence time resolution. Phys Med Biol 63(11):115011

67. Stickel JR (2005) High-resolution PET detector design: modelling components of intrinsic spatial resolution. Phys Med Bio 50(2): 179–195

68. Lecoq P (2017) Pushing the limits in time-of-flight PET imaging. IEEE Trans Rad Plasma Med Sci 1(6):473–485

69. Kang HG, Yamaya T, Han YB, Song SH et al (2020) Crystal surface and reflector optimization for the SiPM-based dual-ended readout TOF-DOI PET detector. Biomed Phys Eng Express 6(6). https://doi.org/10.1088/2057-1976/abc45a

70. Berg E, Roncali E, Cherry SR (2015) Optimizing light transport in scintillation crystals for time-of-flight PET: an experimental and optical Monte Carlo simulation study. Biomed Opt Expres 6(6):2220–2230

71. Spanoudaki V, Levin CS (2010) Photodetectors for time of flight positron emission tomography (ToF-PET). Sensors 10(11): 10484–10505

72. NEMA NU 2-2018 (2018) Performance measurements of positron emission Tomographs (PET). National Electrical Manufacturers Association

73. Defrise M, Kinahan PE, Michel CJ (2005) Image reconstruction algorithms in PET. Springer. ISBN: 978-1-85233-798-8

74. Yang X, Peng H (2015) Study of the relationship between NECR and image SNR for PET systems. J Nucl Med 56(3):1743

75. Tang S, Liu Y, Wang J, Zhao Y et al (2019) Dead time correction method for long axial field-of-view, whole-body PET scanner. J Nucl Med 60(1):458

76. Grant AM, Levin CS (2014) A new dual threshold time-over-threshold circuit for fast timing in PET. Phys Med Biol 59(13): 3421–3430

77. Lecoq P, Auffray E, Knapitsch A (2013) How photonic crystals can improve the timing resolution of scintillators. IEEE Trans Nucl Science 60(3):1653–1657

78. Erickson BJ, Korfiatis P, Akkus Z, Kline TL (2017) Machine learning for medical imaging. Radiographics 37(2):505–515

79. Gerven M, Bohte S (2017) Artificial neural networks as models of neural information processing. Front Comput Neurosci 11:114. https://doi.org/10.3389/fncom.2017.00114

80. Vanderberghe S, Moskal P, Karp JS (2020) State of the art in total body PET. EJNMMI Physics 7(1):35. https://doi.org/10.1186/s40658-020-00290-2

81. Lee JS, Park KS, Lee DS, Lee CW et al (2005) Development and applications of a software for functional image registration (FIRE). Comput Meth Prog Biomed 78(2):157–164

Chapter 21

Practical Considerations for Total-Body PET Acquisition and Imaging

Benjamin A. Spencer, Kristin McBride, Heather Hunt, Terry Jones, Simon R. Cherry, and Ramsey D. Badawi

Abstract

The world's first total-body PET/CT system has been in routine clinical and research use at UC Davis since 2019. The uEXPLORER total-body PET scanner has been designed with an axial field-of-view long enough to completely encompass most human subjects (194 cm or 76 inches long), allowing for a 15–68-fold gain in the PET signal collection efficiency over conventional PET scanners. A high-sensitivity PET scanner that can image the entire subject with a single bed position comes with new benefits and challenges to consider for efficient and practical use. In this chapter, we discuss the common clinical and research imaging protocols implemented at our institution, along with the appropriate technical and practical considerations of total-body PET imaging.

Key words EXPLORER, PET, Total-body imaging, Human imaging, Long axial FOV, Dynamic PET, Low dose imaging

1 Introduction

The University of California, Davis (UC Davis) and United Imaging Healthcare (UIH) have collaborated to develop the world's first total-body PET scanner. The uEXPLORER PET/CT scanner has an axial field-of-view (FOV) of 194.0 cm, allowing PET data collection from the entire human body simultaneously and greatly increasing PET scanner signal collection efficiency. The uEXPLORER scanner was installed at the EXPLORER Molecular Imaging Center (EMIC) in May 2019 and has been operational since June 2019 (Fig. 1).

Developed under an NCI-funded transformative award (R01 CA206187, $15.5 M direct costs), the EXPLORER total-body PET/CT scanner marks a paradigm shift in the capabilities of PET imaging in humans. The 194 cm long PET scanner is the first imaging device that can image the entire human body

Fig. 1 Photograph of the uEXPLORER total-body PET/CT system installed at the EXPLORER Molecular Imaging Center

simultaneously and is one of the most complex imaging devices in the world, with over 500,000 individual detectors, and dataset sizes that commonly exceed 1 TB. In contrast to conventional PET scanners, which have a ~ 20–30 cm axial field-of-view (FOV), the uEXPLORER can collect signal from the entire human body, leading to a 15–68-fold gain in detection efficiency [1]. Additionally, the uEXPLORER scanner was developed with excellent spatial resolution of ~3 mm [1], which is better than any existing whole-body clinical PET scanner. First investigations have shown that the ultra-high sensitivity, coupled with high spatial resolution, leads to exceptional image quality [2]. uEXPLORER is US FDA 510 (k) cleared, with several installations across the world where it is commonly used for high-throughput imaging in regions with high clinical demands [3]. At our institution, this state-of-the-art PET scanner is utilized for both novel research applications and clinical imaging in which an emphasis has been placed on optimizing image quality [4]. There are now multiple vendors selling long (1 m or greater) axial field-of-view (LAFOV) PET scanners [5], as well as other developments in academic labs such as the 140 cm long PennPET EXPLORER [6, 7]; thus, the total-body PET clinical practices and protocols developed at UC Davis will hopefully set the foundations that will guide protocols and usage in future long axial field-of-view and total-body PET systems that will be installed in the coming years.

Initial studies have demonstrated that the uEXPLORER scanner is capable of performing low dose imaging (1/20th standard ^{18}F-2-Fluoro-2-deoxy-D-glucose (^{18}F-FDG) dose), late time point imaging (imaging ^{18}F-FDG up to 12 h post-injection), fast imaging (20–30 s scan duration), and simultaneous total-body dynamic imaging [2]. EXPLORER total-body PET imaging with ultra-fast dynamic imaging at 100 ms frame duration has also been reported [8]. Ongoing experience with clinical and research imaging on the EXPLORER clearly supports the expectation of superior image quality provided by the high scanner sensitivity and spatial resolution compared with conventional PET scanners [4, 9].

This chapter will first give an overview of the uEXPLORER design and performance evaluation, along with the technical considerations related to data collection and image reconstruction, which provide guidance for clinical and research applications of total-body PET. In the methods section, common clinical and research protocols employed at our institution are described and justified. Additionally, some practical considerations specific to total-body PET are discussed.

2   Materials

2.1   The uEXPLORER Total-Body PET/CT Scanner

The characterization and performance evaluation of the uEXPLORER total-body PET scanner has been reported in [1]. The work reports measurements of PET scanner sensitivity, spatial resolution, count-rate performance, time-of-flight (TOF) resolution, and image quality, according to the national electrical manufacturers association (NEMA) NU 2-2018 standard along with additional measurements required to fully characterize long axial FOV PET scanners.

The uEXPLORER uses lutetium-yttrium oxyorthosilicate (LYSO) scintillation crystals (2.76 × 2.76 × 18.1 mm^3) coupled to silicon photomultiplier (SiPM) detectors to detect coincidence photons emitted from positron annihilations. The PET system has a bore diameter of 78.6 cm and an axial length of 194.0 cm separated into eight units of equal length. Each unit can form coincidences with itself and ± 4 adjacent units on either side, entailing an axial acceptance angle of up to 57 degrees. This creates a sensitivity profile in which the central 1 m of axial length has a plateau of high sensitivity, making it optimal for imaging the vital organs of the human body (vertex to pelvis) while still providing diagnostic quality imaging of the extremities in a single acquisition. This provides a peak sensitivity of 18.6% within the central 1 m and an average sensitivity for adult total-body imaging of 14.7% (Fig. 2) [1]. This equates to a vast improvement in PET scanner sensitivity compared to other conventional scanners.
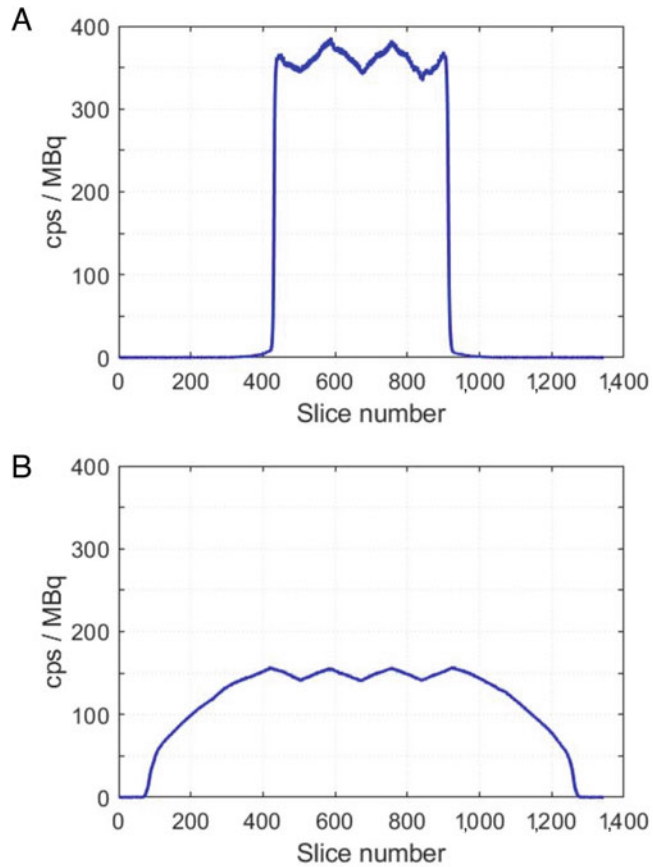
Fig. 2 Axial sensitivity profiles for 70 cm (NEMA NU 2–2018) (**a**) and 170 cm (**b**) line source phantoms. Sinogram slice thickness is 1.444 mm. (Reproduced from Ref. [1] with permission from Journal of Nuclear Medicine)

Although total-body PET is known for its high sensitivity, the uEXPLORER PET scanner also has the highest spatial resolution of any whole-body clinical PET scanner of 3.0 mm measured according to NEMA NU 2 and with the ability to resolve 2.4 mm rods in a mini-Derenzo phantom using iterative reconstruction [1]. Utilization of high spatial resolution in PET imaging requires small voxel image reconstruction, which will suffer from increased image noise unless supported by a high number of detected events. Therefore, the high sensitivity provided by total-body PET is well complemented by high spatial resolution, enabling exceptional image quality in most applications.

2.2 uEXPLORER Data Corrections, Dynamic Range, and Quantitative Accuracy

The high sensitivity of total-body PET enables improved imaging at a very low dose in clinical and research applications, such as ultra-low dose pediatric imaging, ultra-low dose repeat imaging in healthy subjects or subjects with chronic conditions [10], and potentially oncology screening [2].

Fig. 3 Maximum intensity projection image of a research participant injected with ~19 MBq ^{89}Zr-Df-Crefmirlimab and scanned 48 hours after infusion. This ^{89}Zr-labeled mini body is a marker of CD8+ T-lymphocytes. Images were reconstructed with 1.17 mm isotropic voxel size and 60 min duration

Total-body or LAFOV PET can also be utilized for improved imaging of low positron yield tracers such as ^{89}Zr VRC01 [11] or therapy agents such as ^{90}Y. For example, total-body immunoPET imaging of ^{89}Zr-labeled antibodies using only an 18.5 MBq administration of the 22% positron fraction tracer provides exceptional image quality as seen in Fig. 3. Dosimetry verification of therapeutic doses of ^{90}Y is enabled with total-body PET imaging of the 0.003% positron yield of ^{90}Y [12]. Imaging of a therapeutic dose of ^{90}Y is equivalent to imaging ~80 kBq of positron activity, or 2.3 μCi of ^{18}F-FDG [12]. Additionally, the total-body coverage may be used for new research applications such as high-temporal resolution total-body dynamic imaging [8, 13, 14], or improved whole-body clinical scanning of tracers with fast kinetics such as ^{18}F-Fluciclovine [9].
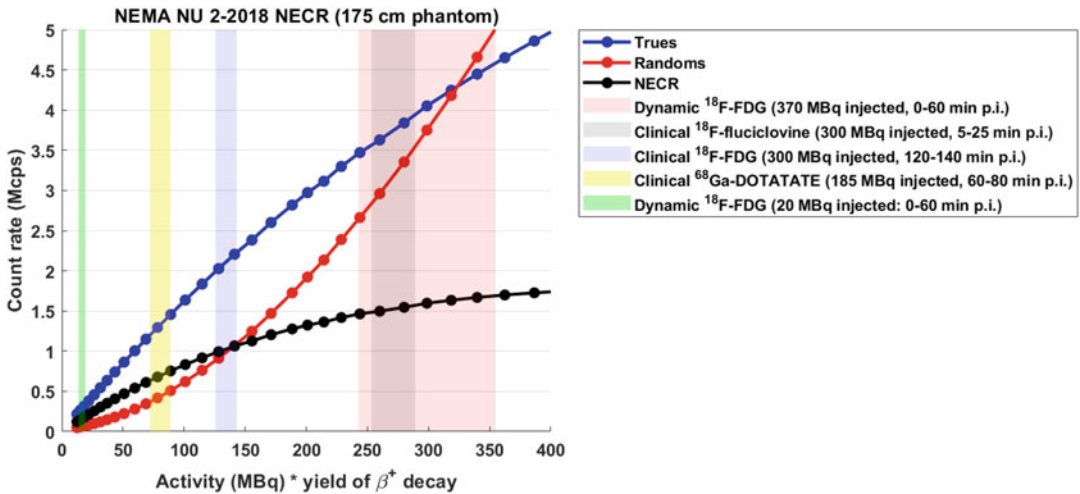
Fig. 4 Range of count rates encountered by the uEXPLORER scanner (throughout the acquisition) in various clinical and research tasks. The count rates were estimated based on the NEMA NU 2–2018 NECR performance assessment using an extended, 175 cm NU 2 scatter phantom. Note: the activity at peak NECR is 528 MBq. (*p.i.* = post-injection). (Reproduced from Ref. [16] with permission)

A PET scanner, which enables imaging applications of tracer activity from as low as 80 kBq (effective positron activity) up to 370 MBq (~4500-fold range), presents a unique challenge in quantitative molecular imaging. This requires accurate data corrections and image reconstruction over a wide signal dynamic range. For very low dose applications, the LYSO background correction must be properly accounted for to allow accurate imaging [15]. Additionally, issues such as the non-negativity constraint in iterative reconstruction must be considered [16]. As activity increases the number of trues increase, whereas the number of randoms increase with the square of activity. Furthermore, because the PET detectors are limited by how fast they can record events, as activity increases detector deadtime losses will increasingly become a factor. This count-rate behavior is captured in the noise equivalent count rate (NECR) plots shown in Fig. 4, which also illustrates the activity ranges of some typical clinical and research protocols. A more in-depth analysis is presented in Spencer et al. [1], where the NECR is presented for both a 70 cm-long phantom (following the NEMA protocol for conventional PET scanners) and a 175 cm-long phantom. The 70 cm phantom can provide an approximation for the count-rate behavior for single-organ imaging using total-body or LAFOV scanners, while the 175 cm phantom more appropriately illustrates the optimal count-rate regime when imaging tracer distribution within the entire human body.

The accuracy of data corrections subsequently translates to quantitatively accurate imaging, which is an essential paradigm of PET imaging [17]. In the case of total-body PET, not only is

quantitative accuracy required over a very large activity range, but consistent quantitative accuracy is sought over the entire axial FOV. The investigation by Leung et al. [16] provides the first evaluation of quantitative accuracy in a total-body PET scanner over a clinically relevant range of activities representative of total-body PET. This study demonstrated that the uEXPLORER quantitative accuracy was between ±3% following the NEMA NU-2 protocol utilizing a 70 cm phantom, and ± 4% accuracy was obtained with a human-sized 175 cm phantom [16]. In addition, this study revealed that the uEXPLORER axial uniformity fell within ±3% across the central 175 cm (90%) of the axial FOV. This prior work provides the necessary validation of the uEXPLORER total-body PET scanner for a wide range of clinical and research applications.

2.3 uEXPLORER Image Reconstruction

PET image reconstruction is achieved using a listmode based time-of-flight (TOF) enabled ordered-subset expectation-maximization (OSEM) iterative reconstruction algorithm. The image reconstruction allows for incorporation of detector normalization factors, deadtime correction, randoms correction, TOF, attenuation correction, Monte Carlo–based scatter correction, and point spread function (PSF) resolution modeling. Along with the correction factors, image pixel size, slice thickness, number of subsets, number of iterations, and optional image smoothing can be specified by the user. In addition, the vendor-provided software allows for limited axial FOV image reconstruction and dynamic framing.

Our institution's commonly used total-body PET image reconstruction protocols are provided in Table 1. Contrary to most conventional PET reconstruction protocols, total-body PET image reconstruction commonly does not require post-reconstruction image smoothing. Given that total-body PET image reconstruction times can be lengthy (*see* Table 2) and are dependent on the reconstruction voxel size, generally image noise can be reduced by employing larger voxel image reconstruction rather than applying post-reconstruction smoothing as seen in the low-resolution reconstruction protocol and high-temporal resolution (2 s frames) dynamic imaging protocol. Larger voxel reconstructions provide noise reduction as well as increased reconstruction speed with the added benefit that the image data sets become more manageable for image viewing and further image processing such as tracer kinetic modeling.

2.4 Practical Consideration for Total-Body PET Data Collection and Reconstruction

Last but not least, the practical considerations of total-body or LAFOV PET imaging must be considered for viable clinical and research applications. For the uEXPLORER PET scanner, the ~eightfold increase in the axial length leads to a large increase in the number of possible lines-of-response (LOR), and thus the raw PET data size increases substantially. The acquired raw data is stored in listmode format after energy window discrimination and

Table 1
Common total-body PET reconstruction protocols

Reconstruction protocol	Voxel size	Matrix size	Iterations & subsets	Corrections	Image smoothing
Standard clinical protocols (*see* Table 3)	2.34 mm³ isotropic	256 × 256 × 828	4 iterations, 20 subsets	Without PSF, with PSF, and without attenuation correction	None
High-resolution or brain imaging	1.17 mm³ isotropic	512 × 512 × 1656	10 iterations, 20 subsets	All corrections with PSF	None
Low-resolution or low dose imaging	4.00 mm³ isotropic	150 × 150 × 486	4 iterations, 20 subsets	All corrections with PSF	None
High-temporal resolution dynamic imaging	4.00 mm³ isotropic	150 × 150 × 486, 66 frames	4 iterations, 20 subsets	All corrections without PSF, 66 frames: 2–300 s duration	None

coincidence processing on the vendor provided 8-node computational cluster. Raw data sizes can become larger than 1 TB for some research applications, such as a 370 MBq 60 minute dynamic acquisition, as shown in Table 2. The raw data produced with clinical imaging protocols is manageable in comparison (*see* Table 2), although the size is still about two orders of magnitude greater compared to conventional PET. Long-term storage of raw data is only required if reprocessing or additional reconstructions are needed, so for most clinical applications, storage of raw data for more than 1 week is typically not necessary.

Sinogram generation becomes unfeasible for total-body PET imaging with up to 92 billion LORs, especially with the incorporation of more than 60 TOF bins. As a result, listmode image reconstruction methods are required for any high-resolution total-body PET applications. The time it takes to go from data acquisition to image generation is due to a combination of several tasks including data pre-processing, Monte Carlo scatter correction, image reconstruction, and DICOM image generation. The duration of these tasks is, for the most part, heavily dependent on the number of events recorded (product of activity and scan duration, bearing in mind radioactive decay), but also vary based on the selected image reconstruction parameters—most notably, the number of reconstruction iterations and the image voxel size. Consequently, the reconstruction time is mostly determined by the clinical or research

Table 2

Typical data sizes and reconstruction times for some common research and clinical protocols

Imaging protocol	Typical raw data size	Reconstruction parameters	Reconstruction time
Research: 296 MBq ^{18}F-FDG, 60 min dynamic acquisition	1000 ± 130 GB	Research high-temporal resolution framing: 66 frames, 4.00 mm isotropic voxels, 4 iterations, 20 subsets	~240 min
Research: 370 MBq ^{18}F-FDG, 20 min acquisition, 90 min post-injection	180 ± 20 GB	Research high-resolution: 1.17 mm isotropic voxels, 4 iterations, 20 subsets	~45 min
Clinical: 296 MBq ^{18}F-FDG, 20 min acquisition, 60 min post-injection	210 ± 30 GB	Clinical protocol: 2.34 mm isotropic voxels, 4 iterations, 20 subsets	~20 min
Clinical: 296 MBq ^{18}F-FDG, 20 min acquisition, 120 min post-injection	130 ± 20 GB	Clinical protocol: 2.34 mm isotropic voxels, 4 iterations, 20 subsets	~15 min
Clinical: 296 MBq ^{18}F-Fluciclovine, 25 min dynamic acquisition	450 ± 60 GB	Clinical protocol: 2.34 mm isotropic voxels, 4 iterations, 20 subsets	~35 min

Reconstruction durations shown are estimated based on hardware and software installed in 2021

Table 3

Standard total-body PET clinical protocols

Clinical protocol	Injected dose	Imaging time point (post-injection)	PET acquisition duration
Standard oncology imaging with ^{18}F-FDG, (non-lymphoma)	296 MBq	120 min	20 min
Lymphoma oncology imaging with ^{18}F-FDG	296 MBq	60 min & 120 min	20 min & 20 min
Neuroendocrine imaging with ^{68}Ga-Dotatate	185 MBq	60 min	20 min
Prostate cancer with ^{18}F-Fluciclovine	296 MBq	Dynamic	25 min

imaging protocol and the image reconstruction parameters. Examples of typical reconstruction durations are given in Table 2; however, these times also vary with factors such as the size of the subject, which influence the number of detected events.

In conclusion, image reconstruction time must be considered if high-throughput clinical imaging is desired, although this can be readily controlled with careful consideration of the imaging protocol and reconstruction parameters. On the other hand, research

protocols such as high-temporal resolution dynamic imaging would be greatly aided with the addition of a separate or dual image reconstruction cluster. If storage of raw data is needed for future reprocessing or research applications, a petabyte scale storage solution is necessary.

3   Methods

The objective of this section is to describe common total-body PET protocols in use at our institution and discuss some practical considerations, which should be taken into account for effective total-body PET imaging in both the clinical and research settings.

Clinical implementation of total-body PET at our institution was designed to increase the benefit to the individual patient rather than just employing it as a high-throughput standard-of-care PET scanner. The goal was to reduce the injected dose and therefore the radiation dose to the patient moderately while simultaneously substantially improving the image quality. For all standard ^{18}F-FDG clinical protocols, the injected dose was reduced by 20% leading to a PET dose, which is similar or less than the dose from the accompanying CT (equivalent to ~1.8 times the average annual background radiation dose in the USA [18]).

To improve image quality, we scan for a similar duration as a typical multi-bed position whole-body scan: a total of 20 min of scan duration. Additionally, we aim to increase tumor to background ratio in oncologic ^{18}F-FDG imaging by doubling the conventional uptake time of the tracer from 60 min post-injection to 120 min post-injection. An additional 60 min of uptake results in further radiotracer decay of ~30%, but according to the total-body PET clinical experience at UCD, the improvements in image quality and lesion detection outweigh the signal loss resulting in a favorable trade-off.

The number of total-body PET research applications and protocols is too numerous and application specific to describe in detail. However, standard dynamic PET imaging protocols currently in use and some practical considerations are outlined below.

3.1   Quality Control and Assurance Procedures for the uEXPLORER Total-Body PET/CT System

Following the manufacturer's recommendations, the uEXPLORER undergoes preventative maintenance and system calibration every 6 months. In the interim, daily and weekly quality control (QC) and quality assurance (QA) procedures are performed to ensure the system is operating properly and accurately. The manufacturer recommends daily and weekly QC procedures for both PET and CT systems. In addition to those, our institution performs our own weekly QA protocol developed to verify quantitative accuracy along the 194 cm axial FOV and monitor any temporal changes in quantitative performance over months to years [19].
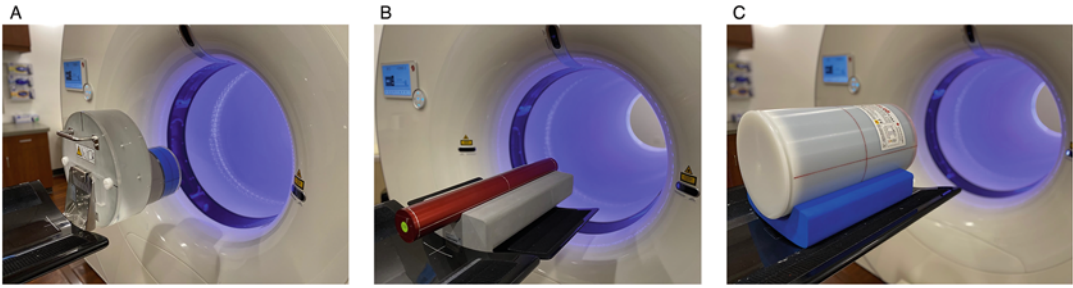
Fig. 5 Pictures of quality control and quality assurance phantoms. (**a**) The water-filled CT phantom with head and body compartments. (**b**) The PET weekly quality control phantom. (**c**) The uniform cylinder phantom, which is scanned at three axial locations for quality assurance

The weekly CT QC procedure utilizes a water-filled phantom with body and head compartments (Fig. 5a). This phantom is attached to the end of the patient table and scanned for approximately 5 min. The procedure checks for image noise, quantitative accuracy (i.e., CT number), uniformity, resolution, and checks for the presence of any CT artifacts. The daily QC procedure involves CT air calibration and does not require a phantom. At our institution, we perform both daily and weekly QC procedures every day of scanning. The manufacturer-recommended PET weekly QC procedure requires a radioactive cylinder source of 52 cm length and 5 cm diameter, which is positioned in the scanner and stepped through the entire axial FOV (Fig. 5b). The radioactive source employed can be either a solid Ge-68 uniform phantom, or a cylinder phantom provided by the manufacturer that can be filled with a uniform radioactive solution. The source strength should be in the range of 37–111 MBq. The weekly QC procedure collects data from two units at a time with a variable acquisition duration from 15 to 40 min depending on the source strength. This ensures sufficient count density to perform all QC assessments. The manufacturer's QC protocol examines the PET calibration crystal map and look up table, the detector energy drift, the time-of-flight status, the detector voltage, temperature, and humidity to verify conditions are within operational standards. In addition, the manufacturer's daily quick QC procedure utilizes the background count rate of the scanner (arising from the presence of small amounts of radioactive ^{176}Lu in the detectors themselves) to verify the state of the PET electronics and detectors. This daily QC can be scheduled to run automatically during off hours and provides information of the detector voltage, temperature, humidity, and background count rates. This daily QC can be performed in about 60 s and automatically verifies the scanner is operational.

At our institution, we designed a secondary QA procedure to ascertain the axial quantitative uniformity and monitor the temporal quantitative performance of the scanner. This QA procedure is

performed weekly, although the frequency could be modified to meet institution-specific needs. The QA evaluation utilizes a standard uniform Ge-68 cylindrical phantom with 30 cm length, 20 cm diameter, and 37–74 MBq activity (Fig. 5c) [19]. This phantom is positioned on the patient bed and scanned at three positions along the axial FOV for 5 min duration at each position [19]. The images are reconstructed following our standard clinical protocol for analysis. A 10 cm diameter circular region of interest is placed approximately at the center of the phantom, and the SUV is recorded for each position and repeated every week. This provides both axial and temporal monitoring of the quantitative accuracy with an in-house designed protocol. Temporal monitoring can reveal changes, which occur between semi-annual calibrations as well as indicate if any changes occurred due to the semi-annual calibration by comparing the weekly QA before and after calibration. QA measurements over 1 year of observations have shown a small drift in SUV ranging from +1% to −3% and consistent axial uniformity within 2%.

3.2 Clinical Total-Body PET/CT Imaging Adult

^{18}F-FDG is used for the assessment of abnormal glucose metabolism to assist in the evaluation of malignancy in patients with known or suspected abnormalities found by other testing modalities, or in patients with an existing diagnosis of cancer. ^{18}F-FDG is the most widely used radiotracer for clinical patients on the total-body uEXPLORER PET/CT scanner. Patients are required to fast for a minimum of 6 hours prior to the injection and must withhold exercise for at least 24 h prior. Oral hydration is encouraged. Transport of ^{18}F-FDG into cells may be affected by fasting or by blood glucose changes associated with diabetes mellitus. Restrictions on diabetic medications vary depending on the category and mechanism of action, but the restricted duration ranges from 4 to 24 h prior to injection. Prior to injection, patients' blood glucose is tested using the standard fingerstick method. Non-diabetic patients should have a fasting blood glucose of 150 mg/dL or less prior to ^{18}F-FDG injection. Diabetic patients should have a fasting blood glucose of 200 mg/dL or less prior to ^{18}F-FDG injection. At our institution, adult clinical patients receive a standard dose of 296 MBq ^{18}F-FDG. Pediatric patients receive weight-based dosing of 4.07 MBq/kg of ^{18}F-FDG with a maximum dose of 296 MBq. Once patients have been injected, they sit quietly in a dimly lit room. Uptake times are dependent upon diagnosis. All patients are asked to void their bladder prior to imaging.

Non-lymphoma patients are imaged for 20 min after a 120 min uptake period for improved lesion detection and tracer clearance from blood or background tissue. Patients receive a low dose CT (140 kV, average 50 mAs) just prior to PET acquisition. Patients with a diagnosis of lymphoma are imaged for 20 min after a 60 min uptake period, in order to comply with the Deauville scale used by physicians for staging and assessment of treatment in lymphoma

patients, and then again at 120 min post-injection. These patients have a low dose CT with the 60 min PET and an ultra-low dose CT (140 kV, average 5 mAs) with the 120 min PET. *See* Table 3 for summary of the standard clinical protocols.

For clinical diagnoses other than head/neck cancer or where PET imaging of the entire body is indicated (e.g., melanoma, multiple myeloma, T cell lymphoma, soft tissue sarcomas), patients are positioned supine on the imaging table with arms above the head in order to reduce attenuation in the torso. Patients who are being evaluated for head/neck cancer or where entire body imaging is indicated are positioned supine on the table and imaged with arms down and stacked across the abdomen to minimize streak artifacts in the torso. Care is taken to ensure the site of disease is within the FOV.

[68]Ga-Dotatate PET/CT imaging is useful for evaluating primary and metastatic well-differentiated neuroendocrine tumors. The standard dose range for ^{68}Ga-Dotatate is 101.4–166.5 MBq. If patients are receiving any somatostatin analog treatments, ^{68}Ga-Dotatate imaging must be scheduled accordingly as non-radioactive somatostatin analogs competitively bind to the same somatostatin receptors as ^{68}Ga-Dotatate. Short-acting analogs of somatostatin should be held at least 24 h prior to imaging with ^{68}Ga-Dotatate. Patients receiving long-acting somatostatin analogs should ideally be imaged with ^{68}Ga-Dotatate just prior to their dosing of somatostatin (same day or 24 h prior). The standard uptake time for ^{68}Ga-Dotatate imaging is 60 min followed by a low dose CT (140 kV, average 5 mAs) and a 20 min PET acquisition.

[18]F-Fluciclovine imaging is indicated in men with suspected prostate cancer recurrence based on elevated blood prostate-specific antigen (PSA) levels following prior treatment. Patients are required to fast for a minimum of 4 hours prior to the injection and must withhold exercise for at least 24 h prior. Oral hydration is encouraged. It is preferable to start an intravenous catheter (IV) in the right upper extremity to avoid potential uptake in the supraclavicular vein as seen with left upper extremity injections. Patients are positioned on the scanner with arms stacked over the abdomen. Prior to injection, patients receive a low dose CT (140 kV, average 50 mAs). A dynamic PET acquisition commences at the start of the injection and is acquired for 25 min. FDA guidelines advise PET imaging to commence 4 min post-injection; in accordance, our institution reconstructs various static images from the dynamic dataset to provide diagnostic quality imaging at various stages of physiologic uptake. As recommended by the FDA, the standard dose of ^{18}F-Fluciclovine for adult patients is 370 MBq ± 20%; however, our institution aims for an injected dose of 296–333 MBq within the −20% allowed variation by the manufacturer.
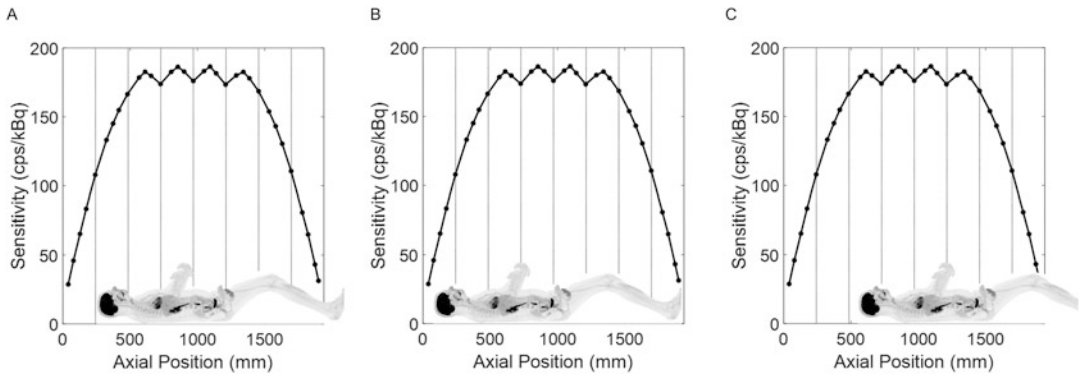
Fig. 6 Clinical or research subject placement within uEXPLORER point-source sensitivity profile. (**a**) The placement for standard clinical imaging (e.g., eyes to thighs imaging) in which the clinical subject's eyes are placed at the center of unit 2, providing optimal use of the uEXPLORER sensitivity profile. (**b**) The participant placement for total-body dynamic studies or clinical total-body scanning (e.g., melanoma). (**c**) The participant placment for clinical or research brain studies in which the subjects brain is positioned at the center of unit three, providing maximum sensitivity in the brain and upper torso regions

3.3 Patient or Research Participant Axial Positioning in Total-Body PET

While the uEXPLORER with its 194 cm axial FOV has the capability to image the entire length of an average-sized adult, patient position within the scanner may be varied according to diagnosis or area of interest taking into consideration the sensitivity profile of the scanner (Fig. 6).

For clinical patient imaging when the priority is to include as much of the entire body as possible, such as with melanoma or multiple myeloma, the entire PET FOV is utilized ensuring the patient's vertex of skull to toes are included within the FOV. Care must be taken with the subset of patients with a height close to or greater than 194 cm to include the site(s) of interest; however, in such cases, it is typically possible to position the subject with their knees bent and elevated to ensure their entire body is within the axial FOV (*see* Fig. 7). If a physician has requested a conventional PET scan (to include the regions between the skull and mid-thigh), the patient is positioned with the skull vertex at the top of the second unit of detector modules, 24 cm from the axial end of the PET detectors (*see* Fig. 6a). For the average adult, the imaging FOV would then include vertex of skull to distal tibia.

Research participant placement varies depending on the research goals of the study. For many total-body dynamic studies, the participant is placed in the center of the FOV to allow total-body kinetic modeling and parametric imaging [13] while also obtaining a total-body ROI-derived quantitative accuracy estimate [16]. In many other studies, the region of primary interest (e.g., brain) would be positioned closer to the center of the FOV to achieve the highest sensitivity (*see* Fig. 6c).
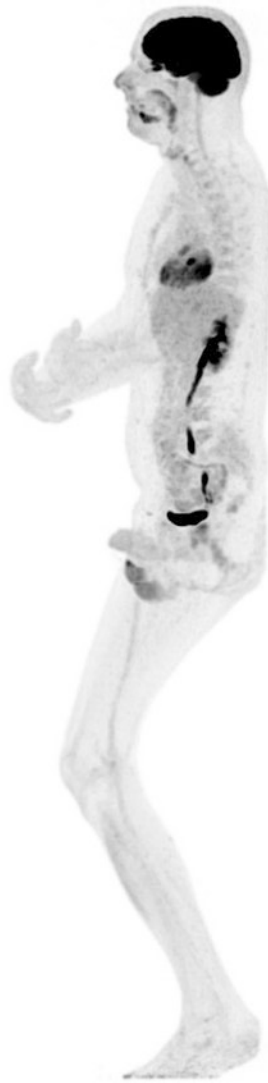
Fig. 7 Maximum intensity projection image of a 196 cm tall (6′5″) research participant injected with 20.7 MBq ^{18}F-FDG and scanned 90 min after injection. The participant conveniently fits in the uEXPLORER's axial FOV with their knees bent

3.4 Pediatric Total-Body PET Imaging

The increased sensitivity of total-body PET has perhaps the greatest benefit to clinical care in pediatric imaging. The pediatric population is of course particularly sensitive to radiation and even more susceptible to patient motion during imaging. In practice, total-body PET allows for the reduction of imaging times and/or the potential for further dose reduction without significantly compromising image quality.

To optimize pediatric patient care, precision imaging protocols can be utilized with total-body PET. Prior to imaging, each

Table 4
Pediatric total-body PET precision imaging using a tranquility scoring system

Pediatric precision imaging tranquility scoring system			
Score	Determination	Scan time	Dosing
1	Needs anesthesia. No prior history, family and child specialist do not feel confident without anesthesia at least as a backup. Refer to other facility with anesthesia capability.	Refer to other facility	Refer to other facility
2	Low-intermediate probability. Child has no prior history of scans, but child specialist has had contact with child and family during other appointments for assessment and is confident child can complete a 5 min scan.	5 min	4.07 MBq/ kg
3	Intermediate probability. Has had prior scans of short durations and was able to hold still. Child specialist has had contact with child and family during other appointments and is confident child can complete a 10 min scan.	10 min	2.04 MBq/ kg
4	High probability. Has proven past ability to lie still for PET or other scans of 20 min or more. Child specialist has had contact with child and family during other appointments for assessment.	20 min	1.02 MBq/ kg

pediatric patient can be assessed and designated with a tranquility score to determine the scan duration and pediatric dosing scale for each individual patient [20]. The tranquility score is based upon a child's capacity to cooperate to either reduce scan time (to avoid general anesthesia) or reduce the dose below SNMMI standards. As seen in Table 4, the tranquility scoring system uses a scale from 1 to 4, with 1 requiring anesthesia and 4 indicating the patient can cooperate for a full 20 min acquisition. A dose reduction proportional to the acceptable scan time reduction can be applied to pediatric patients who can tolerate longer scan durations.

Due to technical limitations, our facility cannot administer anesthesia; however, with the sensitivity provided by this state-of-the-art scanner, we can substantially reduce scan acquisition time to reduce the number of cases where anesthesia would be required. Furthermore, with total-body coverage and listmode data acquisition, the flexibility to identify, separate, and reconstruct relatively motion-free time periods is possible with careful monitoring. For example, if a pediatric patient can tolerate a scan but is susceptible to motion during the scan, the PET data can be acquired for a long duration while monitoring patient motion. The data used for image reconstruction can then be specifically selected and reconstructed to provide a reconstructed frame with relatively low motion and diagnostic image quality provided by the high sensitivity. Data can be selected (1) by technicians observing the patient and only reconstructing the scan time in which the patient was compliant; (2) through the monitoring of real-time count rates of the entire

scanner and each ring individually; and (3) by reconstructing the entire scan with short frames (e.g., 15 s) and by manually reviewing each frame for gross motion. In practice, only the first method would be used for clinical purposes.

3.5 Considerations for Dynamic Total-Body PET Imaging

The uEXPLORER has the capability to acquire total-body dynamic studies. This allows total-body radiotracer biodistribution to be visualized as a function of time across the entire duration of the acquisition. Total-body dynamic studies require special considerations not normally encountered with static imaging or even single-organ dynamic imaging [21]. A total-body PET/CT scanner has a much larger axial FOV than a conventional scanner. Injection technique and length of tubing must be considered, along with length of scan, arm positioning, and patient cooperation.

Our institution has developed a bolus injection technique aimed at delivering the most concentrated bolus possible while limiting the amount of residual activity remaining in the injection syringe and tubing. A 22 g IV or larger is placed in the upper extremity of each patient. If possible, IV placement should be superior to or in the antecubital region. IV placement inferior to the antecubital area leads to a greater likelihood of vessel bifurcation visualized on flow studies, and the potential of a dual time activity curve (TAC). A 1.5 mL microbore extension tube is added to the IV and positioned with the distal tip extended to the superior FOV limit for ease of access for the technologist. After completion of the CT scan, the technologist connects a three-way stop valve and a saline flush to the extension tube. The dose syringe is then connected to the remaining port on the three-way connection. If the volume of the dose is less than 1.5 mL, or the volume the extension tube can hold, the extension tube is pre-loaded with the dose. We then use a saline flush into the dose syringe to rinse any residual activity. The PET acquisition is started just prior to injecting the dose syringe to the patient, and then the saline is immediately flushed directly to the patient. This method delivers the most concentrated bolus, reduces residual in the dose syringe, and ensures the extension tube is flushed appropriately.

When deciding on the duration of a dynamic PET scan, areas of most interest and patient ability to withstand positioning requirements must be taken into consideration. For studies that would benefit most from longer scan durations (60 min or longer) or have areas of interest that would not be hindered from arms positioned down in the field-of-view (brain or lower extremities), patients are positioned with arms down for comfort. If it is determined that arms should be positioned up above the head for image quality, scan duration is, where possible, limited to 30 min for improved patient compliance.

3.6 Methods to Reduce or Correct Patient Motion in Total-Body PET

Patient comfort during scanning is of key importance for reducing image artifacts resulting from intra-scan motion. Due to its increased sensitivity and high spatial resolution, minor motion becomes more apparent on total-body PET imaging. Educating the patient about the scan process and how movement could negatively impact the images is therefore important. Evaluating the patient's pain level and using positioning devices to decrease discomfort may assist in decreasing motion. To reduce motion in the legs and feet, a Velcro strap is usually placed around the patient's feet at the ball of the foot. This allows the patient's feet to relax yet be supported motionless during the scan. In some cases where very fine details (i.e., metacarpophalangeal joints) are being evaluated, further patient immobilization may be useful [22].

The uEXPLORER has available vendor-provided respiratory and cardiac gating capabilities. The respiratory gating utilizes a compression-sensitive respiration belt, which is attached firmly to the subject's chest. The cardiac gating uses a three-lead EKG for cardiac cycle estimation. The vendor-provided reconstruction software then allows flexible incorporation of the gating signals with user-defined settings. However, this has not yet been implemented into routine clinical or research protocols at our institution.

At our institution, data-driven methods of motion correction have been implemented in a research setting for both respiratory and cardiac motion correction, with promising results [23, 24]. Data-driven methods of motion correction are especially advantageous for high-sensitivity total-body PET and could provide effective solutions for future clinical and research applications. Another future direction for total-body PET motion correction may utilize the LYSO background radiation to measure subject motion during the PET acquisition, although this may be more difficult to implement without hardware or software modifications [25].

References

1. Spencer BA, Berg E, Schmall JP et al (2021) Performance evaluation of the uEXPLORER Total-body PET/CT scanner based on NEMA NU 2-2018 with additional tests to characterize long axial field-of-view PET scanners. J Nucl Med 62:861–870

2. Badawi RD, Shi H, Hu P et al (2019) First human imaging studies with the EXPLORER

total-body PET scanner. J Nucl Med 60:299–303

3. Sui X, Liu G, Hu P et al (2021) Total-body PET/computed tomography highlights in clinical practice: experiences from Zhongshan hospital, Fudan University. PET Clinics 16:9–14

4. Nardo L, Abdelhafez YG, Spencer BA et al (2021) Clinical implementation of Total-body PET/CT at University of California, Davis. PET Clinics 16:1–7

5. Conti M, Bharkhada D, Cabello J et al (2020) Design considerations for an ultra-long axial FOV PET/CT scanner. J Nucl Med 61(suppl 1):314

6. Karp JS, Viswanath V, Geagan MJ et al (2020) PennPET Explorer: design and preliminary performance of a whole-body imager. J Nucl Med 61:136–143

7. Pantel AR, Viswanath V, Daube-Withersponn M et al (2020) PennPET Explorer: human imaging on a whole-body imager. J Nucl Med 61:144–151

8. Zhang X, Cherry SR, Zhaoheng X et al (2020) Subsecond total-body imaging using ultrasensitive positron emission tomography. Proc Natl Acad Sci 117:2265–2267

9. Azghadi S, Abdelhafez Y, Parikh M et al (2021) Detectability rates and impact on management from high-sensitivity Total-body 18F-Fluciclovine PET/CT scans in patients with prostate cancer biochemical recurrence. International Journal of Radiation Oncology Biology Physics 111:e264–e265

10. Abdelhafez Y, Hunt H, Caudle DT et al (2021) Ultra-low-dose total-body 18F-FDG PET/CT in patients with autoimmune inflammatory arthritis: evaluation of image quality with shorter scan time. J Nucl Med 62(suppl 1):1697

11. Vera DB, Schulte B, Henrich T et al (2020) First-in-human total-body PET imaging of HIV with 89Zr-VRC01 on the EXPLORER. J Nucl Med 61(suppl 1):545

12. Coelho Alves Costa G, Spencer BA, Omidvari N et al (2021) Radioembolization dosimetry with Total-body 90Y PET. J Nucl Med 63:1101. https://doi.org/10.2967/jnumed.121.263145

13. Wang G, Nardo L, Parikh M et al (2021) Total-body PET multiparametric imaging of cancer using a voxel-wise strategy of compartmental modeling. J Nucl Med 63:1274. https://doi.org/10.2967/jnumed.121.262668

14. Li EJ, Spencer BA, Schmall JP et al (2021) Efficient delay correction for total-body PET kinetic modeling using pulse timing methods. J Nucl Med 63:1266. https://doi.org/10.2967/jnumed.121.262968

15. Nadig V, Herrmann K, Mottaghy FM et al (2021) Hybrid total-body pet scanners—current status and future perspectives. Eur J Nucl Med Mol Imaging 49:445. https://doi.org/10.1007/s00259-021-05536-4

16. Leung EK, Berg E, Omidvari N et al (2021) Quantitative accuracy in total-body imaging using the uEXPLORER PET/CT scanner. Phys Med Biol 66(20):205008

17. Jones T (1996) The imaging science of positron emission tomography. Eur J Nucl Med 23:807–813

18. Wall BF (2009) Ionising radiation exposure of the population of the United States: NCRP Report No. 160. Radiat Prot Dosim 136(2):136–138

19. Nguyen M, McBride K, Hunt H et al (2021) Temporal and axial quantitative uniformity measurements of total-body PET systems. J Nucl Med 62(suppl 1):3041

20. Hunt H, McBride K (2021) Tranquilty scoring to optimize pediatric imaging and reduce radiation exposure on total-body pet scanners. J Nucl Med 62(suppl 1):3018

21. McBride K, Hunt H, Rusnak M et al (2021) Bolus injection technique for uEXPLORER 18F-FDG PET/CT dynamic scans. J Nucl Med 62(suppl 1):3084

22. Hunt H, Nguyen M, Caudle DT et al (2020) Considerations for positioning arthritic patients on the uEXPLORER Total-body PET/CT system. J Nucl Med 61(suppl 1):3125

23. Berg E, Revilla EM, Abdelhafez YG et al (2020) Framework design for comprehensive patient motion compensation in total-body PET. Paper Presented at the IEEE Medical Imaging Conference, Virtual Conference, 5 Nov 2020

24. Sundar LS, Iommi D, Spencer B et al (2021) Data-driven motion compensation using cGAN for total-body [18F]FDG-PET imaging. J Nucl Med 62(suppl 1):35

25. Omidvari N, Berg E, Cheng L et al (2021) Utilization of lutetium background radiation for motion correction in total-body PET Paper Presented at the IEEE Medical Imaging Conference, Virtual Conference, 21 Oct 2021

Chapter 22

Combined PET/MR: Where Anatomical Imaging Meets Cellular Function

Drew R. DeBay and Kimberly D. Brewer

Abstract

Recent technological advances in medical imaging have allowed for both sequential and simultaneous acquisition of magnetic resonance imaging (MRI) and positron emission tomography (PET) data. Simultaneous PET/MRI offers distinct advantages by efficiently capturing functional and metabolic processes with co-localized, high-resolution anatomical images while minimizing time and movement. We will describe some of the technical and logistic requirements for optimizing sequential and simultaneous PET/MRI in the preclinical research setting.

Key words Magnetic resonance imaging (MRI), Positron emission tomography (PET), Hybrid imaging, Sequential acquisition, Simultaneous acquisition, Preclinical imaging, Image registration, Image calibrations, Image corrections, PET/MR workflow

1 Introduction

Hybrid imaging refers to technologies that combine two or more imaging modalities. PET/CT (computed tomography) has been a standard hybrid imaging technique used in both clinical and preclinical studies for many years. Recent technological advances in PET hardware, such as photomultiplier tubes (PMTs) incorporating solid-state systems like avalanche photodiodes (APDs) [1–3] and silicon photomultipliers (SiPMs) [4–9], have not only led to next-generation PET systems, but have spurred the development of new hybrid imaging tools, particularly PET/MRI [10].

MRI is a common clinical modality yielding impressive high-resolution soft tissue contrast for a number of disease indications [11]. However, MRI is not limited to anatomy. MRI offers multi-faceted image contrast including, but not limited to, diffusion (e.g., diffusion tensor imaging or DTI), perfusion, functional MRI, T_1-shortening, and chemical exchange saturation transfer, providing opportunities for immediate sequential monitoring of

multiple processes in the same subject. While many of those processes are often measurable with no external contrast agent, a wide range of MRI probes have been developed to further enhance possible contrast mechanisms. These probes are non-radioactive, stable, easy to transport, readily available, and often used in the clinic, and though they have historically suffered from low sensitivity compared to PET [11], advances in pulse sequence and chemical design methodologies have yielded probes that can be used at reasonable concentrations in animals and humans.

PET/MRI is creating new opportunities for multiparametric analysis with rational probe combinations and advanced imaging acquisition workflows [12–18]. As detailed elsewhere in this book, PET has exquisite sensitivity and an ability to quantify radiotracer uptake. PET/MRI can therefore combine radiotracer quantification with the multiparametric data obtainable from MRI. Quantitative PET becomes more powerful when combined with MRI, as the addition of high-resolution anatomical data allows for co-localization of radiotracer concentrations to smaller substructures. It is also possible to look for correlations of radiotracer concentrations with other physiological parameters as measured by MRI.

Sequential PET/MRI has been possible for several years and requires users to transfer or move samples from the MRI to PET scanner (or vice versa) and co-register or perform necessary corrections in post-processing. However, imaging protocols can vary significantly from lab to lab, and their utility is limited for radio-isotopes with short half-lives, or for temporally correlating functional/metabolic processes characterized with both MRI and PET imaging. Simultaneous PET/MRI does not have these limitations, as both scans are acquired at the same time using hardware with a common isocenter but requires more advanced imaging equipment not available in all labs.

Here, we will discuss recommended materials and procedures for executing both sequential and simultaneous PET/MRI, ranging from pre-scan calibrations to image post-processing. We have tested these procedures in a number of oncology imaging studies, including both ovarian and cervical cancer models (Fig. 1).

The primary choice of simultaneous versus sequential PET/MRI is based on availability of equipment, that is, an integrated PET/MRI system or a PET/MR insert. Currently, most preclinical PET inserts for simultaneous PET/MRI use SiPMs. SiPMs can be seen as an array of submillimeter APD elements connected in parallel and operating in Geiger-mode [5, 6]. They are considered to be an excellent substitute for PMTs. Like a PMT, SiPMs have better signal-to-noise (SNR) and timing properties than APDs, but they are insensitive to magnetic field, which opens their use for PET/MRI. Additionally, SiPMs
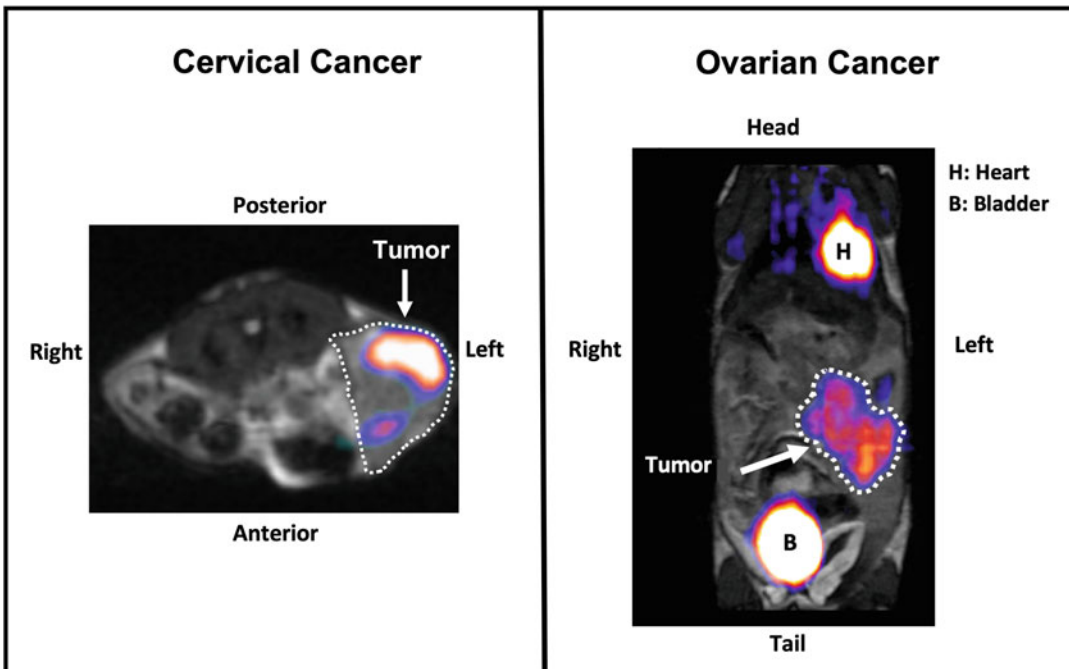
Fig. 1 Sample PET/MRI data from cervical and ovarian cancer studies. Both studies used [¹⁸F]-2-fluorodeox-yglucose (FDG). Left: C57BL/6 mouse implanted with C3 cervical cancer model in left flank (*see* Ref. [47] for mouse/tumor model/MRI details). Imaging was performed 21 days post-implant. While tumor is easily visualized on MRI, PEt allows for monitoring the necrotic core at center of tumor, common in this tumor model. Right: HHD mouse implanted with epithelial ovarian cancer cells directly into the ovary (*see* Ref. [48] for details on mouse/tumor model and PET/MRI). Imaging was done 42 days post-implant. This orthotopic tumor model is difficult to visualize with MRI alone, but it is easily localized with the addition of PET

have a smaller form factor than conventional PMTs, which has distinct advantages for creating physically smaller preclinical imaging systems.

Simultaneous PET/MRI is preferred for a number of reasons. The workflow for simultaneous PET/MRI is much easier with no transport of the animal between scans, allowing for less rigorous registration and image post-processing routines, and acquiring both PET and MRI scans simultaneously saves considerable amounts of time. However, if equipment is not available for simultaneous imaging, sequential PET/MRI is also a viable alternative. Movement of the subject should be minimized between the PET and the MRI to conserve anatomical orientation, which is very helpful when it comes to image registration between modalities in post-processing. Some PET/MRI scanners have the PET ring mounted on the front of the MR scanner, so it is outside of the magnetic field and not considered "simultaneous" MRI since scans are done separately, but still in the same holder and animal transport system. This usually restricts movement for registration to a single plane, improving overall reproducibility and registration accuracy.

2 Materials

1. Integrated PET/MRI system, or PET insert purpose-built for insertion into an MRI.

2. Physiological monitoring system. For optimizing PET acquisition, we recommend a minimum of both temperature and respiration monitoring, as previous work has shown variability of these parameters can significantly affect metabolism and therefore PET quantitation [19–21]. Additionally, maintaining an optimal range for body temperature and respiration rate (surrogate measures of subject's plane of anesthesia) will promote consistent physiology and limit the prospect of motion artifact for both PET and MRI acquisitions.

3. MRI-compatible animal holder/bed. For sequential PET/MRI, this must be able to contain the animal in both scanners without requiring the animal to be repositioned. Some of the more advanced animal holders being developed involve fully sealing the animal within a holder that can be more easily moved between scanners [22]. Animals can then be prepared in a separate room from the scanners, which can be useful for high-volume imaging facilities, and for minimizing exposure to pathogens in certain research applications. These holders often allow a more controlled environment for the animal, which can improve reproducibility of positioning, and also help to maintain optimal physiology and limit motion artifact during scanning.

4. Registration sample. This is particularly helpful for sequential PET/MRI to facilitate fusion of the PET and MRI acquisitions. We recommend using a small capillary tube or spherical phantom filled with both the radioisotope of interest and an MR-visible substance. Manganese or gadolinium-doped water [23] is preferable for ensuring relaxation times similar to tissue. The radioisotope activity level in the capillary tube should be less than ½ or 1/3 of the likely activity in the field of view, which may require some prior testing. Too much activity in the field of view in non-essential regions can interfere with data visualization post-processing, requiring more extensive modification or trimming of images. To maximize logistics, we recommend tubes that can be easily swapped out for each scan, or a tube that will last for several scans. The exact size and position of the registration phantom will be governed by the avoidance of anatomy of interest in a particular application. Prepare a 160×10^{-6} M concentration of $MNCl_2$ as a stock solution. In a small vial, pipette a volume of $MNCl_2$ that you expect to

occupy the volume of capillary tubes or other phantom used. As one example, a general purpose capillary tube (e.g., (1.15/1.5)mm (ID/OD), 75 mm length) can be scored (using a small file) to desired lengths (e.g., 30 mm and 15 mm) and arranged as two intersecting tubes along the axial and trans-axial extent of the animal bed. Radioisotope activity (following the <1/3 rule above) can then be mixed within the small $MNCl_2$ vial. Place capillary tubes in this $MNCl_2$/radioisotope mixture to take up the liquid mixture, seal both ends with clay, and assay/record the activity level using a dosimeter. Tape the capillary to the animal bed prior to imaging in the intersecting configuration indicated above.

Some vendors offer integrated registration markers and auto-registration routines between modalities and other scanner configurations with precise bed positioning that may permit use of an established set of coordinate transformations via a separate registration calibration that can be applied to fuse PET and MRI acquisitions. In this instance, a rotationally asymmetric set of three capillary tubes can be arranged along each imaging plane filled with a mixture of radioisotope and doped water for combined PET/MRI visibility.

5. Radiotracers. The most commonly used and readily available radiotracer is [^{18}F]-2-fluorodeoxyglucose (FDG); however, any PET tracer can be used. This includes but is not limited to a variety of ^{18}F, ^{11}C, and ^{89}Zr probes. These tracers are usually injected via the intravenous tail vein.

6. MRI contrast agents. Depending on the sequences of interest (*see* Subheading 3.3 Sequences), it may be necessary to inject a contrast agent to provide additional information. This includes but is not limited to gadolinium (Gd) and superparamagnetic iron oxide (SPIO) agents. These agents can be added during or prior to scanning.

7. Catheters. If injections of radiotracers must be done during scanning, or while the animal is positioned in such a way that limits access to the tail, a catheter can be used. These catheters are available commercially or can be fashioned in-lab using 30-gauge ½ inch needles (for mice) or 24-gauge ½ inch needles (for rats) and micro tubing (0.025 inches outer diameter and 0.012 inches inner diameter). The tubing should be the minimal length necessary for access mid-scan. Unfortunately, for simultaneous PET/MRI, this can often be quite long, adding excess liquid volume in tubing that must be pushed into the animal. This tends not to be a problem in rats, where it is possible to inject over 1 mL via tail vein, but in mice is a severe limitation where it is only possible to inject 200 μL.

3 Methods

3.1 PET (Pre-scan): Image Quality, Calibrations, and Data Corrections

PET image fidelity is influenced by various physical factors related to the PET scanner hardware, electronics, and more generally, by the nature of coincidence detection, which is susceptible to signal attenuation and undesirable scattered and random coincidences. Metrics used to characterize PET system performance are well established [24, 25] and include measures of (i) spatial resolution; (ii) sensitivity; (iii) signal-to-noise ratio (SNR); (iv) uniformity and performance of applied attenuation and scatter corrections; (v) signal loss at high activities due to detector deadtime; (vi) a noise equivalent count rate (NECR), which reconciles system data corrections of random and scattered coincidences; and (vii) quantitative accuracy of applied attenuation and scatter corrections.

It should be noted that, prior to new technological developments, operating a PET insert within a magnetic field would not be possible. The magnetic fields would interfere with signals from the traditional photomultiplier tubes, resulting in distorted images. Current MR-compatible PET inserts have been designed such that, if all calibrations are done properly, there is no difference in image quality inside or out of the magnetic field, avoiding concerns about effects on image quality. However, these PET systems still require the same corrections as stand-alone PET scanners. For optimal PET scanner performance, a number of routine calibrations and quality control measures are required to mitigate certain performance-degrading characteristics that can be observed in PET imaging.

Normalization—Inherent variations in count rate efficiencies exist between the many thousands of detector elements within a PET scanner. Slight differences in scintillator thickness, light emission, electronics performance, or scintillator ring geometries can alter the detector response to emitted photons [26–28]. The resulting count rate variance between detector lines of response (LORs) at identical activities ultimately compromises the uniformity that can be achieved by the system. Normalization scans are thus performed to determine detector response for all LORs of a scanner and generate a normalization file that can be applied to all acquired data prior to reconstruction in order to correct for this non-uniformity [26–28].

Generally speaking, this procedure involves irradiating the entire PET detector field of view (FOV) with an activity source for a pre-defined number of counts or scan duration (typically long duration scans over several hours to generate high count statistics). Sources could include a ^{68}Ge line source, or a cylindrical or annulus phantom filled with ^{18}F. Normalization scans should be carried out after any scanner hardware changes, at major servicing intervals, or any time that there is a decrease PET image quality or performance

that suggests system uniformity has been compromised. Each PET system vendor will outline protocols and provide recommendations as to the best normalization procedures to follow for their system.

Quantitative Calibrations—The intrinsic output registered by a PET scanner is decay counts or count rate. When corrected for scatter, attenuation, and tracer decay, a reconstructed PET image voxel represents an intensity that is proportional to radioactivity concentration [26, 27]. For direct quantitation of PET data, quantitative calibrations are carried out to compute voxel values that reflect absolute radiotracer concentration (an activity per unit volume, such as MBq/mL). Quantitative calibrations amount to determining an accurate cross-calibration factor between the PET scanner and the specific dose calibrator(s) used to assay injected doses to the subject in the PET imaging workflow. This cross-calibration can then be applied to reconstructed PET data for quantitation. Once carried out, quantified PET data are often expressed as an activity concentration (MBq/mL), a percent injected dose *per* unit volume (%ID/cc) often used for evaluating tracer kinetics [29], or the semi-quantitative standardized uptake values (SUVs) that reflect tracer concentration in a particular volume of interest normalized to the injected dose per body weight of a subject [30].

Quantitative calibration generally involves performing a PET scan of a uniform cylinder of known radiotracer activity and volume and measuring the total counts generated in a representative region of interest on the PET image. From this, a simple calibration factor is generated to convert the voxel intensity of an image to a calibrated activity per unit volume [26–28]. The quantitative accuracy achieved with PET imaging relies heavily on careful execution of these quantitative calibrations; failure to do so can adversely affect the quantitative precision achieved by the system. Quantitative calibrations should be carried out daily or weekly (at minimum) during studies, in order to capture scanner performance on a given imaging day. If using a PET/MRI system that has a PET insert, quantitative calibrations must be done with the insert inside of the MRI system. Ideally, the uniform cylinder used for quantitative calibrations should also be placed on the animal holder to optimize reproducibility.

From the PET equipment perspective, quantitative calibrations should be carried out for each dose calibrator used in the PET workflow (if more than one exists) and should be updated upon dose calibrator calibration (which should be carried out regularly, per the manufacturer's recommendations). Quantitative calibrations should also be generated for each isotope used for imaging (i.e., ^{18}F and ^{11}C), and for protocol-specific applications at the anticipated activity level, scan duration, and reconstruction protocol used for PET imaging. However, the addition of a large magnetic field and varying other pieces of equipment, including

radiofrequency coils, complicates these calibrations. Quantitative calibrations should be done for each RF coil if the RF coil sits between the PET detector and the animal. This is important not only for RF coils used for different animals but also for RF coils that are designed for specialized body parts (i.e., brain vs. abdomen).

It is also important to perform quantitative calibrations at routine intervals to ensure the reproducibility of the calibration over time. If the system calibrations are updated, new quantitative calibrations should also be generated. If there is evidence that the magnetic field may have drifted significantly, the calibrations should be repeated. Some of the newest MR systems are cryogen free and can be brought up to field quickly using electrical power. If there has been a planned (or unplanned) quench of the field on one of these systems, the quantitative calibration scan should be repeated. The quantitative calibration cylinders used should remain consistent. The same type of vessel (i.e., plastic syringe vs. glass vial) should always be used during the dose draw assay of the calibration. If not consistently applied, dose measurement can be differentially attenuated and can cause a significant drop in measurement accuracy. It is also important to ensure the clocks of the PET scanner workstation and dose calibrator are synched to the same date and time to accurately account for isotope decay between dose calibrator and PET measurements.

3.2 MR (Pre-Scan): Image Quality, Calibrations, and Data Corrections

Compared to PET, MRI does not require the same precise calibrations and corrections prior to scanning. Many MR sequences have their own calibrations built in and are optimized for their own contrast and purposes (e.g., calibration of RF transmit power or receiver gain) that are not affected by the presence of PET scanning. The primary concerns for MR imaging quality when adding a PET insert are due to (1) distortion of the main magnetic field, and (2) electronic noise.

Adding anything into a large magnetic field, including the animal or sample being imaged, will cause distortion to the field itself. Active magnetic field shimming, which uses small electric currents to generate magnetic fields in a variety of orientations, has been in use for decades to compensate for these distortions and improve field homogeneity. However, there are limits to active shimming, and using magnetic materials in PET inserts would result in grossly distorted fields. Most of the materials in the PET insert are therefore specially designed to avoid this distortion, and the insert is also generally encapsulated in a RF shield [31]. Shimming is often automated to maximize signal in the area of interest and state-of-the-art PET inserts should not cause any major distortions. However, field mapping can be done for testing purposes if artifacts appear which could be linked to field distortion or signal drop out. This could indicate hardware issues within the insert or a failure in the shield.

Electronic noise in MR images due to a PET insert is also a concern. If not properly shielded, the electronics within the PET insert will generate radiofrequency signals that will be detected by the RF coil. Depending on the type of noise, this could manifest in a variety of ways in MR images. A single frequency unexpectedly picked up by the RF coil could manifest as spike or zipper artifacts [32] depending on the pulse sequence. This should not be a problem that occurs in fully functioning systems, but if MR artifacts linked only to PET scanning begin to occur, the structure of the RF shielding in the insert and cables should be examined.

3.3   Scanning

For the purposes of the following steps, we will describe the recommended procedures for scanning mice, as these are the most commonly used preclinical model. The procedures should be virtually identical for other models such as rats and hamsters, with the exception of a more restricted field of view compared to the total animal size. However, if there may be deviations necessary due to size, we will note this.

Workflow Scheduling—For simultaneous PET/MRI, it is recommended to begin MR scanning first, since it requires more time and can take place during PET tracer uptake. Simultaneous PET/MRI can also be used for dynamic scans to simultaneously measure things such as perfusion (MRI) and initial radiotracer uptake (PET). For sequential PET/MRI, the choice of which modality to use first will depend on certain considerations, including (1) whether the facility is trying to minimize radioactivity within the MRI scanner, (2) the timing and availability of the radiotracer for injection, and (3) decay rate of the radiotracer (^{11}C tracers have a very quick decay rate and very tight timeline).

Figure 2 includes potential workflows for both simultaneous and sequential PET/MRI for static and dynamic imaging (based on Fig. from Ref. [3]). Static imaging occurs after injection and uptake of a radiotracer (or contrast agent), with a single PET (or MR) image permitting quantification and depicting the spatial distribution of the tracer (or contrast agent) at a given time. Dynamic imaging involves continuous scanning during radiotracer/contrast agent administration and uptake, providing an evaluation of tracer/contrast agent concentration as a function of time and, ultimately, insight into the pharmacokinetics of the tracer/contrast agent.

Registration Phantom—Prior to preparing the mouse, it is recommended that a small capillary tube or other phantom be prepared that can be used for registration. The sample should be placed in the animal holder within the field of view (FOV) of both PET and MRI but should be sufficiently distanced from the area of interest of the scan, to minimize signal "spill-in" to voxels of interest (*see* Subheading 2, **item 4** above for detailed phantom information).
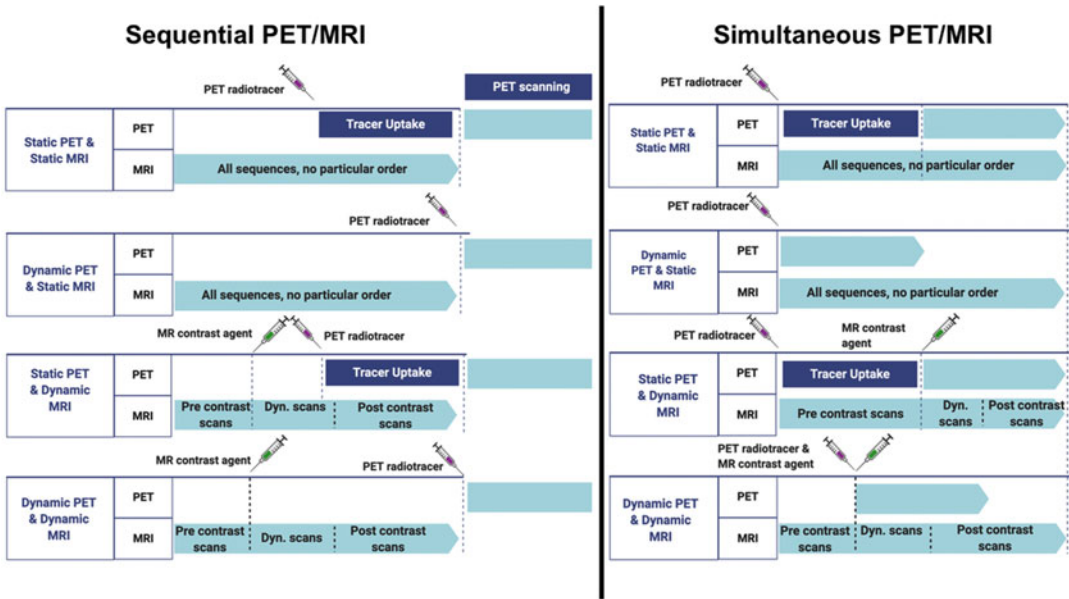
Fig. 2 PET/MRI workflows for sequential (left) and simultaneous (right) PET/MRI, including static and dynamic imaging protocol implementations (based on Figure from Ref. [3], made in BioRender.com). For sequential imaging, workflows assume MRI first for optimal time savings, but it is equally possible to execute PET scanning first with added tracer uptake prior to imaging for static PET studies

Radiotracer Injection—For many PET/MRI scans, mice will receive radiotracer injection prior to being placed in the animal bed, with uptake corresponding to preparation time and time used for MRI scans. High-resolution and specialized MRI scans are often lengthier than PET scans. In these cases, we recommend injecting mice outside of the scan room and then inserting them in the holder. In situations where radiotracer injection must be done when mice are within the PET scanner, the animal must be catheterized prior to imaging. It should be noted that it is very difficult to take a bolus injection machine near a traditional MRI scanner due to the field extending beyond the magnet casing. This may restrict the types of injection being done. Newer magnets, particularly cryogen-free models, often have much smaller stray fields, allowing the use of specialized machinery closer to the magnet.

Anesthesia—Mice can be anesthetized prior to or postinjection, depending on researcher comfort. Tail vein injections are often more difficult in anesthetized mice. Due to stability and ease of modification, we recommend using an inhalable anesthetic like isofluorane or sevoflurane for all imaging studies unless there is a crucial scientific reason or disease basis [21]. Combined with a carrier gas such as oxygen or room air, these inhalable anesthetics result in much stable respiration on behalf of the animals and are safer for longer and/or repeated imaging studies. Depending on the region of interest being studied, additional immobilization may

be added to reduce the likelihood of motion or shifting of the animals. For optimal immobilization, the head, torso, and feet should all be immobilized in some fashion. Immobilization can be done by taping regions of the animal to the bed. For the torso, this would involve using a large piece of tape that attaches to each side of the bed and goes over the animal, pushing it down snugly, but not so much that it restricts natural breathing. If the animal is snugly placed on the bed, it will also result in better physiological monitoring.

Physiological Monitoring—Once the animal is anesthetized, physiological monitoring cables can be affixed. While electrocardiogram (ECG) monitoring can be very useful, we recommend it only if absolutely necessary for advanced MRI analysis (e.g., correlating imaging with cardiac cycles to correct for motion artifacts) since it can also cause image artifacts. Due to the length of most PET/MR imaging studies, respiration monitoring should be used for animal safety and to assess anesthesia depth. The anesthesia regime, including depth, can impact metabolic processes [21] and therefore affect radiotracer uptake. A respiratory bellow/pillow, placed beneath the abdomen of animals in prone position, is the most common choice.

Temperature monitoring is often not strictly required for animal welfare purposes (depending on the length of scans, warming setup, and operator confidence in system stability), but it can be crucial for reproducibility in advanced quantitation [19]. As with anesthetic depth, variations in body temperature can drastically affect metabolic rates, often in unpredictable ways with new radiotracers. Mice are particularly vulnerable to rapidly changing temperatures due to unstable thermoregulation under anesthetic and will die if they get too cold. For scans longer than 15 min, a warming system should absolutely be used. When using forced air warming systems to keep mice at 37 °C, we also recommend that the ears and tail are covered with gauze or plastic to prevent drying, especially if a tail catheter is being used and/or longitudinal imaging is being done. Mice tails and ears are extremely fragile and can dry out and burn very easily.

MRI Sequences—The choice of MRI sequences depends upon the precise scientific question being asked in the experiment and whether the MRI is being used for (a) anatomical images only, (b) generation of an attenuation map, (c) study of a particular physiological parameter (diffusion, perfusion, functional MRI, chemical exchange, etc.), or a combination of all three. A full study of MR sequences is beyond the scope of this work (*see* Ref. [33] for more comprehensive information), and we will focus on some of the most common sequence types.

Those unfamiliar with MRI should be aware that there is always a fundamental trade-off related to the use of the collected MR signal. There is a fixed maximum amount of signal available,

which can only be increased with modified hardware such as a higher magnetic field or the use of hyperpolarization. The three parameters in conflict over the use of this signal are the spatial resolution, scan time, and SNR of the image. Faster, higher-resolution scans will be starved for signal and will appear grainy, making them less useful for combination with PET. As such, MRI scans with sufficient signal and SNR for small animals such as mice are usually much longer than PET and, as mentioned previously (Fig. 2), workflow scheduling should take this into account. For simultaneous acquisitions, this is not a problem and combining the PET with the MRI often saves considerable time overall. But for sequential scanning, the scan time must be considered in concert with the necessary uptake time of the radiotracer prior to PET, along with its radioactive decay.

MR sequences for high-resolution depiction of soft tissue anatomy are commonly used in PET/MRI studies. Most basic studies will obtain either a T_1-weighted sequence, such as a gradient recalled echo (GRE) [34], or a T_2-weighted sequence, such as a rapid acquisition with relaxation enhancement (RARE) [34], or both. T_1-weighted sequences can be chosen to maximize spatial resolution and tissue contrast, particularly gray-white contrast in the brain. T_2-weighted sequences are generally used to evaluate potential pathology in tissues, such as brain tumors. Exact parameters will depend on the field strength of the magnet and the presence of such equipment as multi-channel RF coils, with higher resolution and shorter scans possible at higher fields such as 7.0 T and with newer equipment. However, even at low field strengths of 1.0–1.5 T, it is possible to get resolution on the order of 300 μm, although these scans may take longer to yield sufficient SNR.

Another popular choice for high SNR at lower field strengths is a sequence called balanced steady-state free precession (bSSFP) [35]. This sequence has a mix of T_1 and T_2 contrast and may not be suitable for distinguishing certain tissue types, but due to its high SNR efficiency, it can yield three-dimensional, high-resolution images (i.e., 150 μm or less) more quickly at lower field strengths, such as 3.0 T, making it a strong choice for an anatomical underlay.

MR sequences appropriate for use with attenuation correction algorithms (see post-scan corrections for more details on attenuation correction) tend to either be atlas-based or primarily proton density-weighted [36]. Generally, a short echo time (TE) and long repetition time (TR) in a gradient echo sequence will yield proton density contrast by minimizing T_1 and T_2 contributions. Further modifications include the use of Dixon's method for fat/water separation, which can be used to assign attenuation correction values based on the MR segmentation of water and fatty tissues [37], as well as the use of ultra-short TE (UTE) MRI sequences for more accurate delineation of bone, air and soft tissue [38].

Aside from these PET considerations, a discussion of the large variety of potential MR pulse sequences for studying physiological parameters is beyond the scope of this chapter. However, PET/MRI users are strongly encouraged to consider the use of MRI beyond simply an anatomical underlay. MRI alone has the potential for multiparametric imaging of several physiological parameters, which are not accessible by other imaging modalities (such as diffusion and chemical shift) [33]. These additional scans can often be added to an imaging protocol with minimal impact on the duration of a scanning session and can help maximize informational yield.

3.4   Post-Scan

1. *PET Attenuation Correction*—The attenuation of 511KeV photons within tissues of a scan subject is a significant physical factor that can affect PET image fidelity and quantification accuracy. Attenuation correction methods can be applied to address this by generating separate attenuation coefficient maps, effectively a classification that reflects differences in electron density of tissues in the scanner field of view [26, 28, 39]. Registration of the attenuation correction map and target PET data set permits mathematical correction of these attenuation effects.

   Historically, PET-only scanner configurations performed attenuation corrections based on transmission reference scans using an external rotating ^{68}Ge rod source during and after a subject's PET scan. The advent of hybrid PET/CT scanners enabled the use of low-dose CT scans to generate attenuation maps that can be equivalently scaled to reflect 511KeV attenuation observed in PET [39]. For PET/MR, specialized MR-based attenuation correction approaches have gained utility in recent years. The convenience of simultaneous PET/MR imaging favors MR-based attenuation correction methods; however, the registration and application of separate CT-based attenuation maps is certainly possible if CT is also a part of the PET imaging workflow. Many of the current PET, PET/CT, or PET/MR systems offer built-in attenuation correction methods that are available within the vendor's acquisition and reconstruction software.

   There has been much discussion about whether attenuation correction is necessary for PET/MRI of small animals, particularly mice, due to the small volume and limited attenuation through tissue. For qualitative metrics, it is likely unnecessary, but previous work has demonstrated that, without attenuation correction, quantitative results are underestimated by up to 20% in mice and up to 40% in rats [40, 41]. It is therefore highly recommended to use at least a simplified attenuation correction with PET/MRI, regardless of the source of the attenuation correction (e.g., derived from MRI, CT, or the PET itself).

2. *Scatter, Random Coincidence, and Deadtime Correction*—A PET system with good energy resolution and narrow photopeak energy window and coincidence timing resolution can diminish the effects of scatter and random coincidences [28]. The majority of scanners available today implement a variety of algorithms to calculate and subtract residual scatter and random coincidences, and correction for detector deadtime with signal pileup at high activities providing an estimate of true coincidence events (*see* Ref. [26] for a more thorough treatment of these techniques). These built-in routines provided by the vendor can be applied in post-processing pipelines or are integrated into certain reconstruction strategies and are not significantly affected by the addition of MRI.

3. *PET Reconstruction*—Once PET data are acquired, mathematical algorithms are employed to generate images representing the spatial distribution of radiotracer emissions from the subject within the scanner. There are two main types of image reconstruction in PET, namely, *analytical* and *iterative* reconstruction techniques, which can be applied in 2D or 3D implementations [26, 28, 42].

Conventional reconstruction approaches use *analytical* techniques to reconstruct tomographic PET data. In nuclear medicine, the most ubiquitous is the filtered back projection (FBP) method. The advantages of FBP techniques include relatively fast processing speed that can often achieve high quantitative accuracy [26, 42, 43]. In instances of low count statistics applications, FBP can suffer from streak or star-like artifacts and blurring from the filtering step, resulting in decreased overall image resolution [26, 28, 43]. FBP, on its own, neglects to compensate for some important physical corrections such as random and scatter PET corrections, which would need to be applied independently.

With the advent of faster computer processing speeds in recent years, *iterative* reconstruction approaches have emerged as viable alternatives to analytical methods, offering improvements in spatial resolution and reduction of image noise [28]. In general, these methods start with an initial prediction of some simplified radiotracer distribution, whose constituent projections are then derived by the process of forward projection [26, 39] over successive iterations.

Common iterative algorithms include Maximum Likelihood Expectation Maximization (MLEM) and Ordered Subset Expectation Maximization (OSEM). Advantages of MLEM include the maintenance of spatial resolution with minimal noise amplification in reconstructed images, with the disadvantage of longer processing times due to the often large number of iterations necessary to converge on suitable reconstructed images [27, 42]. OSEM is an adaptation of MLEM that introduces grouped subsets of uniformly

distributed projection data into the algorithm, which are applied to an updated target function at each iteration. The result is accelerated processing time with fewer iterations required to converge on an appropriate solution [27, 42].

Iterative reconstruction methods offer higher contrast images with improved spatial resolution and reduction of noise compared to analytical methods. Additionally, corrections for scatter and attenuation can be integrated directly into these iterative algorithm computations, which is often advantageous. However, iterative methods are computationally expensive and may not be practical in some instances where processing time is prohibitive.

In practice, when selecting the appropriate reconstruction technique to apply in a given research application, one should carefully consider the role of imaging in the study design and what information the imaging results intend to provide. The quantitative accuracy of reconstruction methods should be factored into decision-making and, if applicable, the number of iterations and subsets should be evaluated in representative sample datasets when developing imaging and analysis protocols for specific studies. If using high-resolution MRI scans as the anatomical underlay, PET images of higher resolution will be more useful in localizing activity to certain regions. This is also true if trying to correlate PET activity with an MRI physiological parameter. Trade-offs between processing time, quantitative accuracy, contrast, and achievable resolution will need to be weighed when selecting between analytical and iterative PET reconstruction techniques.

4. *PET/MR Registration*—MR images are usually reconstructed immediately following acquisition as part of automated software procedures. For more specialized and higher-resolution scans, reconstruction may be done offline using internal lab algorithms. Regardless, there is no additional consideration necessary for reconstruction of MR images due to the presence of PET. There are, however, steps necessary before PET and MR images can be merged or overlaid.

Prior to registration, it may be necessary to convert either the PET or MR images to a common image file format such as NIFTI [44] or DICOM [44]. Some imaging scanners output data in proprietary image formats, but most will include software for conversion to more common formats. It is also crucial at this stage to ensure that headers for both images have sufficient information, particularly for quantitative calculations (PET and potentially MRI) and resolution (crucial when images must be resampled for overlay). Once both images are in the same format, the PET can be registered to the MRI.

There are a variety of programs available for image registration, including free software such as imageJ (NIH, USA), FSL (Oxford,

UK), and Automated Image Registration (AIR) [45], and more advanced paid software programs such as Vivoquant and PMOD. Some labs prefer to build their own registration/visualization routines in, for example, Matlab or Python (http://www.python.org). There is publicly available code for reading NIFTI and/or DICOM files into both of these environments. Most programs may resample either the PET or the MR image when overlaying images; for visualization purposes, resampling the PET image and overlaying it on the MRI will result in better defined activation localization. While it is unlikely that this resampling will significantly affect the quantification of PET results, researchers may prefer to measure injected dose/cc or MBq/mL from the original unchanged data.

Simultaneous PET/MRI has significant advantages in requiring minimal registration changes when combining images. There may be a standard translation required due to an offset of the PET center compared to the MRI, but more advanced deformations and rotations should not be necessary. However, researchers should be aware that some imaging systems save images in radiological versus anatomical orientation where left and right are reversed. This can be easily identified in some types of imaging but may be missed in others. Even in simultaneous PET/MRI, the addition of the previously mentioned registration phantom can be very helpful for avoiding simple registration pitfalls by identifying necessary automatic translations. If automated registration routines are used, images should be manually checked at least visually before further analysis is done.

Sequential PET/MRI, particularly when the setup necessitates significant movement between the PET and the MRI, may require more advanced registration. This can be particularly problematic in body transforms where motion is more pronounced over even short time scales. In a multi-modality study of inter- and intra-scan movement of the immobilized hind legs of rats, tumors on the immobilized legs moved between 0.2 and 0.3 mm within the 2 h scan and 0.2 mm between scans [46]. While 0.5 mm may not seem like a large distance, in high-resolution MRI, this can be a shift of several voxels. Regions such as lungs and the abdomen will likely undergo even more movement, emphasizing the need for flexible and accurate registration.

Most imaging programs will have advanced registration routines, both manual and automated. These should be closely and carefully adjusted for each animal to minimize errors. Automated routines tend to work best on regions such as the brain but may fail in more deformable body regions.

3.5 Summary Statement

Exploiting the inherent strengths of both PET and MRI modalities, combined PET/MRI enables the acquisition of more comprehensive information about biological systems. As detailed in this chapter and throughout this book, PET can be used to interrogate

cellular function with incomparable sensitivity. MRI offers not only high-resolution anatomical information but can also provide complementary multiparametric information on a variety of physiological processes. Technological advances that enable simultaneous PET/MRI further improve workflow efficiencies, data quality, and, ultimately, provide an enhanced picture of the underlying biological processes of interest than either modality in isolation.

References

1. Pichler BJ et al (2006) Performance test of an LSO-APD detector in a 7-T MRI scanner for simultaneous PET/MRI. J Nucl Med 47:639–647

2. Catana C et al (2008) Simultaneous in vivo positron emission tomography and magnetic resonance imaging. Proc Natl Acad Sci U S A 105:3705–3710

3. Judenhofer MS et al (2008) Simultaneous PET-MRI: a new approach for functional and morphological imaging. Nat Med 14:459–465

4. Degenhardt C, Prescher G, Nuclear TF (2009) The digital silicon photomultiplier—a novel sensor for the detection of scintillation light ieeexplore.ieee.org. https://doi.org/10.1109/NSSMIC.2009.5402190

5. Frach T, Prescher G, Nuclear CD (2009) The digital silicon photomultiplier—principle of operation and intrinsic detector performance. ieeexplore.ieee.org. https://doi.org/10.1109/NSSMIC.2009.5402143

6. Saveliev V, Golovin V (2000) Silicon avalanche photodiodes on the base of metal-resistor-semiconductor (MRS) structures. Nucl Instrum Methods Phys Res, Sect A 442:223–229

7. Roncali E, Cherry SR (2011) Application of silicon photomultipliers to positron emission tomography. Ann Biomed Eng 39:1358–1377

8. Du J et al (2015) Evaluation of linearly-graded SiPMs for high resolution small-animal PET. Biomed Phys Eng Express 1:045008

9. Krizsan AK et al (2015) A promising future: comparable imaging capability of MRI-compatible silicon photomultiplier and conventional photosensor preclinical PET systems. J Nucl Med 56:1948–1953

10. Cherry SR (2009) Multimodality imaging: beyond PET/CT and SPECT/CT. Semin Nucl Med 39:348–353

11. James ML, Gambhir SS (2012) A molecular imaging primer: modalities, imaging agents, and applications. Physiol Rev 92:897–965

12. Afaq A, Syed R, Bomanji J (2013) PET/MRI: a new technology in the field of molecular imaging. Br Med Bull 108:159–171

13. Mannheim JG et al (2018) PET/MRI hybrid systems. Semin Nucl Med 48:332–347

14. Miles KA, Voo SA, Groves AM (2018) Additional clinical value for PET/MRI in oncology: moving beyond simple diagnosis. J Nucl Med 59:1028–1032

15. Antoch G, Bockisch A (2009) Combined PET/MRI: a new dimension in whole-body oncology imaging? Eur J Nucl Med Mol Imaging 36(Suppl 1):S113–S120

16. Rosenkrantz AB et al (2016) Current status of hybrid PET/MRI in oncologic imaging. AJR Am J Roentgenol 206:162–172

17. Kwon HW, Becker A-K, Goo JM, Cheon GJ (2017) FDG whole-body PET/MRI in oncology: a systematic review. Nucl Med Mol Imaging 51:22–31

18. Ye D et al (2014) Caspase-responsive smart gadolinium-based contrast agent for magnetic resonance imaging of drug-induced apoptosis. Chem Sci 4:3845–3852

19. Hankenson FC, Marx JO, Gordon CJ, David JM (2018) Effects of rodent thermoregulation on animal models in the research environment. Comp Med 68:425–438

20. Vanhoutte G, Verhoye M, Van der Linden A (2006) Changing body temperature affects the T signal in the rat brain and reveals hypothalamic activity. Magn Reson Med 55:1006–1012

21. Tremoleda JL, Kerton A, Gsell W (2012) Anaesthesia and physiological monitoring during in vivo imaging of laboratory rodents: considerations on experimental outcomes and animal welfare. EJNMMI Res 2:1–23

22. Yared WI, Wilson AK, Inc VM (2014) Animal holder for in vivo tomographic imaging with multiple modalities. Visen Medical, Inc

23. Hattori K et al (2013) Development of MRI phantom equivalent to human tissues for 3.0-T MRI. Med Phys 40:32303

24. NEMA (2007) Performance measurements of positron emission tomographs: National Electrical Manufacturers Association (NEMA) Standards Publication NU2-2007

25. NEMA (2008) Performance measurements of small animal positron emission tomographs: National Electrical Manufacturers Association (NEMA) Standards Publication NU4-2008

26. Cherry SR, Sorenson J, Phelps M (2012) Physics in nuclear medicine. Elsevier. https://doi.org/10.1016/C2009-0-51635-2

27. Zanzonico P (2008) Routine quality control of clinical nuclear medicine instrumentation: a brief review. J Nucl Med 49:1114–1131

28. Levin CS (2005) Primer on molecular imaging technology. Eur J Nucl Med Mol Imaging 32: S325–S345

29. Van de Bittner GC, Ricq EL, Hooker JM (2014) A philosophy for CNS radiotracer design. Acc Chem Res 47:3127–3134

30. Boellaard R (2009) Standards for PET image acquisition and quantitative data analysis. J Nucl Med 50(Suppl 1):11S–20S

31. Jung JH, Choi Y, Im KC (2016) PET/MRI: technical challenges and recent advances. Nucl Med Mol Imaging 50:3–12

32. Zhuo J, Gullapalli RP (2006) MR artifacts, safety, and quality control. Radio Graphics 26: 275–297

33. Luisa GMM, Pilar LL (2018) Preclinical MRI: methods and protocols; methods in molecular biology, 1718. Humana Press, New York

34. Bernstein MA, King KF, Zhou XJ (2004) Handbook of MRI pulse sequences. Elsevier

35. Scheffler K, Lehnhardt S (2003) Principles and applications of balanced SSFP techniques. Eur Radiol 13:2409–2418

36. Chen Y, An H (2017) Attenuation correction of PET/MR imaging. Magn Reson Imaging Clin 25:245–255

37. Dixon WT (1984) Simple proton spectroscopic imaging. Radiology 153:189–194

38. Hofmann M, Pichler B, Schölkopf B, Beyer T (2009) Towards quantitative PET/MRI: a review of MR-based attenuation correction techniques. Eur J Nucl Med Mol Imaging 36 (Suppl 1):S93–S104

39. Cabello J, Ziegler SI (2018) Advances in PET/MR instrumentation and image reconstruction. Br J Radiol 91:20160363

40. D'Ambrosio D, Zagni F, Spinelli AE, Marengo M (2013) Attenuation correction for small animal PET images: a comparison of two methods. Comput Math Methods Med 2013: 103476–103412

41. Ali EHH, Bodholdt RP, Jørgensen JT, Myschetzky R, Kjaer A (2012) Importance of attenuation correction (AC) for small animal PET imaging. Diagnostics (Basel) 2:42–51

42. Tarantola G, Zito F, Gerundini P (2003) PET instrumentation and reconstruction algorithms in whole-body applications. J Nucl Med 44: 756–769

43. Turkheimer FE, Veronese M, Dunn J (eds) Experimental design and practical data analysis in positron emission tomography. Create Space Independent Publishing Platform, London. ISBN: 978-1-49929-582-5

44. Larobina M, Murino L (2014) Medical image file formats. J Digit Imaging 27:200–206

45. Woods RP, Grafton ST, Holmes CJ, Cherry SR, Mazziotta JC (1998) Automated image registration: I. general methods and intrasubject, intramodality validation. J Comput Assist Tomogr 22:139–152

46. Zhang M, Huang M, Le C, Medicine PZ (2008) Accuracy and reproducibility of tumor positioning during prolonged and multimodality animal imaging studies. iopscience.iop.org

47. Brewer KD et al (2014) Clearance of depot vaccine SPIO-labeled antigen and substrate visualized using MRI. Vaccine 32:6956–6962

48. Tremblay M-L et al (2020) Abstract 384: T cell infiltration into tumors induced by DPX-Survivac combination immunotherapy demonstrated by PET/MRI imaging in an orthotopic ovarian cancer model. Cancer Res 80:384–384

Chapter 23

Quantitation of Oncologic Image Features for Radiomic Analyses in PET

Travis L. Williams, Mithat Gonen, Rick Wray, Richard K. G. Do, and Amber L. Simpson

Abstract

Radiomics is an emerging and exciting field of study involving the extraction of many quantitative features from radiographic images. Positron emission tomography (PET) images are used in cancer diagnosis and staging. Utilizing radiomics on PET images can better quantify the spatial relationships between image voxels and generate more consistent and accurate results for diagnosis, prognosis, treatment, etc. This chapter gives the general steps a researcher would take to extract PET radiomic features from medical images and properly develop models to implement.

Key words Radiomics, PET, Imaging features, Machine learning, Oncology, Analysis

1 Introduction

Radiomics is a fast-growing and continuously evolving field of study involving the extraction of numerous quantitative features from radiographic images [1]. Software algorithms mine these features by analyzing multiple aspects of the images (i.e., physical, textural, histogram, filter-based, and fractal) [1]. The hope surrounding radiomics stems from the long-held view that medical images contain much more information than what is discernible to trained radiologists [2]. Driven by the potential to capture tumor heterogeneity, radiomic signatures derived from subregions of a tumor with differing biological characteristics may identify unexplored phenotypes [3]. Radiomics have been used to characterize tumor phenotypes for predicting prognosis and therapeutic response for various diseases with a variety of imaging modalities [4, 5].

Positron emission tomography (PET) is a vital tool in the armamentarium of techniques used by clinicians for cancer diagnosis and management [6]. Attempts to quantify PET are well documented: Treatment response and patient survival are predicted by standardized uptake value (SUV) of $[^{18}F]$-4-fluorodeoxyglucose (FDG) in several studies [7–11], but these results can conflict [12]. SUV is dependent on multiple factors (patient weight, blood sugar level, FDG injection timing, dose correction, scanner, and image reconstruction algorithm); therefore, SUV alone does not provide consistent and accurate quantitative information [13]. As a consequence, investigators have sought more robust quantitative image assessment that aids clinical diagnosis and treatment evaluation [14]. Radiomics has been explored to address gaps in existing PET metrics by offering complementary metrics on variation in pixel intensity values and spatial relationships between image voxels [2, 15].

Radiomic features can be derived from the PET scan or the associated diagnostic image (CT or MRI) or jointly and used to create predictive and prognostic models. Radiomic features most often capture variability in pixel intensity values, so features extracted from an anatomic image (CT/MRI) are complementary to those extracted from a molecular image (PET). Figure 1 illustrates the normal PET and CT scans juxtaposed with their granular representations of the pixel variation of each for comparison.

This chapter details the basic building blocks of designing a radiomic model from a PET/CT scan so that a researcher new to the field of radiomics could exploit this exciting technology. While radiomics of PET/MRI have been reported, PET/MRI has not reached widespread adoption clinically so the chapter focuses attention on PET/CT methods [16]. The chapter also addresses the current challenges regarding standardization toward the generation of more robust imaging biomarkers.
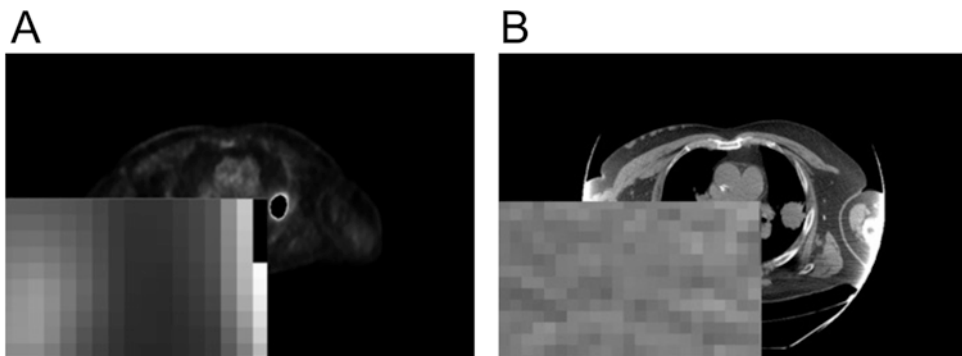
Fig. 1 Pixel variation in both PET (**a**) and CT (**b**), as well as the spatial resolution and voxel intensity differences between the two modalities. Radiomic features extracted from both will have vastly different meanings as a result

2 Materials

2.1 Patient Cohorts

In any imaging study, standard protocols concerning patients and protected health information (PHI) must be strictly adhered to and followed. The anonymization of PHI, having accountability to an institutional review board, and including waivers of informed consent are major examples of protocols to ensure research integrity and fidelity. Clinical factors, set by the research institution, are acquired by reviewing patients' medical records. The criteria for patient inclusion and exclusion should be outlined to explain how the final cohort is formed. Patients should be reviewed for a set duration determined by the research institution, with a second or third cohort from another window of time as a validation set.

2.2 Image Acquisition

Each patient in the protocol has undergone routine imaging whereby PET scans are obtained. The patients are injected with a radiotracer (the most common is fluorodeoxyglucose) and rested for the course of the pharmacokinetics uptake period. The output of these scans is a voxel model, a 3D matrix of raw data expressed as intensity values. Many parameters contribute to the acquisition process, such as voxel size, the specific reconstruction algorithm, and other values of interest for the PET imaging protocols for a particular institution. There is a strong likelihood that the chosen variables will have a significant impact on the computed radiomics features [17, 18]. Certain features are greatly affected, while others are moderately to minimally affected [19], so care should be taken to ensure that the collected images are similarly acquired and reconstructed.

2.3 Preprocessing

The goal of preprocessing the images is to increase the probability of achieving the best, most robust features by reducing noise, emphasizing important features at various scales, thresholding, and resampling the number of bits for the encoding to account for acquisition variability. Spatial filtering methods such as Butterworth, Gaussian, and Laplacian filtering are used to reduce noise or accentuate features [20]. Windowing is applied to create upper and lower bounds for thresholding the data and establishing a set of acceptable values. Typical resampling of the data (usually initially 12–16 bits) compresses it to either four, six, or eight bits prior to feature extraction [20]. Some commercial and open-source software packages for preprocessing mentioned in these studies include: PyRadiomics and MIM Maestro.

2.4 Segmentation

The segmentation of tumor regions of interest (ROI) varies between annotators and studies. Manual segmentation, semi-automatic, and automatic segmentation methods are represented across these studies. The segmentation results are under the supervision of and approved by one or more expert radiologist.

Generally, the resulting segmentations are scaled and normalized, with dilation applied to capture the boundary area. Some commercial and open-source segmentation software packages mentioned in these studies include: PMOD 3.3, MeVisLab©, and MIM Maestro.

3 Methods

Radiomics is an advanced, computer-based algorithm that extracts radiological features from medical images to help identify, diagnose, and predict patient response for numerous diseases. Explicit derivation of radiomic features are done using so-called handcrafted features, while implicit derivation is achieved using deep learning approaches. The general top-level design of the radiomic workflow involves four principle components: image acquisition, tumor segmentation, radiomic signature, and machine learning analysis. Each use case of the workflow is complex, and the application differs across institutions and research labs. Figure 2 gives an overview of the radiomic process from patient to predicted outcome.

3.1 Feature Extraction

Feature extraction involves computing quantitative parameters on the ROI. There are two over-arching methods of calculating features. The first method involves explicit direction from the researchers, duly named "handcrafted features". The second method uses deep learning to implicitly derive features from training on large datasets of images through the learning process of its network. Handcrafted features primarily are subdivided into three types of features based on shape, histogram, and texture. Figure 3 gives a top-level view of features and the two ways they are extracted.

3.1.1 Shape Features

Shape features seek to describe the geometrical characteristics of the ROI. They are computed at the slice level (2D) or from the entire ROI (3D). The main objective is to distinguish between smooth, round, and normal lesions from spiculated, elongated, and abnormal ones [17]. Common shape features are compactness, flatness, elongation, rectangular fit, spherical disproportion, sphericity, surface area, volume, and surface-to-volume ratio [17].
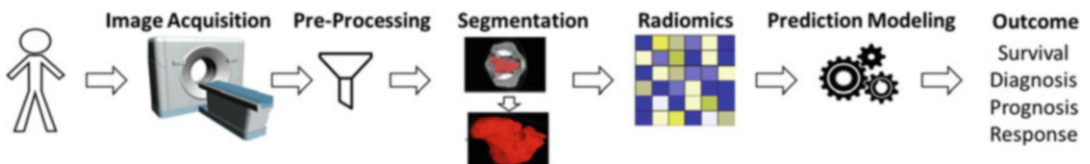
Fig. 2 Overview of the workflow of radiomic analysis from the patient cohort, image acquisition, preprocessing of the images, segmentation of tumors, feature extraction, postprocessing, and analysis of the radiomics by building and evaluating prediction models. The desired outcome is determined by the design of the study
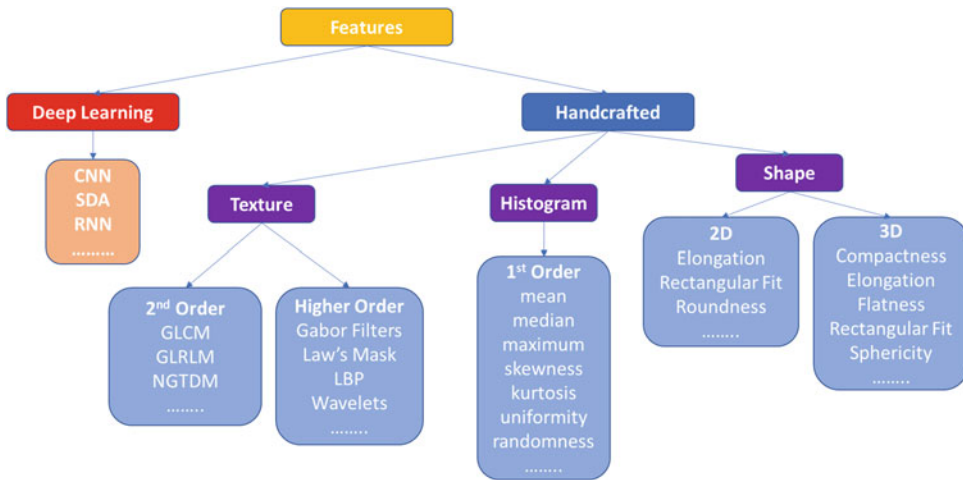
Fig. 3 Top-level view of the two different ways features are extracted from tumor segmentations. Deep learning implicitly derives features from the ROI while handcrafted features are explicitly derived by the researcher from the ROI

3.1.2   Histogram Features

Histogram features, also known as first order statistical features, represent surface texture and intensity concentration throughout the image. These are examples of histogram-based parameters: mean, median, maximum, minimum values of the voxel intensities on the image, skewness (asymmetry), kurtosis (flatness), uniformity, and randomness (entropy) [17].

3.1.3   Texture Features

The purpose of texture features is to quantify the variability of the grey-scale levels in the ROI. They provide a sense of the spatial assignment of the voxel intensities and therefore are able to assess intra-lesion heterogeneity, regarded as a concrete indication of poor prognosis and malignancy [21]. Grey Level Co-occurrence Matrices (GLCM), Grey Level Run-Length Matrices (GLRLM), and Neighborhood Grey-Tone Difference Matrices (NGTDM) are examples of second order statistical texture features [22–24]. Higher order statistical texture features incorporate filters or mathematical transforms to identify various types of patterns, reduce noise, or reveal sharp details of an image. Wavelets, Gabor filters, Laplacian transforms, fractal analysis, and Local Binary Patterns are examples of these types of features [25–28].

3.2   Postprocessing

Once the features are computed by the aforementioned methods, further processing needs to occur to ensure an optimal output (Fig. 4). Depending on the needs of the dataset, this processing may reduce redundancy or increase discrimination capability [29].
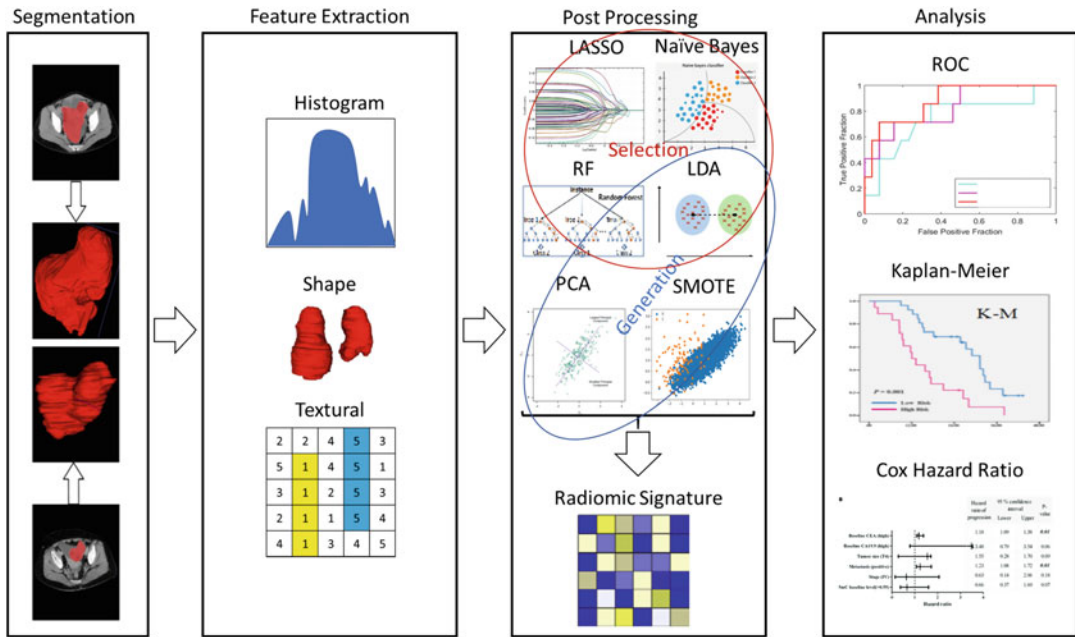
Fig. 4 Operations following the tumor segmentation. The feature extraction and postprocessing of these features create the radiomic signature. The two circular shapes denote examples of feature selection vs feature generation algorithms, with the LDA being enclosed in both to show its dual usage. The output analysis from the prediction modeling is shown by giving examples of an ROC curve, Kaplan-Meier survival curves, and the Cox Hazard ratio plots

3.2.1 Feature Selection

Several different methods of feature selection are used to reduce the number of features. First, duplicate values are removed from the feature list. Secondly, highly correlated features and groupings of highly correlated features are identified by a Pearson linear correlation coefficient (varies by study), and all but the single most significant feature are eliminated [30]. To further reduce the dimensionality, one or more of these techniques are used: least absolute shrinkage and selection operator (LASSO), recursive features elimination based on Naive Bayes (RFE-NB), selection by filter based on linear discriminant analysis (SBF-LDA), and recursive features elimination based on random forest (RFE-RF) [31–33]. The final pruning of features is done by using L1 regularization, Cox modeling, and/or Mann-Whitney U test [34, 35].

3.2.2 Feature Generation

Feature generation uses the features of one or more existing features to create new features. The purpose of this data augmentation is to incorporate new information to be utilized in model construction, hopefully causing it to obtain greater robustness and accuracy. Linear Discriminant Analysis (LDA), Principal Component Analysis (PCA), Synthetic Minority Oversampling Technique (SMOTE), and Multi-Dimensional Scaling (MDS) are some algorithms used for feature generation [36].

3.3 Prediction Modeling

The prediction models constructed are guided by the research question (Fig. 4). Once a classification or regression model is generated, a validation set of patients are evaluated, with the model making predictions. Examples of model outputs include prognosis, recurrence, survival, and therapeutic response. Studies analyzing recurrence or therapeutic response typically use supervised learning methods. Whereas studies analyzing prognosis or survival (disease-free survival (DFS), overall survival (OS), progression-free survival (PFS), and recurrence-free survival (RFS)) typically use unsupervised learning techniques. Common supervised learning algorithms used include LASSO-Cox, LDA, linear regression (LR), multivariate LR (Mult. LR), multivariable modeling (Mult. modeling), random forest (RF), and support vector machines (SVM). Unsupervised learning approaches include k-means clustering, Kaplan-Meier (KM) curves, nonnegative matrix factorization (NMF), and Cox proportion hazard regression.

3.4 Statistical Analysis

To compare groups and assess clinicopathological associations, methods such as the t test, χ^2 test, Fisher's test, or Mann-Whitney U test are used. All statistical tests are two-sided. Statistical significance is shown with a p-value <0.05. Accuracy (Acc), area under the receiver operating characteristic curve (AUC), sensitivity (Sn), and specificity (Sp) are used to evaluate the model performance for supervised learning outcomes like therapeutic response (Fig. 4). Kaplan-Meier curves generate survival curves and are compared using a log-rank test. The Cox proportional hazards model is used for univariate and multivariate analysis to analyze survival with a hazard ratio (HR).

3.5 Deep Learning

Deep learning is a recent advancement in artificial intelligence that incorporates many "deep" layers of computation to extract high-level features from raw input [37]. Survival, image segmentation, and classification are some of the many areas of interests within medical applications that deep learning has been useful. Deep learning algorithms increasingly are implemented in medical imaging and have great promise for research and as a complimentary tool in clinical radiology [38].

Unlike other machine learning algorithms that require hard-coded and handcrafted features generated by the user, deep learning algorithms derive generalized features from learning on a training set. The model constructed through training is tested on an unseen test set and gives predictions of the probability of a certain class (*see* **Note 11**). Convolutional neural networks (CNNs), stacked denoising autoencoders (SDAs), and deep recurrent neural networks (RNNs) are examples of different types of deep neural networks.

3.6 Example PET Radiomics Extraction and Selection

In an effort to give practical advice, the following describes the steps for extracting radiomic features from a PET scan using open source software tools:

1. A PET scan containing a mass in the left lung was obtained (*see* **Note 4**).

2. 3D Slicer was used to manually segment the image [39] (*see* **Notes 6** and **12**).

3. The image was normalized using the NormalizeImageFilter in the SimpleFilter module of 3D Slicer (*see* **Note 5**).

4. The PyRadiomics extension (SlicerRadiomics) that interfaces with 3D Slicer was used to perform feature extraction [40] (first order, GLDM, GLRLM, GLSZM, NGTDM, Shape, and Shape 2D) (*see* **Notes 1**, **3**, **7**, and **9**).

5. The features were stored in a .csv file for further analysis (*see* **Note 1**).

6. Remove duplicate values (*see* **Notes 2** and **8**).

7. Identify and remove highly correlated features using rank correlation with the corr function [30] (*see* **Notes 3** and **10**).

8. Reduce features using random forest with the oobPermuted-PredictorImportance function [32] (*see* **Notes 3** and **8**).

9. Prune final features using L1 regularization with the fitcecoc function [35] (*see* **Notes 3** and **10**).

3.7 Caveats and Future Opportunities for PET Radiomics

Over the past few decades, medical imaging has become an increasingly important fixture in diagnosing and managing cancer. The allure of radiomics is due to its ability to offer non-intrusive, quantitative, high-throughput image analysis and monitoring of tumors to aid in decision-making for clinicians [15]. PET imaging is used as a 3D substitute of tumor biology, with varying biological processes and features exposed depending on the radiotracer injected [15]. Radiomics are, therefore, an exciting method to use to extract biomarkers from the PET images. PET features have correlated with treatment outcomes for tumor entities in various studies [41–44].

Despite the promise and potential of PET radiomic applications, there remain many well-understood challenges and limitations that need to be addressed to create robust markers for clinical use. In many PET radiomic studies, the radiomic features extracted vary greatly, with little consistency in the type and number of features extracted, as well as the methodology adopted to choose the final feature set [14, 45]. Each institution uses different imaging parameters and machines to capture the medical images [14, 45]. Imaging parameter and reconstruction differences make

it difficult to replicate prior experiments. Regarding tumor regions of interest, radiologists must manually segment the images, which is time-consuming to complete. Auto segmentation and semi-automatic segmentation algorithms have been proposed to alleviate this issue, but require supervision and refinement by radiologists. Radiomic studies tend to be singular endeavors, due to the struggle in sharing imaging data, with no external validation of the developed models as a result [46]. Many patient cohorts are too small to conclusively declare that the models generated would perform similarly on larger datasets. Combining datasets from multiple institutions [47] would potentially be a solution to this problem. Unfortunately, the formation of these large datasets is often stymied by medical, industrial, and international politics.

To advance PET radiomic studies past preliminary results, standardization and an adherence to common practices has to occur [45]. Data scalability and multicenter data sharing would allow for deeper research and more robust results [47]. To quell concerns of unsecure data and breaches, one possible solution to safe and secure multicenter data sharing are federated learning techniques. Federated learning collaboratively trains algorithms without exchanging data, which addresses the problem of privacy and data governance [48]. Privatization algorithms are needed to encrypt and secure data from attackers and support federated learning as a trusted method of multicenter data sharing [49]. Furthermore, designing accurate, easily adoptable auto segmentation algorithms would help radiologists quickly analyze more data. Implementing multimodal data approaches integrating quantitative, clinical, histological, genomic, and radiomic data is essential in designing personalized treatments [46].

Proposals to standardize radiomic features and develop strong, adoptable practices for the medical machine learning community have been made based on research by a collaboration of research groups. The Image Biomarker Standardization Initiative (IBSI) is a joint effort between 25 research groups who validated consensus-based reference values for 169 radiomics features [50]. Their study showed the potential for calibration and verification of radiomics software.

Additionally, to curtail the sparse details shown in many studies, transparency in the design and implementation of prediction models is proposed as a solution. The Transparent Reporting of a multivariable prediction model for Individual Prognosis Or Diagnosis (TRIPOD) Initiative was crafted during a series of meetings between health care professionals, methodologists, and journal editors. TRIPOD is a set of recommended guidelines for the reporting of studies developing, validating, or updating a prediction model, whether for diagnostic or prognostic purposes [51].

4   Notes

Here we describe potential sources of error in a standard radiomics pipeline and offer suggestions on how to mitigate the effects of these errors in the design of radiomic studies.

1. In total, 107 features are extracted (if using wavelet-based features this number jumps to 851). The 3D Slicer approach is ideal as the software includes state-of-the-art implementations of segmentation tools. However, if there is a large batch of images, writing a script within 3D Slicer (or modifying the example script given on the PyRadiomics GitHub) would be the better approach. The example radiomic feature extraction script and core code for PyRadiomics can be found here: https://github.com/AIM-Harvard/pyradiomics. 3D Slicer uses PyRadiomics, which enables a smooth transition from code to GUI.

2. In this practical example done in MATLAB, the following steps detail feature selection and the methods used at each step. As stated previously, there are many different ways to implement these steps. The algorithms selected in this example are chosen due to familiarity and prior positive results on other datasets.

3. In a larger dataset, these steps may be repeated empirically to find the best features and reduce the number of features. An example MATLAB script that can be modified for this process is here: https://github.com/tlwilli3/exampleFeatureSelection.

4. Each medical center represented in these studies uses different scanning equipment, parameters, and reconstruction methods in the acquisition of their images. These differences make it difficult to combine efforts across institutions as the images are created and normalized to different standards.

5. Preprocessing is a crucial step in the workflow and may significantly affect the overall outcome, as numerous experiments have demonstrated [52].

6. Manual segmentation is currently the most utilized and reliable method of generating an ROI; however, it is very time-consuming, and many institutions do not have the resources to have every tumor region segmented by hand.

7. Although features originate from the aforementioned types, there is no standard across the field that determines how many features should be extracted. Consequentially, there are studies that extract hundreds of features, while others extract thousands. The extraction of too many features creates a greater risk of overfitting and possibly takes more time to reduce the dimensionality of the features.

8. It is important to utilize the algorithms that are most understood to the individual researcher to perform feature extraction, selection, and generation. Other algorithms can be familiarized in conjunction with the one(s) already implemented to increase the software toolbox and explore the nuances of other methods.

9. Software packages in Python (PyRadiomics) and MATLAB are used by some institutions to generate features. Many develop in-house programs to extract features. This also makes it difficult to standardize the methodology of extracting features across the field.

10. Statistical Product and Service Solutions (SPSS), and R software are the primary software packages used for statistical analysis in many studies. Additionally, some studies used them for feature reduction.

11. A drawback to extracting features from deep neural networks is that it is difficult to understand the decision-making of the model. There are visualization algorithms such as Grad-CAM that attempt to show the activations that the network uses to make predictions [53]. At times, these activated sections are inconsistent with logical results (e.g., activated sites shown on zeroed values outside of the tumor region).

12. The latest version of 3D Slicer should be installed for the best results.

References

1. Lambin P, Rios-Velazquez E, Leijenaar R et al (2012) Radiomics: extracting more information from medical images using advanced feature analysis. Eur J Cancer 48(4):441–446

2. Cook GJ, Azad G, Owczarczyk K et al (2018) Challenges and promises of PET radiomics. Int J Radiat Oncol Biol Phys 102(4):1083–1089

3. Wang H-M, Cheng N-M, Lee L-Y et al (2016) Heterogeneity of 18F-FDG PET combined with expression of EGFR may improve the prognostic stratification of advanced oropharyngeal carcinoma. Int J Cancer 138(3): 731–738

4. Gillies RJ, Kinahan PE, Hricak H (2016) Radiomics: images are more than pictures, they are data. Radiology 278(2):563–577

5. Parekh V, Jacobs MA (2016) Radiomics: a new application from established techniques. Expert Rev Precis Med Drug Dev 1(2): 207–226

6. Grootjans W, de Geus-Oei L-F, Troost EG et al (2015) PET in the management of locally advanced and metastatic NSCLC. Nat Rev Clin Oncol 12(7):395

7. Gupta T, Jain S, Agarwal JP et al (2010) Diagnostic performance of response assessment FDG-PET/CT in patients with head and neck squamous cell carcinoma treated with high-precision definitive (chemo) radiation. Radiother Oncol 97(2):194–199

8. Higgins KA, Hoang JK, Roach MC et al (2012) Analysis of pretreatment FDG-PET SUV parameters in head-and-neck cancer: tumor SUVmean has superior prognostic value. Int J Radiat Oncol Biol Phys 82(2): 548–553

9. Benz MR, Herrmann K, Walter F et al (2011) 18F-FDG PET/CT for monitoring treatment responses to the epidermal growth factor receptor inhibitor erlotinib. J Nucl Med 52(11):1684–1689

10. Takahashi R, Hirata H, Tachibana I et al (2012) Early [18F]fluorodeoxyglucose positron emission tomography at two days of gefitinib treatment predicts clinical outcome in patients with adenocarcinoma of the lung. Clin Cancer Res 18(1):220–228

11. van Gool MH, Aukema TS, Sinaasappel M et al (2016) Tumor heterogeneity on 18F-FDG-PET/CT for response monitoring in non-small cell lung cancer treated with erlotinib. J Thorac Dis 8(3):E200

12. Aukema TS, Kappers I, Olmos RAV et al (2010) Is 18F-FDG PET/CT useful for the early prediction of histopathologic response to neoadjuvant erlotinib in patients with non–small cell lung cancer? J Nucl Med 51(9): 1344–1348

13. Kumar V, Nath K, Berman CG et al (2013) Variance of standardized uptake values for FDG-PET/CT greater in clinical practice than under ideal study settings. Clin Nucl Med 38(3):175

14. Reuzé S, Schernberg A, Orlhac F et al (2018) Radiomics in nuclear medicine applied to radiation therapy: methods, pitfalls, and challenges. Int J Radiat Oncol Biol Phys 102(4): 1117–1142

15. Bogowicz M, Vuong D, Huellner MW et al (2019) CT radiomics and PET radiomics: ready for clinical implementation? Q J Nucl Med Mol Imaging 63:355–370

16. Lohmann P, Kocher M, Ruge MI et al (2010) PET/MRI radiomics in patients with brain metastases. Front Neurol 11:1

17. Rizzo S, Botta F, Raimondi S et al (2018) Radiomics: the facts and the challenges of image analysis. Eur Radiol Exp 2(1):1–8

18. van Velden FH, Kramer GM, Frings V et al (2016) Repeatability of radiomic features in non-small-cell lung cancer [18F]FDG-PET/CT studies: impact of reconstruction and delineation. Mol Imaging Biol 18(5):788–795

19. Traverso A, Wee L, Dekker A et al (2018) Repeatability and reproducibility of radiomic features: a systematic review. Int J Radiat Oncol Biol Phys 102(4):1143–1158

20. Bianconi F, Palumbo I, Spanu A et al (2020) PET/CT radiomics in lung cancer: an overview. Appl Sci 10(5):1718

21. O'Connor JP, Rose CJ, Waterton JC et al (2015) Imaging intratumor heterogeneity: role in therapy response, resistance, and clinical outcome. Clin Cancer Res 21(2):249–257

22. Haralick RM, Shanmugam K, Dinstein IH (1973) Textural features for image classification. IEEE Trans Syst Man Cybern 6:610–621

23. Galloway MM (1975) Texture analysis using gray level run lengths. Comput Graph Image Process 4:172–179

24. Amadasun M, King R (1989) Textural features corresponding to textural properties. IEEE Trans Syst Man Cybern 19(5):1264–1274

25. Dettori L, Semler L (2007) A comparison of wavelet, ridgelet, and curvelet-based texture classification algorithms in computed tomography. Comput Biol Med 37(4):486–498

26. Castellano G, Bonilha L, Li L et al (2004) Texture analysis of medical images. Clin Radiol 59(12):1061–1069

27. Pentland AP (1984) Fractal-based description of natural scenes. IEEE Trans Pattern Anal Mach Intell PAMI-6(6):661–674

28. Peyret R, Bouridane A, Khelifi F et al (2018) Automatic classification of colorectal and prostatic histologic tumor images using multiscale multispectral local binary pattern texture features and stacked generalization. Neurocomputing 275:83–93

29. Bianconi F, Fravolini ML, Palumbo I et al (2019) Shape and texture analysis of radiomic data for computer-assisted diagnosis and prognostication: an overview. In: International conference on design, simulation, manufacturing: the innovation exchange. Springer, pp 3–14

30. Ulrich EJ, Menda Y, Ponto LLB et al (2019) FLT PET radiomics for response prediction to chemoradiation therapy in head and neck squamous cell cancer. Tomography 5(1):161–169

31. Tibshirani R (1997) The LASSO method for variable selection in the Cox model. Stat Med 16(4):385–395

32. Delzell DAP, Peter T, Smith M et al (2019) Machine learning and feature selection methods for disease classification with application to lung cancer screening image data. Front Oncol 9:1393

33. Remeseiro B, Bolon-Canedo V (2019) A review of feature selection methods in medical applications. Comput Biol Med 112:103375

34. Mattonen SA, Davidzon GA, Benson J et al (2019) Bone marrow and tumor radiomics at 18F-FDG PET/CT: impact on outcome prediction in non-small cell lung cancer. Radiology 293(2):451–459

35. Huang S-y, Franc BL, Harnish RJ et al (2018) Exploration of PET and MRI radiomic features for decoding breast cancer phenotypes and prognosis. NPJ Breast Cancer 4(1):1–13

36. Van Der Heijden F, Duin RP, De Ridder D et al (2015) Classification, parameter estimation and state estimation: an engineering approach using MATLAB. Wiley

37. Deng L, Yu D (2014) Deep learning: methods and applications. Found Trends Signal Process 7(3–4):197–387

38. Kaissis G, Braren R (2019) Pancreatic cancer detection and characterization—state of the art

cross-sectional imaging and imaging data analysis. Transl Gastroenterol Hepatol 4:35

39. Fedorov A, Beichel R, Kalpathy-Cramer J et al (2012) 3D slicer as an image computing platform for the quantitative imaging network. Magn Reson Imaging 30(9):1323–1341

40. Van Griethuysen JJ, Fedorov A, Parmar C et al (2017) Computational radiomics system to decode the radiographic phenotype. Cancer Res 77(21):e104–e107

41. Kitajima K, Doi H, Kuribayashi K et al (2017) Prognostic value of pretreatment volume-based quantitative 18F-FDG PET/CT parameters in patients with malignant pleural mesothelioma. Eur J Radiol 86:176–183

42. Stolzenburg A, Lückerath K, Samnick S et al (2018) Prognostic value of [18F]FDG-PET/CT in multiple myeloma patients before and after allogeneic hematopoietic cell transplantation. Eur J Nucl Med Mol Imaging 45(10):1694–1704

43. Liu J, Dong M, Sun X et al (2016) Prognostic value of 18F-FDG PET/CT in surgical non-small cell lung cancer: a meta-analysis. PLoS One 11(1):e0146195

44. Albano D, Familiari D, Gentile R et al (2018) Clinical and prognostic value of 18F-FDG-PET/CT in restaging of pancreatic cancer. Nucl Med Commun 39(8):741–746

45. Lambin P, Leijenaar RT, Deist TM et al (2017) Radiomics: the bridge between medical imaging and personalized medicine. Nat Rev Clin Oncol 14(12):749–762

46. Crivelli P, Ledda RE, Parascandolo N et al (2018) A new challenge for radiologists: radiomics in breast cancer. Biomed Res Int 2018:6120703

47. Qiu Q, Duan J, Yin Y (2020) Radiomics in radiotherapy: applications and future challenges. Precis Radiat Oncol 4(1):29–33

48. Rieke N, Hancox J, Li W et al (2020) The future of digital health with federated learning. NPJ Digit Med 3(1):1–7

49. Kaissis GA, Makowski MR, Rückert D et al (2020) Secure, privacy-preserving and federated machine learning in medical imaging. Nat Mach Intell 2(6):305–311

50. Zwanenburg A, Vallières M, Abdalah MA et al (2020) The image biomarker standardization initiative: standardized quantitative radiomics for high-throughput image-based phenotyping. Radiology 295(2):328–338

51. Collins GS, Reitsma JB, Altman DG et al (2015) Transparent reporting of a multivariable prediction model for individual prognosis or diagnosis (TRIPOD) the TRIPOD statement. Circulation 131(2):211–219

52. Fave X, Zhang L, Yang J et al (2016) Impact of image preprocessing on the volume dependence and prognostic potential of radiomics features in non-small cell lung cancer. Transl Cancer Res 5(4):349–363

53. Selvaraju RR, Cogswell M, Das A et al (2017) Grad-CAM: visual explanations from deep networks via gradient-based localization. In: 2017 IEEE international conference on computer vision (ICCV). IEEE, pp 618–626

Chapter 24

Multiplexing Autoradiography

David Y. Lewis

Abstract

Autoradiography, the direct imaging of radioactive distribution in tissue sections, is a powerful technique that has several key advantages for the validation of PET radiotracers. Using autoradiography, we can localize radiotracer uptake to neighbours of cells, and when multiplexed with additional radiotracers, fluorescent probes, or in situ tissue analysis, autoradiography can help to characterize the mechanism of radiotracer uptake and assess functional heterogeneity in tissue. In this chapter, the author outlines the basic ex vivo autoradiography protocol and shows how it can be multiplexed using dual radionuclides ^{18}F and ^{14}C. They also highlight where autoradiography can be combined with other technologies to provide synergistic information for interrogating spatial biology.

Key words Autoradiography, Dual radionuclides, Carbon-14, Fluorine-18, 2-Deoxy-glucose, Tissue sections, PET, Spatial biology

1 Introduction

Autoradiography directly images radioactive distribution in tissue. The ex vivo method typically involves injecting a radioactive tracer into an animal, waiting for uptake, distribution, and sufficient clearance before culling and harvesting relevant tissues. These tissues are then frozen, cut in a cryostat into thin sections, and directly apposed to a photographic film or a storage phosphor screen, which, after a period of exposure, can be processed and analyzed to produce images and data of radiotracer distribution. The tissues sections can be further processed by histological techniques.

Key discoveries using autoradiography laid the foundation for the development of positron emission tomography (PET). In pioneering experiments, Louis Sokoloff developed a fully quantitative autoradiography technique by combining a glucose analogue, carbon-14 labelled 2-deoxy-D-glucose, with rapid arterial blood sampling and ex vivo cryosectioning to map local cerebral glucose utilization [1]. These early studies demonstrated the potential of autoradiography to quantify spatial biology and provided a

forerunner to clinical imaging with $[^{18}F]$2-fluoro-2-deoxy-glucose ($[^{18}F]$FDG). There have been major advances in PET technology over the last 40 years, and PET has been widely disseminated. However, there is still an important role for autoradiography, and three critical advantages make it an essential tool for all PET scientists.

First, due to positron range and noncollinearity, PET has a fundamental spatial resolution limit of around 1 mm. By close apposition of the imaging plate to tissue and direct measurement of the positron, rather than annihilation photons, autoradiography has a relatively high spatial resolution of around 50 μm for positron emitters. Due to reduced partial volume errors, autoradiography improves the identification and quantification of radiotracer uptake in small structures and improves assessment of PET radiotracer heterogeneity in tissue.

Second, with any PET radiotracer, there is ambiguity in localizing the signal to underlying anatomy and pathology. Radiotracer coregistration to macroscopic anatomy can be performed with dual modality scanners such as PET/CT or PET/MRI, but the precise structures or substructures may be unknown and the pathology cannot be determined using standard structural imaging. Performing autoradiography on tissue sections and correlating with histological staining (Fig. 1a), immunohistochemistry (IHC), immunofluorescence (IF; Fig. 1b, c), or in situ hybridization (ISH) defines the relationship between radiotracer uptake and cell pathology, protein and RNA distribution. This parallel multiplexing informs on radiotracer properties and underlying biology. With increasing availability of new technologies for interrogating spatial biology, multiplexing with autoradiography provides a more comprehensive interpretation of radiotracer distribution than PET imaging alone.

Third, simultaneous comparison of ^{11}C and ^{18}F tracers is not possible with PET as both radionuclides produce gamma emissions that are almost exclusively 511 keV. Multiple radiotracers can be directly compared with autoradiography if their radionuclides have sufficiently different properties, such as differences in radionuclide half-life or the energy of the emitted β particle. By substituting ^{14}C for ^{11}C or ^{3}H for ^{18}F, different radionuclides can be spatially deconvolved. For example, ^{18}F (β^+ emitter) and ^{14}C (β^- emitter) can be separated due to the large differences in their half-life (^{18}F: 109.7 min and ^{14}C: 5730 years) and β energy (^{18}F: 633 keV and ^{14}C: 156 keV). ^{18}F, when injected at 100-fold higher activity, produces an autoradiogram within 3 h with minimal ($<0.1\%$) ^{14}C contamination. When the ^{18}F is left to decay over 26 or more half-lives (<48 h) and the slides are reexposed to a clean imaging plate for several weeks, a ^{14}C image with no ^{18}F contamination is produced (Fig. 2b). Similar approaches can be used to separate radionuclides based on their β energy, for example, ^{3}H and ^{14}C have
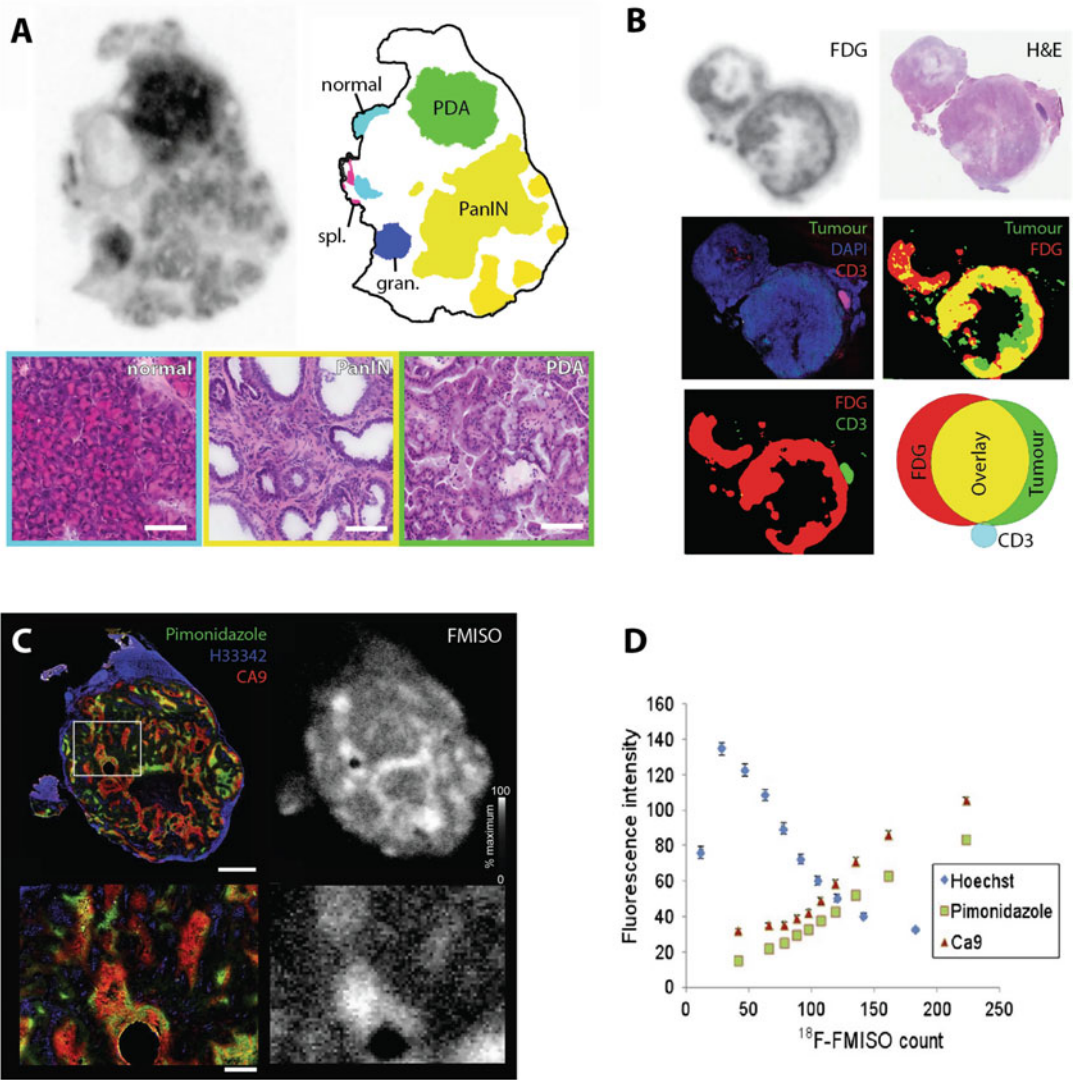
Fig. 1 Multiplexing autoradiography with pathology and immunofluorescence. (**a**) Comparison between [^{18}F] FDG uptake and pathology in the *Kras$^{G12D/+}$ Pdx1-Cre* mouse model of pancreatic ductal adenocarcinoma (PDAC) [2]. (**b**) Alignment and thresholding of [^{18}F]FDG autoradiography, mutant p53 and CD8 immunofluorescence in the *Kras$^{G12D/+}$ Trp53$^{R172H/+}$ Pdx1-Cre* mouse model of PDAC to identify high [^{18}F]FDG in tumour cell but not CD8-postive T cells. (**c**) Microregional comparison of [^{18}F]FMISO and, H33342 perfusion, pimonidazole and CA9 immunostaining. (**d**) Quantitative pixel-by-pixel comparison of [^{18}F]FMISO uptake and H33342 perfusion, pimonidazole and CA9 immunostaining [3].

sufficiently different penetration properties that can be separated using a thin film to block the titrated β but allow passage of the ^{14}C β particle [4]. These approaches can map biological activity in tissue using complementary radiotracers. Two radiotracers provide an additional dimension to single radiotracer autoradiography, for
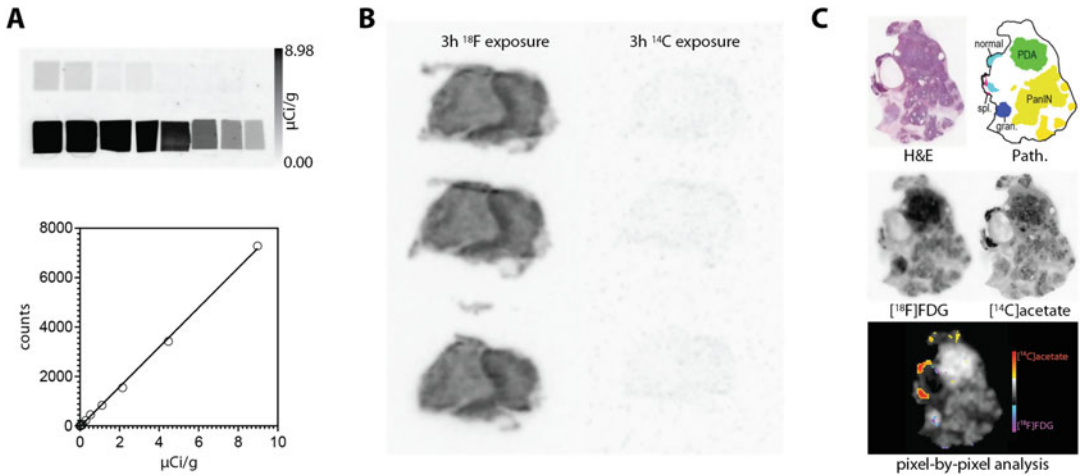
Fig. 2 Quantitative dual ^{18}F and ^{14}C radiotracer autoradiography. (**a**) ^{14}C standards and determination of linear dynamic range of storage phosphor screens. (**b**) A 3 h exposure of ^{18}F and ^{14}C produced an ^{18}F image with <0.1% ^{14}C contamination. After 48 h, a ^{14}C image can be produced in 3 h with zero ^{18}F contamination. (**c**) Dual autoradiography with [^{18}F]FDG and [^{14}C]acetate in the *Kras$^{G12D/+}$ Pdx1-Cre* mouse model of PDAC with pixel-by-pixel comparison of radiotracer uptake and comparison to pathology.

example, [^{14}C]acetate or [^{14}C]valine can be combined with [^{18}F] FDG to spatially compare fatty acid synthesis, protein synthesis, and glucose utilization, respectively (Fig. 2c) [5].

In this chapter, the process for obtaining high-resolution autoradiograms using dual radionuclides is described. The notes section at the end of the chapter provides additional information and describes where autoradiography can be further multiplexed with in situ tissue analysis.

2   Materials

2.1   Preparation of [^{14}C]substrate for Injection

1. ^{14}C-labelled radiochemical (e.g. [1-^{14}C]acetate, 2-[1-^{14}C] deoxy-D-glucose or similar), typically supplied as 37 MBq (1 mCi) in 1–5 mL of ethanol or aqueous solution.

2. Before injection, evaporate ethanol by drying overnight at room temperature or for 2 h under a stream of nitrogen gas in a laminar flow cabinet prior to resuspension in 0.9% NaCl saline solution (e.g., aliquot [^{14}C]acetate into 1.5 mL Eppendorf tubes each containing 3.7 MBq/100 μL). Final concentration will depend on desired radioactive dose (*see* **Note 1**).

3. Radioactive containment tray (460 × 260 mm or similar).

4. 1.5 mL Eppendorf tubes.

5. 0.9% NaCl saline solution in water (bag of 100 mL).

6. Eppendorf rack.

7. P200 and P1000 pipette and tips.

8. Laminar flow cabinet.

9. *Optional*: Nitrogen gas supply and distributor.

2.2 Animal Preparation

1. Tumor-bearing mice (e.g., subcutaneous xenografts, allografts orthotopic models, or genetically engineered mouse model of cancer) or nontumor-bearing control mice.

2. Absorbent paper.

3. Small animal heating chamber.

4. Small animal heating plate.

5. Isoflurane anesthetic machine with medical air or oxygen supply via central distribution system or by pressurized tank or oxygen generator.

6. 1 mL syringes.

7. 30G needles.

8. Heparinized saline: Inject 5 mL sodium heparin solution (5000 I.U.) into 100 mL bag of saline (0.9% NaCl).

9. Polyethylene tubing (0.28 mm Ø).

10. 0.9% NaCl saline solution in water (bag of 100 mL).

11. Heparin sodium 1000 I.U./mL solution for injection, 5 mL ampoule.

12. Needle forceps.

13. Zinc oxide tape (1.25 cm wide).

14. Infrared heat lamp.

15. Topical skin adhesive.

2.3 Preparation of [^{18}F]substrate for Injection

1. Fluorine-18 labelled radiotracer (e.g., [^{18}F]FDG).

2. 5 cm thick lead isotope workstation.

3. Contamination monitor (Geiger-Muller or plastic scintillator type).

4. Vial decapper.

5. Long (30 cm) forceps.

6. 0.9% NaCl saline solution in water (bag of 100 mL).

7. 1 mL syringes.

8. Luer tip syringe caps.

9. Dose calibrator.

2.4 Necropsy and Tissue Freezing

1. Dissection board and pins.

2. Dissection instruments: Fine surgical scissors, fine and blunt forceps.

3. Dry ice.

4. Insulated ice bucket.

5. 200 mL stainless-steel beaker.

6. Isopentane (2-methylbutane), approximately 50 mL.

7. Blunt forceps (approximately 8 cm).

8. 5 × 5 cm square pieces of aluminium foil (approximately).

9. Small grip seal bag.

10. Permanent marker.

11. Freezing embedding media (e.g., optimal cutting temperature (OCT) compound; *see* **Note 2**).

12. *Optional:* Cryomold, for small samples that require support during cryosectioning.

2.5 Cryotomy and Autoradiography

1. Cryostat.

2. Knife holder.

3. Knife blade.

4. Blunt forceps.

5. Specimen stage.

6. Tissue brushes.

7. Standard microscope slides (75 × 25 mm).

8. Slide rack.

9. Razor blade.

10. SR type storage phosphor screen (*see* **Note 3**).

11. Autoradiography cassette (same size as screen, usually 20 × 25 cm).

12. ^{14}C autoradiogram standards (range 0.074–322.26 kBq/g).

13. Storage phosphor scanner.

14. Image Eraser.

2.6 Image Analysis

1. Freely available ImageJ software (https://imagej.nih.gov/ij/) or specialized imaging software.

3 Methods

3.1 Preparation of [^{14}C]substrate for Injection

1. Handle ^{14}C over a containment tray to limit contamination in case of a spill.

2. Prepare final concentration appropriate to the ^{14}C retention of the substrate of interest; for example, prepare [1-^{14}C]acetate as 3.7 MBq/mL in 1 mL of saline or 2-[1-^{14}C]deoxy-D-glucose as 500 kBq/mL in 1 mL saline.

3. Aliquots (100 μL or 1 mL) can be stored at −20 °C for several months until ready for use. Working solutions can be stored at 4 °C. Check degradation rates and quality control methods from manufacturer before using old stock.

3.2 Animal Preparation (Adapted from [6])

1. Switch on the small animal heating chamber 30 min prior to use and set it to 37–40 °C.

2. Line the small animal heating chamber with absorbent paper.

3. Switch on the small animal heating plate and set to 37 °C.

4. Prepare anesthesia machine by filling the isoflurane vaporizer, switching on the medical air or oxygen delivery system, and lining the induction box with absorbent paper.

5. Prepare injection cannulas (one cannula per mouse) using two 30G needles and a 10–15 cm length of polyethylene tubing (0.28 mm Ø). Break one needle by holding with needle forceps and twisting repeatedly until the needle breaks at the plastic end. Place the blunt end of this broken needle into one end of the polyethylene tubing. Place the second 30G needle, needle end first, into the other end of the polyethylene tubing. Finally, ensuring that no bubbles are present, fill a 1 mL syringe with 400 μL heparinized saline and place into the plastic port of the 30G needle. Fill the cannula with heparinized saline by flushing through with about 100 μL.

6. Bring mice to the procedure room and place in heating chamber for 10–30 min prior to cannulation in order to dilate the tail vein.

7. Attach the induction chamber to the isoflurane vaporiser and switch on the gas supply. The isoflurane concentration should be set to 3% for induction of anesthesia.

8. Once the induction chamber is filled with isoflurane, remove one mouse from the heating box and place into the chamber.

9. When the mouse is fully anesthetised, change the flow from the induction box to the anesthetic nose cone. Remove the mouse from the chamber and place on its side on the small heating plate, ensuring the nose is placed fully in the anesthetic nose cone. Change the isofluorane concentration to 2% for cannulation.

10. The heat lamp can also be used to ensure the mouse is warm and tail veins are fully dilated prior to inserting the cannula. Care must be taken not to place to heat lamp too close to the tail to prevent damage to the tail.

11. Stroke the tail moving from a proximal to distal direction to further dilate the vein. Begin cannulation as distally as possible, allowing for more proximal attempts as necessary.

12. To insert the cannula, grasp the mouse tail using the thumb and index finger of the nondominant hand and bend the tail slightly so that the needle and the vein are parallel to each other. Then holding the needle of the cannula in the dominant hand with the bevel up, insert the needle into the lateral tail vein of the mouse and advance the needle a few millimetres. When the cannula is inserted into the vein, blood may flash back into the cannula. Correct placement can be checked by flushing a small amount of saline into the vein; there will be little resistance if the cannula is in the correct place. If there is resistance and the tail around the injection site blanches white, then the needle should be withdrawn and cannulation attempted again.

13. Once the cannula is inserted, secure it to the tail using topical skin adhesive.

14. The isoflurane can be reduced to 1% for maintenance.

15. Similarly, the mouse body temperature should be maintained by changing the set temperature on the animal heating plate as necessary.

3.3 Preparation of [^{18}F] and [^{14}C] substrates for Injection

1. Collect PET tracer directly from supplier or temporary storage location. As ^{18}F has a short half-life, there is a necessity to work quickly.

2. Prepare radioactive doses inside a 5 cm thick lead isotope workstation for radioprotection, and check regularly for personal and laboratory contamination using a contamination monitor.

3. Following ^{18}F collection, the exact concentration of activity in MBq/mL needs to be calculated. This can be achieved by placing 100 μL of the stock solution into the dose calibrator and measuring the total radioactivity. It is important to note the time of this measurement, so all calculations can be decay-corrected.

4. Estimate the time of radiotracer injection into the animal, and use the following equation to calculate the amount of activity at that time:

$$A(t) = A_0 \times e^{-\lambda t} \qquad (1)$$

$A(t)$—radioactive dose at time t (MBq); $A(0)$—original radioactive dose at time zero (MBq); t—elapsed time from initial radioactivity measurement (min); λ—decay constant:

$$\lambda = \frac{\ln(2)}{t_{1/2}} \qquad (2)$$

$t_{1/2}$—radioactive half-life (min); 109.7 min for ^{18}F.

5. From the measured stock activity, calculate the amount of activity required to make a stock solution of 185 MBq/mL at the time of injection; 37 MBq is required per animal (*see* **Note 4**).

6. Once the doses have been calculated for 37 MBq of injected activity, add the exact dose volume required into a 1 mL syringe and place a Luer tip syringe cap on the end (200 µL if using the 185 MBq/mL stock).

7. Using the dose calibrator, measure the syringe activity noting the time $A_1(t_1)$.

8. Prepare the [^{14}C]substrates by defrosting an aliquot and adding 200 µL into a 1 mL syringe, accounting for ~60 µL dead volume, and place a Luer tip syringe cap on the end. Handle ^{14}C over a containment tray to limit contamination in case of a spill.

3.4 Dual Radionuclide Injection

1. Remove the syringe containing heparinized saline from the end of the cannula; remove the luer tip cap from the ^{18}F syringe and place to one side. Place the ^{18}F syringe on the end of the cannula taking care not to introduce air into the injection volume.

2. Inject the mouse with radiotracer over a period of approximately 3 s.

3. Remove the ^{18}F syringe and replace the luer tip cap. Put the syringe containing heparinized saline back into the cannula again taking care not to introduce air, and flush the cannula with 50 µL of heparinized saline.

4. Measure the remaining radioactivity within the activity syringe noting the time, $A_2(t_2)$.

5. Remove the luer tip cap from the ^{14}C syringe, and place to one side. Place the ^{14}C syringe on the end of the cannula.

6. Inject the mouse with radiotracer over a period of about 3 s.

7. Remove the ^{14}C syringe and replace the luer tip cap. Put the syringe containing heparinized saline back into the cannula again taking care not to introduce air, and flush the cannula with 50 µL of heparinized saline.

8. The relative timing of the [^{14}C] and [^{18}F]substrates injections and animal cull is dependant of the kinetics of each tracer (*see* **Note 5**).

9. Florescent agents (e.g., Hoechst 33342; 3 mg/mL, intravenous at 5 mL/kg in saline), pimonidazole (12 mg/mL, injected intravenous at 5 mL/kg in saline), and bromodeoxyuridine (BrdU; 50 mg/kg, injected intraperitoneal at 5 mL/kg in saline) can also be injected, providing additional mapping

of perfusion, hypoxia, and proliferation, respectively. Hoechst 33342, pimonidazole, and BrdU can be injected 2, 60, and 90 min prior to animal cull, respectively.

10. The total volume of multiple injections should adhere to practical and welfare limits (*see* **Note 6**).

3.5 Necropsy and Tissue Freezing

1. Fill a 200 mL steel beaker with 50–100 mL of isopentane (2-methylbutane), and place on dry ice. Use a thermometer to check that temperate is less than -50 °C. If the isopentane is warm, place dry ice pellets directly into the liquid (*see* **Note 7**).

2. Cool a pair of blunt forceps by placing them, tips first, into dry ice. These chilled forceps will be used to remove the frozen tissue from the isopentane.

3. Cull the mouse by a method approved by local and national guidelines (usually cervical dislocation or CO_2 overdose).

4. Confirm euthanasia, splay, and pin the mouse to a dissection board, either in the supine or prone position, depending on the location of the tissue of interest. Remove relevant tissues by creating an incision and performing blunt dissection to expose and then remove the tissue of interest.

5. Carefully drop the piece of tissue directly into steel beaker containing isopentane on dry ice (Fig. 3a). When dropping the tissue, do not let it touch the sides of the beaker, as these will cause the tissue to freeze and adhere to the side causing damage. Small tissues (<200 mg) should be placed in a cryo-mold, which is then filled with optimal cutting temperature (OCT) compound prior to freezing.

6. Once the isopentane bubbling has ceased, usually about 30 s, remove the tissue using the chilled forceps and place it on a square 5×5 cm piece of aluminum foil on dry ice, allowing excess isopentane to drain and evaporate (Fig. 3b). Remove the tissue promptly as leaving in isopentane can cause the tissue block to fracture.

7. Wrap the tissue in aluminum foil and place inside a small grip seal bag with the experimental details written on the outside in permanent marker and return to dry ice.

8. Repeat for further tissues and animals.

9. The tissue needs to be cryosectioned rapidly (within 2 h) due to the short half-life of ^{18}F.

10. Transfer the tissue to the cryostat to warm to the appropriate cutting temperature. This may take up to 30 min (*see* **Note 8**).
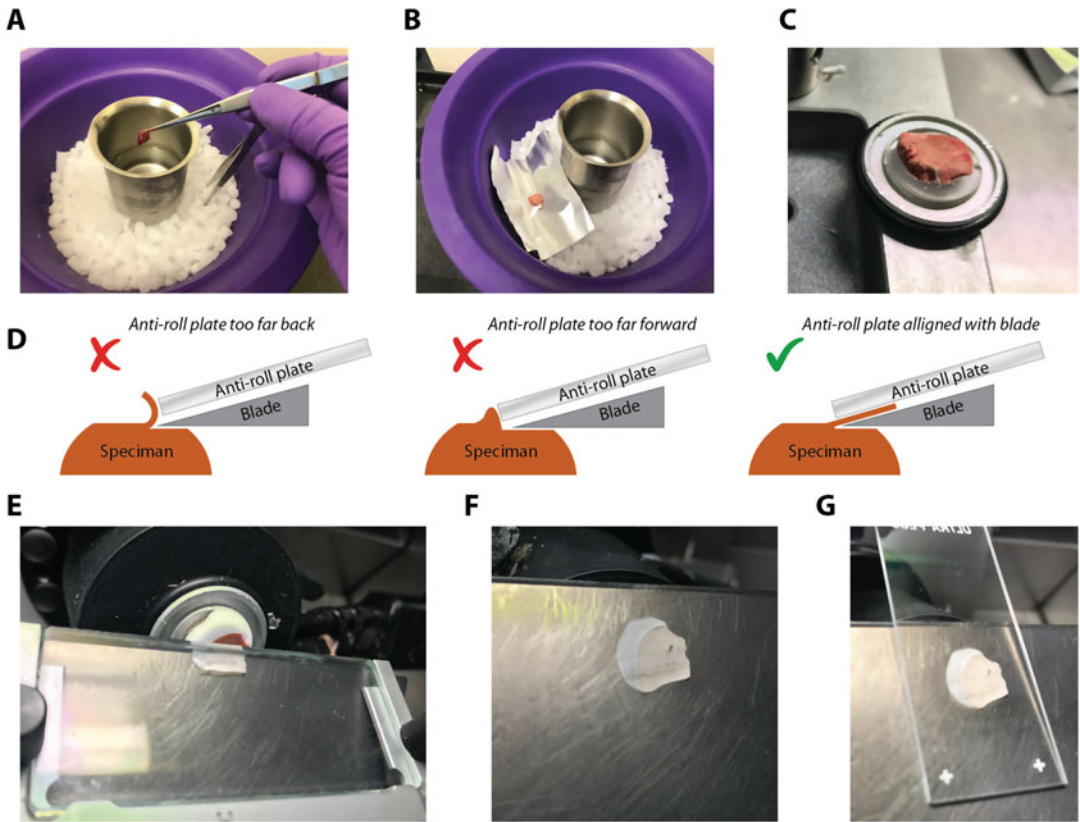
Fig. 3 Sample preparation and cryosectioning. Tissue samples are first frozen in isopentane on dry ice (**a**), before removal (**b**) and attaching to a specimen holder using optimal cutting temperature compound (**c**). Ensure that the anti-roll plate is aligned with the end of the knife blade (**d**). This alignment helps to achieve cleaner cuts between the anti-roll plate and knife holder (**e**). Sections should be flattened on the knife block (**f**) before thaw mounting onto a microscope slide (**g**)

3.6 Cryptomy and Autoradiography

1. Prior to use, place all cryosectioning tools (i.e., knives, brushes, specimen stage, blunt forceps, and razor blades) in the cryostat.

2. Remove tissue from grip seal bag and aluminum foil, setting it aside.

3. Place the specimen stage (i.e., chuck) on the quick-freezing shelf, and apply about 1 mL of OCT compound onto it.

4. Using chilled forceps, hold the tissue perpendicular to the desired cutting plane and place it onto the OCT/specimen stage. Allow the OCT to harden for approximately one minute (Fig. 3c).

5. Wait an additional 2 min until OCT is fully hardened, and then transfer the tissue block and stage to the specimen head. Secure into position by tightening the screw.

6. Insert a new knife blade into the knife holder and secure it. Be careful as the knife blades are very sharp and can cause serious injury if mishandled.

7. Ensure the knife holder, specimen holder, anti-roll system, and all clamps are securely locked into position. Any movement of the knife assembly or specimen except through the cutting wheel can disrupt accurate sectioning.

8. Advance the motorised stage towards the knife block using the course feed until it is almost touching the blade. Align the specimen at the blade's height as you advance the stage.

9. Set the trimming thickness to 30 μm, and manually advance the trimming wheel until it begins to cut the tissue. Continue turning the wheel and cutting sections until you reach the region of interest.

10. Change the section thickness to 10 μm (*see* **Note 9**).

11. Continue turning the cutting wheel until you are close to the region of interest. Lock the wheel and clear away section debris with a large brush.

12. Align the guide-plate (anti-roll system) angle towards the knife so that they both end at the same position (Fig. 3d).

13. Cut a section by turning the hand wheel in a steady, constant motion, observing the cut section emerging between the guide plate and the knife holder (Fig. 3e).

14. Use the tissue brushes to move the section into a central position on the knife holder and flatten any folds (Fig. 3f).

15. In a single motion, thaw mount the section onto a clean microscope slide by placing the slide directly onto the knife holder (Fig. 3g).

16. Place the section on a rack to air dry.

17. For additional analyses like immunohistochemistry, in situ hybridization, or mass spectrometry imaging, cut sections accordingly, air dry them rapidly and store them in a slide box within the cryostat to preserve molecular integrity.

18. Continue cutting and lifting sections until the tissue of interest is sufficiently sampled.

19. Place cut sections, once dry, in an autoradiography cassette, starting from the bottom left-hand corner, making sure all the slides are lying flat and uncovered (*see* **Note 10**).

20. To perform absolute quantification, include a slide with reference autoradiogram standards.

21. Position a recently erased storage phosphor screen against the slides with the phosphor side down in one smooth motion.

22. Firmly close the cassette, ensuringthat the clips are in place.

23. Place the cassette in a secure location for exposure, away from potential movement and exogenous sources of radioactivity.

24. Allow the screen to remain there for up to three half-lives (about 6 h) or overnight at room temperature.

25. Remove the screen and scan the latent image on a storage phosphor imager at 25 μm resolution using the red laser and open filter.

26. Erase the storage phosphor screen using the screen eraser.

27. Leave the slides for 48 h to allow for complete radioactive ^{18}F decay.

28. Erase the screen again and place it on the slides in a closed cassette in a secure location where the cassette will not be moved or exposed to exogenous radiation for an additional 30 days at room temperature (*see* **Note 3**).

29. After 30 days, scan the screen again on a Typhoon imager using the same settings as previously used.

30. Erase the phosphor screen prior to storage.

31. Stain the sections using standard haematoxylin and eosin (H&E; Fig. 1a, b).

32. For further analyses such as IHC, IF, ISH, or other spatial analysis methods like mass spectrometry imaging or spatial transcriptomics, use serial frozen sections.

3.7 Image Analysis

1. Begin by qualitatively comparing the resultant autoradiograms to the underlying pathology observed from H&E sections.

2. Mark out regions of distinct pathology on H&E sections in consultation with a pathologist (Fig. 1a) [2].

3. Compare areas of high and low radiotracer uptake to the pathology map and determine uptake in distinct pathological types using relative (ratiometric) or absolute quantification.

4. For relative quantification, calculate target-to-reference ratios using the following formula (*see* **Note 11**):

$$\text{TRR} = \frac{I_t - I_b}{I_r - I_b} \qquad (3)$$

TRR—target-to-reference ratio; I_t—image intensity in the target region; I_b—image intensity in the background region (outside the tissue); I_r—image intensity in the reference region.

5. Measure target-to-reference ratios for the same regions on both ^{14}C and ^{18}F autoradiograms. Determine the relative radiotracer uptake in distinct regions.

6. For absolute quantification, establish a linear calibration curve from the autoradiogram standards using the pixel intensity and known radioactive concentrations (Fig. 2a). Use this

calibration curve to convert the pixel intensity in the regions of interest into absolute radioactive concentration. Normalize the radioactive concentration to the injected activity and animal body to generate a "standardized uptake value" in a similar way to PET quantification.

7. For multiplex quantification, determine the overlap of autoradiograms and IF signals by thresholding. Create binary masks using an appropriate cut-off value to distinguish positive and negative signals.

8. Analyze the total area of tracer uptake or cell regions and spatially compare the different regions to determine the relative radiotracer uptake in various cell types within the tissue section using ImageJ. Visualise the results with a proportional Venn or Euler diagram representing the areas and overlaps (Fig. 1b) [7].

9. For microdistribution analysis, accurately coregister multiplex autoradiograms and IF images using commercially available programming software or freeware. Analyse each image at the pixel-by-pixel level to compare the radiotracer microdistribution to the underlying perfusion, hypoxia, or protein staining (Figs. 1b, d, and 2c) [3].

4   Notes

1. The radioactive dose required for ^{14}C substrates depends on the retention of the ^{14}C in the target tissue, where a substantial fraction is oxidised and/or excreted the injected dose may need to be increased. To increase signal-to-noise in ^{14}C autoradiography, the storage phosphor screen can be exposed for longer period; however, due to cosmic radiation (increasing background) and dark-decay of the stored image (decreasing signal), this reaches an effective plateau after a few months.

2. Do not use OCT compound as an embedding media when combining autoradiography tissues sections and mass spectrometry imaging, as OCT suppresses ionization particularly for matrix-assisted laser desorption/ionization mass spectrometry (MALDI). Improved hydrogel embedding matrices composed of hydroxypropyl methylcellulose and polyvinylpyrrolidone support multiplexing applications involved mass spectrometry imaging [8].

3. Phosphor screens from Cytiva (previously Amersham/GE Healthcare) are supplied as three main types: MS (multiple purpose standard), TR (tritium), and SR (super resolution). The SR screens are required for pixel resolutions of 50 µm or less and, except for tritium, are recommended for all autoradiography applications.

4. The required injected dose for ^{18}F is dependent on the number of experimental animals and the tissue processing time. For every additional 109.7 min (half-life of ^{18}F), the injected dose should be doubled to provide equivalent signal-to-noise in the resultant autoradiograms. Animals injected at different times but placed on the same imaging plate should be injected with the same stock solution and volume, not the same radioactive dose, this will ensure that the autoradiography intensities are comparable between animals.

5. The timing of $[^{14}$C] and $[^{18}$F]substrate injections should be determined for individual radiotracers. The optimal time to cull an animal and perform autoradiography is when there is maximal radionuclide retention in the metabolic pool of interest, while other pools are at a minimum. This may be different from the peak uptake time or even peak contrast time (peak target-to-background). For $[^{14}$C]acetate and $[^{18}$F]FDG, we have established optimal times of 90 min post injection, appropriate methods for determining the optimal uptake time are described [9].

6. The volume of individual intravenous boluses should not exceed the maximal dose volumes for a single injection in that species (i.e., 10 mL/kg for mice and 5 mL/kg for rats). The total volume of multiple injections should be the minimum required for formulation and accurate dosing, and the total volume and frequency should not exceed the equivalent maximal infusion rates (i.e., 0.04 mL/min for mice and 0.2 mL/min for rats) [10].

7. Rapid freezing of tissue for autoradiography is essential to preserve morphology and prevent the formation of ice crystal artifacts. Isopentane is preferable as a freezing media as it maintains effective contact with the tissue during freezing. Snap freezing warm tissue in liquid nitrogen produces a gas layer that slows down tissue freezing.

8. Set the cryostat to the appropriate temperature depending on the fat content of the tissue; −20 °C is a good starting point for most tissues. Cut tissues with higher fat content at lower temperature than those with higher water content.

9. The spatial resolution and signal in autoradiography is dependent on the tissue thickness. Thick sections will have poorer spatial resolution compared to thin sections, but thin sections will have less signal. In practice, 10 μm is a good compromise between these factors while preserving tissue morphology for pathology and other in situ tissue analysis. For comparable quantitative analysis, it is essential to cut all sections at the same thickness.

10. Some protocols suggest covering the slides with plastic film to prevent contamination of the storage phosphor screen. The SR screen has a protective cover to allow for gentle decontamination so further covering is not necessary, so additional covering should be avoided as it can degrade the signal and resolution.

11. The background region is an area on the slide that contains no tissue. Subtracting the background from the target and reference regions equates to removing the background noise on the imaging plate. The reference region however, should be located within the tissue image but distinct from the area of interest. This region can either be an area with no target uptake, such as the cerebellum for neuroreceptor radiotracers or an area of consistent update that is not affected by your intervention (e.g., liver for FDG studies if the liver is not altered in your experimental and control groups). The reference region normalizes the signal to varying tissue exposure, accounting for radiotracer injection, body weight, and the exposure time. This ratiometric method provides a simple semiquantitative parameter for tracer uptake.

References

1. Kennedy C, Des Rosiers MH, Sakurada O, Shinohara M, Reivich M, Jehle JW, Sokoloff L (1976) Metabolic mapping of the primary visual system of the monkey by means of the autoradiographic [^{14}C]deoxyglucose technique. Proc Natl Acad Sci U S A 73(11): 4230–4234. https://doi.org/10.1073/pnas.73.11.4230

2. Serrao EM, Kettunen MI, Rodrigues TB, Dzien P, Wright AJ, Gopinathan A, Gallagher FA, Lewis DY, Frese KK, Almeida J, Howat WJ, Tuveson DA, Brindle KM (2016) MRI with hyperpolarised [1-^{13}C]pyruvate detects advanced pancreatic preneoplasia prior to invasive disease in a mouse model. Gut 65(3): 465–475. https://doi.org/10.1136/gutjnl-2015-310114

3. Carlin S, Zhang H, Reese M, Ramos NN, Chen Q, Ricketts SA (2014) A comparison of the imaging characteristics and microregional distribution of 4 hypoxia PET tracers. J Nucl Med 55(3):515–521. https://doi.org/10.2967/jnumed.113.126615

4. Yamane Y, Ishide N, Kagaya Y, Takeyama D, Shiba N, Chida M, Sekiguchi Y, Nozaki T, Ido T, Shirato K (1995) Quantitative double-tracer autoradiography with tritium and carbon-14 using imaging plates: application to myocardial metabolic studies in rats. J Nucl Med 36(3):518–524

5. Kirikae M, Diksic M, Yamamoto YL (1989) Quantitative measurements of regional glucose utilization and rate of valine incorporation into proteins by double-tracer autoradiography in the rat brain tumor model. J Cereb Blood Flow Metab 9(1):87–95. https://doi.org/10.1038/jcbfm.1989.12

6. Witney TH, Lewis DY (2019) Imaging cancer metabolism with positron emission tomography (PET). Methods Mol Biol 1928:29–44. https://doi.org/10.1007/978-1-4939-9027-6_2

7. Irkle A, Vesey AT, Lewis DY, Skepper JN, Bird JL, Dweck MR, Joshi FR, Gallagher FA, Warburton EA, Bennett MR, Brindle KM, Newby DE, Rudd JH, Davenport AP (2015) Identifying active vascular microcalcification by (18)F-sodium fluoride positron emission tomography. Nat Commun 6:7495. https://doi.org/10.1038/ncomms8495

8. Dannhorn A, Kazanc E, Ling S, Nikula C, Karali E, Serra MP, Vorng JL, Inglese P, Maglennon G, Hamm G, Swales J, Strittmatter N, Barry ST, Sansom OJ, Poulogiannis G, Bunch J, Goodwin RJ, Takats Z (2020) Universal sample preparation unlocking multimodal molecular tissue imaging. Anal Chem 92(16):11080–11088. https://doi.org/10.1021/acs.analchem.0c00826

9. Lewis DY, Boren J, Shaw GL, Bielik R, Ramos-Montoya A, Larkin TJ, Martins CP, Neal DE, Soloviev D, Brindle KM (2014) Late imaging with [1-^{11}C]acetate improves detection of tumor fatty acid synthesis with PET. J Nucl Med 55(7):1144–1149. https://doi.org/10.2967/jnumed.113.134437

10. Workman P, Aboagye EO, Balkwill F, Balmain A, Bruder G, Chaplin DJ, Double JA, Everitt J, Farningham DA, Glennie MJ, Kelland LR, Robinson V, Stratford IJ, Tozer GM, Watson S, Wedge SR, Eccles SA, Committee of the National Cancer Research Institute (2010) Guidelines for the welfare and use of animals in cancer research. Br J Cancer 102(11):1555–1577. https://doi.org/10.1038/sj.bjc.6605642

Chapter 25

Kinetic Modeling Methods in Preclinical Positron Emission Tomography Imaging

Agne Knyzeliene, Robert Shaw, Viktoria Balogh, and Adriana A. S. Tavares

Abstract

There is an expanding number of applications for preclinical positron emission tomography (PET) imaging. Kinetic modeling of PET data provides rich multiparameter information on radiotracer uptake and binding in tissue from a single experiment. In this chapter, we provide a practical step-by-step protocol to assist with collection of PET data for kinetic modeling studies in rats and mice.

Key words PET imaging, Kinetic modeling, Preclinical, Quantification, Automatic blood sampling, Radiometabolite, Free fraction

1 Introduction

Kinetic modeling of positron emission tomography (PET) imaging data can be instrumental to assess and quantify radiotracer kinetics in vivo via mathematical models that describe the mechanism of radiotracer uptake and binding following their intravenous administration [1]. Although the mathematical principles of kinetic modeling are fundamentally translatable across species, radiotracer kinetics should be characterized for each preclinical species separately due to known physiological differences that can affect kinetic modeling outputs [2].

Typically, the radiotracer's biodistribution and kinetics in tissue can be quantified using dynamic PET imaging combined with arterial blood data collection, including arterial input function and plasma free fraction (f_P). In PET research, f_P describes the fraction of a radiotracer that is unbound to plasma proteins and is therefore available for binding to the target. A simple and practical method to measure f_P in rodent plasma is described in the methods section below.

Alternatively, input functions may be derived from the dynamic PET images themselves by drawing of volumes of interest (VOIs) in a large vessel or using the left ventricle blood pool, as opposed to invasive arterial blood collections. However, when using small animals such as mice and rats, this VOI-based approach can be quantitatively biased versus invasive blood collection owing to the small size of the animal. This small size can impact the VOI measurements due to PET recovery coefficient limits and may require additional corrections [3]. Although blood sampling over time during PET scanning is typically the gold standard for PET kinetic modeling, it also presents with its challenges due to the limited blood volume of mice and rats. Automated blood sampling equipment with peristaltic pumps allows for continuous sampling of the arterial blood through a cannula, followed by reinjection through the venous cannula, while preserving the balance of blood volumes due to low volumes sampled, which is beneficial in preclinical studies [2, 4]. An alternative to invasive kinetic models that require blood measurements includes reference tissue models that can be used when a region devoid of radiotracer binding is available [5] (*see* **Note 1**).

When investigating the kinetics of a radiotracer in vivo, it is essential to gain an understanding on how it is distributed and how it binds to its target in the body. The binding potential of radiotracers that reversibly bind to their target, or in vivo specific binding, can be calculated from the binding associated with the target of the radiotracer and its binding to nonspecific sites or components combined with the rest of the available or "free" radiotracer, that is, the binding potential relative to nondisplaceable binding (BP_{ND}) [6, 7]. Another important outcome measure from kinetic modeling analysis is the volume of distribution (V_T), which describes the distribution volume of total radiotracer uptake in tissue relative to total concentration of radiotracer in plasma.

V_T and BP_{ND} of a radiotracer in vivo can be calculated by using compartmental kinetic models or graphical methods of analysis. One-tissue compartment model is the simplest compartmental model and only derives two rate constants: the rate at which the tracer accumulates in the target tissue when transferred from plasma (K_1) and its retransfer from target tissue after being displaced or no longer bound (k_2) [6] (Fig. 1a). In this case, radiotracer kinetics exchange within the tissue compartments (free, nonspecific, and specific) cannot be distinguished. Alternatively, the two-tissue compartment model allows for the distinction between free and nonspecific (together nondisplaceable) compared to specifically bound radiotracer in the tissue compartment (Fig. 1b). In the two-tissue compartment model, there are two additional rate constants that are important: k_3 and k_4, which describe the two-way transfer of radiotracer from the first compartment of the tissue to the compartment that is specifically bound.

A   One-tissue compartment model
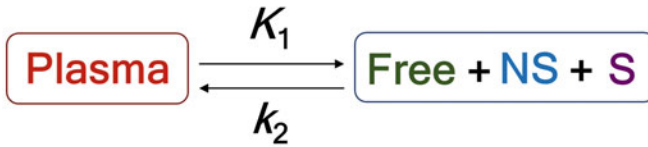
B   Two-tissue compartment model

Fig. 1 One- (**a**) and two-tissue compartment models (**b**) for kinetic modeling. NS—nonspecific binding, S—specific binding

Graphical analysis methods include the Patlak and Logan plots, which can be used for radiotracers that bind their targets irreversibly and reversibly, respectively, and provide an estimation of radiotracer uptake over time [8–10]. There are many more mathematical models available to describe PET radiotracer kinetics, and the selection of which model to use depends on various factors, including radiotracer target, organ physiology, and the research question.

The selection of best model to fit PET data can be further guided by mathematical and statistical analysis. For example, the Akaike Information Criteria (AIC) values are often used to describe the goodness of fit of kinetic models and assist with model choice. Other selection criteria can also be implemented, such as AIC unbiased, Schwartz Criterion, Model Selection Criterion, and F-test [11, 12]. It can also be useful to assess the fitting residuals plot and the estimate error per rate constant and outcome measures, in order to select the most appropriate model to quantify a given PET dataset.

This chapter provides a practical guide on how to conduct PET kinetic modeling experiments in small animals, namely, rats and mice.

2   Materials

Essential materials of each procedure required to conduct kinetic modeling experiments with mice and rats are listed below.

2.1 Anesthesia

1. Anesthetic machine.
2. Anesthetic gas cylinders (oxygen and nitrous oxide).
3. Isoflurane.
4. Perspex anesthetic box (induction chamber) and face mask (maintenance).
5. Heat mat.

2.2 Cannulations (Femoral Vessels)

1. Heat mat.
2. Rectal temperature probe.
3. Hair clippers.
4. Stereomicroscope.
5. Fine Forceps Angled 45°.
6. Fine Forceps Curved Serrated.
7. Clip Applicator Forceps Style.
8. Vannas Spring Scissors Straight 3 mm Cutting Edge.
9. Fine Scissors ToughCut 9 mm.
10. Bulldog Serrafine (Clamp) Straight 35 mm.
11. Dumont #5 45 Forceps Standard Dumoxel.
12. Disinfectant (Povidone-iodine).
13. Cotton buds.
14. 1 mL syringe.
15. Blunt tip needles for polyethylene catheters.
16. Heparinised saline (50 IU for rats and 20 IU for mice).
17. Polyethylene catheters for rats: PE-50 tubing, ID 0.58 mm OD 0.96 mm and 40 cm length.
18. Polyethylene catheters for mice: PE-10 tubing, ID 0.28 mm, OD 0.61 mm, and 35 cm length.
19. Ligature (Silk Suture Thread Size 4-0 and 6-0).
20. Surgical glue.

2.3 Cannulations (Tail Vein)

1. Heat mat.
2. Rectal temperature probe.
3. Cannula for rats: 26 G.
4. Cannula for mice: 27 G, 1/2″ Butterfly needle, polyurethane tubing (ID: 0.013″).
5. Surgical tape.
6. Surgical glue.

2.4 Blood Sampling (Manual)	1. Blood collection tubes. 2. Ice in polystyrene box. 3. Pipettes and tips. 4. Refrigerated centrifuge. 5. Gamma counter.

2.5   Blood Sampling (Automated)

1. Peristaltic pump, tubbing, t-connectors, straight connectors, and Luer connectors.
2. Shielded β-probe.
3. Data acquisition box with coincidence electronics.
4. TCP/IP connection to computer with data acquisition tools.

2.6   PET Image Acquisition and Reconstruction

1. PET scanner.
2. Animal monitoring system.

2.7   Radiometabolite Analysis

1. Refrigerated centrifuge.
2. Gamma counter.
3. High-performance liquid chromatography (HPLC) fitted with radiodetector.
4. Balance.
5. Tissue homogenizer.
6. Vortex mixer.
7. Ice in polystyrene box.
8. Pipettes and tips.
9. Conical centrifuge tubes large enough to hold organs.
10. Blood collection test tubes.
11. Gamma counter compatible tubes.
12. HPLC vials.
13. Distilled water.
14. Acetonitrile.

2.8   Plasma Free Fraction Analysis

1. Refrigerated centrifuge.
2. Gamma counter.
3. Ice in polystyrene box.
4. Pipettes and tips.
5. Blood collection test tubes.
6. Gamma counter compatible tubes.
7. Ultrafiltration units with regenerated cellulose membrane (30,000 NMWL).

3   Methods

3.1   Cannulation of Femoral Vessels

1. Place animal inside the induction chamber prefilled with anesthetic agent (2–2.5% isoflurane in 50/50 O_2/N_2O mixture).

2. Once the animal is unresponsive, remove it from the chamber and immediately transfer to the heat mat, and place its head inside a facemask with anesthetic set at 2–2.5% isoflurane in 50/50 O_2/N_2O mixture. Place the anesthetized animal on a heat mat to maintain temperature within physiological range.

3. Shave the targeted surgical area on the rodent hind limb to be cannulated. Then disinfect the surgical area, lift a small portion of the skin, and make a small incision between the abdominal body wall and the hind limb.

4. Introduce the scissors through the incision and expand incision by gently opening and closing the scissors several times, in order to cut through muscle and connective tissue and until sufficient space is created to gain access and clearly visualize the femoral artery and vein.

5. With the help of a surgical microscope and cotton buds, thoroughly clean the incision wound of any remaining connective tissue. This procedure can be done by extending the connective tissue repeatedly until it breaks and there is a clear access to the femoral artery and vein.

6. Slowly and gently introduce the tip of the forceps between the femoral artery and the vein. Then separate both vessels by opening and closing the forceps to fully disrupt the connective tissue between the femoral vein and artery.

7. Tie a ligature around the caudal end of the vein, and attach a bulldog clamp to the ligature loose ends.

8. Place a 4–6 mm vessel clamp onto the cranial end of the vein to stop blood flow. Care should be taken to avoid clamping any of the surrounding tissue. Place the clamp in such a position that it will allow for maximal length of the accessible vein.

9. Place two loose ligatures around the vein adjacent to the clamp.

10. Make a small incision using 2 mm Vannas spring micro fine scissors in the vein next to the tied ligature, leaving sufficient space to allow insertion of the cannula.

11. Using the tip of the bevel, gently lift the incision and guide the cannula into the vein until levelled with the vessel clamp. The opposite end of the cannula should be connected to a 1 mL syringe filled with 1 mL of heparinized saline.

12. Tie the cannula in place using the two loose ligatures. Two ligatures are required due to the pressure on the tubing from the blood flow.
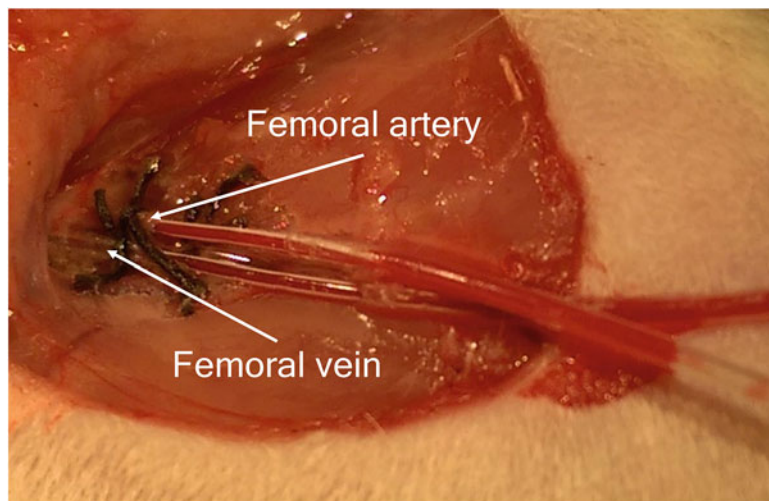
Fig. 2 An image showing unilateral cannulation of femoral artery and vein in a rat. The blood can be seen in the tubing, indicating successful cannulation

13. Remove the bulldog clamp from the end of the ligature and secure the loose ends around the cannula tubing.

14. Remove the vessel clamp. Pull back the plunger of the syringe attached to the catheter. At this point, venous blood should flow into the cannula (Fig. 2).

15. If performing unilateral cannulation, repeat **Steps 6–13** with the femoral artery. If performing bilateral cannulation, repeat **Steps 2–13** with the femoral artery on another hind limb.

16. For additional stability of the cannula inside blood vessel, apply a few drops of surgical glue on the cannula and blood vessel interface.

3.2 Manual Blood Sampling

1. Cannulate a femoral artery for blood sampling (*see* Subheading 3.1).

2. Cannulate a tail vein and secure the cannula in place with tape. This site will be used for the injection of the radiotracer.

3. Carefully but swiftly, transfer the animal onto a PET scanner bed and place the head inside the anesthetic facemask for continual general anesthesia.

4. Following radiotracer injection via tail vein, manually collect arterial blood samples (*mouse:* 10 μL; *rat:* 50 μL) in short time intervals up to 5 min post injection (10–30 s interval) and in longer time intervals after 5 min post injection until the end of a PET scan (e.g., for a 2 h PET scan, this would be 5, 10, 15, 20, 30, 60, 90, and 120 min). Place blood samples on ice and analyze immediately.
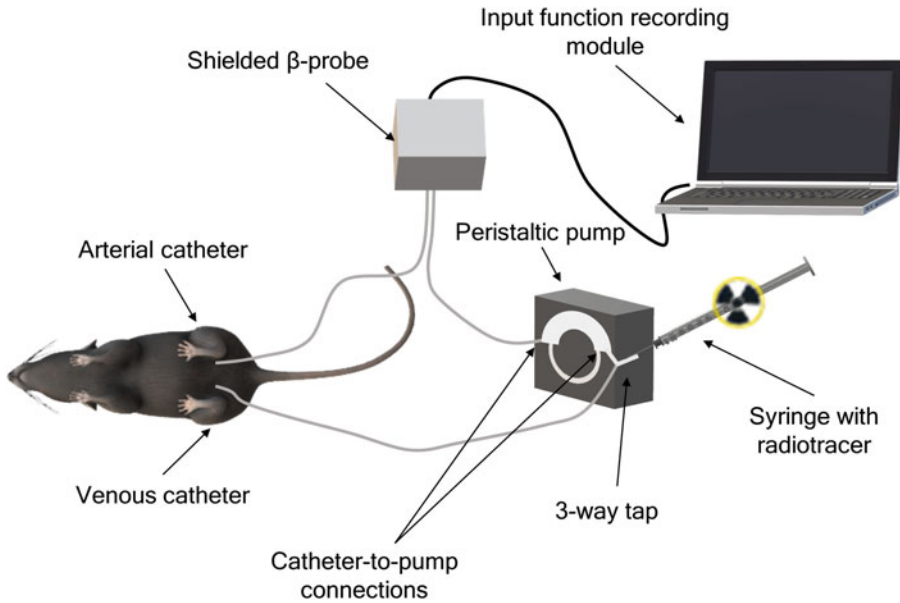
Fig. 3 Diagram showing the experimental setup required to generate an input function using the automated blood sampling system. In this example, bilateral femoral cannulation is shown

5. Measure the activity in the whole blood using a gamma counter. Then centrifuge whole blood at 2000 × *g* for 5 min at 4 °C to obtain plasma and measure its activity using a gamma counter.

3.3 Automated Blood Sampling System (ABSS) Method

1. Cannulate the femoral artery and vein (*see* Subheading 3.1). This procedure can be done either unilaterally (i.e., both artery and vein cannulated on the same leg) or bilaterally (i.e., arterial cannulation on one leg and venous on another; *see* Fig. 3). Whenever possible, the unilateral method is preferred, as it would provide the possibility for acquisition of invasive input function data from the same rodent in two different occasions using one limb per PET experiment.

2. Carefully transfer the animal onto a PET scanner bed, and place its head inside an anesthetic facemask for continued general anesthesia.

3. Prior to connecting the catheters to the ABSS (*see* **Note 2**), move the scanner bed to the position required for PET imaging. Then connect both arterial and venous catheters to ABSS.

4. Make sure that the flow rate of the peristaltic pump is set to mimic the blood flow of the species that is being imaged. Switch the pump on and inspect for any air bubbles in the tubing, obstructed blood flow, and leaks at the sites of cannulation (*see* **Notes 3–5**).

5. Inject the radiotracer using a 3-way tap connected to the venous catheter line attached to the ABSS, while the radioactive concentration in arterial blood coming out of arterial line is measured by the ABSS continuously throughout the duration of the PET scan (*see* **Note 6**).

3.4 Image-Derived Input Function (IDIF) and Reference Tissue Method

1. Cannulate a tail vein and secure the cannula in place with tape. This site will be used for injection of the radiotracer.

2. Carefully but swiftly, transfer the animal onto the PET scanner bed, and place the head inside the anesthetic cone for continued general anesthesia.

3.5 PET Image Acquisition and Reconstruction

1. Insert a rectal temperature probe and attach respiration rate recorder for monitoring of vital signs throughout PET scanning.

2. Inject the radiotracer and start PET data acquisition in a synchronous manner.

3. Acquire dynamic emission images using standard protocols.

4. If your PET system is coupled with a CT system, then perform CT scan for attenuation correction and anatomical information. If your PET system is coupled with a MRI system, perform an MRI scan for anatomical information and generation of pseudo-attenuation maps (*see* **Note 7**).

5. Reconstruct the PET image using standard protocols and upload it onto the kinetic modeling software.

3.6 Radiometabolite Corrections (See Note 8)

1. Induce and maintain general anesthesia.

2. Cannulate one femoral artery (*see* Subheading 3.1).

3. Cannulate a tail vein and secure the cannula in place with tape. This site will be used for injection of a radiotracer.

4. Insert a rectal temperature probe and attach respiration rate recorder for monitoring of vital signs.

5. Collect arterial blood samples (mouse: 7.2 mL/kg, rat: 6.4 mL/kg; or check local regulations) at 2, 5, 10, 20, 30, 60, 120 min post-radiotracer injection (minimum of $n = 3$ per time point).

6. Immediately, place blood samples on ice and measure radioactivity in the whole blood samples using a gamma counter.

7. Centrifuge whole blood at $2000 \times g$ for 5 min at 4 °C to separate whole blood from plasma.

8. Take a plasma sample and measure its radioactivity using a gamma counter (*see* **Note 9**).

9. Cull animals at 2, 5, 10, 20, 30, 60, 120 min post-radiotracer injection (minimum of $n = 3$ per time point).

10. Dissect the target organs, place them on ice, and process immediately.

11. Place each organ in a separate tube, add distilled water in a w/v fixed ratio, and homogenize samples using a tissue homogenizer.

12. Add 1.4 × volume of 100% acetonitrile to plasma and organ homogenate samples and vortex briefly.

13. Centrifuge the samples at 2000 × g for 4 min at 4 °C.

14. Collect the supernatant in an HPLC vial, and inject the sample onto HPLC with a fitted radiodetector (*see* **Notes 10–13**).

15. In order to quantify the parent fraction, integrate all peaks in the radiochromatogram and calculate percentage relative area occupied by parent (i.e., unmetabolised radiotracer) and metabolites (see examples of radio-HPLC chromatograms in Fig. 4).

16. For population-based input functions, correct the whole blood activity measurements obtained using a gamma counter for decay and sample volume. Then convert the gamma counter output units to kBq/mL and normalize the values to injected activity. Plot normalized whole blood kBq/mL values over time to generate a population-based input function (*see* **Note 14**).

17. To calculate plasma-to-whole blood ratios, correct the whole blood and plasma activity measurements obtained using a gamma counter for decay and sample volume. Then convert the gamma counter output units to kBq/mL, and normalize the values to injected activity. Divide plasma values by matched whole blood values and plot the ratio over time. Fit an exponential curve to estimate plasma-to-whole blood ratio at any given time point between 2 and 120 min post injection of the radiotracer.

3.7 Plasma-Free Fraction Corrections

1. Collect an arterial blood sample from a rodent (*mouse*: 7.2 mL/kg; *rat*: 6.4 mL/kg). Place the test tube with sample on ice, and process it immediately.

2. Add a few microliters of a radiotracer to the arterial blood sample, and stir very gently using a pipette tip or by gentle inversion of the blood in the test tube.

3. Centrifuge radiotracer-spiked whole blood sample at 2000 × g for 5 min at 4 °C to separate plasma.

4. Collect a plasma sample and measure the activity using a gamma counter. Note the plasma sample volume.

5. Load an ultrafiltration unit with the plasma sample and centrifuge at 3000 × g for 20 min at 20 °C. Carefully follow the ultrafiltration unit loading instructions provided by the manufacturer.
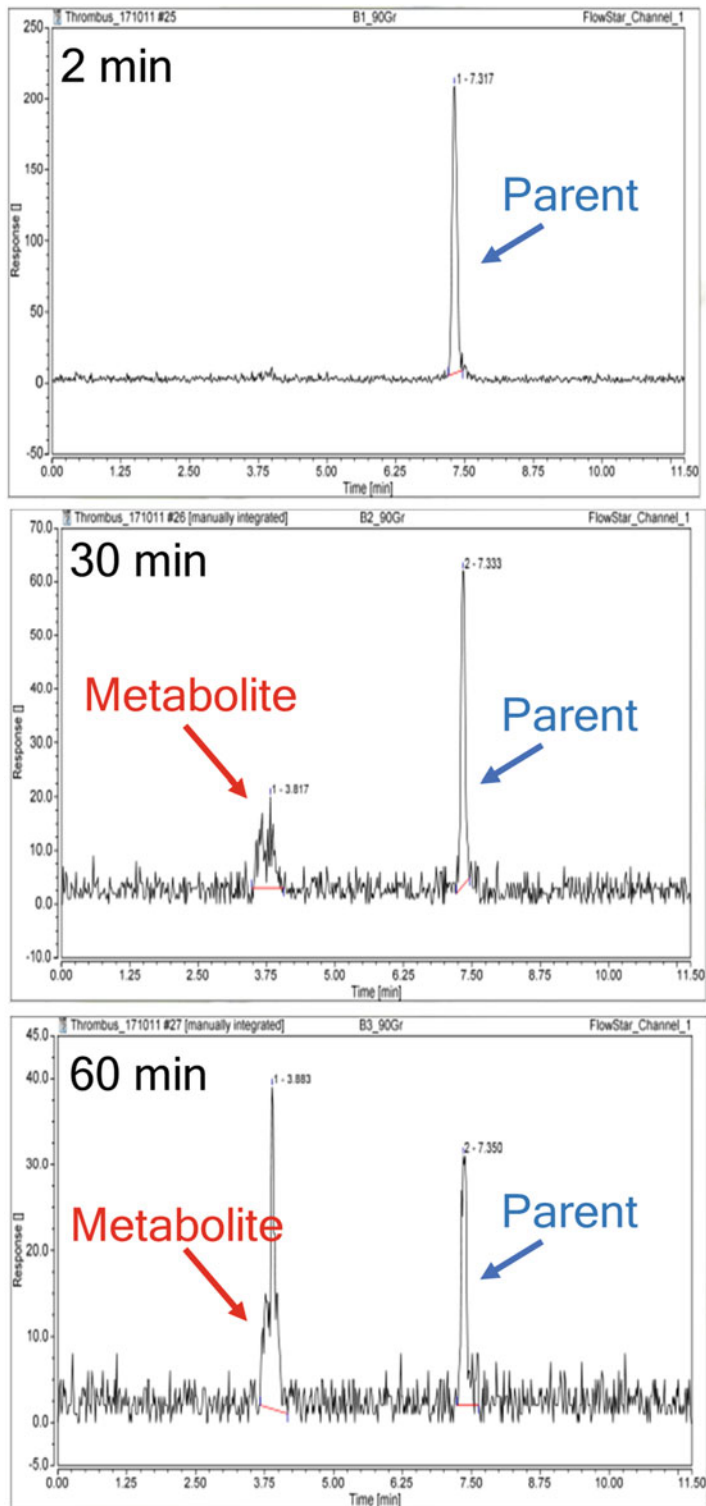
Fig. 4 Example of radiochromatograms obtained following injection of ^{18}F-ENC2015, a radiotracer developed for imaging thrombosis in vivo [13]. A gradual increase in plasma radiometabolite content at 30 and 60 min post ^{18}F-ECN2015 injection can be observed

6. Collect a sample of the ultrafiltrate (i.e., protein-free plasma fraction, or serum), and measure the activity using a gamma counter. Make sure to note the ultrafiltrate sample volume.

7. Correct the plasma and ultrafiltrate values for decay and normalise for sample volume. Then estimate the f_P by dividing ultrafiltrate values by plasma values.

3.8 Image Analysis and Kinetic Modeling

1. Delineate volumes of interest (VOIs) using PET/CT image analysis software, extract the information in each VOI as time activity curves, and upload it to kinetic modeling software.

2. To generate an IDIF, draw a small homogenous VOI (e.g., sphere with 1 mm radius) on a large vessel (e.g., vena cava or descending aorta) or in the left ventricle of the heart.

3. To analyze data using reference tissue methods, select a tissue region devoid of target expression to draw your VOI.

4. For invasive kinetic modeling, upload a whole blood curve, which has been generated using manual sampling (individual or population curve) or ABSS or has been image-derived. Apply plasma-to-whole blood ratio, plasma parent fraction, and plasma-free fraction corrections in order to generate an arterial input function.

5. For both invasive and noninvasive kinetic modeling, use model selection criteria (e.g., AIC) to choose models that best fit the collected data.

6. Extract the desirable kinetic constants, for example, K_1, k_2, k_3, k_4, K_1/k_2, k_3/k_4 (or BP_{ND}), or V_T. The choice of which model to use for quantification of PET data depends on the scientific question, the specific radiotracer used, and the biological process being imaged (*see* **Note 15**).

4 Notes

1. When planning PET experiments, a decision should be made whether kinetic modeling will be performed using an invasive arterial input function sampled manually or using ABSS, or whether an image-derived input function or reference tissue method will be sufficient for quantification of PET data. This decision will dictate the preparation procedures for acquisition of preclinical PET data using small animals and will depend on the radiotracer binding properties, target expression in tissue, and experimental research question (Fig. 5).

2. Make sure that the length and diameter of the catheters used for blood sampling from the arterial site into the detector and from the detector into the venous site are kept constant across all experiments.
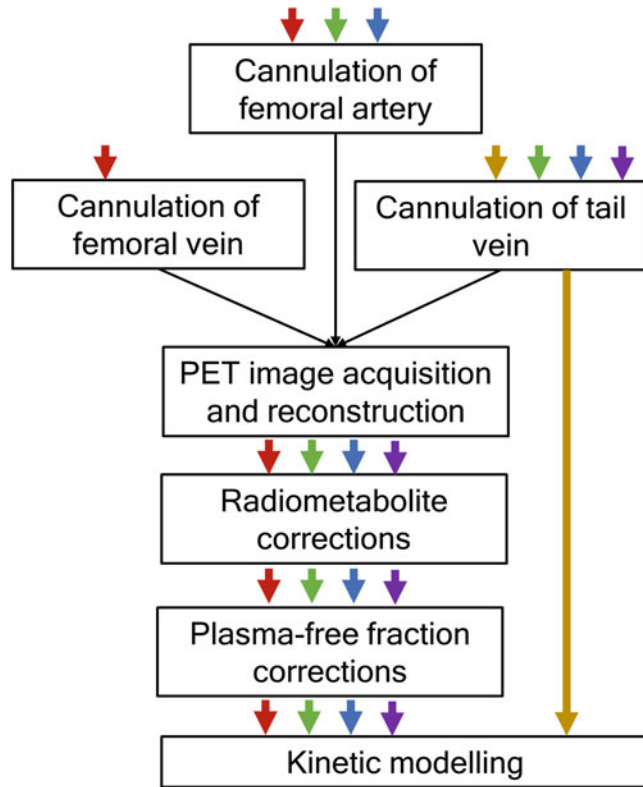
Fig. 5 Schematic flowchart illustrating the experimental workflow for performing kinetic modeling when using different input function methods or reference tissue models. Legend: red = ABSS, green = manual input function, blue = population average input function, purple = image derived input function, yellow = reference tissue model

3. If an air bubble appears inside the arterial catheter, immediately stop the peristaltic pump flow, disconnect the catheter from the ABSS, connect a syringe with heparinized saline to the catheter, and try removing the air bubble by drawing blood from the animal until it fills the entire catheter. Reattach the tubing to the ABSS and turn the pump on again.

4. If the blood flow is obstructed along the arterial catheter, immediately stop the peristaltic pump flow, disconnect the catheter from the ABSS, connect a syringe with heparinized saline to the catheter, and very gently inject a small amount of heparinized saline. This may help to dissolve a blood clot, which may sometimes form at the site of cannulation. Then try drawing the blood using the same preheparinized syringe. If the blood flow obstruction is resolved and blood is now following through the catheter, reconnect the tubing to the ABSS and turn on the pump.

5. If blood is leaking at the site of cannulation (small leaks only!), absorb the blood using a cotton bud and gently press it against the wound to stop the leak. Then a few more drops of surgical glue may be applied to reinforce stability of surgically placed catheters.

6. Make sure the ABSS detector and the acquisition software are switched on prior to injection of the radiotracer.

7. Do not move the animal between the molecular (PET) and the anatomical (CT or MRI) scans.

8. When performing PET kinetic modeling, one important correction to be made is a correction for parent in plasma, that is, a fraction of unmetabolized radiotracer in plasma throughout the period of imaging. Population-based input function and plasma-to-whole blood ratio can also be determined during radiometabolite experiments by measuring radioactive concentration in blood and plasma with a gamma counter. In Subheading 3.6, we provide an example of a method used for quantification of radiometabolites in mice and rats when using fluorine-18-labelled radiotracers and scanning the animals for up to 2 h. This protocol can be adapted for longer scanning intervals or different radioisotopes by adjusting the sampling frequency accordingly.

9. Whenever possible, use the same volumes for measuring whole blood and plasma in the well-type gamma counter to facilitate calculation of plasma-to-whole-blood ratio.

10. The sample volume for HPLC injection should be larger than that typical volumes used for analytical purposes (usually at least 100 μL). However, these volumes should not exceed the loading limits of the loop and HPLC column.

11. The use of semi-prep columns fitted with guard-columns, as opposed to analytical columns, is recommended to minimize pressure buildup from injection of nonfiltered denatured plasma and tissue samples.

12. Filtration of samples prior to HPLC can increase HPLC column longevity, but the filter selected for sample preprocessing must not retain the compound of interest on its membrane.

13. A standard solution (i.e., the radiotracer diluted in mobile phase) should be injected with every experiment.

14. When using the population-based input function for kinetic modeling, remember to correct it for injected dose in that particular animal.

15. When selecting the best kinetic model to describe collected PET data, use the following criteria: Lowest % standard error (%SE) when estimating kinetic constants; or Akaike information criteria (AIC): the lower the better; or Schwartz criterion

(SC): the lower the better; or Model selection criterion (MSC): the higher the better. An approach typically used when assessing best kinetic model includes comparing AIC between different models and selecting the one with lowest AIC. This typically, but not always, translates into the lowest %SE. When two models perform equally well, as per AIC, then the %SE could be used as second line criteria for model selection. Studies comparing pros and cons of different model selection criteria for dynamic PET studies have been published, including a recent detailed study by Golla et al. [12].

References

1. Kuntner C, Stout D (2014) Quantitative preclinical PET imaging: opportunities and challenges. Front Phys 2:12

2. Dupont P, Warwick J (2009) Kinetic modelling in small animal imaging with PET. Methods 48(2):98–103. https://doi.org/10.1016/j.ymeth.2009.03.008

3. Sanabria-Bohorquez SM, Maes A, Dupont P, Bormans G, de Groot T, Coimbra A, Eng W, Laethem T, De Lepeleire I, Gambale J, Vega JM, Burns HD (2003) Image-derived input function for [11C]flumazenil kinetic analysis in human brain. Mol Imaging Biol 5(2): 72–78. https://doi.org/10.1016/s1536-1632(03)00046-5

4. Wu HM, Sui G, Lee CC, Prins ML, Ladno W, Lin HD, Yu AS, Phelps ME, Huang SC (2007) In vivo quantitation of glucose metabolism in mice using small-animal PET and a microfluidic device. J Nucl Med 48(5):837–845. https://doi.org/10.2967/jnumed.106.038182

5. Zanderigo F, Ogden RT, Parsey RV (2013) Reference region approaches in PET: a comparative study on multiple radioligands. J Cereb Blood Flow Metab 33(6):888–897. https://doi.org/10.1038/jcbfm.2013.26

6. Innis RB, Cunningham VJ, Delforge J, Fujita M, Gjedde A, Gunn RN, Holden J, Houle S, Huang SC, Ichise M, Iida H, Ito H, Kimura Y, Koeppe RA, Knudsen GM, Knuuti J, Lammertsma AA, Laruelle M, Logan J, Maguire RP, Mintun MA, Morris ED, Parsey R, Price JC, Slifstein M, Sossi V, Suhara T, Votaw JR, Wong DF, Carson RE (2007) Consensus nomenclature for in vivo imaging of reversibly binding radioligands. J Cereb Blood Flow Metab 27(9):1533–1539. https://doi.org/10.1038/sj.jcbfm.9600493

7. Mintun MA, Raichle ME, Kilbourn MR, Wooten GF, Welch MJ (1984) A quantitative model for the in vivo assessment of drug binding sites with positron emission tomography. Ann Neurol 15(3):217–227. https://doi.org/10.1002/ana.410150302

8. Patlak CS, Blasberg RG (1985) Graphical evaluation of blood-to-brain transfer constants from multiple-time uptake data. Generalizations. J Cereb Blood Flow Metab 5(4): 584–590. https://doi.org/10.1038/jcbfm.1985.87

9. Patlak CS, Blasberg RG, Fenstermacher JD (1983) Graphical evaluation of blood-to-brain transfer constants from multiple-time uptake data. J Cereb Blood Flow Metab 3(1):1–7. https://doi.org/10.1038/jcbfm.1983.1

10. Logan J, Fowler JS, Volkow ND, Wolf AP, Dewey SL, Schlyer DJ, MacGregor RR, Hitzemann R, Bendriem B, Gatley SJ et al (1990) Graphical analysis of reversible radioligand binding from time-activity measurements applied to [N-11C-methyl]-(−)-cocaine PET studies in human subjects. J Cereb Blood Flow Metab 10(5):740–747. https://doi.org/10.1038/jcbfm.1990.127

11. Akaike H (1981) Likelihood of a model and information criteria. J Econ 16(1):3–14

12. Golla SSV, Adriaanse SM, Yaqub M, Windhorst AD, Lammertsma AA, van Berckel BNM, Boellaard R (2017) Model selection criteria for dynamic brain PET studies. EJNMMI Phys 4(1):30. https://doi.org/10.1186/s40658-017-0197-0

13. Andrews JPM, Portal C, Walton T, Macaskill MG, Hadoke PWF, Alcaide Corral C, Lucatelli C, Wilson S, Wilson I, MacNaught G, Dweck MR, Newby DE, Tavares AAS (2020) Non-invasive in vivo imaging of acute thrombosis: development of a novel factor XIIIa radiotracer. Eur Heart J Cardiovasc Imaging 21(6):673–682. https://doi.org/10.1093/ehjci/jez207

INDEX